



HAL
open science

Tridimensional Boundary Conditions for Direct and Large-Eddy Simulation of Turbulent Flows. Sub-Grid Scale Modeling for Near-Wall Region Turbulence

Guido Lodato

► **To cite this version:**

Guido Lodato. Tridimensional Boundary Conditions for Direct and Large-Eddy Simulation of Turbulent Flows. Sub-Grid Scale Modeling for Near-Wall Region Turbulence. Fluid mechanics [physics.class-ph]. INSA de Rouen, 2008. English. NNT : 2008ISAM0024 . tel-00585227

HAL Id: tel-00585227

<https://theses.hal.science/tel-00585227>

Submitted on 12 Apr 2011

HAL is a multi-disciplinary open access archive for the deposit and dissemination of scientific research documents, whether they are published or not. The documents may come from teaching and research institutions in France or abroad, or from public or private research centers.

L'archive ouverte pluridisciplinaire **HAL**, est destinée au dépôt et à la diffusion de documents scientifiques de niveau recherche, publiés ou non, émanant des établissements d'enseignement et de recherche français ou étrangers, des laboratoires publics ou privés.

THÈSE

Présentée par

GUIDO LODATO

Pour l'obtention du grade de

Docteur de l'Institut National des Sciences Appliquées de Rouen

<i>Discipline :</i>	Mécanique.
<i>Spécialité :</i>	Mécanique des Fluides.
<i>Formation Doctorale :</i>	Sciences Physiques, Mathématiques et de l'Information pour l'Ingénieur.
<i>Laboratoire d'Accueil :</i>	UMR-CNRS-6614-CORIA.

Conditions aux Limites Tridimensionnelles pour la Simulation Directe et aux Grandes Échelles des Écoulements Turbulents.

Modélisation de Sous-Maille pour la Turbulence en Région de Proche Paroi.

Le 5 Décembre 2008

Membres du Jury

Rapporteurs :

Franck NICOUD	Professeur, Université de Montpellier II
Pierre SAGAUT	Professeur, Université Pierre et Marie Curie – Paris

Examineurs :

Eric LAMBALLAIS	Professeur, Université de Poitiers
Denis VEYNANTE	Directeur de Recherche CNRS, École Centrale Paris

Directeurs de thèse :

Pascale DOMINGO	Chargée de Recherche CNRS, INSA de Rouen
Luc VERVISCH	Professeur, INSA de Rouen

A mia Moglie Monica

Résumé

Dans cette thèse, différentes problématiques liées à la simulation numérique des écoulements turbulents sont abordées. La simulation d'un jet d'air impactant sur une paroi adiabatique a mis en évidence toute une série de difficultés, notamment numériques et de modélisation de sous-maille de la turbulence, dans le cadre de la Simulation aux Grandes Échelles (SGE).

Deux points essentiels ont été abordés, le traitement des conditions aux limites et la modélisation fine des interactions de sous-maille pour représenter, au mieux, la région de proche paroi.

Pour ce qui concerne le problème des conditions aux limites, leur formulation caractéristique a été considérée et une nouvelle procédure 3D-NSCBC est proposée qui, en assurant une bonne reproduction du comportement physique attendu, induit très peu de perturbations à caractère numérique sur l'écoulement étudié. Inspirée par les Condition Limites Caractéristiques pour les équations de Navier-Stokes développées par Poinso and Lele [58], la procédure proposée dans ce travail autorise la prise en compte des termes de convection et des gradients de pression transverses afin de mieux reproduire la tridimensionnalité de l'écoulement sur les frontières. Les conditions limites précédemment développées supposaient en effet une direction de propagation orthogonale aux frontières du domaine de calcul, ce qui est rarement le cas dans les écoulements turbulents, où la rotation du fluide joue un rôle essentiel. La prise en compte des termes transverses mentionnés ci-dessus pose des difficultés additionnelles au niveau des angles et des coins du maillage de calcul, car les termes transverses des différentes surfaces connectées conduisent à un couplage des ondes caractéristiques voyageant le long des directions orthogonales. De plus, la présence des différentes typologies de frontières pose des problématiques ultérieures de stabilité numérique liées à l'imposition simultanée des variables d'écoulement interconnectées (*e.g.* la pression et la vitesse).

Une méthodologie pour résoudre ce couplage, avec les conditions de compatibilité nécessaires, a été développée et validée pour le cas de conditions aux limites d'entrée et de sortie subsoniques, ainsi que pour des parois adiabatiques.

La deuxième partie du manuscrit s'intéresse à la modélisation numérique de la turbulence dans le cadre de la Simulation des Grandes Échelles, en particulier lorsque l'écoulement est dominé par des interactions de proche paroi. En relation à la simulation d'un jet rond avec un nombre de Reynolds de 23000 et impactant sur une paroi plane, l'utilisation de modèles de sous-maille purement dissipatifs basés sur l'hypothèse de viscosité tourbillonnaire, a mis en évidence des difficultés pour reproduire correctement la dynamique de la turbulence à la paroi. Notamment, la dissipation excessive peut comporter le ralentissement des phénomènes d'évolution des structures tourbillonnaires et un développement insuffisant des petites structures induisant une durée de vie trop longue des grandes structures. Une surestimation des fluctuations de vitesse dans la région de proche paroi est le résultat global de ce mécanisme.

Pour mieux prendre en compte l'anisotropie du tenseur des contraintes de sous-maille, l'adoption d'un modèle structural est envisageable. Un modèle structural fondé sur l'hypothèse de similarité, initialement proposé par Bardina et al. [3], est développé pour des écoulements modérément compressibles. L'insuffisante dissipation d'un modèle de similarité pur conduit à adopter la formulation mixte, comprenant un terme de viscosité tourbillonnaire. Le comportement correct en région de proche paroi est assuré par l'adoption de la formulation WALE proposé par Nicoud and Ducros [53], au lieu d'utiliser une procédure dynamique. La reproduction du transfert local inverse d'énergie des petites échelles aux grandes, *i.e.* *backscatter*, par le modèle proposé s'est révélée être un ingrédient essentiel pour la représentation correcte du transport énergétique moyen dans la couche limite turbulente.

La dernière section de cette thèse présente des Simulations Numériques Directes de la combustion turbulente. Différents aspects ont été considérés. En premier lieu, une procédure pour prendre en compte les termes sources de la chimie dans les conditions aux limites 3D-NSCBC a été développée. Ces termes sont traités de la même façon que les termes transverses et sont, par conséquent, inclus dans les relations qui déterminent les variations temporelles des ondes entrantes. Les résultats obtenus par Simulation Numérique Directe d'une flamme jet prémélangée turbulente de type Bunsen pour des Reynolds de 2000 et 4500 ont été utilisés, entre autre, pour valider un modèle permettant de reconstruire la surface de flamme tridimensionnelle à partir de mesures expérimentales bidimensionnelles.

Table of Contents

Notation	ix
I Numerical Simulation of Turbulence	1
1 Introduction	3
1.1 Background and Motivations	4
1.2 Outline	5
2 Fundamentals	7
2.1 The Governing Equations	8
2.1.1 The Adimensional Formulation	10
2.2 Turbulent Flows	11
3 Mathematical Formulation	17
3.1 The SiTCom Solver	18
3.1.1 The Finite Volume Formulation	19
3.1.2 Convective Numerical Fluxes	22
3.1.3 The Artificial Dissipation Term for LES	23
3.1.4 Viscous Numerical Fluxes	24
3.1.5 Time Integration	26
3.2 Characteristic Boundary Conditions	27
3.2.1 3D Characteristics	32
3.2.2 Characteristic Formulation for Faces	34
3.2.3 Characteristic Formulation for Edges	43
3.2.4 Characteristic Formulation for Corners	51
3.2.5 Testing the 3D-NSCBC	59
3.3 Artificial Turbulence Injection	79
4 Large-Eddy Simulation	83
4.1 Different Levels of Detail	84
4.2 The Filtered Navier-Stokes Equations	85
4.2.1 A Weakly Compressible Approach	88
4.2.2 Near-Wall Scaling	91
4.3 Eddy-Viscosity Hypothesis	92
4.3.1 The Smagorinsky Model	94

4.3.2	The WALE Model	94
4.3.3	The Lagrangian Dynamic Smagorinsky Model	95
4.3.4	The Filtered Structure Function Model	98
4.4	Scale Similarity Hypothesis	100
4.4.1	The WALE-Similarity Model	101
4.4.2	The Explicit Filtering Procedure	105
4.5	Impinging Round-Jet Simulation	108
4.5.1	Boundary Conditions	109
4.5.2	Grid Spacing	110
4.5.3	The Measurement of Statistical Properties	112
4.5.4	$Re_D = 23000$ Test-Case (C1)	113
4.5.5	$Re_D = 23000$ Test-Case (C2)	117
4.5.6	$Re_D = 70000$ Test-Case (C3)	120
4.5.7	Energy Backscatter	124
4.5.8	Flow Field and Scalar Mixing	128
5	Direct Numerical Simulation	133
5.1	Accounting for the Whole Spectrum	134
5.2	The Description of Combustion	135
5.2.1	The Reaction Rate's Boundary Treatment	136
5.2.2	Proper Resolution and Scaling Parameters	138
5.3	Turbulent Bunsen Flame Simulation	142
5.3.1	$Re_D = 600$ Round-Jet Simulation (F1)	144
5.3.2	$Re_D = 2000$ Round-Jet Simulation (F2)	144
5.3.3	$Re_D = 4500$ Slot-Jet Simulation (F3)	147
6	Conclusions & Perspectives	153
6.1	Conclusions	154
6.2	Perspectives	156
II	Archival Publications	159
1	Journal of Computational Physics (2008), 227(10)	161
2	Physics of Fluids (2009), 21(3)	203
3	Proceedings of the Summer Program (2008), Stanford University	227
	Appendices	241
A	The Lagrangian Averaging Operation	243
	Bibliography	247
	Acknowledgments	255

List of Figures

2.1	Qualitative normalized longitudinal 1D spectrum	15
3.1	Schematic representation of the discrete control volume	19
3.2	Four-nodes stencil	21
3.3	Three-nodes boundary stencil	22
3.4	Artificial dissipation test	25
3.5	Impinging jet flow distortion test	30
3.6	Transverse terms influence on boundary accuracy	31
3.7	Schematic representation of a 3D computational domain	32
3.8	Incoming wave indices on 2D computational domain	48
3.9	Vortex test: pressure, velocity, vorticity and Q ($M = 0.00575$)	60
3.10	Vortex test: pressure, velocity, vorticity and Q ($M = 0.575$)	61
3.11	Vortex test: pressure, velocity, vorticity and Q ($M = 0.863$)	62
3.12	Vortex test: pressure contours at the boundary ($M = 0.00575$)	65
3.13	Vortex test: relative error in pressure	66
3.14	Vortex test with flow reversal: initial velocity profile	67
3.15	Vortex test with flow reversal: pressure and vorticity errors	68
3.16	Vortex test with flow reversal: pressure and vorticity errors	69
3.17	Vortex dipole test: pressure maps and velocity contours	70
3.18	Spherical pressure wave test: cutting planes and sampling locations	71
3.19	Spherical pressure wave test T3: pressure map and pressure contours	72
3.20	Spherical pressure wave: local displacement flow	73
3.21	Spherical pressure wave tests T1 and T2: pressure error	74
3.22	Spherical pressure wave test T3: pressure error	75
3.23	Spherical pressure wave test T3: pressure iso-surfaces	76
3.24	Free round-jet test	78
3.25	Free round-jet test: Q iso-contours	79
3.26	Inlet turbulence injection time history	81
4.1	Explicit filtering volume in two dimensions	107
4.2	Schematic of the impinging-jet configuration	108
4.3	Schematic representation of streamwise and radial velocities	112
4.4	$Re_D = 23000$ test C1: statistics	114
4.5	$Re_D = 23000$ test C1: sub-layer scaled statistics	115
4.6	$Re_D = 23000$ test C1: turbulent kinetic energy	116
4.7	$Re_D = 23000$ test C1: statistics (LDA comparison)	117

4.8	Average value of ν_{ratio} over horizontal planes	118
4.9	$Re_D = 23000$ tests C1 and C2: statistics	119
4.10	$Re_D = 23000$ tests C1 and C2: sub-layer scaled statistics	120
4.11	$Re_D = 70000$ test C3: statistics	121
4.12	$Re_D = 70000$ test C3: sub-layer scaled statistics	122
4.13	$Re_D = 70000$ test C3: turbulent kinetic energy	123
4.14	$Re_D = 23000$ test C1: instantaneous backscatter	124
4.15	$Re_D = 23000$ test C2: instantaneous backscatter	125
4.16	$Re_D = 23000$ and 70000 tests C1 and C3: ν_{ratio} maps	126
4.17	$Re_D = 23000$ test C2: ν_{ratio} map	127
4.18	$Re_D = 23000$ and 70000 tests C1 and C3: ν_{ratio} and Q^* maps	128
4.19	$Re_D = 23000$ test C2: statistics of scalar mixing	129
4.20	$Re_D = 23000$ and 70000 tests C1 and C3: 3D flow field	130
4.21	$Re_D = 23000$ and 70000 tests C1 and C3: passive scalar maps	131
5.1	1D laminar flame resolution test	139
5.2	Schematic representation of a conical laminar flame	140
5.3	Viscosity and density versus temperature	141
5.4	Turbulent Bunsen flame DNS: inlet profiles	143
5.5	$Re_D = 600$ test F1: progress variable map and Q^* iso-surfaces	145
5.6	$Re_D = 600$ test F1: progress variable iso-surfaces	146
5.7	$Re_D = 2000$ test F2: progress variable map and Q^* iso-surfaces	147
5.8	$Re_D = 2000$ test F2: progress variable iso-surfaces	148
5.9	$Re_D = 2000$ test F2: progress variable transversal maps	149
5.10	$Re_D = 4500$ test F3: progress variable and Q^* iso-surfaces	150
5.11	$Re_D = 4500$ test F3: progress variable and Q^* iso-surfaces (detail)	151
5.12	$Re_D = 4500$ test F3: progress variable transversal maps	152

List of Tables

3.1	Air properties	59
3.2	Convected vortices test-cases	64
4.1	LES typical mono-dimensional filters	86
4.2	Impinging round-jet simulations' parameters	110
5.1	Turbulent Bunsen flame DNS parameters	142

Notation

Roman symbols

Symbol	Definition
a	Speed of sound, $\sqrt{\gamma p/\rho}$
a_1, a_2	Computational cell's aspect ratios
A_i, B_i, C_i	Near-wall Taylor expansion coefficients
A_{ij}	Deviatoric part of the strain-rate tensor, $S_{ij} - \frac{1}{3}\delta_{ij}S_{kk}$
$\mathcal{AD}_{i+1/2}$	Artificial dissipation
B_{LL}	Longitudinal velocity correlation
c	Progress variable
c_p	Specific heat capacity at constant pressure
c_v	Specific heat capacity at constant volume
C	Courant-Friedrich-Lewis number
C_K	Kolmogorov constant
C_s	Smagorinsky model constant
C_v	Vortex strength
C_w	WALE model constant
$\mathbf{d}, \mathbf{e}, \mathbf{f}$	Characteristic vectors of convective terms along x_1, x_2, x_3
D	Diffusion coefficient; jet's diameter
\mathcal{D}	Diffusion vector in primitive variables' formulation
\mathbf{D}^i	Diffusion vector along i th direction
\mathcal{D}_i	SGS turbulent diffusion of kinetic energy along x_i
D_{LL}	Second-order longitudinal structure function
e	Total energy per unit mass (internal + kinetic)
e_I	Internal energy per unit mass
E_1	Longitudinal one-dimensional energy spectrum
$\mathcal{E}_L, \mathcal{E}_K$	LDSM: lagrangian averaged square errors
f_i	Body force per unit mass in tensor notation
f_{ti}	Turbulence injection frequency
F_2	Second-order structure function
$F_2^{(n)}$	Filtered second-order structure function (n times)
\mathbf{F}^i	Flux vector along i th direction
\mathcal{F}^i	Non-conservative Jacobian matrix, $\partial \mathbf{F}^i / \partial \mathbf{U}$
$\mathcal{FC}_i, \mathcal{FV}_i$	Discrete convective and viscous fluxes
\mathbf{g}	Velocity gradient tensor in vector notation
g_{ij}	Velocity gradient tensor

$G_\Delta, G_{k_c}^*$	Filter operator convolution kernel and transfer function
h	Grid spacing
H_L	Flame height
$HP^{(n)}$	Discrete Laplacian high-pass filter (n times)
$\mathcal{I}_{KH}, \mathcal{I}_{HH}$	LDSM: Lagrangian averages for the energy equation
$\mathcal{I}_{LM}, \mathcal{I}_{MM}$	LDSM: Lagrangian averages for the momentum equation
J_i	Diffusion flux in tensor notation
k	Turbulent kinetic energy
\mathbf{k}, k_i	Tridimensional wave-number (vector and tensor notation)
k_c	Filter cutoff wave-number
K	Pre-exponential factor in the Arrhenius relation
\mathcal{K}_i	LDSM: Modified Leonard terms for the energy equation
$\ell, \ell_R, \ell_u, \ell_v$	Characteristic length-scales
ℓ_0	Integral length-scale
ℓ_τ	Viscous length, ν/u_τ
$\mathcal{L}, \mathcal{M}, \mathcal{N}$	Wave amplitude time variations in vector notation
$\mathcal{L}_i, \mathcal{M}_i, \mathcal{N}_i$	Wave amplitude time variations in tensor notation
L_{ij}, C_{ij}, R_{ij}	Leonard decomposition terms
$\mathcal{L}_{ij}, \mathcal{C}_{ij}, \mathcal{R}_{ij}$	Modified Leonard decomposition terms
$L_k^{e_I}, C_k^{e_I}, R_k^{e_I}$	Leonard decomposition terms at vector level
$\mathcal{L}_k^{e_I}, \mathcal{C}_k^{e_I}, \mathcal{R}_k^{e_I}$	Modified Leonard decomposition terms at vector level
L_x, L_y, L_z	Computational domain's dimensions
Le	Lewis number, Pr/Sc
M	Mach number, u/a
M_0	Reference Mach number, $u_R/\sqrt{\gamma RT_R}$
$\mathcal{M}_{ij}, \mathcal{H}_j$	LDSM: kernel interactions between scales Δ and $\hat{\Delta}$
M_{sgs}	SGS Mach number, $[\tau_{kk}/(\gamma\bar{p})]^{1/2}$
M_{sgs}^*	Reduced SGS Mach number, $[R_{kk}/(\gamma\bar{p})]^{1/2}$
M_t	Turbulent Mach number, $\sqrt{2k}/a$
M_w	Molecular weight
n	Power law profile for turbulent pipe flow exponent
p	Thermodynamic pressure
p_R	Reference pressure, $\rho_R u_R^2$
\mathbf{P}	Conservative to primitive variables' Jacobian, $\partial\mathbf{U}/\partial\mathbf{u}$
Pr	Prandtl number, $\mu c_p/\lambda$
Pr_t	SGS Prandtl number, ν_t/κ_{sgs}
q_i, q_i^Z	Heat flux; SGS energy flux; SGS scalar flux
Q	Second invariant of velocity gradient tensor
Q_F	Heat released per unit mass of fuel
R	Gas constant, \mathcal{R}/M_w
\mathcal{R}	Universal gas constant
\mathfrak{R}	Runge-Kutta residual
R^*	Dimensionless gas constant, $1/(\gamma M_0^2)$
R_p	Characteristic dimension of the pressure pulse
R_v	Vortex radius

Re	Reynolds number, $\rho U \ell / \mu$
Re_0	Reference Reynolds number, $\rho_R u_R \ell_R / \mu_{\text{ref}}$
Re_{cr}	Critical Reynolds number
Re_D	Jet's Reynolds number, $\rho U_b D / \mu$
Re_G, Re_L	Flame Reynolds numbers, $S_L \ell_0 / \nu$ and $S_L \delta_L / \nu$
Re_t	Turbulent Reynolds number, $u' \ell_0 / \nu$
Re_λ	Taylor-scale based Reynolds number, $u' \lambda / \nu$
\mathbf{s}, \mathcal{S}	Conservative and primitive source terms vectors
s_{ij}	Symmetric part of the square of the velocity gradient tensor
S	Sutherland temperature
\mathbf{S}_i	Right eigenvectors matrix for \mathcal{F}^i
$\mathcal{S}, \mathcal{S}_i$	Control volume's frontier
S_{ij}	Strain-rate tensor
$\mathfrak{S}^k, \mathfrak{S}_i^k$	Characteristic source terms $\perp x_k$ (vector and tensor notation)
Sc	Schmidt number, $\mu / (\rho D)$
Sc_t	SGS Schmidt number, $\nu_t / \kappa_{\text{sgs}}^Z$
S_L	Laminar flame speed
t	Time
t_{ij}^{sgs}	SGS stress tensor (incompressible formulation)
t_R	Reference time, ℓ_R / u_R
T	Temperature; time-averaging characteristic time
T_{ref}	Reference temperature (Sutherland's Law)
$\mathcal{T}, \mathcal{T}_i$	Transverse terms (vector and tensor notation)
$\mathcal{T}_{ij}, \mathcal{Q}_j$	SGS stress tensor and heat flux at test filter level
$\mathfrak{T}^k, \mathfrak{T}_i^k$	Characteristic transverse terms $\perp x_k$ (vector and tensor notation)
$\mathfrak{T}_{\text{psd}}^k$	Pseudo-transverse terms, $\mathfrak{T}^k + \mathfrak{S}^k$
$\mathbb{T}_L, \mathbb{T}_K$	LDSM: characteristic times
\mathbf{u}, u_i	Velocity (vector and tensor notation)
u'	Fluctuating velocity scale, $k^{1/2}$
U	Typical velocity scale
\mathbf{U}, \mathbf{u}	Conservative and primitive variables (vector notation)
u_τ	Friction velocity, $\sqrt{\tau_w / \rho_w}$
v_η	Kolmogorov velocity-scale
$\mathcal{V}, \mathcal{V}_i$	Control volume
W	Lagrangian averaging weighting function
\mathbf{x}, x_i	Position vector (vector and tensor notation)
Y_F	Fuel mass fraction
Z	Passive scalar

Greek symbols

Symbol	Definition
α	Heat release parameter, $(T_b - T_0) / T_b$
α^*	Turbulence-flame interaction coefficient, Re_t / Re_G
$\alpha_1, \alpha_2, \beta_1, \beta_2$	Artificial dissipation coefficients
$\alpha_{ij}, \alpha_j, \beta_{ij}, \beta_j$	LDSM: Smagorinsky kernels

β	Zeldovitch number, $\alpha T_{Ac}/T_b$
β_{LL}	Dimensionless self-similar longitudinal structure function
β_t	Transverse relaxation coefficient
γ	Specific heat ration, c_p/c_v
Γ	Turbulence-flame scales ratio, ℓ_0/δ_L
δ	Vortex dipole spacing; pressure pulse amplitude
δ_{ij}	Kronecker delta
δ_L, δ_L^*	Flame thickness
$\Delta, \widehat{\Delta}$	Filter cutoff length
Δ_{eq}	Equivalent filter cutoff length, $(\Delta_1\Delta_2\Delta_3)^{1/3}$
$\Delta p, \Delta u_i$	p, u_i differences from target values
$\Delta t_{\mathcal{I}}, \Delta t_{\mathcal{V}}$	Inviscid and viscous time-steps
$\Delta T, \Delta Z$	T, Z differences from target values
Δx	Grid spacing for mono-dimensional uniform mesh
$\epsilon_i^{(2)}, \epsilon_i^{(4)}, \epsilon_i^{\mathcal{O}4}$	Artificial dissipation factors
ϵ_{ijk}	Levi-Civita symbol
$\bar{\epsilon}$	Average rate of energy dissipation
ϵ_{glb}	Global pressure error
$\epsilon_{ij}^L, \epsilon_j^K$	LDSM: local errors
ϵ_r	Relative error
ϵ_ω	Global vorticity error
η	Kolmogorov length-scale
η_1, \dots, η_6	Subsonic non-reflecting inflow relaxation coefficients
θ^*	Flame semi-aperture angle
θ_L, θ_K	LDSM: characteristic times' coefficients
ϑ	Macrotemperature
ϑ^*	Reduced macrotemperature
$\kappa_{sgs}, \kappa_{sgs}^Z$	SGS thermal and scalar diffusivities
\varkappa	$\gamma - 1$
λ	Thermal conductivity; Taylor micro-scale
$\lambda_1, \dots, \lambda_6$	Characteristic waves' propagation velocities along x_1
$\lambda_{i+1/2}$	Artificial dissipation scaling factor
Λ^i	Eigenvalues' diagonal matrix of \mathcal{F}^i
μ	Dynamic viscosity
μ_1, \dots, μ_6	Characteristic waves' propagation velocities along x_2
μ_{eff}	Effective dynamic viscosity
μ_{ref}	Dynamic viscosity at reference temperature T_{ref}
μ_R	Reference dynamic viscosity, $\rho_R u_R \ell_R$
ν	Kinematic viscosity, μ/ρ
ν_1, \dots, ν_6	Characteristic waves' propagation velocities along x_3
ν_{ratio}	Normalized SGS energy transfer coefficient
ν_t	Eddy-viscosity
ϖ	Macropressure
ϖ^*	Reduced macropressure
Π	Energy flux per unit mass down the cascade process

ρ	Mass density
σ	Subsonic non-reflecting outflow relaxation coefficient
σ_{ij}	Total stress tensor
ς	Characteristic sign switching function
τ_{ij}	Viscous stress tensor; SGS stress tensor
τ_w	Surface shear stress
φ_1	Dimensionless self-similar longitudinal 1D spectrum
Ψ	Stream function
Ψ_i	Pressure sensor
$\boldsymbol{\omega}, \omega_i$	Vorticity (vector and tensor notation)
$\dot{\omega}_c, \dot{\omega}_e, \dot{\omega}_F$	Chemical source terms
ω_Ψ	Pressure sensor's TVD, JST weighting coefficient

Subscripts

Symbol	Definition
Ac	Activation
b	Bulk; burnt
cl	Centerline value
ex	Exact
in	Incoming
$L2$	$L2$ -norm
max	Maximum
min	Minimum
n	Normal component
r	Radial component
R	Normalization reference quantity
ref	Reference value
rnd	Random
s	Streamwise component
sgs	Sub-Grid Scale
w	Wall (surface) value
ϕ	Azimuthal or tangential component
∞	Freestream or far field value

Superscripts

Symbol	Definition
d	Deviatoric part
max	Maximum
min	Minimum
s	Smagorinsky
w	WALE
wsm	WALE-Similarity Model
*	Fourier transformed quantity
*	Dimensionless or normalized quantity

+	Sub-layer scaled value
'	SGS value, $\varphi - \bar{\varphi}$ or $\varphi - \tilde{\varphi}$
//	Fluctuating value, $\varphi - \langle \varphi \rangle$
te	Experimentally measured fluctuating value

Special operators

Symbol	Definition
$\bar{\varphi}$	Filtering
$\tilde{\varphi}$	Favre-filtering, $\overline{\rho\varphi}/\bar{\rho}$
$\langle \varphi \rangle$	Test filtering
$\widehat{\varphi}$	Favre-filtering at test level, $\widehat{\rho\varphi}/\widehat{\rho}$
$\langle \varphi \rangle$	Statistical averaging
$\hat{\varphi}$	Volume averaging

Acronyms

Symbol	Definition
CFD	Computational Fluid Dynamics
DNS	Direct Numerical Simulation
FD	Finite Difference
FSF	Filtered Structure Function
FV	Finite Volume
HWA	Hot-Wire Anemometry
LDA	Laser-Doppler Anemometry
LDSM	Lagrangian Dynamic Smagorinsky Model
LES	Large-Eddy Simulation
NS	Navier-Stokes equations
NSCBC	Navier-Stokes Characteristic Boundary Conditions
3D-NSCBC	Tridimensional NSCBC
PIV	Particle Image Velocimetry
RANS	Reynolds Averaged Navier-Stokes
r.m.s.	Root Mean Square
RNG	Random Number Generator
SGS	Sub-Grid Scale
WALE	Wall-Adapting Local Eddy-viscosity model
WSM	WALE-Similarity Model

Part I

Numerical Simulation of Turbulence

Introduction

The statement that turbulence remains an unsolved problem can hardly be debated. Yet, there is no consensus on how the problem of turbulence should be formulated. Half a century after Kolmogorov's work on the statistical theory of fully developed turbulence, we still wonder how his work can be reconciled with Leonardo's half a millennium old drawings of eddy motion in the study for the elimination of rapids in the river Arno. Here, I shall not even attempt to face this challenge.

U. Frisch, 1991

Contents

1.1	Background and Motivations	4
1.2	Outline	5

Ce 1^{er} Chapitre présente un résumé synthétique des principaux aspects de la simulation numérique appliquée à la Mécanique des Fluides. L'importance que la modélisation de la turbulence revêt dans la représentation numérique des écoulements est examinée.

Les trois principales techniques de simulation de la turbulence, que sont la Simulation Directe, la Simulation aux Grandes Échelles et la Simulation des Équations de Navier-Stokes Moyennées, sont brièvement présentées, et notamment leur niveau de détail dans la représentation du spectre d'énergie cinétique caractérisant l'écoulement étudié.

En particulier, lorsqu'une grande partie du spectre des échelles turbulentes est résolue, les problématiques liées à l'utilisation de schémas discrets avec un niveau d'approximation élevé, et la nécessité de conditions aux limites « transparentes » du point de vue numérique, sont abordées. Ces aspects représenteront les prémisses de la première partie de cette thèse.

Étant donné que la Simulation aux Grandes Échelles et la Simulation des Équations de Navier-Stokes Moyennées sont basées sur une reproduction partielle du spectre énergétique de la turbulence, leurs différences fondamentales sont considérées. Si, d'un côté, les modèles de sous-maille pour la Simulation aux Grandes Échelles sont de caractère plus général, l'utilisation des opérateurs de filtrage au lieu des opérateurs de moyenne (temporelle ou d'ensemble) détermine l'introduction d'une série d'interactions qui doivent être prises en compte. Cette considération sera la base de la deuxième partie de ce travail.

Pour finir, la dernière partie du chapitre introduira le plan de la thèse.

1.1 Background and Motivations

Many engineering applications and fundamental studies are often connected with Fluid Mechanics and, as with any other physical phenomenon which is described by a more or less complex set of partial differential equations, the huge complexity of the relevant mathematical representation make it necessary to rely upon the use of numerical simulations. Computational Fluid Dynamics (CFD), hence, is a standard tool of investigation which has gained considerable attention in the past decades and which still undergoes significant evolution.

In order to be able to make an accurate representation of fluid flows, three main aspects must be considered: (a) turbulence modeling, (b) mathematical theories relevant to the discrete representation of the continuum and (c) efficient algorithms for grid generation. Though, these three ingredients are significantly well connected, turbulence modeling represents one of the driving mechanisms in the definition of standards and requirements that CFD is expected to fulfill. Despite the relatively simple form of the equations that govern the fluid motion, in fact, their solution turns out to be extremely complex, all the relevant details being far from being fully understood, and the numerical schemes used to represent the complexity of the underlining physics with increasing levels of detail need to be continuously improved.

It is probably not far from the reality to affirm that the mathematical tools used in CFD are way more accurate than the turbulence models they solve. And it is also clear that most of the difficulties encountered when dealing with turbulent flows and the relevant transport phenomena come from the non-linear nature of the equations governing fluid dynamics, first of all, because there would not be any turbulence if the equations were linear, but also because non-linear interactions are responsible for the enormous proliferation of the typical scales of fluid motion, which, in principle, should be represented altogether—as well as for the proliferation and amplification of numerical perturbations, which should be avoided by all means—and because discrete representations of the non-linear term pose energy conservation problems which are anything but trivial.

It is indeed the above mentioned broad variety of scales of turbulence, *i.e.*, its broad energy spectrum, that makes it necessary to develop turbulence models, which, in turn, represent generally the *Achille's heel* of Computational Fluid Dynamics. In fact, most of the problems of practical engineering interest are characterized by a spectrum of frequencies that is just too wide to be represented with the available computational resources. Hence, the necessity to represent only part of it and devolve the reproduction of the missing part to the turbulence model. When a large part of the turbulence spectrum is modeled, as when Reynolds Averaged Navier-Stokes (RANS) equations are solved, the model itself is charged with such a variety of physical details and problem dependent features that its generality is often questionable. Moreover, since the relevant solution represents the time- or ensemble-averaged flow, its applicability is limited to configurations which admit a statistically steady solution.

When the model extent is reduced, as for instance in Large-Eddy Simulation (LES), its complexity becomes generally less demanding because a smaller part of the turbulent spectrum, supposedly more universal in character, needs to be reproduced. At the other extremum with respect to RANS, Direct Numerical Simulation (DNS) resolves the entire spectrum and no model is required. The resolved range of scales, of course, is handled by the numerical scheme and the solution becomes necessarily unsteady. Therefore, if on one hand, the range of applicability is extended to unsteady turbulent flows, the additional detail imposes increased accuracy standards to the numerical scheme.

High-order low dissipative—typically centered—numerical schemes which are generally used in Direct and Large-Eddy Simulations are generally more prone to amplify numerical spurious perturbations and the unsteady complex nature of the solution for which they represent the numerical substructure may represent an additional source of disturbances, especially, as far as boundary conditions are concerned. The increasing standards in the definition of numerically “transparent” open boundary conditions motivated the first part of the present work. On these lines, the characteristic formulation of boundary conditions, in particular, was addressed in order to derive a formulation capable of dealing with complex and randomly oriented turbulent flow fields, while maintaining a sufficiently low level numerical reflection.

With regards to LES, the reduction of the modeled frequency range is, supposedly, accompanied by a certain decrease of model complexity. And indeed when Large-Eddy Simulation of free shear flows are performed, even a simple Sub-Grid Scale model based on the eddy-viscosity assumption may perform surprisingly well. Nonetheless, when the energy spectrum is partly modeled different types of interactions between resolved and unresolved scales, requiring more specific treatment, may appear. When the Reynolds-averaging operator used in RANS is regarded as particular sub-class of the filtering operator, in effect, it turns out that it has peculiar properties that the filters generally used in LES do not possess. Notably, the Reynolds-averaging operator is idempotent, whereas the filters which are generally applied in LES are not. Hence, LES unclosed terms contain a series of interaction terms which are not present in RANS.

It is well known, for instance, that turbulence, in average, is a dissipative process where kinetic energy is transferred from the large energy containing scales, down the small dissipative scales, through the energy cascade mechanism. Hence, dissipative turbulence models in RANS are expected to fulfill this requirement. *A priori* tests of DNS results, on the other hand, have revealed that, when local interactions in the neighborhood of a certain frequency within the energy spectrum are observed, local events of reverse energy transfer, namely backscatter, may happen. In such cases, then, purely dissipative models are not expected to perform with sufficient accuracy. LES models should be then properly designed to account for this kind of peculiar features.

This observation was the premise of the second part of this thesis which dealt with the formulation of a structural sub-grid scale model for moderately compressible LES, based on the similarity hypothesis, with particular attention to the correct representation of near-wall dynamics. The model was then tested on the impinging round-jet configuration, which, due to its intrinsic complexity, represents a particularly tough test bench for turbulence modeling. Alongside the validation of the proposed model, some specific features about local energy transfer and scalar mixing within the near-wall region were also addressed.

As a final task, DNS of turbulent Bunsen flames at different Reynolds numbers were performed, in the framework of the last *CTR Summer Program 2008*, in order to achieve more insight into typical issues connected with the comparison of LES results with experimental measurements. Some questions about the treatment of chemical source terms at the boundary and flame resolution were also addressed.

1.2 Outline

The present thesis is organized in 6 chapters:

Chapter 2 contains a brief summary about the physical description of the motion of fluids.

The equations governing compressible viscous flows are presented in Section 2.1 together with the hypothesis and approximations relevant to the present specific applications. Section 2.2 reports a synthetic overview about the phenomenology of turbulence, with particular emphasis on the peculiar features observed in turbulent motion and the relevant typical scalings. At the end of the Section, the main results from the Kolmogorov's K41 Theory are described in some detail.

Chapter 3 describes in detail the problem formulation from the numerical point of view.

The numerical solver which was used during these three years of studies is described in Section 3.1. The boundary conditions' problem and its formulation in characteristic form is detailed in Section 3.2 where the ideas behind the novel 3D-NSCBC procedure are presented together with the numerical tests performed to validate the method. The adaptation of the synthetic turbulence injection method to the 3D-NSCBC technique is described in Section 3.3.

Chapter 4 will introduce some fundamentals about the numerical computation of turbulence

by means of the Large-Eddy Simulation methodology. Section 4.2 deals with the filtering operator and the filtered Navier-Stokes equations when, in particular, compressibility needs to be accounted for, at least partially. Some Sub-Grid Scale functional models based on the Eddy-Viscosity assumption are presented in Section 4.3, where particular emphasis is made on the relevant asymptotic behavior at the wall. In Section 4.4, structural Sub-Grid Scale models based on the Similarity Hypothesis are first described. Then, the new WALE-Similarity Model is presented in detail in a weakly compressible formulation. The validation of the new model follows in Section 4.5, where the WALE-Similarity Model is tested on the impinging round-jet configuration at different Reynolds numbers. Some interesting features about modeled energy backscatter and scalar mixing within the near-wall region are also addressed.

Chapter 5 deals with Direct Numerical Simulation with particular emphasis on turbulent

combustion. The mathematical description of the combustion process is presented in Section 5.2 for lean premixed flames. The treatment of chemical source terms at the boundary making use of the 3D-NSCBC technique and the requirements in terms of flame resolution are also analyzed. Direct Numerical Simulation of the turbulent Bunsen flame is described in detail in Section 5.3 for three Reynolds numbers.

Chapter 6 finally, will contain a summary of the different topics developed and the relevant

conclusions will be drawn. Some possible research perspectives, originating from the present work, will be also put forward.

Part II collects the archival publications relevant to this Ph.D. Thesis, namely the articles about the 3D-NSCBC procedure, the WALE-Similarity Model and the Proceedings of the CTR Summer Program 2008.

Fundamentals

It seems that nature (God?) has a nice sense of irony. On the one hand we have a physical quantity, \mathbf{u} , which behaves in a random fashion, yet is governed by a simple, deterministic equation. On the other hand the statistical properties of \mathbf{u} appear to be well-behaved and reproducible, yet we know of no closed set of equations which described them!

P.A. Davidson, 2004

Contents

2.1	The Governing Equations	8
2.1.1	The Adimensional Formulation	10
2.2	Turbulent Flows	11

Les équations qui gouvernent le mouvement des fluides visqueux, dites équations de Navier-Stokes, sont ici présentées dans le cas d'un écoulement compressible. Une équation de transport additionnelle décrivant l'évolution d'un scalaire passif dans l'écoulement est ajoutée. En particulier, on fera l'hypothèse que le fluide est un gaz parfait Newtonien mono-composant avec une viscosité dynamique décrite par la loi de Sutherland. On fera aussi l'hypothèse que les forces de volume peuvent être négligées et que le transport diffusif de la chaleur et du scalaire passif suivent respectivement la loi de Fourier et de Fick.

Dans la deuxième section, la formulation adimensionnelle des équations susmentionnées, basée sur les grandeurs de référence de densité, vitesse, échelle et température, sera dérivée.

Une introduction synthétique des concepts fondamentaux relatifs à la description phénoménologique de la turbulence est présentée. En particulier, la classification des écoulements laminaires et turbulents sur la base du rapport entre les actions inertielles et visqueuses, notamment le nombre de Reynolds [61], ainsi que les principaux critères de classification des échelles caractéristiques de la turbulence, sont décrits.

Enfin, un résumé très concis de la célèbre Théorie K41 proposée par Kolmogorov [36, 37] est présenté. En particulier, l'existence d'une région d'Équilibre Universel est introduite, et les deux Hypothèses de Similarité relatives sont citées. Leurs formulations en terme de la fonction de structure de deuxième ordre et du spectre d'énergie monodimensionnel longitudinal, respectivement dans la région de dissipation et la sous-gamme inertielle, sont dérivées.

2.1 The Governing Equations

The motion of a compressible viscous fluid is fully described by imposing the conservation laws for mass, momentum and energy. Using Einstein summation convention for repeated indices, the local formulation on a cartesian coordinates system of each conservation law may be formalized with the following transport equations:

- conservation of mass (continuity equation),

$$\frac{\partial \rho}{\partial t} + \frac{\partial \rho u_j}{\partial x_j} = 0, \quad (2.1)$$

where ρ is the fluid's density and u_k is the velocity component along direction x_k ;

- conservation of the three components of momentum,

$$\frac{\partial \rho u_i}{\partial t} + \frac{\partial \rho u_i u_j}{\partial x_j} - \frac{\partial \sigma_{ij}}{\partial x_j} - \rho f_i = 0, \quad (i = 1, 2, 3), \quad (2.2)$$

where $\sigma_{ij} = \tau_{ij} - p\delta_{ij}$ ¹ is the tensor of surface stresses accounting for viscous actions τ_{ij} and thermodynamic pressure p and f_k is the k th component of the body forces per unit mass acting on the fluid element;

- conservation of total energy,

$$\frac{\partial \rho e}{\partial t} + \frac{\partial \rho e u_j}{\partial x_j} - \frac{\partial u_i \sigma_{ij}}{\partial x_j} - \rho u_i f_i + \frac{\partial q_j}{\partial x_j} = 0, \quad (2.3)$$

where $e = e_I + u_k u_k / 2$ is the total energy (internal + kinetic), e_I is the internal energy and q_k is the k th component of the heat flux vector.

The above five equations (two scalar and one vector transport equations) represent the compressible Navier-Stokes (NS) equations set. In the present study, an additional transport equation is introduced to describe the evolution of a scalar quantity Z . For the moment, we will assume that Z is a passive scalar, therefore the relevant transport equation is completely decoupled from the other balanced equations, meaning that Z is transported by the flow field but the flow field itself is not affected by Z :

$$\frac{\partial \rho Z}{\partial t} + \frac{\partial \rho Z u_j}{\partial x_j} + \frac{\partial \rho J_j}{\partial x_j} = 0, \quad (2.4)$$

where J_k is the k th component of the diffusion flux vector.

The following additional hypotheses will be assumed in the present work:

1. the fluid is Newtonian and follows the Stokes Law for mono-atomic gases:

$$\tau_{ij} = 2\mu A_{ij}, \quad (2.5)$$

where μ is the dynamic viscosity and A_{ij} is the deviator of the deformation tensor

$$A_{ij} = \frac{1}{2} \left(\frac{\partial u_i}{\partial x_j} + \frac{\partial u_j}{\partial x_i} \right) - \frac{1}{3} \delta_{ij} \frac{\partial u_k}{\partial x_k}; \quad (2.6)$$

¹ δ_{ij} is the Kronecker's delta

2. the heat flux q_k is given by the Fourier's law

$$q_k = -\lambda \frac{\partial T}{\partial x_k} = -\frac{\mu c_p}{Pr} \frac{\partial T}{\partial x_k}, \quad (2.7)$$

where λ is the thermal conductivity, T is the temperature, c_p is the specific heat capacity at constant pressure and Pr is the Prandtl number;

3. the fluid evolves following the equation of state for a calorically perfect gas:

$$p = \rho RT, \quad (2.8)$$

$$e_I = c_v T \quad (2.9)$$

$$c_p = c_v + R, \quad (2.10)$$

$$\gamma = c_p/c_v, \quad (2.11)$$

where $R = \mathcal{R}/M_w$ is the gas constant computed from the universal gas constant $\mathcal{R} = 8.31451 \text{ J}/(\text{molK})$ and the gas molar weight M_w , c_v is the specific heat capacity at constant volume and $\gamma = 1.4$. The total energy density, in particular, may be expressed as

$$\rho e = \frac{1}{2} \rho u_k u_k + \frac{p}{\gamma - 1}; \quad (2.12)$$

4. the scalar Z diffuses following the Fick's Law:

$$J_k = -D \frac{\partial Z}{\partial x_k} = -\frac{\mu}{\rho Sc} \frac{\partial Z}{\partial x_k}, \quad (2.13)$$

where D is the diffusion coefficient and Sc is the Schmidt number;

5. the dynamic viscosity of the fluid μ may be computed from the temperature T using the Sutherland's law:

$$\mu(T) = \mu_{\text{ref}} \left(\frac{T}{T_{\text{ref}}} \right)^{3/2} \frac{T_{\text{ref}} + S}{T + S}; \quad (2.14)$$

6. body forces can be neglected, *i.e.* $f_k = 0$.

If we introduce the vector of conservative variables,

$$\mathbf{U} = (\rho \quad \rho u_1 \quad \rho u_2 \quad \rho u_3 \quad \rho e \quad \rho Z)^T,$$

and the flux and diffusion vectors \mathbf{F}^k and \mathbf{D}^k the problem may be then conveniently described in vector form by the following equation:

$$\frac{\partial \mathbf{U}}{\partial t} + \frac{\partial \mathbf{F}^k}{\partial x_k} + \frac{\partial \mathbf{D}^k}{\partial x_k} = \mathbf{0}, \quad (2.15)$$

with

$$\mathbf{F}^k = \begin{pmatrix} \rho u_k \\ \rho u_1 u_k + \delta_{1k} p \\ \rho u_2 u_k + \delta_{2k} p \\ \rho u_3 u_k + \delta_{3k} p \\ (\rho e + p) u_k \\ \rho Z u_k \end{pmatrix}, \quad \mathbf{D}^k = \begin{pmatrix} 0 \\ -2\mu A_{1k} \\ -2\mu A_{2k} \\ -2\mu A_{3k} \\ -2\mu u_j A_{kj} - \frac{\mu c_p}{Pr} \frac{\partial T}{\partial x_k} \\ -\frac{\mu}{Sc} \frac{\partial Z}{\partial x_k} \end{pmatrix}, \quad (2.16)$$

2.1.1 The Adimensional Formulation

The numerical solver used in the present work (see Section 3.1) integrates the non-dimensional set of Navier-Stokes equations. The relevant normalization procedure is summarized below.

Let ρ_R , u_R , ℓ_R and T_R be the reference density, velocity, length and temperature respectively. The relevant adimensional quantities are

$$\rho^* = \rho/\rho_R, \quad u_i^* = u_i/u_R, \quad x_i^* = x_i/\ell_R, \quad T^* = T/T_R, \quad (2.17)$$

where the superscript $*$ is now used to address normalized non-dimensional quantities. The reference time, pressure and viscosity may be derived by dimensional analysis as:

$$t_R = \ell_R/u_R, \quad p_R = \rho_R u_R^2, \quad \mu_R = \rho_R u_R \ell_R. \quad (2.18)$$

The dynamic viscosity is adimensionalized dividing Eq. (2.14) by μ_R and using the definition of dimensionless temperature:

$$\mu^*(T^*) = \frac{\mu(T)}{\mu_R} = \frac{\mu_{\text{ref}}}{\rho_R u_R \ell_R} \left(\frac{T^* T_R}{T_{\text{ref}}} \right)^{3/2} \frac{T_{\text{ref}} + S}{T^* T_R + S} = \frac{1}{Re_0} \left(\frac{T^*}{T_{\text{ref}}} \right)^{3/2} \frac{T_{\text{ref}}^* + S^*}{T^* + S^*}, \quad (2.19)$$

where $Re_0 = \rho_R u_R \ell_R / \mu_{\text{ref}}$, $T_{\text{ref}}^* = T_{\text{ref}}/T_R$ and $S^* = S/T_R$. Moreover, the dimensionless equation of state is obtained from Eq. (2.8) as

$$p^* = \rho^* R^* T^*, \quad (2.20)$$

with

$$R^* = \frac{1}{\gamma M_0^2} \quad \text{and} \quad M_0 = \frac{u_R}{\sqrt{\gamma R T_R}}; \quad (2.21)$$

dividing the internal energy by u_R^2 and the total energy by $\rho_R u_R^2$ and using the identity $R^* = R T_R / u_R^2$, the following relations descend immediately:

$$e_I^* = \frac{R^* T^*}{\gamma - 1} = c_v^* T^*, \quad \text{and} \quad \rho^* e^* = \frac{1}{2} \rho^* u_k^* u_k^* + \frac{p^*}{\gamma - 1}, \quad (2.22)$$

where $c_v^* = R^*/(\gamma - 1) = c_v T_R / u_R^2$ is related to γ and M_0 . Evidently, the dimensionless specific heat at constant volume and pressure are related to their dimensional counterparts by the following identities:

$$c_v^* = c_v T_R / u_R^2, \quad \text{and} \quad c_p^* = \gamma c_v^* = c_p T_R / u_R^2. \quad (2.23)$$

Using Eqs. (2.17), (2.18), (2.19), (2.21) and (2.23) and related identities, the dimensionless Navier-Stokes equations become:

$$\frac{\partial \rho^*}{\partial t^*} + \frac{\partial \rho^* u_j^*}{\partial x_j^*} = 0, \quad (2.24)$$

$$\frac{\partial \rho^* u_i^*}{\partial t^*} + \frac{\partial}{\partial x_j^*} (\rho^* u_i^* u_j^* + p^* \delta_{ij}) = \frac{\partial}{\partial x_j^*} (2\mu^* A_{ij}^*), \quad (2.25)$$

$$\frac{\partial \rho^* e^*}{\partial t^*} + \frac{\partial}{\partial x_j^*} [(\rho^* e^* + p^*) u_j^*] = \frac{\partial}{\partial x_j^*} \left(2\mu^* u_i^* A_{ij}^* + \frac{\mu^* c_p^*}{Pr} \frac{\partial T^*}{\partial x_j^*} \right), \quad (2.26)$$

$$\frac{\partial \rho^* Z}{\partial t^*} + \frac{\partial}{\partial x_j^*} (\rho^* Z u_j^*) = \frac{\partial}{\partial x_j^*} \left(\frac{\mu^*}{Sc} \frac{\partial Z}{\partial x_j^*} \right), \quad (2.27)$$

which are formally identical to the dimensional counterparts, with all the quantities replaced by *starred* ones. Based on this consideration, in all the next sections, no distinction will be made anymore between dimensional and dimensionless formulations, being anyway understood that all the results presented have been obtained by numerical integration of the non-dimensional equations. It is worthwhile mentioning the relations existing between the adimensional diffusion coefficients and the dimensionless characteristic numbers of the flow:

$$\mu^* = \frac{f(T^*)}{Re_0}, \quad (2.28)$$

$$\frac{\mu^* c_p^*}{Pr} = \frac{f(T^*)}{(\gamma - 1) Re_0 M_0^2 Pr}, \quad (2.29)$$

$$\frac{\mu^*}{Sc} = \frac{f(T^*)}{Re_0 Sc}, \quad (2.30)$$

where $f(T^*)$ represents the functional relation between non-dimensional dynamic viscosity and temperature (*cf.* Eq. (2.19)).

2.2 Turbulent Flows: A Synthetic Overview

Looking closer to Eq. (2.28)–(2.30), the first thing that can be noticed is that for extremely high values of the parameter Re_0 , the viscous effects become less and less important, hence the flow tends to be almost inviscid. On the other hand, when Re_0 is small, viscous effects become more and more important.

The importance of this parameter was first pointed out by Reynolds [61] while making experimental observations of the flow along straight smooth pipes. He noticed that, for some certain value of the ratio

$$\frac{\rho U \ell}{\mu},$$

with U the average fluid velocity in the pipe and ℓ its radius, the flow was changing radically from “direct” motion into “sinuous” motions, indicating what nowadays is commonly referred to as “laminar” and “turbulent” flow regimes.

If U is the typical velocity of the flow, ℓ_u is the typical length of the streamline pattern and ℓ_v is the typical length of cross-stream velocity gradients, it is easily shown, by simple dimensional considerations, that the inertial and viscous forces for unit volume of fluid scale as $\rho U^2 / \ell_u$ and $\mu U / \ell_v^2$ respectively. Hence, provided that ℓ is properly chosen²,

$$Re = \frac{\rho U \ell}{\mu}, \quad (2.31)$$

namely the Reynolds number, represents the relative intensity of inertial forces compared to the viscous ones. When inertial forces are predominant over viscous forces, the fluid motion is more prone to instabilities. And, since the quadratic nature of the Navier-Stokes equations—expressed by the term $\rho u_i u_j$ in Eq. (2.16)—makes them extremely sensitive to small differences in the initial conditions, chaotic, or turbulent, motion is generally the outcome of those instabilities.

²In the Reynolds’s experiment, for instance, choosing ℓ equal to the length of the tube would have given completely incongruent results.

It should be mentioned that the limiting value Re_{cr} of the Reynolds number, above which transition to turbulence is observed, depends on the intensity, u'/U , of external perturbations affecting the flow. If particular care is made to keep perturbations as low as possible, the value of Re_{cr} , for the same flow configuration, may be generally increased.

If on one hand, there exists a minimum value Re_{cr}^{\min} below which, regardless of the perturbation intensity, the flow is always laminar, on the other hand, a maximum value Re_{cr}^{\max} , *i.e.* the value of Reynolds number for which turbulent transition is ensured for any perturbation, however small, does not always exist. If, for instance, for a boundary layer there seems to be a maximum value of Re_{cr} , of the order of 3×10^6 , above which the flow becomes turbulent no matter how small is the perturbation level, for a pipe flow, a limiting value of the critical Reynolds number does not exist, hence $Re_{cr} \rightarrow \infty$ for $u'/U \rightarrow 0$ and the Reynolds number can be increased indefinitely, while keeping the flow laminar, provided that a sufficiently low level of perturbation can be guaranteed [50].

From a mathematical point of view, if the fluid motion is decomposed into elementary components—*i.e.* it is expanded in terms of orthogonal functions, each of them describing elementary motions at different scales—such that each of them is defined by a limited number of parameters and their energy sum up to the total energy of the flow, then the total number of parameters may be considered as the total number of degrees of freedom of the flow. The elementary functions, as well as the number of degrees of freedom, depend on the initial and boundary conditions for the flow.

For steady laminar flows, the value of the above mentioned parameters, or generalized coordinates, is defined by the boundary conditions, hence the number of degrees of freedom is zero. This is not the case for turbulent flows which can have quite a large amount of degrees of freedom. The total number is anyway limited due to viscosity, which prevents fluctuations of too small scales from existing. If viscosity decreases, smaller and smaller scales are permitted, hence the degrees of freedom increase with increasing Re number. For sufficiently large Reynolds numbers, if N is the total number of degrees of freedom of turbulence in a finite volume, it is well known that

$$N \propto Re^{9/4}, \quad (2.32)$$

where Re is the typical Reynolds number for the flow. We may want, for instance, to make a discrete representation of a turbulent velocity field by means of its Fourier transformation. If N_x , N_y and N_z are the total number of frequencies which are necessary for a sufficiently accurate approximation of the relevant spectra (one for each coordinate direction), then it is clear that the full representation will involve the solution of the Fourier transformed Navier-Stokes equations over, at least, $N = N_x \times N_y \times N_z$ wave-numbers. This number, which corresponds to the total number of grid points in physical space which are necessary to make a full representation of the flow, scales with the Reynolds number as expressed by Eq. (2.32).

In the most simple case of statistically steady turbulence, the velocity field may be decomposed into a mean flow and a random, fluctuating, component of motion:

$$\mathbf{u}(\mathbf{x}, t) = \langle u \rangle(\mathbf{x}) + \mathbf{u}'(\mathbf{x}, t), \quad (2.33)$$

with

$$\langle u \rangle(\mathbf{x}) = \lim_{T \rightarrow \infty} \frac{1}{T} \int_0^T \mathbf{u}(\mathbf{x}, t) dt. \quad (2.34)$$

For fully developed turbulence, the fluctuating velocity \mathbf{u}' may be regarded as a random broad collection of vortices, or eddies, of different typical scales, the bigger being typically comparable, in size, with a characteristic geometric length-scale for the flow, namely the integral length ℓ_0 . Those eddies are created by instabilities and are themselves subject to inertial instabilities, hence, smaller and smaller eddies are generated by break-up of the bigger ones. Kinetic energy is then passed down into a cascade process from big structures to small structures until the typical size of the eddies is so small that they are destroyed by the action of viscous forces. If v_η and η are the typical velocity- and length-scales of the smallest eddies, viscous forces are predominant, hence the relevant Reynolds number is of the order of unity:

$$\frac{v_\eta \eta}{\nu} \sim 1. \quad (2.35)$$

If u' is a measure of the norm of the fluctuating velocity \mathbf{u}' and

$$Re_t = \frac{u' \ell_0}{\nu} \quad (2.36)$$

is sufficiently large, the life-span of a big eddy of size ℓ_0 is of the order of its turn-over time ℓ_0/u' , therefore, as a first approximation, we may conjecture that the rate at which energy per unit mass is passed down the energy cascade is of the order of

$$\Pi \sim \frac{u'^2}{\ell_0/u'} = \frac{u'^3}{\ell_0}. \quad (2.37)$$

On the other hand, considering for simplicity the incompressible case, the rate of energy dissipation $\bar{\varepsilon}$ is of the order of $\nu S_{ij} S_{ij}$, where S_{ij} is the strain rate tensor, and, since dissipation is mainly acting at small scales, where velocity gradients attain the most intense values, we may write:

$$\bar{\varepsilon} \sim \nu \frac{v_\eta^2}{\eta^2}. \quad (2.38)$$

When the conditions are statistically steady, *i.e.*, under the equilibrium hypothesis, the rate at which energy is passed down the cascade, must be equal to the rate of energy dissipation:

$$\Pi \sim \frac{u'^3}{\ell_0} \sim \nu \frac{v_\eta^2}{\eta^2} \sim \bar{\varepsilon}. \quad (2.39)$$

From the above condition and Eq. (2.35), it can be easily verified that:

$$\eta \sim \ell_0 Re_t^{-3/4} \sim (\nu^3/\bar{\varepsilon})^{1/4}, \quad (2.40)$$

$$v_\eta \sim u' Re_t^{-1/4} \sim (\nu \bar{\varepsilon})^{1/4}. \quad (2.41)$$

The scales η and v_η are known as the Kolmogorov microscales. The above relation is in accordance with what has been said about the total number of degrees of freedom in a turbulent flow: if the typical scales characterizing the flow spans from the biggest, of the order of ℓ_0 , to the smallest, of the order of η , then the breadth ℓ_0/η of the scales' range, per integral scale, is of the order of $Re_t^{3/4}$.

Due to the chaotic nature of turbulence, a statistical theory [50, 51] is clearly a powerful tool to tackle the problem. Among the many statistical quantities that can be used, the second-order (longitudinal) structure function,

$$D_{LL}(r) = \langle [u'_1(\mathbf{x} + \mathbf{r}) - u'_1(\mathbf{x})]^2 \rangle, \quad r = |\mathbf{r}|, \quad (2.42)$$

is a particularly useful one.³ In particular, if ℓ_0 , u' , t and ν are the integral scale, the typical velocity of the large eddies, the time and the kinematic viscosity, by dimensional considerations, Eq. (2.42) may be written as:

$$D_{LL}(r) = u'^2 f\left(\frac{r}{\ell_0}, \frac{u't}{\ell_0}, Re_t\right), \quad (2.43)$$

where f is a non-dimensional function of the dimensionless groups in parentheses. The above relation, even if not explicitly stated, is, in general, also a function of the boundary conditions of the flow.

If the Reynolds number is sufficiently large to ensure enough scale separation, although the large scales of motion cannot be assumed to be isotropic, eddies of size $r \ll \ell_0$ are likely not to retain much of the information relevant to the large scales. Moreover, since typical time-scales of small eddies are much smaller than those of the large scales, *i.e.*, small scale dynamics evolves much faster than large scale dynamics, small structures should not directly feel instantaneous changes of large structures. Hence, small scales are more or less unaware of large scales anisotropy (*i.e.*, they are *locally isotropic*) and feel the time evolution of the large scales through the instantaneous flux of energy $\Pi(t)$ only (*i.e.*, small scales are in *statistical equilibrium* with large scales).

Scales $r \ll \ell_0$, under the above hypotheses, represent the *universal equilibrium range* (*cf.* Figure 2.1) envisaged by Kolmogorov in his renowned K41 Theory [36, 37]. In particular, under the *First Similarity Hypothesis*, for sufficiently large Re and $r \ll \ell_0$, the statistical properties of turbulence have a universal nature and depend on $\bar{\varepsilon} = \langle 2\nu S_{ij} S_{ij} \rangle$ and ν , hence, by dimensional considerations, Eq. (2.43) becomes:

$$D_{LL}(r) = v_\eta^2 \beta_{LL}\left(\frac{r}{\eta}\right), \quad \text{for } r \ll \ell_0, \quad (2.44)$$

with η and v_η given in Eqs. (2.40) and (2.41) and β_{LL} a non-dimensional universal function. Introducing the velocity correlation

$$B_{LL}(r) = \langle u'_1(\mathbf{x} + \mathbf{r})u'_1(\mathbf{x}) \rangle, \quad (2.45)$$

its Fourier transformation $E_1(k_1)$, with $k_1 = \pi/r$ the relevant wave-number, represents the longitudinal one-dimensional energy spectrum:

$$E_1(k_1) = \frac{2}{\pi} \int_0^\infty B_{LL}(r) \cos(k_1 r) dr. \quad (2.46)$$

³The fact that in Eq. (2.42) the explicit dependency on r only is indicated, implies that turbulence is assumed to be, at least, locally isotropic [51], hence its statistical properties do not change under translations, rotations and mirror reflections.

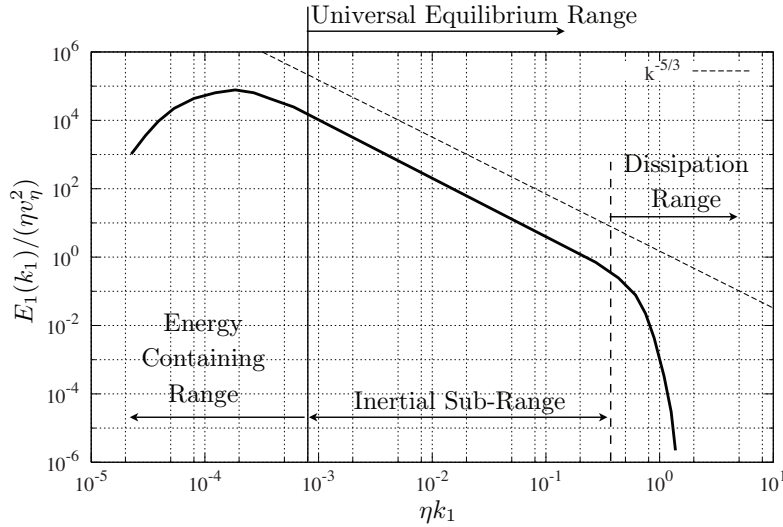


Figure 2.1: Qualitative representation of the normalized longitudinal one-dimensional spectrum $E_1(k_1)/(\eta v_\eta^2)$ as a function of the normalized wave-number ηk_1 .

Resorting again to dimensional considerations, the Kolmogorov's first similarity hypothesis may be written for the longitudinal one-dimensional energy spectrum as follows:

$$E_1(k_1) = \eta v_\eta^2 \varphi_1(\eta k_1), \quad \text{for } k_1 \gg 1/\ell_0, \quad (2.47)$$

with φ_1 another dimensionless universal function [51]. Moreover, there exists a sub-domain, $\eta \ll r \ll \ell_0$, of the universal equilibrium range where scales are sufficiently large not to be affected by viscosity anymore. Accordingly, within this range, the Kolmogorov's *Second Similarity Hypothesis* states that, for sufficiently large Re , the statistical properties of turbulence have a universal nature and depend on $\bar{\varepsilon}$ only. From Eqs. (2.44), (2.40) and (2.41), we have:

$$D_{LL}(r) = (\nu \bar{\varepsilon})^{1/2} \beta_{LL} \left(\frac{r \bar{\varepsilon}^{1/4}}{\nu^{3/4}} \right), \quad (2.48)$$

hence the only possibility to cancel out ν is that $\beta_{LL}(\xi) = C \xi^{2/3}$ and we get:

$$D_{LL}(r) = C \bar{\varepsilon}^{2/3} r^{2/3}, \quad \text{for } \eta \ll r \ll \ell_0, \quad (2.49)$$

and the relevant relation for the longitudinal one-dimensional energy spectrum may be obtained, by analogous reasoning⁴, from Eq. (2.47):

$$E_1(k_1) = C_K \bar{\varepsilon}^{2/3} k_1^{-5/3}, \quad \text{for } 1/\ell_0 \ll k_1 \ll 1/\eta, \quad (2.50)$$

⁴From Eqs. (2.47), (2.40) and (2.41), we have

$$E_1(k_1) = \nu^{5/4} \bar{\varepsilon}^{1/4} \varphi_1 \left(\frac{\nu^{3/4}}{\bar{\varepsilon}^{1/4}} k_1 \right),$$

hence, the only way to cancel out ν is that $\varphi_1(\xi) = C_K \xi^{-5/3}$.

where C_K is commonly indicated as Kolmogorov constant.

The Second Similarity Hypothesis and Eqs. (2.49)–(2.50) define the so called *inertial sub-range*, indicated in Figure 2.1 on a qualitative representation of the one-dimensional longitudinal energy spectrum.

The two similarity hypotheses of the K41 Theory has been extensively demonstrated by experimental measurements. By representing the normalized energy spectrum as in Figure 2.1, in fact, the universal character of the universal equilibrium range implies that spectra extracted from different turbulent flows should collapse onto a single curve. This is indeed the case. The values of the universal constants within the inertial sub-range were found to be $C \simeq 2$ and $C_K \simeq 0.76C \simeq 1.5$ for $Re \rightarrow \infty$ (*cf.* Section 23.3 in Monin and Yaglom [51]).

Mathematical Formulation

The discretization can yield linear but also nonlinear difference equations to determine the unknown velocity components defined at the grid points. The number of unknowns is obtained from the number of grid points. Since the spacing between them must be small in order for the model to be as accurate as possible, the number of unknowns is always large. For this reason, computers must be used to solve the difference equations.

H. Schlichting and K. Gersten, 2000

Contents

3.1	The SiTCom Solver	18
3.1.1	The Finite Volume Formulation	19
3.1.2	Convective Numerical Fluxes	22
3.1.3	The Artificial Dissipation Term for LES	23
3.1.4	Viscous Numerical Fluxes	24
3.1.5	Time Integration	26
3.2	Characteristic Boundary Conditions	27
3.2.1	3D Characteristics	32
3.2.2	Characteristic Formulation for Faces	34
3.2.3	Characteristic Formulation for Edges	43
3.2.4	Characteristic Formulation for Corners	51
3.2.5	Testing the 3D-NSCBC	59
3.3	Artificial Turbulence Injection	79

Les détails mathématiques concernant la mise en œuvre d'une approche Volumes Finis de la résolution des équations de Navier-Stokes, dans leur formulation de type conservative, sont donnés dans ce 3^e Chapitre. Les équations discrètes du code numérique, utilisé dans le cadre de cette thèse, des termes de transport convectif et diffusif, ainsi que des termes de dissipation artificielle employée pour la Simulation aux Grandes Échelles sont présentées en premier lieu.

La formulation caractéristique des conditions aux limites est ensuite décrite. La dérivation de la forme caractéristique des équations de transport, dans le cas tridimensionnel, est présentée et les principales problématiques concernant l'utilisation de l'hypothèse d'écoulement monodimensionnel non-visqueux, propre aux Conditions Limites Caractéristiques des équations de Navier-Stokes [58], sont envisagées.

Puis, une nouvelle procédure pour prendre en compte les effets tridimensionnels dans la solution des dérivées temporelles de l'amplitude des ondes entrantes est proposée. Cette

technique, qui représente l'un des objectifs principaux de cette thèse et qui a été publiée dans Lodato et al. [43], comporte des problèmes de couplage des ondes se déplaçant le long des différentes directions, et les solutions relatives pour les conditions d'entrée/sortie subsoniques non-réfléchissantes et de paroi adiabatique sont détaillées.

Cette procédure, nommée 3D-NSCBC, est, ensuite, testée sur des configurations simplifiées relatives à la convection de tourbillons à différents régimes de Mach, et à la propagation d'une impulsion sonore sphérique. L'application des conditions 3D-NSCBC à la Simulation aux Grandes Échelles d'un jet libre turbulent est aussi présentée afin de tester la robustesse et la stabilité de la nouvelle technique dans le cas d'une configuration complexe.

Enfin, la dernière section sera dédiée à la formulation, non triviale, de la méthode d'injection d'un signal de turbulence corrélé [35] lorsque la condition d'entrée subsonique non-réfléchissante est utilisée.

3.1 The SiTCom Solver

All the simulations presented in this work have been performed using the MPI parallelized implementation of the SiTCom (Simulating Turbulent Combustion) code: a home made solver based on an explicit Finite Volume (FV) scheme written for cartesian grids. This code was previously developed and extensively validated at CORIA in a sequential version [11, 12]. Then, in collaboration with Modelys [18] a parallel version was developed. From this point, this thesis reports on further development concerning boundary conditions, Sub-Grid Scale modeling and massively parallel computations, typically performed on more than 1000 processors.

This solver, which is entirely coded in FORTRAN 77, approximates the convective terms resorting to the fourth-order centered skew-symmetric-like scheme proposed by Ducros et al. [15] and the diffusive terms with a fourth-order centered scheme. The scheme is augmented by a blend of second- and fourth-order artificial dissipation terms [74, 76]; these terms are added in order to suppress spurious oscillations and damp high-frequency modes. Time integration is performed using a particular implementation of the third-order Runge-Kutta scheme [26, 34]. A brief overview of the above mentioned main numerical features is presented in the next sections.

All the boundary conditions are enforced using the 3D-NSCBC approach [43], which constitutes one of the main topics of the present work and that will be discussed in detail in Section 3.2.

With regards to the computation of turbulent flows, the solver can be used to perform either Direct Numerical Simulations (DNS)¹ or Large-Eddy Simulations (LES). LES in particular may be performed choosing between different Sub-Grid Scale (SGS) models, which will be presented in Chapter 4: (a) the Smagorinsky model [70]; (b) the Filtered Structure Function (FSF) model [14]; (c) the Wall Adapting Local Eddy-viscosity (WALE) model [53]; (d) a compressible implementation of the Lagrangian Dynamic Smagorinsky Model (LDSM) originally developed for incompressible flows by Meneveau et al. [48]; (e) and the WALE Similarity mixed Model (WSM), which constitutes the second main topic of this work and which will be described in detail in Section 4.4.1.

¹When DNS are performed, the artificial dissipation is switched off.

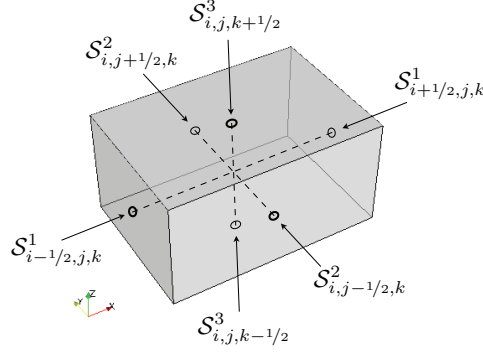


Figure 3.1: Schematic representation of the discrete control volume $\mathcal{V}_{i,j,k}$.

3.1.1 The Finite Volume Formulation

The numerical scheme used within the code is based on the Finite Volume (FV) approach. The governing transport equations, Eqs. (2.15)–(2.16) are therefore rewritten in integral formulation, by integrating over a control volume \mathcal{V} —with frontier \mathcal{S} —and applying the Gauss’ Theorem to the divergence-like terms:

$$\int_{\mathcal{V}} \frac{\partial \mathbf{U}}{\partial t} dV + \int_{\mathcal{S}} \mathbf{F}^j n_j dS + \int_{\mathcal{S}} \mathbf{D}^j n_j dS = \mathbf{0}. \quad (3.1)$$

The above compact equation corresponds to the following integral transport relations:

$$\int_{\mathcal{V}} \frac{\partial \rho}{\partial t} dV + \int_{\mathcal{S}} \rho u_j dS_j = 0, \quad (3.2)$$

$$\int_{\mathcal{V}} \frac{\partial \rho u_i}{\partial t} dV + \int_{\mathcal{S}} (\rho u_i u_j + \delta_{ij} p) dS_j = \int_{\mathcal{S}} 2\mu A_{ij} dS_j, \quad (i = 1, 2, 3), \quad (3.3)$$

$$\int_{\mathcal{V}} \frac{\partial \rho e}{\partial t} dV + \int_{\mathcal{S}} (\rho e + p) u_i dS_i = \int_{\mathcal{S}} \left(2\mu u_j A_{ij} + \frac{\mu c_p}{Pr} \frac{\partial T}{\partial x_i} \right) dS_i, \quad (3.4)$$

$$\int_{\mathcal{V}} \frac{\partial \rho Z}{\partial t} dV + \int_{\mathcal{S}} \rho Z u_i dS_i = \int_{\mathcal{S}} \frac{\mu}{Sc} \frac{\partial Z}{\partial x_i} dS_i, \quad (3.5)$$

where $dS_k = n_k dS$ represent the surface element’s component in the k th direction.

The physical domain is then subdivided in small polyhedral control volumes $\mathcal{V}_{i,j,k}$, which are delimited by a finite number of plane surfaces as depicted in Figure 3.1 (hexahedra in the present case where the computational grid is cartesian), where the equations are solved resorting to the approximations²

$$\int_{\mathcal{V}_{i,j,k}} \varphi dV \simeq \hat{\varphi} \mathcal{V}_{i,j,k} \quad \text{and} \quad \int_{\mathcal{S}} \varphi dS_m \simeq \sum_i [\varphi]_i \mathcal{S}_i^m, \quad (3.6)$$

²In order to overcome the difficulties related to the proliferation of indices when dealing with discrete transport equations, we will stick to the convention that i, j, k indices refer to the discretization (in general, cell numbering along the three coordinate directions) and we will use m, l indices to refer to vector components. To avoid any confusion, Einstein convention won’t be used throughout the remainder of this section when referring to discrete equations and summation, when necessary, will be explicitly indicated.

where $\hat{\varphi}$ is the average value of a generic scalar quantity φ over the control volume $\mathcal{V}_{i,j,k}$ and the summation in the second equation is extended to all the elementary plane surfaces delimiting the control volume; $[\varphi]_i$ is a measure of the value of φ over the i th surface \mathcal{S}_i^m delimiting the discrete control volume $\mathcal{V}_{i,j,k}$.

Considering, in particular, the case of a structured cartesian computational grid, as in the present solver, the discrete flux integral for a generic vector φ_m , at cell location i, j, k , may be written as (see Figure 3.1):

$$\begin{aligned} \int_{\mathcal{S}} \varphi_m dS_m \simeq & [\varphi_1]_{i+1/2,j,k} \mathcal{S}_{i+1/2,j,k}^1 - [\varphi_1]_{i-1/2,j,k} \mathcal{S}_{i-1/2,j,k}^1 \\ & + [\varphi_2]_{i,j+1/2,k} \mathcal{S}_{i,j+1/2,k}^2 - [\varphi_2]_{i,j-1/2,k} \mathcal{S}_{i,j-1/2,k}^2 \\ & + [\varphi_3]_{i,j,k+1/2} \mathcal{S}_{i,j,k+1/2}^3 - [\varphi_3]_{i,j,k-1/2} \mathcal{S}_{i,j,k-1/2}^3. \end{aligned} \quad (3.7)$$

As it can be seen from the above equation, the mathematical details of the numerical scheme used may be conveniently analyzed considering one coordinate direction at a time; this is what it will be done throughout the next sections by addressing the mono-dimensional FV transport equation. Considering the i th control volume \mathcal{V}_i , this may be written on the 1D stencil depicted in Figure 3.2 as:

$$\frac{\partial \hat{\varphi}_i}{\partial t} + \frac{\mathcal{FC}_{i+1/2} \mathcal{S}_{i+1/2} - \mathcal{FC}_{i-1/2} \mathcal{S}_{i-1/2}}{\mathcal{V}_i} = \frac{\mathcal{FV}_{i+1/2} \mathcal{S}_{i+1/2} - \mathcal{FV}_{i-1/2} \mathcal{S}_{i-1/2}}{\mathcal{V}_i}, \quad (3.8)$$

where

$$\mathcal{FC}_{i\pm 1/2} = [\varphi u]_{i\pm 1/2} \quad \text{and} \quad \mathcal{FV}_{i\pm 1/2} = \left[\kappa \frac{\partial \phi}{\partial x} \right]_{i\pm 1/2}$$

are generic convective and viscous discrete fluxes for the transported quantity $\varphi = \rho \phi$ computed on the cell interfaces and κ represent the diffusion coefficient for the relevant primitive variable ϕ .

The Finite Volume Taylor Series

In the framework of the FV technique, Taylor series expansions must be computed taking into account that the value of a generic quantity in cell i is actually its averaged value over the cell volume. Considering the mono-dimensional cartesian grid with uniform spacing Δx , *i.e.* $\mathcal{V}_i = \mathcal{S} \Delta x$, the volume averaged value of φ at cell i may be computed as:

$$\hat{\varphi}_i = \frac{1}{\mathcal{V}_i} \int_{\mathcal{V}_i} \varphi dV = \frac{1}{\Delta x} \int_{\Delta x} \varphi(x) dx.$$

With reference to Figure 3.2, the Taylor expansion of $\varphi(x)$ around the interface location $x_{i+1/2}$ is:

$$\varphi(x) = [\varphi]_{i+1/2} + \varphi' \delta x + \frac{1}{2} \varphi'' \delta x^2 + \frac{1}{6} \varphi''' \delta x^3 + \frac{1}{24} \varphi^{(4)} \delta x^4 + \mathcal{O}(\delta x^5), \quad (3.9)$$

where $\delta x = x - x_{i+1/2}$ and with all the derivatives evaluated at $x_{i+1/2}$.

Eq. (3.9) will be referred as *Finite Difference (FD) Taylor Expansion* in order to distinguish from the *FV Taylor Expansion* formulas which are derived below. The values of $\hat{\varphi}$ at the cell's

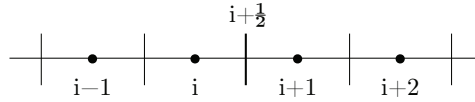


Figure 3.2: Four-nodes stencil used for surface integral approximations.

centers can be expressed in terms of $[\varphi]_{i+1/2}$ by integrating the above Taylor expansion:

$$\begin{aligned}(\hat{\varphi}_{i-1} + \hat{\varphi}_i)\Delta x &= \int_{x-2\Delta x}^x \varphi(x)dx, \\ \hat{\varphi}_i\Delta x &= \int_{x-\Delta x}^x \varphi(x)dx, \\ \hat{\varphi}_{i+1}\Delta x &= \int_x^{x+\Delta x} \varphi(x)dx, \\ (\hat{\varphi}_{i+1} + \hat{\varphi}_{i+2})\Delta x &= \int_x^{x+2\Delta x} \varphi(x)dx,\end{aligned}$$

leading to

$$\hat{\varphi}_{i-1} = [\varphi]_{i+1/2} - \frac{3}{2}\varphi'\Delta x + \frac{7}{6}\varphi''\Delta x^2 - \frac{15}{24}\varphi'''\Delta x^3 + \mathcal{O}(\Delta x^4), \quad (3.10)$$

$$\hat{\varphi}_i = [\varphi]_{i+1/2} - \frac{1}{2}\varphi'\Delta x + \frac{1}{6}\varphi''\Delta x^2 - \frac{1}{24}\varphi'''\Delta x^3 + \mathcal{O}(\Delta x^4), \quad (3.11)$$

$$\hat{\varphi}_{i+1} = [\varphi]_{i+1/2} + \frac{1}{2}\varphi'\Delta x + \frac{1}{6}\varphi''\Delta x^2 + \frac{1}{24}\varphi'''\Delta x^3 + \mathcal{O}(\Delta x^4), \quad (3.12)$$

$$\hat{\varphi}_{i+2} = [\varphi]_{i+1/2} + \frac{3}{2}\varphi'\Delta x + \frac{7}{6}\varphi''\Delta x^2 + \frac{15}{24}\varphi'''\Delta x^3 + \mathcal{O}(\Delta x^4). \quad (3.13)$$

Linear combinations of Eqs. (3.10)–(3.13) with suitable coefficients may be used to determine centered fourth- and second-order approximations of the interface value $[\varphi]_{i+1/2}$ [19]:

$$[\varphi]_{i+1/2}^{\mathcal{O}4} = \frac{7}{12}(\hat{\varphi}_i + \hat{\varphi}_{i+1}) - \frac{1}{12}(\hat{\varphi}_{i+2} + \hat{\varphi}_{i-1}) + \mathcal{O}(\Delta x^4), \quad (3.14)$$

$$[\varphi]_{i+1/2}^{\mathcal{O}2} = \frac{1}{2}(\hat{\varphi}_i + \hat{\varphi}_{i+1}) + \mathcal{O}(\Delta x^2), \quad (3.15)$$

which, evidently, are strictly valid on uniform grids only. With reference to Figure 3.3, the following one-sided third-order approximations, which will be used to compute boundary gradients, can be derived with a similar procedure:

$$[\varphi]_{i+1/2}^{\mathcal{O}3} = \frac{1}{3}\hat{\varphi}_{i+1} + \frac{5}{6}\hat{\varphi}_i - \frac{1}{6}\hat{\varphi}_{i-1} + \mathcal{O}(\Delta x^3). \quad (3.16)$$

$$[\varphi]_{i+3/2}^{\mathcal{O}3} = \frac{11}{6}\hat{\varphi}_{i+1} - \frac{7}{6}\hat{\varphi}_i + \frac{1}{3}\hat{\varphi}_{i-1} + \mathcal{O}(\Delta x^3), \quad (3.17)$$

the last relation being obtained by first deriving the FV Taylor expansion around the interface point $[\varphi]_{i+3/2}$.

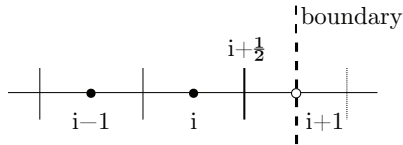


Figure 3.3: Three-nodes boundary stencil (Δx). The open symbol indicate the additional exterior boundary node.

3.1.2 Convective Numerical Fluxes

The numerical flux $\mathcal{FC}_{i+1/2}$ is computed resorting to the fourth-order skew-symmetric-like FV formulation proposed by Ducros et al. [15] on the four-nodes stencil depicted in Figure 3.2:

$$\begin{aligned} \mathcal{FC}_{i+1/2}^{\mathcal{O}4} = & \frac{1}{3} (\hat{\varphi}_i + \hat{\varphi}_{i+1}) (\hat{u}_i + \hat{u}_{i+1}) \\ & - \frac{1}{24} [(\hat{\varphi}_i + \hat{\varphi}_{i+2}) (\hat{u}_i + \hat{u}_{i+2}) + (\hat{\varphi}_{i-1} + \hat{\varphi}_{i+1}) (\hat{u}_{i-1} + \hat{u}_{i+1})] \\ & + \frac{1}{3} \left[\frac{1}{2} (\hat{\varphi}_i \hat{u}_i + \hat{\varphi}_{i+1} \hat{u}_{i+1}) - \frac{1}{4} (\hat{\varphi}_i + \hat{\varphi}_{i+1}) (\hat{u}_i + \hat{u}_{i+1}) \right], \end{aligned} \quad (3.18)$$

where $\varphi = \rho\phi$ is the convected quantity and the $\hat{\cdot}$ operator indicates averaging over the control volume. Plugging Eqs. (3.10)–(3.13) into Eq. (3.18), it can be verified that the first two lines in Eq. (3.18)—which is the strict skew-symmetric formulation as it can be verified in the FD context [15]—are equal to³

$$[\varphi u]_{i+1/2} - \frac{1}{12} \varphi' u' \Delta x^2 + \mathcal{O}(\Delta x^4),$$

and the third line is equal to

$$\frac{1}{12} \varphi' u' \Delta x^2 + \mathcal{O}(\Delta x^4),$$

so that the order of the skew-symmetric-like⁴ formulation above is readily verified:

$$\mathcal{FC}_{i+1/2}^{\mathcal{O}4} = [\varphi u]_{i+1/2} + \mathcal{O}(\Delta x^4).$$

The numerical fluxes on the frontier of the domain are obtained using an additional exterior boundary node (see Figure 3.3)—computed resorting to the 3D-NSCBC procedure [43] which will be presented in detail in Section 3.2—and reducing the order of the scheme. The second-order skew-symmetric-like formulation is then used:

$$\mathcal{FC}_{i+1/2}^{\mathcal{O}2} = \frac{1}{4} (\hat{\varphi}_i + \hat{\varphi}_{i+1}) (\hat{u}_i + \hat{u}_{i+1}), \quad (3.19)$$

which, as it can be immediately verified from Eqs. (3.11) and (3.12), is equivalent to the second-order approximation of the interface flux $[\varphi u]_{i+1/2}$.

³We use the compact notation $[\varphi u]_{i+1/2}$ to indicate $[\varphi]_{i+1/2}[u]_{i+1/2}$.

⁴Strictly speaking, talking of skew-symmetric formulation in the FV context is meaningless as convective fluxes are not computed as $\partial(\varphi u)/\partial x$. This is actually the reason why Eq. (3.18) is referred to as *skew-symmetric-like*: it represent a fourth order approximation of $[\varphi u]_{i+1/2}$, which is formally similar to the FD skew-symmetric scheme.

3.1.3 The Artificial Dissipation Term for LES

In order to suppress spurious oscillations and damp high-frequency modes, the numerical scheme is augmented by the High-Resolution Switched Scheme [76]. This artificial dissipation scheme, originally proposed by Jameson et al. [33], is essentially a blend of fourth- and second-order terms, the former being responsible for high frequency damping and the latter acting in the vicinity of shock waves, if any. The switch between the two terms is done by means of an improved version [74] of the pressure sensor. Moreover, in order to recover a true upwinding for the skew-symmetric-like fourth-order flux, Eq. (3.18), a fourth-order corrective factor $\epsilon^{\mathcal{O}4}$ is added [15].

When the artificial dissipation is active, the convective flux at cell interface $i + 1/2$ is written as:

$$\mathcal{FC}_{i+1/2} = \mathcal{FC}_{i+1/2}^{\mathcal{O}*} - \mathcal{AD}_{i+1/2}, \quad (3.20)$$

where $\mathcal{FC}_{i+1/2}^{\mathcal{O}*}$ is either the fourth- or second-order convective flux computed from Eqs. (3.18)–(3.19) and the artificial dissipation term, for a generic transported variable $\hat{\varphi}$, is defined as:

$$\begin{aligned} \mathcal{AD}_{i+1/2} = & \epsilon_{i+1/2}^{(2)} |\lambda_{i+1/2}| \Delta\varphi_{i+1/2} \\ & - \epsilon_{i+1/2}^{(4)} |\lambda_{i+1/2}| (\Delta\varphi_{i+3/2} - 2\Delta\varphi_{i+1/2} + \Delta\varphi_{i-1/2}) \\ & - \epsilon_{i+1/2}^{\mathcal{O}4} \lambda_{i+1/2} (\Delta\varphi_{i+3/2} - \Delta\varphi_{i-1/2}), \end{aligned} \quad (3.21)$$

with $\Delta\varphi_{i+1/2} = (\hat{\varphi}_{i+1} - \hat{\varphi}_i)$ and

$$\epsilon_{i+1/2}^{(2)} = \min(\alpha_1, \alpha_2 \Psi_{i+1/2}), \quad (3.22)$$

$$\epsilon_{i+1/2}^{(4)} = \max(0, \beta_1 - \beta_2 \epsilon_{i+1/2}^{(2)}), \quad (3.23)$$

$$\epsilon_{i+1/2}^{\mathcal{O}4} = \begin{cases} \frac{1}{6} \epsilon_{i+1/2}^{(2)} & \text{if fourth-order flux is used Eq. (3.18),} \\ 0 & \text{if second-order flux is used Eq. (3.19).} \end{cases} \quad (3.24)$$

The switch $\Psi_{i+1/2}$ is computed as the maximum between the pressure sensors evaluated at cells i and $i + 1$, namely

$$\Psi_{i+1/2} = \max(\Psi_i, \Psi_{i+1}), \quad (3.25)$$

the pressure sensor being defined as:

$$\Psi_i = \frac{|\hat{p}_{i+1} - 2\hat{p}_i + \hat{p}_{i-1}|}{(1 - \omega_\Psi) \mathcal{P}_{\text{TVD}} + \omega_\Psi \mathcal{P}_{\text{JST}} + \epsilon_0}, \quad (3.26)$$

where

$$\mathcal{P}_{\text{TVD}} = |\hat{p}_{i+1} - \hat{p}_i| + |\hat{p}_i - \hat{p}_{i-1}|, \quad (3.27)$$

$$\mathcal{P}_{\text{JST}} = \hat{p}_{i+1} + 2\hat{p}_i + \hat{p}_{i-1}. \quad (3.28)$$

The value of ω_Ψ is typically 0.5 and ϵ_0 is a threshold to ensure that the denominator in Eq. (3.26) cannot be zero. For $\omega_\Psi = 1$ the original JST switch is recovered [33], while for $\omega_\Psi = 0$ a TVD replacement for the switch is obtained [74]; the modified switch is, therefore, a blend of the two.

The variable scaling factor $\lambda_{i+1/2}$ is computed as the convective velocity at cell interface $i + 1/2$, evaluated either from Eq. (3.14) or Eq. (3.15):

$$\lambda_{i+1/2} = \begin{cases} [u]_{i+1/2}^{\mathcal{O}4} & \text{within the computational domain,} \\ [u]_{i+1/2}^{\mathcal{O}2} & \text{at the boundary.} \end{cases} \quad (3.29)$$

In the present work, for all the simulations which have been done using artificial dissipation, the relevant constants have been set at $\alpha_1 = \alpha_2 = 0.5$, $\beta_1 = 0.016$ and $\beta_2 = 1.0$. The α_1 and α_2 coefficients are related to the second-order shock capturing term (first line in Eq. (3.21)) and the relevant values are set in order to scale the diffusion to the upwind level⁵, while β_1 determines the strength of the fourth-order high-frequency damping term (second line in Eq. (3.21)) and β_2 is used to tune the promptness of the scheme in switching off the fourth-order term when a shock wave is detected.

The fourth-order dissipative flux near the boundary is computed resorting to the zeroth-order extrapolation, as suggested by Swanson and Turkel [74]. With reference to Figure 3.3, for instance, the artificial dissipation flux is computed from Eq. (3.21) by simply setting $\Delta\varphi_{i+3/2} = \Delta\varphi_{i+1/2}$:

$$\mathcal{AD}_{i+1/2} = \epsilon_{i+1/2}^{(2)} |\lambda_{i+1/2}| \Delta\varphi_{i+1/2} - \epsilon_{i+1/2}^{(4)} |\lambda_{i+1/2}| (\Delta\varphi_{i-1/2} - \Delta\varphi_{i+1/2}). \quad (3.30)$$

This boundary condition alone produces significant oscillations (see Figure 3.4a) at subsonic non-reflecting inflow and outflow boundaries (*cf.* Section 3.2). Preliminary testing has shown that this numerical noise may be completely eliminated (see Figure 3.4b) by applying a zeroth-order extrapolation, from the interior region, of the *net* artificial dissipation flux at the boundary location. Considering again Figure 3.3, this is actually achieved by subtracting to the convective flux at node $i + 1$ —which is computed using characteristic boundary conditions—a net artificial dissipation term $\Delta_{i+1}^{\mathcal{AD}}$ equal to the one computed in the leftmost neighbor cell:

$$\Delta_{i+1}^{\mathcal{AD}} = \mathcal{AD}_{i+1/2} - \mathcal{AD}_{i-1/2}. \quad (3.31)$$

3.1.4 Viscous Numerical Fluxes

Diffusive fluxes are computed in the following two stages:

⁵Upwinding may be easily checked by switching off the fourth-order term and by setting a uniform velocity u in the vicinity of an hypothetical shock and $\epsilon_{i+1/2}^{(2)} = 1/2$. When the skew-symmetric-like scheme is used, from Eqs. (3.18) and (3.21), we get:

$$\begin{aligned} \mathcal{FC}_{i+1/2}^{\mathcal{O}4} &= \frac{2}{3}u(\hat{\varphi}_i + \hat{\varphi}_{i+1}) - \frac{1}{12}u(\hat{\varphi}_i + \hat{\varphi}_{i+2} + \hat{\varphi}_{i-1} + \hat{\varphi}_{i+1}), \\ \mathcal{AD}_{i+1/2} &= \frac{1}{2}|u|(\hat{\varphi}_{i+1} - \hat{\varphi}_i) - \frac{1}{12}u(\hat{\varphi}_{i+2} - \hat{\varphi}_{i+1} - \hat{\varphi}_i + \hat{\varphi}_{i-1}). \end{aligned}$$

Note that the last term in the above equation is due to the fourth-order corrective factor (third line in Eq. (3.21)). The net numerical flux is then computed from Eq. (3.20) as:

$$\Rightarrow \mathcal{FC}_{i+1/2} = \frac{1}{2}u(\hat{\varphi}_i + \hat{\varphi}_{i+1}) - \frac{1}{2}|u|(\hat{\varphi}_{i+1} - \hat{\varphi}_i) = \begin{cases} u \hat{\varphi}_i & \text{for } u \geq 0, \\ u \hat{\varphi}_{i+1} & \text{for } u < 0. \end{cases}$$

which gives, as expected, a true upwind flux.



Figure 3.4: Normalized pressure map of a convected single-vortex at the instant it goes through a subsonic non-reflecting outflow without specific treatment of the artificial dissipation at the boundary (a) and with zeroth-order extrapolation of the net artificial dissipation flux (b).

1. Gradients are computed resorting to the Gauss' Theorem on the cell's control volume:

$$\int_{\mathcal{V}} \frac{\partial \phi}{\partial x_m} dV = \int_{\mathcal{S}} \phi dS_m \simeq \sum_i [\phi]_i \mathcal{S}_i^m,$$

where, again, the operator $[\cdot]_i$ represent averaging over the i th surface \mathcal{S}_i^m of the control volume \mathcal{V} . In the mono-dimensional case, the last relation leads to the following approximation for the cell-averaged value of the gradient:

$$\left[\frac{\partial \hat{\phi}}{\partial x} \right]_i = \frac{[\phi]_{i+1/2}^{\mathcal{O}4} \mathcal{S}_{i+1/2} - [\phi]_{i-1/2}^{\mathcal{O}4} \mathcal{S}_{i-1/2}}{\mathcal{V}_i}, \quad (3.32)$$

where $[\phi]_{i\pm 1/2}^{\mathcal{O}4}$ are evaluated resorting to the fourth-order average, with Eq. (3.14). It should be noted that, as it can be inferred on a regular mesh where $\mathcal{S}_{i+1/2} = \mathcal{S}_{i-1/2} = \mathcal{S}$ and $\mathcal{V}_i = \mathcal{S} \Delta x$, the above relation gives a third-order approximation of the gradient.

2. Numerical diffusive fluxes at interface $i + 1/2$ are then computed with the fourth-order approximation by applying again Eq. (3.14):

$$\mathcal{FV}_{i+1/2}^{\mathcal{O}4} = \frac{7}{12} \left(\left[\kappa \frac{\partial \hat{\phi}}{\partial x} \right]_i + \left[\kappa \frac{\partial \hat{\phi}}{\partial x} \right]_{i+1} \right) - \frac{1}{12} \left(\left[\kappa \frac{\partial \hat{\phi}}{\partial x} \right]_{i+2} + \left[\kappa \frac{\partial \hat{\phi}}{\partial x} \right]_{i-1} \right), \quad (3.33)$$

where $[\kappa \partial \hat{\phi} / \partial x]_i$ represent the product between the diffusive coefficient and the gradient in the i th cell, *i.e.* $\kappa_i [\partial \hat{\phi} / \partial x]_i$.

At the boundary, gradients are computed switching the scheme to second-order by using one-sided approximations Eqs. (3.16) and (3.17). With reference to Figure 3.3, average

gradients in cell i and the external node $i + 1$ are respectively⁶:

$$\left[\frac{\partial \hat{\phi}}{\partial x} \right]_i = \frac{[\phi]_{i+1/2}^{\mathcal{O}3} \mathcal{S}_{i+1/2} - [\phi]_{i-1/2}^{\mathcal{O}4} \mathcal{S}_{i-1/2}}{\mathcal{V}_i}, \quad (3.34)$$

$$\left[\frac{\partial \hat{\phi}}{\partial x} \right]_{i+1} = \frac{[\phi]_{i+3/2}^{\mathcal{O}3} \mathcal{S}_{i+1/2} - [\phi]_{i+1/2}^{\mathcal{O}3} \mathcal{S}_{i-1/2}}{\mathcal{V}_{i+1}}. \quad (3.35)$$

Moreover, numerical diffusive fluxes at the last fluid-cell interface before the boundary are computed with the third-order approximation by applying again Eq. (3.16):

$$\mathcal{FV}_{i+1/2}^{\mathcal{O}3} = \frac{1}{3} \left[\kappa \frac{\partial \hat{\phi}}{\partial x} \right]_{i+1} + \frac{5}{6} \left[\kappa \frac{\partial \hat{\phi}}{\partial x} \right]_i - \frac{1}{6} \left[\kappa \frac{\partial \hat{\phi}}{\partial x} \right]_{i-1}. \quad (3.36)$$

Normal diffusive fluxes at the boundary location are computed either by imposing the relevant boundary condition (*e.g.*, zero heat flux is imposed on adiabatic walls) or by computing $\mathcal{FV}_{i+3/2}^{\mathcal{O}3}$ using Eq. (3.17), which leads to the second-order one sided difference approximation (*cf.* Footnote 6):

$$\begin{aligned} \left[\frac{\partial}{\partial x} \left(\kappa \frac{\partial \hat{\phi}}{\partial x} \right) \right]_{i+1} &= \frac{\mathcal{FV}_{i+3/2}^{\mathcal{O}3} \mathcal{S}_{i+3/2} - \mathcal{FV}_{i+3/2}^{\mathcal{O}3} \mathcal{S}_{i+3/2}}{\mathcal{V}_i} \\ &= \frac{1}{2\Delta x} \left(3 \left[\kappa \frac{\partial \hat{\phi}}{\partial x} \right]_{i+1} - 4 \left[\kappa \frac{\partial \hat{\phi}}{\partial x} \right]_i + \left[\kappa \frac{\partial \hat{\phi}}{\partial x} \right]_{i-1} \right). \end{aligned} \quad (3.37)$$

3.1.5 Time Integration

The solution is advanced in time using the third-order TVD (Total Variation Diminishing) Runge-Kutta scheme proposed by Gottlieb and Shu [26], which is briefly summarized in this section.

Introducing a first-order approximation of the time derivative, Eq. (3.8) may be conveniently written as:

$$\frac{\hat{\phi}_i^{n+1} - \hat{\phi}_i^n}{\Delta t} + \mathfrak{R}_i(\varphi^n) = 0, \quad (3.38)$$

where the residual \mathfrak{R} includes convective and diffusive fluxes, as well as, the artificial dissipation and source terms, if any, and φ^n represents the solution of the numerical simulation at the n th

⁶Considering a regular mesh, Eq. (3.35) reduces to:

$$\left[\frac{\partial \hat{\phi}}{\partial x} \right]_{i+1} = \frac{3\hat{\phi}_{i+1} - 4\hat{\phi}_i + \hat{\phi}_{i-1}}{2\Delta x} + \mathcal{O}(\Delta x^2),$$

which is formally identical to the one-sided second-order FD approximation of the gradient (the only difference being the *hat* operator on the variable ϕ). This is consistent with the observation that FD and FV approximations can be confused up to the second-order [15].

time-step⁷. Time integration is then performed through the following three steps:

$$\hat{\varphi}_i^{(1)} = \hat{\varphi}_i^n - \Delta t \mathfrak{R}_i(\varphi^n), \quad (3.39)$$

$$\hat{\varphi}_i^{(2)} = \frac{3}{4}\hat{\varphi}_i^n + \frac{1}{4}\hat{\varphi}_i^{(1)} - \frac{1}{4}\Delta t \mathfrak{R}_i(\varphi^{(1)}), \quad (3.40)$$

$$\hat{\varphi}_i^{n+1} = \frac{1}{3}\hat{\varphi}_i^n + \frac{2}{3}\hat{\varphi}_i^{(2)} - \frac{2}{3}\Delta t \mathfrak{R}_i(\varphi^{(2)}), \quad (3.41)$$

The time-step is limited by the Courant-Friedrichs-Lewy (CFL) condition involving an inviscid time $\Delta t_{\mathcal{I}}$ and a viscous time $\Delta t_{\mathcal{V}}$:

$$\frac{\Delta t}{\min(\Delta t_{\mathcal{I}}, \Delta t_{\mathcal{V}})} \leq \mathcal{C}, \quad (3.42)$$

where \mathcal{C} is the CFL coefficient⁸. The inviscid and viscous time-steps are respectively:

$$\Delta t_{\mathcal{I}} = \frac{\mathcal{V}_{i,j,k}}{\sum_m (|\hat{u}_m| + \hat{a}) \mathcal{S}_{i,j,k}^m}, \quad (3.43)$$

$$\Delta t_{\mathcal{V}} = \frac{\hat{\rho} \mathcal{V}_{i,j,k}^2}{2\hat{\mu}_{\text{eff}} \sum_m (\mathcal{S}_{i,j,k}^m \mathcal{S}_{i,j,k}^m)}, \quad (3.44)$$

where the *hat* operator implies volume averaging within $\mathcal{V}_{i,j,k}$, $a = \sqrt{\gamma p/\rho}$ is the speed of sound and $\hat{\mu}_{\text{eff}}$ is the effective dynamic viscosity, which, when Large-Eddy Simulation is performed, includes the contribution of sub-grid viscosity (*cf.* Chapter 4), namely

$$\mu_{\text{eff}} = \begin{cases} \mu & \text{for DNS,} \\ \bar{\mu} + \frac{1}{2} \left| \frac{\sum_l \sum_m \tau_{lm}^d \tilde{A}_{lm}}{\sum_l \sum_m \tilde{A}_{lm} \tilde{A}_{lm}} \right| & \text{for LES}^9. \end{cases} \quad (3.45)$$

3.2 Characteristic Boundary Conditions

The treatment of boundary conditions is one of the most recurrent issues in computational fluid dynamics. Compressible solvers' accuracy, in general, is strongly sensitive to boundary solution, which may be spoiled by spurious numerical reflections generated at open boundaries.

High-order numerical schemes widely used in Direct Numerical Simulation (DNS) and Large-Eddy Simulation (LES), do not dissipate the spurious modes that may be generated at the boundaries and hence, boundary conditions must ensure that physically correct solutions

⁷In general, the residual at cell i is a function of the solution over a certain number of physically neighbor points, the number depending on the used stencil in the discretization scheme.

⁸In the present formulation, the maximum CFL coefficient for the scheme to be TVD is 1 [26].

⁹The formula used to compute the sub-grid viscosity is designed to account for the additional difficulties related to the use of similarity mixed models (*cf.* Section 4.4.1). It is worth underlining that, in the case of eddy-viscosity models, the sub-grid viscosity is automatically recovered:

$$\frac{1}{2} \left| \frac{\sum_l \sum_m \tau_{lm}^d \tilde{A}_{lm}}{\sum_l \sum_m \tilde{A}_{lm} \tilde{A}_{lm}} \right| = \frac{1}{2} \left| \frac{\sum_l \sum_m 2\bar{\rho}\nu_t \tilde{A}_{lm} \tilde{A}_{lm}}{\sum_l \sum_m \tilde{A}_{lm} \tilde{A}_{lm}} \right| = \bar{\rho}\nu_t.$$

are produced, while minimizing the amplitude of any extraneous perturbation. Moreover, in DNS and LES a wide range of length and time scales is resolved and transported by the flow; the open boundaries are therefore invested with a complex set of sound and entropy waves and convected vorticity. Any excess in numerical reflection can lead to the buildup of spurious oscillations, thus negatively affect the physical properties of the flow itself.

Several approaches have been proposed to tackle boundary conditions. Many of them are oriented toward the definition of transparent frontiers for Computational Aero-Acoustics (CAA), where the high standards in this regard, make the task particularly challenging (see Bogy and Bailly [6], Hixon et al. [31], Nicoud [52], Tam [75] for review and applications). Among them, techniques based on characteristics waves have motivated much attention. Initially developed for hyperbolic systems of Euler equations, these approaches decompose the flow in terms of characteristic waves traveling in the direction normal to the boundary, thus reducing the boundary problem to a suitable imposition of the incoming waves. The identification of incoming waves allows a direct control over boundary reflection, as the boundary condition can be designed to prevent incoming perturbations or to damp their amplitude while allowing smooth transients [62, 78, 79]. The extension to the Navier-Stokes equations was then developed, by accounting for viscous terms, leading to the Navier-Stokes Characteristic Boundary Conditions (NSCBC) [5, 54, 58, 73]. A “plane masking” approach for the linear relaxation term was proposed by Polifke et al. [59] in order to reduce of the reflection coefficient low-frequency normal incident waves. A low Mach number expansion has been discussed by Prosser [60], in order to decouple convective and acoustic effects, thus allowing non-reflective conditions for the acoustic length scales.

These methods mostly rely on the assumption that the flow at the boundary can be regarded as Locally One-Dimensional and Inviscid. While, this assumption has proven to perform well when the flow is almost aligned orthogonally to the boundary, flow distortion and high reflection may appear when the flow crosses the boundary along different directions. The role played by the transverse terms was carefully identified by Yoo and Im [84], Yoo et al. [85], who proposed a modification to the NSCBC approach. They showed that an appropriate treatment of the transverse and source terms in the computation of incoming waves improves the accuracy and convergence rate toward target values for selected relaxed quantities, while reducing flow distortion even in regions characterized by strong transverse convection.

Within the framework of the NSCBC procedure [58], the Navier-Stokes equations are rewritten in such a way that their dependency on the characteristic waves traveling across the boundary is made explicit. As it will be shown in more detail in the following sections, characteristic waves are represented by their amplitude time variations \mathcal{L}_i , \mathcal{M}_i and \mathcal{N}_i , corresponding to the three physical-space directions with the subscript ‘ i ’ ranging from 1 to the total number of transport equations used; with reference to Eqs. (2.15) and (2.16) then, there will be a total of 6 characteristic waves in each coordinate direction. In the most general case, *i.e.*, when the characteristic waves traveling along the three coordinate directions are considered altogether, the Navier-Stokes equations assume the form

$$\frac{\partial \mathbf{u}}{\partial t} + \mathbf{f}^1(\mathcal{L}_i) + \mathbf{f}^2(\mathcal{M}_i) + \mathbf{f}^3(\mathcal{N}_i) + \mathcal{D} = \mathbf{0}, \quad (3.46)$$

where \mathbf{u} is the vector of primitive variables¹⁰, \mathbf{f}^k represents the explicit functional relation

¹⁰As it will be shown in the following sections, a formally identical relation may be obtained for conservative variables too (*cf.* Eqs. (3.161) and (3.162)).

existing between convective terms—and pressure gradients—along the k th direction and the relevant characteristic waves and \mathcal{D} includes viscous and diffusive terms only.

A point located on the frontier of the computational domain, the waves propagate in such a way that some of them leave the domain, while the others enter from outside. As outgoing waves can be computed from interior points and one-sided differences by directly applying their definition (*cf.* Eqs. (3.35), (3.66), (3.112) and (3.160)), the boundary problem is reduced to the development of strategies and physical—or numerical—conditions which allow the computation of the unknown incoming waves. Once all the wave amplitude variations and the vector \mathcal{D} are computed, the solution can be advanced in time. Then, the following key points may be identified:

- definition of boundary conditions that allow the computation of all the incoming wave amplitude variations;
- definition of strategies and/or boundary conditions in order to compute viscous and diffusive terms at the boundary.

With regard to the first point, the standard NSCBC approach proposed by Poinot and Lele [58] prescribes that all the incoming wave amplitudes are imposed under the hypothesis that the flow at the boundary can be regarded as Locally One-Dimensional and Inviscid. If the boundary is normal to the x_1 direction, under these hypotheses, \mathbf{f}^2 , \mathbf{f}^3 and \mathcal{D} in Eq. (3.46) are neglected leading to the following relation:

$$\frac{\partial \mathcal{U}}{\partial t} + \mathbf{f}^1(\mathcal{L}_i) = \mathbf{0}. \quad (3.47)$$

The above equation, the so called LODI system (see Eq. (3.71) for more details), represents a direct link between characteristic waves traveling across the boundary and time derivatives of primitive variables, and may be used to translate physical boundary conditions—corresponding to Euler boundary conditions—expressed in terms of time derivatives of the primitive variables, into analytical relations involving the wave amplitude variations, such that the unknown incoming ones can be computed. Well-posedness of boundary conditions for Navier-Stokes equations is then ensured by supplying the necessary additional viscous conditions, thus allowing the computation of the \mathcal{D} term.

When the flow is strongly three-dimensional at boundaries, the LODI assumption becomes too restrictive to keep boundary reflection at an acceptable level and unphysical flow distortions appear, especially in regions where the flow is not aligned with the direction normal to the boundary (*cf.* Figure 3.5). From a mathematical point of view, there appears a residual term \mathcal{R} in the LODI system and this residual, which includes transverse convection and pressure gradients¹¹, is no more negligible:

$$\frac{\partial \mathcal{U}}{\partial t} + \mathbf{f}^1(\mathcal{L}_i) = \mathcal{R}. \quad (3.48)$$

Apart from the already mentioned problems of flow distortion and numerical reflection, in regions where strong convection in the boundary plane exists, this residual may negatively affect

¹¹We will assume that diffusive and viscous effects can be still considered to be much weaker than convection and pressure gradients.

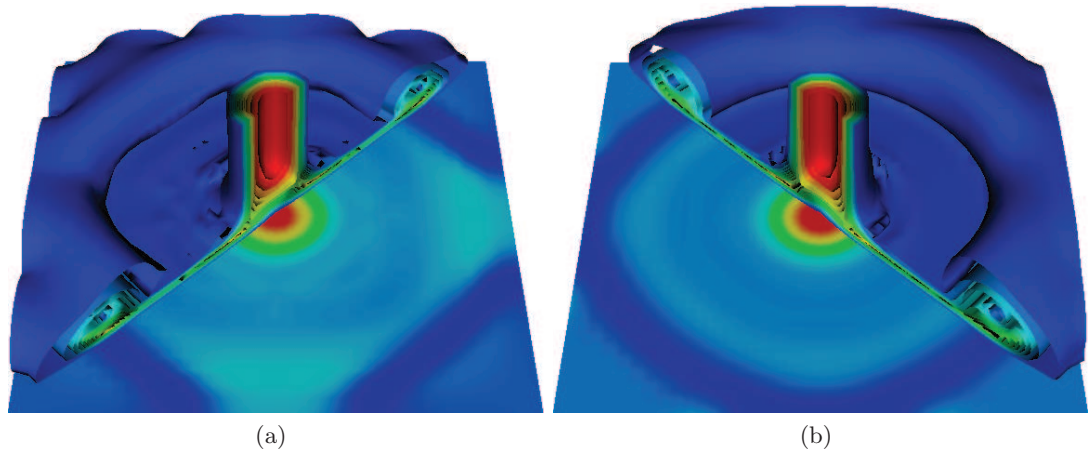


Figure 3.5: Impinging jet simulation using standard LODI non-reflecting outflow boundary conditions (a) and modified NSCBC accounting for transverse effects (b): iso-surfaces of velocity colored by velocity magnitude and pressure map over the impingement wall.

the convergence rate and the accuracy of boundary relaxed quantities¹² toward their physical target value. This problem can be easily shown considering, for simplicity, one single wave propagation direction as follows. With reference to the above equation, a linear transformation \mathbf{A} is introduced in order to have one single wave amplitude variation in each equation:

$$\mathbf{A} \frac{\partial \mathbf{U}}{\partial t} + \mathcal{L} = \mathcal{R}^*, \quad (3.49)$$

where \mathcal{L} is the vector of components \mathcal{L}_i and $\mathcal{R}^* = \mathbf{A} \cdot \mathcal{R}$ is the transformed residual. In the standard NSCBC approach, if we consider the subset \mathcal{L}_{in} of incoming waves, relaxation may be expressed as

$$\mathcal{L}_{\text{in}} = \sigma (\mathbf{U}_{\text{in}} - \mathbf{U}_{\text{in}}^\infty), \quad (3.50)$$

where σ is a matrix defining the relaxation coefficients, \mathbf{U}_{in} is the vector of boundary imposed quantities involved in the computation of incoming waves¹³ and $\mathbf{U}_{\text{in}}^\infty$ represents the relevant target values. In the steady solution limit, if any, *i.e.* when $\partial \mathbf{U} / \partial t \rightarrow \mathbf{0}$, from Eqs. (3.49) and (3.50) we get

$$\lim_{t \rightarrow \infty} \mathbf{U}_{\text{in}} = \mathbf{U}_{\text{in}}^\infty + \sigma^{-1} \mathcal{R}_{\text{in}}^*, \quad (3.51)$$

where $\mathcal{R}_{\text{in}}^*$ is the subset of transverse terms involved in the computation of incoming waves. From the above relation it is evident how strong convection and pressure gradients in the boundary planes will prevent relaxed quantities from reaching the relevant target values unless the relaxation coefficient are high enough to sufficiently reduce the effect of $\mathcal{R}_{\text{in}}^*$, thus increasing the overall level of boundary reflection [59].

¹²Relaxed quantities are often used within characteristic boundary conditions in order to reduce numerical reflection while ensuring convergence of boundary parameters toward prescribed physical states.

¹³In general, \mathbf{U}_{in} may contain either a subset of the components of \mathbf{U} or other physical quantities suitable for the computation of incoming waves.

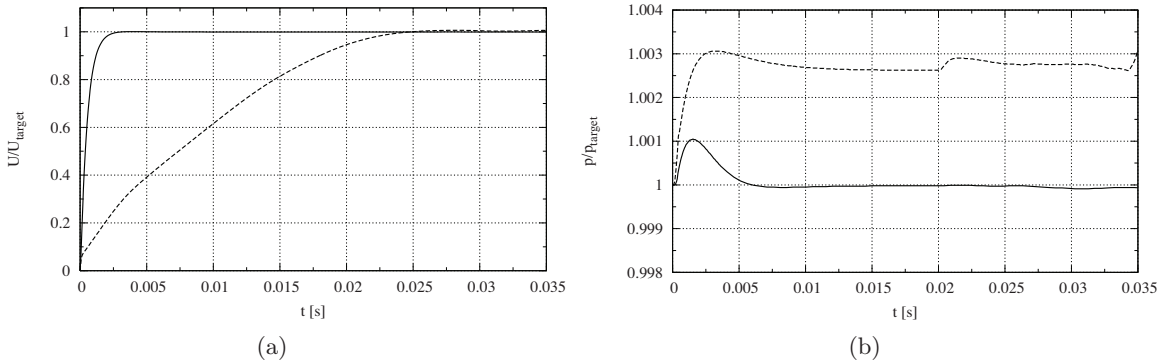


Figure 3.6: Transverse terms influence on boundary accuracy. Time evolution of the normalized computed inlet velocity (a) and outlet pressure (b): ---- standard LODI assumption; — modified NSCBC accounting for transverse effects.

Provided that the $\mathcal{R}_{\text{in}}^*$ terms can be computed at the boundary, the above mentioned problems may be, in principle, solved by including transverse effects in the computation of incoming waves

$$\mathcal{L}_{\text{in}} = \sigma(\mathbf{U}_{\text{in}} - \mathbf{U}_{\text{in}}^{\infty}) + \mathcal{R}_{\text{in}}^*; \quad (3.52)$$

in this way, transverse effects cancel out and the correct target values can be enforced at the boundaries. This is, in summary, what was proposed by Yoo et al. [85] for two-dimensional computations of counterflow flames and then extended to include also transverse diffusion and source terms [84]. Figure 3.6 shows the impact, in terms of convergence toward target values, when transverse effects are neglected in the simulation of an impinging round jet: if, at the inflow, the convergence toward the inlet target velocity is only delayed (during the initial transient the jet tends to spread radially but, eventually, the velocity becomes axially aligned, thus making transverse terms gradually disappear), at the outflow the target pressure is never recovered, because the established flow field is radially oriented (*cf.* Figure 3.5).

Away from edges and corners of the computational domain, transverse terms can be evaluated from the computed solution using interior points. This direct approach, indeed, does not pose additional issues for inlet boundaries but, as already mentioned by Yoo et al. [85], can lead to serious numerical instabilities at outflow boundaries. One effective remedy for this is to add a small relaxation toward a reference value for the transverse terms, thus introducing a transverse damping coefficient β_t , which is directly linked to the typical Mach number in the flow under study [43, 84].

If the inclusion of transverse effects within boundary conditions does not poses particular problems for points located inside a boundary plane, where transverse convective fluxes and pressure gradients are immediately available from in-plane points, at the edges and the corners of the computational domain a specific treatment is, however, necessary. At these locations in fact, transverse terms in a given boundary plane may relate to characteristic waves traveling along directions that are orthogonal to adjacent boundary planes, thus introducing a coupling between characteristic waves traveling along different directions [80]. Moreover, when different types of boundary conditions have to be enforced, it is in general necessary to prescribe compatibility conditions when well-posedness is not inherently ensured. The 3D-NSCBC approach,

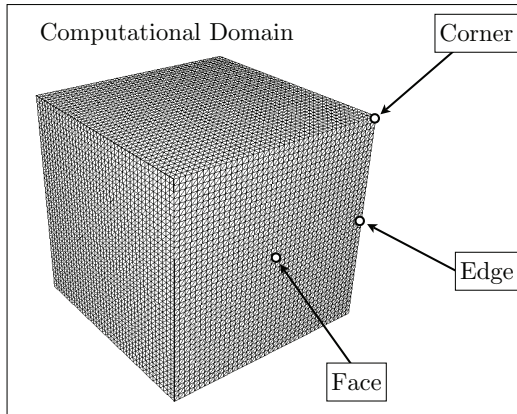


Figure 3.7: Schematic representation of a 3D computational domain.

which will be presented in the following sections, represents a systematic procedure to address 3D characteristic wave coupling and to derive the relevant boundary conditions.

A detailed review of the three-dimensional characteristic formulation of the Navier-Stokes equations is first presented, then the boundary treatment for nodes away from edges and corners will be addressed and, finally, a specific methodology will be proposed for boundary edges (two orthogonal characteristic directions) and corners (three orthogonal characteristic directions).

3.2.1 3D Characteristics

In order to transform the Navier-Stokes equations in characteristic form, it is convenient to reduce conservation laws expressed by Eq. (2.15) in quasi-linear form, apply the transformation matrix from conservative variables to primitive variables and then diagonalize the non-conservative Jacobian matrices [30, 78, 79]. In this way, conservation laws are reformulated such that their dependency on characteristic waves becomes explicit. As it will be shown, the characteristic formulation in both conservative and primitive variables can be readily derived by applying the relevant transformation matrix (namely \mathbf{P} , in what follows).

Let the vector of primitive variables be

$$\mathbf{u} = (\rho \quad u_1 \quad u_2 \quad u_3 \quad p \quad Z)^T,$$

as it can be easily verified, the transformation matrix $\mathbf{P} = \partial \mathbf{U} / \partial \mathbf{u}$, *i.e.* the Jacobian matrix to switch between primitive and conservative variables, reads

$$\mathbf{P} = \begin{pmatrix} 1 & 0 & 0 & 0 & 0 & 0 \\ u_1 & \rho & 0 & 0 & 0 & 0 \\ u_2 & 0 & \rho & 0 & 0 & 0 \\ u_3 & 0 & 0 & \rho & 0 & 0 \\ \frac{1}{2}u_k u_k & \rho u_1 & \rho u_2 & \rho u_3 & 1/\varkappa & 0 \\ Z & 0 & 0 & 0 & 0 & \rho \end{pmatrix}, \quad (3.53)$$

and the relevant inverse matrix is

$$\mathbf{P}^{-1} = \begin{pmatrix} 1 & 0 & 0 & 0 & 0 & 0 \\ -u_1/\rho & 1/\rho & 0 & 0 & 0 & 0 \\ -u_2/\rho & 0 & 1/\rho & 0 & 0 & 0 \\ -u_3/\rho & 0 & 0 & 1/\rho & 0 & 0 \\ \frac{\varkappa}{2}u_k u_k & -\varkappa u_1 & -\varkappa u_2 & -\varkappa u_3 & \varkappa & 0 \\ -Z/\rho & 0 & 0 & 0 & 0 & 1/\rho \end{pmatrix}, \quad (3.54)$$

with $\varkappa = \gamma - 1$.

The quasi-linear form of the Navier-Stokes equations may be obtained pre-multiplying Eq. (2.15) by \mathbf{P}^{-1} and using the identity $\mathbf{P}^{-1}\partial\mathbf{U}/\partial\mathbf{U} = \mathbf{I}^{14}$:

$$\frac{\partial\mathbf{U}}{\partial t} + \mathcal{F}^j \frac{\partial\mathbf{U}}{\partial x_j} + \mathcal{D} = \mathbf{0} \quad (3.55)$$

where

$$\mathcal{D} = \mathbf{P}^{-1} \frac{\partial\mathcal{D}^i}{\partial x_i}$$

includes all the viscous and diffusive terms and $\mathcal{F}^k = \partial\mathbf{F}^k/\partial\mathbf{U}$ is the non-conservative Jacobian matrix relevant to the k th direction. In the present case, we get:

$$\mathcal{F}^k = \begin{pmatrix} u_k & \delta_{1k}\rho & \delta_{2k}\rho & \delta_{3k}\rho & 0 & 0 \\ 0 & u_k & 0 & 0 & \delta_{1k}/\rho & 0 \\ 0 & 0 & u_k & 0 & \delta_{2k}/\rho & 0 \\ 0 & 0 & 0 & u_k & \delta_{3k}/\rho & 0 \\ 0 & \delta_{1k}\gamma p & \delta_{2k}\gamma p & \delta_{3k}\gamma p & u_k & 0 \\ 0 & 0 & 0 & 0 & 0 & u_k \end{pmatrix}. \quad (3.56)$$

The characteristic form is finally obtained after diagonalizing the non-conservative Jacobian matrices \mathcal{F}^k , that is, looking for the linear transformation \mathbf{S}_k that satisfy the following identity:

$$\mathbf{S}_k^{-1} \mathcal{F}^k \mathbf{S}_k = \mathbf{\Lambda}^k \quad (3.57)$$

where $\mathbf{\Lambda}^k$ is a diagonal matrix of the eigenvalues of \mathcal{F}^k . In the present case, if $a = \sqrt{\gamma p/\rho}$ is the speed of sound, we find:

$$\mathbf{\Lambda}^k = \begin{pmatrix} u_k - a & 0 & 0 & 0 & 0 & 0 \\ 0 & u_k & 0 & 0 & 0 & 0 \\ 0 & 0 & u_k & 0 & 0 & 0 \\ 0 & 0 & 0 & u_k & 0 & 0 \\ 0 & 0 & 0 & 0 & u_k + a & 0 \\ 0 & 0 & 0 & 0 & 0 & u_k \end{pmatrix}, \quad (3.58)$$

$$\mathbf{S}_k = \begin{pmatrix} 1/(2a^2) & \delta_{1k}/a^2 & \delta_{2k}/a^2 & \delta_{3k}/a^2 & 1/(2a^2) & 0 \\ -\delta_{1k}/(2\rho a) & 1 - \delta_{1k} & 0 & 0 & \delta_{1k}/(2\rho a) & 0 \\ -\delta_{2k}/(2\rho a) & 0 & 1 - \delta_{2k} & 0 & \delta_{2k}/(2\rho a) & 0 \\ -\delta_{3k}/(2\rho a) & 0 & 0 & 1 - \delta_{3k} & \delta_{3k}/(2\rho a) & 0 \\ 1/2 & 0 & 0 & 0 & 1/2 & 0 \\ 0 & 0 & 0 & 0 & 0 & 1 \end{pmatrix}, \quad (3.59)$$

¹⁴ \mathbf{I} represents the identity matrix.

and

$$\mathbf{S}_k^{-1} = \begin{pmatrix} 0 & -\delta_{1k}\rho a & -\delta_{2k}\rho a & -\delta_{3k}\rho a & 1 & 0 \\ \delta_{1k}a^2 & 1 - \delta_{1k} & 0 & 0 & -\delta_{1k} & 0 \\ \delta_{2k}a^2 & 0 & 1 - \delta_{2k} & 0 & -\delta_{2k} & 0 \\ \delta_{3k}a^2 & 0 & 0 & 1 - \delta_{3k} & -\delta_{3k} & 0 \\ 0 & \delta_{1k}\rho a & \delta_{2k}\rho a & \delta_{3k}\rho a & 1 & 0 \\ 0 & 0 & 0 & 0 & 0 & 1 \end{pmatrix}. \quad (3.60)$$

Depending on the type of boundary condition considered (face, edge or corner), a different number of characteristic directions should be taken into account (one, two or three) simultaneously: the three cases are summarized in the following sections.

3.2.2 Characteristic Formulation Along One Direction for Faces

In the most simple case where the computational point is located inside the boundary surface, a single characteristic direction has to be taken into account, namely the direction orthogonal to the boundary itself. Supposing that the boundary is orthogonal to the x_1 direction, the characteristic waves considered will be those traveling along x_1 ; therefore only \mathcal{F}^1 needs to be diagonalized and Eq. (3.55) can be written as:

$$\frac{\partial \mathcal{U}}{\partial t} + \mathbf{S}_1 \mathbf{\Lambda}^1 \mathbf{S}_1^{-1} \frac{\partial \mathcal{U}}{\partial x_1} + \mathcal{F}^2 \frac{\partial \mathcal{U}}{\partial x_2} + \mathcal{F}^3 \frac{\partial \mathcal{U}}{\partial x_3} + \mathcal{D} = \mathbf{0}, \quad (3.61)$$

where the diagonal matrix of the eigenvalues, *i.e.* the propagation velocities of the characteristic waves, and the transformation matrices are obtained from Eqs. (3.58)– (3.60):

$$\mathbf{\Lambda}^1 = \begin{pmatrix} u_1 - a & 0 & 0 & 0 & 0 & 0 \\ 0 & u_1 & 0 & 0 & 0 & 0 \\ 0 & 0 & u_1 & 0 & 0 & 0 \\ 0 & 0 & 0 & u_1 & 0 & 0 \\ 0 & 0 & 0 & 0 & u_1 + a & 0 \\ 0 & 0 & 0 & 0 & 0 & u_1 \end{pmatrix}, \quad (3.62)$$

$$\mathbf{S}_1 = \begin{pmatrix} 1/(2a^2) & 1/a^2 & 0 & 0 & 1/(2a^2) & 0 \\ -1/(2\rho a) & 0 & 0 & 0 & 1/(2\rho a) & 0 \\ 0 & 0 & 1 & 0 & 0 & 0 \\ 0 & 0 & 0 & 1 & 0 & 0 \\ 1/2 & 0 & 0 & 0 & 1/2 & 0 \\ 0 & 0 & 0 & 0 & 0 & 1 \end{pmatrix}, \quad (3.63)$$

$$\mathbf{S}_1^{-1} = \begin{pmatrix} 0 & -\rho a & 0 & 0 & 1 & 0 \\ a^2 & 0 & 0 & 0 & -1 & 0 \\ 0 & 0 & 1 & 0 & 0 & 0 \\ 0 & 0 & 0 & 1 & 0 & 0 \\ 0 & \rho a & 0 & 0 & 1 & 0 \\ 0 & 0 & 0 & 0 & 0 & 1 \end{pmatrix}. \quad (3.64)$$

Following the procedure proposed by Thompson [78], a vector \mathcal{L} may be conveniently defined as

$$\mathcal{L} = \Lambda^1 \mathbf{S}_1^{-1} \frac{\partial \mathcal{U}}{\partial x_1} \quad (3.65)$$

whose components \mathcal{L}_i are the amplitude time variations of the characteristic waves [58]:

$$\mathcal{L} = \begin{pmatrix} \lambda_1 \left(\frac{\partial p}{\partial x_1} - \rho a \frac{\partial u_1}{\partial x_1} \right) \\ \lambda_2 \left(a^2 \frac{\partial \rho}{\partial x_1} - \frac{\partial p}{\partial x_1} \right) \\ \lambda_3 \frac{\partial u_2}{\partial x_1} \\ \lambda_4 \frac{\partial u_3}{\partial x_1} \\ \lambda_5 \left(\frac{\partial p}{\partial x_1} + \rho a \frac{\partial u_1}{\partial x_1} \right) \\ \lambda_6 \frac{\partial Z}{\partial x_1} \end{pmatrix}, \quad (3.66)$$

where λ_i are the eigenvalues.

Eq. (3.61) is finally rewritten as a function of the wave amplitude variations and the relevant formulation in terms of conservative variables can be obtained pre-multiplying by \mathbf{P} :

$$\frac{\partial \mathcal{U}}{\partial t} + \mathbf{d} + \mathcal{F}^2 \frac{\partial \mathcal{U}}{\partial x_2} + \mathcal{F}^3 \frac{\partial \mathcal{U}}{\partial x_3} + \mathcal{D} = \mathbf{0}, \quad (3.67)$$

$$\frac{\partial \mathbf{U}}{\partial t} + \mathbf{P} \mathbf{d} + \frac{\partial \mathbf{F}^2}{\partial x_2} + \frac{\partial \mathbf{F}^3}{\partial x_3} + \frac{\partial \mathbf{D}^i}{\partial x_i} = \mathbf{0}, \quad (3.68)$$

where

$$\mathbf{d} = \mathbf{S}_1 \mathcal{L} = \begin{pmatrix} \frac{1}{a^2} \left[\mathcal{L}_2 + \frac{1}{2} (\mathcal{L}_5 + \mathcal{L}_1) \right] \\ \frac{1}{2\rho a} (\mathcal{L}_5 - \mathcal{L}_1) \\ \mathcal{L}_3 \\ \mathcal{L}_4 \\ \frac{1}{2} (\mathcal{L}_5 + \mathcal{L}_1) \\ \mathcal{L}_6 \end{pmatrix}, \quad (3.69)$$

and

$$\mathbf{P} \mathbf{d} = \begin{pmatrix} d_1 \\ d_1 u_1 + \rho d_2 \\ d_1 u_2 + \rho d_3 \\ d_1 u_3 + \rho d_4 \\ d_1 \frac{u_k u_k}{2} + \rho u_j d_{j+1} + \frac{d_5}{\gamma - 1} \\ d_1 Z + \rho d_6 \end{pmatrix}. \quad (3.70)$$

Recalling what has been said in the previous section regarding the Locally One-Dimensional and Inviscid assumption of the standard NSCBC procedure [58], the analytical formulation of

the LODI system, for the actual specific choice of primitive variables, can be immediately derived from Eq. (3.67) by simply neglecting transverse derivatives and diffusive terms:

$$\left\{ \begin{array}{l} \frac{\partial \rho}{\partial t} + \frac{1}{a^2} \left[\mathcal{L}_2 + \frac{1}{2} (\mathcal{L}_5 + \mathcal{L}_1) \right] = 0 \\ \frac{\partial u_1}{\partial t} + \frac{1}{2\rho a} (\mathcal{L}_5 - \mathcal{L}_1) = 0 \\ \frac{\partial u_2}{\partial t} + \mathcal{L}_3 = 0 \\ \frac{\partial u_3}{\partial t} + \mathcal{L}_4 = 0 \\ \frac{\partial p}{\partial t} + \frac{1}{2} (\mathcal{L}_5 + \mathcal{L}_1) = 0 \\ \frac{\partial Z}{\partial t} + \mathcal{L}_6 = 0 \end{array} \right. \quad (3.71)$$

Face Boundary Conditions

In the present section, we will make a brief review of the procedure to be followed in order to design boundary conditions accounting for transverse effects when one single direction is to be considered for characteristic waves' propagation, that is, for computational nodes located within a boundary face; we will assume, for the sake of simplicity, that this direction coincides with x_1 , *i.e.*, the boundary is orthogonal to x_1 . This is the first natural step toward the development of boundary conditions involving two characteristic directions (for edge nodes) and three characteristic directions (for corner nodes) and it constitutes, basically, the procedure proposed by Yoo et al. [85].

It is worthwhile stressing again that the numerical solution at the boundary is anyway advanced in time using the full Navier-Stokes equations (3.67) or (3.68). In order to do so, all the wave amplitude variations \mathcal{L}_i needs to be computed; since the outgoing waves can be computed from interior points using one-sided derivatives and Eq. (3.66), the boundary problem is reduced to the computation of incoming waves. More precisely, we need a set of relations linking the wave amplitude variations to primitive variables, which are generally more suitable for physical boundary conditions to be enforced. These relations are obtained from Eq. (3.67) by neglecting viscous and diffusive terms, namely the \mathcal{D} vector, only (*cf.* Eq. (3.71)):

$$\frac{\partial \mathcal{U}}{\partial t} + \mathbf{d} - \mathcal{T} = \mathbf{0}, \quad (3.72)$$

or, in components,

$$\left\{ \begin{array}{l} \frac{\partial \rho}{\partial t} + \frac{1}{a^2} \left[\mathcal{L}_2 + \frac{1}{2} (\mathcal{L}_5 + \mathcal{L}_1) \right] - \mathcal{T}_1 = 0 \\ \frac{\partial u_1}{\partial t} + \frac{1}{2\rho a} (\mathcal{L}_5 - \mathcal{L}_1) - \mathcal{T}_2 = 0 \\ \frac{\partial u_2}{\partial t} + \mathcal{L}_3 - \mathcal{T}_3 = 0 \\ \frac{\partial u_3}{\partial t} + \mathcal{L}_4 - \mathcal{T}_4 = 0 \\ \frac{\partial p}{\partial t} + \frac{1}{2} (\mathcal{L}_5 + \mathcal{L}_1) - \mathcal{T}_5 = 0 \\ \frac{\partial Z}{\partial t} + \mathcal{L}_6 - \mathcal{T}_6 = 0 \end{array} \right. \quad (3.73)$$

where the vector \mathcal{T} represents the transverse fluxes and pressure gradients along x_2 and x_3 :

$$\mathcal{T} = -\mathcal{F}^t \frac{\partial \mathcal{U}}{\partial x_t} = \begin{pmatrix} -\frac{\partial \rho u_t}{\partial x_t} \\ -u_t \frac{\partial u_1}{\partial x_t} \\ -u_t \frac{\partial u_2}{\partial x_t} - \frac{1}{\rho} \frac{\partial p}{\partial x_2} \\ -u_t \frac{\partial u_3}{\partial x_t} - \frac{1}{\rho} \frac{\partial p}{\partial x_3} \\ -u_t \frac{\partial p}{\partial x_t} - \gamma p \frac{\partial u_t}{\partial x_t} \\ -u_t \frac{\partial Z}{\partial x_t} \end{pmatrix}, \quad (t = 2, 3). \quad (3.74)$$

It should be noted that transverse effects, which are expressed in terms of primitive variables' gradients in the above relations, may also be expressed in terms of transverse fluxes computed on conservative variables, as it is often more suitable when using Finite Volume solvers. In fact, by definition, the non-conservative Jacobian matrix \mathcal{F}^k is related to the flux vector \mathbf{F}^k by the following relation:

$$\mathbf{P} \mathcal{F}^k \frac{\partial \mathcal{U}}{\partial x_k} = \frac{\partial \mathbf{F}^k}{\partial x_k}. \quad (3.75)$$

Pre-multiplying by \mathbf{P}^{-1} , the alternative expression for \mathcal{T} then becomes:

$$\mathcal{T} = -\mathbf{P}^{-1} \frac{\partial \mathbf{F}^t}{\partial x_t}, \quad (t = 2, 3), \quad (3.76)$$

with components:

$$\left\{ \begin{array}{l} \mathcal{T}_1 = -\frac{\partial F_1^t}{\partial x_t} \\ \mathcal{T}_2 = -\frac{1}{\rho} \left(\frac{\partial F_2^t}{\partial x_t} - u_1 \frac{\partial F_1^t}{\partial x_t} \right) \\ \mathcal{T}_3 = -\frac{1}{\rho} \left(\frac{\partial F_3^t}{\partial x_t} - u_2 \frac{\partial F_1^t}{\partial x_t} \right) \\ \mathcal{T}_4 = -\frac{1}{\rho} \left(\frac{\partial F_4^t}{\partial x_t} - u_3 \frac{\partial F_1^t}{\partial x_t} \right) \\ \mathcal{T}_5 = -(\gamma - 1) \left(\frac{\partial F_5^t}{\partial x_t} + \frac{u_k u_k}{2} \frac{\partial F_1^t}{\partial x_t} - u_k \frac{\partial F_{k+1}^t}{\partial x_t} \right) \\ \mathcal{T}_6 = -\frac{1}{\rho} \left(\frac{\partial F_6^t}{\partial x_t} - Z \frac{\partial F_1^t}{\partial x_t} \right) \end{array} \right. \quad (3.77)$$

Finally, pre-multiplying Eq. (3.72) by \mathbf{S}_1^{-1} and recalling Eq. (3.69), we obtain the following more appropriate relations between wave amplitude variations and primitive variables' time derivatives (*cf.* Eq. (3.49)):

$$\mathbf{S}_1^{-1} \frac{\partial \mathcal{U}}{\partial t} + \mathcal{L} - \mathfrak{T}^1 = \mathbf{0}. \quad (3.78)$$

Expanding the components of the above vectorial relation we obtain a set of relations expressing each wave amplitude variation as a function of primitive variables and transverse terms:

$$\left\{ \begin{array}{l} \left(\frac{\partial p}{\partial t} - \rho a \frac{\partial u_1}{\partial t} \right) + \mathcal{L}_1 - \mathfrak{T}_1^1 = 0 \\ \left(a^2 \frac{\partial \rho}{\partial t} - \frac{\partial p}{\partial t} \right) + \mathcal{L}_2 - \mathfrak{T}_2^1 = 0 \\ \frac{\partial u_2}{\partial t} + \mathcal{L}_3 - \mathfrak{T}_3^1 = 0 \\ \frac{\partial u_3}{\partial t} + \mathcal{L}_4 - \mathfrak{T}_4^1 = 0 \\ \left(\frac{\partial p}{\partial t} + \rho a \frac{\partial u_1}{\partial t} \right) + \mathcal{L}_5 - \mathfrak{T}_5^1 = 0 \\ \frac{\partial Z}{\partial t} + \mathcal{L}_6 - \mathfrak{T}_6^1 = 0 \end{array} \right. \quad (3.79)$$

where the notation \mathfrak{T}_k^m is now used to indicate a characteristic transverse term in the plane perpendicular to x_m relevant to the k th characteristic variable. In the present case, in particular, we have:

$$\mathfrak{T}^1 = \mathbf{S}_1^{-1} \mathcal{T} = \begin{pmatrix} \mathcal{T}_5 - \rho a \mathcal{T}_2 \\ a^2 \mathcal{T}_1 - \mathcal{T}_5 \\ \mathcal{T}_3 \\ \mathcal{T}_4 \\ \mathcal{T}_5 + \rho a \mathcal{T}_2 \\ \mathcal{T}_6 \end{pmatrix}. \quad (3.80)$$

The unknown incoming waves \mathcal{L}_i are determined from the system (3.79), once physical boundary conditions are provided to approximate the time derivatives of the primitive variable. These physical boundary conditions for subsonic non-reflecting inflows and outflows and for adiabatic no-slip walls are now discussed.

Subsonic Non-Reflecting Outflow. In the case of subsonic non-reflecting outflows, the physical boundary condition may be obtained from the pressure relaxation condition proposed by Rudy and Strikwerda [62] with an additional transverse relaxation term as discussed by Lodato et al. [43], Yoo and Im [84], Yoo et al. [85]. Depending on the sign of the propagation velocities of the characteristic waves, namely the eigenvalues given in Eq. (3.62), and depending on the location of the boundary with respect to the computational domain, some wave amplitude variations \mathcal{L}_i refer to entering waves, which are unknown and need to be determined, while the others refer to waves leaving the domain: the last are known using their definition in Eq. (3.66). For subsonic outflows, there will be only one unknown incoming wave, which is either \mathcal{L}_1 , if the boundary is located at $x_1 = L_x$, or \mathcal{L}_5 , if the boundary is located at $x_1 = 0$.

The former is obtained from the first equation in (3.79) and the latter from the fifth equation in (3.79). These two equations may be conveniently condensed as

$$\left[\frac{\partial p}{\partial t} + \varsigma(\phi)\rho a \frac{\partial u_1}{\partial t} \right] + \mathcal{L}_\phi - \mathfrak{T}_\phi^1 = 0, \quad (3.81)$$

with

$$\mathfrak{T}_\phi^1 = \mathcal{T}_5 + \varsigma(\phi)\rho a \mathcal{T}_2, \quad (3.82)$$

where the wave index ϕ , which is equal to either 1 or 5, selects the unknown entering wave and ς sets the correct sign accordingly:

$$\phi = \begin{cases} 5 & \text{if } x_1 = 0, \\ 1 & \text{if } x_1 = L_x. \end{cases} \quad (3.83)$$

$$\varsigma(\phi) = \frac{\phi - 1}{2} - 1 = \begin{cases} -1 & \text{if } \phi = 1, \\ +1 & \text{if } \phi = 5. \end{cases} \quad (3.84)$$

The relevant physical boundary condition, expressing relaxation toward a target pressure p_∞ and toward a known set of exact transverse terms $\mathfrak{T}_{\phi,\text{ex}}^1$ [85], is:

$$\left[\frac{\partial p}{\partial t} + \varsigma(\phi)\rho a \frac{\partial u_1}{\partial t} \right] + \sigma \frac{a(1 - M_{\text{max}}^2)}{L_x} \Delta p - \beta_t (\mathfrak{T}_\phi^1 - \mathfrak{T}_{\phi,\text{ex}}^1) = 0, \quad (3.85)$$

where σ is the pressure relaxation coefficient, M_{max} is the maximum Mach number, L_x is the characteristic size of the computational domain along x_1 , $\Delta p = p - p_\infty$ is the difference between the actual pressure and its target value and $\beta_t \in [0 : 1]$ is the transverse damping parameter.

For most free shear flows, the boundary condition is expected to well behave with $\mathfrak{T}_{\phi,\text{ex}}^1 = 0$ [43, 84], however, when an analytical steady solution of the flow is known at the boundary, the target value of the transverse term $\mathfrak{T}_{\phi,\text{ex}}^1$ may be obtained applying Eqs. (3.74) and (3.80):

$$\mathfrak{T}_{\phi,\text{ex}}^1 = -\hat{u}_t \frac{\partial \hat{p}}{\partial x_t} - \gamma \hat{p} \frac{\partial \hat{u}_t}{\partial x_t} - \varsigma(\phi) \hat{p} \hat{a} \hat{u}_t \frac{\partial \hat{u}_1}{\partial x_t}, \quad (t = 2, 3), \quad (3.86)$$

where the (\cdot) accent indicates the known analytical solution for the target flow. Further details about the introduced transverse relaxation parameter β_t are given in the next paragraph and in occasion of the presentation of the validation test-cases in Section 3.2.5.

Combining Eq. (3.85) with the corresponding characteristic equation from system (3.79), namely Eq. (3.81), the unknown incoming wave is then obtained as:

$$\mathcal{L}_\phi = \sigma \frac{a(1 - M_{\max}^2)}{L_x} \Delta p + (1 - \beta_t) \mathfrak{T}_\phi^1 + \beta_t \mathfrak{T}_{\phi, \text{ex}}^1. \quad (3.87)$$

It is interesting to note that, for $\mathfrak{T}_{\phi, \text{ex}}^1 = 0$ and $\beta_t = 1$, the standard NSCBC non-reflecting outflow [58] is recovered.

Finally, the Navier-Stokes boundary conditions are obtained by complementing the above inviscid condition with the following viscous conditions:

$$\frac{\partial \tau_{12}}{\partial x_1} = \frac{\partial \tau_{13}}{\partial x_1} = \frac{\partial q_1}{\partial x_1} = \frac{\partial \rho J_1}{\partial x_1} = 0. \quad (3.88)$$

***A priori* choice of the transverse relaxation coefficient β_t .** One of the most striking features of the novel implementation of the subsonic non-reflecting outflow, *i.e.* Eq. (3.87), is the introduction of an additional relaxation parameter, namely, the transverse relaxation coefficient β_t . It seems then, that the improved tridimensional character of the proposed boundary procedure can be achieved at the expense of an additional parameter, which needs to be properly tuned.

And indeed, the transverse relaxation coefficient may play a key role in the correct behavior of the proposed outflow boundary condition. In accordance with the results by Yoo et al. [85], preliminary tests on the proposed technique, without any transverse relaxation, led to problems of numerical stability and to improper reproduction of the flow field, this last showing a marked tendency to align parallel to the boundary plane, as this was a sort of semi-permeable wall.

The above mentioned problems disappeared after introducing a small amount of transverse relaxation. Moreover, tests performed on convected vortices, as those which will be presented later on, suggested a pronounced dependancy of the optimal transverse relaxation to the typical Mach number in the flow [43]. This results is again consistent with the findings of Yoo et al. [85], who suggested that the relaxation coefficient β_t was connected with the flow speed at the outflow.

Applying the asymptotic analysis for low Mach number flows to the simplified two-dimensional case with identically zero exact transverse terms, *i.e.* $\mathfrak{T}_{\phi, \text{ex}}^1 = 0$ in Eq. (3.87), Yoo and Im [84] demonstrated that the leading order continuity equation is violated in the presence of strong transverse velocity gradients unless β_t is set equal to the reference Mach number for the flow, giving evidence of the strong connection existing between the transverse relaxation and the Mach number. It is worthwhile mentioning that all the test performed within the framework of our study highlighted that the underestimation of β_t with respect to the actual Mach may cause catastrophic effects, whereas setting $\beta_t \geq M$ does not pose major problems.

The above considerations suggest that, since β_t is strictly connected with the flow parameters, the additional relaxation parameter cannot be considered just as an additional “tuning” parameter for the boundary condition, but rather as a physical parameter of the tridimensional characteristic formulation. In fact, it is possible to set a proper value for β_t , *a priori*, on the base of the typical Mach number of the flow.

For instance, for all the simulations of free and impinging jets presented in this thesis, a first estimation of the transverse relaxation coefficient, set equal to the Mach number computed on the bulk velocity of the jet, produced correctly behaved outflow boundaries, regardless of the fact that the actual value of the Mach number in the flow regions close to the boundaries was considerably lower than the inlet Mach number. Making a first run with this preliminary estimation of β_t and then reducing it to a more representative local value produced efficient, stable and unperturbed solutions through the outflow boundaries.

In view of the observed Mach dependancy, it may seem reasonable to compute the transverse relaxation coefficient on the base of the local Mach number. Unfortunately, tests performed on different flow configurations, where β_t was set equal to the local time-varying Mach number, were affected by problems of numerical instability at the boundary, in perfect agreement with the observations of Yoo and Im [84]. On the other hand, stable solutions were obtained, by setting the transverse relaxation equal to the maximum Mach number evaluated over the entire boundary plane, in the most critical case of reactive flows (*cf.* 3D-NSCBC implementation for reactive flows in Section 5.2.1). This last approach, which would clearly eliminate the problem of choosing the optimal value for β_t , is currently under more thorough evaluation and suggests that the transverse relaxation may be computed from the local instantaneous properties of the flow, provided that “excessive” variability from point to point is somehow prevented.

Subsonic Non-Reflecting Inflow. For subsonic inflows, the same procedure proposed by Yoo et al. [85] is followed for computational nodes away from edges and corner. At the inlet there will be five entering waves¹⁵, therefore five physical boundary conditions are necessary in order to close the problem. In the present case, we choose to impose temperature, velocity and passive scalar; other choices are possible like density or mass flow rate that will not be discussed here. The characteristic relations relevant to the unknown waves are obtained from Eqs. (3.79) and (3.80):

$$\left[\frac{\partial p}{\partial t} + \varsigma(\phi)\rho a \frac{\partial u_1}{\partial t} \right] + \mathcal{L}_\phi - \mathfrak{T}_\phi^1 = 0, \quad (3.89)$$

$$\left[a^2 \frac{\partial \rho}{\partial t} - \frac{\partial p}{\partial t} \right] + \mathcal{L}_2 - \mathfrak{T}_2^1 = 0, \quad (3.90)$$

$$\frac{\partial u_2}{\partial t} + \mathcal{L}_3 - \mathfrak{T}_3^1 = 0, \quad (3.91)$$

$$\frac{\partial u_3}{\partial t} + \mathcal{L}_4 - \mathfrak{T}_4^1 = 0, \quad (3.92)$$

$$\frac{\partial Z}{\partial t} + \mathcal{L}_6 - \mathfrak{T}_6^1 = 0, \quad (3.93)$$

where \mathfrak{T}_ϕ^1 is obtained according to Eq. (3.82), whereas ϕ and ς are given by Eqs. (3.83) and (3.84) respectively. In the case of subsonic non-reflecting inflow, in particular, no transverse relaxation is necessary and the relevant physical boundary conditions are obtained, according

¹⁵As in the case of the subsonic outflow, in particular, if the boundary is located at $x_1 = 0$ ($x_1 = L_x$), \mathcal{L}_5 (\mathcal{L}_1) enters the computational domain and \mathcal{L}_1 (\mathcal{L}_5) leaves it.

to the suggestion of Yoo et al. [85], as:

$$\left[\frac{\partial p}{\partial t} + \varsigma(\phi)\rho a \frac{\partial u_1}{\partial t} \right] + \eta_\phi \frac{\rho a^2(1 - M_{\max}^2)}{L_x} \Delta u_1 = 0, \quad (3.94)$$

$$\left[a^2 \frac{\partial \rho}{\partial t} - \frac{\partial p}{\partial t} \right] + \eta_2 \frac{\rho a R}{L_x} \Delta T = 0, \quad (3.95)$$

$$\frac{\partial u_2}{\partial t} + \eta_3 \frac{a}{L_x} \Delta u_2 = 0, \quad (3.96)$$

$$\frac{\partial u_3}{\partial t} + \eta_4 \frac{a}{L_x} \Delta u_3 = 0, \quad (3.97)$$

$$\frac{\partial Z}{\partial t} + \eta_6 \frac{a}{L_x} \Delta Z = 0, \quad (3.98)$$

where η_1, \dots, η_6 are relaxation parameters (note that η_1 and η_2 are negative) and $\Delta u_k = u_k - u_{k0}$, $\Delta T = T - T_0$, $\Delta Z = Z - Z_0$ are the differences between the actual values of the velocity components, the temperature and the passive scalar respectively and the relevant target values, denoted by the subscript 0.

The equations for the unknown entering wave amplitudes are obtained from the characteristic relations, Eqs. (3.89)–(3.93), closed with Eqs. (3.94)–(3.98):

$$\mathcal{L}_\phi = \eta_\phi \frac{\rho a^2(1 - M_{\max}^2)}{L_x} \Delta u_1 + \mathfrak{T}_\phi^1, \quad (3.99)$$

$$\mathcal{L}_2 = \eta_2 \frac{\rho a R}{L_x} \Delta T + \mathfrak{T}_2^1, \quad (3.100)$$

$$\mathcal{L}_3 = \eta_3 \frac{a}{L_x} \Delta u_2 + \mathfrak{T}_3^1, \quad (3.101)$$

$$\mathcal{L}_4 = \eta_4 \frac{a}{L_x} \Delta u_3 + \mathfrak{T}_4^1, \quad (3.102)$$

$$\mathcal{L}_6 = \eta_6 \frac{a}{L_x} \Delta Z + \mathfrak{T}_6^1, \quad (3.103)$$

with \mathfrak{T}_ϕ^1 from Eq. (3.82) and the other characteristic transverse terms from Eq. (3.80).

It should be noted that this particular inflow condition does not require any additional viscous condition as the density ρ —the only remaining unknown—is obtained from the continuity equation, which does not involve any viscous term [58].

Adiabatic No-Slip Wall. Even considering transverse effects, the adiabatic no-slip wall boundary condition remains identical to the one proposed by Poinot and Lele [58]. This is due to the fact that the no-slip condition (all the components of velocity are zero) makes the transverse terms involved in the calculation of the incoming wave vanish.

If, for instance, we consider the wall to be normal to x_1 , since the velocity at the wall is zero, the only non-zero wave amplitude variations are \mathcal{L}_1 and \mathcal{L}_5 ; the transverse terms \mathcal{T}_1 , \mathcal{T}_2 , \mathcal{T}_5 and \mathcal{T}_6 are zero as well (*cf.* Eq. (3.74)). The unknown incoming wave amplitude variation is \mathcal{L}_1 (\mathcal{L}_5) when the boundary is located at $x_1 = L_x$ ($x_1 = 0$). The only necessary physical boundary condition prescribes that the normal velocity u_1 , initially set to zero, cannot change value:

$$\frac{\partial u_1}{\partial t} = 0. \quad (3.104)$$

From the second equation in the system (3.73), we get the identity

$$\mathcal{L}_1 = \mathcal{L}_5, \quad (3.105)$$

which allows the computation of the incoming wave amplitude variation from the outgoing one. The viscous conditions for the adiabatic case are obtained by setting to zero normal heat transfer and diffusion:

$$q_1 = 0, \quad J_1 = 0. \quad (3.106)$$

3.2.3 Characteristic Formulation Along Two Directions for Edges

When the computational point is located over an edge joining two different boundary surfaces, two characteristic directions, which are orthogonal to the boundary faces considered, have to be considered simultaneously. As it will be shown in more detail, when dealing with nodes located on the edges of the computational domain, there arise two main issues:

- the two boundaries adjacent to the edge considered may be of different types, thus leading to the necessity for *ad hoc* compatibility conditions;
- the inclusion of transverse effects in the computation of the incoming waves may lead to characteristic waves coupling [80], as the characteristic waves traveling in one direction represent transverse effects in the other direction and *vice versa*.

Supposing that the edge is aligned along x_3 , *i.e.* the boundary is orthogonal to x_1 and x_2 directions, the characteristic waves considered on the connecting edge will be those traveling along x_1 and x_2 ; \mathcal{F}^1 and \mathcal{F}^2 are then diagonalized and Eq. (3.55) is written as:

$$\frac{\partial \mathcal{U}}{\partial t} + \mathbf{S}_1 \mathbf{\Lambda}^1 \mathbf{S}_1^{-1} \frac{\partial \mathcal{U}}{\partial x_1} + \mathbf{S}_2 \mathbf{\Lambda}^2 \mathbf{S}_2^{-1} \frac{\partial \mathcal{U}}{\partial x_2} + \mathcal{F}^3 \frac{\partial \mathcal{U}}{\partial x_3} + \mathcal{D} = \mathbf{0}. \quad (3.107)$$

The eigenvalues and the transformation matrices for \mathcal{F}^1 are obtained from Eqs. (3.62)–(3.64), while the analogous quantities for \mathcal{F}^2 are:

$$\mathbf{\Lambda}^2 = \begin{pmatrix} u_2 - a & 0 & 0 & 0 & 0 & 0 \\ 0 & u_2 & 0 & 0 & 0 & 0 \\ 0 & 0 & u_2 & 0 & 0 & 0 \\ 0 & 0 & 0 & u_2 & 0 & 0 \\ 0 & 0 & 0 & 0 & u_2 + a & 0 \\ 0 & 0 & 0 & 0 & 0 & u_2 \end{pmatrix}, \quad (3.108)$$

$$\mathbf{S}_2 = \begin{pmatrix} 1/(2a^2) & 0 & 1/a^2 & 0 & 1/(2a^2) & 0 \\ 0 & 1 & 0 & 0 & 0 & 0 \\ -1/(2\rho a) & 0 & 0 & 0 & 1/(2\rho a) & 0 \\ 0 & 0 & 0 & 1 & 0 & 0 \\ 1/2 & 0 & 0 & 0 & 1/2 & 0 \\ 0 & 0 & 0 & 0 & 0 & 1 \end{pmatrix}, \quad (3.109)$$

$$\mathbf{S}_2^{-1} = \begin{pmatrix} 0 & 0 & -\rho a & 0 & 1 & 0 \\ 0 & 1 & 0 & 0 & 0 & 0 \\ a^2 & 0 & 0 & 0 & -1 & 0 \\ 0 & 0 & 0 & 1 & 0 & 0 \\ 0 & 0 & \rho a & 0 & 1 & 0 \\ 0 & 0 & 0 & 0 & 0 & 1 \end{pmatrix}. \quad (3.110)$$

Wave amplitude time variations are defined as for the mono-dimensional case as

$$\mathcal{L} = \Lambda^1 \mathbf{S}_1^{-1} \frac{\partial \mathcal{U}}{\partial x_1}, \quad \mathcal{M} = \Lambda^2 \mathbf{S}_2^{-1} \frac{\partial \mathcal{U}}{\partial x_2}, \quad (3.111)$$

where \mathcal{L} is expressed by Eq. (3.66) and the components of \mathcal{M} are:

$$\mathcal{M} = \begin{pmatrix} \mu_1 \left(\frac{\partial p}{\partial x_2} - \rho a \frac{\partial u_2}{\partial x_2} \right) \\ \mu_2 \frac{\partial u_1}{\partial x_2} \\ \mu_3 \left(a^2 \frac{\partial \rho}{\partial x_2} - \frac{\partial p}{\partial x_2} \right) \\ \mu_4 \frac{\partial u_3}{\partial x_2} \\ \mu_5 \left(\frac{\partial p}{\partial x_2} + \rho a \frac{\partial u_2}{\partial x_2} \right) \\ \mu_6 \frac{\partial Z}{\partial x_2} \end{pmatrix}, \quad (3.112)$$

with μ_i the eigenvalues of \mathcal{F}^2 , namely the non-zero elements over the diagonal of Λ^2 . The conservation laws in terms of primitive and conservative variables are respectively:

$$\frac{\partial \mathcal{U}}{\partial t} + \mathbf{d} + \mathbf{e} + \mathcal{F}^3 \frac{\partial \mathcal{U}}{\partial x_3} + \mathcal{D} = \mathbf{0} \quad (3.113)$$

$$\frac{\partial \mathcal{U}}{\partial t} + \mathbf{P}\mathbf{d} + \mathbf{P}\mathbf{e} + \frac{\partial \mathcal{F}^3}{\partial x_3} + \frac{\partial \mathcal{D}^i}{\partial x_i} = \mathbf{0} \quad (3.114)$$

where \mathbf{d} and $\mathbf{P}\mathbf{d}$ are obtained from Eqs. (3.69) and (3.70), while \mathbf{e} and $\mathbf{P}\mathbf{e}$ are:

$$\mathbf{e} = \mathbf{S}_2 \mathcal{M} = \begin{pmatrix} \frac{1}{a^2} \left[\mathcal{M}_3 + \frac{1}{2} (\mathcal{M}_5 + \mathcal{M}_1) \right] \\ \mathcal{M}_2 \\ \frac{1}{2\rho a} (\mathcal{M}_5 - \mathcal{M}_1) \\ \mathcal{M}_4 \\ \frac{1}{2} (\mathcal{M}_5 + \mathcal{M}_1) \\ \mathcal{M}_6 \end{pmatrix}, \quad (3.115)$$

$$\mathbf{P}\mathbf{e} = \begin{pmatrix} e_1 \\ e_1u_1 + \rho e_2 \\ e_1u_2 + \rho e_3 \\ e_1u_3 + \rho e_4 \\ e_1\frac{u_k u_k}{2} + \rho u_j e_{j+1} + \frac{e_5}{\gamma - 1} \\ e_1Z + \rho e_6 \end{pmatrix}. \quad (3.116)$$

Edge Boundary Conditions

The procedure and the formalism which are needed to implement characteristic boundary conditions accounting for transverse effects will be presented now in the case that two different characteristic directions are considered simultaneously; as it has been already mentioned, this is the case when the computational node is located on a boundary edge of the domain. We will suppose that the edge is aligned along x_3 , therefore the face boundaries adjacent to the edge are normal to x_1 and x_2 .

The set of relations linking primitive variables with the wave amplitude variations \mathcal{L}_i and \mathcal{M}_i , traveling along directions x_1 and x_2 , is obtained from the two-dimensional characteristic analysis developed in the previous section and, precisely, by taking Eq. (3.113) and neglecting the viscous and diffusive effects, namely the vector \mathcal{D} :

$$\frac{\partial \mathcal{U}}{\partial t} + \mathbf{d} + \mathbf{e} - \mathcal{T} = \mathbf{0}. \quad (3.117)$$

The above vectorial relation represents the following set of relations:

$$\left\{ \begin{array}{l} \frac{\partial \rho}{\partial t} + \frac{1}{a^2} \left[\mathcal{L}_2 + \frac{1}{2} (\mathcal{L}_5 + \mathcal{L}_1) \right] \\ \quad + \frac{1}{a^2} \left[\mathcal{M}_3 + \frac{1}{2} (\mathcal{M}_5 + \mathcal{M}_1) \right] - \mathcal{T}_1 = 0 \\ \frac{\partial u_1}{\partial t} + \frac{1}{2\rho a} (\mathcal{L}_5 - \mathcal{L}_1) + \mathcal{M}_2 - \mathcal{T}_2 = 0 \\ \frac{\partial u_2}{\partial t} + \mathcal{L}_3 + \frac{1}{2\rho a} (\mathcal{M}_5 - \mathcal{M}_1) - \mathcal{T}_3 = 0 \\ \frac{\partial u_3}{\partial t} + \mathcal{L}_4 + \mathcal{M}_4 - \mathcal{T}_4 = 0 \\ \frac{\partial p}{\partial t} + \frac{1}{2} (\mathcal{L}_5 + \mathcal{L}_1) + \frac{1}{2} (\mathcal{M}_5 + \mathcal{M}_1) - \mathcal{T}_5 = 0 \\ \frac{\partial Z}{\partial t} + \mathcal{L}_6 + \mathcal{M}_6 - \mathcal{T}_6 = 0 \end{array} \right. \quad (3.118)$$

The vector \mathcal{T} now represents the transverse fluxes and pressure gradients along x_3 only:

$$\mathcal{T} = -\mathcal{F}^3 \frac{\partial \mathcal{U}}{\partial x_3} = \begin{pmatrix} -\frac{\partial \rho u_3}{\partial x_3} \\ -u_3 \frac{\partial u_1}{\partial x_3} \\ -u_3 \frac{\partial u_2}{\partial x_3} \\ -u_3 \frac{\partial u_3}{\partial x_3} - \frac{1}{\rho} \frac{\partial p}{\partial x_3} \\ -u_3 \frac{\partial p}{\partial x_3} - \gamma p \frac{\partial u_3}{\partial x_3} \\ -u_3 \frac{\partial Z}{\partial x_3} \end{pmatrix}, \quad (3.119)$$

which, again, may be expressed in terms of flux vector gradients as

$$\mathcal{T} = -\mathbf{P}^{-1} \frac{\partial \mathbf{F}^3}{\partial x_3}. \quad (3.120)$$

A procedure similar to the one discussed for face boundaries may be used. It should be noted, anyway, that, since the transformation matrices \mathbf{S}_1^{-1} and \mathbf{S}_2^{-1} are different¹⁶, a rigorous characteristic form similar to Eq. (3.79) cannot be derived now and the characteristic waves traveling in different directions are then coupled. It is possible, anyway, to write pseudo-characteristic relations where unknown waves traveling along different directions are isolated one at the time. This is basically done pre-multiplying Eq. (3.117) by either \mathbf{S}_1^{-1} or \mathbf{S}_2^{-1} ,

$$\mathbf{S}_1^{-1} \frac{\partial \mathcal{U}}{\partial t} + \mathcal{L} - \mathfrak{T}^1 = \mathbf{0}, \quad (3.121)$$

$$\mathbf{S}_2^{-1} \frac{\partial \mathcal{U}}{\partial t} + \mathcal{M} - \mathfrak{T}^2 = \mathbf{0}, \quad (3.122)$$

the former being formally identical to Eq. (3.79) and the latter giving the following equations:

$$\left\{ \begin{array}{l} \left(\frac{\partial p}{\partial t} - \rho a \frac{\partial u_2}{\partial t} \right) + \mathcal{M}_1 - \mathfrak{T}_1^2 = 0 \\ \frac{\partial u_1}{\partial t} + \mathcal{M}_2 - \mathfrak{T}_2^2 = 0 \\ \left(a^2 \frac{\partial \rho}{\partial t} - \frac{\partial p}{\partial t} \right) + \mathcal{M}_3 - \mathfrak{T}_3^2 = 0 \\ \frac{\partial u_3}{\partial t} + \mathcal{M}_4 - \mathfrak{T}_4^2 = 0 \\ \left(\frac{\partial p}{\partial t} + \rho a \frac{\partial u_2}{\partial t} \right) + \mathcal{M}_5 - \mathfrak{T}_5^2 = 0 \\ \frac{\partial Z}{\partial t} + \mathcal{M}_6 - \mathfrak{T}_6^2 = 0 \end{array} \right. \quad (3.123)$$

Characteristic transverse terms are now computed from the following relations:

$$\mathfrak{T}^1 = \mathbf{S}_1^{-1} (\mathcal{T} - \mathbf{e}), \quad (3.124)$$

$$\mathfrak{T}^2 = \mathbf{S}_2^{-1} (\mathcal{T} - \mathbf{d}), \quad (3.125)$$

¹⁶This is basically due to the fact that Jacobian matrices \mathcal{F}^1 and \mathcal{F}^2 cannot be diagonalized simultaneously.

or, in components,

$$\mathfrak{T}^1 = \begin{pmatrix} \mathcal{T}_5 - \frac{1}{2}(\mathcal{M}_5 + \mathcal{M}_1) - \rho a(\mathcal{T}_2 - \mathcal{M}_2) \\ a^2 \mathcal{T}_1 - \mathcal{T}_5 - \mathcal{M}_3 \\ \mathcal{T}_3 - \frac{1}{2\rho a}(\mathcal{M}_5 - \mathcal{M}_1) \\ \mathcal{T}_4 - \mathcal{M}_4 \\ \mathcal{T}_5 - \frac{1}{2}(\mathcal{M}_5 + \mathcal{M}_1) + \rho a(\mathcal{T}_2 - \mathcal{M}_2) \\ \mathcal{T}_6 - \mathcal{M}_6 \end{pmatrix}, \quad (3.126)$$

$$\mathfrak{T}^2 = \begin{pmatrix} \mathcal{T}_5 - \frac{1}{2}(\mathcal{L}_5 + \mathcal{L}_1) - \rho a(\mathcal{T}_3 - \mathcal{L}_3) \\ \mathcal{T}_2 - \frac{1}{2\rho a}(\mathcal{L}_5 - \mathcal{L}_1) \\ a^2 \mathcal{T}_1 - \mathcal{T}_5 - \mathcal{L}_2 \\ \mathcal{T}_4 - \mathcal{L}_4 \\ \mathcal{T}_5 - \frac{1}{2}(\mathcal{L}_5 + \mathcal{L}_1) + \rho a(\mathcal{T}_3 - \mathcal{L}_3) \\ \mathcal{T}_6 - \mathcal{L}_6 \end{pmatrix}. \quad (3.127)$$

Note that, since by definition

$$e = \mathcal{F}^2 \frac{\partial \mathcal{U}}{\partial x_2},$$

the above expression for \mathfrak{T}^1 is perfectly consistent with Eq. (3.80) and the relevant definition of the vector \mathcal{T} , namely Eq. (3.74).

The equations from system (3.79) and (3.123) can be then still combined with physical boundary conditions to compute the unknown incoming wave amplitude variations of both boundaries but, since these wave amplitude variations are now coupled through the definitions of the transverse terms (*cf.* Eqs. (3.126) and (3.127)), in general, a linear system of equations in the unknown will have to be solved. An additional problem arises when the boundaries sharing the edge are of different kind; in this case, not only different characteristic directions have to be considered simultaneously but, depending on the boundary types, additional compatibility conditions must be introduced to ensure numerical stability.

The physical boundary conditions and the relevant compatibility conditions are now discussed for the following edge typologies:

1. boundary edge between two subsonic non-reflecting outflows;
2. boundary edge between a subsonic non-reflecting outflow and a subsonic non-reflecting inflow;
3. boundary edge between a subsonic non-reflecting outflow and an adiabatic no-slip wall.

Outflow/Outflow Edge. Focusing on the case of a boundary edge located between two outflows, we know from Section 3.2.2 that, for each boundary, there is only one entering wave: in the present case the entering waves are \mathcal{L}_1 (resp. \mathcal{L}_5) if the boundary face normal to x_1 is located at $x_1 = L_x$ (resp. $x_1 = 0$) and \mathcal{M}_1 (resp. \mathcal{M}_5) if the boundary face normal to x_2 is located at $x_2 = L_y$ (resp. $x_2 = 0$).

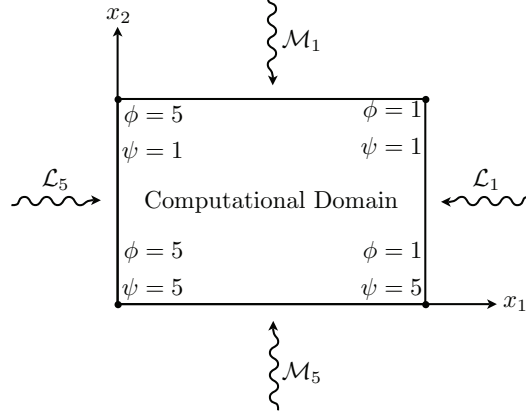


Figure 3.8: Schematic representation of a 2D computational domain showing the values of the indices ϕ and ψ depending on edge location.

The relevant two pseudo-characteristic relations are selected from Eqs. (3.79) and (3.123) and can be conveniently written as

$$\left[\frac{\partial p}{\partial t} + \varsigma(\phi)\rho a \frac{\partial u_1}{\partial t} \right] + \mathcal{L}_\phi - \mathfrak{T}_\phi^1 = 0, \quad (3.128)$$

$$\left[\frac{\partial p}{\partial t} + \varsigma(\psi)\rho a \frac{\partial u_2}{\partial t} \right] + \mathcal{M}_\psi - \mathfrak{T}_\psi^2 = 0, \quad (3.129)$$

with

$$\mathfrak{T}_\phi^1 = \mathcal{T}_5 - \frac{1}{2}(\mathcal{M}_5 + \mathcal{M}_1) + \varsigma(\phi)\rho a(\mathcal{T}_2 - \mathcal{M}_2), \quad (3.130)$$

$$\mathfrak{T}_\psi^2 = \mathcal{T}_5 - \frac{1}{2}(\mathcal{L}_5 + \mathcal{L}_1) + \varsigma(\psi)\rho a(\mathcal{T}_3 - \mathcal{L}_3), \quad (3.131)$$

where ϕ is given in Eq. (3.83), ψ is defined in analogy as

$$\psi = \begin{cases} 5 & \text{if } x_2 = 0, \\ 1 & \text{if } x_2 = L_y. \end{cases} \quad (3.132)$$

(see Figure 3.8) and ς , which is defined in Eq. (3.84), selects the correct signs accordingly.

The two necessary physical boundary conditions are obtained, as before, from Eq. (3.85), which is now written for u_1 and u_2 :

$$\left[\frac{\partial p}{\partial t} + \varsigma(\phi)\rho a \frac{\partial u_1}{\partial t} \right] + \sigma \frac{a(1 - M_{\max}^2)}{L_x} \Delta p - \beta_t (\mathfrak{T}_\phi^1 - \mathfrak{T}_{\phi,\text{ex}}^1) = 0, \quad (3.133)$$

$$\left[\frac{\partial p}{\partial t} + \varsigma(\psi)\rho a \frac{\partial u_2}{\partial t} \right] + \sigma \frac{a(1 - M_{\max}^2)}{L_y} \Delta p - \beta_t (\mathfrak{T}_\psi^2 - \mathfrak{T}_{\psi,\text{ex}}^2) = 0, \quad (3.134)$$

where $\mathfrak{T}_{\phi,\text{ex}}^1$ and $\mathfrak{T}_{\psi,\text{ex}}^2$, if needed, may be computed from a reference steady flow by applying the definition (3.74) written for boundaries orthogonal to x_1 and x_2 respectively:

$$\mathfrak{T}_{\phi,\text{ex}}^1 = -\hat{u}_t \frac{\partial \hat{p}}{\partial x_t} - \gamma \hat{p} \frac{\partial \hat{u}_t}{\partial x_t} - \varsigma(\phi) \hat{\rho} \hat{a} \hat{u}_t \frac{\partial \hat{u}_1}{\partial x_t}, \quad (t = 2, 3) \quad (3.135)$$

$$\mathfrak{T}_{\psi,\text{ex}}^2 = -\hat{u}_t \frac{\partial \hat{p}}{\partial x_t} - \gamma \hat{p} \frac{\partial \hat{u}_t}{\partial x_t} - \varsigma(\psi) \hat{\rho} \hat{a} \hat{u}_t \frac{\partial \hat{u}_2}{\partial x_t}, \quad (t = 1, 3) \quad (3.136)$$

From Eq. (3.128), (3.129), (3.133) and (3.134), the unknown wave amplitude variations may then be computed solving the following linear system of equations:

$$\begin{cases} \mathcal{L}_\phi + \frac{1 - \beta_t}{2} \mathcal{M}_\psi = \sigma \frac{a(1 - M_{\text{max}}^2)}{L_x} \Delta p + (1 - \beta_t) \tilde{\mathfrak{T}}_\phi^1 + \beta_t \mathfrak{T}_{\phi,\text{ex}}^1 \\ \frac{1 - \beta_t}{2} \mathcal{L}_\phi + \mathcal{M}_\psi = \sigma \frac{a(1 - M_{\text{max}}^2)}{L_y} \Delta p + (1 - \beta_t) \tilde{\mathfrak{T}}_\psi^2 + \beta_t \mathfrak{T}_{\psi,\text{ex}}^2 \end{cases} \quad (3.137)$$

with the known terms:

$$\tilde{\mathfrak{T}}_\phi^1 = \mathcal{T}_5 - \frac{\mathcal{M}_{\psi^*}}{2} - \varsigma(\phi) \rho a (\mathcal{M}_2 - \mathcal{T}_2), \quad (3.138)$$

$$\tilde{\mathfrak{T}}_\psi^2 = \mathcal{T}_5 - \frac{\mathcal{L}_{\phi^*}}{2} - \varsigma(\psi) \rho a (\mathcal{L}_3 - \mathcal{T}_3), \quad (3.139)$$

where $\phi^* = 6 - \phi$ and $\psi^* = 6 - \psi$.

It should be noted that, since $0 \leq \beta_t \leq 1$, the system (3.137) always admits solution, the determinant of the relevant matrix of coefficient being zero for $\beta_t = -1$ and $\beta_t = 3$.

Boundary conditions for Navier-Stokes equations are finally obtained after enforcing viscous conditions identical to those used for a face outflow (see Section 3.2.2).

Inflow/Outflow Edge. On the inflow/outflow edge there are 5 incoming waves on the inflow side and 1 incoming wave on the outflow side, therefore six physical boundary conditions. Therefore, inlet and outlet boundary conditions could be, in principle, simultaneously imposed by selecting six suitable relations from Eqs. (3.79) and (3.123), and enforcing inflow (*e.g.*, velocity and temperature) and outflow (pressure) boundary conditions. Nonetheless, it is well known that imposing velocity and pressure represents an ill-posed problem and, even allowing smooth transients for pressure, *i.e.*, using relaxation toward a target pressure, the two boundary conditions have shown problems of stability when simultaneously set.

A simple remedy, which has proven to be effective for the configurations studied in this work, is to set to zero the incoming wave amplitude variation relevant to the outflow boundary (“perfectly non-reflecting” outflow [78]): this is what we call a “compatibility condition” for inflow/outflow edge boundaries. In this way, the pressure is left free to adapt to the local flow field and tends anyway to the expected value due to the effect of the neighboring outflow regions. Furthermore, as the only unknown wave amplitude on the outflow side is directly imposed and set to zero, the edge become decoupled on the two characteristic directions and the remaining incoming waves on the inlet side can be computed directly.

Supposing, for instance, that the inlet is normal to x_1 and the outflow normal to x_2 , the unknown waves are \mathcal{L}_5 (\mathcal{L}_1) and $\mathcal{L}_{2,3,4,6}$ if the edge is located at $x_1 = 0$ ($x_1 = L_x$) and \mathcal{M}_5 (\mathcal{M}_1) if the edge is located at $x_2 = 0$ ($x_2 = L_y$). The characteristic relations are formally

identical to Eqs. (3.89)–(3.93) and the boundary conditions are given by Eqs. (3.94)–(3.98), therefore the expressions for the unknown wave amplitude variations are:

$$\mathcal{L}_\phi = \eta_\phi \frac{\rho a^2 (1 - M_{\max}^2)}{L_x} \Delta u_1 + \mathfrak{T}_\phi^1, \quad (3.140)$$

$$\mathcal{L}_2 = \eta_2 \frac{\rho a R}{L_x} \Delta T + \mathfrak{T}_2^1, \quad (3.141)$$

$$\mathcal{L}_3 = \eta_3 \frac{a}{L_x} \Delta u_2 + \mathfrak{T}_3^1, \quad (3.142)$$

$$\mathcal{L}_4 = \eta_4 \frac{a}{L_x} \Delta u_3 + \mathfrak{T}_4^1, \quad (3.143)$$

$$\mathcal{L}_6 = \eta_6 \frac{a}{L_x} \Delta Z + \mathfrak{T}_6^1. \quad (3.144)$$

From the compatibility condition $\mathcal{M}_\psi = 0$ and Eq. (3.126), the transverse terms in the above relations are:

$$\mathfrak{T}_\phi^1 = \mathcal{T}_5 - \frac{\mathcal{M}_{\psi^*}}{2} + \varsigma(\phi) \rho a (\mathcal{T}_2 - \mathcal{M}_2), \quad (3.145)$$

$$\mathfrak{T}_2^1 = a^2 \mathcal{T}_1 - \mathcal{T}_5 - \mathcal{M}_3, \quad (3.146)$$

$$\mathfrak{T}_3^1 = \mathcal{T}_3 + \frac{\varsigma(\psi)}{2\rho a} \mathcal{M}_{\psi^*}, \quad (3.147)$$

$$\mathfrak{T}_4^1 = \mathcal{T}_4 - \mathcal{M}_4, \quad (3.148)$$

$$\mathfrak{T}_6^1 = \mathcal{T}_6 - \mathcal{M}_6. \quad (3.149)$$

Again, indices ϕ and ψ and the value of ς can be obtained from Eqs. (3.83), (3.132) and Eq. (3.84) (see Figure 3.8) and $\psi^* = 6 - \psi$ is the index relevant to the outgoing wave on the outflow side. The equation for \mathfrak{T}_3^1 , in particular, has been obtained using the compatibility condition and the following identity:

$$\frac{1}{2\rho a} (\mathcal{M}_5 - \mathcal{M}_1) = \frac{\varsigma(\psi)}{2\rho a} (\mathcal{M}_\psi - \mathcal{M}_{\psi^*}) \quad (3.150)$$

As already observed in Section 3.2.2 when talking about the subsonic non-reflecting inflow, the only necessary viscous conditions for the Navier-Stokes equations are those relevant to the outflow side and are identical to those used for a face boundary.

Wall/Outflow Edge. On this kind of edge, in principle, one should impose the pressure for what concerns the outlet condition, and velocity for what concerns the wall condition (the time derivative of the velocity component normal to the wall is set to zero). As suggested by Poinot and Lele, just imposing all these quantities at the same time is not effective, but allowing smooth transient for the pressure, namely relaxing outlet pressure, improves the stability of the boundary condition.

Let the wall be normal to x_1 and the outflow be normal to x_2 . Since the velocity at the wall is zero, the only non-zero wave amplitude variations are $\mathcal{L}_{1,5}$ and $\mathcal{M}_{1,5}$ (those characterized by characteristic speeds $u_1 \mp a$ and $u_2 \mp a$ respectively). Transverse terms \mathcal{T}_1 , \mathcal{T}_2 , \mathcal{T}_3 , \mathcal{T}_5 and \mathcal{T}_6 are zero as well, as it can be verified from Eq. (3.119). The second equation from system (3.118)

and the pseudo-characteristic relation relevant to the outflow side (*cf.* Eq. (3.123)) reduce to:

$$\frac{\partial u_1}{\partial t} + \frac{1}{2\rho a} (\mathcal{L}_5 - \mathcal{L}_1) = 0, \quad (3.151)$$

$$\left[\frac{\partial p}{\partial t} + \varsigma(\psi)\rho a \frac{\partial u_2}{\partial t} \right] + \mathcal{M}_\psi - \mathfrak{T}_\psi^2 = 0, \quad (3.152)$$

with ψ given in Eq. (3.132), ς setting the correct sign according to Eq. (3.84) and

$$\mathfrak{T}_\psi^2 = -\frac{1}{2}(\mathcal{L}_5 + \mathcal{L}_1). \quad (3.153)$$

The physical boundary conditions are expressed by Eq. (3.104) and (3.134) leading to the following solution for the incoming wave amplitude variations \mathcal{L}_ϕ and \mathcal{M}_ψ :

$$\begin{cases} \mathcal{L}_\phi = \mathcal{L}_{\phi^*} \\ \mathcal{M}_\psi = \sigma \frac{a(1 - M_{\max}^2)}{L_y} \Delta p - (1 - \beta_t)\mathcal{L}_{\phi^*} + \beta_t \mathfrak{T}_{\psi,\text{ex}}^2 \end{cases} \quad (3.154)$$

with ϕ given from Eq. (3.83) and $\phi^* = 6 - \phi$. Velocity components u_2 and u_3 are simply forced to zero and $\mathfrak{T}_{\psi,\text{ex}}^2$ may be computed from Eq. (3.136).

Finally, the necessary viscous conditions for the Navier-Stokes equations are added in analogy to what has been done for the other edge typologies in the previous sections.

3.2.4 Characteristic Formulation Along Three Directions for Corners

When the computational point is located on the corner belonging to three boundaries, three characteristic directions need to be considered. This case may be regarded as a generalization of the procedure described in Section 3.2.3 for edges, therefore there remain the main issues of wave coupling and compatibility conditions. As it will be shown in the next section, since now all the flux matrices are diagonalized, there cannot be any \mathcal{T} vector anymore and the characteristic transverse terms \mathfrak{T}^k are computed entirely from wave amplitude variations.

Characteristic waves are considered in all the three directions; all the flux matrices are diagonalized and Eq. (3.55) becomes:

$$\frac{\partial \mathcal{U}}{\partial t} + \mathbf{S}_1 \mathbf{\Lambda}^1 \mathbf{S}_1^{-1} \frac{\partial \mathcal{U}}{\partial x_1} + \mathbf{S}_2 \mathbf{\Lambda}^2 \mathbf{S}_2^{-1} \frac{\partial \mathcal{U}}{\partial x_2} + \mathbf{S}_3 \mathbf{\Lambda}^3 \mathbf{S}_3^{-1} \frac{\partial \mathcal{U}}{\partial x_3} + \mathcal{D} = \mathbf{0}. \quad (3.155)$$

The eigenvalues and the transformation matrices relevant to \mathcal{F}^1 and \mathcal{F}^2 are obtained from Eqs. (3.62)–(3.64) and Eqs. (3.108)–(3.110) respectively and \mathcal{F}^3 is diagonalized with the following matrices:

$$\mathbf{\Lambda}^3 = \begin{pmatrix} u_3 - a & 0 & 0 & 0 & 0 & 0 \\ 0 & u_3 & 0 & 0 & 0 & 0 \\ 0 & 0 & u_3 & 0 & 0 & 0 \\ 0 & 0 & 0 & u_3 & 0 & 0 \\ 0 & 0 & 0 & 0 & u_3 + a & 0 \\ 0 & 0 & 0 & 0 & 0 & u_3 \end{pmatrix}, \quad (3.156)$$

$$\mathbf{S}_3 = \begin{pmatrix} 1/(2a^2) & 0 & 0 & 1/a^2 & 1/(2a^2) & 0 \\ 0 & 1 & 0 & 0 & 0 & 0 \\ 0 & 0 & 1 & 0 & 0 & 0 \\ -1/(2\rho a) & 0 & 0 & 0 & 1/(2\rho a) & 0 \\ 1/2 & 0 & 0 & 0 & 1/2 & 0 \\ 0 & 0 & 0 & 0 & 0 & 1 \end{pmatrix}, \quad (3.157)$$

$$\mathbf{S}_3^{-1} = \begin{pmatrix} 0 & 0 & 0 & -\rho a & 1 & 0 \\ 0 & 1 & 0 & 0 & 0 & 0 \\ 0 & 0 & 1 & 0 & 0 & 0 \\ a^2 & 0 & 0 & 0 & -1 & 0 \\ 0 & 0 & 0 & \rho a & 1 & 0 \\ 0 & 0 & 0 & 0 & 0 & 1 \end{pmatrix}. \quad (3.158)$$

The wave amplitude time variations are defined as

$$\mathcal{L} = \Lambda^1 \mathbf{S}_1^{-1} \frac{\partial \mathcal{U}}{\partial x_1}, \quad \mathcal{M} = \Lambda^2 \mathbf{S}_2^{-1} \frac{\partial \mathcal{U}}{\partial x_2}, \quad \mathcal{N} = \Lambda^3 \mathbf{S}_3^{-1} \frac{\partial \mathcal{U}}{\partial x_3}, \quad (3.159)$$

where \mathcal{L} and \mathcal{M} are expressed by Eq. (3.66) and (3.112) respectively and \mathcal{N} is:

$$\mathcal{N} = \begin{pmatrix} \nu_1 \left(\frac{\partial p}{\partial x_3} - \rho a \frac{\partial u_3}{\partial x_3} \right) \\ \nu_2 \frac{\partial u_1}{\partial x_3} \\ \nu_3 \frac{\partial u_2}{\partial x_3} \\ \nu_4 \left(a^2 \frac{\partial \rho}{\partial x_3} - \frac{\partial p}{\partial x_3} \right) \\ \nu_5 \left(\frac{\partial p}{\partial x_3} + \rho a \frac{\partial u_3}{\partial x_3} \right) \\ \nu_6 \frac{\partial Z}{\partial x_3} \end{pmatrix}, \quad (3.160)$$

ν_i being the eigenvalues of \mathcal{F}^3 . The conservation laws in terms of primitive and conservative variables are respectively:

$$\frac{\partial \mathcal{U}}{\partial t} + \mathbf{d} + \mathbf{e} + \mathbf{f} + \mathcal{D} = \mathbf{0} \quad (3.161)$$

$$\frac{\partial \mathcal{U}}{\partial t} + \mathbf{P}\mathbf{d} + \mathbf{P}\mathbf{e} + \mathbf{P}\mathbf{f} + \frac{\partial \mathcal{D}^i}{\partial x_i} = \mathbf{0} \quad (3.162)$$

where \mathbf{d} , $\mathbf{P}\mathbf{d}$, \mathbf{e} and $\mathbf{P}\mathbf{e}$ are obtained from Eqs. (3.69), (3.70), (3.115), and (3.116) respectively

while \mathbf{f} and $\mathbf{P}\mathbf{f}$ are:

$$\mathbf{f} = \mathbf{S}_3 \mathcal{N} = \begin{pmatrix} \frac{1}{a^2} \left[\mathcal{N}_4 + \frac{1}{2} (\mathcal{N}_5 + \mathcal{N}_1) \right] \\ \mathcal{N}_2 \\ \mathcal{N}_3 \\ \frac{1}{2\rho a} (\mathcal{N}_5 - \mathcal{N}_1) \\ \frac{1}{2} (\mathcal{N}_5 + \mathcal{N}_1) \\ \mathcal{N}_6 \end{pmatrix}, \quad (3.163)$$

$$\mathbf{P}\mathbf{f} = \begin{pmatrix} f_1 \\ f_1 u_1 + \rho f_2 \\ f_1 u_2 + \rho f_3 \\ f_1 u_3 + \rho f_4 \\ f_1 \frac{u_k u_k}{2} + \rho u_j f_{j+1} + \frac{f_5}{\gamma - 1} \\ f_1 Z + \rho f_6 \end{pmatrix}. \quad (3.164)$$

Corner Boundary Conditions

The definition of tools and procedures to be used when solving the corners of the computational domain follows, basically, the same steps discussed in Section 3.2.3: (a) define the relations linking wave amplitude variations to the primitive variables; (b) derive a more suitable pseudo-characteristic formulation and the relevant characteristic transverse terms.

The system relating primitive variables with the characteristic waves is now obtained from Eq. (3.161) by neglecting the \mathcal{D} term as usual:

$$\frac{\partial \mathcal{U}}{\partial t} + \mathbf{d} + \mathbf{e} + \mathbf{f} = \mathbf{0}. \quad (3.165)$$

Note that now, as already mentioned in the previous section, there is no \mathcal{T} vector. The

above compact relation may be written in components as:

$$\left\{ \begin{array}{l} \frac{\partial \rho}{\partial t} + \frac{1}{a^2} \left[\mathcal{L}_2 + \frac{1}{2} (\mathcal{L}_5 + \mathcal{L}_1) \right] \\ \quad + \frac{1}{a^2} \left[\mathcal{M}_3 + \frac{1}{2} (\mathcal{M}_5 + \mathcal{M}_1) \right] \\ \quad \quad + \frac{1}{a^2} \left[\mathcal{N}_4 + \frac{1}{2} (\mathcal{N}_5 + \mathcal{N}_1) \right] = 0 \\ \frac{\partial u_1}{\partial t} + \frac{1}{2\rho a} (\mathcal{L}_5 - \mathcal{L}_1) + \mathcal{M}_2 + \mathcal{N}_2 = 0 \\ \frac{\partial u_2}{\partial t} + \mathcal{L}_3 + \frac{1}{2\rho a} (\mathcal{M}_5 - \mathcal{M}_1) + \mathcal{N}_3 = 0 \\ \frac{\partial u_3}{\partial t} + \mathcal{L}_4 + \mathcal{M}_4 + \frac{1}{2\rho a} (\mathcal{N}_5 - \mathcal{N}_1) = 0 \\ \frac{\partial p}{\partial t} + \frac{1}{2} (\mathcal{L}_5 + \mathcal{L}_1) + \frac{1}{2} (\mathcal{M}_5 + \mathcal{M}_1) + \frac{1}{2} (\mathcal{N}_5 + \mathcal{N}_1) = 0 \\ \quad \quad \quad \frac{\partial Z}{\partial t} + \mathcal{L}_6 + \mathcal{M}_6 + \mathcal{N}_6 = 0 \end{array} \right. \quad (3.166)$$

The relevant pseudo-characteristic relations are obtained from Eq. (3.165) after pre-multiplying by the transformation matrices \mathbf{S}_k^{-1} :

$$\mathbf{S}_1^{-1} \frac{\partial \mathcal{U}}{\partial t} + \mathcal{L} - \mathfrak{T}^1 = \mathbf{0}, \quad (3.167)$$

$$\mathbf{S}_2^{-1} \frac{\partial \mathcal{U}}{\partial t} + \mathcal{M} - \mathfrak{T}^2 = \mathbf{0}, \quad (3.168)$$

$$\mathbf{S}_3^{-1} \frac{\partial \mathcal{U}}{\partial t} + \mathcal{N} - \mathfrak{T}^3 = \mathbf{0}, \quad (3.169)$$

the first two being formally identical to Eqs. (3.79) and (3.123) and the third representing the following system:

$$\left\{ \begin{array}{l} \left(\frac{\partial p}{\partial t} - \rho a \frac{\partial u_3}{\partial t} \right) + \mathcal{N}_1 - \mathfrak{T}_1^3 = 0 \\ \quad \quad \quad \frac{\partial u_1}{\partial t} + \mathcal{N}_2 - \mathfrak{T}_2^3 = 0 \\ \quad \quad \quad \frac{\partial u_2}{\partial t} + \mathcal{N}_3 - \mathfrak{T}_3^3 = 0 \\ \left(a^2 \frac{\partial \rho}{\partial t} - \frac{\partial p}{\partial t} \right) + \mathcal{N}_4 - \mathfrak{T}_4^3 = 0 \\ \left(\frac{\partial p}{\partial t} + \rho a \frac{\partial u_3}{\partial t} \right) + \mathcal{N}_5 - \mathfrak{T}_5^3 = 0 \\ \quad \quad \quad \frac{\partial Z}{\partial t} + \mathcal{N}_6 - \mathfrak{T}_6^3 = 0 \end{array} \right. \quad (3.170)$$

Characteristic transverse terms are computed from the following relations:

$$\mathfrak{T}^1 = -\mathbf{S}_1^{-1}(\mathbf{e} + \mathbf{f}), \quad (3.171)$$

$$\mathfrak{T}^2 = -\mathbf{S}_2^{-1}(\mathbf{d} + \mathbf{f}), \quad (3.172)$$

$$\mathfrak{T}^3 = -\mathbf{S}_3^{-1}(\mathbf{d} + \mathbf{e}), \quad (3.173)$$

which may be explicitly written as

$$\mathfrak{T}^1 = \begin{pmatrix} -\frac{1}{2}(\mathcal{M}_5 + \mathcal{M}_1 + \mathcal{N}_5 + \mathcal{N}_1) + \rho a(\mathcal{M}_2 + \mathcal{N}_2) \\ -\mathcal{M}_3 - \mathcal{N}_4 \\ -\frac{1}{2\rho a}(\mathcal{M}_5 - \mathcal{M}_1) - \mathcal{N}_3 \\ -\mathcal{M}_4 - \frac{1}{2\rho a}(\mathcal{N}_5 - \mathcal{N}_1) \\ -\frac{1}{2}(\mathcal{M}_5 + \mathcal{M}_1 + \mathcal{N}_5 + \mathcal{N}_1) - \rho a(\mathcal{M}_2 + \mathcal{N}_2) \\ -\mathcal{M}_6 - \mathcal{N}_6 \end{pmatrix}, \quad (3.174)$$

$$\mathfrak{T}^2 = \begin{pmatrix} -\frac{1}{2}(\mathcal{L}_5 + \mathcal{L}_1 + \mathcal{N}_5 + \mathcal{N}_1) + \rho a(\mathcal{L}_3 + \mathcal{N}_3) \\ -\frac{1}{2\rho a}(\mathcal{L}_5 - \mathcal{L}_1) - \mathcal{N}_2 \\ -\mathcal{L}_2 - \mathcal{N}_4 \\ -\mathcal{L}_4 - \frac{1}{2\rho a}(\mathcal{N}_5 - \mathcal{N}_1) \\ -\frac{1}{2}(\mathcal{L}_5 + \mathcal{L}_1 + \mathcal{N}_5 + \mathcal{N}_1) - \rho a(\mathcal{L}_3 + \mathcal{N}_3) \\ -\mathcal{L}_6 - \mathcal{N}_6 \end{pmatrix}, \quad (3.175)$$

$$\mathfrak{T}^3 = \begin{pmatrix} -\frac{1}{2}(\mathcal{L}_5 + \mathcal{L}_1 + \mathcal{M}_5 + \mathcal{M}_1) + \rho a(\mathcal{L}_4 + \mathcal{M}_4) \\ -\frac{1}{2\rho a}(\mathcal{L}_5 - \mathcal{L}_1) - \mathcal{M}_2 \\ -\mathcal{L}_3 - \frac{1}{2\rho a}(\mathcal{M}_5 - \mathcal{M}_1) \\ -\mathcal{L}_2 - \mathcal{M}_3 \\ -\frac{1}{2}(\mathcal{L}_5 + \mathcal{L}_1 + \mathcal{M}_5 + \mathcal{M}_1) - \rho a(\mathcal{L}_4 + \mathcal{M}_4) \\ -\mathcal{L}_6 - \mathcal{M}_6 \end{pmatrix}. \quad (3.176)$$

The physical boundary conditions and the relevant compatibility conditions are now discussed for the following corner typologies:

1. boundary corner belonging to three subsonic non-reflecting outflows;
2. boundary corner belonging to two subsonic non-reflecting outflows and a subsonic non-reflecting inflow;
3. boundary corner belonging to two subsonic non-reflecting outflows and an adiabatic no-slip wall.

Outflow/Outflow/Outflow Corner. Since there are three unknown entering waves, one for each direction, three pseudo-characteristic relations are taken from Eqs. (3.79), (3.123) and (3.170). Depending on the location of the corner, the incoming waves are \mathcal{L}_5 (\mathcal{L}_1) for $x_1 = 0$ ($x_1 = L_x$), \mathcal{M}_5 (\mathcal{M}_1) for $x_2 = 0$ ($x_2 = L_y$) and \mathcal{N}_5 (\mathcal{N}_1) for $x_3 = 0$ ($x_3 = L_z$); the relevant pseudo-characteristic relations are written as:

$$\left[\frac{\partial p}{\partial t} + \varsigma(\phi)\rho a \frac{\partial u_1}{\partial t} \right] + \mathcal{L}_\phi - \mathfrak{T}_\phi^1 = 0, \quad (3.177)$$

$$\left[\frac{\partial p}{\partial t} + \varsigma(\psi)\rho a \frac{\partial u_2}{\partial t} \right] + \mathcal{M}_\psi - \mathfrak{T}_\psi^2 = 0, \quad (3.178)$$

$$\left[\frac{\partial p}{\partial t} + \varsigma(\chi)\rho a \frac{\partial u_3}{\partial t} \right] + \mathcal{N}_\chi - \mathfrak{T}_\chi^3 = 0, \quad (3.179)$$

with

$$\mathfrak{T}_\phi^1 = -\frac{1}{2}(\mathcal{M}_5 + \mathcal{M}_1 + \mathcal{N}_5 + \mathcal{N}_1) - \varsigma(\phi)\rho a(\mathcal{M}_2 + \mathcal{N}_2), \quad (3.180)$$

$$\mathfrak{T}_\psi^2 = -\frac{1}{2}(\mathcal{L}_5 + \mathcal{L}_1 + \mathcal{N}_5 + \mathcal{N}_1) - \varsigma(\psi)\rho a(\mathcal{L}_3 + \mathcal{N}_3), \quad (3.181)$$

$$\mathfrak{T}_\chi^3 = -\frac{1}{2}(\mathcal{L}_5 + \mathcal{L}_1 + \mathcal{M}_5 + \mathcal{M}_1) - \varsigma(\chi)\rho a(\mathcal{L}_4 + \mathcal{M}_4), \quad (3.182)$$

where ϕ and ψ are given in Eqs. (3.83) and (3.132) respectively, χ identifies the entering wave along x_3

$$\chi = \begin{cases} 5 & \text{if } x_3 = 0, \\ 1 & \text{if } x_3 = L_z. \end{cases} \quad (3.183)$$

and ς (see Eq. (3.84)) selects the correct signs accordingly.

The three necessary boundary conditions are obtained from Eq. (3.85) plus analogous relations for u_2 and u_3 :

$$\left[\frac{\partial p}{\partial t} + \varsigma(\phi)\rho a \frac{\partial u_1}{\partial t} \right] + \sigma \frac{a(1 - M_{\max}^2)}{L_x} \Delta p - \beta_t (\mathfrak{T}_\phi^1 - \mathfrak{T}_{\phi,\text{ex}}^1) = 0, \quad (3.184)$$

$$\left[\frac{\partial p}{\partial t} + \varsigma(\psi)\rho a \frac{\partial u_2}{\partial t} \right] + \sigma \frac{a(1 - M_{\max}^2)}{L_y} \Delta p - \beta_t (\mathfrak{T}_\psi^2 - \mathfrak{T}_{\psi,\text{ex}}^2) = 0, \quad (3.185)$$

$$\left[\frac{\partial p}{\partial t} + \varsigma(\chi)\rho a \frac{\partial u_3}{\partial t} \right] + \sigma \frac{a(1 - M_{\max}^2)}{L_z} \Delta p - \beta_t (\mathfrak{T}_\chi^3 - \mathfrak{T}_{\chi,\text{ex}}^3) = 0, \quad (3.186)$$

Exact transverse terms $\mathfrak{T}_{\phi,\text{ex}}^1$, $\mathfrak{T}_{\psi,\text{ex}}^2$ and $\mathfrak{T}_{\chi,\text{ex}}^3$, if needed, may be computed for a reference steady flow, respectively, from Eqs. (3.135), (3.136) and the following relation:

$$\mathfrak{T}_{\chi,\text{ex}}^3 = -\hat{u}_t \frac{\partial \hat{p}}{\partial x_t} - \gamma \hat{p} \frac{\partial \hat{u}_t}{\partial x_t} - \varsigma(\chi) \hat{\rho} \hat{a} \hat{u}_t \frac{\partial \hat{u}_3}{\partial x_t}, \quad (t = 1, 2) \quad (3.187)$$

Combining the pseudo-characteristic relations in Eqs. (3.177)–(3.182) with the physical boundary conditions Eqs. (3.184)–(3.186), the following linear system of equations is obtained

to solve for the wave amplitude variations of the unknown incoming waves:

$$\begin{cases} \mathcal{L}_\phi + \frac{1-\beta_t}{2}\mathcal{M}_\psi + \frac{1-\beta_t}{2}\mathcal{N}_\chi = \sigma \frac{a(1-M_{\max}^2)}{L_x} \Delta p + (1-\beta_t)\tilde{\mathfrak{T}}_\phi^1 + \beta_t \mathfrak{T}_{\phi,\text{ex}}^1 \\ \frac{1-\beta_t}{2}\mathcal{L}_\phi + \mathcal{M}_\psi + \frac{1-\beta_t}{2}\mathcal{N}_\chi = \sigma \frac{a(1-M_{\max}^2)}{L_y} \Delta p + (1-\beta_t)\tilde{\mathfrak{T}}_\psi^2 + \beta_t \mathfrak{T}_{\psi,\text{ex}}^2 \\ \frac{1-\beta_t}{2}\mathcal{L}_\phi + \frac{1-\beta_t}{2}\mathcal{M}_\psi + \mathcal{N}_\chi = \sigma \frac{a(1-M_{\max}^2)}{L_z} \Delta p + (1-\beta_t)\tilde{\mathfrak{T}}_\chi^3 + \beta_t \mathfrak{T}_{\chi,\text{ex}}^3 \end{cases} \quad (3.188)$$

with the known terms

$$\tilde{\mathfrak{T}}_\phi^1 = -\frac{1}{2}(\mathcal{M}_{\psi^*} + \mathcal{N}_{\chi^*}) - \varsigma(\phi)\rho a(\mathcal{M}_2 + \mathcal{N}_2), \quad (3.189)$$

$$\tilde{\mathfrak{T}}_\psi^2 = -\frac{1}{2}(\mathcal{L}_{\phi^*} + \mathcal{N}_{\chi^*}) - \varsigma(\psi)\rho a(\mathcal{L}_3 + \mathcal{N}_3), \quad (3.190)$$

$$\tilde{\mathfrak{T}}_\chi^3 = -\frac{1}{2}(\mathcal{L}_{\phi^*} + \mathcal{M}_{\psi^*}) - \varsigma(\chi)\rho a(\mathcal{L}_4 + \mathcal{M}_4), \quad (3.191)$$

and starred indices $\phi^* = 6 - \phi$, $\psi^* = 6 - \psi$ and $\chi^* = 6 - \chi$. Observe that the determinant of the relevant coefficients matrix is $-\frac{1}{4}\beta_t^3 + \frac{3}{4}\beta_t + \frac{1}{2}$ and is zero for $\beta_t = -1$ (two coincident roots) and $\beta_t = 2$, therefore the system (3.188) always admits solution for $\beta_t \in [0 : 1]$.

Inflow/Outflow/Outflow Corner. The presence of the inlet boundary condition makes it necessary to impose compatibility conditions and, in analogy to what is done on inflow/outflow edge boundaries, the “perfectly non-reflecting” condition is imposed on the outflows, thus decoupling the inlet from the outlets.

If, for instance, the inflow is normal to x_1 and the outflows are normal to x_2 and x_3 respectively, then, the compatibility conditions are:

$$\mathcal{M}_\psi = 0, \quad \mathcal{N}_\chi = 0, \quad (3.192)$$

where ψ and χ are given in Eqs. (3.132) and (3.183) respectively.

Since the inflow is decoupled from the outflows, the unknown wave amplitude variations on the inflow side are directly solved from the characteristic relations (3.89)–(3.93) and the boundary conditions (3.94)–(3.98):

$$\mathcal{L}_\phi = \eta_\phi \frac{\rho a^2 (1 - M_{\max}^2)}{L_x} \Delta u_1 + \mathfrak{T}_\phi^1, \quad (3.193)$$

$$\mathcal{L}_2 = \eta_2 \frac{\rho a R}{L_x} \Delta T + \mathfrak{T}_2^1, \quad (3.194)$$

$$\mathcal{L}_3 = \eta_3 \frac{a}{L_x} \Delta u_2 + \mathfrak{T}_3^1, \quad (3.195)$$

$$\mathcal{L}_4 = \eta_4 \frac{a}{L_x} \Delta u_3 + \mathfrak{T}_4^1, \quad (3.196)$$

$$\mathcal{L}_6 = \eta_6 \frac{a}{L_x} \Delta Z + \mathfrak{T}_6^1, \quad (3.197)$$

Making use of the compatibility conditions, the characteristic transverse terms in the above relations are obtained from Eq. (3.174):

$$\mathfrak{T}_\phi^1 = -\frac{1}{2}(\mathcal{M}_{\psi^*} + \mathcal{N}_{\chi^*}) - \varsigma(\phi)\rho a(\mathcal{M}_2 + \mathcal{N}_2), \quad (3.198)$$

$$\mathfrak{T}_2^1 = -\mathcal{M}_3 - \mathcal{N}_4, \quad (3.199)$$

$$\mathfrak{T}_3^1 = \frac{\varsigma(\psi)}{2\rho a}\mathcal{M}_{\psi^*} - \mathcal{N}_3, \quad (3.200)$$

$$\mathfrak{T}_4^1 = \frac{\varsigma(\chi)}{2\rho a}\mathcal{N}_{\chi^*} - \mathcal{M}_4, \quad (3.201)$$

$$\mathfrak{T}_6^1 = -\mathcal{M}_6 - \mathcal{N}_6, \quad (3.202)$$

with $\psi^* = 6 - \psi$ and $\chi^* = 6 - \chi$. An analogous identity as in Eq. (3.150) has been used to derive the equation for \mathfrak{T}_4^1 :

$$\frac{1}{2\rho a}(\mathcal{N}_5 - \mathcal{N}_1) = \frac{\varsigma(\chi)}{2\rho a}(\mathcal{N}_\chi - \mathcal{N}_{\chi^*}) \quad (3.203)$$

Wall/Outflow/Outflow Corner. In analogy with the wall/outflow edge condition, the adiabatic no-slip condition is imposed on the wall side while allowing smooth transients for the pressure, through relaxation, on the outflow sides.

Let the wall be normal to x_1 and the outflows be normal to x_2 and x_3 . Since the velocity at the wall is zero, the only non-zero wave amplitude variations are $\mathcal{L}_{1,5}$, $\mathcal{M}_{1,5}$ and $\mathcal{N}_{1,5}$ (*i.e.*, those characterized by characteristic speeds $u_1 \mp a$, $u_2 \mp a$ and $u_3 \mp a$ respectively). Consequently, the characteristic transverse terms \mathfrak{T}_2^1 , \mathfrak{T}_6^1 , \mathfrak{T}_3^2 , \mathfrak{T}_6^2 , \mathfrak{T}_4^3 and \mathfrak{T}_6^3 are zero, as it can be verified from Eqs. (3.174)–(3.176).

The characteristic relations to be used are obtained from Eqs. (3.166), (3.123) and (3.170):

$$\frac{\partial u_1}{\partial t} + \frac{1}{2\rho a}(\mathcal{L}_5 - \mathcal{L}_1) = 0, \quad (3.204)$$

$$\left[\frac{\partial p}{\partial t} + \varsigma(\psi)\rho a \frac{\partial u_2}{\partial t} \right] + \mathcal{M}_\psi - \mathfrak{T}_\psi^2 = 0, \quad (3.205)$$

$$\left[\frac{\partial p}{\partial t} + \varsigma(\chi)\rho a \frac{\partial u_3}{\partial t} \right] + \mathcal{N}_\chi - \mathfrak{T}_\chi^3 = 0, \quad (3.206)$$

with

$$\mathfrak{T}_\psi^2 = -\frac{1}{2}(\mathcal{L}_5 + \mathcal{L}_1 + \mathcal{N}_5 + \mathcal{N}_1), \quad (3.207)$$

$$\mathfrak{T}_\chi^3 = -\frac{1}{2}(\mathcal{L}_5 + \mathcal{L}_1 + \mathcal{M}_5 + \mathcal{M}_1), \quad (3.208)$$

ψ , χ and ς being defined, as usual, through Eqs. (3.132), (3.183) and (3.84) respectively.

The boundary conditions are obtained from Eq. (3.104) and Eqs. (3.185)–(3.186) respectively, which, combined with the above characteristic relations, lead to the equality between incoming and outgoing waves traveling along x_1 , namely

$$\mathcal{L}_\phi = \mathcal{L}_{\phi^*}, \quad (\phi \text{ from Eq. (3.83) and } \phi^* = 6 - \phi), \quad (3.209)$$

	Value	Ref.
M_w	28.9×10^{-3} kg/mol	Eq. (2.8)
γ	1.4	
Pr	0.72	
Sc	0.72	
μ_{ref}	1.827×10^{-5} kg/(m s)	Eq. (2.14)
T_{ref}	291.15 K	Eq. (2.14)
S	120.0 K	Eq. (2.14)

Table 3.1: Air properties.

and to the following linear system of two equations in the unknown incoming waves on the outflow sides:

$$\begin{cases} \mathcal{M}_\psi + \frac{1 - \beta_t}{2} \mathcal{N}_\chi = \sigma \frac{a(1 - M_{\text{max}}^2)}{L_y} \Delta p + (1 - \beta_t) \tilde{\mathfrak{T}}_\psi^2 + \beta_t \mathfrak{T}_{\psi,\text{ex}}^2 \\ \frac{1 - \beta_t}{2} \mathcal{M}_\psi + \mathcal{N}_\chi = \sigma \frac{a(1 - M_{\text{max}}^2)}{L_z} \Delta p + (1 - \beta_t) \tilde{\mathfrak{T}}_\chi^3 + \beta_t \mathfrak{T}_{\chi,\text{ex}}^3 \end{cases} \quad (3.210)$$

with the known transverse terms

$$\tilde{\mathfrak{T}}_\psi^2 = -\mathcal{L}_{\phi^*} - \frac{1}{2} \mathcal{N}_{\chi^*}, \quad (3.211)$$

$$\tilde{\mathfrak{T}}_\chi^3 = -\mathcal{L}_{\phi^*} - \frac{1}{2} \mathcal{M}_{\psi^*}, \quad (3.212)$$

and $\psi^* = 6 - \psi$ and $\chi^* = 6 - \chi$. Exact transverse terms $\mathfrak{T}_{\psi,\text{ex}}^2$ and $\mathfrak{T}_{\chi,\text{ex}}^3$, if needed, are computed from Eqs. (3.136) and (3.187) respectively.

3.2.5 Testing the 3D-NSCBC

Tests of 3D-NSCBC on simple flow configurations are presented in this section. These tests are mainly designed to assess the behavior of the boundary conditions when perturbations of various type travel across open boundaries. Some of the configurations presented have been chosen to allow a direct comparison with other characteristic boundary conditions that can be found in literature [58, 60].

All the simulations presented in the next sections have been performed with air, the relevant properties being summarized in Table 3.1. Qualitative results from a Large-Eddy Simulation¹⁷ of a turbulent free-jet are also presented.

Single Vortex Test-Case

This is a classical test-case for open boundary conditions and it is often adopted to assess the behavior of non-reflecting outflows when coherent vortical structures, like those characterizing turbulent flows, cross the boundary. A single vortex is superimposed to a uniform flow field,

¹⁷Details about Large-Eddy Simulations and the relevant modeling techniques will be analyzed in the next chapter.

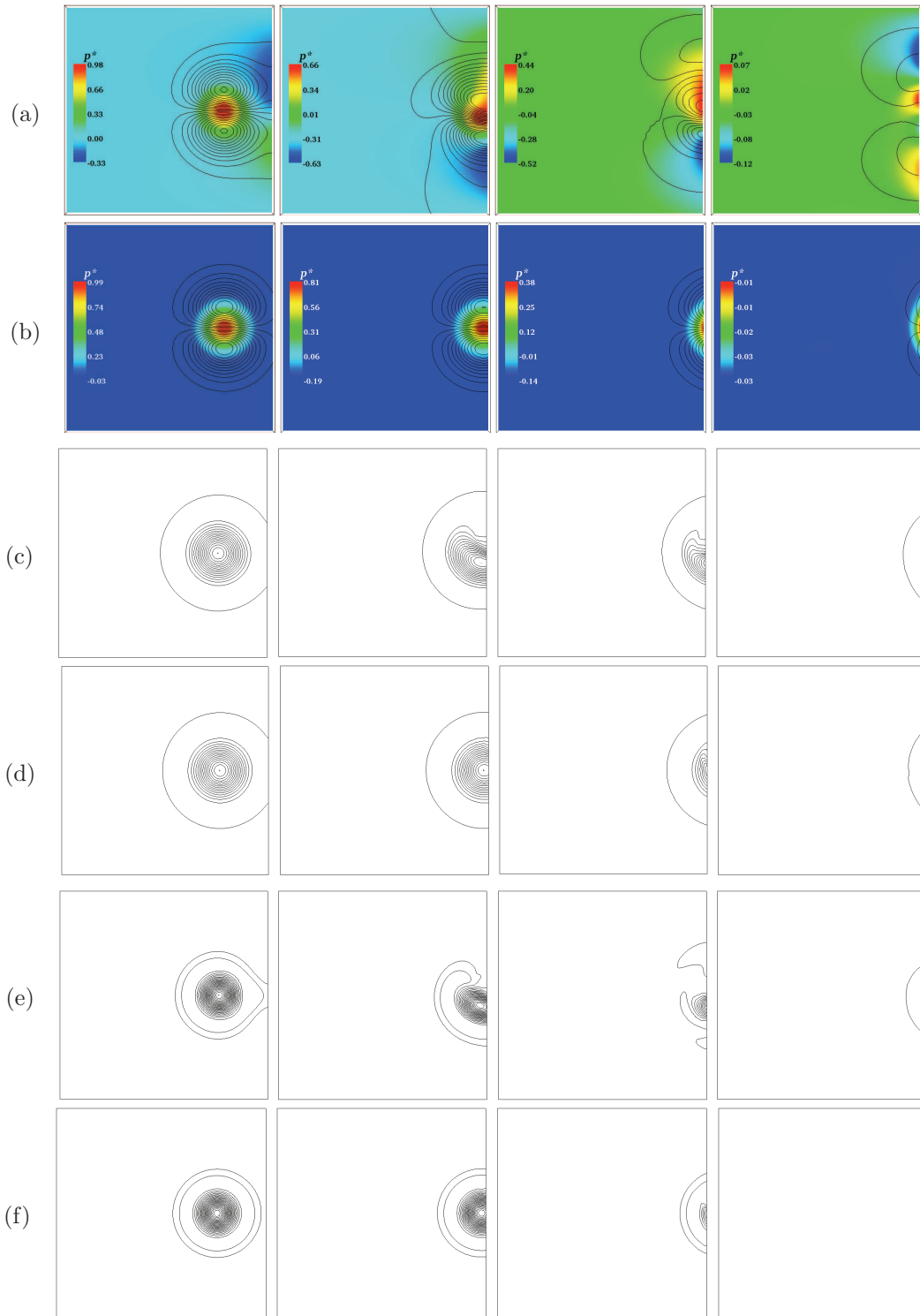


Figure 3.9: Vortex test: $M = 0.00575$. Standard NSCBC (a-c-e) and 3D-NSCBC (b-d-f). Normalized pressure field (see Eq. (3.220)) and longitudinal velocity contours (a-b); vorticity contours (c-d); Q contours (e-f). Frames at increasing time from left to right.

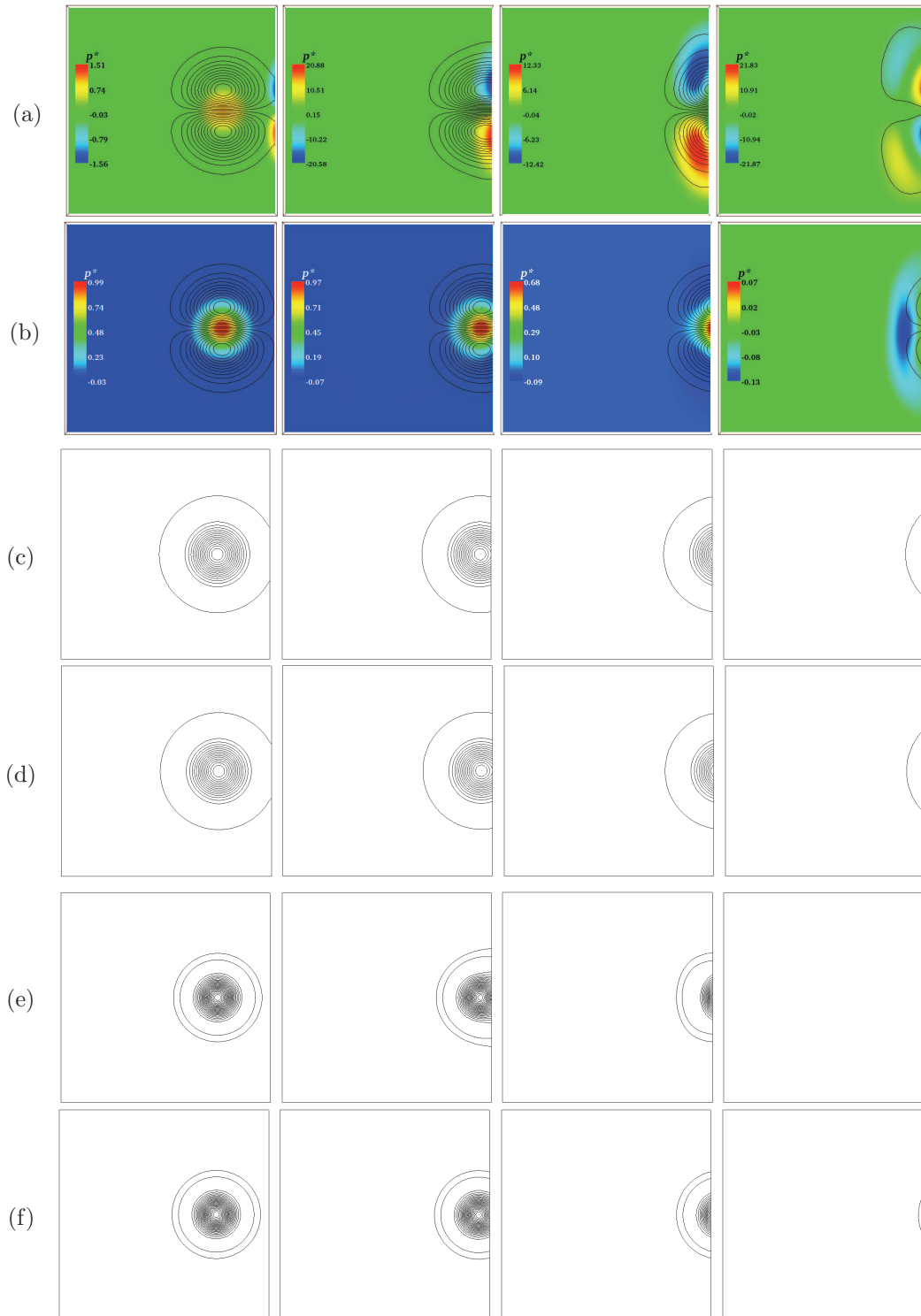


Figure 3.10: Vortex test: $M = 0.575$. Standard NSCBC (a-c-e) and 3D-NSCBC (b-d-f). Normalized pressure field (see Eq. (3.220)) and longitudinal velocity contours (a-b); vorticity contours (c-d); Q contours (e-f). Frames at increasing time from left to right.

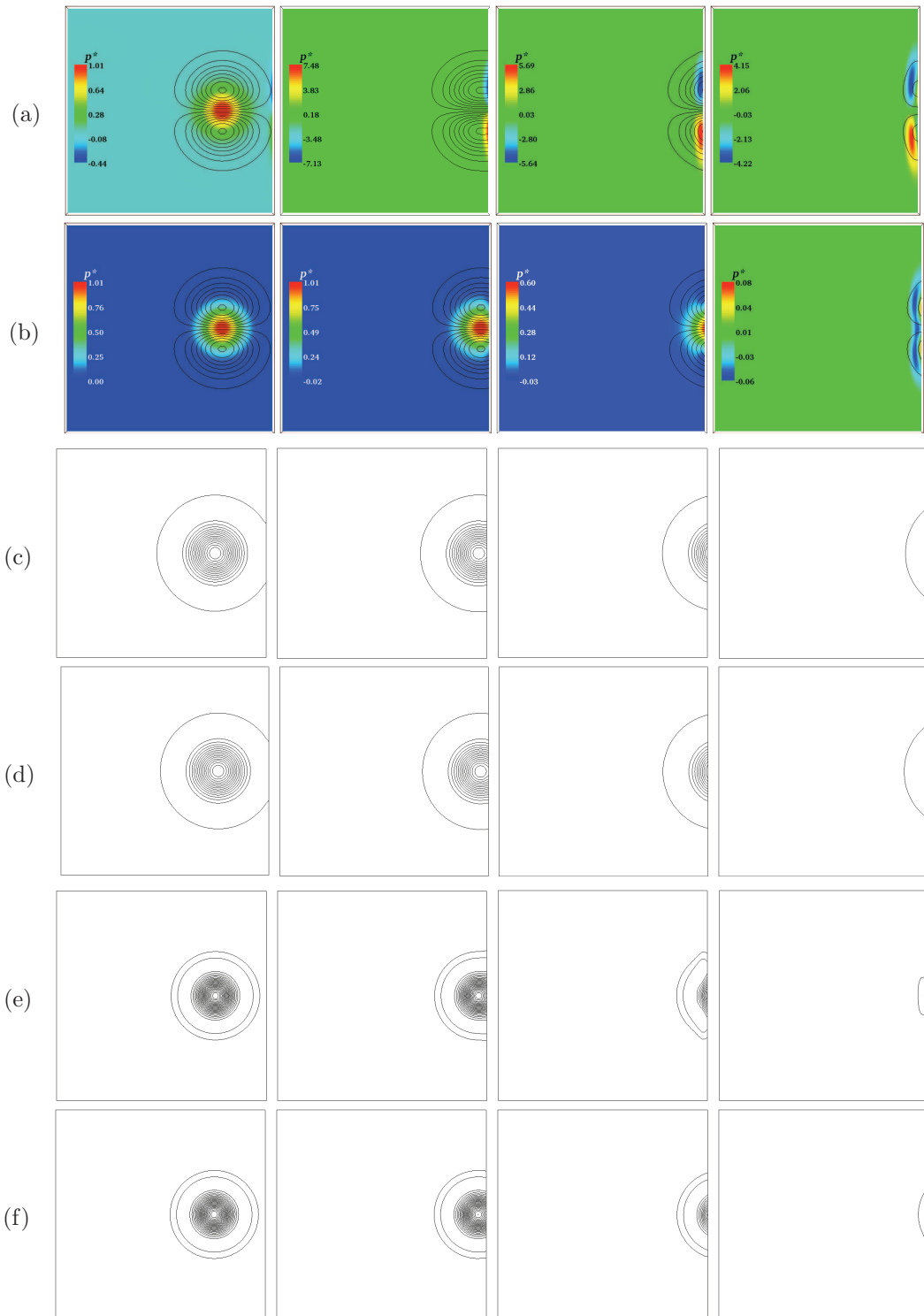


Figure 3.11: Vortex test: $M = 0.863$. Standard NSCBC (a-c-e) and 3D-NSCBC (b-d-f). Normalized pressure field (see Eq. (3.220)) and longitudinal velocity contours (a-b); vorticity contours (c-d); Q contours (e-f). Frames at increasing time from left to right.

which is aligned along the x_1 direction in the present case, and convected downstream through the outflow. The relevant vorticity is then expected to be conserved¹⁸, the accompanying low pressure core (*cf.* Eq. (3.217)) remaining unchanged. The initial flow field is defined in terms of the stream function as:

$$\Psi = C_v \exp\left(-\frac{r^2}{2R_v^2}\right) + U_0 x_2, \quad (3.213)$$

$$u_1 = \frac{\partial \Psi}{\partial x_2}, \quad u_2 = -\frac{\partial \Psi}{\partial x_1}, \quad (3.214)$$

where C_v is the vortex strength, $r = \sqrt{x_1^2 + x_2^2}$ is the radial distance from the vortex's axis x_3 and R_v is a measure of the vortex radius. U_0 is the speed of the uniform flow field along x_1 . The pressure, density and temperature can be obtained from an analytical solution. In fact, by imposing the balance of centrifugal forces by the pressure distribution, it can be shown [7] that the pressure is solution of the following equation:

$$\frac{\partial p}{\partial r} = \frac{\rho u_\phi^2}{r}, \quad (3.215)$$

where u_ϕ is the tangential velocity field in a reference frame attached to the vortex center, *i.e.*,

$$u_\phi = \frac{C_v r}{R_v^2} \exp\left(-\frac{r^2}{2R_v^2}\right). \quad (3.216)$$

Assuming that the temperature is constant and equal to T_0 , the initial pressure and density distributions can be computed integrating Eq. (3.215) as:

$$p(r) = p_\infty \exp\left[-\frac{\gamma}{2} \left(\frac{C_v}{aR_v}\right)^2 \exp\left(-\frac{r^2}{R_v^2}\right)\right], \quad (3.217)$$

$$\rho(r) = \frac{p(r)}{RT_0}, \quad (3.218)$$

with $a = \sqrt{\gamma RT_0}$ the sound speed.

In order to assess the behavior of the 3D-NSCBC at different Mach numbers, three test-cases with increasing Mach number have been performed on a square computational domain of side L ; the relevant details are summarized in Table 3.2 (SV1). Note that the Reynolds and Mach numbers are defined from the convective velocity U_0 , the characteristic size of the vortex R_v and the temperature T_0 .

The right side of the computational domain is a subsonic non-reflecting outflow with the pressure relaxation parameter σ set at 0.28, which corresponds to the optimal value proposed by Rudy and Strikwerda [62]. Increasing this value leads to a more reflective boundary condition. All the other boundaries are periodic.

Figures 3.9, 3.10 and 3.11 show a comparison of results obtained using the standard LODI assumption of the NSCBC non-reflecting outflow and the 3D-NSCBC. The represented quantities are the normalized pressure field, the vorticity contours, the longitudinal velocity contours

¹⁸Strictly speaking, no change of vorticity in the fluid element due to vortex stretching may happen (*cf.* terms $\omega_i \partial u_j / \partial x_j$ and $-\omega_j \partial u_i / \partial x_j$ in the vorticity compressible transport equation) because vorticity is orthogonal to the velocity gradient and the flow is divergence-free; therefore, the only vorticity variation mechanism is related to viscous forces.

	SV1			SV2	VD
L [m]	0.013				
p_∞ [atm]	1				
T_0 [K]	300				
R_v	10% L				
δ	–			–	15% L
C_v [m ² /s]	5×10^{-3}			3×10^{-1}	1.25×10^{-3}
U_0 [m/s]	2	200	300	100	0.5
M	0.00575	0.575	0.863	0.286	0.00144
Re	166	16600	24900	8300	42

Table 3.2: Convected vortices test-cases' parameters: single vortex (SV1), single vortex with flow inversion (SV2) and vortex dipole (VD).

and the contours of the second invariant of the velocity gradient tensor:

$$Q = -\frac{1}{2} \frac{\partial u_i}{\partial x_j} \frac{\partial u_j}{\partial x_i} = -\frac{1}{2} \left(S_{ij} S_{ij} - \frac{1}{2} \boldsymbol{\omega}^2 \right), \quad (3.219)$$

where S_{ij} is the strain rate tensor and $\boldsymbol{\omega}$ is the vorticity vector (ϵ_{kij} is the Levi-Civita symbol):

$$S_{ij} = \frac{1}{2} \left(\frac{\partial u_i}{\partial x_j} + \frac{\partial u_j}{\partial x_i} \right), \quad \text{and} \quad \omega_i = \epsilon_{ijk} \frac{\partial u_k}{\partial x_j}.$$

The frames have been taken at four different times and each figure refers to a different Mach number test. The pressure, in particular, is expressed in terms of its relative value, with respect to the far field pressure p_∞ , normalized by the initial maximum pressure drop at the center of the vortex:

$$p^*(\mathbf{x}, t) = \frac{p_\infty - p(\mathbf{x}, t)}{p_\infty - p(\mathbf{0}, 0)}. \quad (3.220)$$

The initial map of p^* is then expected to be equal to 1 in the vortex center and 0 in the far field; once the vortex has left the domain, p^* is expected to be identically 0 all over the domain.

All the computations have been done setting $\mathfrak{T}_{1,\text{ex}}^1 = 0$ (*cf.* Eq. (3.87)); as already observed, under this particular assumption—motivated by the fact that no transverse terms are expected for such a flow after the vortex has left the domain—the standard LODI assumption is retrieved in the limit of the transverse damping parameter β_t equal to 1. As it was discussed in Section 3.2.2, it may be shown that, in general, the optimal value for β_t is related to the typical Mach number for the specific flow [43, 84]. For $M \geq 1$, therefore, we would expect the modified boundary condition to recover the standard NSCBC conditions, which, in agreement with the $M = 1.1$ test case presented by Poinso and Lele [58], produces negligible flow distortion; moreover, no acoustic waves (either physical or numerical) can re-enter the domain as the flow regime is supersonic.

When the flow is subsonic, the standard NSCBC is still able to prevent fairly well distortion of vorticity iso-lines when the vortex leaves the domain. This is true for $M = 0.575$ and $M = 0.863$ but not for very low Mach number flows (see Figure 3.9a): in agreement with the results

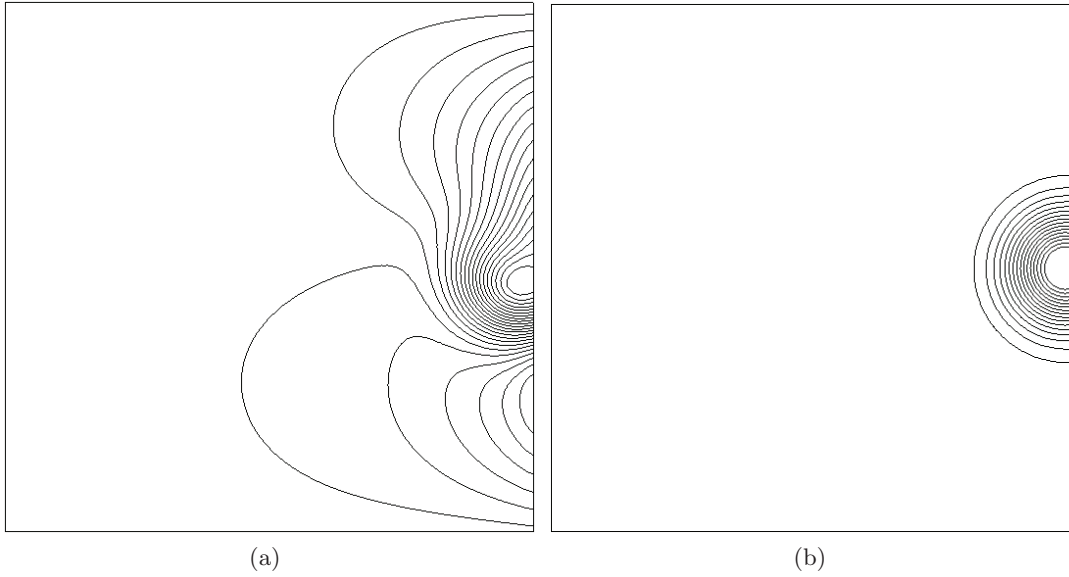


Figure 3.12: Vortex test: pressure contours as the vortex crosses the boundary ($M = 0.00575$). Standard NSCBC non-reflecting outflow (a); 3D-NSCBC non-reflecting outflow (b).

obtained by Prosser [60], vorticity, the contours of which are expected to remain concentric circles, undergoes significant distortion at the boundary. Moreover, the standard non-reflecting boundary produces significant distortion of the longitudinal velocity and Q contours: the effect is more and more pronounced when reducing the Mach number but it seems that these quantities are slightly more affected than the vorticity. This can be explained observing that the flow tends to align orthogonally to the boundary producing an unphysical disturbance in the strain rate, thus leading to the observed variation in Q .

On the other hand, the pressure field shows a somehow opposed behavior: boundary generated pressure noise amplitude becomes more and more important when increasing the Mach number but, obviously, also less and less able to re-enter the domain. For the $M = 0.575$ test, a pressure perturbation with a total amplitude that is about 44 times higher than the initial vortex pressure drop is observed at the boundary (see Figure 3.10a). Pressure field distortion is more important at low Mach, as shown in Figure 3.12a, but the accompanying disturbance is much less pronounced than in higher Mach number flows.

The proposed 3D-NSCBC produces almost no distortion in vorticity, longitudinal velocity and Q contours: vorticity is well conserved and the inclusion of transverse effects prevents additional strain to be generated at the boundary at any Mach number (Figures 3.9, 3.10 and 3.11 b-d-f). At low Mach, the pressure field distortion is dramatically reduced: pressure contours for the low Mach number case are shown in Figure 3.12b where the expected profiles—concentric circles—are perfectly reproduced. The residual pressure perturbation amplitude is reduced of about a factor 6, 214 and 60 for the low, mid and high Mach test-cases respectively, with a maximum amplitude of about 20% of the initial pressure drop at $M = 0.575$.

The error on the computed centerline boundary pressure (at $x_1 = L/2$ and $x_2 = 0$) has been quantified by comparison with a benchmark solution computed over an extended domain

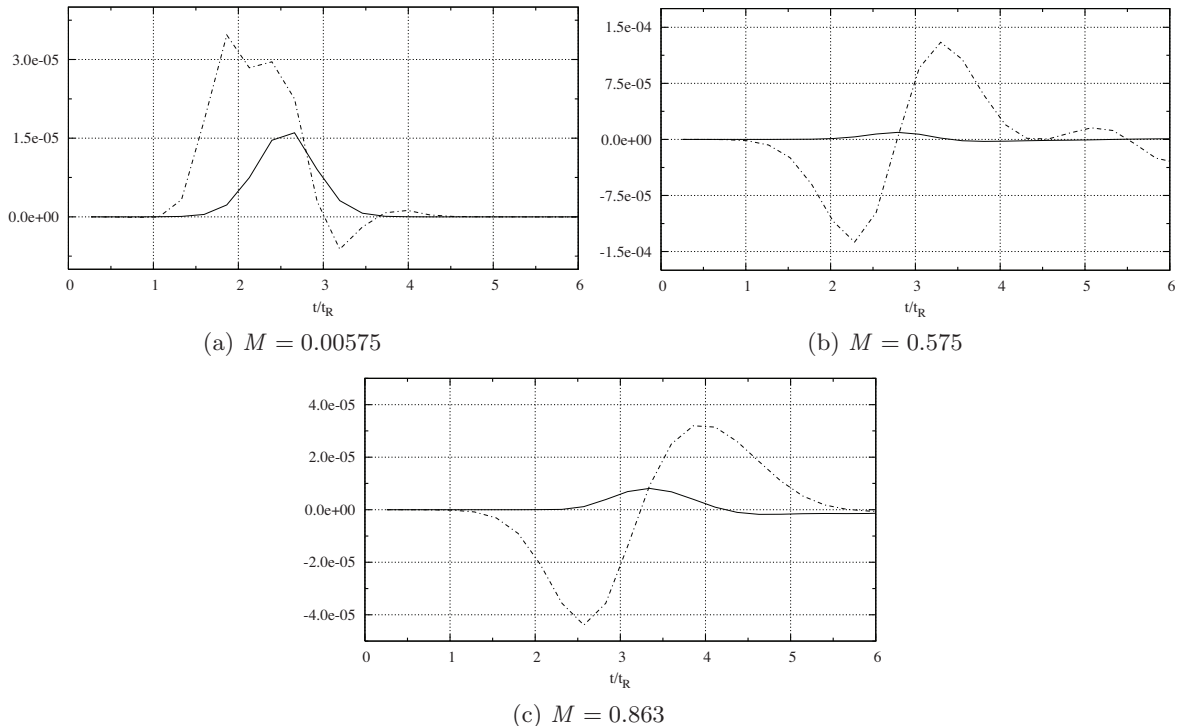


Figure 3.13: Vortex test: time evolution of the relative error in pressure $\varepsilon_r(\mathbf{x}_0, t)$ with respect to the benchmark solution on the extended domain: — , 3D-NSCBC; -- , Standard LODI. Sampling point \mathbf{x}_0 is located at the boundary, on the vortex centerline; $t_R = L/(5U_0)$.

of length $2L$. The relative error for the three tests, computed as

$$\varepsilon_r(\mathbf{x}, t) = \frac{p(\mathbf{x}, t) - p^0(\mathbf{x}, t)}{p^0(\mathbf{x}, t)}, \quad (3.221)$$

with \mathbf{x} the sampling location and p^0 the pressure computed on the benchmark simulation, is shown in Figure 3.13.

The improvement with the modified boundary condition is more evident at higher Mach numbers where the amplitude of the pressure disturbance generated using the LODI non-reflecting outflow is higher; in these cases, using the modified approach, the spurious pressure wave is almost completely damped down and the computed solution follows quite well the benchmark one. Even at low Mach, the new proposed method reduces the error of about a factor 2. In any case, the novel approach avoids any oscillatory behavior: the relative error is always positive during all the vortex transition event, meaning that the pressure drop at the vortex core is slightly under-predicted when the vortex reaches the boundary.

Single Vortex with Flow Inversion

Another two-dimensional vortex test is presented in this section. The vortex strength C_v has now been increased in order to produce a relatively strong reversed flow at the outflow. This is a particularly stringent test for non-reflecting boundary conditions, as the reversed flow requires

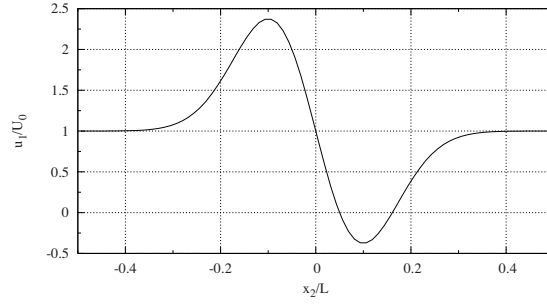


Figure 3.14: Vortex test with flow reversal: initial u_1 velocity profile along a vertical plane passing through the vortex center.

the specification of additional informations, coming from the outside of the computational domain, which are hard to be prescribed *a priori*.

The computation's parameters are summarized in Table 3.2 (SV2). With regards to the outflow boundary, the relaxation parameter for pressure σ is set at 0.28 and the transverse terms are relaxed toward $\mathfrak{T}_{1,\text{ex}}^1 = 0$ with relaxation coefficient β_t equal to 0.286, the reference Mach number for this flow.

The value of C_v is now high enough to create a region of reversed flow, as it can be observed from the initial velocity profile in Figure 3.14, where the horizontal velocity attains a negative peak of about 40 m/s for $0.0007 < x_2 < 0.002$. In those parts of the outflow boundary where reversed flow is created, the standard perfectly non-reflecting procedure [78, 79] is applied and all the entering waves traveling with convective velocity u_1 —namely, \mathcal{L}_2 , \mathcal{L}_3 , \mathcal{L}_4 and \mathcal{L}_6 —are set to zero.

Figure 3.15 shows the behavior of the 3D-NSCBC technique compared to the standard NSCBC in terms of pressure and vorticity errors; as in the previous section, the error has been estimated over a benchmark solution computed on an extended computational domain (2 times longer). The top plot in Figure 3.15a shows a normalized global error measure defined as:

$$\varepsilon_{\text{glb}}(t) = \frac{\left[\sum_{i,j,k} (p_{i,j,k}(t) - p_{i,j,k}^0(t))^2 \right]^{1/2}}{\left[\sum_{i,j,k} (p_{i,j,k}^0(t))^2 \right]^{1/2}}, \quad (3.222)$$

where the i, j, k subscript refers to the grid location and p^0 is the pressure computed on the benchmark simulation. The bottom plot on the same figure is the relative error measured on a point located at the outflow boundary on the vortex centerline (*cf.* Eq. (3.221)).

Figure 3.15b shows the normalized global error in vorticity, which is defined in analogy with Eq. (3.222) as:

$$\varepsilon_{\omega}(t) = \frac{\left[\sum_{i,j,k} (\omega_{i,j,k}(t) - \omega_{i,j,k}^0(t))^2 \right]^{1/2}}{\left[\sum_{i,j,k} (\omega_{i,j,k}^0(0))^2 \right]^{1/2}}. \quad (3.223)$$

Even when the vortex strength is enough to create flow inversion at the outflow, a certain improvement is observed over the standard NSCBC approach, when using the 3D-NSCBC technique. In terms of normalized global measures, pressure error is reduced by a factor of

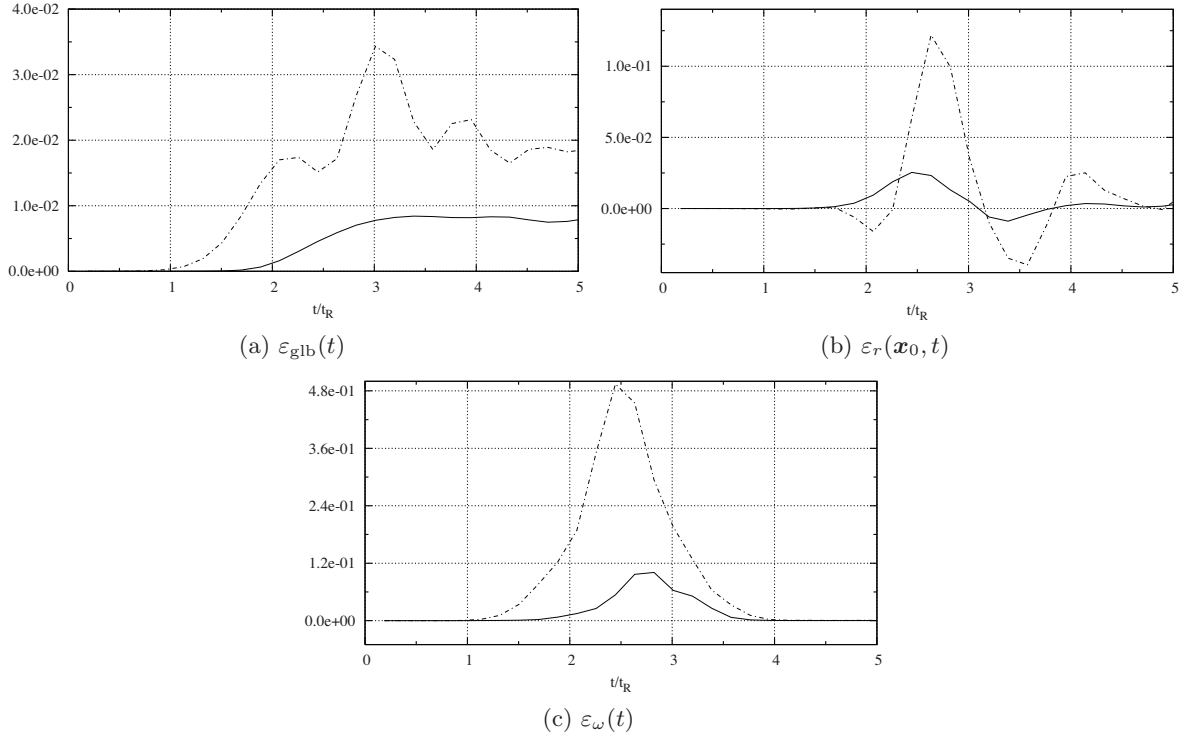


Figure 3.15: Vortex test with flow reversal: time evolution of the normalized global pressure error (a), the relative error on the centerline boundary point \mathbf{x}_0 (b) and the vorticity normalized error (c): — , 3D-NSCBC; - - , Standard LODI. $t_R = L/(5U_0)$.

about 2; with regards to the vorticity, the error peak is more than 4 times less than in the simulation performed with standard mono-dimensional boundary conditions. This is not surprising, as the 3D-NSCBC approach is expected to get advantage by the inclusion of transverse effects, therefore allowing a correct propagation of vorticity across the boundary.

Vortex Dipole

In this section a convected dipole of co-rotating vortices is analyzed in order to assess the 3D-NSCBC for problems characterized by a certain level of unsteadiness. The two vortices, in fact, slowly rotate around each other while being convected downstream. The flow field is initialized with the following stream function [60]:

$$\Psi = C_v \left[\exp\left(-\frac{r_1^2}{2R_v^2}\right) + \exp\left(-\frac{r_2^2}{2R_v^2}\right) \right] + U_0 x_2, \quad (3.224)$$

with

$$r_1 = \sqrt{x_1^2 + (x_2 + \delta)^2}, \quad (3.225)$$

$$r_2 = \sqrt{x_1^2 + (x_2 - \delta)^2}, \quad (3.226)$$

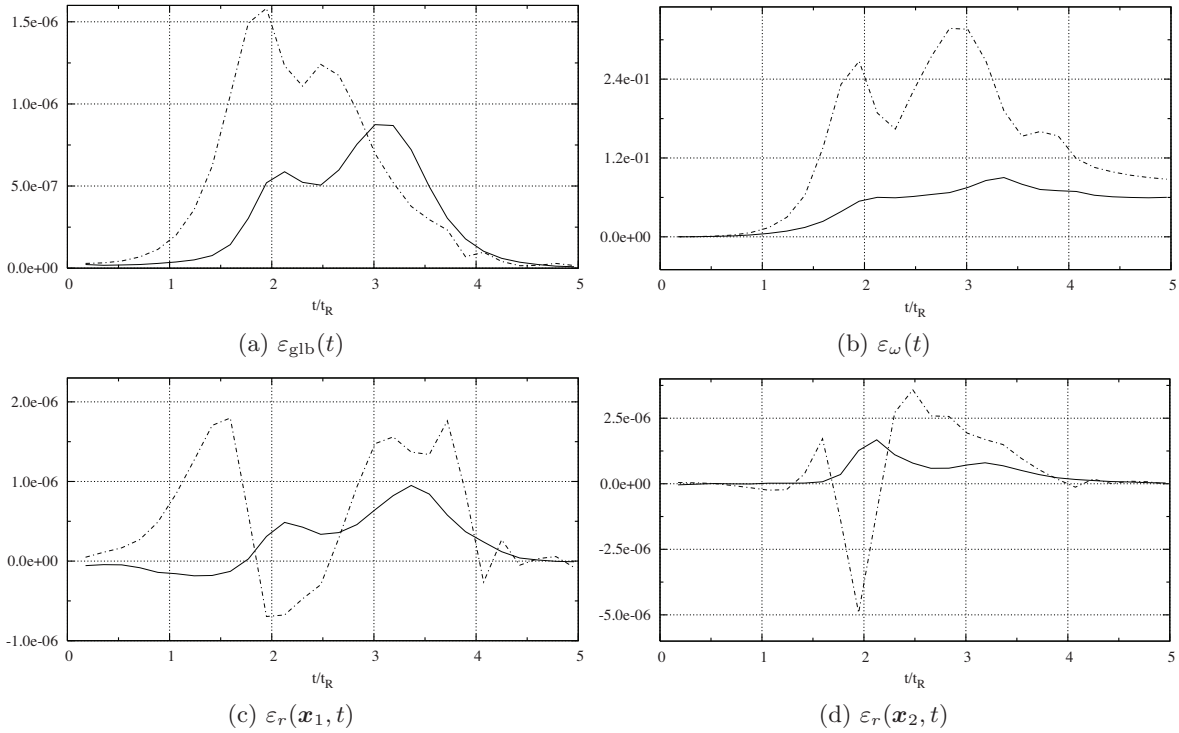


Figure 3.16: Vortex test with flow reversal: time evolution of the normalized global pressure error (a), the normalized vorticity error (b), the boundary pressure relative error at the upper vortex centerline \mathbf{x}_1 (c) and at the lower vortex centerline \mathbf{x}_2 (d): — , 3D-NSCBC; --- , Standard LODI. $t_R = L/(5U_0)$.

the relevant parameters being listed in Table 3.2 (VD). The relaxation parameter for pressure σ and the transverse relaxation parameter β_t are 0.28 and 0.00144 respectively ($\mathfrak{T}_{1,\text{ex}}^1 = 0$), the latter being the reference Mach number computed on the convective velocity U_0 .

A reference simulation is performed over a longer domain of length $2L$ in order to have a benchmark solution to compare with. The relevant results, in terms of pressure (Eqs. (3.221) and (3.222)) and vorticity (Eq. (3.223)) errors are shown in Figure 3.16. Local relative error, in particular, has been sampled at the boundary on two points, P1 and P2, corresponding approximately to the upper and lower vortex centers respectively.

Pressure and vorticity errors are generally in line with those observed on the single vortex test case. Due to the slow rotation of the two vortices around each other, the lower and the upper vortex's centers cross the outflow boundary at different times: these may be inferred observing the pressure time history on the benchmark solution—*i.e.*, looking for the instant the low pressure peak in the vortex's core reach the $x_1 = L/2$ plane—and are equal to $\simeq 2.1t_R$ and $\simeq 3.2t_R$ respectively. As the maximum normalized pressure error is, in general, attained at the moment the vortex core leave the domain, the two peaks in the global normalized error curve (Figure 3.16a) indicate precisely those two instants. Interestingly, the standard NSCBC boundary produces a shift to the left of the peaks, indicating that the pressure field is perturbed in such a way that the two vortices seem to leave the domain earlier than expected. On the

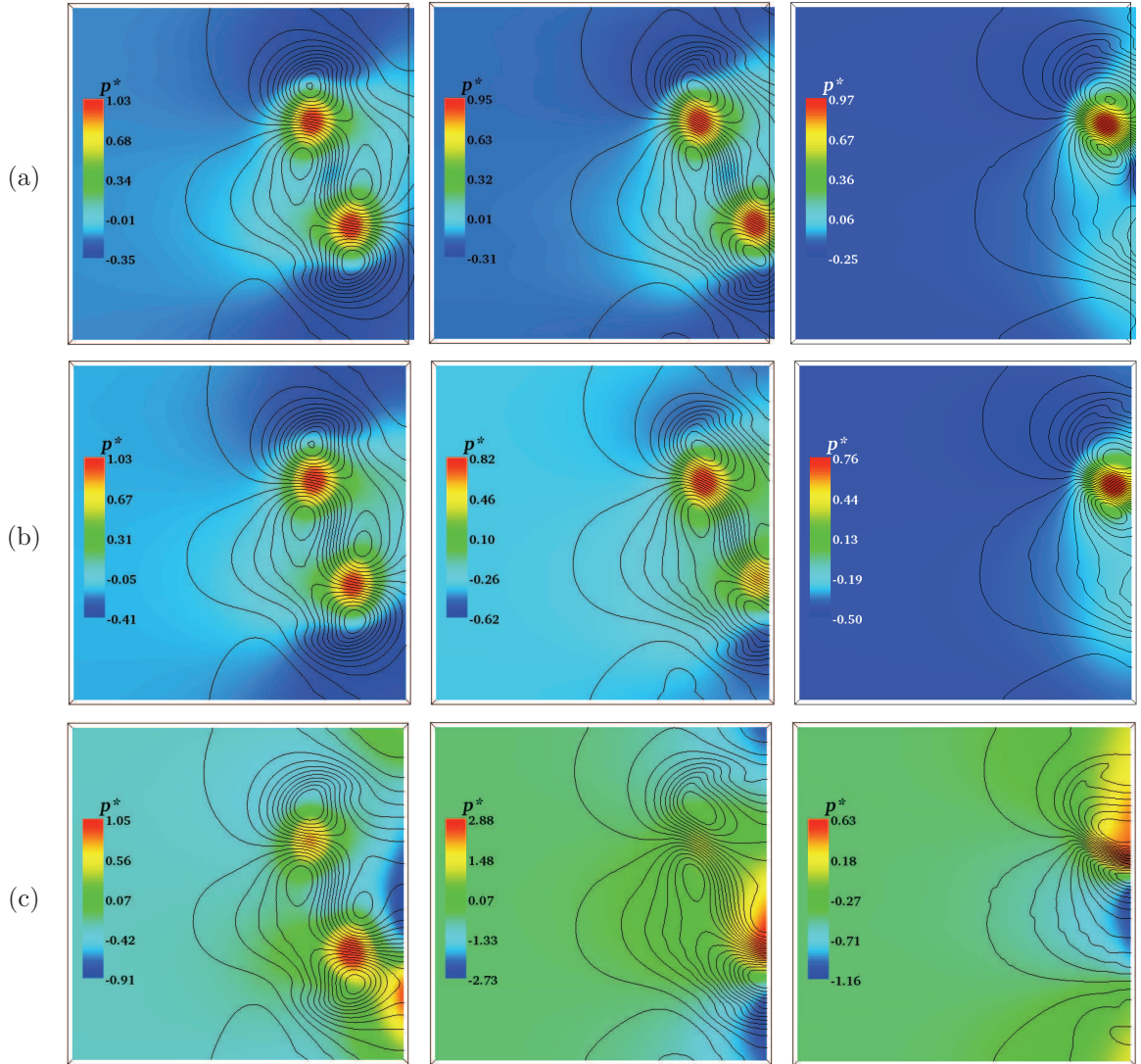


Figure 3.17: Vortex dipole test. Benchmark solution on first half of domain (a), 3D-NSCBC (b) and Standard NSCBC (c) on full domain. Normalized pressure field (see Eq. (3.220)) color map and longitudinal velocity contours. Frames at increasing time from left to right.

other hand, no shift is observed in the error curve relevant to the simulation performed using the 3D-NSCBC outflow.

The inclusion of transverse effects, again, produces a significant reduction in vorticity perturbations, leading to a reduction of about 3 times in the relevant normalized global error.

The normalized pressure p^* (*cf.* Eq. (3.220)) and the iso-contours of the longitudinal velocity component u_1 at three consecutive instants in time are shown in Figure 3.17. The benchmark solution over the first half of its computational domain is depicted on top (Figure 3.17a), the solution computed using the 3D-NSCBC approach in the middle (Figure 3.17b) and the solution computed using the standard NSCBC at the bottom (Figure 3.17c). The frames have been chosen to show the moment the lower vortex leaves the domain. The 3D-NSCBC is still

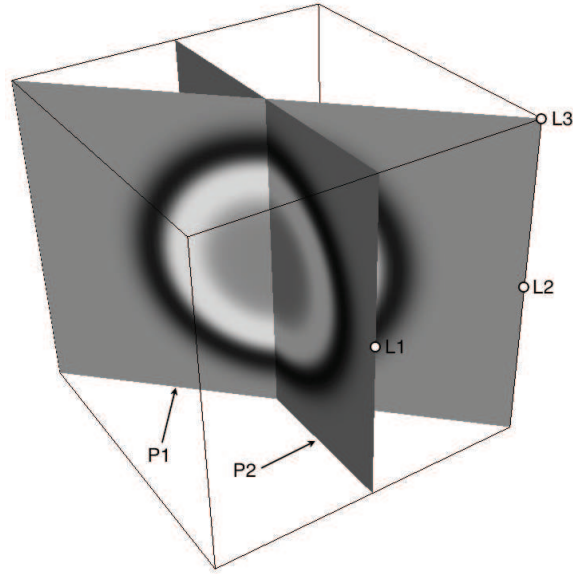


Figure 3.18: Spherical pressure wave test: position of the cutting planes P1 and P2 and of the sampling locations L1, L2 and L3.

able to allow a fairly good reproduction of the expected solution, both in terms of pressure map and velocity field, whereas the standard LODI assumption produces a strong perturbation on the pressure field—a peak in the pressure perturbation’s total amplitude which is about 5.6 times the initial pressure drop can be observed in the second frame of Figure 3.17b—and the velocity field undergoes significant distortion, especially after the lower vortex has left the domain.

Spherical Pressure Wave

The behavior of the proposed approach for edges and corners is assessed on this tridimensional flow configuration where a spherical pressure pulse is left free to develop within a cubic computational domain of side $L = 0.013$ m with subsonic non-reflecting outflows on its 6 faces; the 12 edges are solved using the outflow/outflow boundary condition and outflow/outflow/outflow conditions are enforced on the relevant 8 corners.

The pressure field is initialized with a Gaussian-shaped pressure pulse of amplitude δ and, assuming a constant temperature T_0 , the initial density distribution is obtained from the state equation:

$$p(r) = p_\infty \left[1 + \delta \exp\left(-\frac{r^2}{2R_p^2}\right) \right], \quad (3.227)$$

$$\rho(r) = \frac{p(r)}{RT_0}, \quad (3.228)$$

where $r = \sqrt{x_1^2 + x_2^2 + x_3^2}$ is the distance from the center of the computational domain and R_p is the characteristic dimension of the pressure pulse.

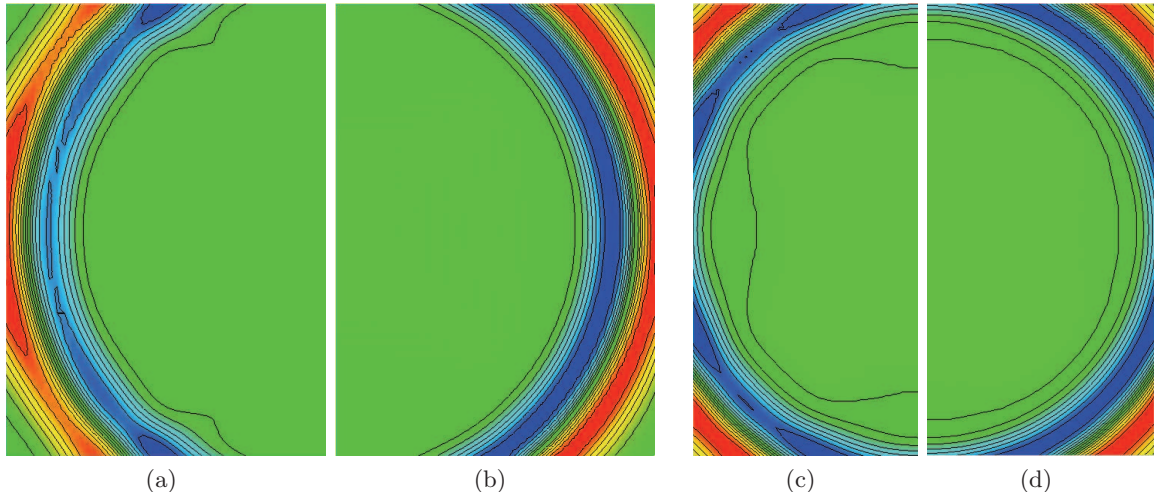


Figure 3.19: Spherical pressure wave test T3: pressure map and pressure contours on plane P1 (a,b) and P2 (c,d). Standard NSCBC non-reflecting outflows (a,c); 3D-NSCBC non-reflecting outflows (b,d).

The flow field has been initialized at rest with $\delta = 0.001$, $R_p = 0.05L$, $p_\infty = 1$ atm, and $T_0 = 300$ K. The 3D-NSCBC are assessed checking the correct evolution of the spherical pressure wave front, especially when it approaches the computational domain edges and corners.

As in the previous tests, the computation has been done setting $\mathfrak{T}_{*,ex}^k = 0$ (subscript $*$ equal to 1 or 5 depending on the outflow's location and $k = 1, 2, 3$) over all the outflows, as the steady state is expected to be characterized by uniform pressure and zero velocity. With regards to the transverse damping parameter β_t , a typical Mach number for this kind of flow—computed on the maximum local fluid displacement produced by the acoustic wave—has been used at first with fairly good results. On the other hand, some tests carried out varying β_t have given an optimal value of about 0.5, which is 4 order of magnitude higher than the mentioned Mach number. We report in what follows the results from three tests which have been made changing both the transverse relaxation coefficient and the pressure relaxation coefficient: (T1) $\beta_t = M_{\max}$ and $\sigma = 0.28$; (T2) $\beta_t = M_{\max}$ and $\sigma = 3.00$; (T3) $\beta_t = 0.5$ and $\sigma = 0.28$.

With regards to test T3, Figure 3.19 shows the pressure field and pressure contours over the two cutting planes P1 and P2 depicted in Figure 3.18; two slightly different time-steps have been selected in order to show the moment when the pressure wave fronts are well cut by the domain boundaries. As the flow field is characterized by spherical symmetry, this represent a typical example where the introduction of transverse effects at the boundaries helps in reducing flow distortion. The LODI assumption is strictly applicable only at the center of the boundary surfaces; the spherical acoustic wave front tends to become distorted, especially in regions where the flow field is not perpendicular to the outlet (*i.e.* toward edges and corners). The 3D-NSCBC technique helps in preserving pressure wave front curvature, whereas the standard non-reflecting outflow shows a tendency to reduce curvature or even to reverse it (*cf.* pressure contours at the top left corner of Figure 3.19c). The level of numerical reflection is significantly reduced too, as it can be observed in the region just behind the pressure wave. The results

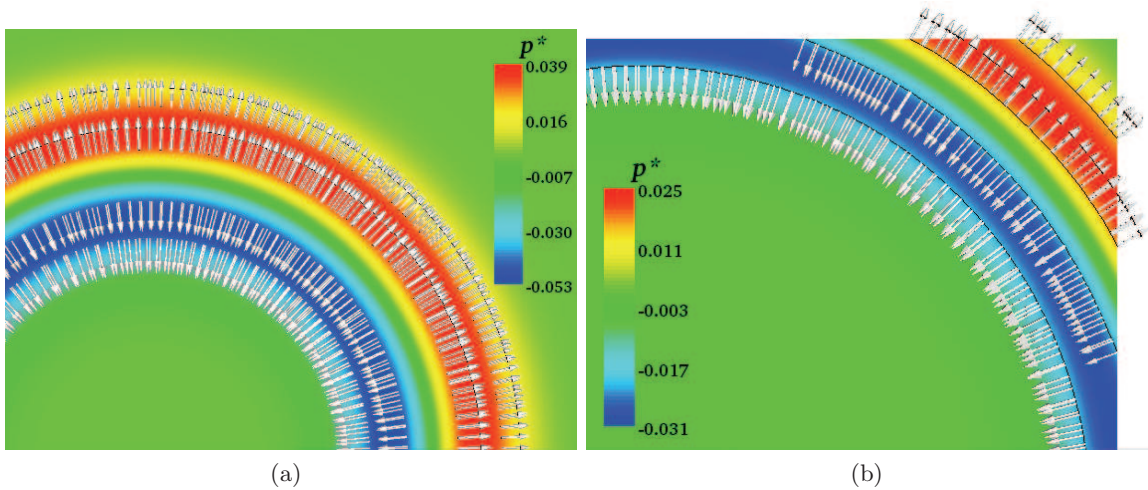


Figure 3.20: Spherical pressure wave: visualization of the local displacement flow on the benchmark simulation (a) and of the back-flow occurring on simulation T3 (b). Velocity field and normalized pressure map, $p^* = (p - p_\infty)/(\delta p_\infty)$, on plane P1.

from tests T1 and T2 (not shown) are slightly worse but, still, the inclusion of transverse effects helps in preserving the pressure wave shape. Interestingly, no significant difference has been observed in tests T1 and T2, meaning that the modified NSCBC allow a certain freedom in the choice of the pressure relaxation coefficient σ .

It is worthwhile mentioning that the present configuration is a particularly tough test-case for both NSCBC and 3D-NSCBC non-reflecting outflows. The pressure wave, in fact, is accompanied by two opposed local displacements, as depicted in Figure 3.20a, where the velocity field is superimposed to the normalized pressure map. The presence of local back-flow regions at the outlet (see Figure 3.20b) poses the additional problem of imposing incoming characteristic waves traveling with the convective velocity, namely characteristic waves with indices 2, 3, 4 and 6. Previous tests have shown that just “ignoring” the possibility of a reversed flow event and keep computing the relevant entering characteristic wave amplitudes using interior points may lead to instability problems, especially when the back-flow is particularly persistent in time. An efficient solution is to set these convected incoming waves to zero in regions of local back-flow. The drawback of this simplistic approach is, of course, a slight reduction of boundary transparency.

A measure of the error has been extracted using a benchmark solution computed on a two times wider domain. Three different locations on the boundary (see Figure 3.18) have been taken into account: (L1) boundary face center, (L2) boundary edge center and (L3) boundary corner. The local relative absolute error on pressure for these points has been measured as:

$$\varepsilon_r(\mathbf{x}, t) = \frac{|p(\mathbf{x}, t) - p^0(\mathbf{x}, t)|}{p^0(\mathbf{x}, t)}, \quad (3.229)$$

where \mathbf{x} denotes the sampling location and p^0 is the pressure computed on the reference simulation. Furthermore, the overall performance of the 3D-NSCBC approach has been quantified resorting to the normalized global error measure defined in Eq. (3.222).

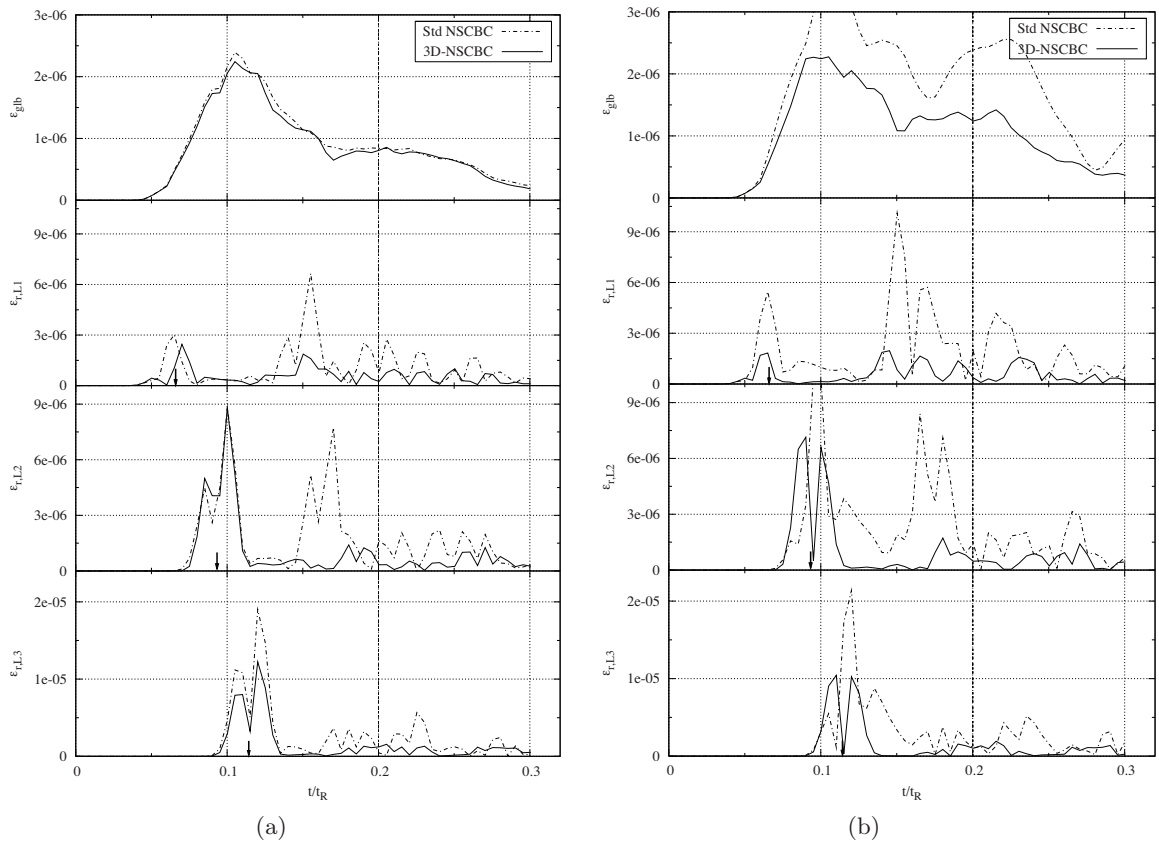


Figure 3.21: Spherical pressure wave test: normalized error on pressure for test-case T1 (a) and test-case T2 (b). Global normalized error on the top graph (see Eq. (3.222)) and local relative error at boundary locations L1, L2 and L3. The vertical arrows mark the instants when the pressure pulse crosses locations L1, L2 and L3 respectively ($t_R = 2.8 \times 10^{-4}$ s).

Figures 3.21 and 3.22 show the relevant results. It should be noted that for $t/t_R \simeq 0.2$ the reference solution on the wider domain is expected to become more and more affected by its own boundary and the comparison becomes meaningless: this is marked by a vertical dashed line limiting the region of interest.

In general, the maximum error—as per Eq. (3.222)—occurs, of course, during the period when the boundaries are crossed by the pressure pulse. With regards to tests T1 with low relaxation the error level is less than about 0.14% and no significant improvement is observed using 3D-NSCBC approach (*cf.* Figures 3.21a). On the other hand, when the relaxation coefficient is increased (Figures 3.21b), the simulation performed resorting to the LODI hypothesis is characterized by a higher error, meaning that the boundary conditions are less transparent and numerical reflected pressure waves have higher amplitude. The 3D-NSCBC, on the other hand, maintains the error almost unchanged, and the level of boundary reflection is only slightly increased.

In terms of local relative error, the novel approach gives, in general, more accurate results, showing a favorable tendency to produce numerical reflected waves of small amplitude; when

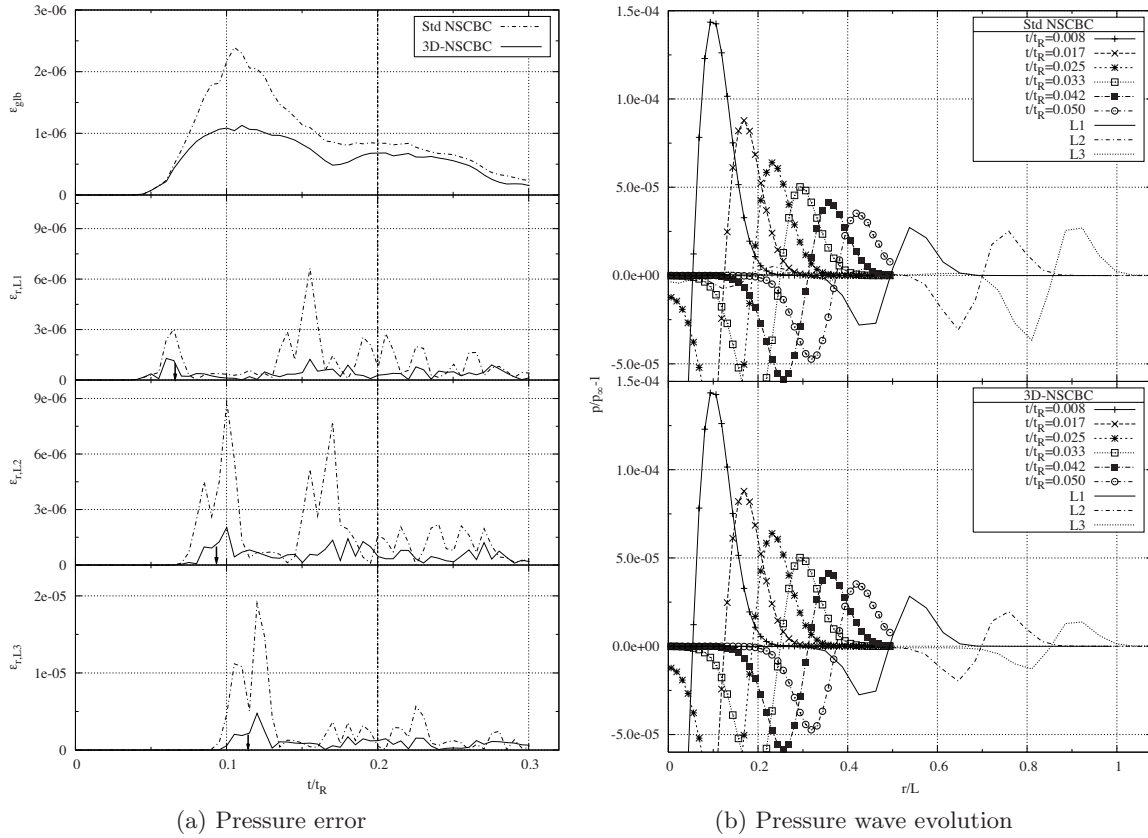


Figure 3.22: Spherical pressure wave test T3: normalized error on pressure (a) and normalized pressure wave evolution (b). Plot (a): global normalized error on the top graph (*cf.* Eq. (3.222)) and local relative error at boundary locations L1, L2 and L3. Plot (b): symbols represent radial pressure plots at different normalized time-steps; lines are temporal pressure plots at locations L1, L2 and L3 rescaled as radial plots under the assumption that the pressure pulse is a signal traveling with speed $a \simeq 347.6$ m/s. ($t_R = 2.8 \times 10^{-4}$ s)

the pressure relaxation coefficient σ is increased, the LODI approximation produces higher reflection, whereas the modified approach remains significantly more transparent, the level of boundary reflection being marginally affected by the pressure relaxation coefficient. Test-case T3 gives the better performance (*cf.* Figure 3.22a). In this particular case, the normalized maximum error is reduced of about a factor 2 and the local relative error is significantly reduced even when the pressure pulse crosses the critical locations (L2) and (L3).

Figure 3.22b shows a comparison about the evolution of the pressure wave. The pressure wave was looked at different time-steps before it had reached the boundary and radial plots were extracted at each time-step (symbols). As expected for a spherical wave, the pulse amplitude decreases continuously as the wave front expands. Regarding the pressure pulse as a signal traveling with the speed of sound a , the time evolution of pressure can be rescaled as a radial

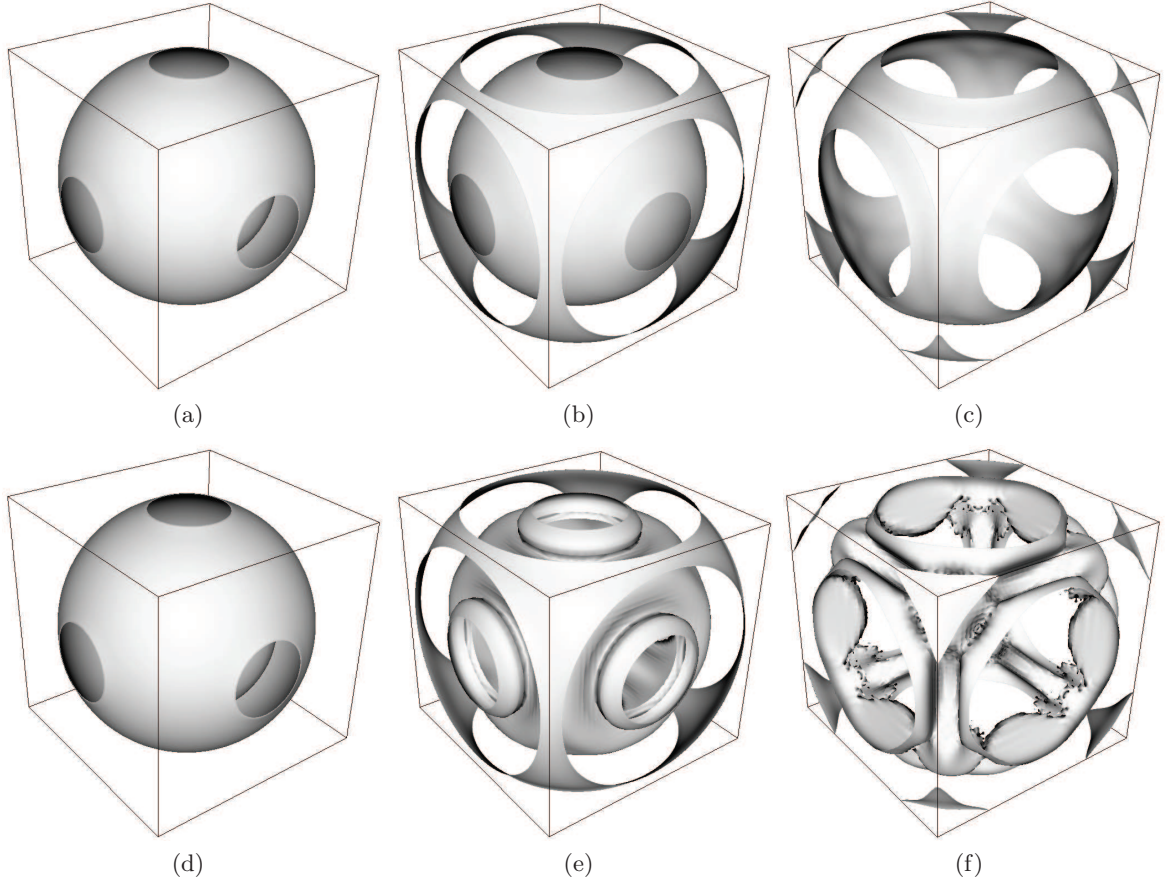


Figure 3.23: Spherical pressure wave test T3: pressure iso-surfaces evolution (iso-value $p/p_R = 1000.98$). 3D-NSCBC non-reflecting outflows (a–c), standard NSCBC non-reflecting outflows (d–f).

plot using the following equivalence relation between space and time for such a wave:

$$\begin{aligned} f(r - ct_0) &= f(r_0 - at), \quad \text{with } at_0 = r_0, \\ &\Rightarrow r - r_0 = r_0 - at, \end{aligned}$$

with $a \simeq 347.6 \text{ m/s}$ and r_0 the radial distance of the time signal's sampling location.

Once the pressure front meets the boundary, the LODI assumption is unable to retain the correct physical information about the tridimensionality of the flow: the pressure front stops behaving as a spherical wave and reaches the edge and, later on, the corner, retaining almost the same amplitude. The 3D-NSCBC outflow and the proposed edge/corner procedure is remarkably capable of preserving the correct physical information and the pressure front reaches the boundary edges and corners with a reduced amplitude.

Deformation of the wave front is assessed by a qualitative comparison of the computed wave front at three subsequent time-steps, as shown in Figure 3.23. The wave front is shown by means of pressure iso-surfaces relevant to a normalized pressure value of 1000.98 ($p_R = 101.23 \text{ Pa}$) and is expected to be perfectly spherical; results are relevant to the test-

case T3. The innermost and the outermost surfaces have been chosen in order to enclose the pressure pulse. Spurious numerical reflection is expected to be generated starting from the moment the outermost surface crosses the boundary; the effects are then visible on what follows, namely, the innermost surface. As it can be observed, the 3D-NSCBC outflows allow the wave front curvature to be correctly preserved. Negligible reflection is produced and the wave front undergoes minimal distortion even when the pressure pulse is well outside the computational domain (Figure 3.23c). Significant distortion of the core pressure field is observed when transverse effects are not accounted for; the outermost surface itself is progressively deformed with local regions of reversed curvature (*cf.* Figures 3.23e and 3.23f).

Turbulent Free Round-Jet

We have analyzed some basic test-cases on simple configurations so far, in order to assess the behavior of the 3D-NSCBC non-reflecting outflows when compared to the standard LODI (NSCBC) assumption. In this section we present qualitative results from the more complex geometry of a compressible turbulent free round-jet. Though only qualitative this test reveals some interesting features of the novel approach on a configuration involving non-reflecting inlet/outlet coupling.

This simulation, which is mainly intended to assess boundary reflection in the presence of complex and chaotically oriented vortical structures and to test the inlet/outlet proposed compatibility condition, was performed in turbulent regime resorting to the Large-Eddy Simulation technique, the details of which are deferred to Chapter 4. The computational domain is a box of dimensions $14D \times 5D \times 5D$ with $D = 0.0026$ m the jet diameter ($200 \times 80 \times 80$ grid points). The grid is uniform along x_1 and slightly stretched along x_2 and x_3 in order to better resolve the jet shear layer; transverse refinement was limited to maintain a maximum stretching ratio of about 1.06 over consecutive cells. The resulting grid spacing is: $\Delta x_t/D \simeq 0.0527$ on the axis, $\Delta x_t/D \simeq 0.0431$ at $x_t = \pm D/2$ and $\Delta x_t/D \simeq 0.1312$ at $x_t = \pm 2.5D$ ($t = 2, 3$).

The inflow is located at $x_1 = 0$ and the modified subsonic non-reflecting inflow is used, with the velocity relaxation parameter η_5 set at 3.58. The same value is used for the other inlet relaxation parameters: $\eta_2 = -3.58$ and $\eta_3 = \eta_4 = \eta_6 = 3.58$. The target inlet velocity is prescribed using the power law profile for turbulent pipe flow:

$$\frac{U(r)}{U_{cl}} = \left(1 - \frac{2r}{D}\right)^{1/n}, \quad (3.230)$$

where $r = \sqrt{x_2^2 + x_3^2}$ is the distance from the jet axis, U_{cl} is the centerline velocity and the parameter $n = 7.4$; the ratio between bulk velocity U_b and centerline velocity U_{cl} is about 0.82. The value of U_b has been computed fixing the value of the jet's Reynolds number at 23000: $Re_D = \rho U_b D / \mu = 23000$. A correlated random noise [35] is superimposed to the velocity profile with an intensity of 0.8% of the bulk velocity U_b . The inlet temperature is fixed at 300 K.

The lateral and downstream boundaries are subsonic non-reflecting outflows with pressure relaxation parameter $\sigma = 0.28$ and target pressure equal to 1 atm. No assumed exact transverse terms have been imposed. The transverse relaxation parameter β_t is equal to 0.19, a typical value of the Mach number for this specific flow, as it was evaluated from a precursor simulation performed with β_t equal to U_b/a . Inflow/Outflow edge conditions are used on the 4 bottom edges and Inflow/Outflow/Outflow corner conditions are used on the relevant 4

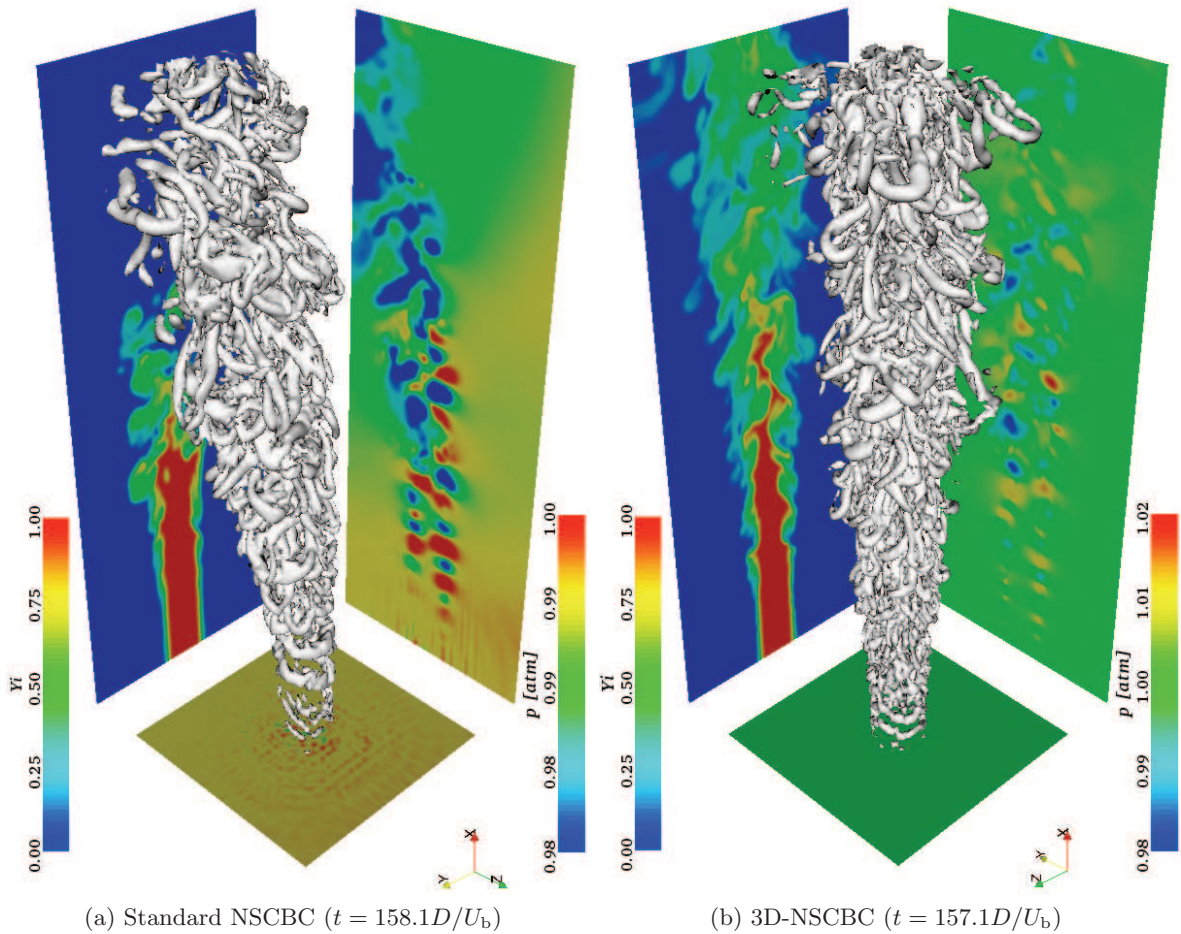


Figure 3.24: Free round-jet with standard NSCBC (a) and 3D-NSCBC (b): $Q = 0.5$ contours (center), passive scalar (left) and pressure (right) distributions over orthogonal axial planes.

joining corners; Outflow/Outflow edge conditions are used on the 8 remaining edges and Outflow/Outflow/Outflow corner conditions on the 4 top corners (see Figure 3.24). The simulation was started from fluid at rest and at reference condition (1 atm, 300 K) all over the domain.

The developed flow field is depicted in Figure 3.24b, where the coherent vortical structures are represented resorting to the iso-surfaces of $Q = 0.5$, Q being the second invariant of the velocity gradient tensor normalized by the jet diameter D and the bulk velocity U_b . Pressure and passive scalar distributions over axial planes are also shown. Despite the fairly narrow computational domain used, no perturbation coming from the boundaries is observed. The pressure field reflects the presence of vortical structures with alternating low- and high-pressure regions but maintains the expected target value in regions not affected by the flow. The compatibility conditions for inlet/outlet edges and corners allow perfect transition from the inlet to the outflow boundaries without producing any unphysical pressure disturbance. Regardless of their orientation with respect to the boundary plane, the complex ensemble of vortical structures which develops along the jet, is able to leaves the domain through the outflows without being significantly perturbed (see Figure 3.25).

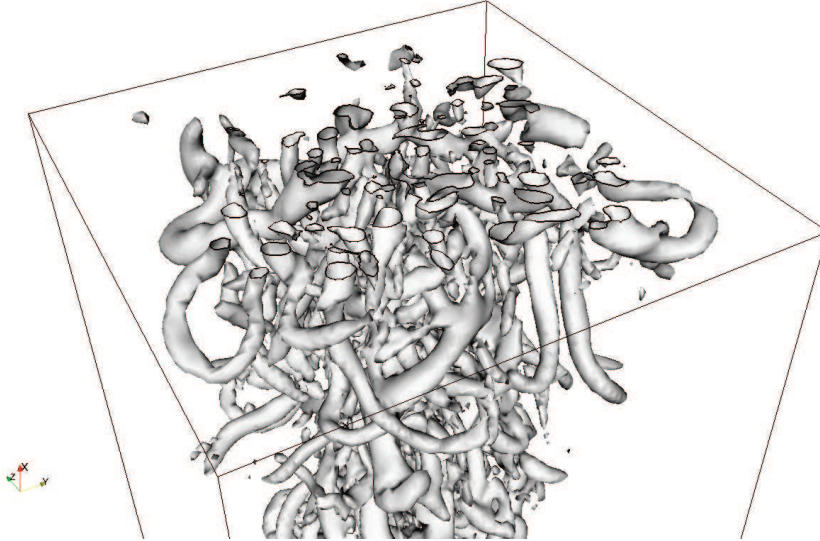


Figure 3.25: Free round-jet with 3D-NSCBC: detail of $Q = 0.5$ contours at the boundary.

On the other hand, the same simulation performed using the standard NSCBC approach underwent a destabilization of the pressure, originating on an outflow's corner with a peak of low pressure; this destabilization caused the jet to collapse toward the low pressure region as it can be observed in Figure 3.24a. Moreover, the inlet side is far more noisy and a chessboard pattern is visible on the pressure map at the inlet plane. Coherent vortical structures at the beginning of the jet appear to be less developed. The problem is clearly linked to the observed inlet pressure noise (see axial pressure map on the right of Figure 3.24a), which, interacting with the shear layer development, prevents the appearance of Kelvin-Helmholtz-type instabilities up to a distance of about one diameter from the jet's nozzle.

The above results suggest that such a simulation with standard NSCBC would have required: (a) a greater value of the pressure relaxation coefficient σ in order to better control the pressure at the boundary (thus leading to higher reflection); (b) a wider computational domain in order to limit the influence of the boundaries on turbulence development and to prevent the jet from falling into a lateral outflow. This notwithstanding, the inlet noise could remain an issue.

3.3 Artificial Turbulence Injection

When performing Direct or Large-Eddy Simulations, it is generally necessary to prescribe a specific time signal at the inlet in order to: (a) comply with the specific configuration to be studied (*e.g.*, the simulation of turbulence development in a jet originating from a fully developed pipe flow, which is not included in the computational domain); (b) trigger particular modes or instabilities which would be otherwise absent in the numerical simulation (*e.g.*, all those stochastic small perturbation, which characterize a real experiment and which cannot

be reproduced by mathematical models¹⁹). In both cases, a random perturbation may be necessary and this can be obtained, for instance, by stochastic reconstruction of its time evolution from a prescribed energy spectrum, by precursor simulations or by some sort of extraction/re-scaling technique [63]. In any case, a Random Numbers Generator (RNG) is often needed, thus obtaining what is typically referred to as a synthetic signal.

The simplest way to generate a turbulent inlet signal is to superimpose random fluctuations to the prescribed mean velocity profile. Since RNGs are generally designed to reproduce random signals with flat frequency spectrum, the so called *white noise*, the relevant pseudo-turbulence is immediately damped due to a lack of energy in the low wave number range [35]. In order to have a more realistic representation of inlet turbulence, the synthetic signal should have the same statistical features of the real one.

We adopt the technique described by Klein et al. [35], who propose the use of digital filters in order to reproduce a correlated random noise with prescribed correlation length-scales, starting from a white noise.

Instead of computing the correlated noise for each time step, as suggested by Klein et al., in particular, assuming that the random perturbation enters the computational domain with a typical velocity U_b , the sampling frequency of the pseudo-turbulent signal is computed from the inlet grid spacing Δx in the direction normal to the inflow boundary:

$$f_{ti} = U_b/\Delta x. \quad (3.231)$$

When characteristic boundary conditions are used, wave amplitude time variations are imposed at the inlet (*cf.* Section 3.2), therefore any prescribed inlet signal must be imposed specifying its time derivative rather than its time evolution itself. In the case of the subsonic non-reflecting inflow, if dU_k^0/dt ($k = 1, 2, 3$), dT^0/dt and dZ^0/dt are the time derivatives of prescribed time-evolving signals for the velocity, the temperature and the scalar respectively, Eqs. (3.99)–(3.103) are rewritten as [58]:

$$\mathcal{L}_\phi = \eta_\phi \frac{\rho a^2 (1 - M_{\max}^2)}{L_x} \Delta u_1 + \mathfrak{F}_\phi^1 - \varsigma(\phi) \rho a \frac{dU_1^0}{dt}, \quad (3.232)$$

$$\mathcal{L}_2 = \eta_2 \frac{\rho a R}{L_x} \Delta T + \mathfrak{F}_2^1 + \gamma \rho R \frac{dT^0}{dt}, \quad (3.233)$$

$$\mathcal{L}_3 = \eta_3 \frac{a}{L_x} \Delta u_2 + \mathfrak{F}_3^1 - \frac{dU_2^0}{dt}, \quad (3.234)$$

$$\mathcal{L}_4 = \eta_4 \frac{a}{L_x} \Delta u_3 + \mathfrak{F}_4^1 - \frac{dU_3^0}{dt}, \quad (3.235)$$

$$\mathcal{L}_6 = \eta_6 \frac{a}{L_x} \Delta Z + \mathfrak{F}_6^1 - \frac{dZ^0}{dt}. \quad (3.236)$$

Therefore, focusing on the fluctuating velocity signal only, the time derivative of the correlated random noise needs to be reconstructed from its discrete sequence of values with the requirement that the variance of the resulting velocity is equal to the variance of the correlated noise, thus ensuring the injection of the proper amount of turbulent energy.

If U_{rnd}^n is the sequence of realizations of a correlated random noise of variance $I^2 U_b^2$ (I is the intensity of the injected noise) and sampling frequency f_{ti} (*i.e.*, n is incremented every

¹⁹Roundoff errors of the numerical scheme may be, in principle, regarded as a source of perturbation. However, their stochastic nature is questionable.

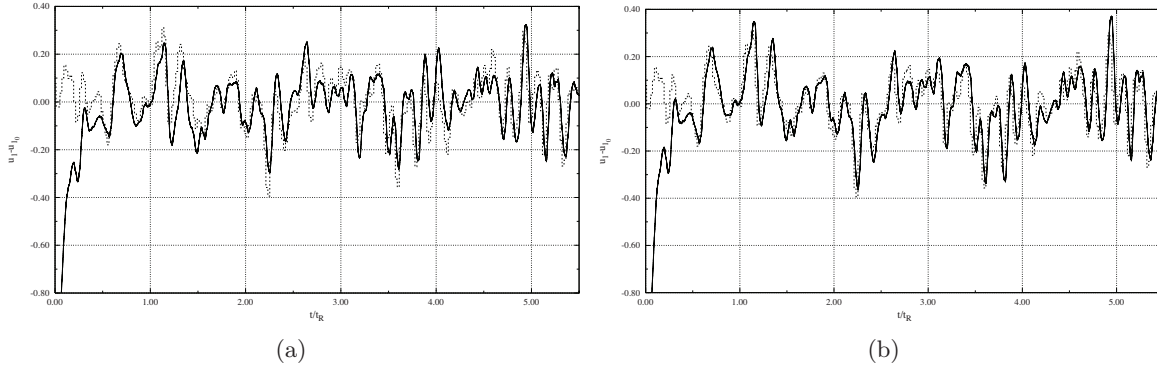


Figure 3.26: Time evolution of the fluctuating inlet velocity imposing inlet turbulence through the reconstructed time derivative only (a) and adding the correction of the target value (b). — , computed velocity at the first grid point; ····· , discrete correlated random noise.

$1/f_{\text{ti}}$ seconds), the simplest way to approximate its time derivative is to connect the discrete values by straight lines, thus setting

$$\frac{dU_{\text{rnd}}}{dt} \simeq f_{\text{ti}} \Delta U_{\text{rnd}}^n, \quad \text{for } t \in [t^n : t^{n+1}], \quad (3.237)$$

with $\Delta U_{\text{rnd}}^n = (U_{\text{rnd}}^{n+1} - U_{\text{rnd}}^n)$. Unfortunately, when this approximation is used, due to the time response of the characteristic implementation of the boundary condition, the variance of the resulting signal is significantly underestimated: the above approximation is too weak to reproduce the injected noise through Eq. (3.232). Better results are obtained if the discrete values of the random sequence are linked together using a sinusoidal curve:

$$U_{\text{rnd}}(t) = U_{\text{rnd}}^n + \frac{1}{2} \Delta U_{\text{rnd}}^n \left\{ 1 - \cos[\pi f_{\text{ti}}(t - t^n)] \right\}, \quad \text{for } t \in [t^n : t^{n+1}], \quad (3.238)$$

Since $f_{\text{ti}} = 1/(t^{n+1} - t^n)$, it is easy to show that the above relation represent a sinusoidal change from U_{rnd}^n to U_{rnd}^{n+1} . The approximation of the time derivative of the signal in the interval $[t^n : t^{n+1}]$ is then obtained as:

$$\frac{dU_{\text{rnd}}}{dt} \simeq \frac{\pi}{2} f_{\text{ti}} \Delta U_{\text{rnd}}^n \sin[\pi f_{\text{ti}}(t - t^n)], \quad \text{for } t \in [t^n : t^{n+1}]. \quad (3.239)$$

This approximation, which gives a maximum value of the time derivative $\pi/2$ times higher than the first-order approximation in Eq. (3.237), allow good representation of the injected noise with a relatively correct value for the variance. The time history of the velocity field computed at the first grid point is depicted in Figure 3.26a, where the difference between the computed inlet velocity signal u_1 and the relevant target value u_{1_0} (solid line) is compared to the original sequence of correlated random numbers (dotted line): after the initial transient, during which the solution reaches the target value, the velocity starts following the injected random noise and the resulting variance is about 18% lower than expected.

The above error in the variance is directly linked to the relaxation procedure toward the target value. When the time derivative of the injected noise makes the velocity move away from its target value, the relaxation term (first term on the right-hand side of Eq. (3.232))

acts in opposition. The resulting variance is then reduced and this reduction depends on the relaxation coefficient for the velocity. A simple and effective way to “neutralize” the relaxation term contribution, is to correct the target velocity by accounting for the injected noise. If u_{10} is the target value of velocity, then the term Δu_1 in Eq. (3.232) is rewritten as:

$$\Delta u_1 = u_1 - u_{10} - U_{\text{rnd}}^{n+1}, \quad \text{for } t \in [t^n : t^{n+1}]. \quad (3.240)$$

With the above correction on the relaxation term and the reconstructed derivative from Eq. (3.239), the error in the variance of the inlet velocity with respect to the injected noise is reduced to about 3% (*cf.* Figure 3.26b). It is worthwhile underlining that the target velocity correction alone would be ineffective as the velocity would never be able to follow the fluctuating signal unless being characterized by a time constant much smaller than the injection period $1/f_{\text{ti}}$.²⁰

²⁰The time constant of the inlet velocity response may be evaluated taking Eq. (3.94) and neglecting the effect of the pressure:

$$\frac{\partial \Delta u_1}{\partial t} = -\frac{\eta_\phi}{\varsigma(\phi)} \frac{a(1 - M_{\text{max}}^2)}{L_x} \Delta u_1.$$

Since $\eta_1 < 0$ and $\eta_5 > 0$, $\eta_\phi/\varsigma(\phi) = |\eta_\phi|$, therefore, approximating the above relation as an ordinary first-order differential equation, the time response of the inlet velocity results equal to:

$$\Delta u_1(t) = C \exp\left(-\frac{t}{\tau_u}\right), \quad \text{with } \tau_u = \frac{L_x}{|\eta_\phi|a(1 - M_{\text{max}}^2)},$$

where C is a constant of integration and τ_u is the the time constant. Evidently, for the inlet velocity to be able to follow a signal that changes value with frequency f_{ti} , we should have a sufficiently small value of $\tau_u f_{\text{ti}}$, which is not always the case.

Large-Eddy Simulation (LES)

[...] *However, for turbulent motion, an enormous number of degrees of freedom are always excited, and hence the variation with time on any physical value will be described here by functions containing a vast number of Fourier components, i.e., by functions of an extremely complicated nature.*

A.S. Monin and A.M. Yaglom, 1971

Contents

4.1	Different Levels of Detail	84
4.2	The Filtered Navier-Stokes Equations	85
4.2.1	A Weakly Compressible Approach	88
4.2.2	Near-Wall Scaling	91
4.3	Eddy-Viscosity Hypothesis	92
4.3.1	The Smagorinsky Model	94
4.3.2	The WALE Model	94
4.3.3	The Lagrangian Dynamic Smagorinsky Model	95
4.3.4	The Filtered Structure Function Model	98
4.4	Scale Similarity Hypothesis	100
4.4.1	The WALE-Similarity Model	101
4.4.2	The Explicit Filtering Procedure	105
4.5	Impinging Round-Jet Simulation	108
4.5.1	Boundary Conditions	109
4.5.2	Grid Spacing	110
4.5.3	The Measurement of Statistical Properties	112
4.5.4	$Re_D = 23000$ Test-Case (C1)	113
4.5.5	$Re_D = 23000$ Test-Case (C2)	117
4.5.6	$Re_D = 70000$ Test-Case (C3)	120
4.5.7	Energy Backscatter	124
4.5.8	Flow Field and Scalar Mixing	128

Au regard de l'extraordinaire variété d'échelles qui caractérise les écoulements turbulents d'intérêt pratique, une approche « simplifiée » est souvent nécessaire.

Le caractère aléatoire de la turbulence et, en même temps, sa description statistique extrêmement régulière, ont historiquement suggéré l'analyse statistique comme un instrument puissant d'investigation numérique. Et, en effet, la plupart des applications d'ingénierie est souvent concernée par des écoulements stationnaires, au sens statistique, pour lesquelles, la

connaissance des moyennes donne déjà un important niveau de détail. D'ailleurs, la non-linéarité des équations de Navier-Stokes empêche la formulation mathématique des grandeurs statistiques sans encourir des problèmes complexes de fermeture.

Néanmoins, lorsque le phénomène étudié n'est pas stationnaire, sa description en termes de moyennes temporelles devient impossible, et les variations temporelles doivent être prise en compte, au moins de manière grossière. Si un niveau de détail plus élevé nécessite donc des ressources de calcul plus importantes, la nature plus universelle des termes de fermeture détermine une certaine simplification des modèles de turbulence utilisés. La Simulation aux Grandes Échelles (SGE ou LES) est basée sur cette considération et devient, de plus en plus, un instrument d'analyse d'intérêt pratique.

Ce 4^e Chapitre présente une introduction de la formulation mathématique à la base de la SGE et l'opérateur de filtrage utilisé dans ce contexte est défini. Ensuite, la formulation des équations de Navier-Stokes filtrées, lorsque les effets de compressibilité sont partiellement pris en compte, est détaillée. Certains modèles de sous-maille, basés sur l'hypothèse de viscosité tourbillonnaire, sont analysés, avec une attention particulière quant à leur comportement asymptotique en présence d'une paroi.

Ensuite, une introduction des modèles de sous-maille structurels, basés sur l'hypothèse de similarité [3, 4], sera faite et un nouveau modèle de sous-maille de similarité mixte, spécifiquement conçu pour conserver un comportement correct en région de proche paroi, est proposé.

Le nouveau modèle est, tout d'abord, testé lors de la simulation d'un jet d'air impactant sur une paroi plane et les résultats obtenus par différents modèles de sous-maille sont comparés. Le transport inverse d'énergie turbulente, notamment le *backscatter*, est identifié comme un mécanisme clé pour la représentation correcte des dynamiques turbulentes en région de proche paroi. Enfin, une brève analyse du caractère statistique du mélange du scalaire passif dans la configuration étudiée est aussi présentée.

4.1 Different Levels of Detail

Turbulent flows are generally characterized by a very broad variety of length- and time-scales, therefore, in order to make an accurate representation of the relevant features, numerical resolution should be high enough to capture each and every detail. Such an approach, namely the Direct Numerical Simulation (DNS) of turbulence, turns out to be so computationally demanding that its applicability remains quite limited, even with computer resources available today.

Considering for instance the most simple case of homogeneous isotropic turbulence, by typical scaling considerations, it is possible to show that, if ℓ is the size of the most energetic length-scale, the number of degrees of freedom necessary to fully represent all the length-scales is of the order of $Re^{3/4}$ in each coordinate direction; the same holds for characteristic time scales, so that, the numerical simulation of the evolution of the solution within a cube ℓ^3 for a duration equal to the characteristic time of the most energetic scale, would require the integration of the Navier-Stokes equations $\sim Re^3$ times. The situation may get even worse when multi-physical phenomena are addressed—as is it the case, for instance, when chemical reactions take place—and the range of typical scales of turbulent motion is just a subset of the whole range of physically relevant scales.

A possible way to tackle the problem is to try to obtain as much information as it is

necessary from a reduce set of degrees of freedom. The numerical integration of Reynolds Averaged Navier-Stokes (RANS) equations, for example, pushes this concept to the limit and aims at finding a numerical solution of the statistically averaged (often time averaged) Navier-Stokes equations. If, on one hand, the statistical properties of turbulent flows are generally quite well-behaved and *smooth*, thus requiring a comparatively low resolution to be represented, on the other hand the non-linear interactions between scales of different size makes it necessary to model, in a statistical sense, the effect of scales which are not resolved. Considering the Fourier representation of the solution, RANS solve the zero mode only, *i.e.* the mean, and hence the entire spectrum needs to modeled, leading generally to a big deal of model complexity, especially when some level of generality is looked for¹.

Midway between DNS and RANS, Large-Eddy Simulations (LES) try to split the spectrum in an optimized way. Starting from the consideration that the large scale structures of the flow are supposedly strongly related to the flow configuration (boundary conditions, external excitations, etc.), thus being typically highly problem-dependant, and that there exist a range of small scales which is expected to have a more *universal* character, LES aim at resolving the large scales while modeling the small ones. This is the reason why LES are particularly appealing from the modeling point of view: the so called Sub-Grid Scale (SGS) model, which represents the coupling term arising from the non-linear convective term, is not supposed to show a strong problem-dependancy, except near the wall, this last statement motivating this study.

4.2 The Filtered Navier-Stokes Equations

Length-scale separation, on a generic quantity $\varphi(\mathbf{x}, t)$, is achieved in physical space by means of the convolution product

$$\overline{\varphi}(\mathbf{x}, t) = \int_{-\infty}^{+\infty} \varphi(\boldsymbol{\xi}, t) G_{\Delta}(\mathbf{x} - \boldsymbol{\xi}) d^3 \boldsymbol{\xi}, \quad (4.1)$$

where G_{Δ} is the convolution kernel associated to the filter operation at cutoff length Δ^2 . Using the superscript $*$ to indicate Fourier transformed quantities, Eq. (4.1) correspond, through the Convolution Theorem, to point-wise multiplication in Fourier space:

$$\overline{\varphi}^*(\mathbf{k}, \omega) = \varphi^*(\mathbf{k}, \omega) G_{k_c}^*(\mathbf{k}), \quad (4.2)$$

where $G_{k_c}^*(\mathbf{k})$ is the transfer function, namely the Fourier transform, associated with the convolution kernel $G_{\Delta}(\mathbf{x})$, \mathbf{k} and ω are the wavenumber and the phase respectively and $k_c = 2\pi/\Delta$ is the cutoff wave-number. The spectral representation of φ may be then truncated at wave-number k_c by an appropriately chosen low-pass filter $G_{k_c}^*$. For the filtered Navier-Stokes to be tractable, the filter has to:

¹The most energetic scales are directly affected by boundary conditions and external forcing, therefore a general model should be able to efficiently adapt to a quite broad range of flow configurations.

²The filter is assumed here isotropic. Moreover the tridimensional kernel G_{Δ} is assumed to be the product of mono-dimensional kernels:

$$G_{\Delta}(\mathbf{x} - \boldsymbol{\xi}) = \prod_{i=1,3} G_{i\Delta}(x_i - \xi_i).$$

	$G_\Delta(x_i - \xi_i) =$	$G_{k_c}^*(k_i) =$
Top-Hat	$\begin{cases} \frac{1}{\Delta} & \text{for } x_i - \xi_i \leq \frac{\Delta}{2}, \\ 0 & \text{otherwise.} \end{cases}$	$\frac{\sin(k_i \Delta/2)}{k_i \Delta/2}$
Gaussian	$\sqrt{\frac{\Gamma}{\pi \Delta^2}} \exp\left(\frac{-\Gamma x_i - \xi_i ^2}{\Delta^2}\right)$	$\exp\left(\frac{-\Delta^2 k_i^2}{4\Gamma}\right)$
Cutoff	$\frac{\sin[k_c(x_i - \xi_i)]}{k_c(x_i - \xi_i)}$	$\begin{cases} 1 & \text{for } k_i \leq k_c = \pi/\Delta, \\ 0 & \text{otherwise.} \end{cases}$

Table 4.1: Convolution kernels and transfer functions of typical mono-dimensional filters at cutoff length-scale Δ . Γ is a parameter of the Gaussian filter, typically taking a value of 6 [63].

- conserve constant values; this is equivalent to the normalization condition [63]

$$\int_{-\infty}^{+\infty} G_\Delta(\boldsymbol{\xi}) d^3 \boldsymbol{\xi} = 1;$$

- be linear, *i.e.* $\overline{\varphi + \psi} = \overline{\varphi} + \overline{\psi}$;
- commute with derivation in space and time:

$$\overline{\frac{\partial \varphi}{\partial t}} = \frac{\partial \overline{\varphi}}{\partial t}, \quad \overline{\frac{\partial \varphi}{\partial x_i}} = \frac{\partial \overline{\varphi}}{\partial x_i}.$$

The first two requirements are generally met with a properly defined filter (the second condition, in particular, is ensured by the linearity of the convolution operation). The third requirement is a bit more complex in nature. Commutation errors arise when the filter is anisotropic (*e.g.*, when solid boundaries are present or when the computational grid is not uniform) or, for instance, when Favre-filtering (the relevant definition will be given later) is adopted. On this regard, additional approximations will be made case by case. In all the developments which follow, it is assumed that the filter operator commutes with spatial and temporal differentiation.

Typical filters used to perform spatial scale separation are the top-hat, the Gaussian and the spectral cutoff filters which are summarized in Table 4.1. The top-hat and Gaussian filters allow frequency overlap between $\overline{\varphi}$ and $\varphi' = \varphi - \overline{\varphi}$, while the sharp cutoff filter does not. Moreover, the cutoff filter is idempotent in spectral space, *i.e.*, $G_{\text{cutoff}}^*(k_i)G_{\text{cutoff}}^*(k_i) = G_{\text{cutoff}}^*(k_i)$, thus for this filter we have: $\overline{\overline{\varphi}} = \overline{\varphi}$.

Using the above definitions and applying the commutation property, the filtered Navier-Stokes equations are obtained after applying the *bar* filter operator to Eq. (2.15):

$$\frac{\partial \overline{U}}{\partial t} + \frac{\partial \overline{F}^k}{\partial x_k} + \frac{\partial \overline{D}^k}{\partial x_k} = \mathbf{0}, \quad (4.3)$$

with

$$\bar{\mathbf{U}} = \begin{pmatrix} \bar{\rho} \\ \overline{\rho u_1} \\ \overline{\rho u_2} \\ \overline{\rho u_3} \\ \overline{\rho e} \\ \overline{\rho Z} \end{pmatrix}, \quad \bar{\mathbf{F}}^k = \begin{pmatrix} \overline{\rho u_k} \\ \overline{\rho u_1 u_k} + \delta_{1k} \bar{p} \\ \overline{\rho u_2 u_k} + \delta_{2k} \bar{p} \\ \overline{\rho u_3 u_k} + \delta_{3k} \bar{p} \\ (\overline{\rho e} + \bar{p}) u_k \\ \overline{\rho Z u_k} \end{pmatrix}, \quad \bar{\mathbf{D}}^k = \begin{pmatrix} 0 \\ -2\overline{\mu A_{1k}} \\ -2\overline{\mu A_{2k}} \\ -2\overline{\mu A_{3k}} \\ -2\overline{\mu u_j A_{kj}} - \frac{\mu c_p}{Pr} \frac{\partial T}{\partial x_k} \\ -\frac{\mu}{Sc} \frac{\partial Z}{\partial x_k} \end{pmatrix}, \quad (4.4)$$

the filtered energy and the filtered equation of state being given by the following relations

$$\overline{\rho e} = \overline{\rho c_v T} + \frac{1}{2} \overline{\rho u_k u_k} = \frac{\bar{p}}{\gamma - 1} + \frac{1}{2} \overline{\rho u_k u_k}, \quad \text{and} \quad \bar{p} = \overline{\rho R T}. \quad (4.5)$$

Following the same methodology generally applied when solving the compressible RANS equations, in order to avoid unclosed SGS terms in the continuity equation, a density-weighted Favre filter operator *tilde* may be introduced; this operator, which represents *filtering per unit filtered density*, is defined for a given quantity φ as³:

$$\tilde{\varphi} = \frac{\overline{\rho \varphi}}{\bar{\rho}}, \quad \Rightarrow \quad \overline{\rho \tilde{\varphi}} = \overline{\rho \varphi}. \quad (4.6)$$

The non-linear interaction terms in the flux vector $\bar{\mathbf{F}}^k$ are then decomposed in resolved and SGS parts, the former being accessible from the filtered solution and the latter, namely the SGS terms now included into the diffusive flux vector $\bar{\mathbf{D}}^k$, requiring modeling:

$$\bar{\mathbf{F}}^k = \begin{pmatrix} \overline{\rho u_k} \\ \overline{\rho u_1 \tilde{u}_k} + \delta_{1k} (\bar{p} - \frac{1}{3} \tau_{jj}) \\ \overline{\rho u_2 \tilde{u}_k} + \delta_{2k} (\bar{p} - \frac{1}{3} \tau_{jj}) \\ \overline{\rho u_3 \tilde{u}_k} + \delta_{3k} (\bar{p} - \frac{1}{3} \tau_{jj}) \\ (\overline{\rho e} + \bar{p}) \tilde{u}_k \\ \overline{\rho Z \tilde{u}_k} \end{pmatrix}, \quad \bar{\mathbf{D}}^k = \begin{pmatrix} 0 \\ -2\overline{\mu A_{1k}} - \tau_{1k}^d \\ -2\overline{\mu A_{2k}} - \tau_{2k}^d \\ -2\overline{\mu A_{3k}} - \tau_{3k}^d \\ -2\overline{\mu u_j A_{kj}} - \frac{\mu c_p}{Pr} \frac{\partial T}{\partial x_k} - q_k \\ -\frac{\mu}{Sc} \frac{\partial Z}{\partial x_k} - q_k^Z \end{pmatrix}, \quad (4.7)$$

³It should be mentioned that, contrary to the more traditional Favre time averaging, if the turbulent field is decomposed, based on the Favre-filter operator, as

$$\varphi = \tilde{\varphi} + \varphi',$$

we have the following inequalities:

$$\begin{aligned} \overline{\rho \tilde{\varphi}} &= \overline{\rho \tilde{\varphi}} \neq \overline{\rho \varphi} \\ \Rightarrow \quad \tilde{\varphi} &\neq \tilde{\varphi} \quad \text{and} \quad \tilde{\varphi}' \neq 0. \end{aligned}$$

Moreover, as already mentioned, the Favre-filter operator does not commute with the derivative. This is readily verified:

$$\frac{\partial \tilde{\varphi}}{\partial x_i} = \frac{\partial}{\partial x_i} \left[\frac{\overline{\rho \varphi}}{\bar{\rho}} \right] = \frac{1}{\bar{\rho}} \frac{\partial (\overline{\rho \varphi})}{\partial x_i} + \overline{\rho \varphi} \frac{\partial (1/\bar{\rho})}{\partial x_i} = \frac{1}{\bar{\rho}} \frac{\partial (\overline{\rho \varphi})}{\partial x_i} - \frac{\overline{\rho \varphi}}{\bar{\rho}^2} \frac{\partial \bar{\rho}}{\partial x_i} = \frac{\partial \tilde{\varphi}}{\partial x_i} + \underbrace{\frac{1}{\bar{\rho}} \frac{\partial \bar{\rho}}{\partial x_i} - \frac{\tilde{\varphi}}{\bar{\rho}} \frac{\partial \bar{\rho}}{\partial x_i}}_{\text{Commutation Error}}.$$

where τ_{ij} , q_k and q_k^Z are the unclosed SGS terms

$$\tau_{ij} = \overline{\rho u_i \tilde{u}_j} - \overline{\rho u_i} \tilde{u}_j, \quad (4.8)$$

$$\begin{aligned} q_k &= (\overline{\rho e} + \bar{p}) \tilde{u}_k - \overline{(\rho e + p) u_k} = c_v (\overline{\rho T \tilde{u}_k} - \overline{\rho T} u_k) \\ &\quad + \bar{p} \tilde{u}_k - \overline{p u_k} \\ &\quad + \frac{1}{2} (\overline{\rho u_j u_j} \tilde{u}_k - \overline{\rho u_j u_j} u_k), \end{aligned} \quad (4.9)$$

$$q_k^Z = \overline{\rho Z \tilde{u}_k} - \overline{\rho Z} u_k, \quad (4.10)$$

whereas superscript ‘d’ denotes the deviatoric part of the SGS stress tensor $\tau_{ij}^d = \tau_{ij} - \frac{1}{3} \delta_{ij} \tau_{kk}$.

Using the above decomposition and the Favre-filtering operator, Eq. (4.5) becomes:

$$\overline{\rho e} = \bar{\rho} c_v \tilde{T} + \frac{1}{2} \overline{\rho u_k \tilde{u}_k} - \frac{1}{2} \tau_{kk} = \frac{\bar{p}}{\gamma - 1} + \frac{1}{2} \overline{\rho u_k \tilde{u}_k} - \frac{1}{2} \tau_{kk}, \quad \text{and} \quad \bar{p} = \bar{\rho} R \tilde{T}. \quad (4.11)$$

4.2.1 A Weakly Compressible Approach

As mentioned, in the Eq. (4.7) above, some terms can be computed from the resolved flow field, namely the convective terms in $\overline{\mathbf{F}}$, whereas the other are unclosed SGS terms which need to be modeled. Among them, two main groups may be recognized: (a) the terms related to sub-grid turbulent transport, τ_{ij} , q_k and q_k^Z , from Eqs. (4.8), (4.9) and (4.10) respectively; (b) the remaining terms in $\overline{\mathbf{D}}$ which are related to sub-grid viscous and diffusive transport. With regards to the SGS stresses, an issue which needs some particular attention is related to the necessity to model separately the deviator of τ_{ij} and its spherical part $\frac{1}{3} \tau_{kk}$. The latter is present in the momentum equation as well as in the filtered total energy through Eq. (4.11).

A separate model for this term is derived by Yoshizawa [86] under the assumption that length and time scales of the fluctuating fields were small compared to those of the main field: this hypothesis restricts the use of the model to low Mach number flows with small density fluctuations. Even at low Mach numbers, the modeled isotropic SGS stress shows poor correlation with the exact one, with a correlation coefficient of about 15% at $\langle M \rangle = 0.1^4$ [16, 72]. A dynamic version of this model is then developed by [49] and tested on isotropic decaying turbulence at $M_t = 0.519$.

Erlebacher et al. [16], Speziale et al. [72] proposed a compressible version of the similarity mixed model [4]—with fixed model constants determined from *a priori* analysis of DNS data—where the Yoshizawa’s model is retained for the trace of the SGS Reynolds stress tensor (more details about similarity models will be discussed in Section 4.4.1). At $\langle M \rangle = 0.1$, a correlation coefficient of 0.85 is obtained for the isotropic SGS stress but is also pointed out that this has a negligible influence on the modeled total stresses on the vector and scalar level up to $\langle M \rangle = 0.4$.

Erlebacher et al. [17] conjectured that the trace of the SGS stress tensor is dominated by the thermodynamic pressure for SGS Mach numbers $M_{\text{sgs}} < 0.4$, with $M_{\text{sgs}}^2 = \overline{\rho u'_k u'_k} / (\gamma \bar{p})$ computed from the SGS Reynolds stress, and hence neglected the isotropic part of the SGS Reynolds term. This assumption is confirmed by Zang et al. [88].

An alternative solution is proposed by Ducros et al. [13], Lesieur et al. [40], who incorporate the trace of the SGS stress tensor within a *macropressure* and *macrotemperature*. Hence, the

⁴ $\langle M \rangle$ is the average Mach number over the computational domain.

isotropic SGS stress is not modeled. This approach, which is briefly summarized below, when applied to similarity mixed modeling (*cf.* Section 4.4.1) leads to a condition over the SGS Mach number, which is similar but less stringent than the one suggested by Erlebacher et al. [17].

The resolved macropressure is defined as the sum of the resolved pressure and the trace of the SGS stress tensor,

$$\overline{\varpi} = \overline{p} - \frac{1}{3}\tau_{kk}, \quad (4.12)$$

hence, the flux vector $\overline{\mathbf{F}}^k$ in Eq. (4.7) is rewritten as:

$$\overline{\mathbf{F}}^k = \begin{pmatrix} \overline{\rho}u_k \\ \overline{\rho}u_1\tilde{u}_k + \delta_{1k}\overline{\varpi} \\ \overline{\rho}u_2\tilde{u}_k + \delta_{2k}\overline{\varpi} \\ \overline{\rho}u_3\tilde{u}_k + \delta_{3k}\overline{\varpi} \\ (\overline{\rho e} + \overline{\varpi})\tilde{u}_k \\ \overline{\rho Z}\tilde{u}_k \end{pmatrix}, \quad (4.13)$$

where, since the filtered pressure \overline{p} is no more accessible from LES, the SGS energy flux q_k has been redefined in terms of the resolved macropressure:

$$q_k = (\overline{\rho e} + \overline{\varpi})\tilde{u}_k - \overline{(\rho e + p)u_k}. \quad (4.14)$$

Moreover, observing that the filtered total energy (*cf.* Eq. (4.11)) contains the trace of the SGS stresses, a resolved macrotemperature may be defined in such a way that the total energy is computable from resolved quantities:

$$\overline{\rho e} = \overline{\rho}c_v\tilde{\vartheta} + \frac{1}{2}\overline{\rho}u_k\tilde{u}_k, \quad \text{with} \quad \tilde{\vartheta} = \tilde{T} - \frac{1}{2\overline{\rho}c_v}\tau_{kk}. \quad (4.15)$$

The filtered state equation in terms of macropressure and macrotemperature reads:

$$\overline{\varpi} = \overline{\rho}R\tilde{T} - \frac{1}{3}\tau_{kk} = \overline{\rho}R\tilde{\vartheta} + \overline{\rho}R\frac{1}{2\overline{\rho}c_v}\tau_{kk} - \frac{1}{3}\tau_{kk} = \overline{\rho}R\tilde{\vartheta} + \frac{3\gamma - 5}{6}\tau_{kk}, \quad (4.16)$$

suggesting that, for τ_{kk} sufficiently small, macropressure and macrotemperature may be related by the usual equation of state, *i.e.*,

$$\overline{\varpi} = \overline{\rho}R\tilde{\vartheta} \quad (4.17)$$

Defining the sub-grid Mach number as

$$M_{\text{sgs}}^2 = \frac{\tau_{kk}}{\overline{\rho}a^2} = \frac{\tau_{kk}}{\overline{\rho}p}, \quad (4.18)$$

this condition becomes:

$$\frac{|3\gamma - 5|}{6}\gamma M_{\text{sgs}}^2 \ll 1. \quad (4.19)$$

For $\gamma = 1.4$ for instance, this condition is ~ 1.6 times less restrictive on M_{sgs} than just neglecting the effects of the SGS stress' trace compared to the filtered thermodynamic pressure:

$$\frac{1}{3}\tau_{kk} \ll \overline{p}, \quad \Rightarrow \quad \frac{1}{3}\gamma M_{\text{sgs}}^2 \ll 1.$$

A final remark needs to be done regarding the definition of the SGS energy flux, which is now defined using Eq. (4.15) as:

$$\begin{aligned}
 q_k &= (\overline{\rho e} + \overline{\varpi})\tilde{u}_k - \overline{(\rho e + p)u_k} = \overline{\rho}c_v(\overline{\vartheta}\tilde{u}_k - \overline{T}u_k) \\
 &\quad + \overline{\varpi}\tilde{u}_k - \overline{p}u_k \\
 &\quad + \frac{1}{2}\overline{\rho}(\tilde{u}_j\tilde{u}_j\tilde{u}_k - \overline{u_j u_j u_k}),
 \end{aligned} \tag{4.20}$$

Using Eqs. (2.8) and (4.17) and introducing the internal energy $e_I = c_v T$ and the resolved internal energy $\tilde{e}_I = c_v \tilde{\vartheta}$, the SGS energy flux becomes finally

$$q_k = \gamma\overline{\rho}(\tilde{e}_I\tilde{u}_k - \overline{e_I}u_k) + \overline{\rho}\mathcal{D}_k + \frac{1}{2}\tau_{jj}\tilde{u}_k. \tag{4.21}$$

where $\overline{\rho}\mathcal{D}_k = \frac{1}{2}\overline{\rho u_j u_j \tilde{u}_k} - \frac{1}{2}\overline{\rho u_j u_j u_k}$ represents the SGS turbulent diffusion of kinetic energy.

Furthermore, according to the approach proposed by Lesieur et al. [40], viscous and diffusive sub-grid contributions, arising from the non-commutativity of Favre-filtering (*cf.* note 3 at page 87), are neglected. This is consistent with compressible LES models derived by different authors [17, 38, 39, 49, 72, 88]. From *a priori* tests on compressible turbulent mixing layer, Vreman [81], Vreman et al. [82], in particular, show that SGS viscous diffusion and SGS thermal diffusion may be neglected for a reasonably wide range of Mach numbers (tests are performed up to $M = 1.2$), namely

$$2\overline{\mu u_j A_{kj}} - 2\overline{\mu}\tilde{u}_j\tilde{A}_{kj} \simeq 0, \tag{4.22}$$

$$\frac{\overline{\mu c_p \partial T}}{Pr \partial x_k} - \frac{\overline{\mu} c_p \partial \tilde{\vartheta}}{Pr \partial x_k} \simeq 0. \tag{4.23}$$

From the same tests, they also conclude that the SGS viscous term in the momentum equation is much smaller than the SGS stress tensor:

$$2\overline{\mu A_{ij}} - 2\overline{\mu}\tilde{A}_{ij} \simeq 0. \tag{4.24}$$

In a similar fashion, we assume that the SGS scalar diffusion is also negligible:

$$\frac{\overline{\mu \partial Z}}{Sc \partial x_k} - \frac{\overline{\mu} \partial \tilde{Z}}{Sc \partial x_k} \simeq 0. \tag{4.25}$$

The SGS viscous diffusion, in particular, is found to be the smallest of the SGS terms in the total energy equation in Martín et al. [46]. Its contribution, which, from *a priori* tests on decaying isotropic turbulence at turbulent Mach number $M_t = u''/c = 0.52$ (the velocity u'' here represents the fluctuating velocity extracted from Reynolds time averaging), is about 5% of the divergence of the SGS heat flux $\overline{\rho T \tilde{u}_k} - \overline{\rho T}u_k$ and may be reasonably neglected: the relatively poor performances of the SGS viscous diffusion model proposed therein [46] do not justify the additional modeling effort for such a small term.

Based on the above considerations, the filtered diffusive flux $\overline{\mathbf{D}}^k$ is then written as:

$$\overline{\mathbf{D}}^k \simeq \begin{pmatrix} 0 \\ -2\overline{\mu}\tilde{A}_{1k} - \tau_{1k}^d \\ -2\overline{\mu}\tilde{A}_{2k} - \tau_{2k}^d \\ -2\overline{\mu}\tilde{A}_{3k} - \tau_{3k}^d \\ -2\overline{\mu}\tilde{u}_j\tilde{A}_{kj} - \frac{\overline{\mu}c_p}{Pr}\frac{\partial \tilde{\vartheta}}{\partial x_k} - q_k \\ -\frac{\overline{\mu}}{Sc}\frac{\partial \tilde{Z}}{\partial x_k} - q_k^Z \end{pmatrix}, \tag{4.26}$$

where \tilde{A}_{ij} is the deviator of the deformation tensor computed on the resolved velocity field using Eq. (2.6),

$$\tilde{A}_{ij} = \frac{1}{2} \left(\frac{\partial \tilde{u}_i}{\partial x_j} + \frac{\partial \tilde{u}_j}{\partial x_i} \right) - \frac{1}{3} \delta_{ij} \frac{\partial \tilde{u}_k}{\partial x_k}, \quad (4.27)$$

and the dynamic viscosity $\bar{\mu}$ is computed with Eq. (2.14) from the resolved macrotemperature:

$$\bar{\mu}(\tilde{\vartheta}) = \mu_{\text{ref}} \left(\frac{\tilde{\vartheta}}{T_{\text{ref}}} \right)^{3/2} \frac{T_{\text{ref}} + S}{\tilde{\vartheta} + S}. \quad (4.28)$$

It should be noted that all the above equations have been derived under the implicit assumption that the gas constant R and the specific heat capacities, c_v and c_p , are constant—as it is the case for a calorically perfect gas—or, at least, constant to the filtering operator.

4.2.2 Near-Wall Scaling

Before going on with the description of sub-grid scale modeling procedures for the SGS stress tensor, it is worthwhile deriving some useful relations regarding near-wall scaling, which will be used in the next sections to assess SGS models' behavior close to solid boundaries. Supposing that the wall is orthogonal to x_2 , Taylor series expansions at the wall of the instantaneous velocity field in the x_2 direction may be used in order to check proper wall scaling. If the wall is located at $x_2 = 0$, the above expansions read:

$$u_1(x_1, x_2, x_3) = A_0(x_1, x_3) + A_1(x_1, x_3)x_2 + A_2(x_1, x_3)x_2^2 + \mathcal{O}(x_2^3), \quad (4.29)$$

$$u_2(x_1, x_2, x_3) = B_0(x_1, x_3) + B_1(x_1, x_3)x_2 + B_2(x_1, x_3)x_2^2 + \mathcal{O}(x_2^3), \quad (4.30)$$

$$u_3(x_1, x_2, x_3) = C_0(x_1, x_3) + C_1(x_1, x_3)x_2 + C_2(x_1, x_3)x_2^2 + \mathcal{O}(x_2^3), \quad (4.31)$$

where the coefficients A_k , B_k and C_k represent the k th-order derivatives of the velocity components with respect to x_2 , evaluated at the wall, namely

$$A_k = \frac{1}{k!} \left. \frac{\partial^k u_1}{\partial x_2^k} \right|_{x_2=0}, \quad B_k = \frac{1}{k!} \left. \frac{\partial^k u_2}{\partial x_2^k} \right|_{x_2=0}, \quad C_k = \frac{1}{k!} \left. \frac{\partial^k u_3}{\partial x_2^k} \right|_{x_2=0}. \quad (4.32)$$

From the no-slip condition, the zeroth-order terms, of course, have to be identically zero: $A_0 = B_0 = C_0$, $\forall (x_1, x_3) \in \mathbb{R}^2$. Moreover, the incompressibility constraint⁵ on the divergence of the velocity field reads:

$$\frac{\partial u_k}{\partial x_k} = \frac{\partial A_1}{\partial x_1} x_2 + B_1(x_1, x_3) + \frac{\partial C_1}{\partial x_3} x_2 + \mathcal{O}(x_2^2) = 0, \quad (4.33)$$

which, for $x_2 = 0$, implies that also B_1 must be identically zero, hence, the following Taylor expansions in x_2 are obtained [53]:

$$u_1(x_1, x_2, x_3) = A_1(x_1, x_3)x_2 + A_2(x_1, x_3)x_2^2 + \mathcal{O}(x_2^3), \quad (4.34)$$

$$u_2(x_1, x_2, x_3) = B_2(x_1, x_3)x_2^2 + \mathcal{O}(x_2^3), \quad (4.35)$$

$$u_3(x_1, x_2, x_3) = C_1(x_1, x_3)x_2 + C_2(x_1, x_3)x_2^2 + \mathcal{O}(x_2^3). \quad (4.36)$$

⁵Due to the weakly compressible nature of the present implementation, we assume reasonable to neglect density fluctuations within the viscous sublayer.

From the above relations we may conclude that, in the near-wall region, the average velocity components scale as [42, 63]:

$$\langle u_1 \rangle \sim x_2, \quad \langle u_2 \rangle \sim x_2^2, \quad \langle u_3 \rangle \sim x_2,$$

where angled brackets designate statistical averaging. Moreover, the velocity gradient tensor $g_{ij} = \partial u_i / \partial x_j$ shows the following wall-scaling:

$$\mathbf{g} = \begin{pmatrix} \frac{\partial A_1}{\partial x_1} x_2 + \mathcal{O}(x_2^2) & A_1 + 2A_2 x_2 + \mathcal{O}(x_2^2) & \frac{\partial A_1}{\partial x_3} x_2 + \mathcal{O}(x_2^2) \\ \frac{\partial B_2}{\partial x_1} x_2^2 + \mathcal{O}(x_2^3) & 2B_2 x_2 + \mathcal{O}(x_2^2) & \frac{\partial B_2}{\partial x_3} x_2^2 + \mathcal{O}(x_2^3) \\ \frac{\partial C_1}{\partial x_1} x_2 + \mathcal{O}(x_2^2) & C_1 + 2C_2 x_2 + \mathcal{O}(x_2^2) & \frac{\partial C_1}{\partial x_3} x_2 + \mathcal{O}(x_2^2) \end{pmatrix}, \quad (4.37)$$

where the explicit indication of the dependence on x_1 and x_3 has been omitted for simplicity of notation. Consequently, the near-wall behavior of the average strain rate tensor is obtained as:

$$\langle S_{11} \rangle \sim x_2, \quad \langle S_{22} \rangle \sim x_2, \quad \langle S_{33} \rangle \sim x_2, \quad (4.38)$$

$$\langle S_{12} \rangle \sim 1, \quad \langle S_{13} \rangle \sim x_2, \quad \langle S_{23} \rangle \sim 1, \quad (4.39)$$

where the notation ~ 1 is used to indicate that the leading term in the relevant Taylor expansion is constant with respect to x_2 . Wall-scaling for the deviator of the strain rate tensor is immediately obtained from the above relations by subtracting the trace of $\langle S_{ij} \rangle$ from its own diagonal components:

$$\langle A_{11} \rangle \sim x_2, \quad \langle A_{22} \rangle \sim x_2, \quad \langle A_{33} \rangle \sim x_2, \quad (4.40)$$

$$\langle A_{12} \rangle \sim 1, \quad \langle A_{13} \rangle \sim x_2, \quad \langle A_{23} \rangle \sim 1. \quad (4.41)$$

Finally, the wall scaling of turbulent stresses may be derived from the theory of turbulent boundary layers [50, 66] and, accordingly, the statistical asymptotic behavior of the sub-grid stress is expected to be:

$$\langle \tau_{11} \rangle \sim x_2^2, \quad \langle \tau_{22} \rangle \sim x_2^4, \quad \langle \tau_{33} \rangle \sim x_2^2, \quad (4.42)$$

$$\langle \tau_{12} \rangle \sim x_2^3, \quad \langle \tau_{13} \rangle \sim x_2^2, \quad \langle \tau_{23} \rangle \sim x_2^3. \quad (4.43)$$

If we consider the deviator of the SGS stress tensor, the above scalings are still valid except that $\langle \tau_{22} \rangle$ now scales as x_2^2 . All the above results will be used in the next sections to check near-wall SGS models' behavior.

4.3 Eddy-Viscosity Hypothesis

The Eddy-Viscosity or Sub-Grid Viscosity models belong to the class of *Functional Models* in physical space, *i.e.*, models that aim at reproducing the effects of sub-grid terms on the resolved flow field, without necessarily reproduce also their structure [63]. Considering, for instance, the momentum transport equation, the effects of the sub-grid scales on the resolved field is linked to the divergence of the SGS stress tensor $\partial \tau_{ij} / \partial x_j$. Functional models try to compute

this divergence without necessarily reproduce the SGS tensor itself and its components and hence, they correlate with the SGS stresses *at vector level*⁶.

If the energy transfer from the resolved to the sub-grid scales is assumed to be similar to the molecular diffusion mechanism—which involves the kinematic viscosity and the thermal or scalar diffusivity—the sub-grid contributions may be modeled by introducing the eddy-viscosity ν_t , the sub-grid thermal diffusivity κ_{sgs} and the sub-grid diffusivity κ_{sgs}^Z and by resorting to the Boussinesq assumption and the Prandtl analogy [50, 66], which, in the LES perspective, lead to the following approximations:

$$(\overline{\rho u_i \tilde{u}_j} - \overline{\rho u_i} \tilde{u}_j)^d \simeq 2\overline{\rho} \nu_t \tilde{A}_{ij}, \quad (4.44)$$

$$\overline{\rho \vartheta \tilde{u}_k} - \overline{\rho T} \tilde{u}_k \simeq \overline{\rho} \kappa_{\text{sgs}} \frac{\partial \tilde{\vartheta}}{\partial x_k} = \frac{\overline{\rho} \nu_t}{Pr_t} \frac{\partial \tilde{\vartheta}}{\partial x_k}, \quad (4.45)$$

$$\overline{\rho Z \tilde{u}_k} - \overline{\rho Z} \tilde{u}_k \simeq \overline{\rho} \kappa_{\text{sgs}}^Z \frac{\partial \tilde{Z}}{\partial x_k} = \frac{\overline{\rho} \nu_t}{Sc_t} \frac{\partial \tilde{Z}}{\partial x_k}, \quad (4.46)$$

where Pr_t and Sc_t are the sub-grid Prandtl and Schmidt numbers respectively⁷. Supposing that the SGS turbulent diffusion \mathcal{D}_k and the isotropic SGS stress term $\tau_{jj} \tilde{u}_k$ in Eq. (4.21) are much smaller than the SGS heat flux, the SGS total energy flux becomes

$$q_k \simeq \frac{\overline{\rho} c_p \nu_t}{Pr_t} \frac{\partial \tilde{\vartheta}}{\partial x_k} = \gamma \frac{\overline{\rho} \nu_t}{Pr_t} \frac{\partial \tilde{e}_I}{\partial x_k}. \quad (4.47)$$

Using the above approximations, the flux vectors Eqs. (4.26) and (4.13) may be conveniently rewritten in the following form:

$$\overline{\mathbf{F}}^k = \begin{pmatrix} \overline{\rho u}_k \\ \overline{\rho u}_1 \tilde{u}_k + \delta_{1k} \overline{\varpi} \\ \overline{\rho u}_2 \tilde{u}_k + \delta_{2k} \overline{\varpi} \\ \overline{\rho u}_3 \tilde{u}_k + \delta_{3k} \overline{\varpi} \\ (\overline{\rho e} + \overline{\varpi}) \tilde{u}_k \\ \overline{\rho Z} \tilde{u}_k \end{pmatrix}, \quad \overline{\mathbf{D}}^k \simeq \begin{pmatrix} 0 \\ -2(\overline{\mu} + \overline{\rho} \nu_t) \tilde{A}_{1k} \\ -2(\overline{\mu} + \overline{\rho} \nu_t) \tilde{A}_{2k} \\ -2(\overline{\mu} + \overline{\rho} \nu_t) \tilde{A}_{3k} \\ -2\overline{\mu} \tilde{u}_j \tilde{A}_{kj} - \frac{\overline{\mu} c_p}{Pr} \frac{\partial \tilde{\vartheta}}{\partial x_k} - \gamma \frac{\overline{\rho} \nu_t}{Pr_t} \frac{\partial \tilde{e}_I}{\partial x_k} \\ -\left(\frac{\overline{\mu}}{Sc} + \frac{\overline{\rho} \nu_t}{Sc_t}\right) \frac{\partial \tilde{Z}}{\partial x_k} \end{pmatrix}, \quad (4.48)$$

with

$$\overline{\rho e} = \overline{\rho} c_v \tilde{\vartheta} + \frac{1}{2} \overline{\rho u}_k \tilde{u}_k = \frac{\overline{\varpi}}{\gamma - 1} + \frac{1}{2} \overline{\rho u}_k \tilde{u}_k, \quad (4.49)$$

$$\tilde{e}_I = c_v \tilde{\vartheta} = \frac{\overline{\rho e}}{\overline{\rho}} - \frac{1}{2} \tilde{u}_k \tilde{u}_k. \quad (4.50)$$

⁶The performances of SGS models may be checked, in a statistical sense, *a priori*, by comparison with exact SGS contributions extracted from Direct Numerical Simulation (DNS) data or, *a posteriori*, by analysis of experimental measurements. Correlations coefficients between modeled and exact sub-grid terms may be then computed. Since functional SGS models reproduce the divergence of the SGS stress tensor, correlation coefficients can be computed, at most, on the three components of the divergence vector.

With regards to scalar transport equations (*e.g.*, the energy equation), the divergence of the SGS flux vector is modeled, hence the correlations can be checked *at scalar level* only.

⁷The subscript ‘t’, *i.e.* “turbulent”, is frequently used and is reminiscent of the terminology commonly adopted for Reynolds averaged Navier-Stokes equations. Anyway, in this context, it would be more appropriate to use symbols like ν_{sgs} , Pr_{sgs} or Sc_{sgs} to underline the fact that we are really talking about “sub-grid scale” quantities.

The problem is closed once ν_t , Pr_t and Sc_t are specified. The next two sections will provide two examples of eddy-viscosity models, resorting to static or dynamically computed model constants, which have been used in the present work.

4.3.1 The Smagorinsky Model (SM)

Among the most used sub-grid scale eddy-viscosity models, the Smagorinsky model [70] computes the sub-grid viscosity ν_t as:

$$\nu_t = C_s^2 \Delta^2 |\tilde{S}|, \quad (4.51)$$

where the tensor norm term is computed from the resolved strain rate tensor with the following relation

$$|\tilde{S}| = (2\tilde{S}_{ij}\tilde{S}_{ij})^{1/2}, \quad (4.52)$$

and Δ is the grid level filter width, which, in the present case, is evaluated as: resorting to the formula,

$$\Delta = f(a_1, a_2)\Delta_{\text{eq}}, \quad (4.53)$$

where $\Delta_{\text{eq}} = (\Delta_1\Delta_2\Delta_3)^{1/3}$ [10]— Δ_k being the local grid spacing in the k th direction—and $f(a_1, a_2)$ is the corrective factor for anisotropic grids proposed by Scotti et al. [69], where a_1 and a_2 are the aspect ratios of the two smaller sides of the computational cell to the biggest one.

The model constant C_s can be theoretically determined, from *Local Equilibrium Hypothesis* considerations or adapted for the specific problem. Typical values range from 0.1 to 0.2 (*cf.* Sagaut [63] and therein cited references for more details).

The Smagorinsky model alone shows quite poor wall-scaling properties. In fact, as it can be easily deduced from Eqs. (4.38), (4.39), (4.40) and (4.41), the predicted sub-grid viscosity scales as $\langle\nu_t\rangle \sim 1$, leading to an over-dissipative behavior in the near-wall region [42]:

$$\langle\tau_{11}^s\rangle \sim x_2, \quad \langle\tau_{22}^s\rangle \sim x_2, \quad \langle\tau_{33}^s\rangle \sim x_2, \quad (4.54)$$

$$\langle\tau_{12}^s\rangle \sim 1, \quad \langle\tau_{13}^s\rangle \sim x_2, \quad \langle\tau_{23}^s\rangle \sim 1. \quad (4.55)$$

On this regard, a possible remedy is to introduce *ad hoc* damping functions that try to recover the correct scaling toward solid boundaries. Alternatively, the dynamic procedure, which is presented in Section 4.3.3, may be adopted.

4.3.2 The WALE Model

Specifically designed to reproduce correct scaling when wall boundary conditions are present, the Wall-Adapting Local Eddy-viscosity (WALE) model proposed by Nicoud and Ducros [53] computes the eddy-viscosity ν_t from the velocity gradient tensor's invariants resorting to the following relation:

$$\nu_t = C_w^2 \Delta^2 \frac{(\tilde{s}_{ij}^d \tilde{s}_{ij}^d)^{3/2}}{(\tilde{S}_{ij}\tilde{S}_{ij})^{5/2} + (\tilde{s}_{ij}^d \tilde{s}_{ij}^d)^{5/4}}, \quad (4.56)$$

where C_w is a true model constant, Δ is evaluated from Eq. (4.53), $\tilde{S}_{ij} = 1/2(\partial\tilde{u}_i/\partial x_j + \partial\tilde{u}_j/\partial x_i)$ is the strain rate tensor of the resolved field and \tilde{s}_{ij}^d is the traceless symmetric part

of the square of the resolved velocity gradient tensor $\tilde{g}_{ij} = \partial\tilde{u}_i/\partial x_j$, namely

$$\tilde{s}_{ij}^d = \frac{1}{2}(\tilde{g}_{ij}^2 + \tilde{g}_{ji}^2) - \frac{1}{3}\delta_{ij}\tilde{g}_{kk}^2, \quad (4.57)$$

with $\tilde{g}_{ij}^2 = \tilde{g}_{ik}\tilde{g}_{kj}$. Moreover, sub-grid thermal and scalar diffusivities are computed from the eddy-viscosity assuming constant Pr_t and Sc_t respectively. A model constant value $C_w = 0.5$ was found to be optimal from *a priori* tests on freely decaying isotropic homogeneous turbulence [53].

Using the results obtained in Section 4.2.2, it is easy to show that the eddy-viscosity from Eq. (4.56) is of the order of x_2^3 [53], thus leading to the following behavior for the deviatoric part of the SGS modeled stress tensor (*cf.* Eq. (4.44)):

$$\langle\tau_{11}^w\rangle \sim x_2^4, \quad \langle\tau_{22}^w\rangle \sim x_2^4, \quad \langle\tau_{33}^w\rangle \sim x_2^4, \quad (4.58)$$

$$\langle\tau_{12}^w\rangle \sim x_2^3, \quad \langle\tau_{13}^w\rangle \sim x_2^4, \quad \langle\tau_{23}^w\rangle \sim x_2^3. \quad (4.59)$$

As a direct consequence of the fact that $\langle\nu_t\rangle \sim x_2^3$, the most important sub-grid stress components in the near wall region [63], namely $\langle\tau_{12}^w\rangle$ and $\langle\tau_{23}^w\rangle$, retain the correct scaling. Furthermore, the other components are two order of magnitude smaller than expected from theory. This last fact will play a key role in the development of the WALE-Similarity Model, which will be presented in Section 4.4.1.

4.3.3 The Compressible Lagrangian Dynamic Smagorinsky Model (LDSM)

When the eddy-viscosity model is not able to retain the expected near-wall behavior, as it is the case for the Smagorinsky model, dynamic procedures for computing sub-grid model constants may be adopted in order to minimize an estimate of the error introduced by the model itself, in the least square sense [25, 41, 49]. One of the major drawbacks of dynamic models is the need to resort to a constant regularization procedure, typically based on averaging operations along homogeneous directions, in order to prevent numerical instabilities related to anti-dissipative model predictions.

In the Lagrangian Dynamic Smagorinsky Model (LDSM), originally developed by Meneveau et al. [48] for incompressible flows, in particular, averaging is performed along fluid particles trajectories, thus extending the applicability of the dynamic procedures to complex geometries, for which the definition of homogeneous directions is seldom possible.

The main features of the model are summarized below. In parallel, the Lagrangian dynamic procedure is extended to the computation of the turbulent Prandtl number in the compressible case as suggested by Moin et al. [49]⁸. The least squares procedures proposed by Lilly [41], in particular, will be adopted.

Following the idea of Germano et al. [25], the dynamic procedure aims at evaluating SGS model constants using the information contained in the resolved flow field. Introducing the *hat* test filter operator at cutoff length $\hat{\Delta} = 2\Delta$, the following identities are introduced:

$$\mathcal{L}_{ij}^d = \hat{\tau}_{ij}^d - \mathcal{T}_{ij}^d, \quad (4.60)$$

$$\mathcal{K}_j = \hat{q}_j - \mathcal{Q}_j, \quad (4.61)$$

⁸Even though the turbulent Schmidt number could also be dynamically computed, we assume unity SGS Lewis number, hence the turbulent Schmidt number is set equal to the turbulent Prandtl number.

where \mathcal{T}_{ij} and \mathcal{Q}_j represent the SGS stress tensor and the SGS heat flux as they would have been computed from a LES at the test filter level, $\widehat{\tau}_{ij}$ and \widehat{q}_j are the SGS terms at level Δ filtered at the test level; \mathcal{L}_{ij} and \mathcal{K}_j are the modified Leonard terms [24] expressing interactions between scales Δ and $\widehat{\Delta}$:

$$\mathcal{T}_{ij}^d = (\widehat{\rho\tilde{u}_i\tilde{u}_j} - \widehat{\rho\tilde{u}_i\tilde{u}_j})^d, \quad \mathcal{Q}_j = \gamma(\widehat{\rho e_I\tilde{u}_j} - \widehat{\rho e_I\tilde{u}_j}), \quad (4.62)$$

$$\widehat{\tau}_{ij}^d = (\widehat{\rho\tilde{u}_i\tilde{u}_j} - \widehat{\rho\tilde{u}_i\tilde{u}_j})^d, \quad \widehat{q}_j = \gamma(\widehat{\rho e_I\tilde{u}_j} - \widehat{\rho e_I\tilde{u}_j}), \quad (4.63)$$

$$\mathcal{L}_{ij}^d = (\widehat{\rho\tilde{u}_i\tilde{u}_j} - \widehat{\rho\tilde{u}_i\tilde{u}_j})^d, \quad \mathcal{K}_j = \gamma(\widehat{\rho e_I\tilde{u}_j} - \widehat{\rho e_I\tilde{u}_j}). \quad (4.64)$$

with the *tilde-hat* operator being used to symbolically indicate mass wighted Favre-filtering at the test level:

$$\widehat{\tilde{\varphi}} \equiv \frac{\widehat{\rho\tilde{\varphi}}}{\widehat{\rho}}.$$

Note that \mathcal{L}_{ij}^d and \mathcal{K}_j are computable from the resolved field, therefore, if the Smagorinsky model is used to approximate the SGS eddy-viscosity, the relevant errors in the Germano's identity read

$$\varepsilon_{ij}^L = \mathcal{L}_{ij}^d - \widehat{C_s^2\alpha_{ij}} + C_s^2\beta_{ij} = \mathcal{L}_{ij}^d - C_s^2\mathcal{M}_{ij}, \quad (4.65)$$

$$\varepsilon_j^K = \mathcal{K}_j - \widehat{\frac{C_s^2}{Pr_t}\alpha_j^{eI}} + \frac{C_s^2}{Pr_t}\beta_j^{eI} = \mathcal{K}_j - \frac{C_s^2}{Pr_t}\mathcal{H}_j, \quad (4.66)$$

where, using Eqs. (4.44) and (4.47) and the Smagorinsky model, Eq. (4.51), to express the sub-grid viscosity ν_t , we may write the various terms as:

$$\alpha_{ij} = 2\bar{\rho}\Delta^2|\tilde{S}|\tilde{A}_{ij}, \quad \beta_{ij} = 2\widehat{\rho}\widehat{\Delta}^2|\widehat{S}|\widehat{A}_{ij}, \quad \mathcal{M}_{ij} = \widehat{\alpha}_{ij} - \beta_{ij}, \quad (4.67)$$

$$\alpha_j^{eI} = \gamma\bar{\rho}\Delta^2|\tilde{S}|\frac{\partial\tilde{e}_I}{\partial x_j}, \quad \beta_j^{eI} = \gamma\widehat{\rho}\widehat{\Delta}^2|\widehat{S}|\frac{\partial\widehat{e}_I}{\partial x_j}, \quad \mathcal{H}_j = \widehat{\alpha}_j^{eI} - \beta_j^{eI}, \quad (4.68)$$

with the tensor norms $|\tilde{S}|$ and $|\widehat{S}|$ being computed, according to Eq. (4.52), from the filtered and test filtered strain tensors respectively. It is worthwhile underlining that both Δ and $\widehat{\Delta}$ may be computed, in analogy to Eq. (4.53), including the relevant anisotropic corrective factor [67, 68].

The last equality in Eqs. (4.65) and (4.66) is obtained under the assumption of scale-invariance of the model constant C_s and the turbulent Prandtl number Pr_t ⁹.

If $\mathbf{z}(t')$ is the position of the fluid particle at some earlier time t' , the Lagrangian averaged square errors are defined as:

$$\mathcal{E}_L = \int_{-\infty}^t \varepsilon_{ij}^L(\mathbf{z}(t'), t')\varepsilon_{ij}^L(\mathbf{z}(t'), t')W(t-t')dt', \quad (4.69)$$

$$\mathcal{E}_K = \int_{-\infty}^t \varepsilon_j^K(\mathbf{z}(t'), t')\varepsilon_j^K(\mathbf{z}(t'), t')W(t-t')dt', \quad (4.70)$$

⁹Even if not explicitly indicated, the model constant, in general, is a parameter which depends on the filter size. The scale-invariance assumption states that this dependency may be neglected between Δ and $\widehat{\Delta}$, thus allowing taking the model constant out of the test filtering operator:

$$\widehat{C_s^2\alpha_{ij}} \simeq C_s^2\widehat{\alpha}_{ij}, \quad \text{and} \quad \widehat{\frac{C_s^2}{Pr_t}\alpha_j^{eI}} \simeq \frac{C_s^2}{Pr_t}\widehat{\alpha}_j^{eI}.$$

where $W(t - t')$ is a weighting function introduced to control the *memory* of the total error function with respect to earlier times. The above errors can be minimized in the least squares sense, with respect to a model constant C^2 , by solving the following general condition:

$$\frac{\partial \mathcal{E}}{\partial C^2} = \int_{-\infty}^t 2\varepsilon \frac{\partial \varepsilon}{\partial C^2} W(t - t') dt' = 0. \quad (4.71)$$

which is applied to \mathcal{E}_L and \mathcal{E}_K in order to minimize the error with respect to C_s^2 and the ratio C_s^2/Pr_t respectively. Using Eq. (4.65) and (4.66), we finally get

$$C_s^2(\mathbf{x}, t) = \frac{\mathcal{I}_{LM}}{\mathcal{I}_{MM}}, \quad \text{and} \quad \left[\frac{C_s^2}{Pr_t} \right](\mathbf{x}, t) = \frac{\mathcal{I}_{KH}}{\mathcal{I}_{HH}}, \quad (4.72)$$

with

$$\mathcal{I}_{LM} = \int_{-\infty}^t \mathcal{L}_{ij}^d \mathcal{M}_{ij}(\mathbf{z}(t'), t') W(t - t') dt', \quad (4.73)$$

$$\mathcal{I}_{MM} = \int_{-\infty}^t \mathcal{M}_{ij} \mathcal{M}_{ij}(\mathbf{z}(t'), t') W(t - t') dt', \quad (4.74)$$

$$\mathcal{I}_{KH} = \int_{-\infty}^t \mathcal{K}_j \mathcal{H}_j(\mathbf{z}(t'), t') W(t - t') dt', \quad (4.75)$$

$$\mathcal{I}_{HH} = \int_{-\infty}^t \mathcal{H}_j \mathcal{H}_j(\mathbf{z}(t'), t') W(t - t') dt'. \quad (4.76)$$

Choosing exponential weighting functions, the above integrals may be obtained as the solution of the following relaxation-transport equations (a demonstration of this statement is reported in Appendix A):

$$\frac{D\mathcal{I}_{LM}}{Dt} = \frac{1}{\mathbb{T}_L} (\mathcal{L}_{ij}^d \mathcal{M}_{ij} - \mathcal{I}_{LM}), \quad \frac{D\mathcal{I}_{MM}}{Dt} = \frac{1}{\mathbb{T}_L} (\mathcal{M}_{ij} \mathcal{M}_{ij} - \mathcal{I}_{MM}), \quad (4.77)$$

$$\frac{D\mathcal{I}_{KH}}{Dt} = \frac{1}{\mathbb{T}_K} (\mathcal{K}_j \mathcal{H}_j - \mathcal{I}_{KH}), \quad \frac{D\mathcal{I}_{HH}}{Dt} = \frac{1}{\mathbb{T}_K} (\mathcal{H}_j \mathcal{H}_j - \mathcal{I}_{HH}), \quad (4.78)$$

which are solved in a Lagrangian sense as suggested by Meneveau et al. [48]¹⁰.

According to the original formulation of the Lagrangian dynamic model, both \mathcal{I}_{LM} and \mathcal{I}_{KH} are clipped to zero in order to avoid negative values of the constants, thus preventing the

¹⁰The generic transport equation

$$\frac{D\phi}{Dt} = \frac{1}{\mathbb{T}} [f(\mathbf{x}, t) - \phi(\mathbf{x}, t)],$$

is approximated as

$$\frac{\phi^{n+1}(\mathbf{x}) - \phi^n(\mathbf{x} - \tilde{\mathbf{u}}^n \Delta t)}{\Delta t} = \frac{1}{\mathbb{T}^n} [f^{n+1}(\mathbf{x}) - \phi^{n+1}(\mathbf{x})],$$

where the value of ϕ^n at the upstream location $\mathbf{x} - \tilde{\mathbf{u}}^n \Delta t$ is obtained by multilinear interpolation. The new value ϕ^{n+1} is then obtained as a weighted sum of the interpolated prior value and the current source term at the grid point location:

$$\phi^{n+1}(\mathbf{x}) = \epsilon f^{n+1}(\mathbf{x}) + (1 - \epsilon) \phi^n(\mathbf{x} - \tilde{\mathbf{u}}^n \Delta t),$$

with $\epsilon = \Delta t / (\mathbb{T}^n + \Delta t)$.

model from predicting energy backscatter; by dimensional considerations, the characteristic times \mathbb{T}_L and \mathbb{T}_K are computed as:

$$\mathbb{T}_L = \frac{\theta_L \Delta \bar{\rho}^{1/2}}{(\mathcal{I}_{LM} \mathcal{I}_{MM})^{1/8}}, \quad \text{with } \theta_L = 1.5, \quad (4.79)$$

$$\mathbb{T}_K = \frac{\theta_K \Delta \bar{\rho}^{1/3}}{(\mathcal{I}_{KH} \mathcal{I}_{HH})^{1/12}}, \quad \text{with } \theta_K = 3.5. \quad (4.80)$$

The different value of the coefficient θ_K , which is proportional to the amount of memory of the Lagrangian averaging procedure, was chosen based on preliminary tests in order to limit the excessive oscillatory behavior of the dynamically computed Prandtl number. It is reasonable to expect that the difference between θ_L and θ_K is related to the different magnitude of the other terms involved in the computation of \mathbb{T}_L and \mathbb{T}_K respectively. The eddy-viscosity and the diffusivity coefficients are finally obtained:

$$\nu_t = C_s^2(\mathbf{x}, t) \Delta^2 |\tilde{S}|, \quad (4.81)$$

$$\kappa_{\text{sgs}} = \left[\frac{C_s^2}{Pr_t} \right](\mathbf{x}, t) \Delta^2 |\tilde{S}|, \quad (4.82)$$

$$\kappa_{\text{sgs}}^Z = \left[\frac{C_s^2}{Pr_t} \right](\mathbf{x}, t) Le_t \Delta^2 |\tilde{S}|, \quad (4.83)$$

where Le_t is the SGS Lewis number, which, as already mentioned, is actually set to 1.

With regards to wall scaling, observing that $\langle |S| \rangle \sim 1$ and that $\langle \mathcal{L}_{ij} \rangle$ and $\langle \mathcal{M}_{ij} \rangle$ scale as $\langle \tau_{ij} \rangle$ and $\langle A_{ij} \rangle$ respectively [42], it is easy to show that $\langle \mathcal{L}_{ij}^d \mathcal{M}_{ij} \rangle \sim x_2^3$ and that $\langle \mathcal{M}_{ij} \mathcal{M}_{ij} \rangle \sim 1$ and hence, from Eq. (4.72), that the eddy-viscosity retain the proper x_2^3 scaling leading to the same near-wall behavior observed for the WALE model (*cf.* Eqs. (4.58) and (4.59)).

4.3.4 The Filtered Structure Function Model (FSF)

The Filtered Structure Function (FSF) model, developed by Ducros et al. [14] for LES of turbulent transition in the boundary layer, evaluates the sub-grid viscosity from the energy of the highest resolved frequencies $E(k_c)$, computed from the second order structure function of the resolved velocity field:

$$F_2(\mathbf{x}, \Delta, t) = \langle \|\tilde{\mathbf{u}}(\mathbf{x} + \mathbf{r}, t) - \tilde{\mathbf{u}}(\mathbf{x}, t)\| \rangle_{\|\mathbf{r}\|=\Delta}, \quad (4.84)$$

where angled brackets indicate spatial averaging.

In order to better select resolved high frequency modes, the structure function is evaluated after applying a high-pass filter on the resolved velocity field, which is actually implemented resorting to a discrete Laplacian filter in physical space¹¹

$$\begin{aligned} \text{HP}^{(1)}(\tilde{\mathbf{u}}_{i,j,k}) &= \tilde{\mathbf{u}}_{i+1,j,k} - 2\tilde{\mathbf{u}}_{i,j,k} + \tilde{\mathbf{u}}_{i-1,j,k} \\ &\quad + \tilde{\mathbf{u}}_{i,j+1,k} - 2\tilde{\mathbf{u}}_{i,j,k} + \tilde{\mathbf{u}}_{i,j-1,k} \\ &\quad + \tilde{\mathbf{u}}_{i,j,k+1} - 2\tilde{\mathbf{u}}_{i,j,k} + \tilde{\mathbf{u}}_{i,j,k-1}, \end{aligned} \quad (4.85)$$

$$\text{HP}^{(n)}(\tilde{\mathbf{u}}_{i,j,k}) = \text{HP}^{(1)}[\text{HP}^{(n-1)}(\tilde{\mathbf{u}}_{i,j,k})], \quad (4.86)$$

¹¹The used high-pass filter is actually the discrete approximation of the Laplacian operator [63]:

$$\text{HP}^{(1)}(\tilde{\mathbf{u}}) \simeq \Delta^2 \nabla^2 \tilde{\mathbf{u}}.$$

iterated, as recommended by Ducros et al. [14], 3 times:

$$\begin{aligned}
 F_2^{(3)}(\mathbf{x}, \Delta, t) &= \langle \|\tilde{\mathbf{u}}^{(3)}(\mathbf{x} + \mathbf{r}, t) - \tilde{\mathbf{u}}^{(3)}(\mathbf{x}, t)\| \rangle_{\|\mathbf{r}\|=\Delta} \\
 &\simeq \frac{1}{6} \left(\|\tilde{\mathbf{u}}_{i+1,j,k}^{(3)} - \tilde{\mathbf{u}}_{i,j,k}^{(3)}\| + \|\tilde{\mathbf{u}}_{i,j,k}^{(3)} - \tilde{\mathbf{u}}_{i-1,j,k}^{(3)}\| \right. \\
 &\quad + \|\tilde{\mathbf{u}}_{i,j+1,k}^{(3)} - \tilde{\mathbf{u}}_{i,j,k}^{(3)}\| + \|\tilde{\mathbf{u}}_{i,j,k}^{(3)} - \tilde{\mathbf{u}}_{i,j-1,k}^{(3)}\| \\
 &\quad \left. + \|\tilde{\mathbf{u}}_{i,j,k+1}^{(3)} - \tilde{\mathbf{u}}_{i,j,k}^{(3)}\| + \|\tilde{\mathbf{u}}_{i,j,k}^{(3)} - \tilde{\mathbf{u}}_{i,j,k-1}^{(3)}\| \right), \tag{4.87}
 \end{aligned}$$

with $\tilde{\mathbf{u}}^{(3)} = \text{HP}^{(3)}(\tilde{\mathbf{u}})$.

The value of the sub-grid viscosity is then obtained as:

$$\nu_t = 0.0014 C_K^{-3/2} \Delta \sqrt{F_2^{(3)}(\mathbf{x}, \Delta, t)}, \tag{4.88}$$

where $C_K \sim 1.5$ is the Kolmogorov constant in the five-thirds law [51] (*cf.* Eq. (2.50) at page 15) and Δ is computed from Eq. (4.53).

It should be noted that, when Eq. (4.87) is evaluated as a local statistical average of square velocity differences over the six neighbor nodes (on cartesian grids), then $\langle F_2^{(3)} \rangle \sim 1$ and hence near-wall scaling for the sub-grid viscosity is of the same order [53]. Better results may be obtained averaging (and filtering) on four neighbor nodes lying on the plane parallel to the wall [14].¹² In that case, the structure function scales as x_2^2 , hence, the eddy viscosity behaves like $\langle \nu_t \rangle \sim x_2$, therefore zero eddy-viscosity is recovered at the wall, even though not as fast as expected.¹³

¹²If the wall is orthogonal to x_2 , the four nodes formulations for Eqs. (4.85) and (4.87) become:

$$\begin{aligned}
 \text{HP}^{(1)}(\tilde{\mathbf{u}}_{i,j,k}) &= \tilde{\mathbf{u}}_{i+1,j,k} - 2\tilde{\mathbf{u}}_{i,j,k} + \tilde{\mathbf{u}}_{i-1,j,k} \\
 &\quad + \tilde{\mathbf{u}}_{i,j,k+1} - 2\tilde{\mathbf{u}}_{i,j,k} + \tilde{\mathbf{u}}_{i,j,k-1}, \\
 F_2^{(3)}(\mathbf{x}, \Delta, t) &\simeq \frac{1}{4} \left(\|\tilde{\mathbf{u}}_{i+1,j,k}^{(3)} - \tilde{\mathbf{u}}_{i,j,k}^{(3)}\| + \|\tilde{\mathbf{u}}_{i,j,k}^{(3)} - \tilde{\mathbf{u}}_{i-1,j,k}^{(3)}\| \right. \\
 &\quad \left. + \|\tilde{\mathbf{u}}_{i,j,k+1}^{(3)} - \tilde{\mathbf{u}}_{i,j,k}^{(3)}\| + \|\tilde{\mathbf{u}}_{i,j,k}^{(3)} - \tilde{\mathbf{u}}_{i,j,k-1}^{(3)}\| \right).
 \end{aligned}$$

¹³If r_k is the k th component of the spacing \mathbf{r} used to compute the structure function, form Eqs. (4.34)–(4.36) is readily verified that:

$$\begin{aligned}
 \delta_1[u_1] &= \delta_1[A_1]x_2 + \mathcal{O}(x_2^2), & \delta_2[u_1] &= A_1 r_2 + \mathcal{O}(x_2), & \delta_3[u_1] &= \delta_3[A_1]x_2 + \mathcal{O}(x_2^2), \\
 \delta_1[u_2] &= \delta_1[B_2]x_2^2 + \mathcal{O}(x_2^3), & \delta_2[u_2] &= B_2 r_2^2 + \mathcal{O}(x_2), & \delta_3[u_2] &= \delta_3[B_2]x_2^2 + \mathcal{O}(x_2^3), \\
 \delta_1[u_3] &= \delta_1[C_1]x_2 + \mathcal{O}(x_2^2), & \delta_2[u_3] &= C_1 r_2 + \mathcal{O}(x_2^2), & \delta_3[u_3] &= \delta_3[C_1]x_2 + \mathcal{O}(x_2^2),
 \end{aligned}$$

where the notation $\delta_k[\cdot]$ has been introduced to synthetically indicate a difference between locations x_k and $x_k + r_k$. From these relations, the norms of the velocity differences along the three coordinate axes have scalings:

$$\begin{aligned}
 \|\delta_1[\mathbf{u}]\| &= \delta_1[u_1]^2 + \delta_1[u_2]^2 + \delta_1[u_3]^2 \sim x_2^2, \\
 \|\delta_2[\mathbf{u}]\| &= \delta_2[u_1]^2 + \delta_2[u_2]^2 + \delta_2[u_3]^2 \sim 1, \\
 \|\delta_3[\mathbf{u}]\| &= \delta_3[u_1]^2 + \delta_3[u_2]^2 + \delta_3[u_3]^2 \sim x_2^2,
 \end{aligned}$$

hence, when the structure function is evaluated with the six neighbor formulation, the leading term is $\mathcal{O}(1)$ relevant to $\|\delta_2[\mathbf{u}]\|$, whereas in the four neighbor formulation the leading term is $\mathcal{O}(x_2^2)$ from in-plane differences only, $\|\delta_1[\mathbf{u}]\|$ and $\|\delta_3[\mathbf{u}]\|$.

4.4 Scale Similarity Hypothesis

As opposed to Functional Models, as those based on the Eddy-Viscosity hypothesis, the *Structural Models* are designed to make the best approximation of the sub-grid scale contributions using informations contained within the resolved scales. Considering the momentum transport equation, for instance, structural models aim at reproducing the SGS stress tensor and its structural features, hence they would be expected to well correlate *at tensor level* also.

Among the Structural Models, similarity models are based on the hypothesis that the statistical features of tensors constructed on the sub-grid scales are similar to those of analogous tensors computed on the basis of the smallest resolved scales [1, 3, 4, 42].

Focusing on the incompressible case, if $t_{ij}^{\text{sgs}} = \overline{u_i u_j} - \overline{u_i} \overline{u_j}$ is the SGS stress tensor relevant to a LES at filter size Δ , corresponding to the *bar* filter operator, the Leonard decomposition reads

$$-t_{ij}^{\text{sgs}} = \underbrace{\overline{u_i u_j} - \overline{u_i} \overline{u_j}}_{L_{ij}} + \underbrace{\overline{u_i u'_j} + \overline{u'_i u_j}}_{C_{ij}} + \underbrace{\overline{u'_i u'_j}}_{R_{ij}}, \quad (4.89)$$

where $u'_i = u_i - \overline{u_i}$ is the sub-grid velocity and L_{ij} , C_{ij} and R_{ij} are the Leonard term, the Cross term and the SGS Reynolds term respectively. Since the Leonard term is computable from the resolved flow field, the closure problem reduces to the approximation of the Cross and Reynolds terms only, which are computed on the SGS velocity u'_i . Under the scale similarity assumption, we may construct those tensors on the small-scale components of the resolved field, which may be estimated as the difference between the filtered field and the twice-filtered field, this difference representing a reasonable estimate of the filtered SGS velocity [3].

Assuming that $\overline{u'_i u'_j} \simeq \overline{u'_i} \overline{u'_j}$ and that $\overline{u_i u'_j} \simeq \overline{u_i} \overline{u'_j}$ and approximating $\overline{u'_i}$ with $\overline{u_i} - \overline{\overline{u_i}}$, the Cross and SGS Reynolds terms become

$$C_{ij} \simeq \overline{\overline{u_i}} (\overline{u_j} - \overline{\overline{u_j}}) + (\overline{u_i} - \overline{\overline{u_i}}) \overline{\overline{u_j}}, \quad (4.90)$$

$$R_{ij} \simeq (\overline{u_i} - \overline{\overline{u_i}}) (\overline{u_j} - \overline{\overline{u_j}}), \quad (4.91)$$

which, using Eq. (4.89), lead to the following approximation for the SGS stress tensor, namely the original Bardina et al. [4] model¹⁴:

$$-t_{ij}^{\text{sgs}} \simeq \overline{\overline{u_i u_j}} - \overline{u_i} \overline{u_j} + \underbrace{\overline{u_i u_j} - \overline{\overline{u_i u_j}}}_{C_{ij} + R_{ij}} = \overline{\overline{u_i u_j}} - \overline{u_i} \overline{u_j}, \quad (4.94)$$

The above hypothesis was then generalized by Liu et al. [42] splitting the energy spectrum into a certain number of bands and filtering at two different levels, Δ and $\widehat{\Delta} = \alpha \Delta$ (with $\alpha \geq 1$):

$$-t_{ij}^{\text{sgs}} = C_L (\widehat{\overline{u_i u_j}} - \widehat{\overline{u_i}} \widehat{\overline{u_j}}), \quad (4.95)$$

¹⁴The same approximation may be obtained using the generalized central moments proposed by Germano [24] and neglecting the modified Cross and Reynolds terms:

$$-t_{ij}^{\text{sgs}} = \underbrace{\overline{\overline{u_i u_j}} - \overline{\overline{u_i}} \overline{\overline{u_j}}}_{\mathcal{L}_{ij}} + \underbrace{\overline{u_i u'_j} + \overline{u'_i u_j} - \overline{\overline{u_i u'_j}} - \overline{\overline{u'_i u_j}}}_{\mathcal{C}_{ij}} + \underbrace{\overline{u'_i u'_j} - \overline{\overline{u'_i u'_j}}}_{\mathcal{R}_{ij}}, \quad (4.92)$$

$$C_{ij} \simeq 0, \mathcal{R}_{ij} \simeq 0, \Rightarrow -t_{ij}^{\text{sgs}} \simeq \mathcal{L}_{ij}. \quad (4.93)$$

where the model coefficient C_L may be assigned *a priori*—typically C_L is set equal to one in order to preserve Galilean invariance of the model [71]—or dynamically computed [42].

Differently from models based on the eddy-viscosity assumption, similarity models remove the hypothesis of alignment between the proper axes of the sub-grid scale stress tensor and those of the resolved shear stress tensor, thus achieving very good correlation between expected and computed SGS stresses. Good correlation was also observed between real and modeled local SGS energy flux, even in regions characterized by energy backscatter, meaning that the Leonard tensor is able to predict reversed energy transfer on a reasonable physical ground [42, 64].

On the other hand, tests performed on LES show that similarity models are not dissipative and the addition of an eddy-viscosity term is anyway advisable in practice [3, 4]. The resulting closures are the so-called similarity mixed models and a number of versions have been proposed which, generally, resort to the classical eddy viscosity Smagorinsky model and to dynamic modeling, in order to retain the correct wall-scaling that the eddy-viscosity term may have affected [1, 2, 64, 89]. In the perspective of the modified Leonard decomposition (*cf.* Eq. (4.92)), a similarity mixed model may be obtained by neglecting C_{ij} and the second term in \mathcal{R}_{ij} and by modeling the first term in the modified SGS Reynolds term using the eddy-viscosity hypothesis [64]:

$$-t_{ij}^{\text{sgs}} \simeq \overline{\tilde{u}_i \tilde{u}_j} - \overline{\tilde{u}_i} \overline{\tilde{u}_j} + \overline{u'_i u'_j} \simeq \overline{\tilde{u}_i \tilde{u}_j} - \overline{\tilde{u}_i} \overline{\tilde{u}_j} - 2\bar{\rho} \nu_t \tilde{S}_{ij} \quad (4.96)$$

The similarity mixed model was generalized to the compressible case using the Favre-filtering formalism and *a priori* determined model coefficients—namely, C_L for the modified Leonard term and C_s for the eddy-viscosity term—by Erlebacher et al. [16, 17], Speziale et al. [72]. A dynamic version of the same model was then proposed by Salvetti and Banerjee [64]. Strong correlation at tensor level was observed in both cases.

4.4.1 The WALE-Similarity Model (WSM)

In the perspective of developing a similarity mixed model with proper near-wall scaling without resorting to dynamic procedures, we put forward the idea of modeling the eddy-viscosity term resorting to the WALE formulation. In this way, on one hand, the explicit filtering operator is applied for the computation of the modified Leonard tensor only, whereas a dynamic procedure would require additional test filtering to apply the Germano's identity (*cf.* Eq. (4.60)); on the other hand, no spatial or Lagrangian averaging, generally required when dynamic procedures are implemented, is needed.

Introducing the velocity decomposition into resolved and unresolved parts, namely $u_j = \tilde{u}_j + u'_j$, the SGS stress tensor is decomposed according to the Leonard decomposition and the modified Leonard decomposition as

$$-\tau_{ij} = \underbrace{L_{ij} + C_{ij} + R_{ij}}_{\text{Leonard decomposition}} = \underbrace{\mathcal{L}_{ij} + C_{ij} + \mathcal{R}_{ij}}_{\text{modified Leonard decomposition}}, \quad (4.97)$$

with

$$L_{ij} = \bar{\rho}(\widetilde{\tilde{u}_i \tilde{u}_j} - \tilde{u}_i \tilde{u}_j), \quad \mathcal{L}_{ij} = \bar{\rho}(\widetilde{\tilde{u}_i \tilde{u}_j} - \tilde{u}_i \tilde{u}_j), \quad (4.98)$$

$$C_{ij} = \bar{\rho}(\widetilde{\tilde{u}_i u'_j} + u'_i \tilde{u}_j), \quad C_{ij} = \bar{\rho}(\widetilde{\tilde{u}_i u'_j} + u'_i \tilde{u}_j - \tilde{u}_i u'_j - u'_i \tilde{u}_j), \quad (4.99)$$

$$R_{ij} = \overline{\rho u'_i u'_j}, \quad \mathcal{R}_{ij} = \bar{\rho}(u'_i u'_j - \tilde{u}'_i \tilde{u}'_j). \quad (4.100)$$

The compressible extension of the similarity mixed model [3, 4] is obtained by neglecting \mathcal{C}_{ij} and the second term in \mathcal{R}_{ij} or, equivalently, by using the approximation $C_{ij} \simeq \bar{\rho} \tilde{u}_i \tilde{u}_j - \overline{\tilde{u}_i \tilde{u}_j}$; the SGS stress tensor is then modeled as:

$$-\tau_{ij} \simeq \underbrace{\bar{\rho}(\tilde{u}_i \tilde{u}_j - \overline{\tilde{u}_i \tilde{u}_j})}_{\mathcal{L}_{ij}} + \underbrace{\overline{\rho u'_i u'_j}}_{R_{ij}}, \quad (4.101)$$

and, modeling the deviatoric part of the SGS true Reynolds term with the eddy-viscosity hypothesis (Eq. (4.44)), the sub-grid stress becomes:

$$-\tau_{ij} \simeq \bar{\rho}(\tilde{u}_i \tilde{u}_j - \overline{\tilde{u}_i \tilde{u}_j}) - 2\bar{\rho}\nu_t \tilde{A}_{ij} + \frac{1}{3}\delta_{ij} \overline{\rho u'_k u'_k}. \quad (4.102)$$

The last term in the above relation, namely the trace of R_{ij} , may be modeled, as proposed by Speziale et al. [72], Zang et al. [88], who use the formulation by Yoshizawa [86], or neglected as in Erlebacher et al. [17]¹⁵. In this work, a modified version of the already discussed procedure of Ducros et al. [13], Lesieur et al. [40] is adopted, in which *reduced* macropressure $\overline{\varpi}^*$ and macrotemperature ϑ^* are defined accounting for the trace of the SGS Reynolds term only. In fact, since the modified Leonard tensor is directly accessible from the resolved field, there is no need to incorporate its spherical part into the macropressure and the filtered momentum and total energy transport equation can be rewritten as (*cf.* Eq. (4.7))¹⁶:

$$\frac{\partial \overline{\rho u_i}}{\partial t} + \frac{\partial}{\partial x_j} [\overline{\rho u_i \tilde{u}_j} + \delta_{ij}(\overline{\varpi}^* + \frac{1}{3}\mathcal{L}_{kk})] = \frac{\partial}{\partial x_j} (2\bar{\mu} \tilde{A}_{1k} + \tau_{ij}^d), \quad (4.104)$$

$$\frac{\partial \overline{\rho e}}{\partial t} + \frac{\partial}{\partial x_k} [(\overline{\rho e} + \overline{\varpi}^*) \tilde{u}_k] = \frac{\partial}{\partial x_k} \left(2\bar{\mu} \tilde{u}_j \tilde{A}_{kj} + \frac{\bar{\mu} c_p}{Pr} \frac{\partial \vartheta^*}{\partial x_k} + q_k \right), \quad (4.105)$$

where

$$\overline{\varpi}^* = \bar{p} + \frac{1}{3} \overline{\rho u'_k u'_k} = \bar{p} + \frac{1}{3} R_{kk}, \quad (4.106)$$

and

$$\tau_{ij}^d = 2\bar{\rho}\nu_t \tilde{A}_{ij} - \bar{\rho}(\tilde{u}_i \tilde{u}_j - \overline{\tilde{u}_i \tilde{u}_j})^d. \quad (4.107)$$

In a similar fashion, the reduced macrotemperature may be defined from the filtered total energy using Eq. (4.11) and Eq. (4.102):

$$\overline{\rho e} = \bar{\rho} c_v \tilde{T} + \frac{1}{2} \overline{\rho u_k \tilde{u}_k} - \frac{1}{2} \tau_{kk} = \bar{\rho} c_v \vartheta^* + \frac{1}{2} \overline{\rho u_k \tilde{u}_k} + \frac{1}{2} \mathcal{L}_{kk}, \quad (4.108)$$

¹⁵It is interesting to note that *a priori* tests on moderately compressible isotropic homogeneous turbulence by [88] revealed almost no change in the results when varying the model coefficient for the isotropic part of the SGS true Reynolds term between 0 and 10 times its standard value. This result corroborate the choice of Erlebacher et al. [17], who neglected the Yoshizawa term for turbulent Mach number up to 0.4.

¹⁶Consistently with the definition of reduced macrotemperature, it is assumed that:

$$\frac{\bar{\mu} c_p}{Pr} \frac{\partial \tilde{T}}{\partial x_k} - \frac{\bar{\mu} c_p}{Pr} \frac{\partial \vartheta^*}{\partial x_k} \simeq 0.$$

Moreover, the dynamic viscosity $\bar{\mu}$ is computed from Eq. (2.14) using the reduced macrotemperature:

$$\bar{\mu}(\vartheta^*) = \mu_{\text{ref}} \left(\frac{\vartheta^*}{T_{\text{ref}}} \right)^{3/2} \frac{T_{\text{ref}} + S}{\vartheta^* + S}. \quad (4.103)$$

where

$$\tilde{\vartheta}^* = \tilde{T} + \frac{1}{2\bar{\rho}c_v} \overline{\rho u'_k u'_k} = \tilde{T} + \frac{1}{2\bar{\rho}c_v} R_{kk}, \quad (4.109)$$

and the filtered internal energy is now expressed as

$$\tilde{e}_I = c_v \tilde{\vartheta}^* = \frac{\bar{\rho}e}{\bar{\rho}} - \frac{1}{2} \tilde{u}_k \tilde{u}_k - \frac{1}{2} \frac{\mathcal{L}_{kk}}{\bar{\rho}}. \quad (4.110)$$

Provided that the *true* SGS Mach number is sufficiently small (*cf.* Section 4.2.1), namely

$$M_{\text{sgs}}^{*2} = \frac{\overline{\rho u'_k u'_k}}{\gamma \bar{p}} = \frac{R_{kk}}{\gamma \bar{p}}, \quad (4.111)$$

$$\frac{|3\gamma - 5|}{6} \gamma M_{\text{sgs}}^{*2} \ll 1, \quad (4.112)$$

the reduced macropressure and macrotemperature are related by the usual equation of state,

$$\bar{\omega}^* = \bar{\rho} R \tilde{\vartheta}^*. \quad (4.113)$$

In the present case, where $\gamma = 1.4$, the condition Eq. (4.112) is ~ 1.6 times less restrictive on M_{sgs}^* than the analogous one prescribed by Erlebacher et al. [17].

Due to the present redefinition of macropressure, macrotemperature and filtered energy (Eqs. (4.106), (4.108) and (4.109)), the sub-grid total energy flux q_k is now rewritten as:

$$\begin{aligned} q_k &= (\bar{\rho}e + \bar{\omega}^*) \tilde{u}_k - \overline{(\rho e + p) u_k} = \bar{\rho} c_v (\tilde{\vartheta}^* \tilde{u}_k - \tilde{T} u_k) \\ &\quad + \bar{\omega}^* \tilde{u}_k - \bar{p} u_k \\ &\quad + \frac{1}{2} \bar{\rho} (\tilde{u}_j \tilde{u}_j \tilde{u}_k - \widetilde{u_j u_j u_k}) + \frac{1}{2} \mathcal{L}_{jj} \tilde{u}_k, \end{aligned} \quad (4.114)$$

Using Eqs. (4.110), (2.8) and (4.113), the first two terms on the right-hand side in the above equation may be written as

$$\bar{\rho} c_v (\tilde{\vartheta}^* \tilde{u}_k - \tilde{T} u_k) + \bar{\omega}^* \tilde{u}_k - \bar{p} u_k = \gamma \bar{\rho} (\tilde{e}_I \tilde{u}_k - \widetilde{e_I u_k}), \quad (4.115)$$

whilst the last two terms are rearranged using the definition of SGS turbulent diffusion \mathcal{D}_k (*cf.* Section 4.2.1):

$$\frac{1}{2} \bar{\rho} (\tilde{u}_j \tilde{u}_j \tilde{u}_k - \widetilde{u_j u_j u_k}) + \frac{1}{2} \mathcal{L}_{jj} \tilde{u}_k = \frac{1}{2} (\bar{\rho} \widetilde{u_j u_j} - \overline{\rho u_j u_j} + \mathcal{L}_{jj}) \tilde{u}_k + \bar{\rho} \mathcal{D}_k. \quad (4.116)$$

Under the scale-similarity hypothesis, the term in parentheses in the above equation is equal to the trace of the SGS true Reynolds term, hence the SGS energy flux becomes:

$$q_k = \gamma \bar{\rho} (\tilde{e}_I \tilde{u}_k - \widetilde{e_I u_k}) + \frac{1}{2} R_{jj} \tilde{u}_k + \bar{\rho} \mathcal{D}_k. \quad (4.117)$$

Assuming that $\bar{\rho} \mathcal{D}_k$ and $R_{jj} \tilde{u}_k$ are much smaller than the SGS heat flux and introducing the internal energy decomposition $e_I = \tilde{e}_I + e'_I = c_v (\tilde{\vartheta}^* + T')$ ¹⁷, the SGS energy is written, resorting to the usual triple decompositions, as:

$$-q_k = \underbrace{L_k^{e_I} + C_k^{e_I} + R_k^{e_I}}_{\text{Leonard decomposition}} = \underbrace{\mathcal{L}_k^{e_I} + C_k^{e_I} + \mathcal{R}_k^{e_I}}_{\text{modified Leonard decomposition}}, \quad (4.118)$$

¹⁷It is worthwhile underlining that, since both the temperature and the reduced macrotemperature are present, *i.e.*,

$$\tilde{e}_I \tilde{u}_k - \widetilde{e_I u_k} = c_v (\tilde{\vartheta}^* \tilde{u}_k - \tilde{T} u_k),$$

with

$$L_k^{eI} = \gamma \bar{\rho} (\widetilde{e_I \tilde{u}_k} - \tilde{e}_I \tilde{u}_k), \quad \mathcal{L}_k^{eI} = \gamma \bar{\rho} (\widetilde{\tilde{e}_I \tilde{u}_k} - \tilde{e}_I \tilde{u}_k), \quad (4.119)$$

$$C_k^{eI} = \gamma \bar{\rho} (\widetilde{e_I u'_k} + \widetilde{e'_I \tilde{u}_k}), \quad \mathcal{C}_k^{eI} = \gamma \bar{\rho} (\widetilde{\tilde{e}_I u'_k} + \widetilde{e'_I \tilde{u}_k} - \tilde{e}_I \tilde{u}'_k - \tilde{e}'_I \tilde{u}_k), \quad (4.120)$$

$$R_k^{eI} = \overline{\gamma \rho e'_I u'_k}, \quad \mathcal{R}_k^{eI} = \gamma \bar{\rho} (\widetilde{e'_I u'_k} - \tilde{e}'_I \tilde{u}'_k). \quad (4.121)$$

Assuming the validity of the scale similarity hypothesis, namely neglecting \mathcal{C}_k^{eI} and the second term in \mathcal{R}_k^{eI} , and using the eddy-viscosity hypothesis, Eq. (4.47), to model the SGS true Reynolds term R_k^{eI} , the similarity mixed model for the SGS energy becomes:

$$q_k \simeq \gamma \frac{\bar{\rho} \nu_t}{Pr_t} \frac{\partial \tilde{e}_I}{\partial x_k} - \gamma \bar{\rho} (\widetilde{\tilde{e}_I \tilde{u}_k} - \tilde{e}_I \tilde{u}_k). \quad (4.122)$$

In the perspective of the similarity mixed model, the sub-grid flux for the passive scalar Z may be easily obtained by introducing the decomposition $Z = \tilde{Z} + Z'$ and following a similar reasoning:

$$q_k^Z \simeq \frac{\bar{\rho} \nu_t}{Sc_t} \frac{\partial \tilde{Z}}{\partial x_k} - \bar{\rho} (\widetilde{\tilde{Z} \tilde{u}_k} - \tilde{Z} \tilde{u}_k). \quad (4.123)$$

The WALE Similarity Model (WSM) is finally obtained by computing the eddy-viscosity ν_t in Eqs.(4.107), (4.122) and (4.123) resorting to the WALE closure, Eq(4.56), with fixed model constants $C_w = 0.5$, Pr_t and Sc_t . For the sake of clarity, the filtered flux vectors, namely Eqs. (4.13) and (4.26), are summarized below for the WSM formulation:

$$\mathbf{F}^k = \begin{pmatrix} \overline{\rho u}_k \\ \overline{\rho u}_1 \tilde{u}_k + \delta_{1k} (\overline{\varpi^*} + \frac{1}{3} \mathcal{L}_{jj}) \\ \overline{\rho u}_2 \tilde{u}_k + \delta_{2k} (\overline{\varpi^*} + \frac{1}{3} \mathcal{L}_{jj}) \\ \overline{\rho u}_3 \tilde{u}_k + \delta_{3k} (\overline{\varpi^*} + \frac{1}{3} \mathcal{L}_{jj}) \\ (\overline{\rho e} + \overline{\varpi^*}) \tilde{u}_k \\ \overline{\rho Z} \tilde{u}_k \end{pmatrix}, \quad \mathbf{D}^k = \begin{pmatrix} 0 \\ -2\bar{\mu} \tilde{A}_{1k} - \tau_{1k}^d \\ -2\bar{\mu} \tilde{A}_{2k} - \tau_{2k}^d \\ -2\bar{\mu} \tilde{A}_{3k} - \tau_{3k}^d \\ -2\bar{\mu} \tilde{u}_j \tilde{A}_{kj} - \frac{\bar{\mu} c_p}{Pr} \frac{\partial \tilde{\vartheta}^*}{\partial x_k} - q_k \\ -\frac{\bar{\mu}}{Sc} \frac{\partial \tilde{Z}}{\partial x_k} - q_k^Z \end{pmatrix}, \quad (4.124)$$

the decomposition in terms of resolved and unresolved internal energy may, in principle, pose an issue. In fact, by analogy with the procedure used to obtain the Leonard decomposition for the SGS stress tensor, the temperature and the reduced macrotemperature must be decomposed into their resolved and unresolved parts:

$$T = \tilde{T} + T', \quad \vartheta^* = \tilde{\vartheta}^* + \vartheta'.$$

It should be noted, anyway, that the *fully resolved* reduced macrotemperature ϑ^* is physically meaningless, being the macrotemperature strictly connected with the introduction of sub-grid terms in the filtered set of equations. Nonetheless, we may observe that, if a resolved macrotemperature ϑ^* could be defined, this would be the temperature field obtained from a very well resolved LES, *i.e.*, the Direct Numerical Simulation (DNS) limit of $\tilde{\vartheta}^*$. Observing that, in the DNS limit, the trace of the SGS true Reynolds term R_{kk} vanishes, we conclude, from Eq. (4.109), that $\vartheta^* \equiv T$. It is therefore assumed that, if the temperature is decomposed as $T = \tilde{\vartheta}^* + T'$ (*i.e.*, the unresolved temperature T' is defined as the difference between the temperature T and the reduced macrotemperature $\tilde{\vartheta}^*$), then the same decomposition will hold for the fully resolved macrotemperature, namely $\vartheta^* = \tilde{\vartheta}^* + T'$, and we can write:

$$\tilde{\vartheta}^* = \widetilde{\vartheta^*} + T',$$

with $T' = T - \tilde{\vartheta}^* \equiv \vartheta^* - \widetilde{\vartheta^*}$. The above decomposition allows the definition of a consistent measure of the sub-grid internal energy as $e'_I = c_v T'$

with

$$\overline{\rho e} = \overline{\rho} c_v \tilde{\vartheta}^* + \frac{1}{2} \overline{\rho} \tilde{u}_k \tilde{u}_k + \frac{1}{2} \mathcal{L}_{kk} = \frac{\overline{\omega}^*}{\gamma - 1} + \frac{1}{2} \overline{\rho} \tilde{u}_k \tilde{u}_k + \frac{1}{2} \mathcal{L}_{kk}, \quad (4.125)$$

$$\tilde{e}_I = \tilde{e} - \frac{1}{2} \tilde{u}_k \tilde{u}_k - \frac{1}{2} \frac{\mathcal{L}_{kk}}{\overline{\rho}}. \quad (4.126)$$

With regard to wall-scaling, since the modified Leonard tensor is, by construction, characterized by correct wall scaling on each of its components,

$$\begin{aligned} \langle \mathcal{L}_{11}^d \rangle &\sim x_2^2, & \langle \mathcal{L}_{22}^d \rangle &\sim x_2^2, & \langle \mathcal{L}_{33}^d \rangle &\sim x_2^2, \\ \langle \mathcal{L}_{12}^d \rangle &\sim x_2^3, & \langle \mathcal{L}_{13}^d \rangle &\sim x_2^2, & \langle \mathcal{L}_{23}^d \rangle &\sim x_2^3, \end{aligned}$$

using the WALE closure scaling, Eqs. (4.58)–(4.59), the SGS stress wall-scaling results correctly predicted by the WSM:

$$\langle \tau_{11}^{\text{wsm}} \rangle \sim x_2^2, \quad \langle \tau_{22}^{\text{wsm}} \rangle \sim x_2^2, \quad \langle \tau_{33}^{\text{wsm}} \rangle \sim x_2^2, \quad (4.127)$$

$$\langle \tau_{12}^{\text{wsm}} \rangle \sim x_2^3, \quad \langle \tau_{13}^{\text{wsm}} \rangle \sim x_2^2, \quad \langle \tau_{23}^{\text{wsm}} \rangle \sim x_2^3, \quad (4.128)$$

the above relations referring to the deviator of the modeled sub-grid stress when the wall is orthogonal to x_2 .

4.4.2 The Explicit Filtering Procedure

The SGS contributions are modeled by means of an eddy-viscosity term, which is computed from resolved quantities, and the modified Leonard term, which involves explicit filtering of resolved quantities. Within the framework of mixed similarity modeling [3, 4], scale invariance is assumed to postulate that the structure of the velocity field at scales below a certain length-scale Δ is similar to that at scales above Δ . As already mentioned, this idea was then generalized [42] by subdividing the inertial subrange in a series of contiguous narrow bands of length-scales, thus introducing filtering at two different levels, Δ and $\hat{\Delta} \geq \Delta$. Accordingly, the WSM closures are, more generally, rewritten as:

$$\tau_{ij}^d = 2\overline{\rho} \nu_t \tilde{A}_{ij} - \overline{\rho} (\widehat{\tilde{u}_i \tilde{u}_j} - \widehat{\tilde{u}_i} \widehat{\tilde{u}_j})^d, \quad (4.129)$$

$$q_k = \gamma \frac{\overline{\rho} \nu_t}{Pr_t} \frac{\partial \tilde{e}_I}{\partial x_k} - \gamma \overline{\rho} (\widehat{\tilde{e}_I \tilde{u}_k} - \widehat{\tilde{e}_I} \widehat{\tilde{u}_k}), \quad (4.130)$$

$$q_k^Z = \frac{\overline{\rho} \nu_t}{Sc_t} \frac{\partial \tilde{Z}}{\partial x_k} - \overline{\rho} (\widehat{\tilde{Z} \tilde{u}_k} - \widehat{\tilde{Z}} \widehat{\tilde{u}_k}), \quad (4.131)$$

the *hat* operator now representing filtering at cutoff length $\hat{\Delta} = \alpha \Delta$, with $\alpha \geq 1$. The spherical part of the modified Leonard term in Eqs.(4.124), (4.125) and (4.126) is computed accordingly as

$$\mathcal{L}_{kk} = \overline{\rho} (\widehat{\tilde{u}_k \tilde{u}_k} - \widehat{\tilde{u}_k} \widehat{\tilde{u}_k}). \quad (4.132)$$

It is worthwhile emphasizing that, from *a priori* analysis of filtered experimental data, Liu et al. [42] obtained very low correlation when using a spectral cutoff filter. Hence they concluded that, in order to preserve similarity between scales, the filter used should have

enough localization in physical space. In particular, similar level of correlation at tensor level was achieved with the top-hat or Gaussian filters. Different choices of α have been proposed: filtering at the grid level ($\alpha = 1$) is a possible solution [3, 4, 17, 64, 89], whereas Liu et al. [42] and Akhavan et al. [1] use $\alpha = 2$ and $\alpha = 4/3$ respectively.

Akhavan et al., in particular, in their Dynamic Two-component SGS Model (DTM), distinguish two contributions: (a) the non-local interactions which are responsible for a low-intensity forward energy transfer and (b) the local interactions near the cutoff length scale which are responsible for intense and coherent regions of forward and reverse energy transfer. The former contribution is modeled by the eddy-viscosity assumption, while the latter is represented by an approximation of the modified Leonard term, measuring the interactions between the resolved scales and a narrow band of sub-grid wavenumbers. This idea is then applied using pseudo-spectral methods and results from incompressible LES of turbulent planar jet and turbulent channel flow are validated against DNS data obtaining quite good agreement.

The same assumption, generalized to the compressible case, is adopted in this study, where the Leonard terms are computed filtering the resolved field using a discrete top-hat filter of characteristic width $4/3\Delta$, the details of which are presented in the next section.

The 4/3 Discrete Filter

The filtering operation at length-scale $4/3\Delta$ has been obtained as a generalization of the discrete filter used by Zang et al. [89]. With reference to Figure 4.1, in the case of uniform grid, the filtered quantity $\widehat{\varphi}$ is obtained with the trapezoidal rule as:

$$\begin{aligned} \widehat{\varphi}_{i,j,k} = & \frac{1}{8} \left(\varphi_{i+\frac{1}{3},j+\frac{1}{3},k+\frac{1}{3}} + \varphi_{i-\frac{1}{3},j+\frac{1}{3},k+\frac{1}{3}} \right. \\ & + \varphi_{i+\frac{1}{3},j-\frac{1}{3},k+\frac{1}{3}} + \varphi_{i-\frac{1}{3},j-\frac{1}{3},k+\frac{1}{3}} \\ & + \varphi_{i+\frac{1}{3},j+\frac{1}{3},k-\frac{1}{3}} + \varphi_{i-\frac{1}{3},j+\frac{1}{3},k-\frac{1}{3}} \\ & \left. + \varphi_{i+\frac{1}{3},j-\frac{1}{3},k-\frac{1}{3}} + \varphi_{i-\frac{1}{3},j-\frac{1}{3},k-\frac{1}{3}} \right), \end{aligned} \quad (4.133)$$

where each of the values in parentheses is obtained by multilinear interpolation of the surrounding nodes. The explicit formulation for interpolated quantities—indicated in Figure 4.1 with solid circles—can be expressed as

$$\begin{aligned} \varphi_{i\pm\frac{1}{3},j\pm\frac{1}{3},k\pm\frac{1}{3}} = & \frac{1}{27}\varphi_{i\pm 1,j\pm 1,k\pm 1} + \frac{8}{27}\varphi_{i,j,k} \\ & + \frac{2}{27}(\varphi_{i\pm 1,j\pm 1,k} + \varphi_{i\pm 1,j,k\pm 1} + \varphi_{i,j\pm 1,k\pm 1}) \\ & + \frac{4}{27}(\varphi_{i\pm 1,j,k} + \varphi_{i,j\pm 1,k} + \varphi_{i,j,k\pm 1}), \end{aligned} \quad (4.134)$$

where the signs in the triplets of indices of the terms on the right-hand side must be chosen in accordance with the signs in the triplet of indices of the relevant interpolated quantity on the left-hand side.

The above formulation may be readily generalized to the case of non-uniform grids. An isotropic filter operator can be built, in this particular case, by computing a different set of the interpolation coefficients for each grid point, thus ensuring the correct filtering cutoff length along the three coordinate directions. The local value of the grid length-scale Δ , in particular, may be conveniently computed resorting to the anisotropic grid correction factor proposed by Scotti et al. [69]. It is worth stressing that maintaining moderate grid anisotropy [63]

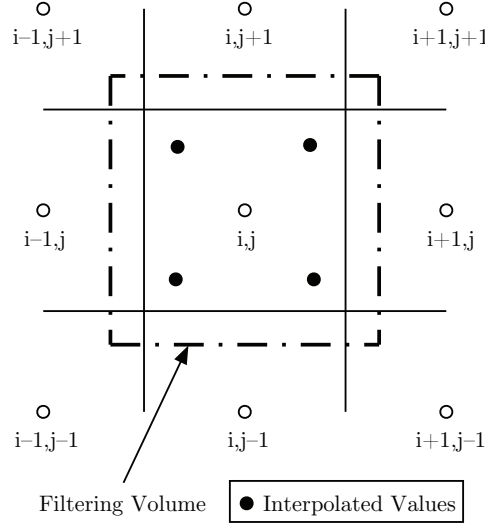


Figure 4.1: Explicit filtering volume in two dimensions.

and paying particular attention to pencil-like computational cells [67, 68] is anyway advisable. If $\widehat{\Delta} = 4/3\Delta$ is the filter cutoff length-scale, the non-uniform grids version of Eqs. (4.133) and (4.134) may be rewritten as

$$\begin{aligned} \widehat{\varphi}_{i,j,k} = \frac{1}{8} & [\varphi(x^+, y^+, z^+) + \varphi(x^-, y^+, z^+) \\ & + \varphi(x^+, y^-, z^+) + \varphi(x^-, y^-, z^+) \\ & + \varphi(x^+, y^+, z^-) + \varphi(x^-, y^+, z^-) \\ & + \varphi(x^+, y^-, z^-) + \varphi(x^-, y^-, z^-)], \end{aligned} \quad (4.135)$$

with

$$\begin{aligned} \varphi(x^\pm, y^\pm, z^\pm) = a_0 \varphi_{i\pm 1, j\pm 1, k\pm 1} + b_0 \varphi_{i,j,k} \\ + c_1 \varphi_{i\pm 1, j\pm 1, k} + c_2 \varphi_{i\pm 1, j, k\pm 1} + c_3 \varphi_{i, j\pm 1, k\pm 1} \\ + d_1 \varphi_{i\pm 1, j, k} + d_2 \varphi_{i, j\pm 1, k} + d_3 \varphi_{i, j, k\pm 1}, \end{aligned} \quad (4.136)$$

and $x^\pm = x_i \pm \widehat{\Delta}/4$, $y^\pm = y_j \pm \widehat{\Delta}/4$ and $z^\pm = z_k \pm \widehat{\Delta}/4$.

Again the signs in the triplets of indices on the right-hand side must be chosen according to the location of the interpolated quantity with respect to the filtering location; the same signs shall be used when computing all the following relevant quantities. The multilinear interpolation coefficients in Eq. (4.136) are defined by the following relations:

$$\begin{aligned} a_0 = \xi^\pm \eta^\pm \zeta^\pm, \quad b_0 = [1 - \xi^\pm][1 - \eta^\pm][1 - \zeta^\pm], \\ c_1 = \xi^\pm \eta^\pm [1 - \zeta^\pm], \quad d_1 = \xi^\pm [1 - \eta^\pm][1 - \zeta^\pm], \\ c_2 = \xi^\pm [1 - \eta^\pm] \zeta^\pm, \quad d_2 = [1 - \xi^\pm] \eta^\pm [1 - \zeta^\pm], \\ c_3 = [1 - \xi^\pm] \eta^\pm \zeta^\pm, \quad d_3 = [1 - \xi^\pm][1 - \eta^\pm] \zeta^\pm. \end{aligned}$$

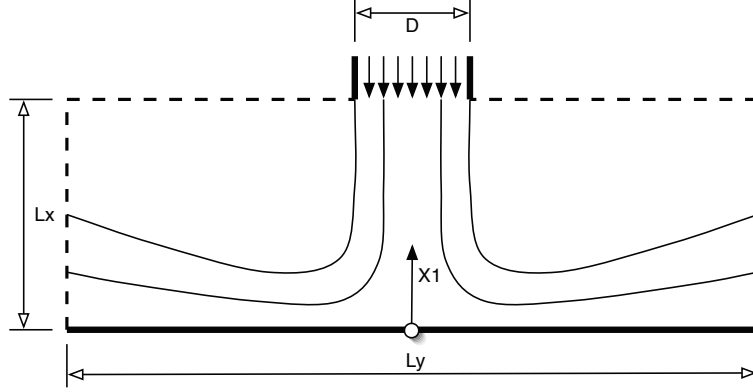


Figure 4.2: Schematic of the flow configuration and position of the coordinate system.

ξ^\pm , η^\pm and ζ^\pm being computed as the ratio between $\hat{\Delta}/4$ and the separation along the three coordinate axes between the filtering location and the neighbor nodes:

$$\xi^\pm = \frac{\hat{\Delta}}{4|x_{i\pm 1} - x_i|}, \quad \eta^\pm = \frac{\hat{\Delta}}{4|y_{j\pm 1} - y_j|}, \quad \zeta^\pm = \frac{\hat{\Delta}}{4|z_{k\pm 1} - z_k|}.$$

As it can be easily verified, Eq. (4.133)—or the analogous non-uniform grid version from Eq. (4.135)—reduces, globally, to a linear combination of the 27 points involved in the multilinear interpolation procedure:

$$\hat{\varphi}_{i,j,k} = \sum_{\varepsilon} \alpha_{i+\varepsilon, j+\varepsilon, k+\varepsilon} \varphi_{i+\varepsilon, j+\varepsilon, k+\varepsilon}, \quad (4.137)$$

the factors α being computed from the multilinear interpolation coefficients and the summation being performed over all the possible combinations of indices obtained for $\varepsilon = -1, 0, 1$.

The presence of wall boundary conditions poses an additional problem within the near-wall region, when the filter size becomes greater than the available distance to the wall. In this case, the filtering volume is cut by the wall and a strictly isotropic filter is difficult to define. In the present implementation, the scheme is switched to bi-dimensional filtering over the plane parallel to the solid boundary whenever the filter cutoff length becomes greater than the distance from the wall.

4.5 Impinging Round-Jet Simulation

The flow configuration under study consists of an unconfined impinging round-jet as schematized in Figure 4.2. The jet axis is aligned along x_1 and the coordinate system origin is located at the impingement wall. The jet-nozzle to wall distance, L_x , is equal to twice the jet diameter D . Two values of jet Reynolds number have been studied on three test-cases: (C1) $Re_D = 23000$ on a 2.9 M nodes coarse grid, (C2) $Re_D = 23000$ on a 5.5 M nodes refined grid and (C3) $Re_D = 70000$ on a 3.5 M nodes coarse grid, Re_D being defined with the bulk velocity U_b ,

$$Re_D = \frac{\rho U_b D}{\mu}. \quad (4.138)$$

This configuration has been chosen in order to directly compare numerical results against the experimental database provided by Cooper et al. [8], for both turbulence regimes, and by Geers [22], Geers et al. [23] for the lower Reynolds number test-case. The computational domain is a cartesian grid of dimensions $2D \times 7D \times 7D$ for test-case C1, $2D \times 6D \times 6D$ for test-case C2 and $2D \times 5D \times 5D$ for test-case C3.

All the simulations which will be presented, have been performed using the parameters summarized in Table 3.1 at page 59. In particular, for the WALE and the WSM models, Pr_t and Sc_t have been set at 0.5 [17, 72].

4.5.1 Boundary Conditions

Details about the numerical solver and the implementation of boundary conditions may be found in Sections 3.1 and 3.2. The bottom boundary is an adiabatic no-slip wall, the lateral sides are subsonic non-reflecting outflows while the top side is a subsonic non-reflecting inflow. The following edge/corner boundary conditions have been used:

- Inflow/Outflow edge conditions on the 4 top edges;
- Wall/Outflow edge conditions on the 4 bottom edges;
- Outflow/Outflow edge conditions on the 4 lateral edges;
- Inflow/Outflow/Outflow corner conditions on the 4 top corners;
- Wall/Outflow/Outflow corner conditions on the 4 bottom corners.

In order to ensure acceptable accuracy within the wall-layer, the computational grid is stretched toward the wall. This stretching is included in the computation of the filter cutoff length Δ , used to obtain the eddy-viscosity for the WALE model (*cf.* Eq. (4.56)) and in the determination of the cutoff length in the explicit filter operator $\hat{\Delta}$ used in the WALE-Similarity Model, by means of a corrective function for non-uniform grids [69] (*cf.* Eq. (4.53)).

The lateral open boundaries, in particular, are characterized by the pressure relaxation coefficient $\sigma = 0.28$ and transverse relaxation coefficient $\beta_t = 0.18$; no target transverse terms have been prescribed, therefore $\mathfrak{T}_k^n = 0$ (*cf.* Eq. (3.87)). On this regard, it should be noted that the three test-cases have been designed in order to have the same Mach number, which is equal to about 0.4 based on the bulk velocity.

In the inflow section, the relaxation coefficient η_5 is set at 3.28. Target velocity components are prescribed using the Power Law profile for turbulent pipe flow, Eq. (3.230), the coefficient n being set at 7.23, 7.42 and 8.3 for the test-cases C1, C2 and C3 respectively. These values have been chosen in order to attain the same ratio of bulk and centerline inlet velocities as in the experiments by Cooper et al. [8]:

$$\frac{U_b}{U_{cl}} = 0.811 + 0.038[\log(Re_D) - 4]. \quad (4.139)$$

To reproduce a turbulent inflow condition, a correlated random noise [35] is superimposed to the average velocity profile with a sampling rate computed from the jet's characteristic time-scale (*cf.* Section 3.3). The amplitude of the injected noise varies along the jet diameter from $0.028U_b$ at the axis, to a peak value of $0.075U_b$ within the jet's shear layer.

Re_D	23000		70000
D	2.6 mm		8 mm
U_b	141 m/s		139.4 m/s
M	0.41		0.40
$30\eta/D$	3.2×10^{-2}		1.4×10^{-2}
$\Delta_{1_{\min}}/D$	3.5×10^{-3}	9.3×10^{-4}	1.7×10^{-3}
$\Delta_{1_{\max}}/D$	4.6×10^{-2}	3.5×10^{-2}	4.3×10^{-2}
$\Delta_{2,3}/D$	4.0×10^{-2}	3.1×10^{-2}	2.8×10^{-2}
$\ell_0/6D$	8.3×10^{-2}		8.3×10^{-2}
Δ_1^+	4.7–6.3	1.2–1.7	5.7–8.4
$\Delta_{r,\phi}^+$	64.2–87.4	49.7–67.7	113.3–165.7
Nodes	90×178^2	146×194^2	110×178^2
CPU time	1360 h	18650 h	2510 h
Processors	32	512	128

Table 4.2: Impinging round-jet simulations: computational grid properties. Subscript 1 indicates wall-normal direction (minimum spacing is attained at the wall, whereas maximum spacing refers to the inlet) and subscript 2 and 3 indicate lateral directions. Subscripts r and ϕ refer to radial and azimuthal directions respectively.

4.5.2 Grid Spacing

The computational grids and the relevant spacing have been chosen fulfilling three main requirements:

1. maintain the low-pass filter cutoff length within the inertial subrange in order to perform correctly resolved LES;
2. ensure proper resolution of the wall-layer while keeping grid stretching to a minimum;
3. retain a reasonable computational cost.

With regards to the first point, the assumption has been made that the inertial subrange includes length-scales from approximately $\ell_0/6$ down to length-scales of the order of 30η [21], $\ell_0 \sim D/2$ being an estimation of the integral length-scale and $\eta \sim \ell_0 Re^{-3/4}$ being the Kolmogorov length-scale, with $Re = u_0 \ell_0 / \nu$ and $u_0^2 \sim 0.1 U_b^2$ (10% turbulence is assumed).

Regarding to the second point, it should be noted that the numerical scheme which has been used, is designed for uniform grids. This choice, motivated by the necessity of conserving stability properties of the scheme, leads to a variable local discretization error [15]. In order to limit accuracy reductions and commutation errors in the refined regions, grid stretching has been done maintaining the maximum stretching ratio between contiguous cells below 1.04.

Indicating, as usual, with the superscript $+$ distances measured in wall units¹⁸, in the wall-jet region, namely for radial distance $r/D \geq 1.0$, wall-normal grid spacing Δ_1^+ ranges from

¹⁸If τ_w is the value of the shear stress measured at the wall and $u_\tau = \sqrt{\tau_w}$ is the relevant friction velocity, wall units are obtained by normalizing with respect to the viscous length $l_\tau = \nu/u_\tau$. In the present case, in particular, τ_w has been approximated from the experimental average velocity profiles [8] by applying the definition:

$$u_\tau = \sqrt{\nu \left. \frac{\partial u_r}{\partial x_1} \right|_w},$$

~ 4.7 to ~ 6.3 for test-case C1, from ~ 1.2 to ~ 1.7 for test-case C2 and from ~ 5.7 to ~ 8.4 for the higher Reynolds number test-case C3, the maximum values being attained near the stagnation region where the average shear stress is higher.

Due to the use of a cartesian grid, both radial and azimuthal spacings vary going around the jet's axis, from a minimum of $\Delta_{2,3}$ to a maximum of $\sqrt{2}\Delta_{2,3}$, where $\Delta_{2,3}$ is the grid resolution measured along the coordinate axes x_2 or x_3 (equal grid spacing is used along the lateral directions). We will refer, for simplicity, to its average value $\sim 1.2\Delta_{2,3}$. Radial and azimuthal spacings Δ_r^+ and Δ_ϕ^+ , for the lower Reynolds number case, are in the range 64.2–87.4 for test-case C1 and 49.7–67.7 for the more resolved test-case C2; for the higher Reynolds number test-case, radial and azimuthal spacings are in the range 113.3–165.7. Again, maximum values are attained close to the stagnation region. A detailed summary of grid dimensions and mesh spacing for the three test-cases is reported in Table 4.2.

Grid resolution for test-cases C1 and C3 is quite low, compared, for instance, to the recommendations given by Zang [87], who suggests that the minimum spacing to capture near-wall dynamics should be $\Delta_{\text{str}}^+ < 80$ and $\Delta_{\text{spn}}^+ < 30$ in the streamwise and spanwise directions respectively, with a minimum of three points for $\Delta_1^+ < 10$ in the wall-normal direction. A very strong influence of grid resolution in LES of detached boundary layers was reported by Temmerman et al. [77], who found high sensitivity of the reattachment position to grid spacing—especially in the streamwise direction—around the mean separation position. They concluded that the use of the no-slip condition at the location where detachment occurs, in conjunction with insufficient grid resolution in the streamwise direction, may lead to substantial errors, even if sufficient wall-normal resolution is used.

Nevertheless, the relevant computational effort when increasing resolution at high Reynolds number may grow significantly (*cf.* Table 4.2), therefore it is of practical interest to assess the model behavior in cases where a significant percentage of the energy is in the sub-grid scales and when the near-wall resolution is marginal. Moreover, the impinging jet features some peculiarities which make it profoundly different from other wall-bounded flows. As opposed to turbulent boundary layers, where length scales are usually determined by the distance from the wall, the impinging jet is characterized by local turbulent length scales in the near-wall region that are strongly affected by the scales of the jet's turbulence. Hence, the criteria on mesh resolution developed for turbulent boundary layers may not be used as guide line for an impinging jet.

It should be mentioned, again, that for LES of channel flow at high Reynolds numbers, Piomelli [55] used grid spacings $\Delta_{\text{str}}^+ = 172$, $\Delta_{\text{spn}}^+ = 26$, $\Delta_1^+ \in [1.25 : 51]$ for $Re = 23700$ (based on the centerline velocity) and $\Delta_{\text{str}}^+ = 244$, $\Delta_{\text{spn}}^+ = 40$, $\Delta_1^+ \in [1.5 : 77]$ for $Re = 47100$. Despite the fairly coarse grids used, first- and second-order statistical moments were predicted accurately. The author conjectured that the explanation for that was to be related to the model ability to reproduce backscatter. Purely dissipative models necessitate the energy production events to be resolved by the grid, hence, under-resolution of near-wall dynamics may lead to underestimation of the related energy production. On the other hand, models which are able to account for reverse energy transfer, like the WALE-Similarity Model presented in this work, may effectively give a correction to the average sub-grid dissipation, which is reduced due to sufficiently frequent local backscatter. This point will be further discussed in Section 4.5.7.

where u_r denotes the velocity component in the radial direction, x_1 is the direction normal to the wall and subscript 'w' indicate that the relevant quantity is evaluated at the wall.

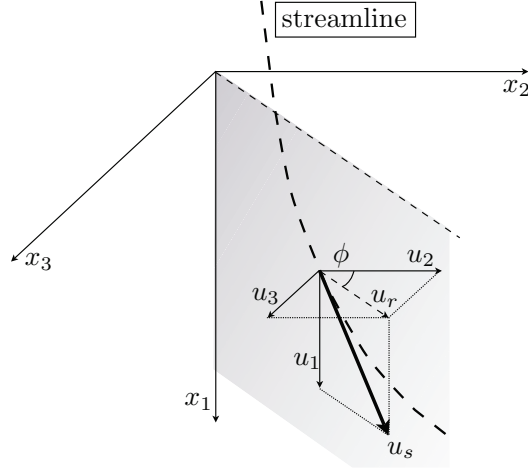


Figure 4.3: Schematic representation of the geometrical relations between the streamwise and radial components of velocity, u_s and u_r and the relevant components along the coordinate axes.

Moreover, for $Re_D = 23000$, the impact of grid resolution in the wall-boundary layer will be assessed comparing the results from the above mentioned two different computational grids C1 and C2.

4.5.3 The Measurement of Statistical Properties

Statistical results have been evaluated by time averaging an ensemble of 600 samples of the resolved quantities for a total period of about $17 D/U_b$ and $13 D/U_b$ for test-cases C1 and C3 respectively. Due to the reduction in time-step of the higher resolved simulation C2 at $Re_D = 23000$ and the relatively high computational cost, an ensemble of 900 samples for a period of just $\sim 8 D/U_b$ was collected. Global statistical convergence for the three test-cases has been checked continuously calculating the $L2$ -norm of the change in the statistical quantity $\langle \phi \rangle$ of interest between two successive samplings, indicated with superscripts n and $n - 1$:

$$\langle \phi \rangle_{L2}^{\{n\}} = \sqrt{\sum_{i,j,k} \left(\langle \phi \rangle_{i,j,k}^{\{n\}} - \langle \phi \rangle_{i,j,k}^{\{n-1\}} \right)^2}, \quad (4.140)$$

where the summation is extended to the whole computational domain. In particular, statistical sampling was stopped for $L2$ -norm of first-order moments below 10^{-1} and $L2$ -norm of second-order moments below 10^{-2} . Assuming the validity of the Taylor hypothesis, statistical convergence has been further improved by averaging around the jet's axis, for a total statistical ensemble spanning from 50400 to 637200 depending on the radial location and the computational grid used. Time/space averaging will be denoted by angled brackets hereafter.

According to the experimental setup used by Cooper et al. [8], velocity components and relevant second-order moments are measured along the streamwise and wall-normal directions with Hot-Wire Anemometry (indicated as HWA hereafter), whereas Geers [22], Geers et al.

[23] measure radial and wall-normal components using Laser-Doppler Anemometry (LDA) and Particle Image Velocimetry (PIV). Subscripts s , r and n will be used to indicate “streamwise”, “radial” and “wall-normal” directions respectively. In order to avoid confusion with sub-grid scale quantities, which have been indicated with the prime mark so far, the “” accent will be used to refer to statistically fluctuating quantities¹⁹. If, on one hand, wall-normal statistics are directly obtained from the u_1 component of velocity, radial and streamwise velocities have been computed as (*cf.* Figure 4.3):

$$\tilde{u}_r = \tilde{u}_2 \cos(\phi) + \tilde{u}_3 \sin(\phi), \quad (4.141)$$

$$\tilde{u}_s = \sqrt{\tilde{u}_1^2 + [\tilde{u}_2 \cos(\phi) + \tilde{u}_3 \sin(\phi)]^2}, \quad (4.142)$$

where ϕ is the azimuthal angle relevant to the plane where the projection take place. The relevant second order moments are then obtained from the relations

$$\langle u_r'' u_r'' \rangle = \langle \tilde{u}_r \tilde{u}_r \rangle - \langle \tilde{u}_r \rangle \langle \tilde{u}_r \rangle, \quad (4.143)$$

$$\langle u_s'' u_s'' \rangle = \langle \tilde{u}_s \tilde{u}_s \rangle - \langle \tilde{u}_s \rangle \langle \tilde{u}_s \rangle, \quad (4.144)$$

$$\langle u_s'' u_n'' \rangle = \langle \tilde{u}_s \tilde{u}_1 \rangle - \langle \tilde{u}_s \rangle \langle \tilde{u}_1 \rangle. \quad (4.145)$$

When needed (*cf.* Section 4.5.6), the projected average sub-grid stress tensor in cylindrical coordinates, $\langle \boldsymbol{\tau}^c \rangle$, is obtained by means of the following transformation:

$$\langle \boldsymbol{\tau}^c \rangle = \boldsymbol{\Phi} \langle \boldsymbol{\tau} \rangle \boldsymbol{\Phi}^{-1}, \quad (4.146)$$

where $\boldsymbol{\Phi}$ is the matrix of rotation around the jet’s axis,

$$\boldsymbol{\Phi} = \begin{pmatrix} 1 & 0 & 0 \\ 0 & \cos(\phi) & \sin(\phi) \\ 0 & -\sin(\phi) & \cos(\phi) \end{pmatrix}; \quad (4.147)$$

the stress tensor components in the axial plane are then computed as

$$\langle \tau_{nn}^c \rangle = \langle \tau_{11} \rangle, \quad (4.148)$$

$$\langle \tau_{rr}^c \rangle = \langle \tau_{22} \rangle \cos^2(\phi) + \langle \tau_{33} \rangle \sin^2(\phi) + 2 \langle \tau_{23} \rangle \sin(\phi) \cos(\phi), \quad (4.149)$$

$$\langle \tau_{rn}^c \rangle = \langle \tau_{12} \rangle \cos(\phi) + \langle \tau_{13} \rangle \sin(\phi). \quad (4.150)$$

4.5.4 $Re_D = 23000$ Test-Case (C1)

Results for the $Re_D = 23000$ test-case are shown in Figures 4.4–4.6, error-bars relevant to HWA measurement uncertainties [8] are displayed for experimental second order moments. In order to better show the results in the near-wall region, streamwise average velocity and streamwise velocity variance are also represented in Figure 4.5, on logarithmic scale, with respect to the wall distance normalized with the viscous length (see note 18 at page 111). For the same configuration, Figure 4.7 shows the comparison between the results obtained using the WSM and the LDSM and the experimental measurements obtained by Geers [22], Geers

¹⁹Note that, right after the stagnation point, the average field becomes almost completely aligned parallel to the wall, hence $\langle u_s \rangle \simeq \langle u_r \rangle$ and $\langle u_s'' u_s'' \rangle \simeq \langle u_r'' u_r'' \rangle$. This is readily verified comparing the experimental data from Cooper et al. and Geers et al..

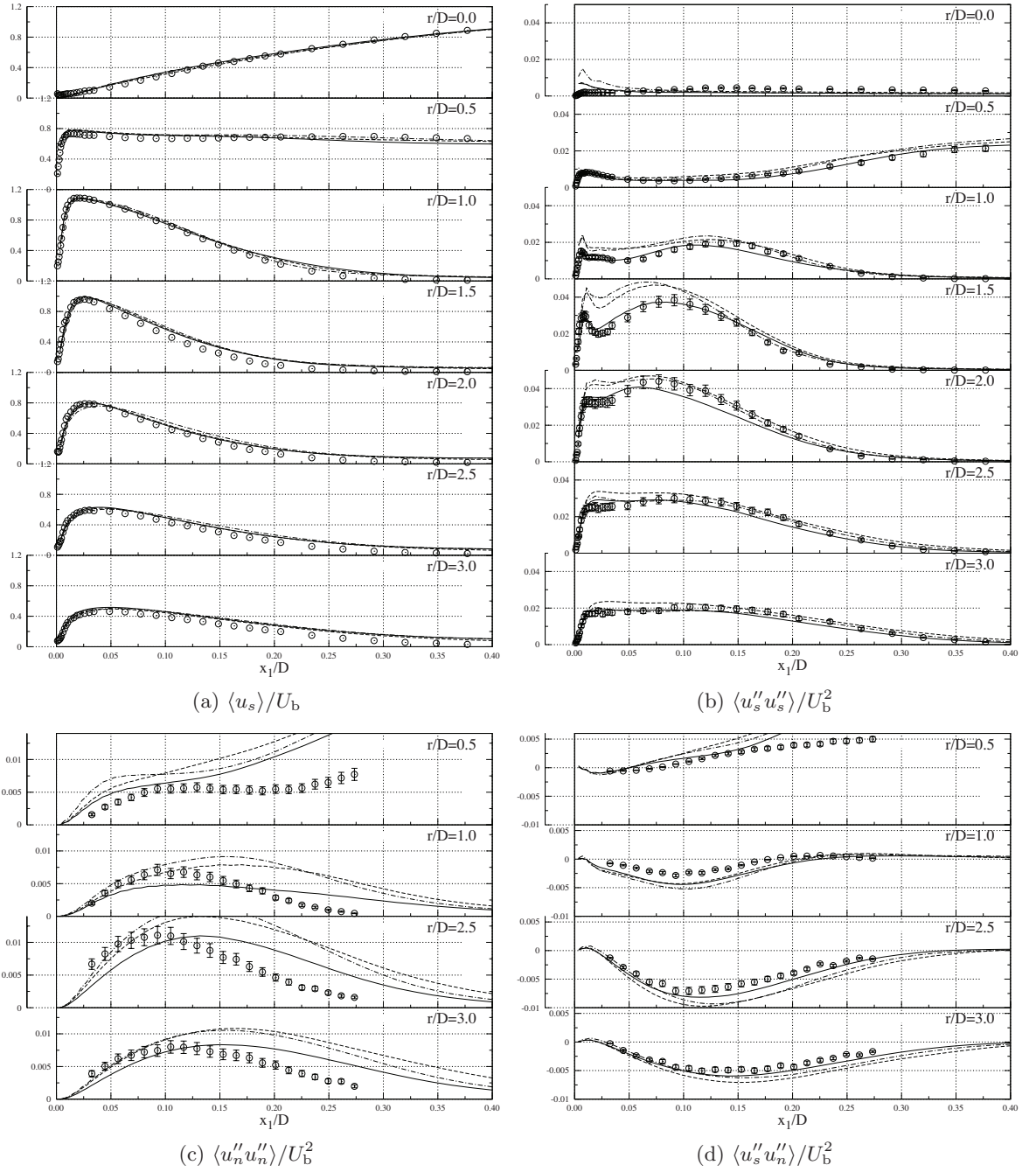


Figure 4.4: $Re_D = 23000$ test-case C1. Streamwise average velocity (a), streamwise fluctuating velocity (b), wall-normal fluctuating velocity (c) and turbulent shear stress (d): — , WSM; ---- , WALE; -.- , LDSM; \circ , HWA measurements [8].

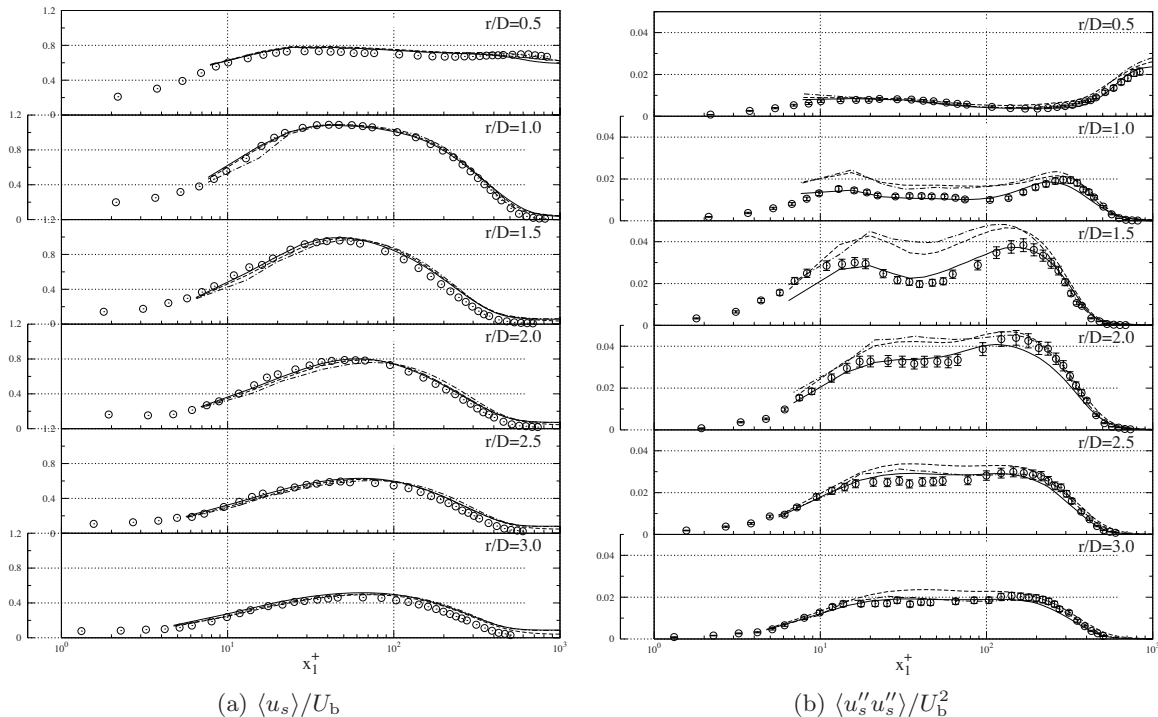


Figure 4.5: $Re_D = 23000$ test-case C1. Streamwise average velocity (a) and streamwise fluctuating velocity (b), represented with logarithmic scale in wall units: —, WSM; ----, WALE; - · -, LDSM; \circ , HWA measurements [8].

et al. [23] using LDA technique. The WSM is compared to the standard WALE model and the Lagrangian Dynamic Smagorinsky model. Test filtering for the latter model has been performed using the same isotropic filter implementation described in Section 4.4.2, but with cutoff length equal to 2Δ .

With regards to the average velocity profiles (*cf.* Figures 4.4a and 4.5), all three models perform well and no appreciable difference between them is visible. In any case, the correct slope down to the viscous sub-layer indicates clearly that correct scaling of SGS stresses is achieved as expected by the three models and no additional sub-grid viscosity is produced in regions where this is not expected to be present.

On the other hand, the three models perform quite differently in terms of resolved second order moments. With regards to the streamwise fluctuations, both the WALE and the LDSM models predict fairly well measurements far from the wall, for $x_1/D \geq 0.1$, but produces a significant overestimation in the near-wall region, especially between the buffer layer and the logarithmic layer, for $x_1^+ \in (20 : 200)$, where the flow undergoes strong curvature (*cf.* Figures 4.4b–4.5b). It seems reasonable to affirm that the dynamic computation of the model constant in the LDSM and the relatively moderate SGS dissipation of the WALE model allow for a correct reproduction of sub-grid interactions far from the wall. Nonetheless, close to the wall, even the dynamic procedure is not able to adjust properly the sub-grid model viscosity. These shortcomings are probably due to the fact the both the WALE and the LDSM do not allow backscatter and require alignment of the SGS stress and the resolved deformation tensors,

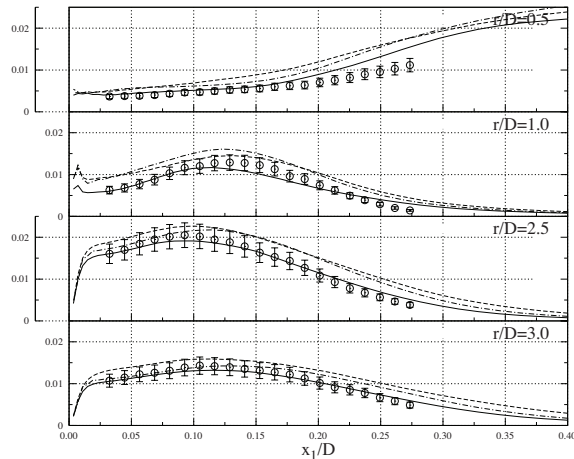


Figure 4.6: $Re_D = 23000$ test-case C1. Turbulent kinetic energy $\frac{1}{2}(\langle u_s''u_s'' \rangle + \langle u_n''u_n'' \rangle)/U_b^2$: — , WSM; ···· , WALE; --- , LDSM; ○ , HWA measurements [8].

the former mechanism being anyway the main responsible, as it will be shown in Section 4.5.7.

The introduction of the modified Leonard term in the WSM has a strong impact on the resolved streamwise velocity fluctuations, these last being just slightly underestimated far from the wall in the wall-jet region. It is reasonable to expect, on this regard, a certain improvement in the results if the isotropic SGS contribution is included before comparing with the measurements, as it will be shown for the $Re_D = 70000$ test-case.

With regards to wall-normal fluctuations, different behaviors are observed when comparing with HWA (Figure 4.4c) and LDA (Figure 4.7c) measurements. The WALE and the LDSM models predict significant overestimation of vertical fluctuations in the wall-jet region ($r/D \geq 2.5$). This fact, combined with the observed tendency to overestimate streamwise fluctuations in the near-wall region, leads to the prediction of an excess of resolved turbulent kinetic energy (Figure 4.6). Since significant backward energy cascade may be generally observed within the buffer layer [28, 29], purely dissipative models are then expected to give poor results, such as the WALE and the LDSM²⁰. On the other hand, as already mentioned, the WSM intrinsically allows backscatter and this could be one of the leading mechanism involved in the significant reduction in vertical fluctuations compared to the other two models. The mentioned reduction allows for a significant improvement of the results in terms of turbulent kinetic energy.

Moreover, it is interesting to note that the WALE model is able to give results analogous to the more expensive LDSM. This fact is not surprising considering that both formulations are eddy-viscosity models with relatively low SGS dissipation and correct wall-scaling.

If a particularly bad agreement in vertical fluctuations is observed when comparing with HWA measures, results from the WSM are in fairly good agreement with the experimental data extracted from LDA measurements (*cf.* Figure 4.7c). Good agreement is also observed on average profiles (Figure 4.7a,b) and radial fluctuations (Figure 4.7d). The discrepancies observed between the experimental results by Cooper et al. and by Geers et al. in the measurements of the vertical fluctuations, makes it difficult to draw conclusions on this regard.

²⁰As in the original formulation by Meneveau et al., the dynamically computed model constant is clipped to prevent it from assuming complex values, thus not allowing backscatter.

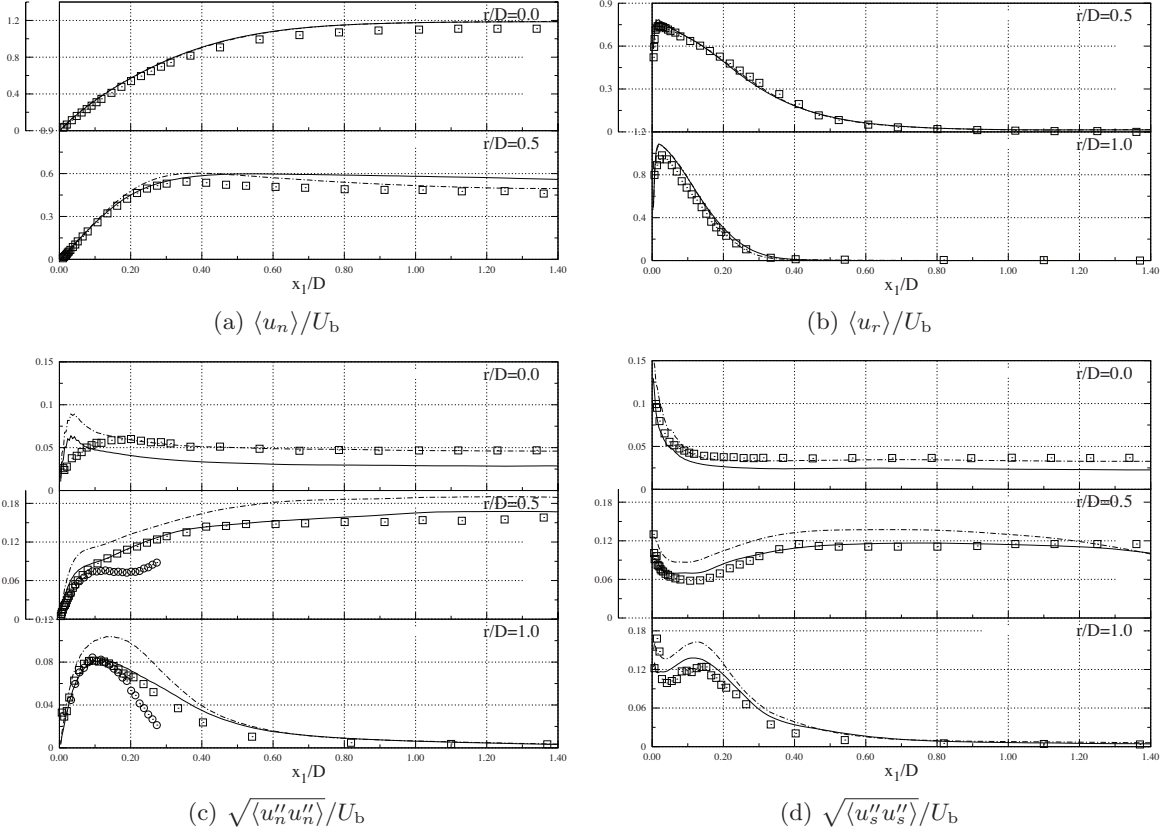


Figure 4.7: $Re_D = 23000$ test-case C1. Average wall-normal velocity (a), average radial velocity (b), r.m.s. wall-normal velocity (c) and r.m.s. radial velocity (d): —, WSM; ---, LDSM; \square , LDA measurements [22, 23]; \circ , HWA measurements [8].

Turbulent shear stress (Figure 4.4d) results are quite satisfactory, the proposed WSM giving the best agreement. The observed disagreement in statistical quantities relevant the vertical component of velocity does not allow an unbiased assessment of the curves, especially at $r/D \leq 1.0$. Alternative measurements of the shear stress are not available anyway.

4.5.5 $Re_D = 23000$ Test-Case (C2)

In order to better quantify LES resolution, a normalized SGS energy transfer coefficient is computed as:

$$\nu_{\text{ratio}} = \frac{\tau_{ij}^d \tilde{A}_{ij}}{2\tilde{\mu} \tilde{A}_{ij} \tilde{A}_{ij}}, \quad (4.151)$$

which measures the relative intensity between sub-grid and viscous energy transfers; note that ν_{ratio} reduces to the ratio ν_t/ν for an eddy-viscosity model and becomes negative in regions characterized by backward SGS energy transfer. The average value of ν_{ratio} has to be positive anyway, *i.e.*, even if, locally, reverse energy transfer may happen, globally, turbulence is a

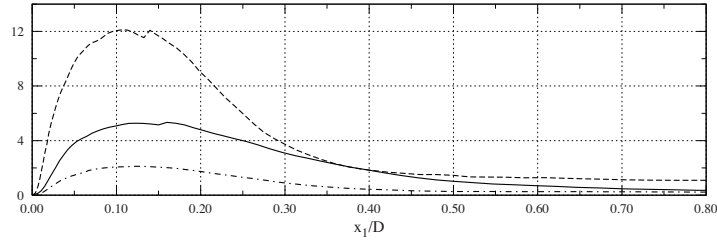


Figure 4.8: Average value of ν_{ratio} over horizontal planes: — , $Re_D = 23000$ test-case (coarse grid); -- , $Re_D = 23000$ test-case (refined grid); -.- , $Re_D = 70000$ test-case.

dissipative phenomenon and the relevant kinetic energy is expected to flow down the energy cascade.

Experience shows that a typical threshold for a well resolved LES is ν_{ratio} , in average, less than about 10. Figure 4.8 shows the average value of ν_{ratio} produced by the WSM over horizontal planes. With regards to the $Re_D = 23000$ test-case, the computation performed on the coarse mesh is well resolved, the average ν_{ratio} being always below 6, whereas the computation carried out on the more refined grid has even less energy within the sub-grid scales and $\nu_{\text{ratio}} < 2$ everywhere in the wall-jet region. The higher Reynolds number test-case, on the other hand, appears slightly under-resolved, with ν_{ratio} taking values up to ~ 12 . This is consistent with the results which will be presented in the next section, where the resolved turbulent kinetic energy results slightly under predicted for the $Re_D = 70000$ test-case.

With regard to the 23000 Reynolds number jet simulations, the statistical moments computed using the proposed WSM, extracted from the coarse 2.8 M nodes mesh and the highly refined 5.5 M nodes mesh, are compared in Figures 4.9; again, wall units logarithmic representations are depicted in Figure 4.10 for streamwise average velocity and relevant fluctuations. First order moments match almost perfectly, while some slight difference is visible on second order moments. The only curve which shows significant improvement is the one related to wall-normal fluctuations at $r/D = 1.0$ (*cf.* Figure 4.9c). Clearly the more resolved simulation has less energy in the sub-grid scales and statistical fluctuations extracted from the resolved flow field give a more accurate representation of the data obtained from the experiments.

No significant improvement of results is observed in the near-wall region where the better resolution of the viscous sub-layer in the more refined grid would have suggested a more marked improvement. Model behavior in the coarser grid simulation, for $x_1^+ \leq 20$, appears quite remarkable (*cf.* Figure 4.10). This result confirm what has been previously said about the positive impact that a model allowing correct energy backscatter may produce when dealing with not well resolved wall-bounded flows like those presented in this work.

It is worthwhile mentioning that, in order to obtain equivalent results, the more refined computational grid required about 14 times more CPU time than that required by the coarse grid simulation (*cf.* Table 4.2); the increase in computational time was marginally due to the increased number of grid points and mostly related to the reduction of the allowed time-step, due to the use of explicit time integration and the application of the relevant CFL limitation within the viscous sub-layer. Moreover, the reduced time-step resulted also in a significant reduction of statistical convergence rate; sufficiently converged statistical data required about 56% of the total computational resources.

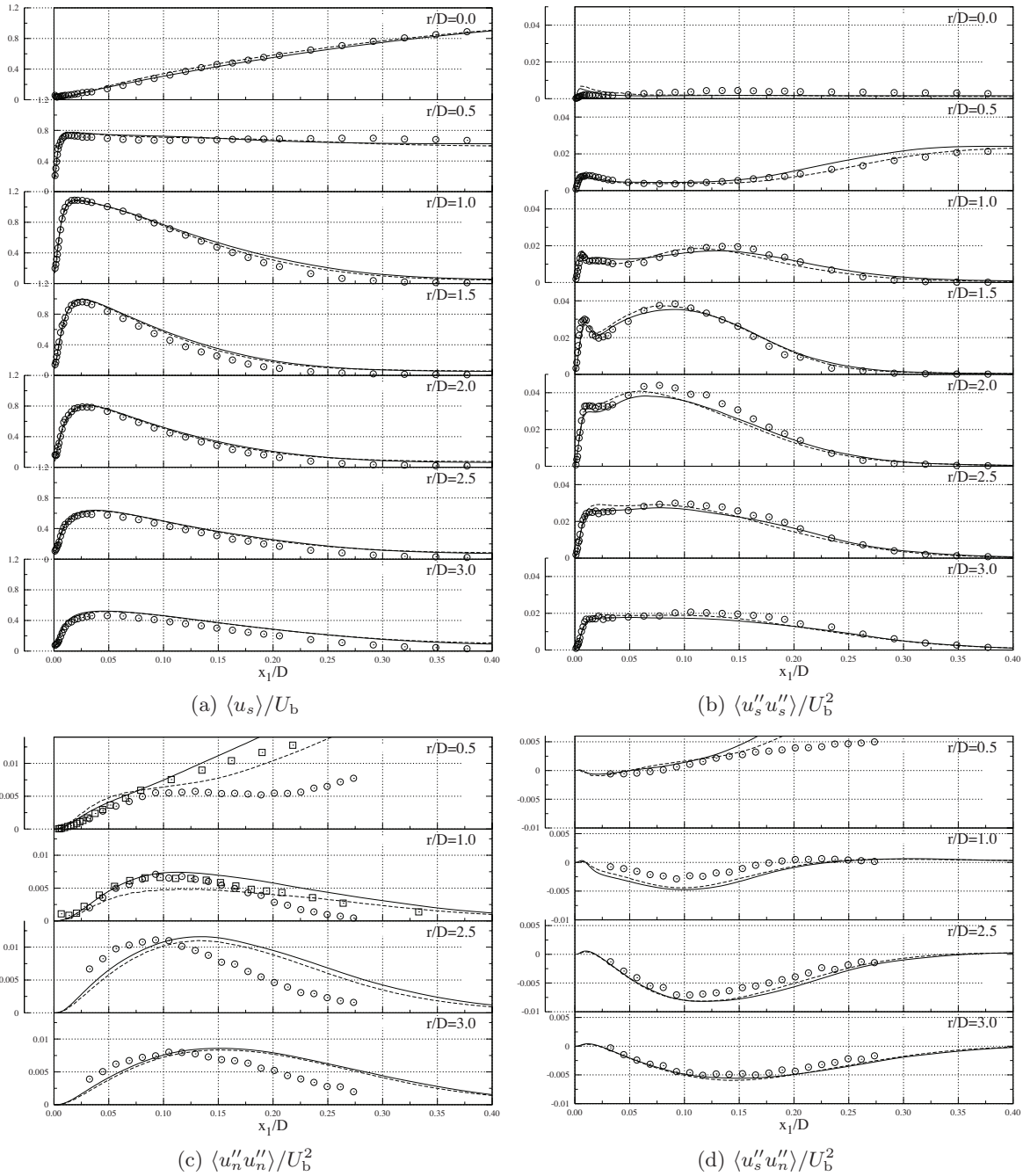


Figure 4.9: $Re_D = 23000$ test-case. Streamwise average velocity (a), streamwise fluctuating velocity (b), wall-normal fluctuating velocity (c) and turbulent shear stress (d): —, WSM on refined grid (C2); ----, WSM on coarse grid (C1); \circ , HWA measures [8]; \square , LDA measures [22, 23].

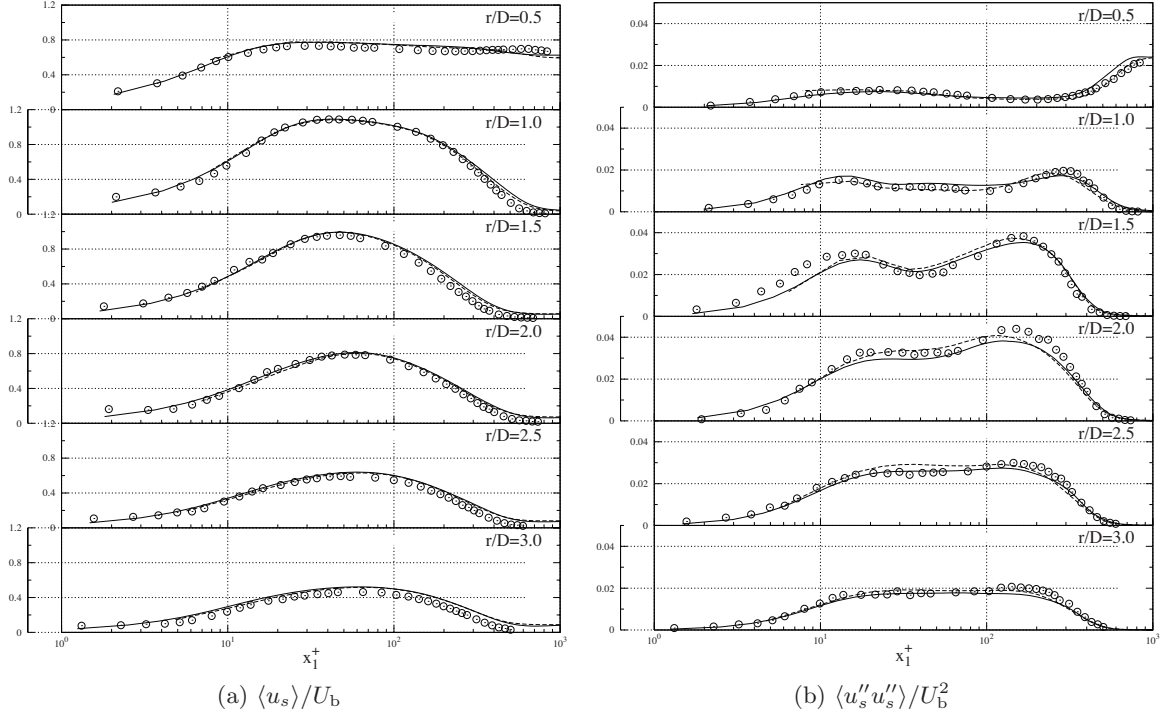


Figure 4.10: $Re_D = 23000$ test-case. Streamwise average velocity (a) and streamwise fluctuating velocity (b), represented with logarithmic scale in wall units: —, WSM on refined grid (C2); ----, WSM on coarse grid (C1); \circ , HWA measures [8]; \square , LDA measures [22, 23].

In view of these results and the significant extra-cost that follows from increasing resolution, especially for relatively high Reynolds numbers as in the present study, and considering the small improvements in the results which may be expected, the suitability of such a computational effort is questionable. We would rather envisage the possibility of developing improved modeling for the spherical part of the SGS stress tensor, in order to better reproduce streamwise and normal fluctuations for slightly under-resolved LES.

4.5.6 $Re_D = 70000$ Test-Case (C3)

The results obtained with the WSM on the $Re_D = 70000$ test-case are shown in Figures 4.11–4.13. Also in this case, error-bars are shown to indicate measurement errors on second order moments. Solid curves refer to statistical quantities extracted directly from the resolved flow field (as in the previous test-case), while dashed lines have been obtained including the SGS contribution. If the statistical fluctuation of the resolved velocity is expressed as \tilde{u}_i'' and $u_i^{e''}$ is the exact fluctuation (measured from experiments or obtained from DNS), we may write [63]:

$$\langle u_i^{e''} u_j^{e''} \rangle \simeq \langle \tilde{u}_i'' \tilde{u}_j'' \rangle + \langle \tau_{ij} \rangle, \quad (4.152)$$

where τ_{ij} is the SGS stress tensor used within the simulation or computed from the resolved field with another SGS model. In the present case, we adopt the former choice and compute the SGS contribution by time/space averaging the WALE-Similarity SGS stress tensor used to

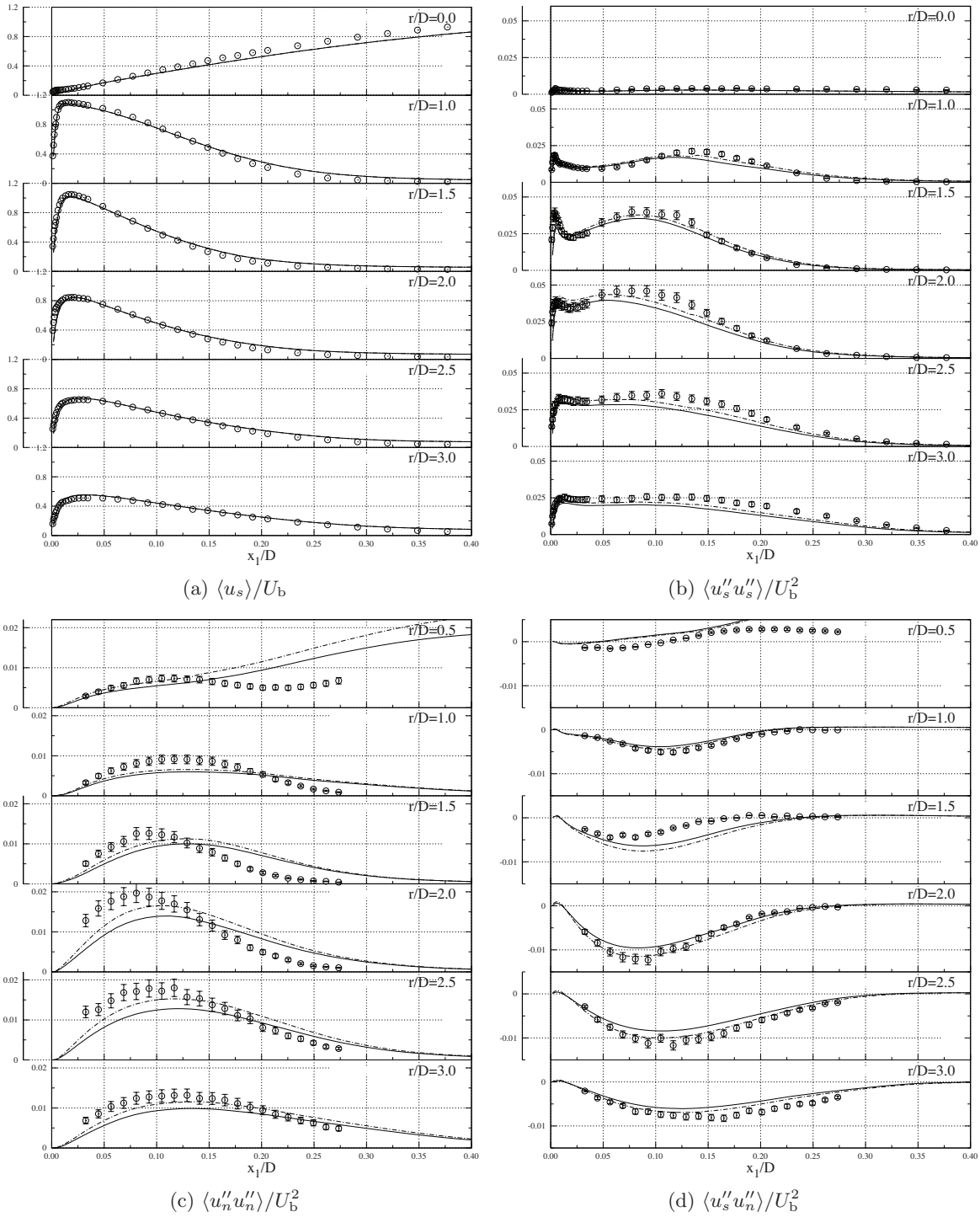


Figure 4.11: $Re_D = 70000$ test-case C3. Streamwise average velocity (a), streamwise fluctuating velocity (b), wall-normal fluctuating velocity (c) and turbulent shear stress (d): — , resolved fluctuations; - - , resolved fluctuations plus SGS contributions; \circ , HWA measurements [8].

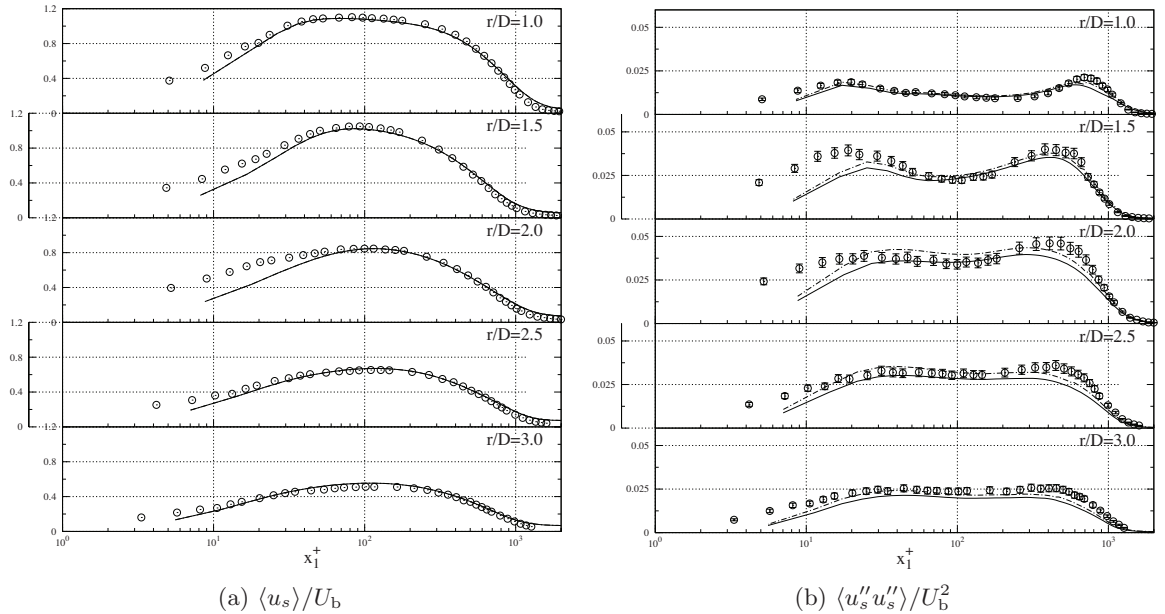


Figure 4.12: $Re_D = 70000$ test-case C3. Streamwise average velocity (a) and streamwise fluctuating velocity (b), represented with logarithmic scale in wall units: —, resolved fluctuations; ---, resolved fluctuations plus SGS contributions; \circ , HWA measurements [8].

perform the simulations (*cf.* Eq. (4.102)),

$$\langle \tau_{ij} \rangle = \langle 2\bar{\rho}\nu_t \tilde{A}_{ij} - \mathcal{L}_{ij} \rangle, \quad (4.153)$$

and extracting the relevant components in the axial plane from Eqs. (4.148)–(4.150). Note that \mathcal{L}_{ij} accounts for both the deviatoric and spherical parts, whereas the spherical part of the SGS true Reynolds term, *i.e.* $\overline{\rho u'_k u'_k}$, which is included into the reduced macropressure (*cf.* Eq. (4.106)), is still not included.

For the average velocity profiles, depicted in Figures 4.11a and 4.12a, the matching between experimental data and computed solution is satisfactory but not perfect, as it can be seen from the logarithmic plots. Close to the wall, for $x_1^+ \leq 40$, profiles tend to become underestimated.

Similar trend is observed with streamwise fluctuations in the near-wall region (*cf.* Figure 4.12b). As for the lower Reynolds number test-case, streamwise fluctuations at the far end of the buffer layer and in the following regions departing from the wall are well predicted and the “saddle” shaped behavior observed where the flow undergoes strong curvature is well captured. The second peak around $x_1/D \simeq 0.1$ is slightly underestimated. The inclusion of the SGS part produces better agreement but, still, results remain below the measurement errors, especially far from the jet’s axis. No significant improvement is obtained close to the wall. Since it is the spherical part of the SGS stress tensor which plays the key role in this context, it is reasonable to expect that the inclusion of the modeled trace of the SGS true Reynolds term, would further improve the results (as it has been pointed out, this is the only missing contribution in the presented results). In the near-wall region, anyway, it seems more reasonable to connect the observed error to insufficient grid resolution or excess of dissipation.

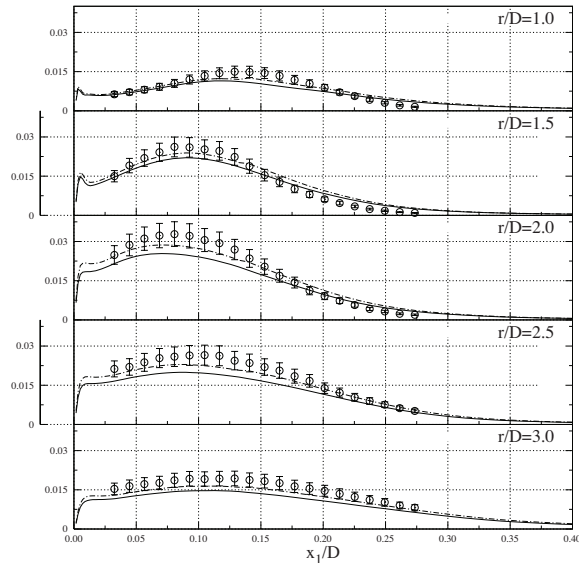


Figure 4.13: $Re_D = 70000$ test-case C3. Turbulent kinetic energy $\frac{1}{2}(\langle u_s'' u_s'' \rangle + \langle u_n'' u_n'' \rangle)/U_b^2$: — , resolved fluctuations; - - , resolved fluctuations plus SGS contributions; \circ , HWA measurements [8].

Results for wall-normal fluctuations (Figure 4.11c), again, shows the most marked deviation from the experimental measurements. In sight of the discrepancy observed between HWA and LDA measurements for the lower Reynolds number test-case, it would have been interesting to compare computed vertical fluctuations against alternative measurements; unfortunately such a database is not available for this Reynolds number. The only reasonable conclusion which may be drawn is that vertical fluctuations profiles display similar trends as those observed at $Re_D = 23000$.

Turbulent shear stresses (*cf.* Figure 4.11d) are well predicted everywhere, except at $r/D = 0.5$ and 1.5 . Results are globally consistent with those obtained for the previous test-cases; the bad agreement on the $r/D = 1.5$ profile is quite strange though, considering that the two profiles right ahead and behind it show results in much better agreement with experimentally measured shear stresses. The inclusion of the SGS part, which in this case accounts for all the modified Leonard decomposition's terms, produces a relatively significant improvement in results representing about 10% of the expected turbulent shear stress (note that error-bars in the relevant plot represent 9% error [8]).

Despite the problems observed in streamwise fluctuations in the near-wall region, the overall behavior of the WSM, as it may be inferred from the computed turbulent kinetic energy, represented in Figure 4.13, is satisfactory. Although a certain tendency to “align” to the bottom limit of the error range is observed, all the curves fall within the measurement uncertainties. This behavior clearly reflects similar tendencies observed in the streamwise and wall-normal directions and could, in principle, be improved by accounting for the full trace of the SGS stress tensor.

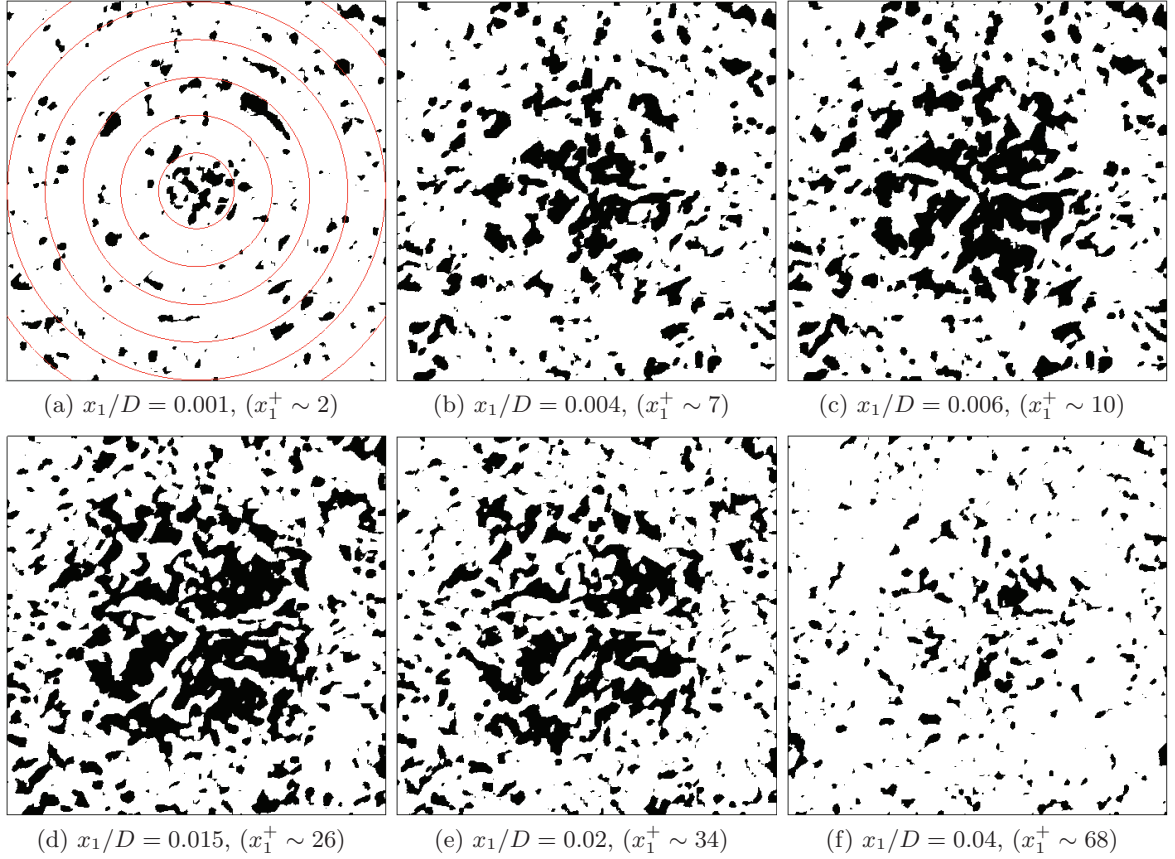


Figure 4.14: $Re_D = 23000$ test-case C1. Localization of regions of negative ν_{ratio} (Eq. (4.151)) over horizontal planes at different heights. Red circle in (a) indicate radial distances in steps of $0.5D$.

4.5.7 Energy Backscatter

Even though kinetic energy, in average, is always transferred from the mean motion to the fluctuating one through the well known energy cascade process, the possibility of the existence of isolated events of reverse energy transfer, or backscatter, from the turbulent motion to the mean flow was already envisaged by Monin and Yaglom [50] and extensively demonstrated using results from DNS, for turbulent boundary layer in particular, by many authors [27–29, 32, 55–57]. In all these studies, strong anisotropy in *a priori* evaluated sub-grid stresses was observed, the mean responsible for energy backscatter being identified in the wall SGS shear stress. Therefore, structural SGS models capable of capturing energy backscatter, as it is the case for similarity mixed models, appear to be particularly suited for wall bounded turbulent flows.

In certain regions of the turbulent boundary layer, in fact, typically within the buffer layer [27–29], the backward energy cascade can become largely dominant over the forward energy cascade. As it has been already observed in Section 4.5.4, both the standard WALE model and the LDSM show a marked tendency to overestimate velocity fluctuations in the

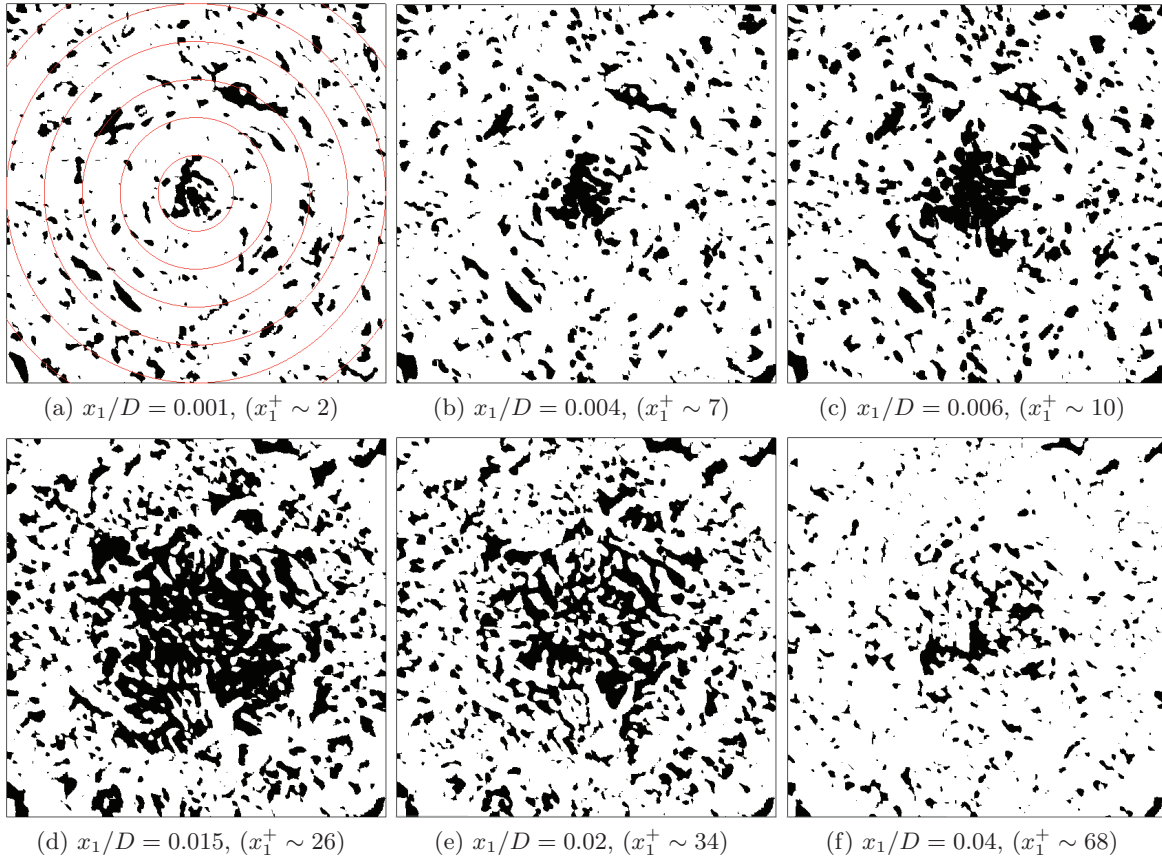


Figure 4.15: $Re_D = 23000$ test-case C2. Localization of regions of negative ν_{ratio} (Eq. (4.151)) over horizontal planes at different heights. Red circle in (a) indicate radial distances in steps of $0.5D$.

near-wall region, whereas the WSM gives much better results. It is then natural to expect that this behavior may be connected with intrinsic differences between these SGS closures, *e.g.*, the ability of reproducing backscatter, and that computations performed using the WSM should feature some backward energy transfer close to the wall. It is worthwhile mentioning that the similarity closure for the cross and Reynolds terms (*cf.* Eqs. (4.90) and (4.91)) play a crucial role for backscattering within the buffer layer [32]. This fact was confirmed by Härtel and Kleiser [27], who also emphasize the importance of maintaining Galilean invariance of the model in order to prevent it from reproducing reverse energy transfer in regions where there should not be any.

Energy backscatter is quantified resorting to the normalized SGS energy transfer coefficient from Eq. (4.151). For the $Re_D = 23000$ test-case on the coarse grid (C1), in Figure 4.14, black regions indicate the occurrence of backscatter over horizontal planes, of dimension $5D \times 5D$, located at different distances from the impingement wall. Approaching the wall, reverse energy transfer regions become more and more numerous, the maximum backscatter activity being observed at a distance $x_1/D \simeq 0.015$ ($x_1^+ \simeq 26$), and then tend to disappear closer to the viscous sub-layer (note that data on the plane at $x_1/D = 0.001$ were extracted from the first

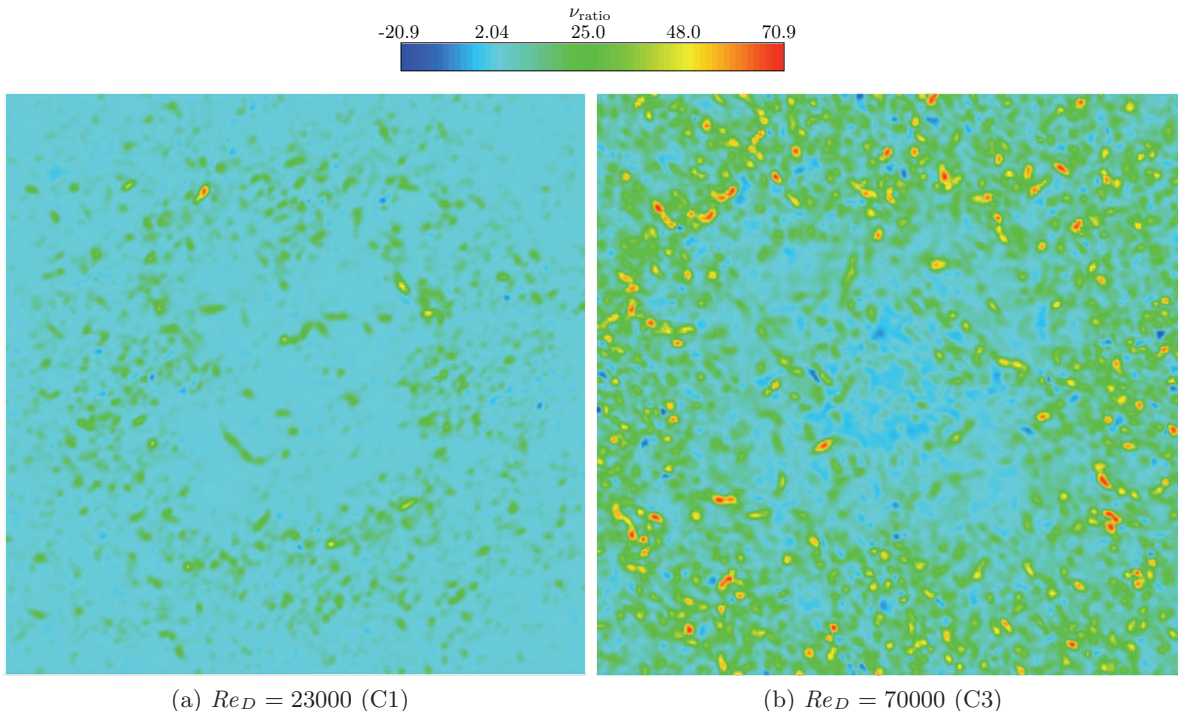


Figure 4.16: Maps of normalized SGS energy transfer coefficient ν_{ratio} Eq. (4.151) over an horizontal plane located at $x_1/D = 0.1$.

computational cell at the wall). Intense backscatter appears for x_1/D in the range 0.006–0.02 ($x_1^+ \sim 10$ –34), which corresponds pretty well with the region where the WALE and the LDSM produce excessive streamwise fluctuations (*cf.* Figure 4.4b). The most intense activity is visible in the stagnation region, approximately for $r < 1.5$, which is also in agreement with the observed behavior of the three models. For the $Re_D = 70000$ test-case (not shown), maximum backscatter activity was registered slightly closer to the wall, at $x_1/D \simeq 0.01$ ($x_1^+ \simeq 40$), which is consistent with the thinning of the boundary layer at higher Reynolds number.²¹

The same plots for the more resolved grid (C2) are depicted in Figure 4.15. The overall behavior is similar to that observed with the less refined mesh. The less frequent events of energy backscatter, registered in the refined grid at x_1/D equal to 0.004 and 0.006, confirm that reverse energy transfer plays a key role in under-resolved turbulent boundary layers, giving a sort of automatic compensation mechanism that results anyway in the correct amount of average sub-grid dissipation being produced [55].

The visual examination of Figure 4.14 also agrees with the observations of Piomelli et al. [56], who found the fraction of points, in planes parallel to the wall, experiencing backscatter to be between 30% to 50%, when a box filter in physical space was applied to DNS data from channel simulations at different Reynolds numbers, including transitional turbulence and compressible isotropic decay. No dependence on Mach number was observed, on this regard, in the case of compressible turbulence.

²¹Due to the boundary layer evolution going radially outwards, sub-layer scaled heights of the planes depicted in Figures 4.14 and 4.15 are estimated from the average value of the viscous length ℓ_τ within the region of interest.

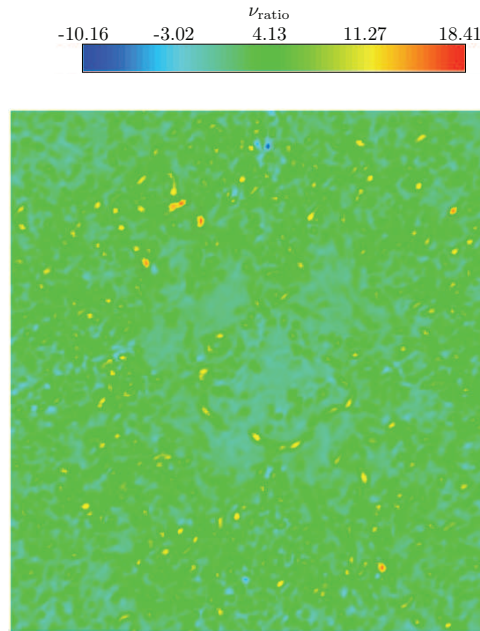


Figure 4.17: $Re_D = 23000$ test-case C2: map of normalized SGS energy transfer coefficient ν_{ratio} over an horizontal plane located at $x_1/D = 0.1$.

The occurrence of reverse energy transfer is little affected by the Reynolds number [28], even though higher Reynolds number flows are typically slightly more susceptible to show backscatter [56]. More frequent occurrence of energy backscatter is expected, anyway, when the near-wall dynamics of the flow are under-resolved [55]. This is consistent with the above mentioned dependency on the Reynolds number, as, increasing Re , grid resolution requirements become more stringent.

Instantaneous spatial distributions of ν_{ratio} over a horizontal plane located at $x_1/D = 0.1$ reveal that, when the Reynolds number is increased, sub-grid energy transfer becomes much more intermittent, with more frequent occurrence of high peaks of forward energy transfer (*cf.* Figures 4.16 and 4.17). Note that, although the two maps in Figures 4.16 are represented with the same scale in order to allow direct comparison, the range of values for the lower Reynolds number case was from -12.5 to 96.7 , the maximum being attained in the single red spot which can be observed in the upper left quadrant of Figure 4.16a; that is the only location where values of ν_{ratio} greater than ~ 55 were measured. Also note that, due to the much lower level of SGS energy in the refined $Re_D = 23000$ test-case C2, the relevant map in Figure 4.17 is represented with its own scale. Some regions of backscatter are observed in the stagnation region (less visible in the low Reynolds number case due to the used scale) where the flow field undergoes significant straining. Anyway, at this height forward energy transfer is dominant.

Figure 4.18 shows maps of ν_{ratio} and the the normalized second invariant of the resolved velocity gradient tensor,

$$Q^* = -\frac{D^2}{2U_b^2} \frac{\partial \tilde{u}_i}{\partial x_j} \frac{\partial \tilde{u}_j}{\partial x_i}, \quad (4.154)$$

over a radial plane extending from the wall up to $x_1/D = 0.8$. Consistently with the findings

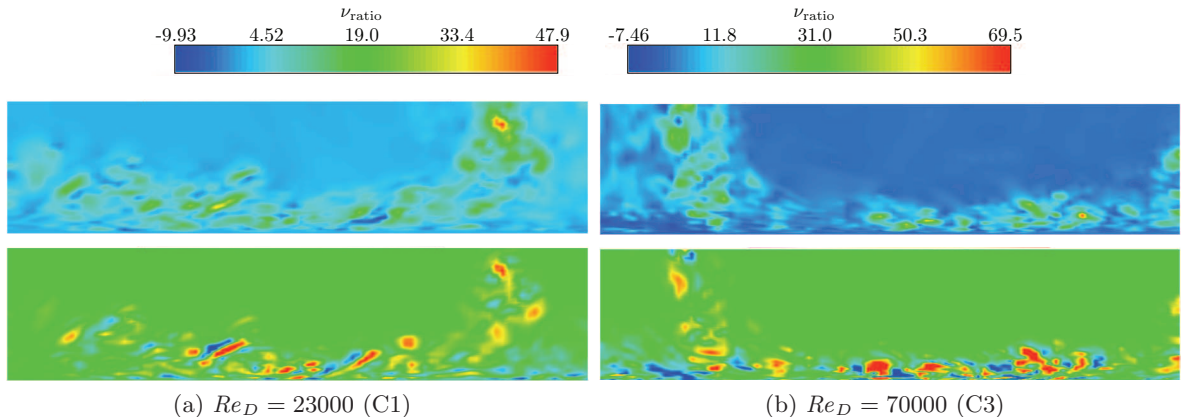


Figure 4.18: Maps of normalized SGS energy transfer coefficient ν_{ratio} (top) and second invariant of the resolved velocity gradient tensor Q^* (bottom) over a vertical axial plane in the range $x_1/D \in [0 : 0.8]$. For the Q^* maps, regions of strong vorticity are colored in red, whereas regions of intense strain are colored in blue.

of Piomelli et al. [57], peaks in forward scatter are well correlated with regions of strong vorticity (indicated in red in the Q^* maps), for the most coming from the jet's shear layer, and backscatter events generally occur in the middle of intense forward scatter regions. Long and thin pockets of fluid, where backward energy transfer is predominant, originate mostly near the wall and propagate into the boundary layer and downstream in the wall-jet. As expected, regions of negative ν_{ratio} are relatively well correlated with regions of negative Q^* (in blue), meaning that the most important events of SGS energy backscatter are observed where the resolved flow field undergoes intense straining, due to sweeping motions induced by coherent vortical structures.

4.5.8 Flow Field and Scalar Mixing

In this section we present a brief qualitative comparison of the two test-cases, with particular emphasis on the observed differences in turbulence development and scalar mixing.

With regards to scalar mixing, in particular, Figure 4.19 shows the relevant statistical quantities extracted at $Re_D = 23000$ from the refined simulation (C2). The profiles are plotted with respect to wall-units normalized distance to the wall x_1^+ . Even though the flow field undergoes continuous transition within the region under study, *i.e.*, the computed wall-jet region is too short and too close to the stagnation region to allow fully developed turbulence to be established, some sort of similarity between profiles at various radial distances is visible. Right after $r/D = 1.5$, all the curves are fairly well scalable between each other and the maximum values are located at the same wall distance.

Scalar variance (see Figure 4.19b) peaks at $x_1^+ \simeq 300$, corresponding, approximately, to the maximum in turbulent kinetic energy, and a nearly logarithmic behavior may be seen in the range $x_1^+ > 30$, $x_1^+ < 100$. Within the region of strong flow curvature ($r/D \leq 1.5$), a peak in streamwise turbulent scalar transport is observed between $x_1^+ \simeq 10$ and $x_1^+ \simeq 20$ (*cf.* Figure 4.19c). This corresponds exactly with the analogous peak observed in streamwise velocity fluctuations and is probably mostly related to the interactions between coherent struc-

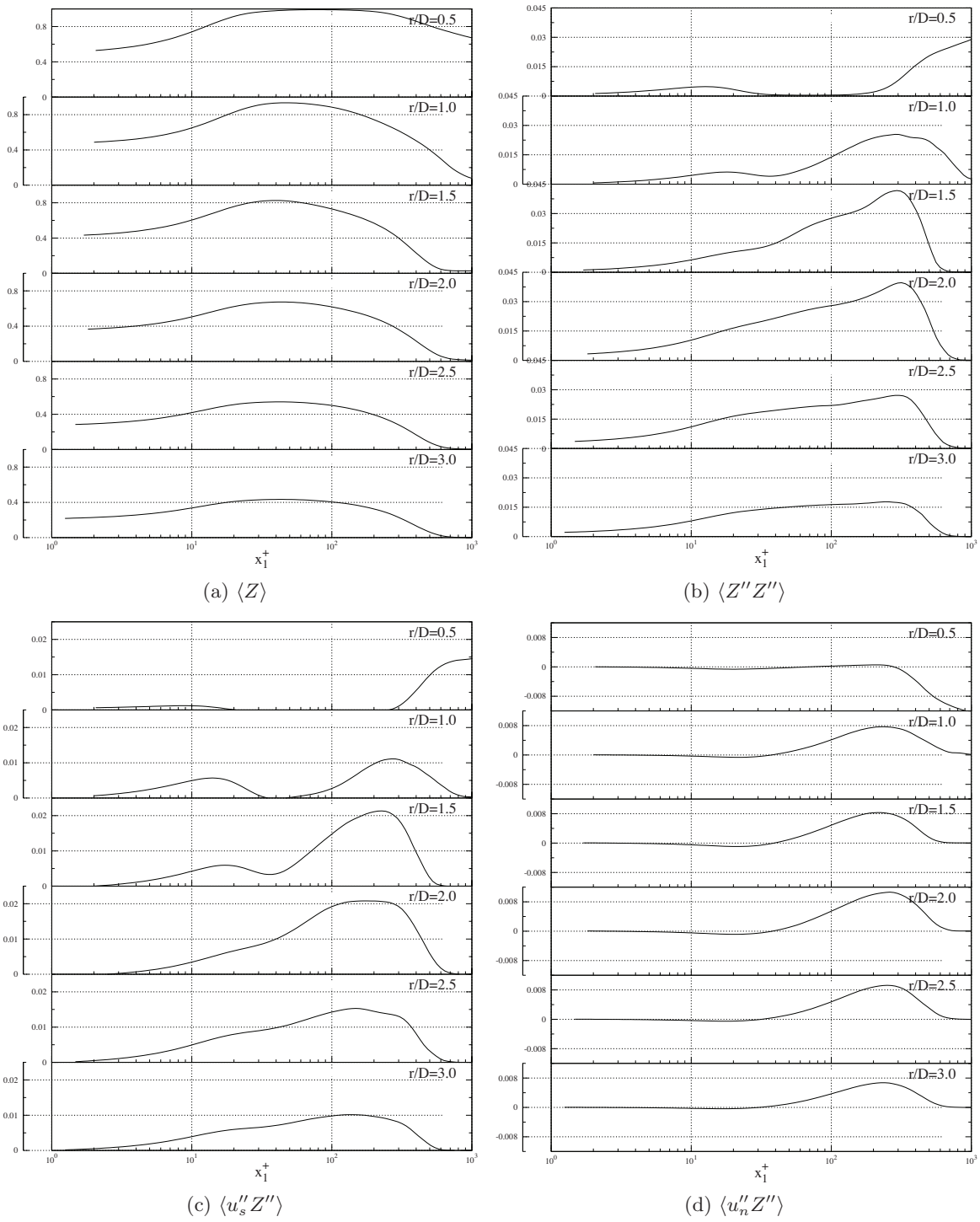


Figure 4.19: $Re_D = 23000$ test-case C2. Average scalar (a), scalar variance (b), streamwise scalar flux (c) normal scalar flux (d). The distance to the wall is indicated in wall-units (viscous length obtained from experimental average velocity profiles [8]).

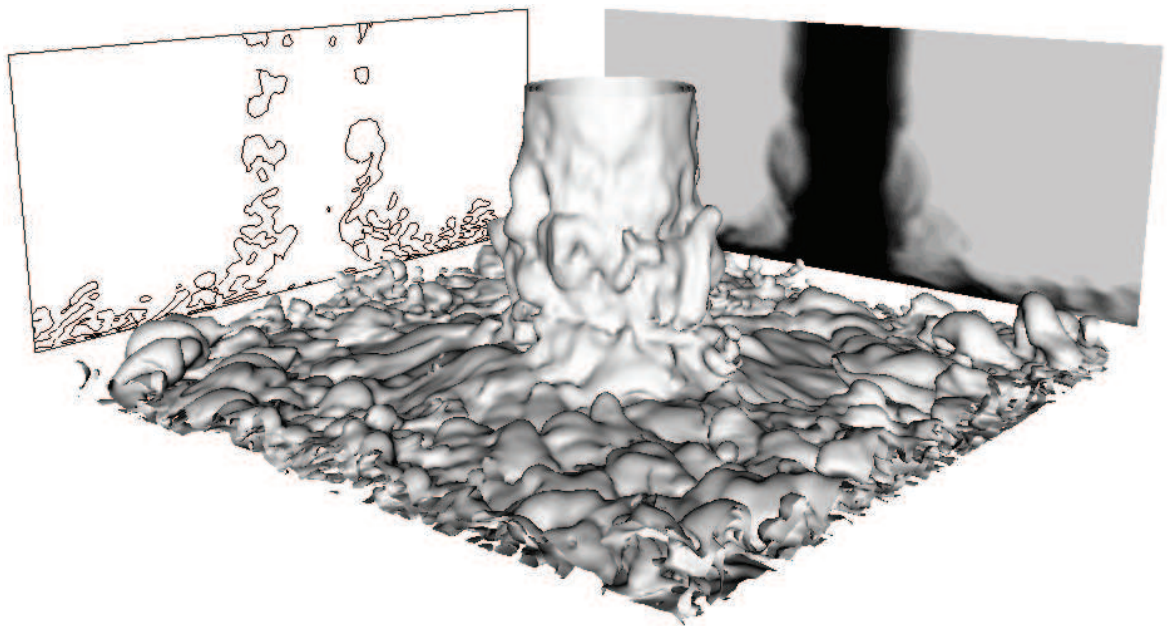
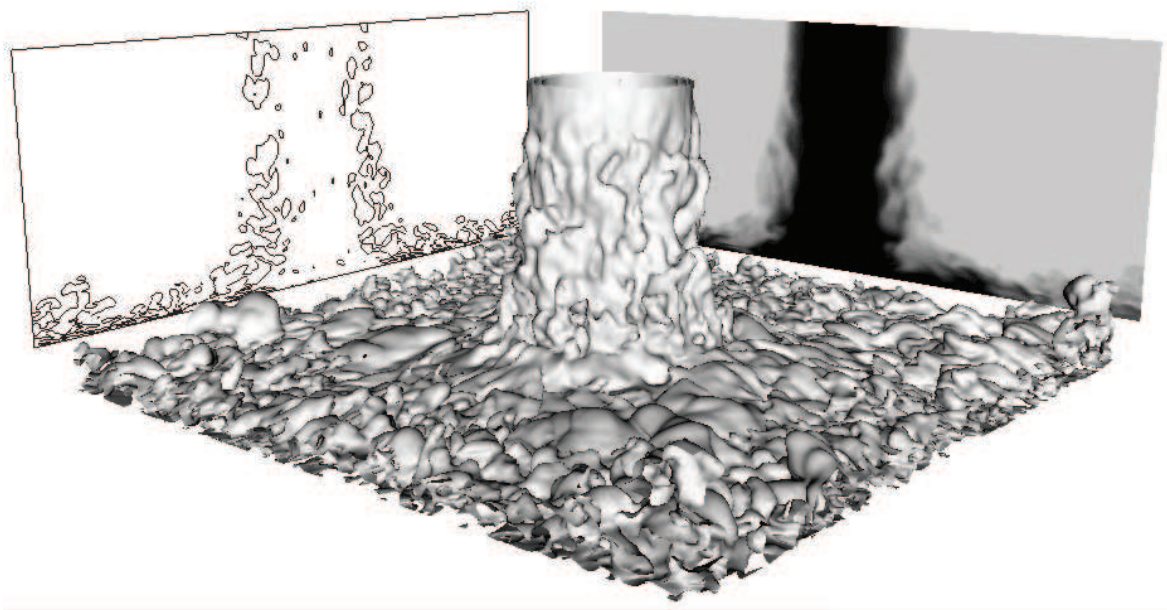
(a) $Re_D = 23000$ (C1)(b) $Re_D = 70000$ (C3)

Figure 4.20: Tridimensional visualization of the flow: iso-surfaces of passive scalar Z (center), iso-contours of $Q^* = 0.5$ (left) and passive scalar map (right) over axial planes.

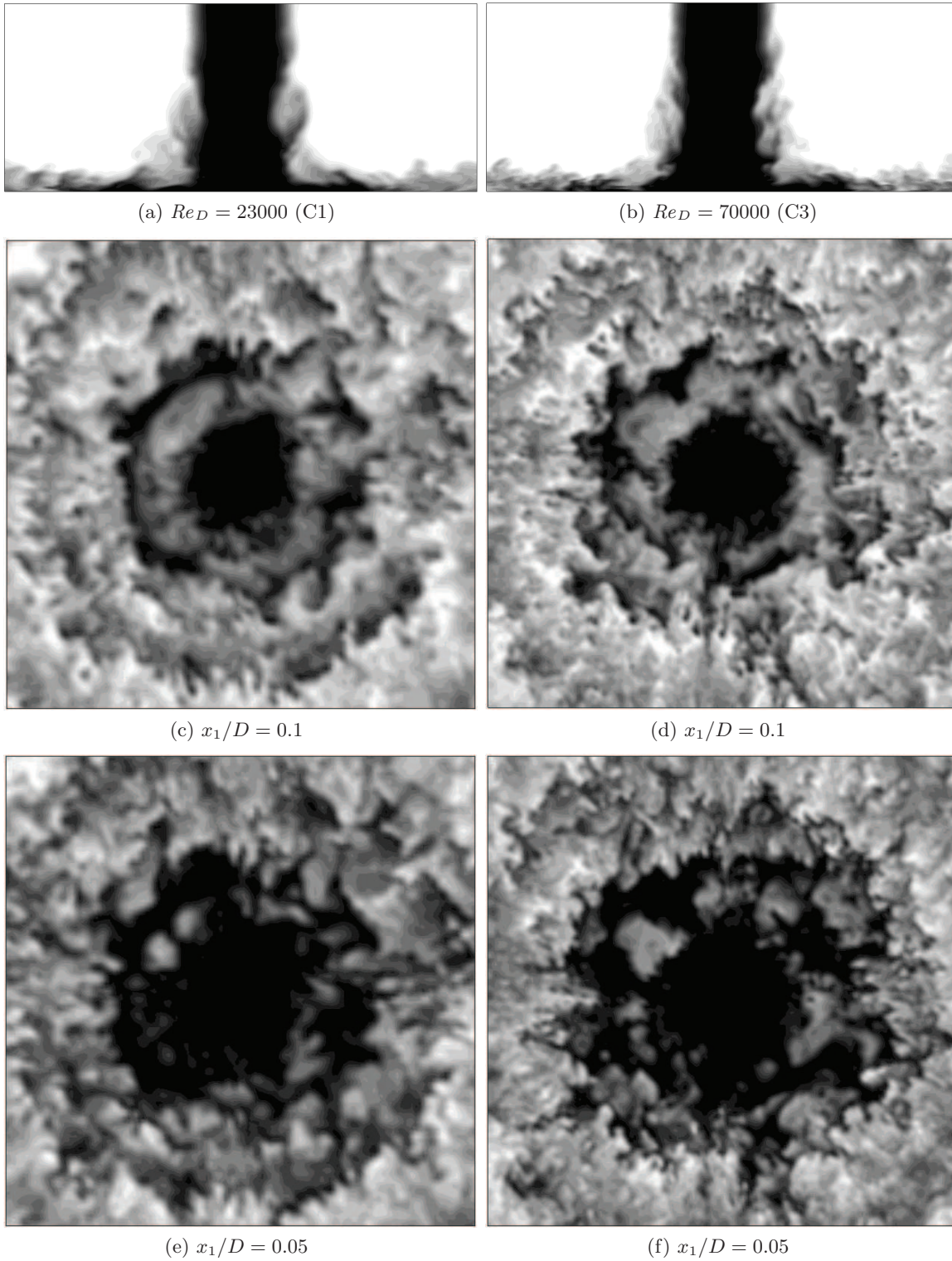


Figure 4.21: Maps of passive scalar $Z \in [0 : 1]$ over axial planes (a,b) and horizontal planes at $x_1/D = 0.1$ (c,d) and $x_1/D = 0.05$ (e,f). $Re_D = 23000$ (a,c,d) and $Re_D = 70000$ (b,d,e).

tures coming from the jet's shear layer and secondary structures originating at the wall. A second more intense peak is attained at $x_1^+ \simeq 200$, corresponding to the region of maximum turbulent kinetic energy. No significant wall-normal turbulent scalar transport is observed, in Figure 4.19d, until $x_1^+ \simeq 30$, corresponding to approximately $x_1/D = 0.017$, which is consistent with the initial flat zone visible at the beginning of the wall-normal velocity fluctuations' profiles (*cf.* Figure 4.9). The maximum in vertical turbulent transport is located at $x_1^+ \simeq 130$ and corresponds fairly well with the maximum value of scalar variance $\langle Z''Z'' \rangle$.

A tridimensional representation of the flow field is presented in Figure 4.20 for the two test-cases. Instantaneous iso-surfaces of passive scalar Z are shown, together with its distribution over an axial plane; the development of coherent vortical structures is also represented by means of iso-contours of Q^* . Passive scalar distribution over axial planes and horizontal planes at $x_1/D = 0.1$ and $x_1/D = 0.05$ for the two Reynolds numbers is also shown in Figure 4.21.

As expected, the higher Reynolds number test-case presents an earlier development of turbulence within the jet's shear layer, which is characterized by finer structures and increased intermittency, which is particularly evident from the distributions of Z parallel to the impingement wall. Also, increased mixing in the near-wall region is promoted at higher Reynolds number, as it may be inferred from the presence of numerous and extended white pockets of fluid with $Z \sim 0$, just around the stagnation region (*cf.* Figure 4.21f).

Direct Numerical Simulation (DNS)

To make an accurate numerical simulation (i.e., a full time-dependent three-dimensional solution) of a turbulent flow, all physically relevant scales must be resolved. While more and more progress is being made with such simulations, computers of the early 1990's have insufficient memory and speed to solve any turbulent flow problem of practical interest.

D.C. Wilcox, 1993

Contents

5.1	Accounting for the Whole Spectrum	134
5.2	The Description of Combustion	135
5.2.1	The Reaction Rate's Boundary Treatment	136
5.2.2	Proper Resolution and Scaling Parameters	138
5.3	Turbulent Bunsen Flame Simulation	142
5.3.1	$Re_D = 600$ Round-Jet Simulation (F1)	144
5.3.2	$Re_D = 2000$ Round-Jet Simulation (F2)	144
5.3.3	$Re_D = 4500$ Slot-Jet Simulation (F3)	147

Le 5^e Chapitre de cette thèse est dédié à la Simulation Numérique Directe (ou DNS) des écoulements turbulents. Dans ce contexte, le spectre d'énergie est résolu complètement, c'est-à-dire que le maillage de calcul, ainsi que le schéma numérique adopté, sont conçus pour représenter la gamme entière des échelles caractéristiques du phénomène étudié.

La très grande taille du spectre d'énergie des écoulements d'intérêt pratique nécessite, en général, un énorme effort du point de vue de l'utilisation de ressources de calcul. La DNS reste donc souvent confinée à l'analyse des configurations plutôt simplifiées.

Néanmoins, la simulation directe représente un instrument d'investigation capable de fournir un niveau de détail que même les moyens d'analyse expérimentale les plus sophistiqués ne peuvent donner.

Dans ce chapitre, la DNS est adoptée dans le but d'analyser les détails topologiques de la surface d'une flamme prémélangée de type Bunsen et d'évaluer l'erreur commise lorsque les données bidimensionnelles obtenues par mesure expérimentale sont comparées aux résultats tridimensionnels d'une simulation numérique. La formulation mathématique de la chimie est d'abord présentée. Par la suite, les problématiques liées à l'introduction des termes sources de la chimie, dans le contexte de la méthodologie 3D-NSCBC développée dans la Section 3.2,

sont détaillées et la généralisation des conditions aux limites d'entrée/sortie subsoniques est présentée.

Ensuite, les paramètres pour la définition de la résolution minimale nécessaire à la simulation directe d'une telle flamme sont analysés. Il sera montré, notamment, que la résolution de l'épaisseur de la zone de réaction, pour une flamme de longueur fixée, peut représenter une contrainte bien plus forte que la résolution du spectre d'énergie turbulente.

En dernier lieu, trois simulations directes d'une flamme Bunsen turbulente à différents nombres de Reynolds sont détaillées. Les résultats de deux d'entre elles ont été utilisés pendant le *CTR Summer Program 2008* de l'Université de Stanford, dont les *Proceedings* sont joints dans la Deuxième Partie de la thèse.

5.1 Accounting for the Whole Spectrum

As already mentioned at the beginning of the previous Chapter, when the numerical scheme and grid spacing are able to resolve the whole spectrum of time- and length-scales of the physical phenomenon under study, the Navier-Stokes equations can be directly integrated. This means that, on one hand, the number of grid points and of time-steps per second is sufficiently large to represent all the degrees of freedom of the problem and, on the other hand, the discrete numerical scheme used to perform time- and space-integration is accurate enough to prevent numerical errors from polluting the solution. When these two requirements are met, we talk about Direct Numerical Simulation (DNS) of turbulence.

Remembering that the number of degrees of freedom is of the order of $\sim Re^3$ ($Re^{9/4}$ in the tridimensional space and $Re^{3/4}$ in time), it is clear that DNS of configurations of practical interest, from the engineering point of view, may be just unfeasible, even with the enormous computational power which is available nowadays. It is worthwhile underlining that the above scaling refers to homogeneous isotropic turbulence. Other physical phenomena, characterized by smaller scales, may be generally involved making the situation even worse. Nonetheless, when simple configurations are considered, DNS may represent a quite powerful tool in order to obtain a number of informations and a richness of detail that laboratory experimental setups cannot generally provide.

Hence, Direct Numerical Simulation represents an alternative “experimental” procedure, as well as a powerful diagnostic tool to assess, *a priori*, the performances of Sub-Grid Scale models for Large-Eddy Simulation¹.

In summary, given the energy spectrum of the physical problem to be solved, RANS does not resolve it all, LES resolves part of it and DNS resolves it all, the transition between one approach to the other requiring more and more computational effort. In partial compensation of this, modeling complexity is reduced: since DNS resolves the entire spectrum, there does not need to be any model, therefore the Navier-Stokes equations are integrated directly without any additional unclosed term.

¹As opposed to *a posteriori* evaluation of model performances by comparing the relevant statistical results with experimental or DNS data from an identical flow configuration, *a priori* evaluation is performed when the comparison is made between exact and modeled quantities extracted from the same experimental/DNS data. The large amount of details that can be extracted from DNS, makes it a unique tool for *a priori* evaluation of LES models. Since DNS data represent the full spectrum, both resolved and unresolved quantities are available. Hence, filtered DNS data can be used to compute exact SGS stresses, as well as modeled ones, thus allowing direct comparison.

Although in principle, the transition between LES and DNS could be regarded as a “continuous” process, in which, increasing resolution, the SGS model contribution progressively disappears, thus attaining DNS conditions, there turns out to be a discontinuity. In fact, SGS models are often designed under the assumption that the cutoff wave-number lies in the inertial subrange, therefore, when the resolution is such that the spectrum is cut within high-frequencies of the dissipation range, some corrections to the model should be anyway introduced, as proposed by Meneveau and Lund [47] for the dynamic model (*cf.* Section 4.3.3 at page 95). The same holds true for the transition between RANS and LES. If, on one hand, LES models are not designed for the spectrum being truncated within the low-frequencies of the production range, on the other hand, RANS models are designed to represent the effect of the entire spectrum in strictly statistically steady turbulent flows. Hence, “coarse LES” or “unsteady RANS” are meaningless, unless the models are re-adapted for the particular case.

In the following sections, Direct Numerical Simulation of the turbulent Bunsen flame at three different Reynolds numbers is presented. The relevant DNS database were used in occasion of the Summer Program 2008 at the Center for Turbulence Research (CTR), Stanford University. The article [44] that followed is included in the second Part of this thesis.

5.2 The Description of Combustion

A simplified mathematical representation of premixed combustion is sufficient for the purposes of the present study, which is focused on flame surface’s topology and reaction rate’s statistical description. It is then assumed that the mixture is very lean (*i.e.*, combustion takes place in excess of air) and that combustion weakly modifies the oxidizer mass fraction. Under these hypotheses, the burning rate of the fuel mass fraction Y_F may be described by means of an Arrhenius relation of the form:

$$\dot{\omega}_F = -\rho K Y_F \exp\left(-\frac{E_{Ac}}{RT}\right), \quad (5.1)$$

where K is the pre-exponential factor, $E_{Ac} = RT_{Ac}$ is the activation energy (T_{Ac} is the relevant activation temperature) and T the temperature. Moreover, the combustion process may be described introducing an adimensional scalar $c \in [0 : 1]$, representing the progress of reaction, which is equal to 0 where no reaction has yet taken place and 1 where combustion has been completed:

$$c = \frac{T - T_0}{T_b - T_0}, \quad (5.2)$$

T_0 and T_b being the temperature of the fresh ($c = 0$) and burnt gases ($c = 1$) respectively. The activation temperature, in particular, may be obtained from the Zeldovitch number, namely

$$\beta = \alpha \frac{T_{Ac}}{T_b}, \quad (5.3)$$

where $\alpha = (T_b - T_0)/T_b$ is the heat release parameter, using the following relation:

$$T_{Ac} = T_b \frac{\beta}{\alpha} = \frac{\beta T_0}{\alpha(1 - \alpha)}. \quad (5.4)$$

If Pr is the Prandtl number and Sc is the Schmidt number related to the diffusion process of the fuel mass fraction Y_F , when the Lewis number $Le = Pr/Sc$ [66] is equal to one, equivalence

between scalar and temperature diffusion is achieved. Therefore, assuming unity Lewis number, the progress of reaction, Eq. (5.2), may be also computed as

$$c = 1 - \frac{Y_F}{Y_{F,0}}, \quad (Le = 1), \quad (5.5)$$

with $Y_{F,0}$ the fuel mass fraction in the fuel jet. The burning rate Eq. (5.1) then becomes:

$$\dot{\omega}_F = -\rho K Y_{F,0} (1 - c) \exp\left(-\frac{T_{Ac}}{T}\right). \quad (5.6)$$

Furthermore, since from Eq. (5.5) it is readily verified that

$$\frac{\partial c}{\partial t} = -\frac{1}{Y_{F,0}} \frac{\partial Y_F}{\partial t}, \quad (5.7)$$

and since, by definition, $\dot{\omega}_F = \partial Y_F / \partial t$, a source term for the progress of reaction c may be defined as:

$$\dot{\omega}_c = \rho K (1 - c) \exp\left(-\frac{T_{Ac}}{T}\right). \quad (5.8)$$

Finally, the amount of heat release per unit mass of fuel Q_F is related to the reference temperatures T_0 and T_b through the relation

$$Q_F = c_p (T_b - T_0) = c_p T_0 \left(\frac{\alpha}{1 - \alpha}\right), \quad (5.9)$$

leading to the following relevant source term for the energy equation:

$$\dot{\omega}_e = c_p T_0 \left(\frac{\alpha}{1 - \alpha}\right) \dot{\omega}_c. \quad (5.10)$$

In the perspective of the above description of combustion, therefore, the compressible Navier-Stokes equations set which describes the problem under study is obtained from Eq. (2.15) by introducing the source term vector \mathbf{s} and by replacing the passive scalar Z with the progress variable c :

$$\frac{\partial \mathbf{U}}{\partial t} + \frac{\partial \mathbf{F}^k}{\partial x_k} + \frac{\partial \mathbf{D}^k}{\partial x_k} = \mathbf{s}, \quad (5.11)$$

with \mathbf{F}^k and \mathbf{D}^k given by Eq. (2.16) and

$$\mathbf{s} = (0 \quad 0 \quad 0 \quad 0 \quad \dot{\omega}_e \quad \dot{\omega}_c)^T. \quad (5.12)$$

5.2.1 The Reaction Rate's Boundary Treatment

In order to better control the behavior of relaxed boundary quantities under the presence of heat release by chemical reactions, the source terms may be accounted for in the computation of characteristic incoming waves [73, 84]. Source terms, in fact, can be treated in analogy to what has been described in Section 3.2 with regards to transverse convective terms and transverse pressure gradients. The modification to be introduced in the subsonic non-reflecting inflow and outflow boundary conditions, will now be described, for simplicity, in the case of face

boundaries, where a single characteristic direction—say x_1 —is considered (*cf.* Section 3.2.2). The generalization for edges and corners is straightforward and will be omitted.

Taking Eq. (5.11) and pre-multiplying by \mathbf{P}^{-1} , defined in Eq. (3.54), and following the same procedure that has been described in Section 3.2, the relationship linking primitive variables to wave amplitude variations and the relevant characteristic formulation read respectively:

$$\frac{\partial \mathcal{U}}{\partial t} + \mathbf{d} - \mathcal{T} = \mathcal{S}, \quad (5.13)$$

$$\mathbf{S}_1^{-1} \frac{\partial \mathcal{U}}{\partial t} + \mathcal{L} - \mathfrak{T}^1 = \mathfrak{S}^1, \quad (5.14)$$

with \mathbf{S}_1^{-1} being obtained from Eq. (3.64) and

$$\mathbf{S} = \mathbf{P}^{-1} \mathbf{s} = \begin{pmatrix} 0 \\ 0 \\ 0 \\ 0 \\ (\gamma - 1)\dot{\omega}_e \\ \dot{\omega}_c/\rho \end{pmatrix}, \quad \mathfrak{S}^1 = \mathbf{S}_1^{-1} \mathbf{S} = \begin{pmatrix} (\gamma - 1)\dot{\omega}_e \\ -(\gamma - 1)\dot{\omega}_e \\ 0 \\ 0 \\ (\gamma - 1)\dot{\omega}_e \\ \dot{\omega}_c/\rho \end{pmatrix}, \quad (5.15)$$

Using now Eq. (5.14) in place of Eq. (3.78) and combining it with boundary conditions Eq. (3.85) and Eqs. (3.94)–(3.98), the unknown incoming wave amplitude variations, relevant to the subsonic non-reflecting inflow and outflow respectively, take the form:

$$\begin{cases} \mathcal{L}_\phi = \eta_\phi \frac{\rho a^2 (1 - M_{\max}^2)}{L_x} \Delta u_1 + \mathfrak{T}_\phi^1 + \mathfrak{S}_\phi^1, \\ \mathcal{L}_2 = \eta_2 \frac{\rho a R}{L_x} \Delta T + \mathfrak{T}_2^1 + \mathfrak{S}_2^1, \\ \mathcal{L}_3 = \eta_3 \frac{a}{L_x} \Delta u_2 + \mathfrak{T}_3^1, \\ \mathcal{L}_4 = \eta_4 \frac{a}{L_x} \Delta u_3 + \mathfrak{T}_4^1, \\ \mathcal{L}_6 = \eta_6 \frac{a}{L_x} \Delta c + \mathfrak{T}_6^1 + \mathfrak{S}_6^1, \end{cases} \quad (5.16)$$

$$\mathcal{L}_\phi = \sigma \frac{a (1 - M_{\max}^2)}{L_x} \Delta p + (1 - \beta_t) (\mathfrak{T}_\phi^1 + \mathfrak{S}_\phi^1) + \beta_t \mathfrak{T}_{\phi, \text{ex}}^1, \quad (5.17)$$

where \mathfrak{T}_k^1 and \mathfrak{S}_k^1 are the k th components of the vectors given in Eq. (3.80) and (5.15) respectively. With regards to the outflow, in particular, it has to be noted that, due to numerical stability issues altogether similar to those related to the transverse convective terms themselves, the boundary condition is much better behaved when also the source terms are relaxed. In the above Eq. (5.17), the same relaxation coefficient β_t is used and source terms' relaxation is performed toward zero reaction rate, *i.e.* $\mathfrak{S}_{\phi, \text{ex}}^1 = 0$.

It is worthwhile mentioning that the above relations could have been obtained by defining pseudo-transverse terms $\mathfrak{T}_{\text{psd}}^k = \mathfrak{T}^k + \mathfrak{S}^k$, with $\mathfrak{S}^k = \mathbf{S}_k^{-1} \mathbf{P}^{-1} \mathbf{s}$, and computing the incoming waves by applying the same relations obtained in Section 3.2 with $\mathfrak{T}_{\text{psd}}^k$ in place of \mathfrak{T}^k . Bearing this in mind, the 3D-NSCBC for edges and corners are readily generalized to the reactive case.²

²This is strictly true for the simplified description of the chemical process herein presented. More complex chemistry may lead to additional difficulties (*cf.* Baum et al. [5]).

5.2.2 Proper Resolution and Scaling Parameters

When DNS of a turbulent flame is to be performed, it is of course necessary to check that grid resolution is sufficiently high to represent the entire range of length-scales involved, namely turbulence length-scales and combustion length-scales. The first, by usual turbulence scaling, may be estimated as extending from the integral length-scale ℓ_0 , down to the Kolmogorov microscale η , these two being related by the following relation:

$$\eta \sim \ell_0 Re_t^{-3/4}, \quad \text{with} \quad Re_t = \frac{u' \ell_0}{\nu}, \quad (5.18)$$

u' being a measure of turbulence activity extracted from the turbulent kinetic energy per unit mass k

$$u'^2 \sim 2k = \langle u'_i u'_i \rangle.$$

With regard to the combustion process, when the study is focused on a particular flame surface topology, as in the present case, there turn out to be a certain number of interlinked parameters, which make their determination not quite immediate. First of all, the computational grid must be fine enough to resolve the flame thickness. If δ_L is the real flame thickness³ and S_L is the laminar flame speed, which is directly linked to the pre-exponential factor (cf. Eq. (5.8)), experience shows that the flame Reynolds number

$$Re_L = \frac{S_L \delta_L}{\nu}, \quad (5.19)$$

for a typical hydrocarbon fuel, is ~ 5 , hence, we may assume that $\delta_L \sim 5\nu/S_L$ and define a flame scaling parameter

$$\delta_L^* = \frac{\nu}{S_L}. \quad (5.20)$$

It is then evident that, in order for the grid to be able to resolve the flame, the maximum grid spacing must be a certain fraction of δ_L^* . A practical way to define a flame resolution criterion, is to perform a direct numerical simulation of a laminar 1D flame and check that the plot of the reaction rate versus the progress of reaction is well resolved.

On the other hand, on a reference frame moving with the flame speed, the mono-dimensional transport equation for the progress of reaction c becomes:

$$S_L \frac{d(\rho c)}{dx} + \frac{d}{dx} \left(\frac{\rho \nu}{Sc} \frac{dc}{dx} \right) = \dot{\omega}_c, \quad (5.21)$$

which, integrated over a control volume $[x_0 : x_b]$ long enough to sufficiently enclose the flame, *i.e.* $dc/dx = 0$ over the control volume's frontier, $c(x_0) = 0$ and $c(x_b) = 1$ (cf. Figure 5.1a), gives the following relation:

$$S_L = \frac{1}{\rho_b} \int_{x_0}^{x_b} \dot{\omega}_c dx, \quad (5.22)$$

with ρ_b the density of the burnt gases. Hence, on the same simulation, the actual flame speed may be obtained by integrating the reaction rate across the flame front.

³Practically, δ_L is of the order of the flame thickness measured from the temperature profiles through the flame:

$$\delta_L \simeq \frac{T_b - T_0}{\max(\partial T / \partial x_n)},$$

where subscript n indicates the direction orthogonal to the flame front.

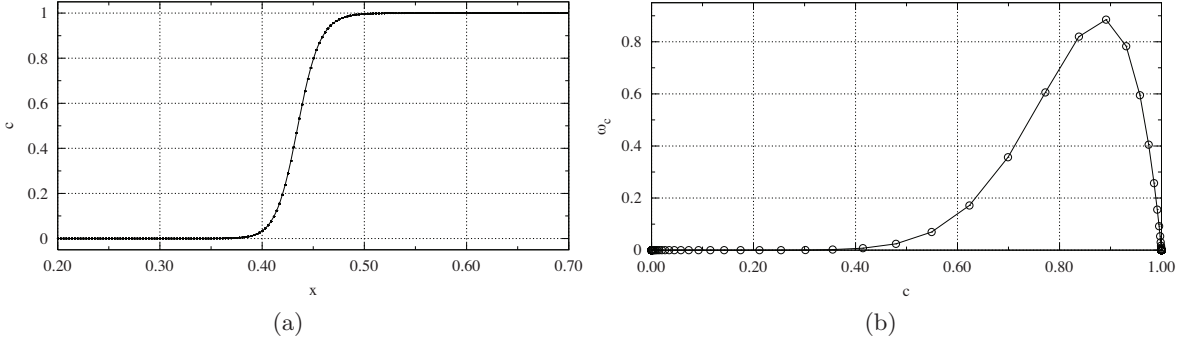


Figure 5.1: Mono-dimensional laminar flame test: progress variable c versus x (a); reaction rate ω_c versus progress variable c (b). The flame speed was set at $S_{L,\max}$ according to Eq. (5.24).

These tests have revealed that a good estimation of the maximum grid spacing h_{\max} , needed to resolve a flame that propagates at velocity S_L , can be evaluated from the parameter δ_L^* as:

$$h_{\max} \simeq 0.3 \delta_L^*, \quad (5.23)$$

therefore, for a given computational grid with resolution h (assumed, for simplicity, to be the same in each coordinate direction), there exist a maximum resolvable flame speed, which is approximately equal to:

$$S_{L,\max} \simeq 0.3 \frac{\nu}{h}. \quad (5.24)$$

Figure 5.1b shows the plot of ω_c versus progress variable c for a 1D laminar flame obtained setting the maximum flame speed according to the threshold given in Eq. (5.24). As it can be seen, although c is fairly well resolved in physical space (Figure 5.1a), in composition space, the grid is just able to resolve the peak of reaction rate with about 3 points, which may be regarded as a minimum requirement. Turning now the attention on the average flame shape, referring to Figure 5.2, if D is the diameter of the Bunsen burner, injecting fresh mixture with bulk velocity U_b , the semi-aperture angle $\theta^* \in (0 : \pi/2)$ of the conical laminar flame satisfies the following relations:

$$\tan(\theta^*) = \frac{D}{2H_L}, \quad \text{and} \quad \sin(\theta^*) = \frac{S_L}{U_b}, \quad (5.25)$$

The flame height may be then computed as:

$$H_L = \frac{D/2}{\tan[\sin^{-1}(S_L/U_b)]}. \quad (5.26)$$

Therefore, from Eq. (5.24), the maximum semi-aperture angle or, otherwise, the minimum flame height, that can be resolved on a given mesh may be obtained as

$$\sin(\theta_{\max}^*) \simeq \frac{0.3D}{hRe_D}, \quad (5.27)$$

$$H_{\min} \simeq \frac{0.5D}{\tan\left[\sin^{-1}\left(\frac{0.3D}{hRe_D}\right)\right]}, \quad (5.28)$$

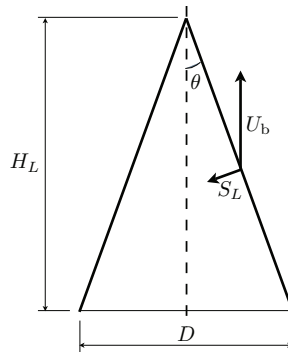


Figure 5.2: Schematic representation of a conical laminar flame.

where $Re_D = U_b D / \nu$ is the jet's Reynolds number. If $N = D/h$ is the number of nodes along the diameter, the above relation states that, for a given flame semi-aperture angle θ^* , the number of degrees of freedom necessary to resolve a tridimensional conical flame scales as $\sim Re^3$, which is even more demanding than the classical turbulence resolution requirement, namely $\sim Re^{9/4}$.

Just to fix the ideas, should we intend to perform a direct numerical simulation of the wrinkled laminar flame presented by A. Yoshida in the book by Samimy et al. [65], we may want to make an *a priori* estimation of the necessary resolution to resolve both chemistry and turbulence. The experiment was conducted with a Propane/Air mixture injected through a diameter of 30 mm and bulk velocity of 2.36 m/s (with an annular pilot flame). The equivalence ratio was 0.68, the flame height was ~ 85 mm, corresponding to a semi-aperture angle $\theta^* \simeq 10^\circ$, and the laminar flame speed, obtained from the flame height, the diameter and the bulk velocity, was ~ 0.41 m/s.

Considering a kinematic viscosity of $1.59 \times 10^{-5} \text{ m}^2/\text{s}$, the jet's Reynolds number is ~ 4440 , hence, from Eq. (5.27), the maximum grid spacing to resolve chemistry is

$$h \simeq \frac{0.3D}{\sin(\theta^*)Re_D} = \frac{0.3 \times 0.03 \text{ m}}{0.1736 \times 4440.0} \simeq 11.6 \mu\text{m}.$$

With regards to turbulence resolution, the Taylor micro-scale λ was about 1.81 mm and the relevant Reynolds number was $Re_\lambda \simeq 17.4$, corresponding to $u' \simeq 0.15$ m/s and $Re_t \simeq 303$ [30], hence we have:

$$\ell_0 \simeq \frac{\nu Re_t}{u'} \simeq 30 \text{ mm}, \quad \text{and} \quad \eta \sim \ell_0 Re_t^{-3/4} \sim 0.4 \text{ mm}.$$

For this particular problem the Kolmogorov scale is around 40 times bigger than the estimated limit for sufficient chemistry resolution. It should be noted that Eq. (5.24) represents an approximate upper limit for resolvable flame speed, *i.e.*, a DNS based on that criterion would represent the less resolved DNS which can be made still sufficiently resolving the flame. Supposing that we want to economize CPU time, and design the grid using the maximum allowed spacing in the three directions, for a tridimensional cartesian computational grid $2D$ wide and $4D$ long, the total number of mesh points would be $\sim 2.8 \times 10^{11}$.⁴ As it will be shown in the

⁴Of course, using grid stretching the mesh may be optimized but, still, the above estimation gives an idea of the computational effort for such a relatively small Reynolds number.

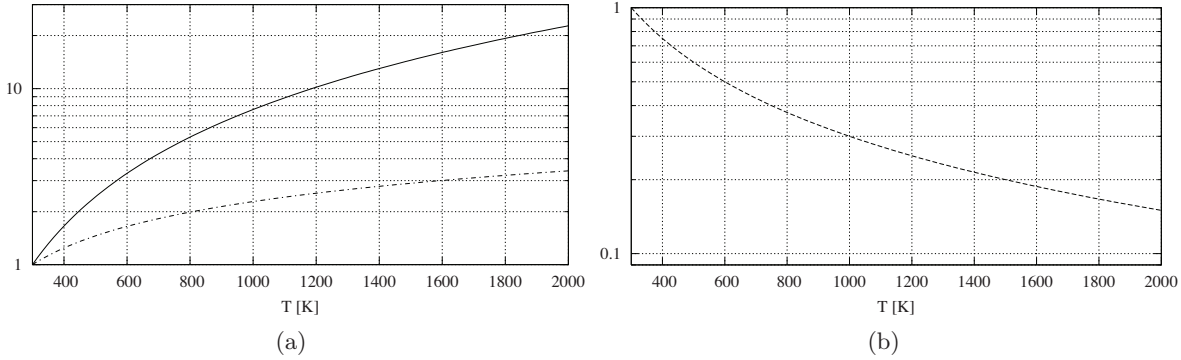


Figure 5.3: Viscosity (a) and density (b) variations as a function of temperature: — , normalized kinematic viscosity ν/ν_0 ; --- , normalized dynamic viscosity μ/μ_0 ; ---- , normalized density ρ/ρ_0 (ν_0 , μ_0 and ρ_0 evaluated at 300 K).

next sections, in order to be able to compute a Bunsen flame with Reynolds number of 4500 and with a reasonable computational cost, the angle θ^* must be so small, that the resulting flame becomes actually almost tubular, hence the need for robust boundary conditions which allow the flame to pass through without posing major stability issues (*cf.* Section 5.2.1).

Another important issue, when dealing with turbulent Bunsen flames, regards the way the expected behavior of the flame and its interactions with the flow field can be prescribed. When the flame is quite close to the burner, turbulence in jet's shear layer cannot generally develop early enough to interact with the flame, unless the jet's Reynolds number is high enough to allow full development within a relatively short distance. If the interactions between turbulence and the flame front need to be investigated, clearly, fully developed turbulence must be already available at the jet's nozzle. For instance, the flame may be fed by artificially generated grid turbulence, as in the case of the above mentioned wrinkled flame. And, indeed, such turbulence must be strong enough in order for it not to be damped by the significant increase of viscosity arising from higher temperature in the burnt gases. If, for instance, Re_t is the turbulent Reynolds number measured in the fresh gases just before the flame front, a temperature jump from 300 K to 1200 K would increase the kinematic viscosity of a factor 10 (*cf.* Figure 5.3), thus leading to a 10 times lower Re_t right after the flame front. Therefore, if

$$Re_t = \frac{u' \ell_0}{\nu},$$

either u' or ℓ_0 must be sufficiently high.⁵

Two useful parameters in order to control flame wrinkling are the ratio Γ between the integral scale of turbulence ℓ_0 and the flame thickness δ_L and the ratio α^* between the typical velocity fluctuation u' and the laminar flame speed S_L . The ratio between the turbulent integral length scale and the flame thickness may be written as:

$$\Gamma = \frac{\ell_0}{\delta_L} = \frac{Re_G}{Re_L}, \quad \text{with} \quad Re_G = \frac{\ell_0 S_L}{\nu}. \quad (5.29)$$

⁵It should be mentioned that both u' and ℓ_0 are limited. The former cannot be more than a fraction of U_b (*e.g.*, $u' \sim 0.5U_b$ can be considered as a huge velocity fluctuation to be superimposed on the inlet profile and the gain is just 25% turbulent intensity). The latter, of course, cannot be more than just a fraction of the jet's diameter D . Increasing those limits, in the end, is a matter of increasing Re_D .

Re_D	600 (F1)	2000 (F2)	4500 (F3)
Type	Round Jet	Round Jet	Slot Jet
D	0.1 mm	0.5 mm	1.0 mm
U_b	95.61 m/s	63.74 m/s	71.71 m/s
T_0	300.0 K	300.0 K	300.0 K
M	0.28	0.18	0.21
η	$\sim 0.9 \mu\text{m}$	$\sim 1.8 \mu\text{m}$	$\sim 1.7 \mu\text{m}$
h/η	0.50–3.88	1.49–7.96	1.98–15.2
ℓ_0/D	0.04	0.04	0.025
S_L	12.0 m/s	1.7 m/s	1.4 m/s
$S_{L,\text{max}}$	8.6 m/s	1.72 m/s	1.41 m/s
θ_{max}^*	5.15°	1.55°	1.13°
u'/S_L	2.5	11.9	16.4
ℓ_0/δ_L	~ 2.2	~ 2.1	~ 2.2
Re_t	7.5	25.4	36.0
Re_G	3.0	2.1	2.2
α	0.3	0.8	0.8
β	8	8	8
K	$7.0 \times 10^{19} \text{ s}^{-1}$	$6.0 \times 10^{10} \text{ s}^{-1}$	$1.2 \times 10^{11} \text{ s}^{-1}$
T_b	428.6 K	1500.0 K	1500.0 K
Nodes	214×162^2	226×194^2	610×386^2
Dimensions	$4D \times 2D \times 2D$	$4D \times 2D \times 2D$	$3D \times 3D \times 1.3D$
Processors	256	2048	4096

Table 5.1: Turbulent Bunsen flame DNS parameters.

Moreover, the turbulent Reynolds number can be written as:

$$Re_t = \frac{u'\ell_0}{\nu} = \frac{u'\ell_0}{S_L\delta_L} Re_L = \alpha^* Re_G = \alpha^* \Gamma Re_L, \quad (5.30)$$

with

$$\alpha^* = \frac{u'}{S_L}. \quad (5.31)$$

Hence, as a preliminary criterion, in order to have a sufficiently wrinkled flame, turbulent fluctuations must be strong enough to interact with the flame, *i.e.* $\alpha^* = u'/S_L > 1$, and the integral scales must be large enough to distort the flame front, *i.e.* $\Gamma = \ell_0/\delta_L > 1$; using the above relations we must have $Re_t > Re_G$ and $Re_G > Re_L$, therefore Re_t must be greater than Re_L .

5.3 Turbulent Bunsen Flame Simulation

All the results presented in this section were obtained using the SiTCOM solver (see Section 3.1) without artificial dissipation and setting the physical properties of the fluid according to the

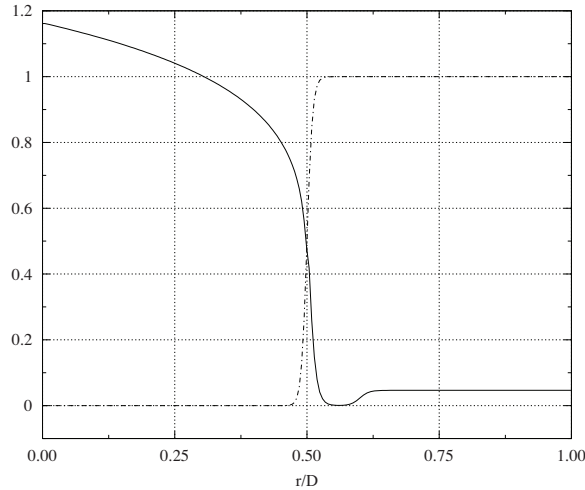


Figure 5.4: Prescribed inlet profiles: — , axial velocity component normalized by the bulk velocity U_b ; - - , progress variable or, equivalently, normalized temperature $T^* = (T - T_0)/(T_b - T_0)$.

values in Table 3.1 at page 59. Three different flow configurations have been computed at different Reynolds numbers: (F1) a $Re_D = 600$ round conical flame, (F2) a $Re_D = 2000$ round tubular flame and (F3) a $Re_D = 4500$ slot tubular flame, with Re_D , as usual, computed on the bulk velocity U_b and on the viscosity in the fresh mixture, *i.e.* at 300 K. Round flames were computed using subsonic non-reflecting inlet condition at $x_1 = 0$ ($\eta_5 = -\eta_2 = \eta_3 = \eta_4 = \eta_6 = 3.28$) and subsonic non-reflecting outflows ($\sigma = 0.28$ and β_t set according to the characteristic Mach number of the flow) on all the other five boundaries, whereas the slot burner configuration had periodic boundary conditions in the spanwise direction. Boundary conditions were enforced using the 3D-NSCBC technique [43] with the modification described in Section 5.2.1. Outlet target pressure was set at 1 atm and inlet target velocity profile was obtained using the Power Law profile for turbulent pipe flow, Eq. (3.230), with a small $4\%U_b$ coflow of burnt gases at temperature T_b . Inlet target progress variable and temperature were set at 0 and 300 K respectively (*cf.* Eqs. (5.16) and (5.17)) by means of a slightly smoothed top-hat profile (see Figure 5.4). All the chamber was initially filled with burnt gases at temperature T_b .

In any case, turbulence was promoted by injecting a correlated random noise [35], with specified correlation length l_t and uniform intensity u' throughout the inlet (see Section 3.3 at page 79). A summary of the parameters of the three computations is reported in Table 5.1.

Note that $\alpha = 0.3$ for test-case F1, corresponding to a temperature in the burnt gases of just ~ 430 K. This unrealistic parameter was chosen in order to limit the increase of kinematic viscosity to a factor of about 2 (*cf.* Figure 5.3), hence preventing turbulent fluctuations from being completely damped within the burnt gases. Thanks to the higher Reynolds number, the other two flames have a more realistic value of $T_b = 1500$ K. Also note that flame speed in simulation F1 is higher than the maximum limit from Eq. (5.24), hence chemistry is not completely resolved. That value of S_L was set in order to prevent the flame from reaching the outlet, by increasing the semi-aperture angle θ^* to a value of about 7.2° .

Grid spacing has been chosen in order to correctly resolve all the relevant scales of turbulence, as well as the flame thickness based on the criteria developed in the previous section (*cf.* Eq. (5.24)). With regards to the first point, the Kolmogorov length-scale η has been evaluated from the classical scaling $\eta \sim \ell_0 Re_t^{-3/4}$, where ℓ_0 is the correlation length of the injected noise (grid turbulence is assumed at the inlet) and $Re_t \sim u' \ell_0 / \nu$, with u' set at $0.32U_b$, corresponding to $\sim 10\%$ turbulence. As it can be seen in Table 5.1, grid spacing h is of the order of η in flow regions; the maximum values, which are reported for the sake of completeness, refer to the far lateral ends of the computational domain.⁶

5.3.1 $Re_D = 600$ Round-Jet Simulation (F1)

Qualitative results from test-case F1 are depicted in Figures 5.5 and 5.6. The map of progress variable is shown in Figure 5.5a and the iso-surfaces of the normalized second invariant of the velocity gradient (*cf.* Eq. (4.154) at page 127) colored by density indicate coherent vortical structures in Figure 5.5b. The black lines indicate the trace of the theoretic flame cone as it may be inferred from Eq. (5.25).

It is worthwhile mentioning that, as already said, the flame in this simulation was under-resolved. Going on with the computation, this fact led to a numerical instability in a small pocket of reacting mixture which had detached from the flame tip. This pocket is visible in Figure 5.5a as a small orange spot right ahead of the flame tip. Hence the key role of correct flame resolution in this kind of DNS.

At this Reynolds number, the damping effect of the increased temperature may be observed, despite the relatively small increase in viscosity, looking at the coherent vortical structures (*cf.* Figure 5.5b). Injected turbulence propagates downstream for about $1.6D$ and then almost disappears; the relevant Re_t is reduced down to about 3.75 by the increased kinematic viscosity (*cf.* Tabel 5.1). The few structures which are observed further downstream are reminiscent of Kelvin-Helmholtz instabilities generated in the jet's shear layer.

As it can be seen in Figure 5.6 by observing the typical size of the flame front's wrinkling, the lower part of the flame interacts mainly with the finer structures of the injected turbulence, whereas, further downstream interactions with bigger structures from the shear layer are dominant. Hence the importance of both mechanisms: lower Reynolds number, *i.e.*, higher temperature in the burnt gases in this case, would have laminarized the jet's shear layer and the flame front would have been almost perfectly smooth and conical with the base only slightly wrinkled.

The damping effect of temperature may be also noted by comparing the local curvature of the flame front at $c = 0.2$, *i.e.* $T \simeq 326$ K, (Figure 5.6a) and at $c = 0.8$ (Figure 5.6b), where the temperature is around 403 K.

5.3.2 $Re_D = 2000$ Round-Jet Simulation (F2)

When the Reynolds number is increased, as already mentioned, correct flame resolution translate in a requirement over the semi-aperture angle θ^* , hence, in order to keep the computational

⁶In order to allow some reduction in computational cost, while ensuring a sufficiently wide domain, the grid for test-cases F1 and F2 was stretched in the lateral direction with the maximum refinement toward the center. The computational grid for test-case F3 was stretched in the transverse direction and uniform in the spanwise direction (*i.e.* the direction of periodicity).

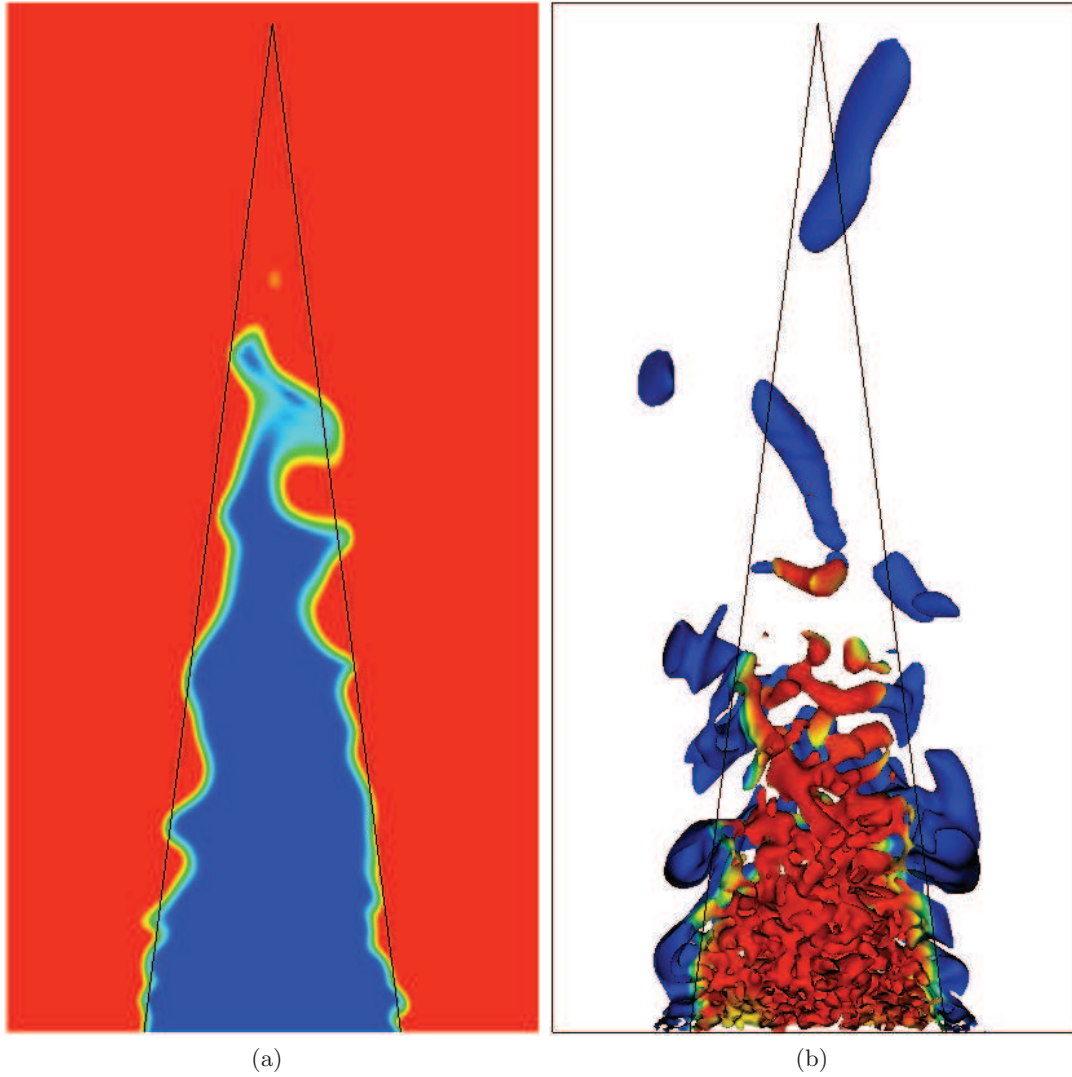


Figure 5.5: $Re_D = 600$ test-case F1. Map of progress variable c over an axial plane (a) and iso-surfaces of normalized $Q^* = 0.5$ colored by density (b). In (a): $c = 0$ colored in blue and $c = 1$ colored in red. In (b): $\rho/\rho_0 = 1$ colored in red and $\rho/\rho_0 = 0.7$ colored in blue ($\rho_0 = 1.174 \text{ kg/m}^3$). Black lines indicate $\theta^* = 7.2^\circ$.

cost reasonably low, it is necessary to switch to tubular shaped flames. At $Re_D = 2000$, a computational domain $4D$ long and $2D$ wide, with around 8.5 M nodes, allows a maximum θ^* of about 1.5° , these data referring to sufficiently resolved chemistry (*cf.* Table 5.1).

Figure 5.7 shows the map of progress variable c over an axial plane and the iso-surfaces of $Q^* = 0.5$, cut over the same plane, colored by the density. As expected, the increased Reynolds number allows turbulence to develop and propagate further downstream, despite the fact that, in this case, the temperature in the burnt gases is around 1500 K, with a consequent kinematic viscosity more than 10 times higher than in the fresh mixture.

Again, the reaction zone undergoes distortion due to the interactions between the injected

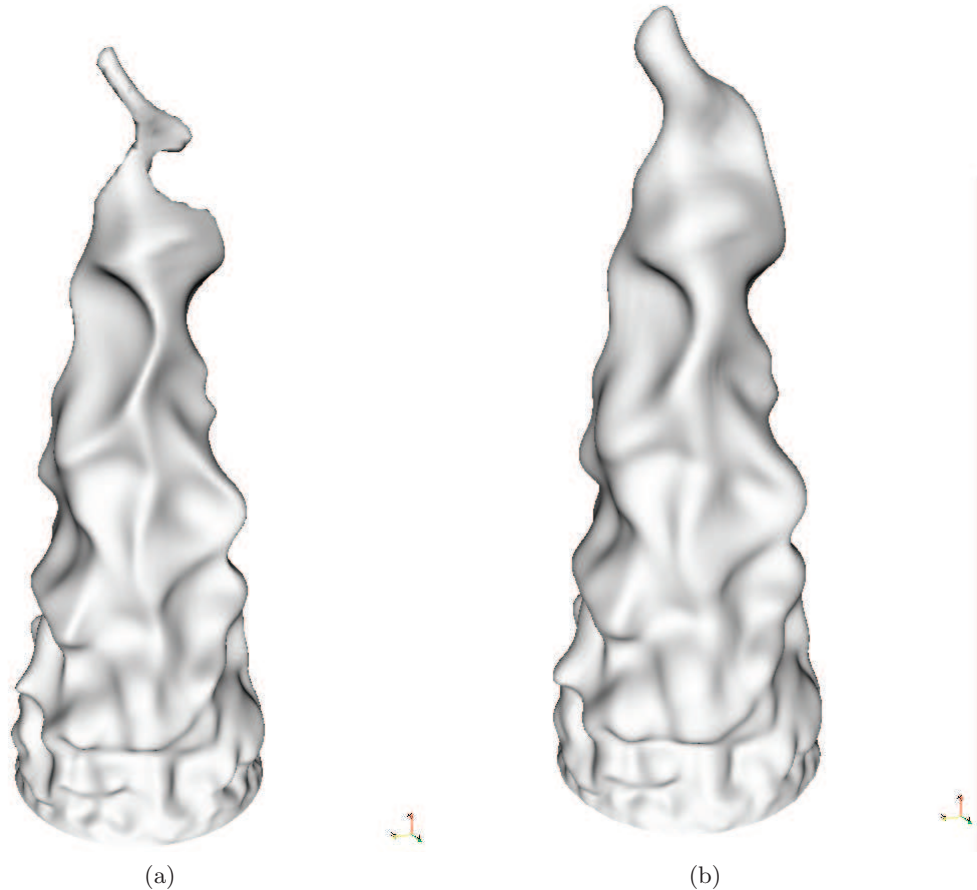


Figure 5.6: $Re_D = 600$ test-case F1. Iso-surfaces of progress variable $c = 0.2$ (a) and $c = 0.8$ (b).

turbulence and the instabilities generated within the jet's shear layer, the two mechanisms having quite different typical length-scales. The damping effect of temperature is now particularly strong, as it can be observed in Figure 5.8, where the flame front at 540 K is characterized by strong local curvature, whereas at 1260 K the surface appears much smoother.

Instantaneous cross-sections of the flame at various streamwise positions are depicted in Figure 5.9, where contours of $Q^* = 0.5$ (in black) are superimposed to the maps of progress variable. Close to inlet, the core of the flame is populated by a variety of coherent structures, coming from the inlet turbulence, which, interacting with the flame front, induce strong local curvature. The increased viscosity through the reaction zone, induce the reduction of local curvature due to dissipation. Few bigger structures are visible in the burnt gases' side; these last, according to Figure 5.7b are mostly related to the jet's shear layer development. Further downstream, small structures tend to disappear and, at $x_1/D = 3.0$, only few big structures are still visible. The flame front is now heavily distorted but the local curvature is much lower and reflects the typical size of the remaining coherent structures. Indeed, since the hot gases do not allow turbulent development of the jet itself (*i.e.*, there is no external forcing), on a reference frame moving with the flow, the situation may be considered similar to freely decaying

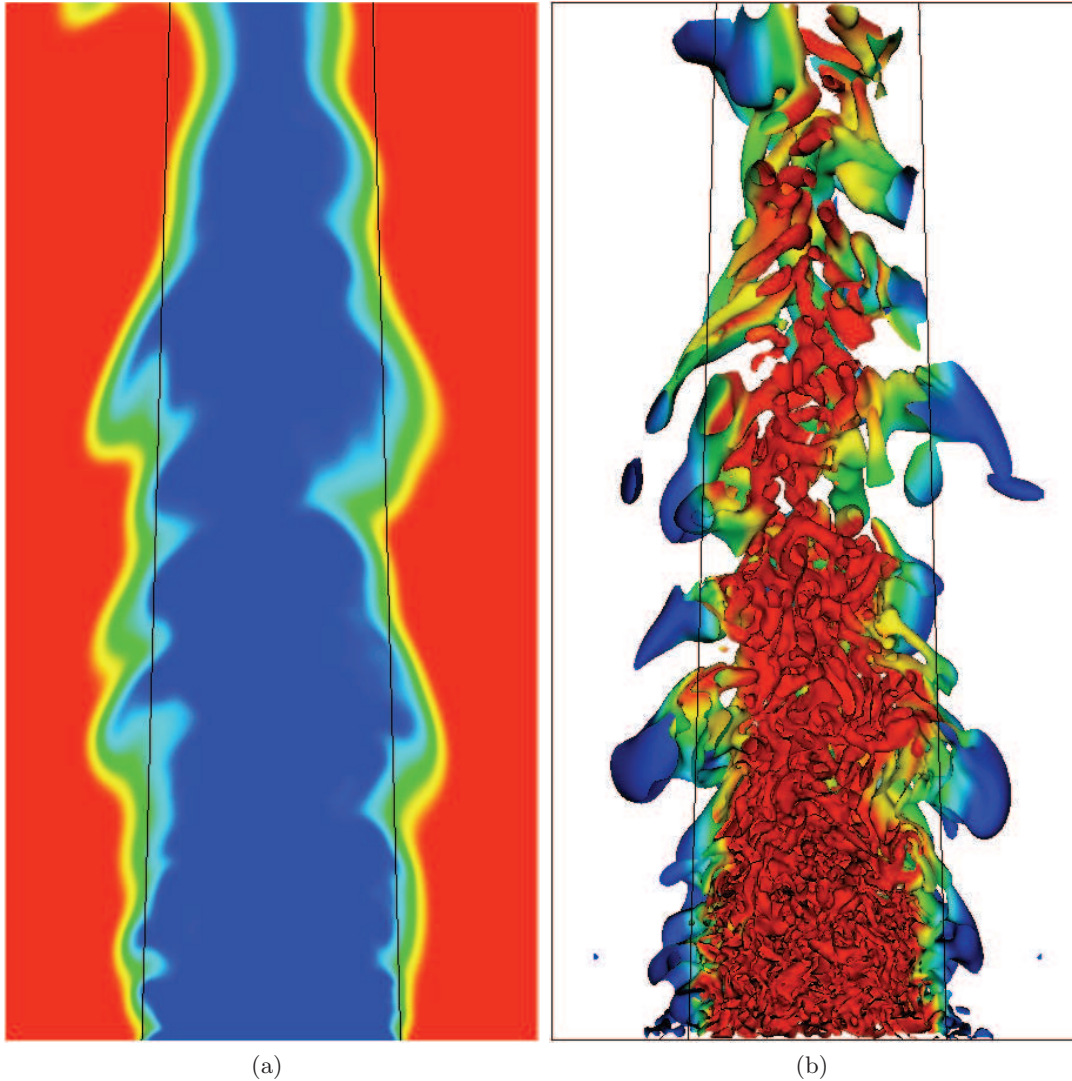


Figure 5.7: $Re_D = 2000$ test-case F2. Map of progress variable c over an axial plane (a) and iso-surfaces of normalized $Q^* = 0.5$ colored by density (b). In (a): $c = 0$ colored in blue and $c = 1$ colored in red. In (b): $\rho/\rho_0 = 1$ colored in red and $\rho/\rho_0 = 0.2$ colored in blue ($\rho_0 = 1.174 \text{ kg/m}^3$). Black lines indicate $\theta^* = 1.53^\circ$.

turbulence, where the total turbulent kinetic energy declines due to viscous dissipation, with the smallest eddies decaying fastest. This is the reason why, obtaining a highly wrinkled flame is so difficult: the high kinematic viscosity depletes any external forcing. The solution, clearly, is to increase Reynolds.

5.3.3 $Re_D = 4500$ Slot-Jet Simulation (F3)

The image of the wrinkled laminar flame by A. Yoshida [65], which has been described in Section 5.2.2 served as inspiration for this last test-case. Of course, according to chemistry

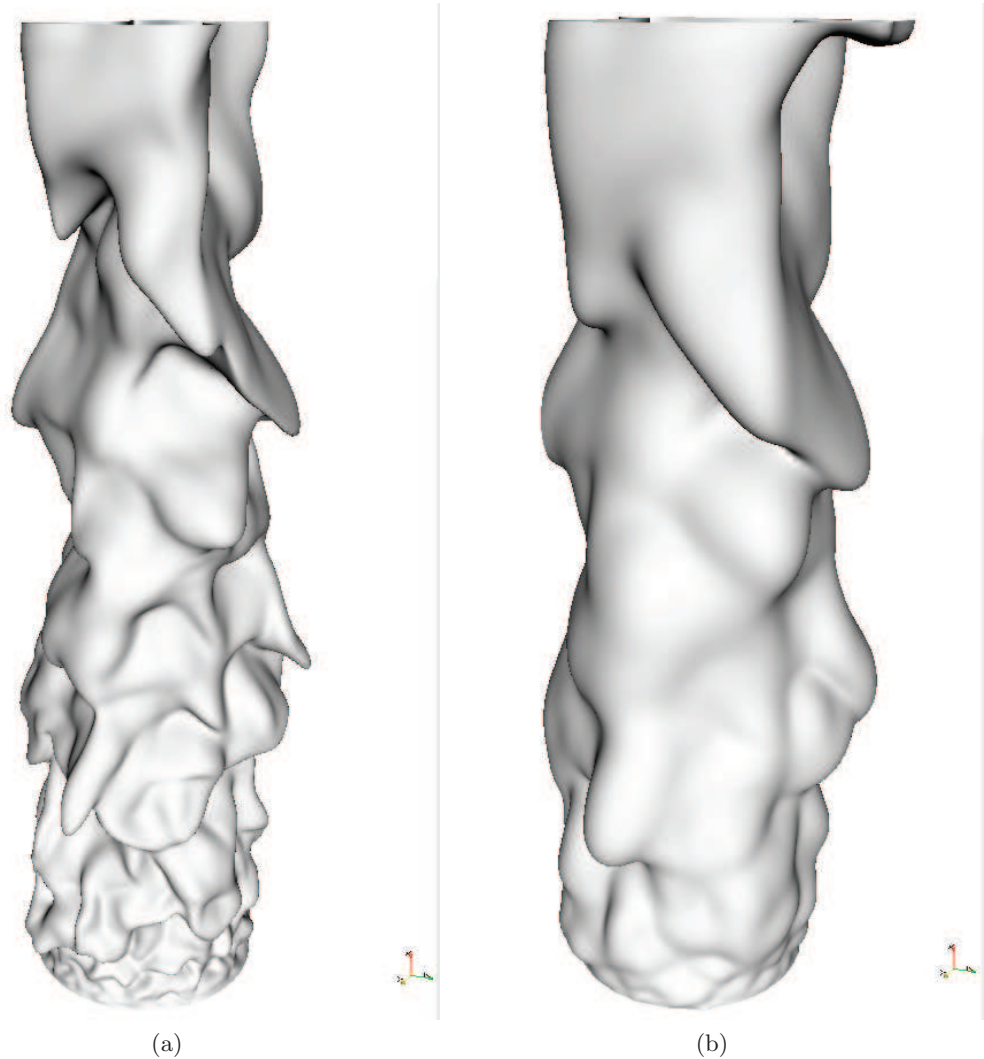


Figure 5.8: $Re_D = 2000$ test-case F2. Iso-surfaces of progress variable $c = 0.2$ (a) and $c = 0.8$ (b).

resolution issues already discussed, the semi-aperture angle θ^* was reduced from the 10° of the experiment to about 1.13° . Yet the computational grid was around 91 M nodes and the simulation required 4096 processors on an IBM Blue Gene/P machine. Moreover, it was decided to switch to a bi-dimensional configuration for reasons connected to the studies carried out during the CTR Summer Program 2008⁷, namely to check for the influence of anisotropies on the statistical behavior of the flame curvature's parameters. The details of the simulation are summarized in Table 5.1.

The general features of the flame are, again, represented in Figure 5.10 by means of the coherent vortical structures, colored by the density, and the flame front obtained from the

⁷The relevant proceedings are reported at the end of Part II, where the archival publications relevant to this thesis are collected.

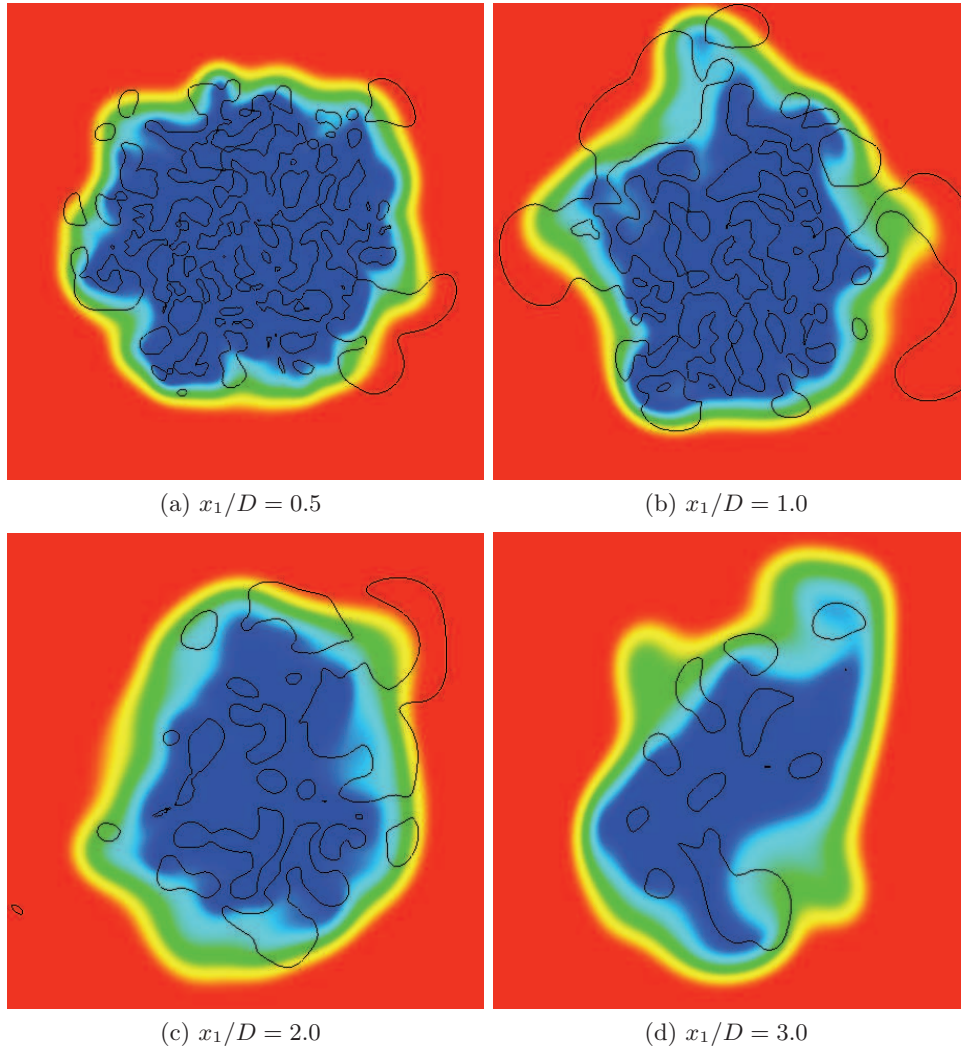


Figure 5.9: $Re_D = 2000$ test-case F2. Maps of progress variable over transversal sections at various heights. Black contours are iso-lines of $Q^* = 0.5$.

iso-surface of $c = 0.2$. Even if not shown in this case, the theoretical semi-aperture angle was confirmed by the simulation. Accordingly, the flame speed was well reproduced.

Again the two mechanisms of jet's instabilities and injected grid noise can be observed. The increased Reynolds number promotes, as expected, a wider spectrum of wave-lengths. Also note that the correlation length of the injected noise was 1.6 times lower than in the previous test. The ratio ℓ_0/δ_L , anyway, was the same.

Looking closer at the flame structure in Figure 5.11, nothing really new is observed with respect to the other two test-cases, except that now the flame is way more distorted, even on the hot side (*cf.* Figure 5.11b). After about $0.7D$ (note that the spanwise dimension is $1.3D$), the smallest scales coming from the inlet have almost disappeared. Jet's instabilities, which are visible in red (*i.e.*, within the hot gases) in Figure 5.11c, are damped out after about one diameter. What remains, again, is freely decaying turbulence that, this time, has increased

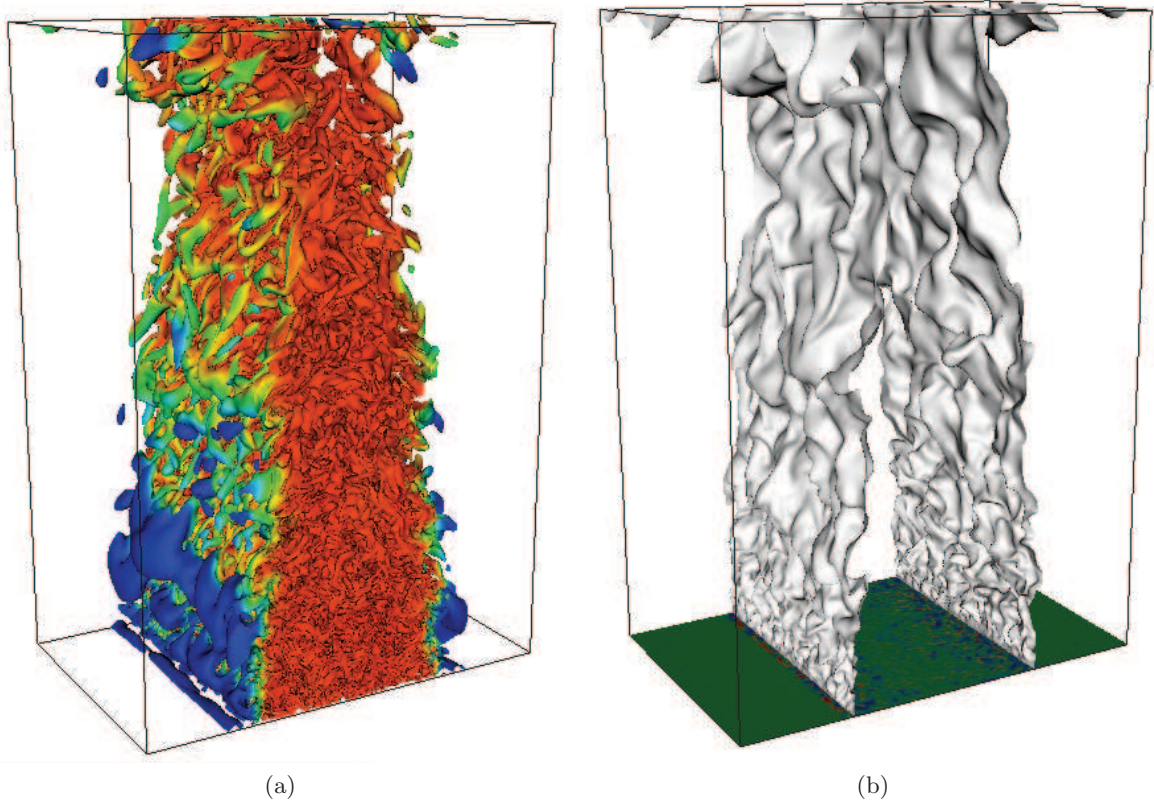


Figure 5.10: $Re_D = 4500$ test-case F3. Iso-surfaces of normalized $Q^* = 0.5$ colored by density (a) and iso-surfaces of progress variable $c = 0.2$ (b). In (b): $\rho/\rho_0 = 1$ colored in red and $\rho/\rho_0 = 0.2$ colored in blue ($\rho_0 = 1.174 \text{ kg/m}^3$).

“life” thanks to the higher Re_D . This fact is readily confirmed by analyzing the cross-sections in Figure 5.12 where, again, the iso-contours of $Q^* = 0.5$ are shown over the maps of progress variable.

It is reasonable to expect that a shorter flame, *i.e.*, a larger θ^* , for this Reynolds number, would have been significantly more distorted by earlier interaction with core turbulence. This notwithstanding, the qualitative examination of the DNS results is in fairly good agreement with the above mentioned wrinkled *laminar* (conical) flame.

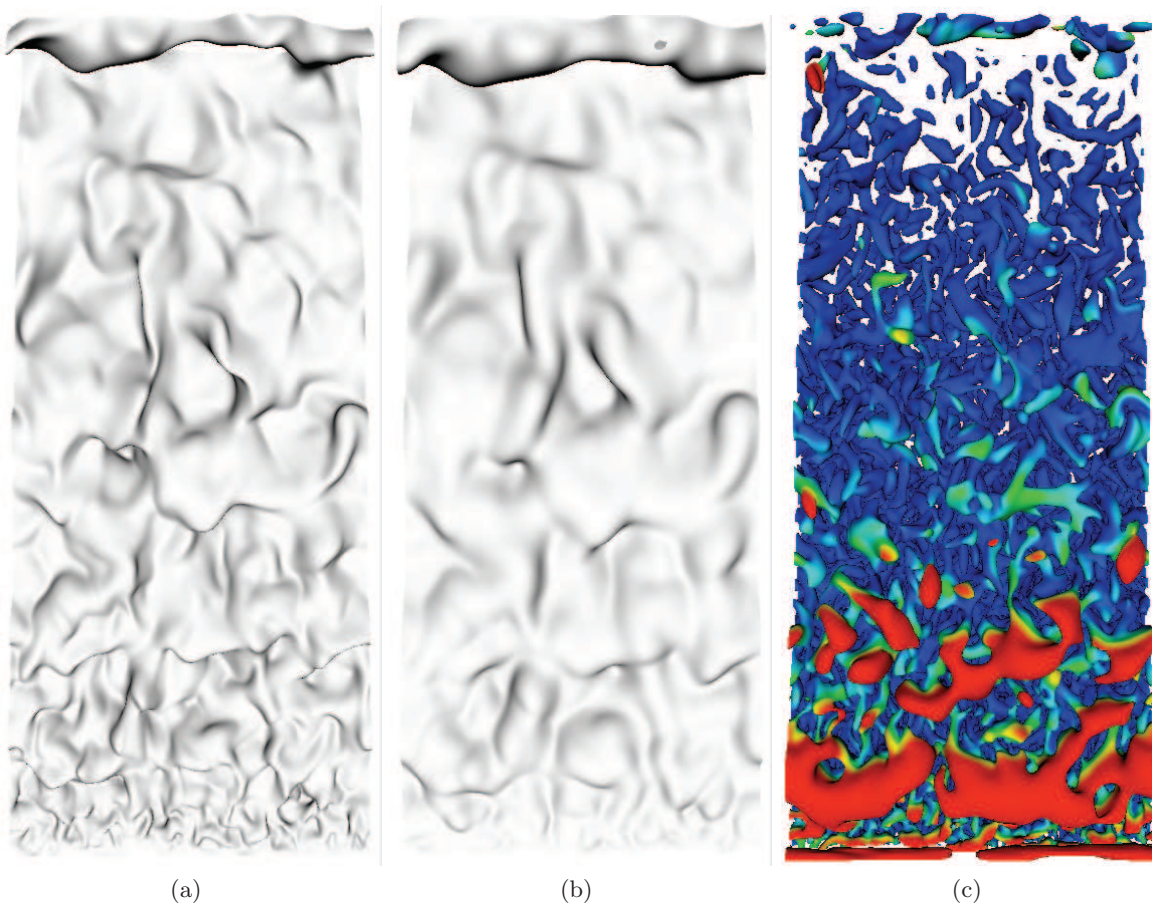


Figure 5.11: $Re_D = 4500$ test-case F3. Iso-surfaces of progress variable $c = 0.2$ (a), $c = 0.8$ (b) and $Q^* = 0.5$ colored by c (c).

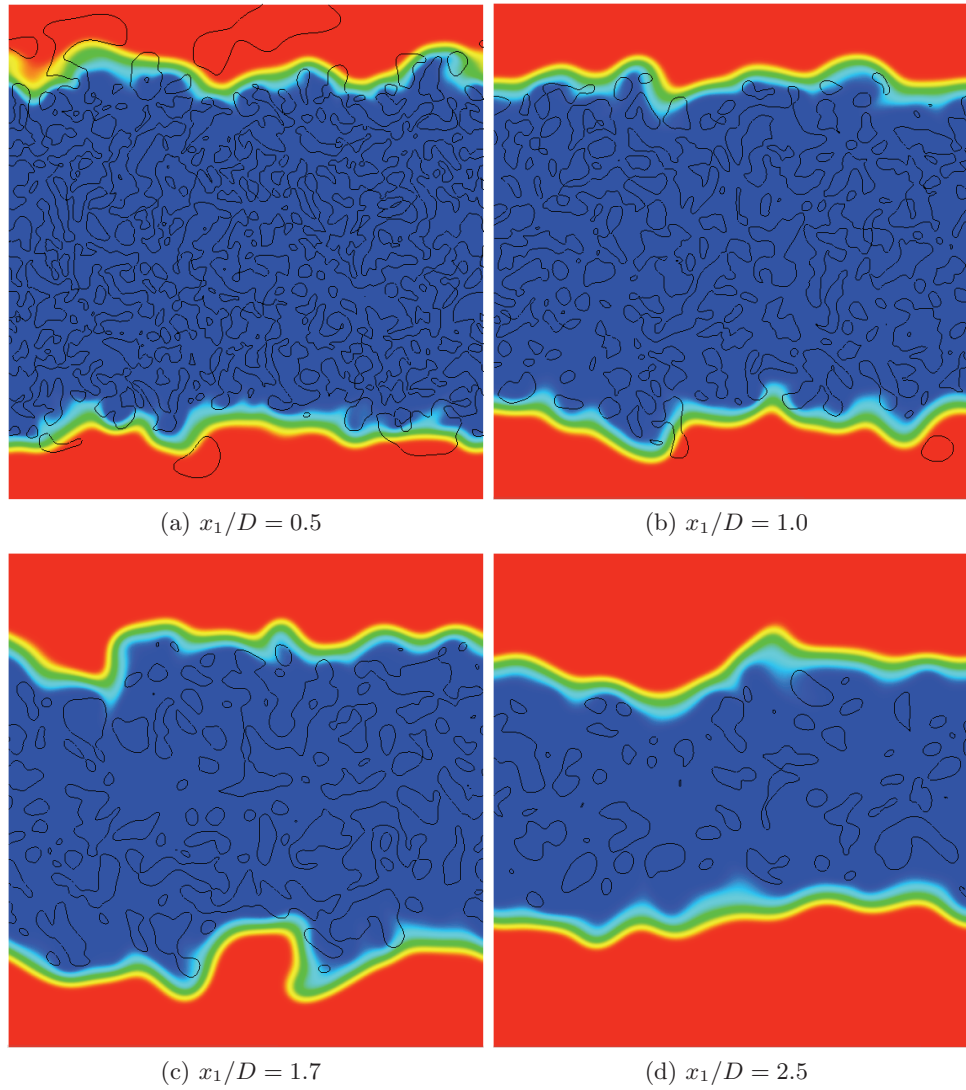


Figure 5.12: $Re_D = 4500$ test-case F3. Maps of progress variable over transversal sections at various heights. White contours are iso-lines of $Q^* = 0.5$.

Conclusions & Perspectives

Cette thèse, essentiellement axée autour de la Simulation Directe et aux Grandes Échelles des écoulements turbulents caractérisés par une faible compressibilité, peut être divisée en deux parties principales : (a) la formulation des conditions caractéristiques tridimensionnelles non-réfléchissantes basées sur le méthode NSCBC [58] et (b) la dérivation d'un modèle de sous-maille structurel, basé sur l'hypothèse de similarité [3, 4], capable de conserver un comportement asymptotique correct dans la région de proche paroi.

En ce qui concerne le premier point, une méthodologie, dénommée 3D-NSCBC [43], a été développée, tandis que, pour le deuxième point, le Modèle WALE-Similarity (ou WSM) a été présenté et testé sur un jet d'air impactant sur une paroi plane.

En prenant en compte les termes de convection et les gradients de pression transverse par rapport à la surface frontière du domaine de calcul, la méthode 3D-NSCBC a démontré sa capacité de reproduction fidèle de la tridimensionnalité de l'écoulement ; réduisant ainsi le niveau des perturbations numériques au bord, même lorsque l'écoulement est caractérisé par des structures tourbillonnaires très complexes. De plus, le niveau de contrôle sur les variables relaxées, typiques des conditions aux limites non-réfléchissantes, peut être amélioré, même si les coefficients de relaxation imposés sont très faibles.

À ce propos, la prise en compte des termes transverses engendre des problèmes de couplage des ondes caractéristiques se déplaçant le long des directions orthogonales, ainsi que la nécessité d'imposer des conditions de compatibilité, lorsque différentes typologies de frontières se rejoignent aux coins et aux arêtes du domaine de calcul. Des procédures systématiques pour résoudre le couplage des ondes, et des conditions de compatibilité, ont été développées et détaillées dans le 3^e Chapitre, en particulier, pour toutes les combinaisons des conditions d'entrée/sortie subsoniques et de paroi adiabatique. Plusieurs tests sur des configurations simplifiées et sur un jet libre turbulent ont été aussi présentés.

Au sujet des modèles de sous-maille pour la Simulation aux Grandes Échelles (SGE), la simulation d'un jet d'air impactant sur une paroi plane à deux différents nombres de Reynolds a mis en évidence les limites des modèles purement dissipatifs basés sur l'hypothèse de viscosité tourbillonnaire (*i.e.*, *eddy-viscosity*), qui : (a) en imposant les mêmes axes propres au tenseur des contraintes de sous-maille et au tenseur du taux de déformation, ne peuvent pas reproduire correctement les anisotropies des interactions de sous-maille ; (b) en utilisant l'hypothèse de

Boussinesq, ne peuvent pas, en général, donner une représentation correcte des interactions particulières de l'opérateur de filtrage, qui, habituellement, ne satisfait pas les propriétés des opérateurs de Reynolds. De cette dernière considération, dérive, par exemple, l'incapacité des modèles à viscosité tourbillonnaire de reproduire des événements locaux de transfert inverse d'énergie turbulente, *i.e. backscatter*, à moins de recourir à des procédures dynamiques qui, néanmoins, ont souvent besoin d'opérations de moyenne afin d'assurer la stabilité numérique (à ce propos, le modèle Dynamique Lagrangien [48] utilisé dans cette thèse ne peut en aucune manière engendrer du *backscatter*).

D'ailleurs, les modèles structuraux peuvent s'adapter de façon plus efficace au contexte de la SGE et démontrent généralement un degré très élevé de corrélation au niveau du tenseur. C'est pourquoi un modèle de similarité mixte employant un terme de viscosité tourbillonnaire de type WALE [53] a été proposé. Par cette formulation, on peut démontrer que le comportement asymptotique correct vers la paroi est conservé pour chacune des composantes du tenseur des contraintes de sous-maille. De plus, l'introduction des termes de Leonard croisés, typique de la formulation de similarité, a montré sa capacité de reproduction d'un transfert énergétique global correct, surtout en région de proche paroi. Cette propriété s'est révélée être un mécanisme clé pour la modélisation de la dynamique de la couche limite turbulente, notamment dans le cas de la configuration étudiée, qui a montré un taux très élevé de *backscatter* dans la région de stagnation et aussi dans la région du jet à la paroi.

Le comportement statistique du mélange du scalaire passif en région de proche paroi a été aussi brièvement analysé.

Pour finir, une application de la Simulation Numérique Directe au le cas d'une flamme pré-mélangée Bunsen turbulente a été détaillée. La méthode 3D-NSCBC a été adaptée pour prendre en compte la présence des termes source chimiques dans le calcul des amplitudes des ondes entrantes aux frontières dans le cas de conditions aux limites d'entrée/sortie subsoniques. Cette procédure est basée sur la définition des termes pseudo-transverses, et peut donc être aisément généralisée à la formulation présentée pour les coins et les arêtes. Par ailleurs, il a été démontré que la résolution d'une telle flamme peut représenter une contrainte bien plus forte que la résolution de la turbulence même. Par conséquent, la simulation directe avec un nombre de Reynolds relativement élevé, pour un coût de calcul raisonnable, a nécessité la réduction de l'angle de semi-ouverture du cône de la flamme, jusqu'à avoir une forme quasi-tubulaire.

6.1 Conclusions

This thesis, which is mainly concerned with Direct and Large-Eddy Simulation of turbulence, may be considered as a twofold work: (a) on one side, numerical aspects regarding the implementation of numerically transparent boundary conditions were addressed; (b) on the other side, a structural SGS model for LES of weakly compressible turbulent confined flows was proposed.

A three-dimensional procedure for characteristic boundary conditions at edges and corners was discussed. This very sensitive point of boundary conditions was found to be closely related to convection and pressure gradient developing in the direction parallel to boundary faces, also called transverse terms.

A method involving the inclusion of these transverse effects in the computation of the incoming wave amplitude variations was presented. This method, which is based on the NSCBC

approach [58], removes the original one-dimensional inviscid assumption that is, in general, too stringent to correctly deal with turbulent flows. The work was grounded on the method proposed by Yoo and Im [84], which, nonetheless, poses additional problems of wave coupling at the edges and corners of three-dimensional computational domains. Hence, a systematic procedure to solve edges and corners was presented and compatibility conditions for mixed boundaries were discussed.

The presented technique showed significant reduction of flow distortion and boundary reflection even when the configuration is characterized by high tridimensionality of the flow field, accompanied by obliquely propagating waves. The obtained 3D-NSCBC non-reflecting out-flow, in particular, is characterized by an additional relaxation parameter for transverse terms. On this regard, tests performed on different flow configurations demonstrated that, for the majority of the flows, transverse relaxation can be done toward identically zero terms and, in agreement with the findings of Yoo and Im [84], the optimal choice for the transverse relaxation parameter is, in general, related to the typical Mach number for the flow considered.

The proposed solution to the edge/corner wave coupling problem and the relevant compatibility conditions for connecting regions of different boundary types, revealed good numerical stability and low level of spurious boundary reflection for acoustic waves traveling toward the edges and corners of the computational domain, thus allowing high boundary transparency even when computing complex flows.

The 3D-NSCBC method is applicable to compressible turbulent flows in the full subsonic range and is then suitable for a wide range of flow configurations and engineering applications. The method was extended to chemically reacting flows and tested on DNS of turbulent Bunsen flames. The increased level of control over relaxed quantities, which may be achieved by accounting for chemical source terms in the computation of incoming waves, allowed the simulation of “tubular” flames crossing the boundary.

With regards to LES of weakly compressible turbulent flows, a WALE-Similarity mixed model was presented and tested on the impinging round-jet at Reynolds numbers 23000 and 70000. The difficulties of purely dissipative functional models based on the eddy-viscosity hypothesis, when dealing with such a complex flow, were addressed and the necessity to improve the modeling strategy by better accounting for the peculiar interaction terms arising from the use of non Reynolds operators was analyzed.

The eddy-viscosity term together with the modified Leonard tensor allows good representation of non-local interactions as well as local interactions near the cutoff length, these last being responsible for reverse energy transfer, a key mechanism in near-wall dynamics. The use of the WALE model [53], in particular, allows proper wall scaling of the wall shear stresses without the necessity of a dynamic procedure. Near wall scaling of each component of the SGS stress tensor was checked and the proposed model was found to correctly reproduce the average theoretical scaling within the viscous sub-layer.

The model was compared to the standard WALE model and a compressible implementation of the Lagrangian Dynamic Smagorinsky model [48] on the lower Reynolds number test-case on a relatively coarse grid. A significant improvement in the results in terms of second order moments was observed, especially in the near-wall region, where the other two models have a marked tendency to overestimate streamwise turbulent fluctuations due to excessive dissipation and, supposedly, incorrect azimuthal redistribution of turbulent energy.

On the higher Reynolds number test-case, the new model provided quite satisfactory results. The relatively low grid resolution used for such a high Reynolds number, made it necessary to

account for SGS contributions when comparing with experiments. By accounting for the SGS part, results were generally improved. Yet, the necessity to either increase near wall resolution or introduce an efficient model for the spherical part of the SGS tensor was observed for this Reynolds number.

Correct representation of energy backscatter was found to play an essential role for the estimation of the average sub-grid dissipation, especially when the computational grid does not allow for sufficient resolution in the near-wall region. In that case, it was found that energy backscatter by the SGS model may determine a sort of automatic compensation process for energy production events related to under-resolved near-wall dynamics. The impinging round-jet, in particular, was found to be extremely prone to show energy backscatter in the vicinity of the stagnation region. This fact would clearly explain the difficulties encountered by purely dissipative models in reproducing the early development of the wall jet region. Statistical properties of near wall scalar mixing and relevant qualitative features were also briefly investigated.

Alongside these two topics, Direct Numerical Simulations of a turbulent Bunsen flame at three different Reynolds numbers were performed. The inclusion of the chemical source terms within the 3D-NSCBC procedure to solve subsonic non-reflecting inflows and outflows was detailed. In particular, it was found that the formalism developed in the case of non-reacting flows may be conveniently extended to the case where reactions take place by simply defining pseudo-transverse terms that include the relevant source terms, as they appear in the characteristic formulation of the Navier-Stokes equations. This procedure allowed the simulation of tubular-shaped flames which cross the outflow boundaries without major problems of numerical stability.

Moreover, scaling criteria for the specific case under study were analyzed. It was found that the number of degrees of freedom, in space, of a conical Bunsen flame of specified height, *i.e.*, of specified semi-aperture angle, scale as the third power of the characteristic Reynolds number. Hence, in this specific case, the resolution of chemistry was found to be a more stringent requirement than the resolution of turbulence that, according to typical scaling criteria, would require at least a number of degrees of freedom of the order of the Reynolds number to the power of nine fourths, *i.e.* 2.25.

Considering the stabilizing effect connected to the increase of kinematic viscosity within the burnt gases, on the base of the above mentioned findings, DNS of turbulent Bunsen flames with a “reasonable” computational cost and with sufficiently high Reynolds number, *i.e.*, with sufficiently developed turbulence, required the reduction of the flame’s semi-aperture angle, thus leading to tubular-shaped configurations.

6.2 Perspectives

The present work has highlighted some interesting aspects that possibly would deserve further investigation. Although, as already mentioned in the first introductory chapter, numerical and modeling aspects should be considered as closely interconnected features of Computational Fluid Dynamics, considering the “dual” nature of the work described in this thesis, the possible relevant perspectives will be put forward here subdivided in two main groups: (a) boundary conditions and (b) LES modeling of compressible flows.

3D Characteristic Boundary Conditions, as it has been demonstrated may represent a

powerful strategy for dealing with Direct and Large-Eddy Simulation of turbulent flows. The reason is essentially twofold and pertains to the necessity of preventing numerical perturbations that high-order numerical schemes would further amplify and to the attainable reduction in computational effort that the reduction of computational domain size—permitted by the use of sufficiently “transparent” frontiers—would imply.

The 3D-NSCBC procedure has proven to be an efficient and relatively simple method to produce low boundary reflection when complex flows, with cylindrical and spherical symmetries, are computed within cartesian orthogonal grids. Yet, the necessity for an additional parameter, namely the transverse relaxation coefficient β_t , has been underlined in relation with subsonic non-reflecting outflows.

Although the majority of flows do not pose particular issues on this regard, for certain configurations, a proper choice of this parameter may be crucial (*cf.* the spherical pressure wave test). The DNS of turbulent Bunsen flames for instance, highlighted the necessity for a properly chosen value of β_t when the reactive front crosses the boundary. On the other hand, a certain dependency of this parameter on the Mach number was observed and this feature is, indeed, quite promising: the transverse relaxation parameter could be in principle automatically determined by the flow itself.

Further investigation on the exact mathematical and physical meaning of the transverse relaxation parameter in order to better establish the envisaged properties would be advisable.

Alongside this aspect, the extension of the edge/corner strategy to other different types of Dirichlet boundary conditions, as well as to Neumann boundary problems would be of sure interest.

In Chapter 5, the possible extension of 3D-NSCBC strategy to the solution of reactive flows was anticipated in the case of a quite simplified description of chemistry. The use of more complex combustion models, in consideration of the extremely delicate nature of the interconnections between characteristic boundary conditions and density variations, would require better understanding and further investigation.

The WALE-Similarity Model has demonstrated good performances, especially in consideration of the complexity of the analyzed configuration and the relatively simple implementation.

Nonetheless, the proposed SGS model entails a series of assumption and approximations which limit its range of applicability. Notably, the inclusion of part of the trace of the sub-grid scale stress tensor within the reduced macropressure and macrotemperature imposes a limit on the maximum SGS Mach number, hence a limit to the level of compressibility that the model can take charge of.

In consideration of the increasing interest in transonic and hypersonic turbulent flows, for instance, removing any limitation on the Mach number would represent an attractive perspective from the engineering point of view.

The necessity of modeling the isotropic part of the sub-grid contribution has been already mentioned. On the other hand, existing models often fail to live up to expectations [17, 72] and further investigation is still needed. Moreover, when the flow is characterized by strong interactions with boundary layers, Smagorinsky-type models [86] do not possess the correct asymptotic behavior, this fact being supposedly a limiting factor. Hence, the generalization of the WSM model to the fully compressible case, though non-

trivial, should involve a more suitable definition of the modeled spherical part of the SGS true Reynolds term.

Other approximations were made with particular regard to the SGS energy flux term. The neglected terms, in general, are not supposed to have strong impact to the flow, anyway some of them, notably the SGS turbulent diffusion term $\overline{\rho}\mathcal{D}_k$, may be comparable with the divergence of the SGS heat flux [46]. Better understanding of the physical relevance of similar unclosed terms, especially in the presence of significant density fluctuations, is clearly of great interest in the perspective of applications to high Mach number flows.

A final remark needs to be made with regards to the discrete explicit filter operation. The WSM model presented in this thesis makes use of a discrete box filter in physical space, which was implemented resorting to the trapezoidal rule.

It has been shown that this kind of implementation may not be particularly accurate in reproducing the expected filter width [45]. Although the impact of this kind of inaccuracy on a similarity mixed model is, supposedly, considerably less influential if compared to the dynamic procedure, where a discrepancy between the assumed and effective test filter size introduces a systematic error, more insight on this regard would be clearly advisable, as well as on the possibility to implement more accurate discrete filtering techniques in the near-wall region.

Part II

Archival Publications

G. Lodato, P. Domingo and L. Vervisch. Three-dimensional boundary conditions for Direct and Large-Eddy Simulation of compressible viscous flows, *Journal of Computational Physics*, **227(10)**: pp. 5105–5143 (2008).



Three-dimensional boundary conditions for direct and large-eddy simulation of compressible viscous flows

Guido Lodato^{*}, Pascale Domingo, Luc Vervisch

*INSA – Rouen, UMR-CNRS-6614-CORIA, Campus du Madrillet, Avenue de l'Université, BP 8,
76801 Saint Etienne du Rouvray Cedex, France*

Received 24 September 2007; received in revised form 18 January 2008; accepted 22 January 2008
Available online 7 February 2008

Abstract

Navier–Stokes characteristic boundary conditions (NSCBC) usually assume the flow to be normal to the boundary plane. In this paper, NSCBC is extended to account for convection and pressure gradients in boundary planes, resulting in a 3D-NSCBC approach. The introduction of these additional transverse terms requires a specific treatment for the computational domain's edges and corners, as well as a suited set of compatibility conditions for boundaries joining regions associated to different flow properties, as inlet, outlet or wall. A systematic strategy for dealing with edges and corners is derived and compatibility conditions for inlet/outlet and wall/outlet boundaries are proposed. Direct numerical simulation (DNS) tests are carried out on simplified flow configurations at first. 3D-NSCBC brings a drastic reduction of flow distortion and numerical reflection, even in regions of strong transverse convection; the accuracy and convergence rate toward target values of flow quantities is also improved. Then, 3D-NSCBC is used for large-eddy simulation (LES) of a free jet and an impinging round-jet. Edge and corner boundary treatment, combining multidirectional characteristics and compatibility conditions, yields stable and accurate solutions even with mixed boundaries characterized by bad posedness issues (e.g. inlet/outlet). LES confirms the effectiveness of the proposed boundary treatment in reproducing mean flow velocity and turbulent fluctuations up to the computational domain limits.

© 2008 Elsevier Inc. All rights reserved.

Keywords: Non-reflecting boundary conditions; Compressible flows; Direct numerical simulation; Large-eddy simulations

1. Introduction

The treatment of boundary conditions is one of the most recurrent issues in computational fluid dynamics. Compressible solvers' accuracy, in general, is strongly sensitive to boundary solution, which may be spoiled by spurious numerical reflections generated at open boundaries. This motivates the necessity for strategies to reduce reflection and set up transparent boundary conditions.

^{*} Corresponding author.

E-mail addresses: guido.lodato@coria.fr, guido.lodato@gmail.com (G. Lodato), pascale.domingo@coria.fr (P. Domingo), luc.vervisch@coria.fr (L. Vervisch).

The boundary conditions provide a way to anticipate the flow behavior at the very limit of the computational domain. The flow properties at the boundaries must derive from the knowledge of the inside of the computational domain, coupled with some approximations of the outside flow features. Departures between inside and boundary flows add numerical noise to the solutions. High-order numerical schemes widely used in direct numerical simulation (DNS) and large-eddy simulation (LES), do not dissipate the spurious modes that may be generated at the boundaries; the boundary conditions must therefore be designed so that physically correct solutions are produced, while minimizing the amplitude of any extraneous perturbation added to the flow.

The situation gets even more complicated when dealing with turbulent flows, where an excess of numerical reflection at open boundaries can significantly affect important physical flow properties, such as vorticity. As opposed to Reynolds-averaged Navier–Stokes computations (RANS), in LES a wide range of length and time scales is resolved and transported by the flow; the open boundaries are therefore, invested with a complex set of sound and entropy waves and convected vorticity. Any excess in numerical reflection can lead to the buildup of spurious oscillations, which, being superposed to the computed solution, negatively affect the physical properties of the flow itself.

Several approaches have been proposed to tackle boundary conditions. Many of them are oriented toward the definition of transparent frontiers for computational aero-acoustics (CAA), where the high standards in this regard, make the task particularly challenging (see [19,9,6,2] for review and applications). Among them, techniques based on characteristic waves have motivated much attention. Initially developed for hyperbolic systems of Euler equations, these approaches decompose the flow in terms of characteristic waves traveling in the direction normal to the boundary, thus reducing the boundary problem to a suitable imposition of the incoming waves. The identification of incoming waves allows, in principle, a direct control over boundary reflection, as the boundary condition can be designed to prevent incoming perturbations [21,22] or to damp their amplitude while allowing smooth transients [15]. An extension to the Navier–Stokes equations has been thoroughly discussed by Poinso and Lele [12], who have developed a systematic approach to account for viscous terms, known as Navier–Stokes characteristic boundary conditions (NSCBC). The method has been extended to multicomponent reactive flows [1,11] with different choices of primitive variables along with the inclusion of chemical source terms at the domain's frontiers [17]. Polifke et al. [13] proposed a reduction of the reflection coefficient for low-frequency normal incident waves, using a “plane masking” approach for the linear relaxation term. A low Mach number expansion has been discussed by Prosser [14], in order to decouple convective and acoustic effects, thus allowing non-reflective conditions for the acoustic length scales.

These methods mostly rely on the assumption that the flow at the boundary can be regarded as locally one-dimensional, aligned with the normal to the boundary. The incoming waves are therefore computed resorting to the so-called LODI system, which directly derives from the Navier–Stokes equations written for primitive variables in characteristic form. The terms involving derivatives in the directions defining the local boundary plane (convection, pressure gradient and viscous fluxes) are then computed from the interior of the computational domain, but without any specific coupling with the boundary treatment. In the following, these in-plane directions are called ‘transverse directions’ and the related terms are called ‘transverse terms’. The single-dimensionality assumption, combined with transverse terms computed from the known interior, has proven to perform well when the flow is almost aligned orthogonally to the boundary. Nevertheless, flow distortion and high reflection appear when the flow crosses the boundary along different directions. The role played by the transverse terms in these distortions has been carefully identified by Yoo et al. [24], who proposed a modification to the NSCBC approach for two-dimensional turbulent counterflow flames. They show that an appropriate treatment of the transverse terms in the computation of incoming waves improves the accuracy and convergence rate toward target values for selected relaxed quantities, while reducing flow distortion even in regions characterized by strong transverse convection.

When transverse effects are included in three-dimensional computation of incoming waves, the problem arises on how to enforce proper boundary conditions on the edges and the corners of the computational domain. As discussed by Valorani and Favini [23], transverse terms on edges and corners are coupled with characteristic waves traveling along directions orthogonal to adjacent boundaries. Therefore, three-dimensional characteristic coupled waves must be considered. Furthermore, when different types of boundary conditions have to be enforced, it is in general necessary to prescribe compatibility conditions for those boundary conditions whose well-posedness is not inherently ensured (e.g. inlet/outlet boundary conditions where veloc-

ity, temperature and pressure are simultaneously imposed). Not much on this regard can be found in literature and the formulation of boundary conditions for edges and corners remains a feature somehow related to each specific problem.

The objective of this paper is threefold. First the NSCBC improvement proposed by Yoo et al. [24], who included transverse terms in the boundary analysis, is extended to three-dimensional flows. A systematic procedure to deal with three-dimensional computational domain's edges and corners is then proposed. Finally, compatibility conditions for inlet/outlet and wall/outlet nodes are presented. The resulting 3D-NSCBC approach is tested on simplified configurations. LES results of a turbulent free jet and a turbulent impinging round-jet are also reported. For the sake of clarity, all the details of the three-dimensional characteristic formulation leading to the explicit derivation of the equations for the edges and corners solution are recalled in [Appendix A](#).

2. Governing equations

The dynamics of compressible viscous flow is described by the Navier–Stokes equations, which impose the conservation of mass, momentum and energy within the fluid element. In the present case, the system is augmented with an additional transport equation for a passive scalar Z (diffusing according to the Fick law), which carries informations on turbulent scalar mixing. In cartesian coordinates (with the Einstein summation convention) the system of equations reads

$$\frac{\partial \rho}{\partial t} + \frac{\partial}{\partial x_i} (m_i) = 0, \quad (1)$$

$$\frac{\partial m_i}{\partial t} + \frac{\partial}{\partial x_j} (m_i u_j) + \frac{\partial p}{\partial x_i} = \frac{\partial \tau_{ij}}{\partial x_j} \quad (i = 1, 2, 3), \quad (2)$$

$$\frac{\partial \rho E}{\partial t} + \frac{\partial}{\partial x_i} [(\rho E + p) u_i] = \frac{\partial}{\partial x_i} (u_j \tau_{ij}) - \frac{\partial q_i}{\partial x_i}, \quad (3)$$

$$\frac{\partial \rho Z}{\partial t} + \frac{\partial}{\partial x_i} (\rho Z u_i) = \frac{\partial}{\partial x_i} \left(\rho D \frac{\partial Z}{\partial x_i} \right), \quad (4)$$

where ρ is the fluid mass density, p is the thermodynamic pressure, $m_i = \rho u_i$ is the momentum density along the direction x_i and ρE is the total energy density (kinetic + thermal); under the assumption that the fluid is Newtonian and described by the ideal single-component gas law, the above system is closed by the following relations:

$$\frac{p}{\rho} = \mathcal{R} T, \quad (5)$$

$$\rho E = \frac{1}{2} \rho u_k u_k + \frac{p}{\gamma - 1}, \quad (6)$$

$$A_{ij} = \frac{1}{2} \left(\frac{\partial u_i}{\partial x_j} + \frac{\partial u_j}{\partial x_i} \right) - \frac{1}{3} \delta_{ij} \frac{\partial u_k}{\partial x_k}, \quad (7)$$

$$\tau_{ij} = 2\mu A_{ij}. \quad (8)$$

Here, T is the absolute temperature, \mathcal{R} is the gas constant \mathcal{R}^*/M_w , where $\mathcal{R}^* = 8.32 \text{ J}/(\text{mol K})$ and M_w is the gas molar weight; $\gamma = c_p/c_v$ is the ratio between specific heat capacities at constant pressure and constant volume, which, in the present case, are expressed as

$$c_v = \frac{\mathcal{R}}{\gamma - 1}, \quad (9)$$

$$c_p = c_v + \mathcal{R}. \quad (10)$$

The dynamic viscosity of the fluid μ is expressed by the Sutherland's law:

$$\mu(T) = \mu_{\text{ref}} \left(\frac{T}{T_{\text{ref}}} \right)^{3/2} \frac{T_{\text{ref}} + S}{T + S}. \quad (11)$$

Finally, the heat flux along x_i , namely q_i , is described by the Fourier law, while the thermal conductivity λ and the diffusion coefficient D are expressed from the dynamic viscosity, the Prandtl and Schmidt numbers:

$$q_i = -\lambda \frac{\partial T}{\partial x_i}, \quad \lambda = \frac{\mu c_p}{Pr}, \quad D = \frac{\mu}{\rho Sc} \quad (12)$$

(see Table 2 for a summary of the parameters' values used for the test-cases presented in the present paper).

3. Three-dimensional NSCBC

In NSCBC [12] the Navier–Stokes equations are written in their characteristic form to make explicit their dependency on the acoustic waves traveling across the boundary. Characteristic waves are represented by their amplitude time variations \mathcal{L}_i , \mathcal{M}_i and \mathcal{N}_i , corresponding to the three physical-space directions (see Appendix A for details). The waves propagate in such a way that some of them leave the domain, while the others enter from outside. Incoming waves must be specified to close the boundary problem, as the outgoing ones can be computed from interior points and one-sided differences by directly applying their definition (Eqs. (A.16), (A.26) and (A.37)). The NSCBC approach prescribes that all the incoming wave amplitudes are imposed under the hypothesis that the flow at the boundary can be regarded as locally one-dimensional and inviscid. The resulting LODI system (A.20) is used to translate physical boundary conditions, expressed in terms of time derivatives of the primitive variables, into analytical relations involving the wave amplitude variations, such that the unknown incoming ones can be computed [12]. Once all the wave amplitudes are known, balance equations are used to advance the solution in time ((A.17) or (A.18) if the solver integrates the equations in conservative form).

When the flow is strongly three-dimensional at boundaries, the LODI assumption becomes too restrictive to keep boundary reflection at an acceptable level and nonphysical flow distortions appear, especially in regions where the flow is not aligned with the direction normal to the boundary. Furthermore, the pressure and any other relaxed quantity cannot reach the relevant physical target value in regions where strong convection in the boundary plane exists. Improved results are obtained by including in the computation of incoming wave amplitudes the transverse terms, namely convection and pressure gradients developing in the boundary plane [24].

Away from edges and corners of the computational domain, transverse terms can be evaluated from the computed solution using interior points. This direct approach, indeed, does not pose additional issues for inlet boundaries but, as already mentioned by Yoo et al. [24], can lead to serious numerical instabilities at outflow boundaries. One effective remedy for this is to add a small relaxation toward a reference value for the transverse terms, thus introducing a transverse damping coefficient β . As it will be shown when presenting results from selected test-cases, an expression can be proposed to relate β to flow properties and dynamically adjust this additional parameter.

At edges and corners of three-dimensional simulations a specific treatment is, however, needed. At these locations, transverse terms in a given boundary plane relate to characteristic waves traveling along directions that are orthogonal to adjacent boundary planes. The corresponding characteristic waves become coupled, leading to the need for a 3D-NSCBC approach.

The boundary treatment is first discussed for nodes away from edges and corners, then a specific method is proposed for edges and corners. In all the developments below, well-posedness of boundary conditions for Navier–Stokes equations is ensured following the approach used by Poinso and Lele [12]: inviscid relations, corresponding to Euler boundary conditions, are first obtained and the correct number of boundary conditions for the Navier–Stokes equations is then achieved supplying additional viscous conditions. For each boundary type, the modification proposed in the present paper does not affect viscous conditions, which are then identical to those used by Poinso and Lele.

3.1. Face boundaries

The solution at a face boundary is advanced in time using the Navier–Stokes equations (A.17) or (A.18). These equations have been written in terms of wave amplitudes \mathcal{L}_i .

For a boundary that is orthogonal to x_1 , the \mathcal{L}_i are obtained from their relations with time derivative of primitive variables, which are given by the system including transverse terms (in plane pressure gradient and convection) obtained from Eq. (A.17) by neglecting the viscous and diffusive terms \mathbf{D} only:

$$\begin{cases} \frac{\partial \rho}{\partial t} + \frac{1}{c^2} [\mathcal{L}_2 + \frac{1}{2}(\mathcal{L}_5 + \mathcal{L}_1)] - \mathcal{T}_1 = 0, \\ \frac{\partial u_1}{\partial t} + \frac{1}{2\rho c}(\mathcal{L}_5 - \mathcal{L}_1) - \mathcal{T}_2 = 0, \\ \frac{\partial u_2}{\partial t} + \mathcal{L}_3 - \mathcal{T}_3 = 0, \\ \frac{\partial u_3}{\partial t} + \mathcal{L}_4 - \mathcal{T}_4 = 0, \\ \frac{\partial p}{\partial t} + \frac{1}{2}(\mathcal{L}_5 + \mathcal{L}_1) - \mathcal{T}_5 = 0, \\ \frac{\partial Z}{\partial t} + \mathcal{L}_6 - \mathcal{T}_6 = 0 \end{cases} \quad (13)$$

with the transverse contribution:

$$\mathcal{T} = \begin{pmatrix} -\frac{\partial m_t}{\partial x_t} \\ -u_t \frac{\partial u_1}{\partial x_t} \\ -u_t \frac{\partial u_2}{\partial x_t} - \frac{1}{\rho} \frac{\partial p}{\partial x_2} \\ -u_t \frac{\partial u_3}{\partial x_t} - \frac{1}{\rho} \frac{\partial p}{\partial x_3} \\ -u_t \frac{\partial p}{\partial x_t} - \gamma p \frac{\partial u_t}{\partial x_t} \\ -u_t \frac{\partial Z}{\partial x_t} \end{pmatrix} \quad (t = 2, 3). \quad (14)$$

An alternative definition of \mathcal{T} , using transverse fluxes computed on conservative variables, is given in Appendix B. The waves \mathcal{L}_i are determined from this system, once physical boundary conditions are provided to approximate $\partial \rho / \partial t$, $\partial \mathbf{u} / \partial t$, $\partial p / \partial t$, $\partial Z / \partial t$. These physical boundary conditions are now discussed on the basis of Eq. (13) reorganized in terms of characteristic variables:

$$\begin{cases} (\frac{\partial p}{\partial t} - \rho c \frac{\partial u_1}{\partial t}) + \mathcal{L}_1 - \mathbb{T}_1^1 = 0, \\ (c^2 \frac{\partial p}{\partial t} - \frac{\partial p}{\partial t}) + \mathcal{L}_2 - \mathbb{T}_1^2 = 0, \\ \frac{\partial u_2}{\partial t} + \mathcal{L}_3 - \mathbb{T}_1^3 = 0, \\ \frac{\partial u_3}{\partial t} + \mathcal{L}_4 - \mathbb{T}_1^4 = 0, \\ (\frac{\partial p}{\partial t} + \rho c \frac{\partial u_1}{\partial t}) + \mathcal{L}_5 - \mathbb{T}_1^5 = 0, \\ \frac{\partial Z}{\partial t} + \mathcal{L}_6 - \mathbb{T}_1^6 = 0, \end{cases} \quad (15)$$

where \mathbb{T}_k^m indicates a characteristic transverse term in the plane perpendicular to x_k relevant to the m th characteristic variable

$$\begin{cases} \mathbb{T}_1^1 = \mathcal{T}_5 - \rho c \mathcal{T}_2, \\ \mathbb{T}_1^2 = c^2 \mathcal{T}_1 - \mathcal{T}_5, \\ \mathbb{T}_1^3 = \mathcal{T}_3, \\ \mathbb{T}_1^4 = \mathcal{T}_4, \\ \mathbb{T}_1^5 = \mathcal{T}_5 + \rho c \mathcal{T}_2, \\ \mathbb{T}_1^6 = \mathcal{T}_6. \end{cases} \quad (16)$$

3.1.1. Subsonic non-reflecting outflow

The physical boundary condition, which links primitive variables to wave amplitudes, is obtained from the pressure relaxation condition proposed by Rudy and Strikwerda [15] with an additional transverse relaxation term as discussed by Yoo et al. [24]. The waves velocities are given by Eqs. (A.8)–(A.10) and depending on their sign, \mathcal{L}_i are entering (unknown and needing an equation to be determined) or leaving the domain

(known). For boundaries orthogonal to x_1 , depending on their location, the unknown incoming wave is either \mathcal{L}_1 (at $x_1 = L_x$) or \mathcal{L}_5 (at $x_1 = 0$). The relevant boundary condition can be conveniently expressed as follows:

$$\left(\frac{\partial p}{\partial t} + \varsigma \rho c \frac{\partial u_1}{\partial t}\right) + \sigma \frac{c(1 - \mathcal{M}^2)}{L_x} (p - p_\infty) - \beta(\mathbb{T}_1^\phi - \mathbb{T}_{1,\text{ex}}^\phi) = 0, \quad (17)$$

where σ is the pressure relaxation coefficient, \mathcal{M} is the maximum Mach number, L_x is the characteristic size of the computational domain along x_1 and $\beta \in [0 : 1]$ is a transverse damping parameter. ς is a function which sets the correct sign for the velocity term depending on the value of the wave index ϕ :

$$\varsigma(\phi) = \frac{\phi - 1}{2} - 1 = \begin{cases} -1 & \text{if } \phi = 1, \\ +1 & \text{if } \phi = 5. \end{cases} \quad (18)$$

For most free shear flows, the boundary condition is expected to well behave with $\mathbb{T}_{1,\text{ex}}^\phi = 0$, as shown in the next section. However, when an analytical steady solution of the flow is known at the boundary, the target value of the transverse term $\mathbb{T}_{1,\text{ex}}^\phi$ is obtained applying equations (14) and (16):

$$\Rightarrow \mathbb{T}_{1,\text{ex}}^\phi = -\hat{u}_t \frac{\partial \hat{p}}{\partial x_t} - \gamma \hat{p} \frac{\partial \hat{u}_t}{\partial x_t} - \varsigma \hat{\rho} \hat{c} \hat{u}_t \frac{\partial \hat{u}_1}{\partial x_t} \quad (t = 2, 3), \quad (19)$$

where the (\cdot) accent indicates the known analytical solution for the target flow.

Combining Eq. (17) with the corresponding characteristic equation from system (15), the unknown incoming wave becomes

$$\mathcal{L}_\phi = \sigma \frac{c(1 - \mathcal{M}^2)}{L_x} (p - p_\infty) + (1 - \beta)\mathbb{T}_1^\phi + \beta\mathbb{T}_{1,\text{ex}}^\phi \quad (20)$$

with

$$\mathbb{T}_1^\phi = \mathcal{T}_5 + \varsigma \rho c \mathcal{T}_2. \quad (21)$$

Navier–Stokes boundary conditions are obtained by complementing the above inviscid condition with the following viscous conditions:

$$\frac{\partial \tau_{12}}{\partial x_1} = \frac{\partial \tau_{13}}{\partial x_1} = \frac{\partial q_1}{\partial x_1} = \frac{\partial}{\partial x_1} \left(\rho D \frac{\partial Z}{\partial x_1} \right) = 0. \quad (22)$$

3.1.2. Subsonic non-reflecting inflow

The procedure of Yoo et al. [24] is followed for inflow, away from edges and corner. The inlet is composed of five entering waves, leading to five closures for boundary conditions. Here it is chosen to impose temperature and velocity and passive scalar; other choices are possible like density or mass flow rate that will not be discussed here. The closed system reads

$$\left(\frac{\partial p}{\partial t} + \varsigma \rho c \frac{\partial u_1}{\partial t}\right) + \eta_\phi \frac{\rho c^2 (1 - \mathcal{M}^2)}{L_x} (u_1 - u_{1_0}) = 0, \quad (23)$$

$$\left(c^2 \frac{\partial \rho}{\partial t} - \frac{\partial p}{\partial t}\right) + \eta_2 \frac{\rho c \mathcal{R}}{L_x} (T - T_0) = 0, \quad (24)$$

$$\frac{\partial u_2}{\partial t} + \eta_3 \frac{c}{L_x} (u_2 - u_{2_0}) = 0, \quad (25)$$

$$\frac{\partial u_3}{\partial t} + \eta_4 \frac{c}{L_x} (u_3 - u_{3_0}) = 0, \quad (26)$$

$$\frac{\partial Z}{\partial t} + \eta_6 \frac{c}{L_x} (Z - Z_0) = 0 \quad (27)$$

with η_1, \dots, η_6 relaxation parameters (η_1 and η_2 negative) and the subscript 0 denoting target values for the relevant quantities. In Eq. (23) the index ϕ is equal to 1 or 5 depending whether the inlet is located at $x_1 = L_x$ or $x_1 = 0$, respectively; ς sets the sign accordingly (Eq. (18)).

The equations for the unknown entering wave amplitudes are obtained from system (15) closed with Eqs. (23)–(27):

$$\mathcal{L}_\phi = \eta_\phi \frac{\rho c^2(1 - \mathcal{M}^2)}{L_x} (u_1 - u_{1_0}) + (\mathcal{T}_5 + \zeta \rho c \mathcal{T}_2), \tag{28}$$

$$\mathcal{L}_2 = \eta_2 \frac{\rho c \mathcal{R}}{L_x} (T - T_0) + (c^2 \mathcal{T}_1 - \mathcal{T}_5), \tag{29}$$

$$\mathcal{L}_3 = \eta_3 \frac{c}{L_x} (u_2 - u_{2_0}) + \mathcal{T}_3, \tag{30}$$

$$\mathcal{L}_4 = \eta_4 \frac{c}{L_x} (u_3 - u_{3_0}) + \mathcal{T}_4, \tag{31}$$

$$\mathcal{L}_6 = \eta_6 \frac{c}{L_x} (Z - Z_0) + \mathcal{T}_6. \tag{32}$$

It should be noted that this particular inflow condition does not require any additional viscous condition as the density ρ —the only remaining unknown—is obtained from the continuity equation, which does not involve any viscous term [12].

3.2. Edge boundaries

Supposing that the edge is aligned along x_3 (face boundaries composing the edge are normal to x_1 and x_2), the system linking primitive variables with amplitude of the waves \mathcal{L}_i and \mathcal{M}_i , traveling in both directions x_1 and x_2 is obtained from a two-dimensional characteristic analysis (Eq. (A.27)) by neglecting the \mathbf{D} term only:

$$\begin{cases} \frac{\partial \rho}{\partial t} + \frac{1}{c^2} [\mathcal{L}_2 + \frac{1}{2}(\mathcal{L}_5 + \mathcal{L}_1)] + \frac{1}{c^2} [\mathcal{M}_3 + \frac{1}{2}(\mathcal{M}_5 + \mathcal{M}_1)] - \mathcal{T}_1 = 0, \\ \frac{\partial u_1}{\partial t} + \frac{1}{2\rho c} (\mathcal{L}_5 - \mathcal{L}_1) + \mathcal{M}_2 - \mathcal{T}_2 = 0, \\ \frac{\partial u_2}{\partial t} + \mathcal{L}_3 + \frac{1}{2\rho c} (\mathcal{M}_5 - \mathcal{M}_1) - \mathcal{T}_3 = 0, \\ \frac{\partial u_3}{\partial t} + \mathcal{L}_4 + \mathcal{M}_4 - \mathcal{T}_4 = 0, \\ \frac{\partial p}{\partial t} + \frac{1}{2}(\mathcal{L}_5 + \mathcal{L}_1) + \frac{1}{2}(\mathcal{M}_5 + \mathcal{M}_1) - \mathcal{T}_5 = 0, \\ \frac{\partial Z}{\partial t} + \mathcal{L}_6 + \mathcal{M}_6 - \mathcal{T}_6 = 0 \end{cases} \tag{33}$$

with

$$\mathcal{T} = \begin{pmatrix} -\frac{\partial m_3}{\partial x_3} \\ -u_3 \frac{\partial u_1}{\partial x_3} \\ -u_3 \frac{\partial u_2}{\partial x_3} \\ -u_3 \frac{\partial u_3}{\partial x_3} - \frac{1}{\rho} \frac{\partial p}{\partial x_3} \\ -u_3 \frac{\partial p}{\partial x_3} - \gamma p \frac{\partial u_3}{\partial x_3} \\ -u_3 \frac{\partial Z}{\partial x_3} \end{pmatrix}. \tag{34}$$

A procedure similar to the one discussed for face boundaries may be used. System (33) is combined with physical boundary conditions to compute the unknown incoming wave amplitude variations of both boundaries. These wave amplitude variations are now coupled, therefore, in general, a linear system in the unknown waves has to be solved. An additional problem arises when the boundaries sharing the edge are of different kind; in this case, not only different characteristic directions have to be considered simultaneously but, depending on the boundary types, additional compatibility conditions must be introduced to ensure numerical stability.

Note that the wall boundary condition presented in what follows is always considered as adiabatic no-slip, therefore, the relevant inviscid conditions are augmented by the addition of the following viscous conditions:

$$q_n = 0, \quad \rho D \frac{\partial Z}{\partial x_n} = 0, \tag{35}$$

subscript n indicating the direction normal to the wall. Viscous conditions for inflow and outflow boundaries are enforced as for face boundaries (see Sections 3.1.1 and 3.1.2).

3.2.1. Outflow/outflow edge

Two characteristic-type relations may be written combining the second, the third and the fifth equations in system (33):

$$\left(\frac{\partial p}{\partial t} + \varsigma(\phi)\rho c \frac{\partial u_1}{\partial t}\right) + \mathcal{L}_\phi + \underbrace{\frac{\mathcal{M}_5 + \mathcal{M}_1}{2} - \mathcal{T}_5 + \varsigma(\phi)\rho c(\mathcal{M}_2 - \mathcal{T}_2)}_{-\mathbb{T}_1^\phi} = 0, \tag{36}$$

$$\left(\frac{\partial p}{\partial t} + \varsigma(\psi)\rho c \frac{\partial u_2}{\partial t}\right) + \mathcal{M}_\psi + \underbrace{\frac{\mathcal{L}_5 + \mathcal{L}_1}{2} - \mathcal{T}_5 + \varsigma(\psi)\rho c(\mathcal{L}_3 - \mathcal{T}_3)}_{-\mathbb{T}_2^\psi} = 0, \tag{37}$$

where ϕ and ψ are indices taking either the values 1 or 5 depending on the location of the edge as summarized in Table 1; ς is the switch defined in Eq. (18).

The boundary conditions are obtained from Eq. (17) written for u_1 and u_2 :

$$\left(\frac{\partial p}{\partial t} + \varsigma(\phi)\rho c \frac{\partial u_1}{\partial t}\right) + \sigma \frac{c(1 - \mathcal{M}^2)}{L_x} (p - p_\infty) - \beta(\mathbb{T}_1^\phi - \mathbb{T}_{1,\text{ex}}^\phi) = 0, \tag{38}$$

$$\left(\frac{\partial p}{\partial t} + \varsigma(\psi)\rho c \frac{\partial u_2}{\partial t}\right) + \sigma \frac{c(1 - \mathcal{M}^2)}{L_y} (p - p_\infty) - \beta(\mathbb{T}_2^\psi - \mathbb{T}_{2,\text{ex}}^\psi) = 0, \tag{39}$$

where $\mathbb{T}_{1,\text{ex}}^\phi$ and $\mathbb{T}_{2,\text{ex}}^\psi$ may be computed from a reference steady flow by applying definition (14) written for boundaries orthogonal to x_1 and x_2 , respectively:

$$\mathbb{T}_{1,\text{ex}}^\phi = -\hat{u}_t \frac{\partial \hat{p}}{\partial x_t} - \gamma \hat{p} \frac{\partial \hat{u}_t}{\partial x_t} - \varsigma(\phi) \hat{\rho} \hat{c} \hat{u}_t \frac{\partial \hat{u}_1}{\partial x_t} \quad (t = 2, 3), \tag{40}$$

$$\mathbb{T}_{2,\text{ex}}^\psi = -\hat{u}_t \frac{\partial \hat{p}}{\partial x_t} - \gamma \hat{p} \frac{\partial \hat{u}_t}{\partial x_t} - \varsigma(\psi) \hat{\rho} \hat{c} \hat{u}_t \frac{\partial \hat{u}_2}{\partial x_t} \quad (t = 1, 3). \tag{41}$$

From Eqs. (36)–(39), the unknown waves are then solution of the system:

$$\begin{cases} \mathcal{L}_\phi + \frac{1-\beta}{2} \mathcal{M}_\psi = \sigma \frac{c(1 - \mathcal{M}^2)}{L_x} (p - p_\infty) + (1 - \beta) \tilde{\mathbb{T}}_1^\phi + \beta \mathbb{T}_{1,\text{ex}}^\phi, \\ \frac{1-\beta}{2} \mathcal{L}_\phi + \mathcal{M}_\psi = \sigma \frac{c(1 - \mathcal{M}^2)}{L_y} (p - p_\infty) + (1 - \beta) \tilde{\mathbb{T}}_2^\psi + \beta \mathbb{T}_{2,\text{ex}}^\psi \end{cases} \tag{42}$$

with the known terms

$$\tilde{\mathbb{T}}_1^\phi = \mathcal{T}_5 - \frac{\mathcal{M}_{\psi^*}}{2} - \varsigma(\phi)\rho c(\mathcal{M}_2 - \mathcal{T}_2), \tag{43}$$

$$\tilde{\mathbb{T}}_2^\psi = \mathcal{T}_5 - \frac{\mathcal{L}_{\phi^*}}{2} - \varsigma(\psi)\rho c(\mathcal{L}_3 - \mathcal{T}_3), \tag{44}$$

Table 1
Values of the indices ϕ and ψ depending on edge location

		ϕ	ψ	ϕ	ψ
$x_2 \backslash x_1$	0	0		L_x	
	L_y	5	1	1	1

where $\phi^* = 6 - \phi$ and $\psi^* = 6 - \psi$. It should be noted that, since $0 \leq \beta \leq 1$, system (42) always admits solution, the determinant of the relevant matrix of coefficient being zero for $\beta = -1$ and $\beta = 3$; nonetheless, some care has to be taken in general as, depending on the particular boundaries considered, a check on this regard is recommended.

3.2.2. Inflow/outflow edge

An analogous procedure as the one used for the outflow/outflow boundary edge could be followed in this case. On the inflow/outflow edge, in fact, there are five incoming waves on the inflow side and one incoming wave on the outflow side for a total number of six physical boundary conditions. Therefore, inlet and outlet boundary conditions could be, in principle, simultaneously imposed. Nonetheless, even allowing smooth transients for pressure, the two boundary conditions have shown problems of stability when simultaneously imposed. A simple remedy, which has proven effective for the configurations studied in this work, is to set to zero the incoming wave amplitude relevant to the outflow boundary (“perfectly non-reflecting” outflow). In this way, the pressure is left free to adapt to the local flow field and tends anyway to the expected value due to the effect of the neighboring regions. Furthermore, as the only unknown wave amplitude on the outflow side is directly imposed, the edge become uncoupled on the two characteristic directions and the remaining incoming waves can be computed directly from system (33) and Eqs. (23)–(27).

Supposing for instance the inlet normal to x_1 and the outflow normal to x_2 , the expression for the unknown wave amplitude variations are

$$\mathcal{M}_\psi = 0 \quad (\text{compatibility condition}), \tag{45}$$

$$\mathcal{L}_\phi = \eta_\phi \frac{\rho c^2 (1 - \mathcal{M}^2)}{L_x} (u_1 - u_{1_0}) - \frac{\mathcal{M}_{\psi^*}}{2} + \mathcal{T}_5 + \zeta(\phi) \rho c (\mathcal{T}_2 - \mathcal{M}_2), \tag{46}$$

$$\mathcal{L}_2 = \eta_2 \frac{\rho c \mathcal{R}}{L_x} (T - T_0) - \mathcal{M}_3 + (c^2 \mathcal{T}_1 - \mathcal{T}_5), \tag{47}$$

$$\mathcal{L}_3 = \eta_3 \frac{c}{L_x} (u_2 - u_{2_0}) + \frac{\zeta(\psi)}{2\rho c} \mathcal{M}_{\psi^*} + \mathcal{T}_3, \tag{48}$$

$$\mathcal{L}_4 = \eta_4 \frac{c}{L_x} (u_3 - u_{3_0}) - \mathcal{M}_4 + \mathcal{T}_4, \tag{49}$$

$$\mathcal{L}_6 = \eta_6 \frac{c}{L_x} (Z - Z_0) - \mathcal{M}_6 + \mathcal{T}_6, \tag{50}$$

where the indices ϕ and ψ and the value of ζ can be obtained from Table 1 and Eq. (18) and $\psi^* = 6 - \psi$. The equation for \mathcal{L}_3 has been obtained using the following identity:

$$\frac{1}{2\rho c} (\mathcal{M}_5 - \mathcal{M}_1) = \frac{\zeta(\psi)}{2\rho c} (\mathcal{M}_\psi - \mathcal{M}_{\psi^*}). \tag{51}$$

3.2.3. Wall/outflow edge

On this kind of edge, in principle, one should impose the pressure for what concerns the outlet condition, and velocity for what concerns the wall condition (the time derivative of the velocity component normal to the wall is set to zero). As suggested by Poinso and Lele [12], just imposing all these quantities at the same time is not effective, but allowing smooth transient for the pressure, namely relaxing outlet pressure, improves the stability of the boundary condition.

Let the wall be normal to x_1 and the outflow be normal to x_2 . Since the velocity at the wall is zero, the only non-zero wave amplitude variations are $\mathcal{L}_{1,5}$ and $\mathcal{M}_{1,5}$ (those characterized by characteristic speeds $u_1 \mp c$ and $u_2 \mp c$, respectively). $\mathcal{T}_1, \mathcal{T}_2, \mathcal{T}_3$ and \mathcal{T}_5 are zero as well. The physical boundary conditions are expressed by

$$\frac{\partial u_1}{\partial t} = 0 \tag{52}$$

and Eq. (17) (written for u_2). From system (33) the relevant equations are

$$\frac{\partial u_1}{\partial t} + \frac{1}{2\rho c}(\mathcal{L}_5 - \mathcal{L}_1) = 0, \tag{53}$$

$$\left(\frac{\partial p}{\partial t} + \varsigma(\psi)\rho c \frac{\partial u_2}{\partial t}\right) + \mathcal{M}_\psi + \underbrace{\frac{1}{2}(\mathcal{L}_5 + \mathcal{L}_1)}_{-\mathbb{T}_2^\psi} = 0 \tag{54}$$

and the solving system for the unknown \mathcal{L}_ϕ and \mathcal{M}_ψ reads

$$\begin{cases} \mathcal{L}_\phi = \mathcal{L}_{\phi^*}, \\ \mathcal{M}_\psi = \sigma \frac{c(1-M^2)}{L_y}(p - p_\infty) - (1 - \beta)\mathcal{L}_{\phi^*} + \beta\mathbb{T}_{2,\text{ex}}^\psi \end{cases} \tag{55}$$

with $\phi^* = 6 - \phi$. Velocity components u_2 and u_3 are simply forced to zero and $\mathbb{T}_{2,\text{ex}}^\psi$ is expressed by Eq. (41).

3.3. Corner boundaries

The system relating primitive variables with the characteristic waves is obtained from Eq. (A.38) by neglecting the \mathbf{D} term as before

$$\begin{cases} \frac{\partial p}{\partial t} + \frac{1}{c^2}[\mathcal{L}_2 + \frac{1}{2}(\mathcal{L}_5 + \mathcal{L}_1)] + \frac{1}{c^2}[\mathcal{M}_3 + \frac{1}{2}(\mathcal{M}_5 + \mathcal{M}_1)] + \frac{1}{c^2}[\mathcal{N}_4 + \frac{1}{2}(\mathcal{N}_5 + \mathcal{N}_1)] = 0, \\ \frac{\partial u_1}{\partial t} + \frac{1}{2\rho c}(\mathcal{L}_5 - \mathcal{L}_1) + \mathcal{M}_2 + \mathcal{N}_2 = 0, \\ \frac{\partial u_2}{\partial t} + \mathcal{L}_3 + \frac{1}{2\rho c}(\mathcal{M}_5 - \mathcal{M}_1) + \mathcal{N}_3 = 0, \\ \frac{\partial u_3}{\partial t} + \mathcal{L}_4 + \mathcal{M}_4 + \frac{1}{2\rho c}(\mathcal{N}_5 - \mathcal{N}_1) = 0, \\ \frac{\partial p}{\partial t} + \frac{1}{2}(\mathcal{L}_5 + \mathcal{L}_1) + \frac{1}{2}(\mathcal{M}_5 + \mathcal{M}_1) + \frac{1}{2}(\mathcal{N}_5 + \mathcal{N}_1) = 0, \\ \frac{\partial Z}{\partial t} + \mathcal{L}_6 + \mathcal{M}_6 + \mathcal{N}_6 = 0. \end{cases} \tag{56}$$

The procedure is similar to the one used for face and edge boundaries, except that in this case all the transverse terms are expressed by wave amplitude variations. Once the incoming waves are solved using physical boundary conditions, viscous conditions are enforced and the boundary nodes are advanced in time.

As in Section 3.2, we will only consider adiabatic no-slip wall boundary conditions and the relevant additional viscous conditions are obtained from Eq. (35). Viscous conditions for inflow and outflow boundaries are enforced as for face boundaries (see Sections 3.1.1 and 3.1.2).

3.3.1. Wall/outflow/outflow corner

Let the wall be normal to x_1 and the outflows be normal to x_2 and x_3 . Since the velocity at the wall is zero, the only non-zero wave amplitude variations are $\mathcal{L}_{1,5}$, $\mathcal{M}_{1,5}$ and $\mathcal{N}_{1,5}$ (those characterized by characteristic speeds $u_1 \mp c$, $u_2 \mp c$ and $u_3 \mp c$, respectively). The boundary conditions are expressed by Eq. (17) (written for u_2 and u_3) and Eq. (52). From system (56) the equations to be considered are

$$\frac{\partial u_1}{\partial t} + \frac{1}{2\rho c}(\mathcal{L}_5 - \mathcal{L}_1) = 0, \tag{57}$$

$$\left(\frac{\partial p}{\partial t} + \varsigma(\psi)\rho c \frac{\partial u_2}{\partial t}\right) + \mathcal{M}_\psi + \underbrace{\frac{\mathcal{L}_5 + \mathcal{L}_1 + \mathcal{N}_5 + \mathcal{N}_1}{2}}_{-\mathbb{T}_2^\psi} = 0, \tag{58}$$

$$\left(\frac{\partial p}{\partial t} + \varsigma(\chi)\rho c \frac{\partial u_3}{\partial t}\right) + \mathcal{N}_\chi + \underbrace{\frac{\mathcal{L}_5 + \mathcal{L}_1 + \mathcal{M}_5 + \mathcal{M}_1}{2}}_{-\mathbb{T}_3^\chi} = 0, \tag{59}$$

where ψ and χ are indices taking either the values 1 or 5 depending on the location of the corner and ς is the switch defined by Eq. (18). In particular, ψ is obtained from Table 1 and χ , by analogy, is equal to 1 for $x_3 = L_z$ and 5 for $x_3 = 0$. The incoming wave relevant to the wall condition is readily solved by setting $\mathcal{L}_1 = \mathcal{L}_5$; there-

fore, the remaining unknown waves can be solved by applying a procedure similar to the one described for outflow/outflow edges. The solving system then reads

$$\begin{cases} \mathcal{L}_\phi = \mathcal{L}_{\phi^*}, \\ \mathcal{M}_\psi + \frac{1-\beta}{2}\mathcal{N}_\chi = \sigma \frac{c(1-\mathcal{M}^2)}{L_y}(p - p_\infty) + (1 - \beta)\tilde{\mathbb{T}}_2^\psi + \beta\mathbb{T}_{2,\text{ex}}^\psi, \\ \frac{1-\beta}{2}\mathcal{M}_\psi + \mathcal{N}_\chi = \sigma \frac{c(1-\mathcal{M}^2)}{L_z}(p - p_\infty) + (1 - \beta)\tilde{\mathbb{T}}_3^\chi + \beta\mathbb{T}_{3,\text{ex}}^\chi \end{cases} \quad (60)$$

with $\mathbb{T}_{2,\text{ex}}^\psi$ computed from Eq. (41) and

$$\tilde{\mathbb{T}}_2^\psi = -\mathcal{L}_{\phi^*} - \frac{1}{2}\mathcal{N}_{\chi^*}, \quad (61)$$

$$\tilde{\mathbb{T}}_3^\chi = -\mathcal{L}_{\phi^*} - \frac{1}{2}\mathcal{M}_{\psi^*}, \quad (62)$$

$$\mathbb{T}_{3,\text{ex}}^\chi = -\hat{u}_t \frac{\partial \hat{p}}{\partial x_t} - \gamma \hat{p} \frac{\partial \hat{u}_t}{\partial x_t} - \varsigma(\chi) \hat{\rho} \hat{c} \hat{u}_t \frac{\partial \hat{u}_3}{\partial x_t} \quad (t = 1, 2), \quad (63)$$

where $\phi^* = 6 - \phi$, $\psi^* = 6 - \psi$ and $\chi^* = 6 - \chi$.

3.3.2. Inflow/outflow/outflow corner

The presence of the inlet condition makes it necessary to impose compatibility conditions. In analogy to what is done on inflow/outflow boundaries, the “perfectly non-reflecting” condition is imposed on the outflows, thus decoupling the inlet from the outlets.

Let the inflow be normal to x_1 and the outflows be normal to x_2 and x_3 , respectively. Then, the compatibility conditions are

$$\mathcal{M}_\psi = 0, \quad (64)$$

$$\mathcal{N}_\chi = 0 \quad (65)$$

and the unknown wave amplitude variations on the inflow side are directly solved from the system (56) and the boundary conditions (23)–(27):

$$\mathcal{L}_\phi = \eta_\phi \frac{\rho c^2(1 - \mathcal{M}^2)}{L_x}(u_1 - u_{1_0}) - \frac{\mathcal{M}_{\psi^*} + \mathcal{N}_{\chi^*}}{2} - \varsigma(\phi)\rho c(\mathcal{M}_2 + \mathcal{N}_2), \quad (66)$$

$$\mathcal{L}_2 = \eta_2 \frac{\rho c \mathcal{R}}{L_x}(T - T_0) - \mathcal{M}_3 - \mathcal{N}_4, \quad (67)$$

$$\mathcal{L}_3 = \eta_3 \frac{c}{L_x}(u_2 - u_{2_0}) + \frac{\varsigma(\psi)}{2\rho c}\mathcal{M}_{\psi^*} - \mathcal{N}_3, \quad (68)$$

$$\mathcal{L}_4 = \eta_4 \frac{c}{L_x}(u_3 - u_{3_0}) + \frac{\varsigma(\chi)}{2\rho c}\mathcal{N}_{\chi^*} - \mathcal{M}_4, \quad (69)$$

$$\mathcal{L}_6 = \eta_6 \frac{c}{L_x}(Z - Z_0) - \mathcal{M}_6 - \mathcal{N}_6 \quad (70)$$

with $\psi^* = 6 - \psi$ and $\chi^* = 6 - \chi$. An analogous identity as in Eq. (51) has been used to derive the equation for \mathcal{L}_4 .

3.3.3. Outflow/outflow/outflow corner

The three characteristic equations relevant to the unknown wave amplitude variations are obtained from system (56):

$$\left(\frac{\partial p}{\partial t} + \varsigma(\phi)\rho c \frac{\partial u_1}{\partial t}\right) + \mathcal{L}_\phi + \underbrace{\frac{\mathcal{M}_5 + \mathcal{M}_1 + \mathcal{N}_5 + \mathcal{N}_1}{2}}_{-\mathbb{T}_1^\phi} + \varsigma(\phi)\rho c(\mathcal{M}_2 + \mathcal{N}_2) = 0, \quad (71)$$

$$\left(\frac{\partial p}{\partial t} + \varsigma(\psi)\rho c \frac{\partial u_2}{\partial t}\right) + \mathcal{M}_\psi + \underbrace{\frac{\mathcal{L}_5 + \mathcal{L}_1 + \mathcal{N}_5 + \mathcal{N}_1}{2}}_{-\mathbb{T}_2^\psi} + \varsigma(\psi)\rho c(\mathcal{L}_3 + \mathcal{N}_3) = 0, \quad (72)$$

$$\left(\frac{\partial p}{\partial t} + \varsigma(\chi)\rho c \frac{\partial u_3}{\partial t}\right) + \mathcal{N}_\chi + \underbrace{\frac{\mathcal{L}_5 + \mathcal{L}_1 + \mathcal{M}_5 + \mathcal{M}_1}{2}}_{-\mathbb{T}_3^\chi} + \varsigma(\chi)\rho c(\mathcal{L}_4 + \mathcal{M}_4) = 0. \quad (73)$$

The three necessary boundary conditions are obtained from Eq. (17) plus analogous relations for u_2 and u_3 . The unknown waves are then computed by solving the following system:

$$\begin{cases} \mathcal{L}_\phi + \frac{1-\beta}{2}\mathcal{M}_\psi + \frac{1-\beta}{2}\mathcal{N}_\chi = \sigma \frac{c(1-\mathcal{M}^2)}{L_x}(p - p_\infty) + (1-\beta)\tilde{\mathbb{T}}_1^\phi + \beta\mathbb{T}_{1,\text{ex}}^\phi, \\ \frac{1-\beta}{2}\mathcal{L}_\phi + \mathcal{M}_\psi + \frac{1-\beta}{2}\mathcal{N}_\chi = \sigma \frac{c(1-\mathcal{M}^2)}{L_y}(p - p_\infty) + (1-\beta)\tilde{\mathbb{T}}_2^\psi + \beta\mathbb{T}_{2,\text{ex}}^\psi, \\ \frac{1-\beta}{2}\mathcal{L}_\phi + \frac{1-\beta}{2}\mathcal{M}_\psi + \mathcal{N}_\chi = \sigma \frac{c(1-\mathcal{M}^2)}{L_z}(p - p_\infty) + (1-\beta)\tilde{\mathbb{T}}_3^\chi + \beta\mathbb{T}_{3,\text{ex}}^\chi \end{cases} \quad (74)$$

with $\mathbb{T}_{1,\text{ex}}^\phi$, $\mathbb{T}_{2,\text{ex}}^\psi$ and $\mathbb{T}_{3,\text{ex}}^\chi$ obtained from Eqs. (40), (41) and (63), respectively and

$$\tilde{\mathbb{T}}_1^\phi = -\frac{\mathcal{M}_{\psi^*} + \mathcal{N}_{\chi^*}}{2} - \varsigma(\phi)\rho c(\mathcal{M}_2 + \mathcal{N}_2), \quad (75)$$

$$\tilde{\mathbb{T}}_2^\psi = -\frac{\mathcal{L}_{\phi^*} + \mathcal{N}_{\chi^*}}{2} - \varsigma(\psi)\rho c(\mathcal{L}_3 + \mathcal{N}_3), \quad (76)$$

$$\tilde{\mathbb{T}}_3^\chi = -\frac{\mathcal{L}_{\phi^*} + \mathcal{M}_{\psi^*}}{2} - \varsigma(\chi)\rho c(\mathcal{L}_4 + \mathcal{M}_4), \quad (77)$$

where $\phi^* = 6 - \phi$, $\psi^* = 6 - \psi$ and $\chi^* = 6 - \chi$. Observe that the determinant of the relevant coefficients matrix is $-\frac{1}{4}\beta^3 + \frac{3}{4}\beta + \frac{1}{2}$ and is zero for $\beta = -1$ (two coincident roots) and $\beta = 2$, therefore, system (74) always admits solution for $\beta \in [0 : 1]$.

4. Results

Tests of 3D-NSCBC have been performed by means of a parallel solver based on the explicit finite volumes (FV) scheme for cartesian grids. The convective terms are computed resorting to the fourth-order centered skew-symmetric-like scheme proposed by Ducros et al. [4], while the diffusive terms are computed using a fourth-order centered scheme. In LES tests, a blend of second- and fourth-order artificial dissipation terms [20,18] is added in order to suppress spurious oscillations and damp high-frequency modes. Time integration is performed using a third-order Runge–Kutta scheme [7]. Within the framework of the FV scheme, the boundary problem reduces to the computation of boundary fluxes. On the other hand, the NSCBC approach is generally well suited for finite differences (FD) schemes, therefore its implementation, in the present case, requires the use of a hybrid FV–FD scheme at the boundary. We compute, then, boundary fluxes using values of the flow variables computed on an extra grid point located at the center of each computational cell's boundary face, the extra nodes being computed using the FD approach in order to integrate the relevant equation in conservative form (see Eqs. (A.18), (A.28) and (A.39)).

All the tests presented in the following sections have been performed using air and the relevant properties are summarized in Table 2.

4.1. Single vortex test-case

The first test is the two-dimensional compressible vortex convected through a non-reflecting boundary. This is a typical test used to evaluate boundary conditions and it is particularly suited to assess non-reflecting outflows for turbulent flow simulations. The configuration corresponds to a single vortex superimposed on a uniform flow field aligned along the x_1 -direction. The initial flow field is defined in terms of the stream function as

Table 2
Air properties

	Value	Ref.
M_w	28.9×10^{-3} kg/mol	Eq. (5)
γ	1.4	Eq. (9)
Pr	0.72	Eq. (12)
Sc	0.72	Eq. (12)
Pr_T	0.90	
Sc_T	0.90	
μ_{ref}	1.827×10^{-5} kg/(m s)	Eq. (11)
T_{ref}	291.15 K	Eq. (11)
S	120.0 K	Eq. (11)

Pr_T and Sc_T are the turbulent Prandtl and Schmidt numbers, respectively, which have been used in LES computations.

$$\Psi = C_v \exp\left(-\frac{r^2}{2R_v^2}\right) + U_0 x_2, \quad (78)$$

$$u_1 = \frac{\partial \Psi}{\partial x_2}, \quad (79)$$

$$u_2 = -\frac{\partial \Psi}{\partial x_1}, \quad (80)$$

where C_v is the vortex strength, $r = \sqrt{x_1^2 + x_2^2}$ is the radial distance from the reference frame's x_3 axis and R_v is the vortex radius. U_0 is the speed of the uniform flow field along x_1 . The pressure, density and temperature can be obtained from an analytical solution. In fact, it can be shown [3] that the pressure distribution is solution of

$$\frac{\partial p}{\partial r} = \frac{\rho u_\theta^2}{r}, \quad (81)$$

where u_θ is the tangential velocity field in a reference frame attached to the vortex center:

$$u_\theta = \frac{C_v r}{R_v^2} \exp\left(-\frac{r^2}{2R_v^2}\right). \quad (82)$$

Assuming that the temperature is constant and equal to T_0 , the initial pressure and density distributions can be computed as

$$p(r) = p_\infty \exp\left[-\frac{\gamma}{2} \left(\frac{C_v}{cR_v}\right)^2 \exp\left(-\frac{r^2}{R_v^2}\right)\right], \quad (83)$$

$$\rho(r) = \frac{p(r)}{\mathcal{R}T_0} \quad (84)$$

with $c = \sqrt{\gamma \mathcal{R}T_0}$ the sound speed.

For the present tests, C_v was set at 5×10^{-3} m²/s, R_v was set at 10% of the domain size L ; p_∞ and T_0 were 1 atm, and 300 K, respectively.

Three test-cases are presented with U_0 equal to 2 m/s, 200 m/s and 300 m/s, respectively, in order to assess 3D-NSCBC at different Mach numbers ($Ma = 0.00575$, 0.575 and 0.863, respectively, based on the velocity U_0). The Reynolds number (computed from the velocity U_0 and the vortex radius R_v) for the three tests is about 166, 16,600 and 24,900, respectively.

The computational domain is a square of dimension $L = 0.013$ m with uniform U_0 inlet velocity at the left ($x_1 = -0.0065$ m) boundary, and non-reflecting outflow at the right boundary; the relaxation parameter for pressure σ was equal to 0.28 for all the tests, which corresponds to the optimal value proposed by Rudy and Strikwerda [15]. Increasing this value leads to a more reflective boundary condition. All the other boundaries were periodic.

Figs. 1–3 show a comparison of results obtained using the standard NSCBC non-reflecting outflow and the 3D-NSCBC. The represented quantities are the pressure field, the vorticity contours, the longitudinal velocity contours and the contours of the velocity gradient tensor invariant Q defined as

$$Q = -\frac{1}{2} \frac{\partial u_i}{\partial x_j} \frac{\partial u_j}{\partial x_i} = -\frac{1}{2} \left(S_{ij} S_{ij} - \frac{1}{2} \omega^2 \right), \quad (85)$$

where S_{ij} is the strain tensor and ω is the vorticity vector (ϵ_{kij} is the Levi–Civita symbol):

$$S_{ij} = \frac{1}{2} \left(\frac{\partial u_i}{\partial x_j} + \frac{\partial u_j}{\partial x_i} \right), \quad (86)$$

$$\omega_i = \epsilon_{ijk} \frac{\partial u_k}{\partial x_j}. \quad (87)$$

The frames have been taken at three different times and each figure refers to a different Mach number test. The pressure, in particular, is expressed in terms of its relative value, with respect to the far field pressure p_∞ , normalized by the initial maximum pressure drop at the center of the vortex:

$$p^*(\mathbf{x}, t) = \frac{p(\mathbf{x}, t) - p_\infty}{p(\mathbf{0}, 0) - p_\infty}. \quad (88)$$

The initial map of p^* is then expected to be equal to 1 in the vortex center and 0 in the far field; once the vortex has left the domain, p^* is expected to be identically 0 all over the domain.

All the computations have been done setting $\mathbb{T}_{1,\text{ex}}^1 = 0$ (see Eq. (20)); it is interesting to note that, under this particular assumption—motivated by the fact that no transverse terms are expected for such a flow after the vortex has left the domain—the standard LODI assumption is retrieved in the limit of the transverse damping parameter β equal to 1. On the other hand, from numerical tests performed, it appears that in general the optimal value for β is related to the typical Mach number for the specific flow. For the vortex problem, indeed, the best choice for the transverse relaxation coefficient is

$$\beta \simeq Ma = \frac{U_0}{\sqrt{\gamma \mathcal{R} T_0}}. \quad (89)$$

For $Ma \geq 1$, therefore, we would expect the modified boundary condition to recover the standard LODI assumption, which, in agreement with the $Ma = 1.1$ test-case presented by Poinot and Lele [12], produces negligible flow distortion and no acoustic waves re-entering the domain as the flow regime is supersonic.

When the flow is subsonic, standard NSCBC is still able to prevent fairly well distortion of vorticity iso-lines when the vortex leaves the domain; this is true for $Ma = 0.575$ and $Ma = 0.863$ but not for very low Mach number flows (see Fig. 1(a)), as already shown by Prosser [14], where vorticity contours undergo significant distortion at the boundary. Furthermore, the standard non-reflecting boundary produces significant distortion of the longitudinal velocity and Q contours: also in this case, the effect is more and more pronounced when reducing the Mach number but it seems that these quantities are slightly more affected (the flow tends to align orthogonally to the boundary and a disturbance in the strain is produced). On the other hand, the pressure field shows a somehow opposed behavior: boundary generated pressure noise amplitude becomes more and more important when increasing the Mach number but, obviously, also less and less able to re-enter the domain. For the $Ma = 0.575$ test, a pressure perturbation with a total amplitude that is about 43 times higher than the initial vortex pressure drop is observed at the boundary (see Fig. 2(a)). Nonetheless, even at low Mach, the pressure field is significantly distorted as shown in Fig. 4(a).

The proposed 3D-NSCBC produces almost no distortion in vorticity, longitudinal velocity and Q contours meaning that vorticity is well conserved and no additional strain is generated at the boundary for all the Mach numbers (Figs. 1–3(b–d–f)). Furthermore, the pressure field distortion is dramatically reduced and the pressure perturbation amplitude is reduced of about a factor 6, 214 and 60 for the low, mid and high Mach test-cases, respectively. Pressure contours for the low Mach number case are shown in Fig. 4(b) where the expected profiles—concentric circles—are quite well reproduced.

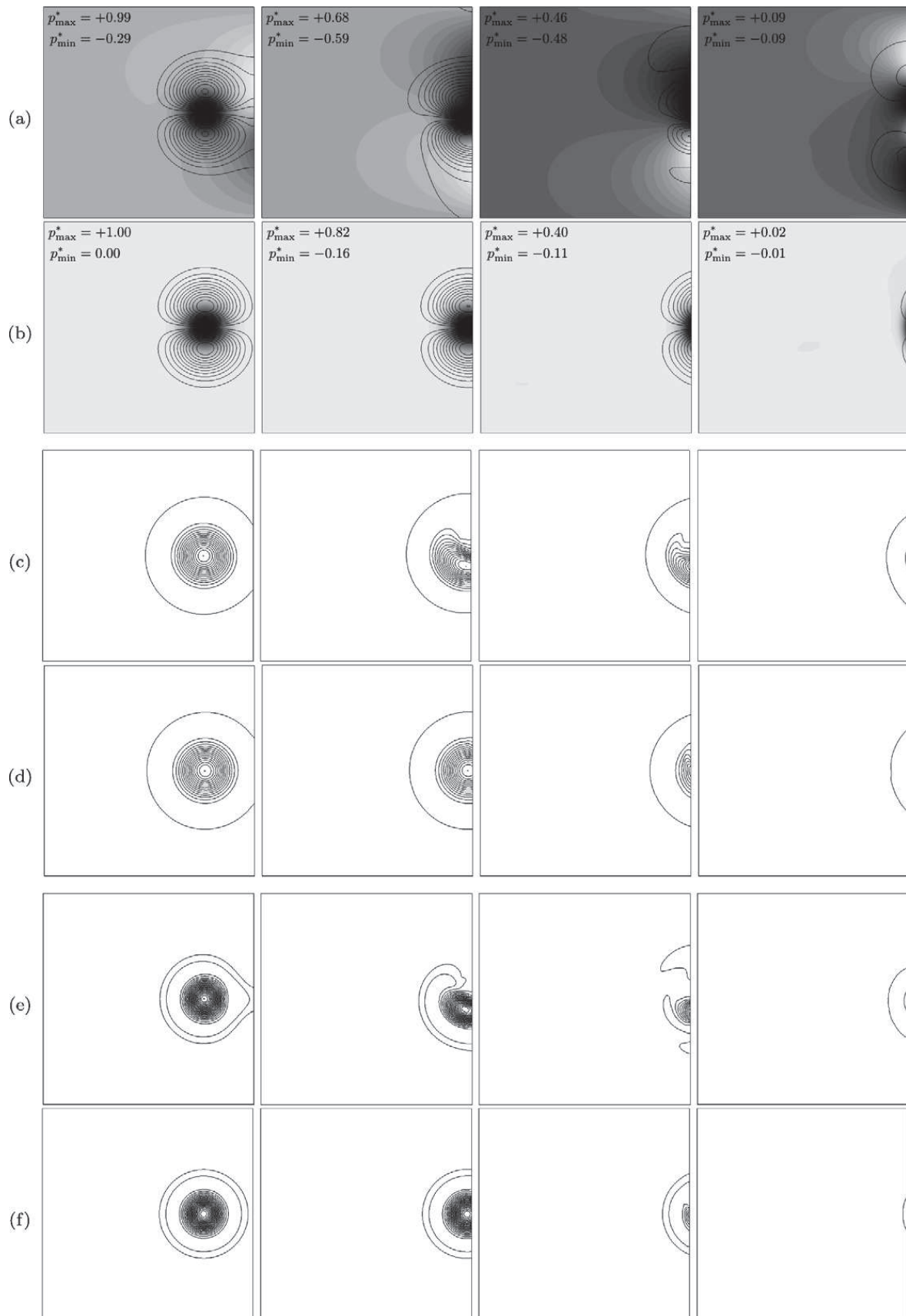


Fig. 1. Vortex test: $Ma = 0.00575$. Standard NSCBC (a–c) and 3D-NSCBC (b–d–f). Normalized pressure field (see Eq. (88)) and longitudinal velocity contours (a, b); vorticity contours (c, d); Q contours (e, f). Frames at increasing time from left to right.

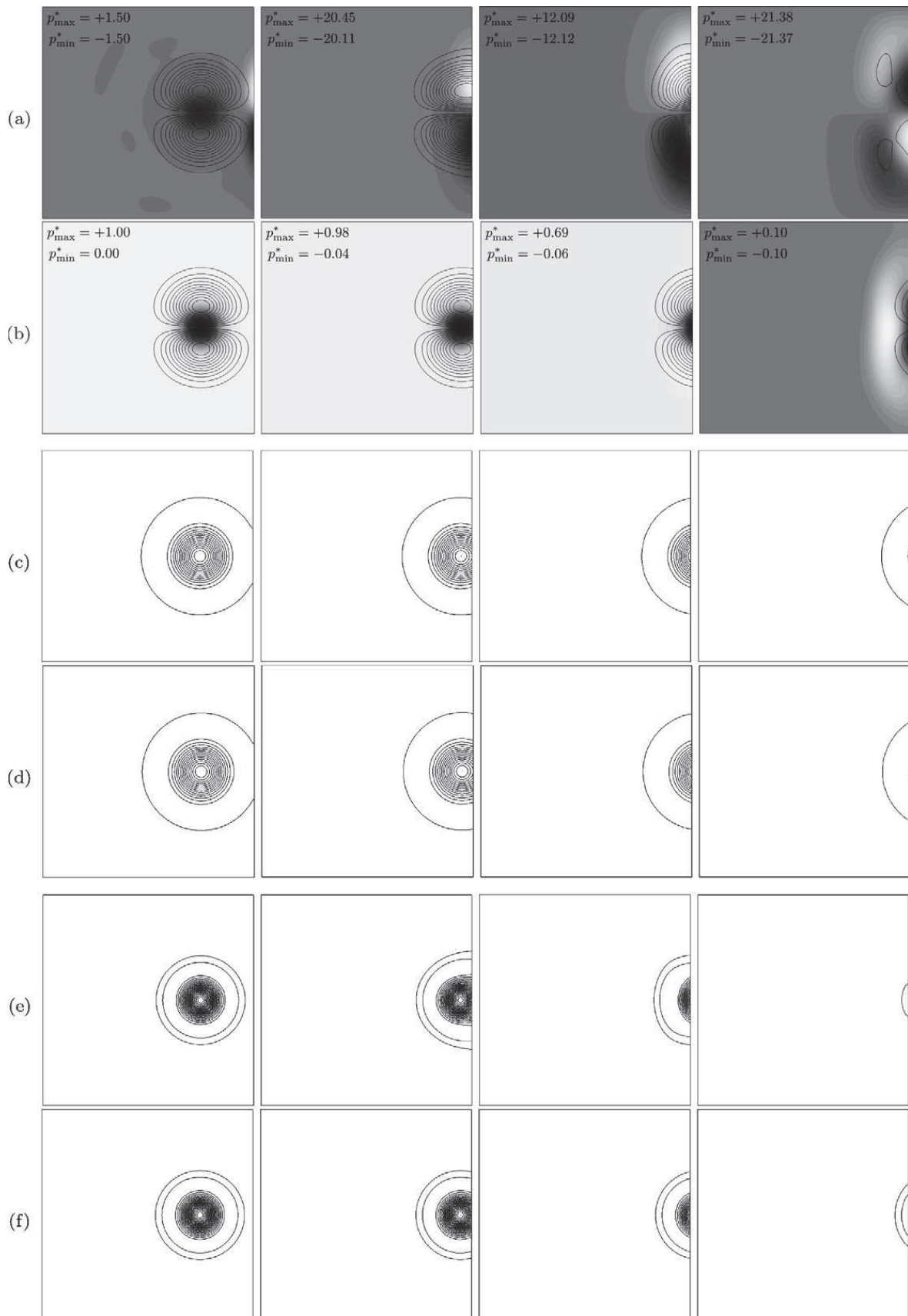


Fig. 2. Vortex test: $Ma = 0.575$. Standard NSCBC (a–c–e) and 3D-NSCBC (b–d–f). Normalized pressure field (see Eq. (88)) and longitudinal velocity contours (a, b); vorticity contours (c, d); Q contours (e, f). Frames at increasing time from left to right.

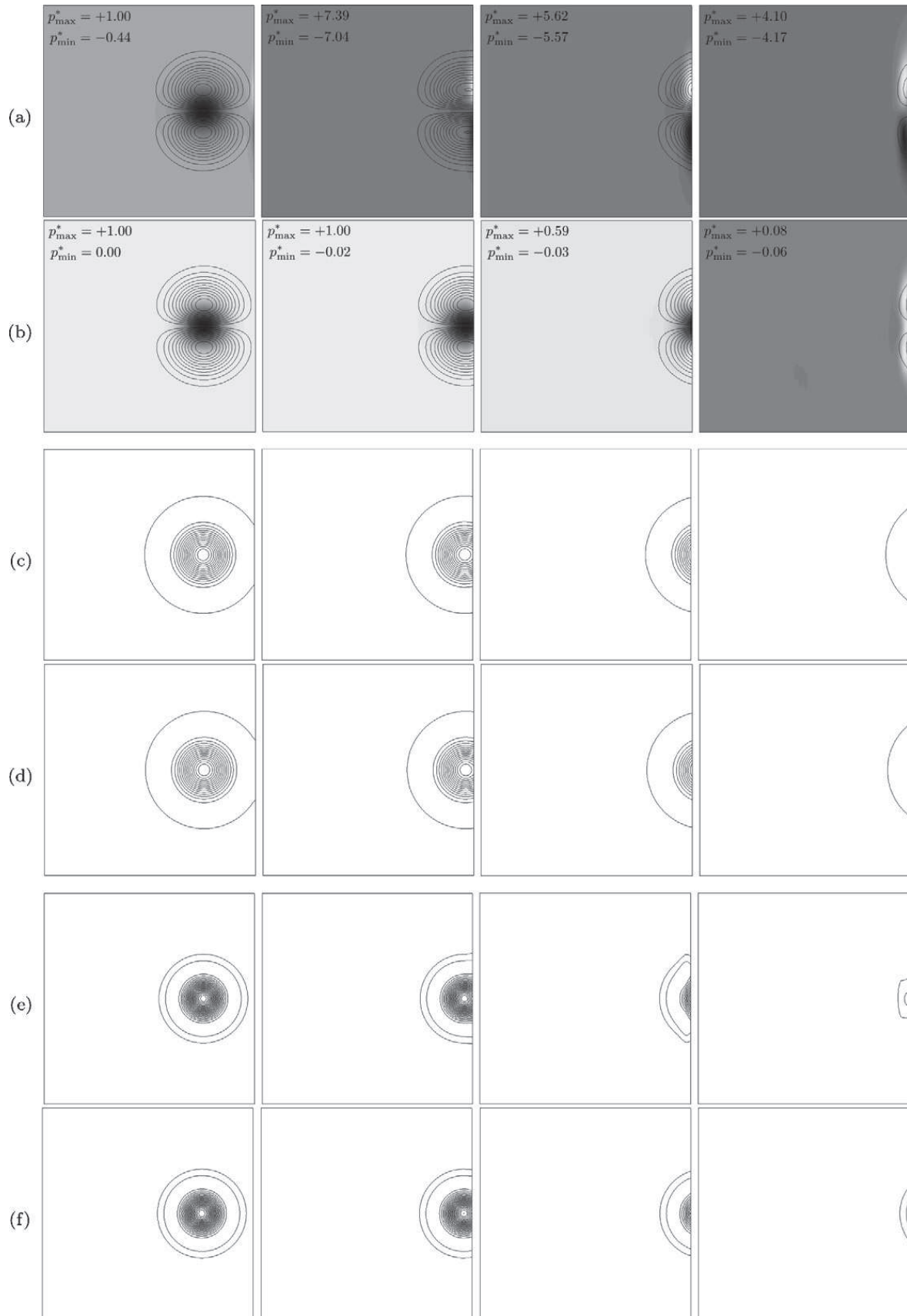


Fig. 3. Vortex test: $Ma = 0.863$. Standard NSCBC (a–c–e) and 3D-NSCBC (b–d–f). Normalized pressure field (see Eq. (88)) and longitudinal velocity contours (a, b); vorticity contours (c, d); Q contours (e, f). Frames at increasing time from left to right.

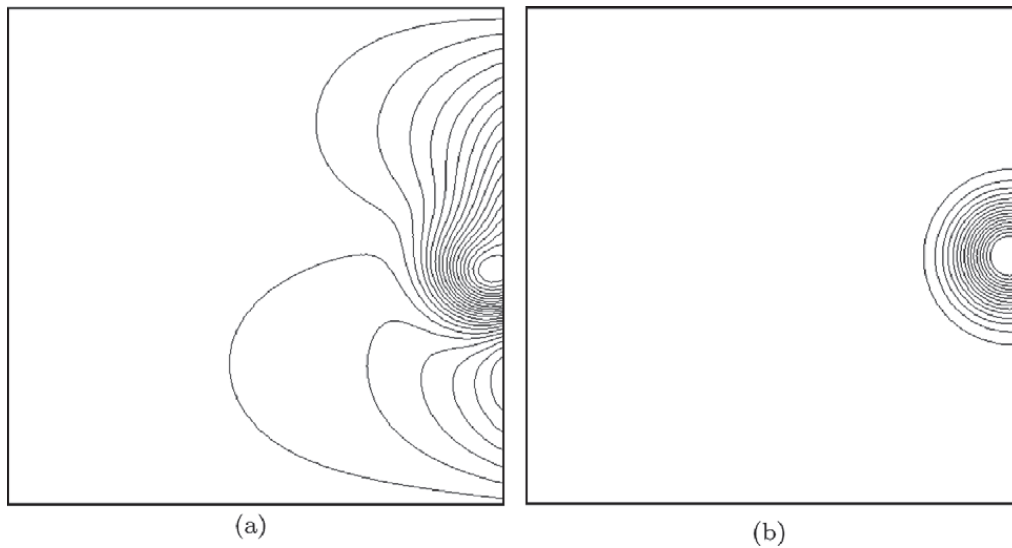


Fig. 4. Vortex test: pressure contours as the vortex crosses the boundary ($Ma = 0.00575$). Standard NSCBC non-reflecting outflow (a); 3D-NSCBC non-reflecting outflow (b).

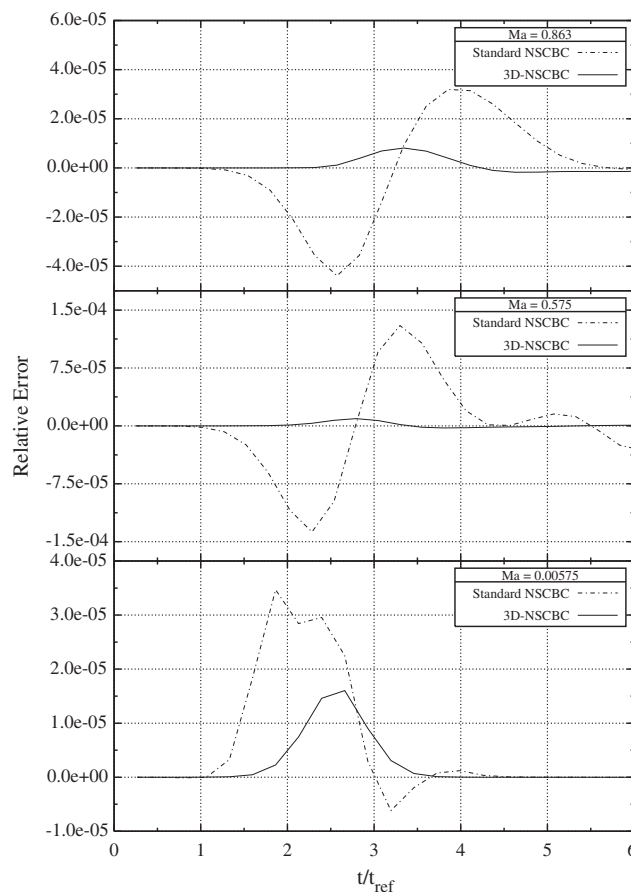


Fig. 5. Vortex test: time evolution of the relative error in pressure with respect to the benchmark solution on the extended domain. Sampling point is located at the boundary, on the vortex centerline; $t_{ref} = L/(5U_0)$.

Fig. 5 shows, for the three test-cases, the error on the computed centerline boundary pressure (at $x_1 = L/2$ and $x_2 = 0$) relative to a benchmark solution computed over an extended domain of length $2L$:

$$\varepsilon_r(\mathbf{x}, t) = \frac{p(\mathbf{x}, t) - p^0(\mathbf{x}, t)}{p^0(\mathbf{x}, t)}, \tag{90}$$

where \mathbf{x} denotes the sampling location and p^0 is the pressure computed on the benchmark simulation.

As expected, the improvement with the modified boundary condition is more evident at higher Mach numbers where the amplitude of the pressure disturbance generated using the LODI non-reflecting outflow is higher; in these cases, using the modified approach, the spurious pressure wave is almost completely avoided and the computed solution follows quite well the benchmark solution. Even at low Mach, the new proposed method reduces the error of about a factor 2. In any case, the novel approach avoids any oscillatory behavior: the relative error is always positive during all the vortex transition event, meaning that the pressure drop at the vortex core is slightly under-predicted when the vortex reaches the boundary.

4.2. Single vortex with flow inversion

Another two-dimensional vortex test is presented in this section. The vortex strength C_v has now been increased in order to produce a relatively strong reversed flow at the outflow. This is a particularly stringent test for non-reflecting boundary conditions, as the reversed flow requires the specification of additional information, coming from the outside of the computational domain, which is hard to be prescribed a priori.

For the present test, $C_v = 3 \times 10^{-1} \text{ m}^2/\text{s}$, R_v was set at 10% of the domain size L , $p_\infty = 1 \text{ atm}$, $T_0 = 300 \text{ K}$ and the convective velocity U_0 was set at 100 m/s ($Ma = 0.286$ and $Re = \rho U_0 R_v / \mu \simeq 8300$). The relaxation parameter for pressure σ was set at 0.28 and the transverse relaxation parameter $\beta = 0.286$ ($\mathbb{T}_{1,\text{ex}}^1 = 0$).

The value of C_v is now high enough to create a region of reversed flow, as it can be observed in the initial velocity profile in Fig. 6, where horizontal velocity attains a negative peak of about 40 m/s for $0.0007 < x_2 < 0.002$. In those parts of the outflow boundary where reversed flow is created, the standard perfectly non-reflecting procedure is applied and all the entering waves traveling with convective velocity u_1 —namely, $\mathcal{L}_2, \mathcal{L}_3, \mathcal{L}_4$ and \mathcal{L}_6 —are set to zero.

Fig. 7 shows the behavior of the 3D-NSCBC technique compared to the standard NSCBC in terms of pressure error; as in the previous section, the error has been estimated over a benchmark solution computed on an extended computational domain (two times longer). The top plot shows a normalized global error measure defined as

$$\varepsilon(t) = \frac{\left[\sum_{i,j,k} (p_{i,j,k}(t) - p_{i,j,k}^0(t))^2 \right]^{1/2}}{\left[\sum_{i,j,k} (p_{i,j,k}^0(t))^2 \right]^{1/2}}, \tag{91}$$

where the i, j, k subscript refers to the grid location and p^0 is the pressure computed on the benchmark simulation. The bottom plot shows the relative error measured on a point located at the outflow boundary on the vortex centerline (see Eq. (90)).

Fig. 8 shows the normalized global error in vorticity, which is defined in analogy with Eq. (91) as

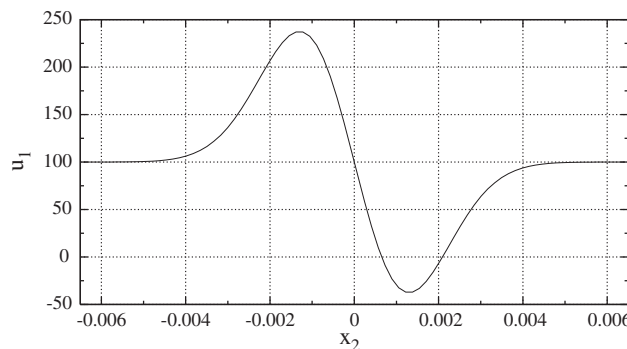


Fig. 6. Vortex test with flow reversal: initial u_1 velocity profile along a vertical plane passing through the vortex center.

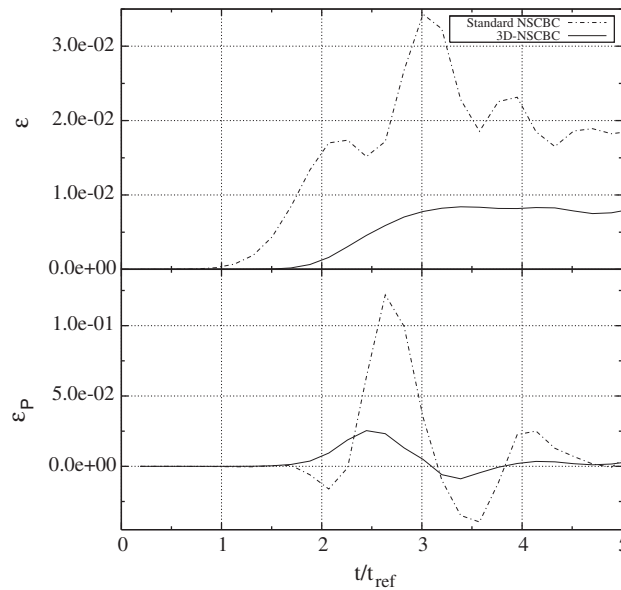


Fig. 7. Vortex test with flow reversal: time evolution of the pressure error. Global normalized error (top); relative error (bottom) for a point located at the boundary, on the vortex centerline; $t_{\text{ref}} = L/(5U_0)$.

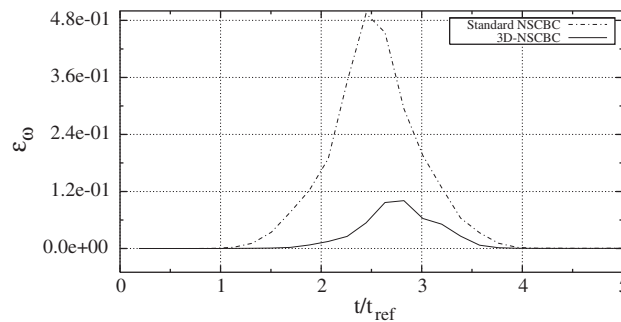


Fig. 8. Vortex test with flow reversal: time evolution of vorticity normalized error; $t_{\text{ref}} = L/(5U_0)$.

$$\varepsilon_{\omega}(t) = \frac{\left[\sum_{i,j,k} (\omega_{i,j,k}(t) - \omega_{i,j,k}^0(t))^2 \right]^{1/2}}{\left[\sum_{i,j,k} (\omega_{i,j,k}^0(0))^2 \right]^{1/2}}. \quad (92)$$

Even when the vortex strength is enough to create flow inversion at the outflow, a certain improvement is observed over the standard NSCBC approach, when using the 3D-NSCBC technique. In terms of normalized global measures, pressure error is reduced by a factor of about 2; with regards to the vorticity, the error peak is more than four times less than in the simulation performed with standard mono-dimensional boundary conditions. This is not surprising, as the 3D-NSCBC approach is expected to get advantage by the inclusion of transverse effects, therefore allowing a correct propagation of vorticity across the boundary.

4.3. Vortex dipole

In this section a test is presented concerning a convected dipole of co-rotating vortices. This problem is characterized by a certain level of unsteadiness as the two vortices slowly rotate around each other. The flow field is initialized with the following stream function [14]:

$$\Psi = C_v \left[\exp\left(-\frac{r_1^2}{2R_v^2}\right) + \exp\left(-\frac{r_2^2}{2R_v^2}\right) \right] + U_0 x_2 \quad (93)$$

with

$$r_1 = \sqrt{x_1^2 + (x_2 + \delta)^2}, \quad (94)$$

$$r_2 = \sqrt{x_1^2 + (x_2 - \delta)^2}. \quad (95)$$

The vortex strength C_v was equal to $1.25 \times 10^{-3} \text{ m}^2/\text{s}$, R_v and δ were set at 10% and 15% of the transverse domain size L , respectively and the free-stream velocity U_0 was set at 0.5 m/s ($\text{Ma}=0.00144$ and $Re = \rho U_0 R_v / \mu \simeq 42$). The relaxation parameter for pressure σ and the transverse relaxation parameter β were 0.28 and 0.00144, respectively ($\mathbb{T}_{1,\text{ex}}^1 = 0$).

Again in this case we performed a reference simulation over a longer domain of length $2L$ in order to have a benchmark solution to compare with. The relevant results, in terms of pressure (Eqs. (90) and (91)) and vorticity (Eq. (92)) errors are shown in Figs. 9 and 10, respectively. Local relative error, in particular, has been sampled at the boundary on two points, P1 and P2, corresponding approximately to the upper and lower vortex centers, respectively.

Results, both in terms of pressure and vorticity errors, are generally in line with those presented in the previous sections. It should be noted that, due to the slow rotation of the two vortices around each other, the lower and the upper vortex's centers cross the outflow boundary at different times, namely $t/t_{\text{ref}} \simeq 2.1$ and $t/t_{\text{ref}} \simeq 3.2$, respectively (as it was inferred observing the pressure field computed on the benchmark solution). As the maximum normalized pressure error is, in general, attained at the moment the vortex core leave the domain, the two peaks in the global normalized error curve (Fig. 9 on top) indicate precisely those two moments. Interestingly, the standard NSCBC boundary produces a shift to the left of the peaks: the pressure field is perturbed in such a way that the two vortices seem to leave the domain earlier than expected. On the

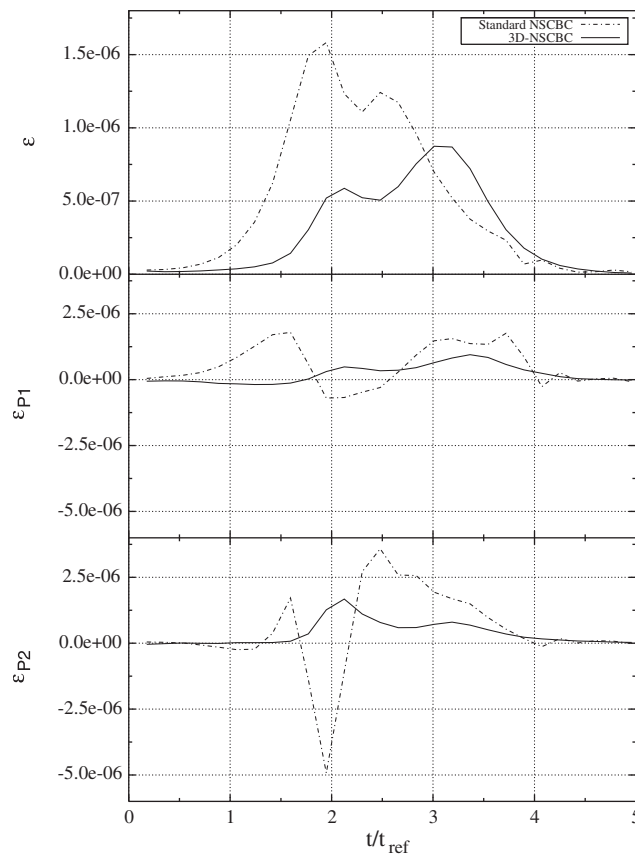


Fig. 9. Vortex dipole test: time evolution of the pressure error. Global normalized error (top); relative error for a point located at the boundary, on the upper vortex centerline (middle); relative error for a point located at the boundary, on the lower vortex centerline (bottom); $t_{\text{ref}} = L/(5U_0)$.

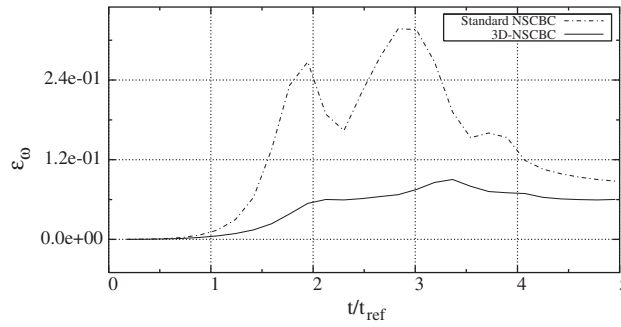


Fig. 10. Vortex dipole test: time evolution of vorticity normalized error; $t_{ref} = L/(5U_0)$.

other hand, no shift is observed in the error curve relevant to the simulation performed using the 3D-NSCBC outflow.

Again, the most evident improvement is obtained in terms of vorticity, the relevant normalized global error is about three times lower when using the 3D-NSCBC technique.

Fig. 11 shows the normalized pressure p^* (see Eq. (88)) and the iso-contours of the longitudinal velocity u_1 at three consecutive instants in time. The benchmark solution over the first half of its computational domain is depicted on top (Fig. 11(a)), the solution computed using the 3D-NSCBC approach in the middle (Fig. 11(b)) and the solution computed using the standard NSCBC at the bottom (Fig. 11(c)). The frames have been chosen to show the moment the lower vortex leaves the domain. The 3D-NSCBC is still able to allow a fairly good reproduction of the expected solution, both in terms of pressure map and velocity field. On the other hand, the

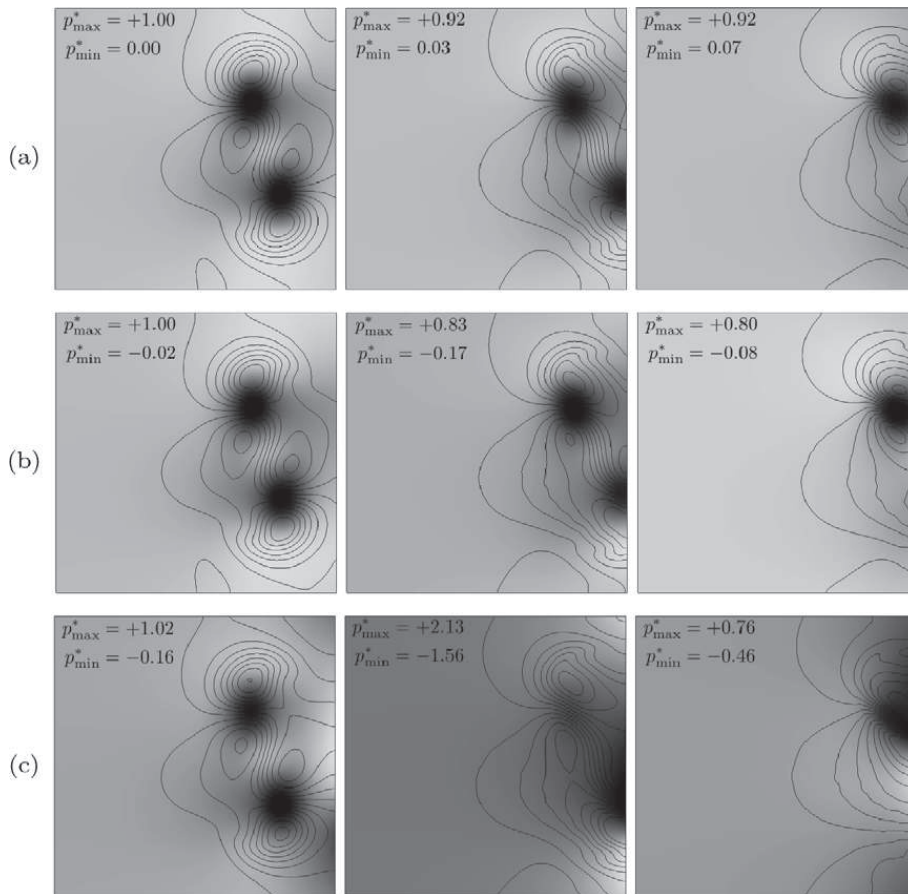


Fig. 11. Vortex dipole test. Benchmark solution on first half of domain (a), 3D-NSCBC (b) and Standard NSCBC (c) on full domain. Normalized pressure field (see Eq. (88)) color map and longitudinal velocity contours. Frames at increasing time from left to right.

standard NSCBC produces a strong perturbation to the pressure field—a pressure perturbation with a total amplitude of about 370% the initial pressure drop is observed in the second frame of Fig. 11(b)—and the vector field becomes quite distorted, especially after the lower vortex has left the domain.

4.4. Spherical pressure wave

The fourth test-case is a tridimensional flow configuration designed to assess the behavior of the proposed approach for edges and corners. The computational domain is a cube of side $L = 0.013$ m with non-reflecting outflows on all the six faces, Outflow/outflow edge conditions on all the 12 edges and Outflow/outflow/outflow corner conditions on all the eight corners.

The pressure field was initialized with a spherical pressure pulse of amplitude δ :

$$p(r) = p_\infty \left[1 + \delta \exp \left(-\frac{r^2}{2R_p^2} \right) \right], \quad (96)$$

where $r = \sqrt{x_1^2 + x_2^2 + x_3^2}$ is the distance from the center of the computational domain and R_p is the characteristic dimension of the pressure pulse. Assuming that the temperature is constant and equal to T_0 , the initial density distribution can be computed from the state equation: $\rho(r) = p(r)/(\mathcal{R}T_0)$.

For the present test, δ was set at 0.001, R_p was set at 5% of the domain size L , $p_\infty = 1$ atm, and $T_0 = 300$ K. The flow field was initialized at rest and then left to evolve in order to compare the evolution of the spherical pressure wave front—especially when approaching the computational domain edges and corners—when using standard NSCBC and 3D-NSCBC approach.

As in the previous test, the computation was done setting $\mathbb{T}_{k,\text{ex}}^* = 0$ (superscript * equal to 1 or 5 depending on the outflow's location and $k = 1, 2, 3$) over all the outflows, as the steady state is expected to be characterized by uniform pressure and zero velocity. With regards to the transverse damping parameter β , considering what has been observed in the vortex test-case, it seemed reasonable to use a value somehow related to a typical Mach number for this particular flow. A possible choice is then the maximum Mach number relevant to the local fluid displacement produced by the acoustic wave. As it will be shown, this simple approach gives fairly good results. On the other hand, some tests carried out varying β have given an optimal value of about 0.5, which is 4 order of magnitude higher than the mentioned Mach number. We report in what follows the results from three tests which have been made changing both the transverse relaxation coefficient and the pressure relaxation coefficient: $\beta = Ma_{\text{max}}$ and $\sigma = 0.28$; $\beta = Ma_{\text{max}}$ and $\sigma = 3.00$; $\beta = 0.5$ and $\sigma = 0.28$.

Qualitative results in terms of pressure field have been extracted over the two cutting planes P1 and P2 depicted in Fig. 12. These planes were chosen to assess the pressure field distortion on corners and edges, respectively.

With regards to test T3, Fig. 13 shows the pressure field and pressure contours, at two slightly different time-steps, when the pressure wave fronts are well cut by the domain boundaries. As expected, the LODI assumption (standard NSCBC) is too restrictive for such a tridimensional flow and the introduction of transverse effects at the boundary helps in reducing flow distortion, especially in regions where the flow field is not perpendicular to the outlet (i.e. toward edges and corners). The 3D-NSCBC technique, instead, is able to preserve pressure wave front curvature, whereas the standard non-reflecting outflow shows a tendency to reduce curvature or even to reverse it (see, for instance, pressure contours at the top left corner of Fig. 13(c)). The level of numerical reflection is significantly reduced too, as it can be observed in the region just behind the pressure wave. The results from tests T1 and T2 (not shown) are slightly worse but still better than those obtained with the LODI assumption. Moreover, no significant difference has been observed when increasing σ , meaning that the modified NSCBC allow a certain freedom in the choice of the pressure relaxation coefficient.

It should be noted that the present configuration is a particularly tough test-case for both NSCBC and 3D-NSCBC non-reflecting outflows. The pressure wave, as expected, is accompanied by two opposed local displacements of equal amplitude, as it is shown in Fig. 14, where the velocity field is superimposed to the pressure map. The presence of local back-flow regions at the outlet poses the additional problem about how incoming characteristic waves traveling with the convective velocity (i.e. characteristic waves with indices 2, 3, 4 and 6) should be imposed. Previous tests have shown that just “ignoring” the possibility of a reversed flow

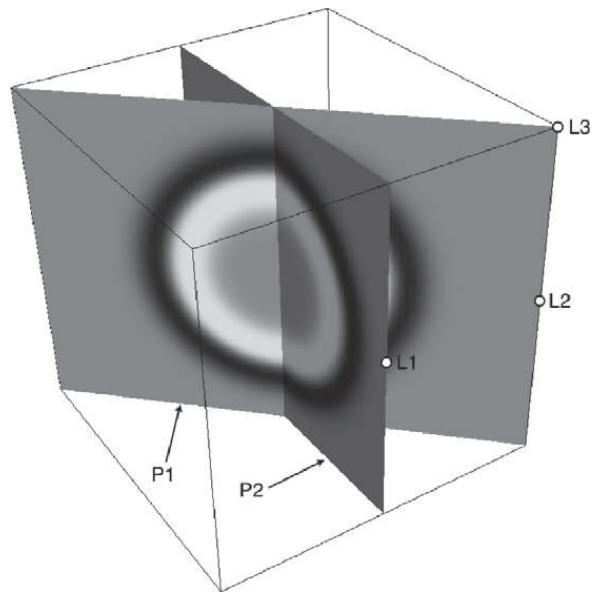


Fig. 12. Spherical pressure wave test: position of the cutting planes P1 and P2 and of the sampling locations L1, L2 and L3.

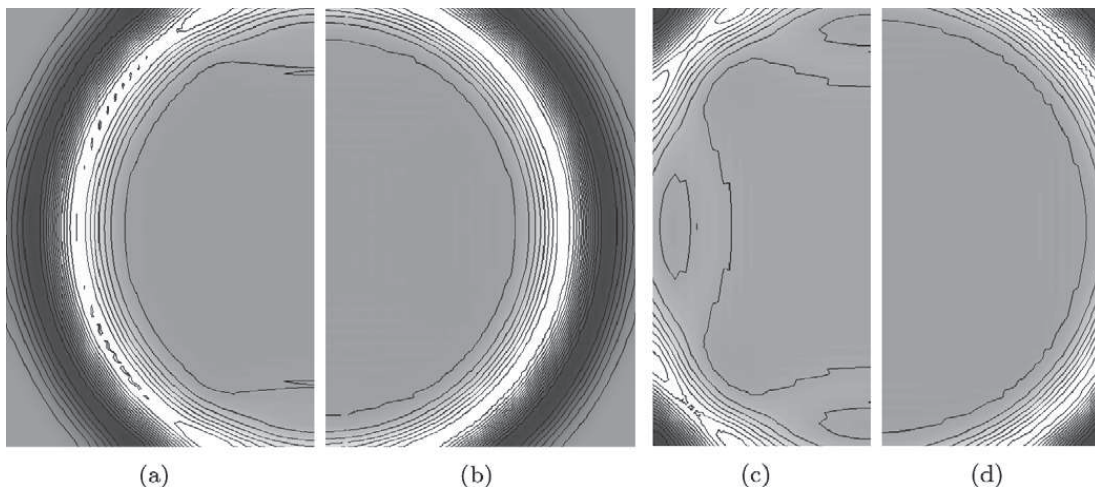


Fig. 13. Spherical pressure wave test T3: pressure map and pressure contours on plane P1 (a,b) and P2 (c,d). Standard NSCBC non-reflecting outflows (a, c); 3D-NSCBC non-reflecting outflows (b, d).

event and keep computing the relevant characteristic wave amplitudes using interior points may lead to instability problems, especially when the back-flow is particularly persistent in time. An efficient solution is to set these convected incoming waves to zero in regions of local back-flow. The drawback of this simplistic approach is, of course, a slight reduction of boundary transparency.

A measure of the error has been extracted using a benchmark solution computed on a two times wider domain. Three different locations on the boundary (see Fig. 12) have been taken into account: boundary face center (L1), boundary edge center (L2) and boundary corner (L3). The local relative absolute error on pressure for these points has been measured as

$$\varepsilon_r(\mathbf{x}, t) = \frac{|p(\mathbf{x}, t) - p^0(\mathbf{x}, t)|}{p^0(\mathbf{x}, t)}, \quad (97)$$

where \mathbf{x} denotes the sampling location and p^0 is the pressure computed on the reference simulation. Furthermore, the overall performance of the 3D-NSCBC approach has been quantified resorting to the normalized error measure defined in Eq. (91).

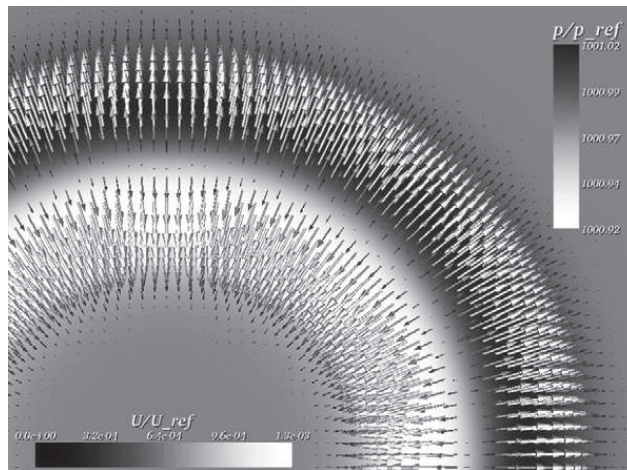


Fig. 14. Spherical pressure wave test: velocity field and pressure map on plane P1 (benchmark simulation). $U_{ref} = 9.29$ m/s, $p_{ref} = 101.23$ Pa.

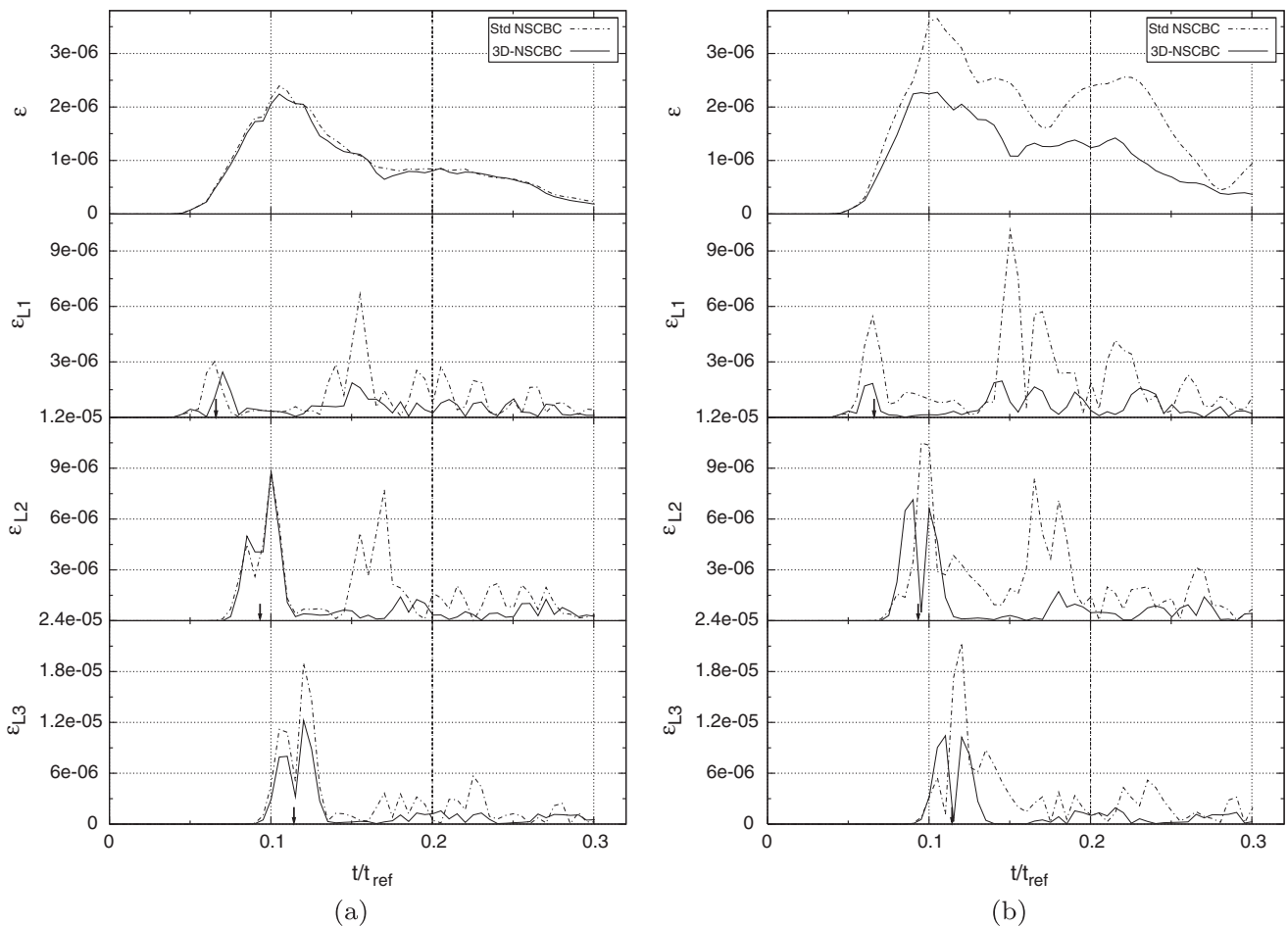


Fig. 15. Spherical pressure wave test: normalized error on pressure for test-case T1 (a) and test-case T2 (b). Global normalized error on the top graph (see Eq. (91)) and local relative error at boundary locations L1, L2 and L3. The vertical arrows mark the instants when the pressure pulse crosses locations L1, L2 and L3, respectively ($t_{ref} = 2.8 \times 10^{-4}$ s).

Figs. 15 and 16 show the relevant results. It should be noted that for $t/t_{ref} \simeq 0.2$ the reference solution (bigger domain) is expected to become more and more affected by its own boundary and the comparison becomes meaningless: this is marked by a vertical dashed line limiting the region of interest.

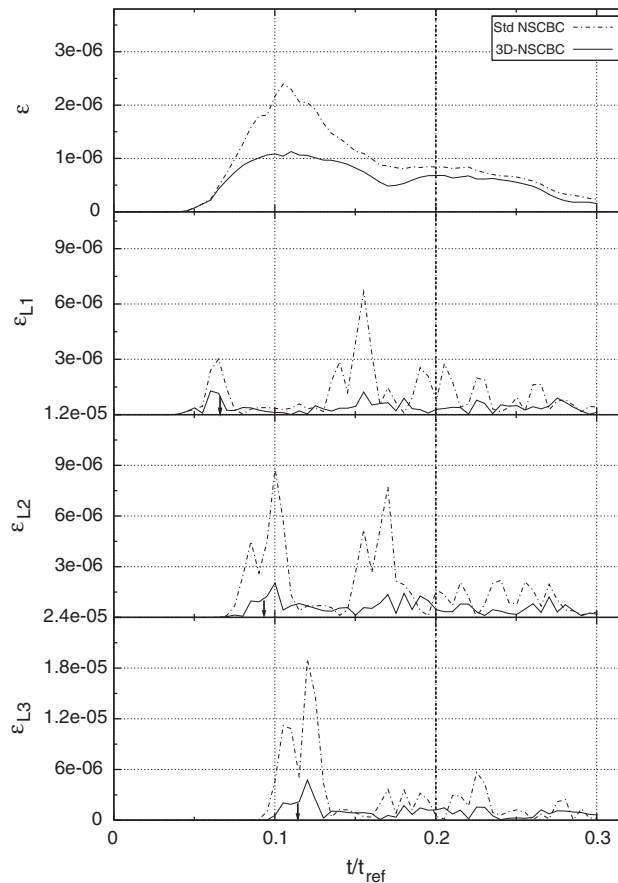


Fig. 16. Spherical pressure wave test: normalized error on pressure for test-case T3. Global normalized error on the top graph (see Eq. (91)) and local relative error at boundary locations L1, L2 and L3. The vertical arrows mark the instants when the pressure pulse crosses locations L1, L2 and L3, respectively ($t_{\text{ref}} = 2.8 \times 10^{-4}$ s).

In general, the maximum error—as per Eq. (91)—occurs, of course, during the period when the boundaries are crossed by the pressure pulse. With regards to tests T1 (low relaxation) the error level is less than about 0.14% and no significant improvement is observed using 3D-NSCBC approach. On the other hand, when the relaxation coefficient is increased (T2), the simulation performed resorting to NSCBC hypothesis is characterized by a higher error, meaning that the boundary conditions are less transparent and numerical reflected pressure waves have higher amplitude. The 3D-NSCBC, on the other hand, maintains the error almost unchanged, and the level of boundary reflection is only slightly increased.

In terms of local relative error, the novel approach gives, in general, more accurate results, showing a favorable tendency to produce numerical reflected waves of small amplitude; also in this case, when increasing σ , the LODI approximation (standard NSCBC) produces higher reflection, whereas the modified approach remains significantly more transparent, the level of boundary reflection being marginally affected by the pressure relaxation coefficient σ .

Test-case T3 gives the better performance (see Fig. 16). In this particular case, the normalized maximum error is reduced of about a factor 2 and the local relative error is significantly reduced even when the pressure pulse crosses the critical locations L2 and L3.

Fig. 17 shows a comparison about the evolution of the pressure wave. The pressure wave was looked at different time-steps before it had reached the boundary and radial plots were extracted at each time-step (symbols). As expected for a spherical wave, the pulse amplitude decreases continuously as the wave front expands. Regarding the pressure pulse as a signal traveling with the speed of sound c , the time evolution of pressure can be rescaled as a radial plot using the following equivalence relation between space and time for such a wave:

$$f(r - ct_0) \equiv f(r_0 - ct) \quad \text{with } ct_0 = r_0, \quad (98)$$

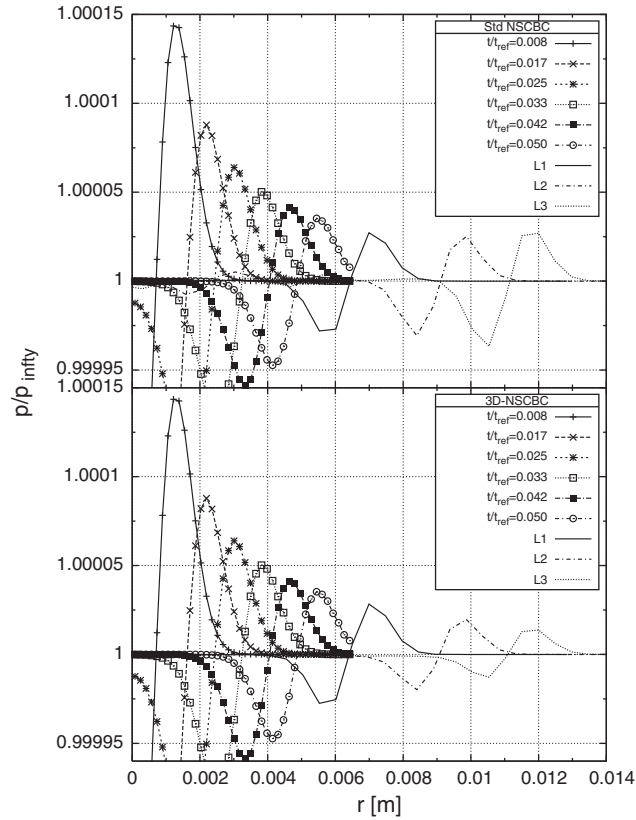


Fig. 17. Spherical pressure wave test: normalized pressure wave evolution r for test-case T3. Symbols are radial pressure plots at different normalized time-steps ($t_{\text{ref}} = 2.8 \times 10^{-4}$ s); lines are temporal pressure plots at locations L1, L2 and L3 rescaled as radial plots under the assumption that the pressure pulse is a signal traveling with speed $c \simeq 347.6$ m/s.

$$\Rightarrow r - r_0 = r_0 - ct \quad (99)$$

with $c \simeq 347.6$ m/s and r_0 the radial distance of the time signal's sampling location.

Once the pressure front meets the boundary, the LODI assumption is unable to retain the correct physical information about the tridimensionality of the flow: the pressure front stops behaving as a spherical wave and reaches the edge and, later on, the corner retaining almost the same amplitude. On the other hand, the 3D-NSCBC outflow and the proposed edge/corner technique, is remarkably capable of preserving the correct physical information and the pressure front reaches the boundary edges and corners with the expected reduced amplitude.

Finally, a qualitative comparison of the computed wave front at three subsequent time-steps is shown in Fig. 18. The wave front is shown by means of pressure iso-surfaces relevant to a normalized pressure value of 1000.98 ($p_{\text{ref}} = 101.23$ Pa) and is expected to be perfectly spherical; results are relevant to the test-case T3. The innermost and the outermost surfaces have been chosen in order to “enclose” the pressure pulse. Spurious numerical reflection is expected to be generated starting from the moment the outermost surface crosses the boundary; the effects are then visible on what follows, namely, the innermost surface. As it can be observed, the 3D-NSCBC outflows allow the wave front curvature to be correctly preserved. Negligible reflection is produced and the wave front undergoes minimal distortion even when the pressure pulse is well outside the computational domain (Fig. 18(c)). On the contrary, the computation performed resorting to the LODI assumption is characterized by significant distortion of the core pressure field; even the outermost surface itself is progressively deformed with local regions where the curvature is reversed (see Fig. 18(e) and (f)).

4.5. Jet flow configurations

We have analyzed some basic test-cases on simple configurations so far, in order to assess the behavior of the 3D-NSCBC non-reflecting outflows when compared to the standard LODI (NSCBC) assumption. In this

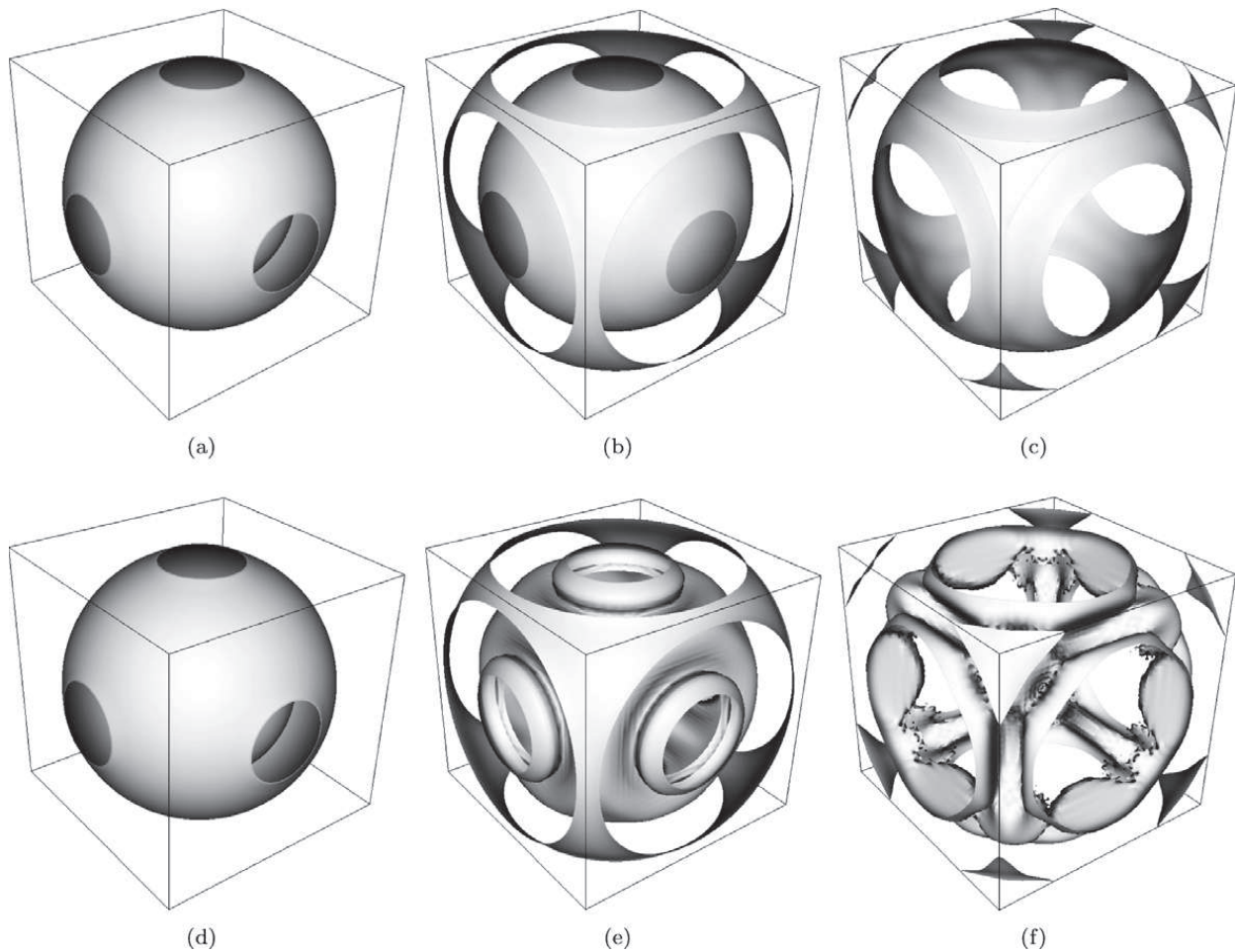


Fig. 18. Spherical pressure wave test (T3): pressure iso-surfaces evolution (iso-value $p/p_{ref} = 1000.98$). 3D-NSCBC non-reflecting outflows (a–c), standard NSCBC non-reflecting outflows (d–f).

section we present qualitative results from two simulation of more complex geometries: (a) LES of compressible turbulent free round-jet and (b) LES of compressible turbulent impinging round-jet.

Though only qualitative, as already said, these test were chosen to apply the novel approach on configurations involving non-reflecting inlet/outlet coupling, as well as all the types of edge/corner conditions presented in the precedent sections.

As just mentioned, both the simulation were performed in turbulent regime resorting to the LES technique. Within the framework of LES approach, the Navier–Stokes equations are filtered with a low-pass filter, the low-frequency components of the flow field—those which represent the large scale structures of the flow—being directly resolved, and the coupling term arising from the non-linear convective term being modeled by the sub-grid scale (SGS) model. We adopt an implicit filtering approach, therefore, the filter's cutoff length Δ is equal to the local grid spacing, while SGS terms are modeled using the eddy viscosity assumption of the wall-adapting local eddy-viscosity model proposed by Nicoud and Ducros [10].

4.5.1. Turbulent free round-jet

The computational domain is a box of dimensions $14D \times 5D \times 5D$ with $D = 0.0026$ m the jet diameter ($200 \times 80 \times 80$ grid points). The grid is uniform along x_1 and slightly stretched along x_2 and x_3 in order to better resolve the jet shear layer; transverse refinement was limited to maintain a maximum stretching ratio of about 1.06 over consecutive cells. The resulting grid spacing is: $\Delta x_1/D \simeq 0.0527$ on the axis, $\Delta x_i/D \simeq 0.0431$ at $x_i = \pm D/2$ and $\Delta x_i/D \simeq 0.1312$ at $x_i = \pm 2.5D$ ($t = 2, 3$).

The inflow is located at $x_1 = 0$ and the modified subsonic non-reflecting inflow is used, with the velocity relaxation parameter η_5 set at 3.58. The same value was set for the other inlet relaxation parameters:

$\eta_2 = -3.58$ and $\eta_3 = \eta_4 = \eta_6 = 3.58$. The target inlet velocity was imposed using the power law profile for turbulent pipe flow:

$$\frac{U(r)}{U_{cl}} = \left(1 - \frac{2r}{D}\right)^{1/n}, \quad (100)$$

where $r = \sqrt{x_2^2 + x_3^2}$ is the distance from the jet axis, U_{cl} is the centerline velocity and the parameter n was set at 7.4; the ratio between bulk velocity U_b and centerline velocity U_{cl} is about 0.82. The value of U_b was computed fixing the value of the jet's Reynolds number: $Re_D = \rho U_b D / \mu = 23,000$. A correlated random noise [8] was superimposed to the velocity profile with an intensity of 0.8% of the bulk velocity U_b . The inlet temperature was fixed at 300 K.

All the other boundaries are non-reflecting outflows with pressure relaxation parameter σ set at 0.28 and target pressure equal to 1 atm. The assumed exact transverse terms were set at zero, which seemed a reasonable approach in consideration of the results obtained in the previous tests. The transverse relaxation parameter β was set at 0.19, a typical value of the Mach number for this specific flow, as it has been evaluated from a precursor simulation performed with β equal to U_b/c . Inflow/outflow edge conditions are used on the four bottom edges and Inflow/outflow/outflow corner conditions are used on the relevant four joining corners; Outflow/outflow edge conditions are used on the eight remaining edges and Outflow/Outflow/Outflow corner conditions on the four top corners (see Fig. 19). The simulation was started from fluid at rest and at reference condition (1 atm, 300 K) all over the domain.

The developed flow field is depicted in Fig. 19, where the coherent vortical structures are represented resorting to the Q criterion. Pressure and passive scalar distributions over axial planes are shown too. Despite the fairly small computational domain used, no perturbation coming from the boundaries is observed: the

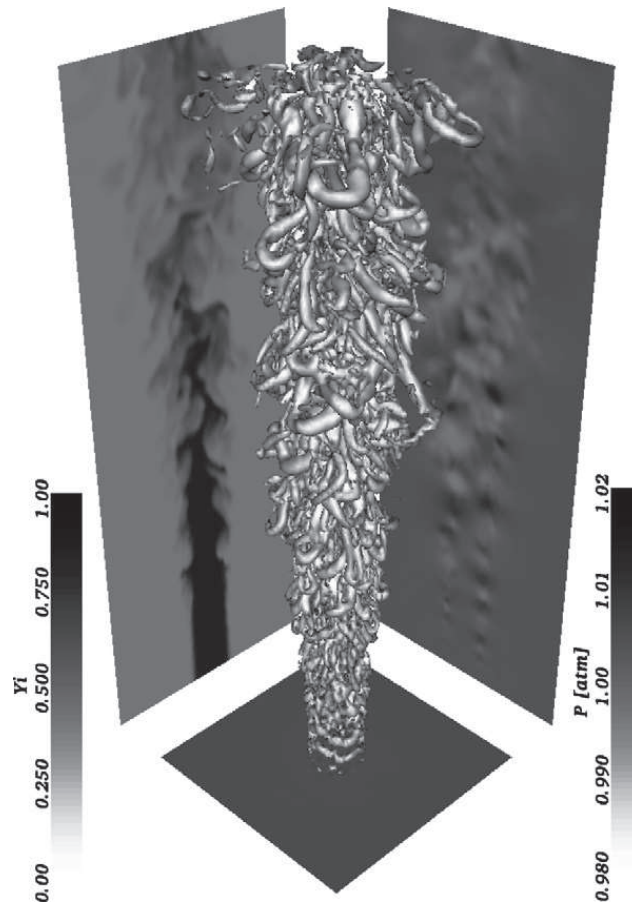


Fig. 19. Free round-jet with 3D-NSCBC: $Q = 0.5$ contours (center), passive scalar (left) and pressure (right) distributions over orthogonal axial planes ($t = 157.1D/U_b$).

pressure field reflects the presence of vortical structures and is smooth and on the target values in regions not affected by the flow. The compatibility conditions for inlet/outlet edges and corners allow perfect transition from the inlet to the outflow boundaries without producing any “square-shaped” pressure pattern. The complex of vortical structures which develops along the jet, is able to leave the domain through the outflows without being significantly perturbed (see Fig. 20).

On the other hand, the same simulation performed using the standard NSCBC approach—see Fig. 21—underwent a destabilization of the pressure, originating on an outflow’s corner with a peak of low pressure; this destabilization caused the jet to collapse toward the low pressure region as it can be observed in the figure. Moreover, the inlet side is far more noisy and a chessboard pattern is visible on the pressure map over the inlet plane. Looking at the vortical structures, turbulent structures seem a bit less developed, especially at the beginning of the jet. The problem is clearly linked to the observed inlet pressure noise (see axial pressure map on the right of Fig. 21), which interacts with the shear layer development and prevents the appearance of Kelvin–Helmholtz-type instabilities up to a distance of about one diameter from the jet’s nozzle.

From the above results, it is clear that such a simulation is not feasible with standard NSCBC unless: (a) a greater value of the pressure relaxation coefficient σ is used in order to better control the pressure at the boundary (thus leading to higher reflection); (b) a wider computational domain is used in order to prevent the jet from *falling* into a lateral outflow. This notwithstanding, the inlet noise could remain an issue.

4.5.2. Turbulent impinging round-jet

For this last test-case, the computational domain is a box of dimensions $2D \times 7D \times 7D$ with $D = 0.0026$ m the jet diameter ($90 \times 146 \times 146$ grid points). The grid is refined along x_1 in the near-wall region and slightly stretched along x_2 and x_3 in order to better resolve the jet shear layer; refinements in the three directions were limited to maintain a maximum stretching ratio of about 1.04 over consecutive cells. The resulting grid spacing along x_1 is: $\Delta x_1/D \simeq 0.0443$ at the jet’s nozzle exit and $\Delta x_1/D \simeq 0.0042$ at the wall. The grid spacing along x_2 and x_3 is: $\Delta x_t/D \simeq 0.033$ on the axis, $\Delta x_t/D \simeq 0.0261$ at $x_t = \pm D/2$ and $\Delta x_t/D \simeq 0.1251$ at $x_t = \pm 3.5D$ ($t = 2, 3$).

The inflow is located at $x_1 = 0$ with the following inlet relaxation parameters: $\eta_{3,4,5,6} = -\eta_2 = 1.28$. The target inlet velocity was imposed using the power law profile for turbulent pipe flow (Eq. (100)) with $n = 7.215$ ($U_b/U_{cl} = 0.8247$). The value of U_b was computed fixing the value of the jet’s Reynolds number: $Re_D = \rho U_b D / \mu = 23,000$. Also in this case, a correlated random noise was superimposed to the velocity profile (intensity $0.8\% U_b$) and the imposed inlet temperature was fixed at 300 K.

The four lateral boundaries are non-reflecting outflows with $\sigma = 0.28$ and target pressure equal to 1 atm. The assumed exact transverse terms were set according to the inviscid potential solution for the *axisymmetric stagnation-point flow* [16] with $\beta = 0.18$, the typical outflow Mach number for this flow. The bottom boundary is an adiabatic no-slip wall. Inflow/outflow edge conditions are used on the four top edges and inflow/outflow/outflow corner conditions are used on the relevant four joining corners; outflow/outflow edge conditions are

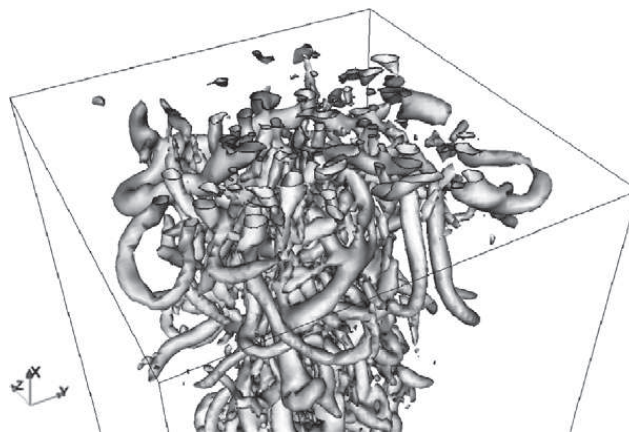


Fig. 20. Free round-jet with 3D-NSCBC: detail of $Q = 0.5$ contours at the boundary.

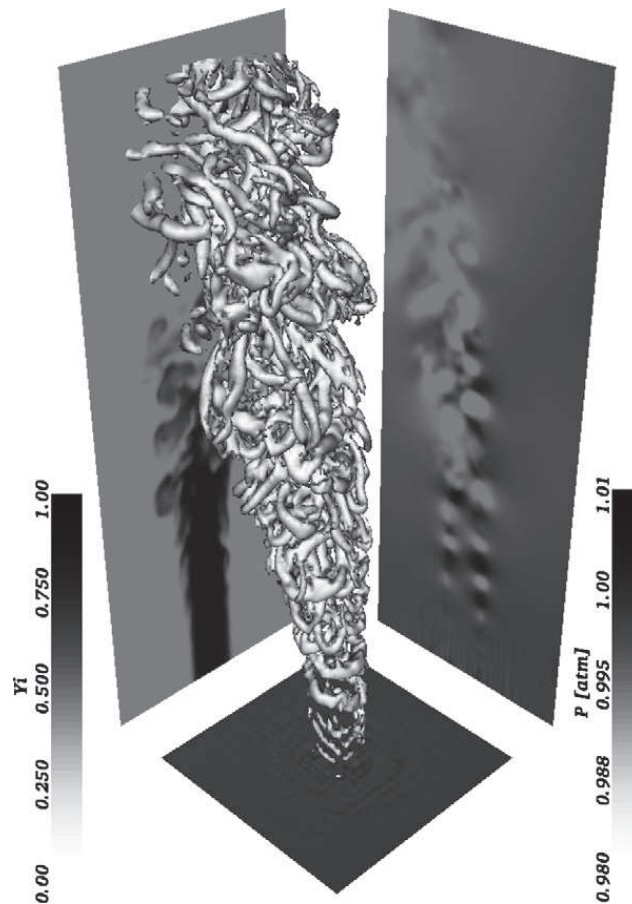


Fig. 21. Free round-jet with standard NSCBC: $Q = 0.5$ contours (center), passive scalar (left) and pressure (right) distributions over orthogonal axial planes ($t = 158.1D/U_b$).

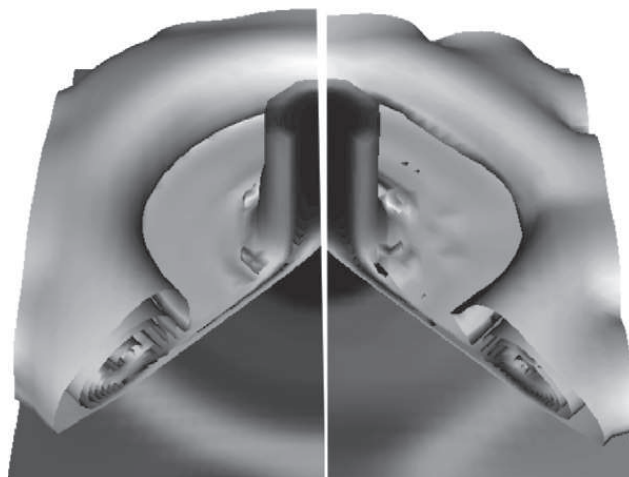


Fig. 22. Impinging round-jet: transverse terms influence on flow distortion. Iso-surfaces of velocity field and wall pressure map in the early stages of the simulation with standard NSCBC boundary conditions (right) and with 3D-NSCBC (left).

used on the four lateral edges, wall/outflow edge conditions are used on the four bottom edges and wall/outflow/outflow corner conditions are used on the four bottom corners (see Fig. 23). The simulation was started from fluid at rest and at reference condition (1 atm, 300 K) all over the domain.

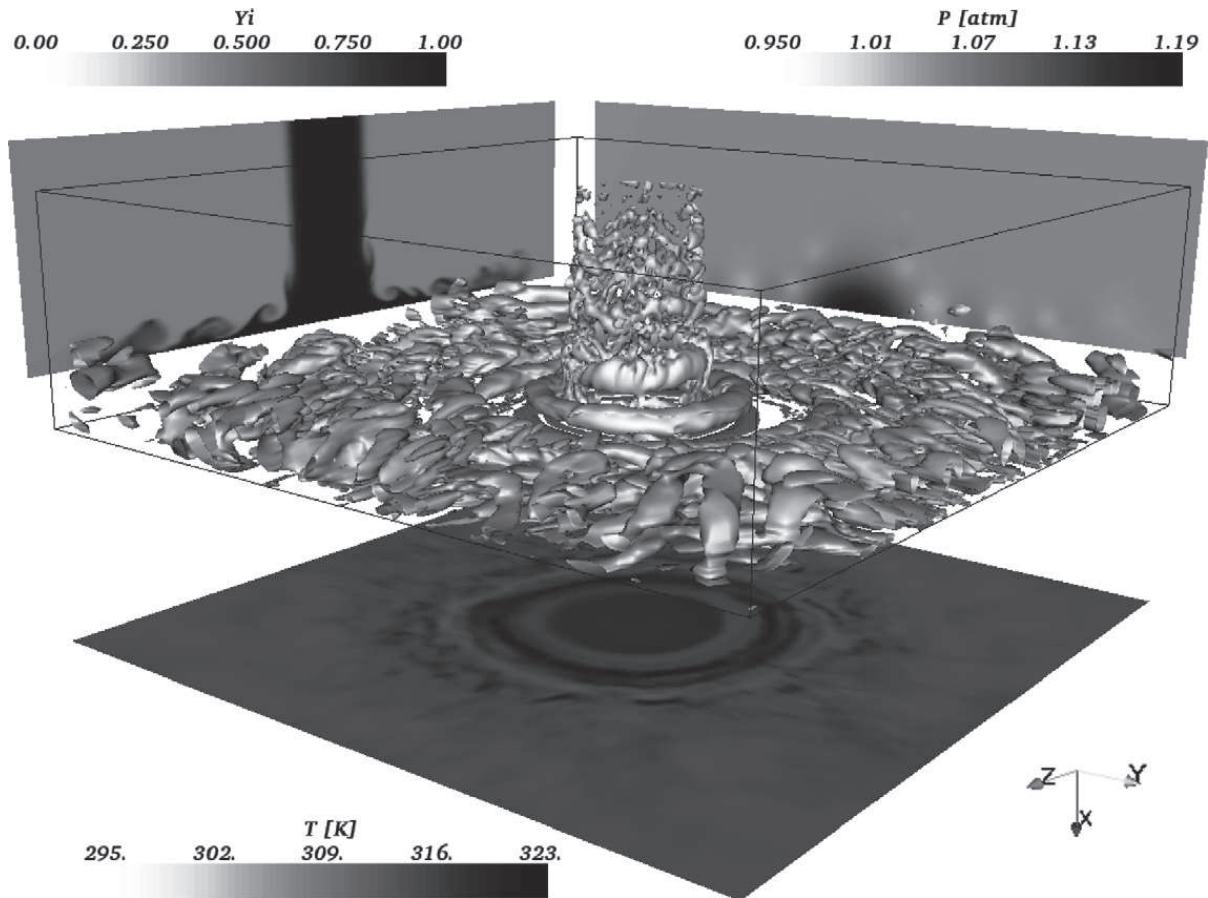


Fig. 23. Impinging round-jet: $Q = 0.5$ contours (center), passive scalar (left) and pressure (right) distributions over orthogonal axial planes and temperature (bottom) distribution over the impingement wall ($t = 52.4D/U_b$).

A preliminary test, made on a quite coarse mesh ($20 \times 42 \times 42$ grid points), is presented in Fig. 22 where the standard NSCBC non-reflecting outflow is compared with the 3D-NSCBC in terms of flow-field distortion. Iso-surfaces of velocity and wall pressure map are shown at the moment the big initial toroidal vortex encounters the domain boundaries. The inclusion of transverse terms allows for a significant reduction in terms of flow distortion and numerical noise; the latter, can be observed as a small perturbation in the vicinity of the impingement zone.

The developed flow field is shown by its coherent vortical structures ($Q = 0.5$ iso-surfaces) in Fig. 23. Pressure and passive scalar distributions over axial planes are projected to the sides and the wall temperature map is shown at the bottom. No significant numerical perturbation is observed on turbulence development, nor in the pressure field; moreover, the wall/outflow compatibility conditions exhibit fairly good robustness and numerical stability.

5. Concluding remarks

A three-dimensional treatment of boundary conditions at edges and corners of fully compressible flow computational domains has been discussed. This very sensitive point of boundary condition was found related to the treatment of convection and pressure gradient developing in the direction parallel to boundary faces, also called transverse terms.

A method involving the inclusion of these transverse effects in the computation of the incoming wave amplitude variations is presented. This method removes the original LODI assumption which is, in general, too stringent to correctly deal with turbulent flows. The work is grounded on the method proposed by Yoo et al. [24] regarding bidimensional flows, which poses additional problems of wave coupling at the edges

and corners of three-dimensional computational domain. A systematic approach to solve edges and corners has been presented and compatibility conditions for inflow/outflow and wall/outflow boundaries discussed. The general methodology to organize the incoming and outgoing waves approximation is based on the NSCBC approach by Poinso and Lele [12].

The novel technique has shown significant reduction of flow distortion and boundary reflection even when the configuration is characterized by high tridimensionality of the flow field, accompanied by obliquely propagating waves. The obtained 3D-NSCBC non-reflecting outflow, in particular, is characterized by an additional relaxation parameter for transverse terms damping. This poses the problem of specifying a reasonable exact solution for the flow under study. The tests performed have revealed a quite interesting feature on this regard: even when no information is available a priori for the steady solution, transverse relaxation can still be done toward identically zero terms. However, the optimal choice for the transverse relaxation parameter is, in general, related to the typical Mach number for the flow considered.

The proposed solution to the edge/corner wave coupling problem, as well as the compatibility conditions for inflow/outflow and wall/outflow connecting regions, have revealed good numerical stability and low level of spurious boundary reflection for acoustic waves traveling toward the edges and corners of the computational domain, thus allowing high boundary transparency even when computing complex flows.

The 3D-NSCBC method is applicable to compressible turbulent flows in the full subsonic range and is then suitable for a wide range of flow configurations and engineering applications. Furthermore, the method can be readily extended to chemically reacting flows with some additional development.

Acknowledgment

Support was provided by the project NICE (New Integrated Combustion system for Future Passenger Car Engines), TIP3-CT-2004-50620 within the 6th Framework program of the European Union. Computing resources were provided by IDRIS-CNRS (<http://www.idris.fr/>) and CRIHAN (<http://www.crihan.fr/>).

Appendix A. The characteristic form of the Navier–Stokes equations

Eqs. (1)–(4) are more conveniently recast in vector form as follows:

$$\frac{\partial \tilde{U}}{\partial t} + \frac{\partial \tilde{F}^i}{\partial x_i} + \frac{\partial \tilde{D}^i}{\partial x_i} = \mathbf{0}, \tag{A.1}$$

where $\tilde{U} = |\rho \ \rho u_1 \ \rho u_2 \ \rho u_3 \ \rho E \ \rho Z|^T$ is the vector of conservative variables and \tilde{F}^k is the flux vector of conservative variables along direction x_k ; vectors \tilde{D}^k represent viscous and diffusive terms only. \tilde{F}^k and \tilde{D}^k are explicitly written as follows (δ_{ij} is Kronecker’s delta):

$$\tilde{F}^k = \begin{pmatrix} \rho u_k \\ m_1 u_k + \delta_{1k} p \\ m_2 u_k + \delta_{2k} p \\ m_3 u_k + \delta_{3k} p \\ (\rho E + p) u_k \\ \rho Z u_k \end{pmatrix}, \quad \tilde{D}^k = \begin{pmatrix} 0 \\ -2\mu A_{1k} \\ -2\mu A_{2k} \\ -2\mu A_{3k} \\ -2\mu u_j A_{kj} + q_k \\ -\rho D \frac{\partial Z}{\partial x_k} \end{pmatrix}, \tag{A.2}$$

the relevant quantities being defined in Section 2.

Let the vector of primitive variables be $U = |\rho \ u_1 \ u_2 \ u_3 \ p \ Z|^T$; following the same analysis proposed by Hirsch [5] and Thompson [21,22], Eq. (A.1) is then rewritten in terms of primitive variables as

$$\frac{\partial U}{\partial t} + F^i \frac{\partial U}{\partial x_i} + D = \mathbf{0}, \tag{A.3}$$

where $D = P^{-1} \partial \tilde{D}^i / \partial x_i$ includes all the viscous and diffusive terms and F^k is the non-conservative Jacobian matrix relevant to the k th direction. In the present case

$$F^k = \begin{pmatrix} u_k & \delta_{1k}\rho & \delta_{2k}\rho & \delta_{3k}\rho & 0 & 0 \\ 0 & u_k & 0 & 0 & \delta_{1k}/\rho & 0 \\ 0 & 0 & u_k & 0 & \delta_{2k}/\rho & 0 \\ 0 & 0 & 0 & u_k & \delta_{3k}/\rho & 0 \\ 0 & \delta_{1k}\gamma P & \delta_{2k}\gamma P & \delta_{3k}\gamma P & u_k & 0 \\ 0 & 0 & 0 & 0 & 0 & u_k \end{pmatrix}. \tag{A.4}$$

$P = \partial \tilde{U} / \partial U$ is the Jacobian matrix to switch between primitive and conservative variables:

$$P = \begin{pmatrix} 1 & 0 & 0 & 0 & 0 & 0 \\ u_1 & \rho & 0 & 0 & 0 & 0 \\ u_2 & 0 & \rho & 0 & 0 & 0 \\ u_3 & 0 & 0 & \rho & 0 & 0 \\ \frac{1}{2}u_k u_k & \rho u_1 & \rho u_2 & \rho u_3 & \frac{1}{\kappa} & 0 \\ Z & 0 & 0 & 0 & 0 & \rho \end{pmatrix}, \tag{A.5}$$

$$P^{-1} = \begin{pmatrix} 1 & 0 & 0 & 0 & 0 & 0 \\ -u_1/\rho & 1/\rho & 0 & 0 & 0 & 0 \\ -u_2/\rho & 0 & 1/\rho & 0 & 0 & 0 \\ -u_3/\rho & 0 & 0 & 1/\rho & 0 & 0 \\ \frac{\kappa}{2}u_k u_k & -\kappa u_1 & -\kappa u_2 & -\kappa u_3 & \kappa & 0 \\ -Z/\rho & 0 & 0 & 0 & 0 & 1/\rho \end{pmatrix} \tag{A.6}$$

with $\kappa = \gamma - 1$.

Each F^k may be diagonalized resorting to the usual transformation:

$$S_k^{-1} F^k S_k = \Lambda^k, \tag{A.7}$$

the eigenvalues being

$$\lambda_1^k = u_k - c, \tag{A.8}$$

$$\lambda_{2,3,4,6}^k = u_k, \tag{A.9}$$

$$\lambda_5^k = u_k + c, \tag{A.10}$$

where c is the speed of sound and

$$S_k = \begin{pmatrix} \frac{1}{2c^2} & \frac{\delta_{1k}}{c^2} & \frac{\delta_{2k}}{c^2} & \frac{\delta_{3k}}{c^2} & \frac{1}{2c^2} & 0 \\ -\frac{\delta_{1k}}{2\rho c} & 1 - \delta_{1k} & 0 & 0 & \frac{\delta_{1k}}{2\rho c} & 0 \\ -\frac{\delta_{2k}}{2\rho c} & 0 & 1 - \delta_{2k} & 0 & \frac{\delta_{2k}}{2\rho c} & 0 \\ -\frac{\delta_{3k}}{2\rho c} & 0 & 0 & 1 - \delta_{3k} & \frac{\delta_{3k}}{2\rho c} & 0 \\ \frac{1}{2} & 0 & 0 & 0 & \frac{1}{2} & 0 \\ 0 & 0 & 0 & 0 & 0 & 1 \end{pmatrix}, \tag{A.11}$$

$$S_k^{-1} = \begin{pmatrix} 0 & -\delta_{1k}\rho c & -\delta_{2k}\rho c & -\delta_{3k}\rho c & 1 & 0 \\ \delta_{1k}c^2 & 1 - \delta_{1k} & 0 & 0 & -\delta_{1k} & 0 \\ \delta_{2k}c^2 & 0 & 1 - \delta_{2k} & 0 & -\delta_{2k} & 0 \\ \delta_{3k}c^2 & 0 & 0 & 1 - \delta_{3k} & -\delta_{3k} & 0 \\ 0 & \delta_{1k}\rho c & \delta_{2k}\rho c & \delta_{3k}\rho c & 1 & 0 \\ 0 & 0 & 0 & 0 & 0 & 1 \end{pmatrix}. \tag{A.12}$$

Depending on the type of boundary condition considered (face/edge/corner), a different number of characteristic directions should be taken into account (one/two/three) simultaneously: the three cases are summarized in the following sections.

A.1. Characteristic formulation along one direction for faces

Supposing that the boundary is orthogonal to the x_1 direction, the characteristic waves considered will be those traveling along x_1 ; therefore, only \mathbf{F}^1 needs to be diagonalized and Eq. (A.3) can be then written as

$$\frac{\partial \mathbf{U}}{\partial t} + \mathbf{S}_1 \mathbf{\Lambda}^1 \mathbf{S}_1^{-1} \frac{\partial \mathbf{U}}{\partial x_1} + \mathbf{F}^2 \frac{\partial \mathbf{U}}{\partial x_2} + \mathbf{F}^3 \frac{\partial \mathbf{U}}{\partial x_3} + \mathbf{D} = \mathbf{0}. \tag{A.13}$$

The eigenvalues (i.e. the propagation velocities of the characteristic waves) are

$$\lambda_1 = u_1 - c, \quad \lambda_{2,3,4,6} = u_1, \quad \lambda_5 = u_1 + c. \tag{A.14}$$

Following the procedure proposed by Thompson [21], a vector \mathcal{L} may be conveniently defined as

$$\mathcal{L} = \mathbf{\Lambda}^1 \mathbf{S}_1^{-1} \frac{\partial \mathbf{U}}{\partial x_1}, \tag{A.15}$$

whose components \mathcal{L}_i are the amplitude time variations of the characteristic waves [12]:

$$\mathcal{L} = \begin{pmatrix} \lambda_1 \left(\frac{\partial p}{\partial x_1} - \rho c \frac{\partial u_1}{\partial x_1} \right) \\ \lambda_2 \left(c^2 \frac{\partial \rho}{\partial x_1} - \frac{\partial p}{\partial x_1} \right) \\ \lambda_3 \frac{\partial u_2}{\partial x_1} \\ \lambda_4 \frac{\partial u_3}{\partial x_1} \\ \lambda_5 \left(\frac{\partial p}{\partial x_1} + \rho c \frac{\partial u_1}{\partial x_1} \right) \\ \lambda_6 \frac{\partial Z}{\partial x_1} \end{pmatrix}. \tag{A.16}$$

Eq. (A.13) is finally rewritten as a function of the wave amplitude variations and the relevant formulation in terms of conservative variables can be obtained pre-multiplying by \mathbf{P} :

$$\frac{\partial \mathbf{U}}{\partial t} + \mathbf{d} + \mathbf{F}^2 \frac{\partial \mathbf{U}}{\partial x_2} + \mathbf{F}^3 \frac{\partial \mathbf{U}}{\partial x_3} + \mathbf{D} = \mathbf{0}, \tag{A.17}$$

$$\frac{\partial \tilde{\mathbf{U}}}{\partial t} + \mathbf{P} \mathbf{d} + \frac{\partial \tilde{\mathbf{F}}^2}{\partial x_2} + \frac{\partial \tilde{\mathbf{F}}^3}{\partial x_3} + \frac{\partial \tilde{\mathbf{D}}^i}{\partial x_i} = \mathbf{0}, \tag{A.18}$$

where

$$\mathbf{d} = \mathbf{S}_1 \mathcal{L} = \begin{pmatrix} \frac{1}{c^2} \left[\mathcal{L}_2 + \frac{1}{2} (\mathcal{L}_5 + \mathcal{L}_1) \right] \\ \frac{1}{2\rho c} (\mathcal{L}_5 - \mathcal{L}_1) \\ \mathcal{L}_3 \\ \mathcal{L}_4 \\ \frac{1}{2} (\mathcal{L}_5 + \mathcal{L}_1) \\ \mathcal{L}_6 \end{pmatrix}. \tag{A.19}$$

It should be noted that Eq. (A.17) without transverse derivatives and diffusive terms constitutes the so-called LODI system of the standard NSCBC approach [12]:

$$\begin{cases} \frac{\partial \rho}{\partial t} + \frac{1}{c^2} [\mathcal{L}_2 + \frac{1}{2}(\mathcal{L}_5 + \mathcal{L}_1)] = 0, \\ \frac{\partial u_1}{\partial t} + \frac{1}{2\rho c} (\mathcal{L}_5 - \mathcal{L}_1) = 0, \\ \frac{\partial u_2}{\partial t} + \mathcal{L}_3 = 0, \\ \frac{\partial u_3}{\partial t} + \mathcal{L}_4 = 0, \\ \frac{\partial p}{\partial t} + \frac{1}{2}(\mathcal{L}_5 + \mathcal{L}_1) = 0, \\ \frac{\partial Z}{\partial t} + \mathcal{L}_6 = 0. \end{cases} \tag{A.20}$$

A.2. Characteristic formulation along two directions for edges

Supposing that the boundary is orthogonal to x_1 - and x_2 -directions, the characteristic waves considered on the connecting edge will be those traveling along x_1 and x_2 ; F^1 and F^2 are then diagonalized and Eq. (A.3) is written, with a slightly different notation, as

$$\frac{\partial U}{\partial t} + S_1 \Lambda S_1^{-1} \frac{\partial U}{\partial x_1} + S_2 M S_2^{-1} \frac{\partial U}{\partial x_2} + F^3 \frac{\partial U}{\partial x_3} + D = 0. \tag{A.21}$$

The eigenvalues of F^1 and F^2 are λ_i and μ_i , respectively:

$$\lambda_1 = u_1 - c, \quad \lambda_{2,3,4,6} = u_1, \quad \lambda_5 = u_1 + c, \tag{A.22}$$

$$\mu_1 = u_2 - c, \quad \mu_{2,3,4,6} = u_2, \quad \mu_5 = u_2 + c. \tag{A.23}$$

Wave amplitude time variations are defined as

$$\mathcal{L} = \Lambda S_1^{-1} \frac{\partial U}{\partial x_1}, \tag{A.24}$$

$$\mathcal{M} = M S_2^{-1} \frac{\partial U}{\partial x_2}, \tag{A.25}$$

where \mathcal{L} is expressed by Eq. (A.16) and \mathcal{M} is

$$\mathcal{M} = \begin{pmatrix} \mu_1 \left(\frac{\partial p}{\partial x_2} - \rho c \frac{\partial u_2}{\partial x_2} \right) \\ \mu_2 \frac{\partial u_1}{\partial x_2} \\ \mu_3 \left(c^2 \frac{\partial \rho}{\partial x_2} - \frac{\partial p}{\partial x_2} \right) \\ \mu_4 \frac{\partial u_3}{\partial x_2} \\ \mu_5 \left(\frac{\partial p}{\partial x_2} + \rho c \frac{\partial u_2}{\partial x_2} \right) \\ \mu_6 \frac{\partial Z}{\partial x_2} \end{pmatrix}. \tag{A.26}$$

Conservation laws in terms of primitive and conservative variables are respectively:

$$\frac{\partial U}{\partial t} + d + e + F^3 \frac{\partial U}{\partial x_3} + D = 0, \tag{A.27}$$

$$\frac{\partial \tilde{U}}{\partial t} + Pd + Pe + \frac{\partial \tilde{F}^3}{\partial x_3} + \frac{\partial \tilde{D}^i}{\partial x_i} = 0, \tag{A.28}$$

where d is expressed by Eq. (A.19) and e is

$$e = S_2 \mathcal{M} = \begin{pmatrix} \frac{1}{c^2} [\mathcal{M}_3 + \frac{1}{2}(\mathcal{M}_5 + \mathcal{M}_1)] \\ \mathcal{M}_2 \\ \frac{1}{2\rho c} (\mathcal{M}_5 - \mathcal{M}_1) \\ \mathcal{M}_4 \\ \frac{1}{2}(\mathcal{M}_5 + \mathcal{M}_1) \\ \mathcal{M}_6 \end{pmatrix}. \tag{A.29}$$

A.3. Characteristic formulation along three directions for corners

Characteristic waves are considered in all the three directions; all the flux matrix are diagonalized and Eq. (A.3) becomes

$$\frac{\partial \mathbf{U}}{\partial t} + \mathbf{S}_1 \mathbf{\Lambda} \mathbf{S}_1^{-1} \frac{\partial \mathbf{U}}{\partial x_1} + \mathbf{S}_2 \mathbf{M} \mathbf{S}_2^{-1} \frac{\partial \mathbf{U}}{\partial x_2} + \mathbf{S}_3 \mathbf{N} \mathbf{S}_3^{-1} \frac{\partial \mathbf{U}}{\partial x_3} + \mathbf{D} = \mathbf{0}. \tag{A.30}$$

The eigenvalues of \mathbf{F}^1 , \mathbf{F}^2 and \mathbf{F}^3 are λ_i , μ_i and ν_i , respectively:

$$\lambda_1 = u_1 - c, \quad \lambda_{2,3,4,6} = u_1, \quad \lambda_5 = u_1 + c, \tag{A.31}$$

$$\mu_1 = u_2 - c, \quad \mu_{2,3,4,6} = u_2, \quad \mu_5 = u_2 + c, \tag{A.32}$$

$$\nu_1 = u_3 - c, \quad \nu_{2,3,4,6} = u_3, \quad \nu_5 = u_3 + c. \tag{A.33}$$

Wave amplitude time variations are defined as

$$\mathcal{L} = \mathbf{\Lambda} \mathbf{S}_1^{-1} \frac{\partial \mathbf{U}}{\partial x_1}, \tag{A.34}$$

$$\mathcal{M} = \mathbf{M} \mathbf{S}_2^{-1} \frac{\partial \mathbf{U}}{\partial x_2}, \tag{A.35}$$

$$\mathcal{N} = \mathbf{N} \mathbf{S}_3^{-1} \frac{\partial \mathbf{U}}{\partial x_3}, \tag{A.36}$$

where \mathcal{L} and \mathcal{M} are expressed by Eqs. (A.16) and (A.26), respectively and \mathcal{N} is

$$\mathcal{N} = \begin{pmatrix} \nu_1 \left(\frac{\partial p}{\partial x_3} - \rho c \frac{\partial u_3}{\partial x_3} \right) \\ \nu_2 \frac{\partial u_1}{\partial x_3} \\ \nu_3 \frac{\partial u_2}{\partial x_3} \\ \nu_4 \left(c^2 \frac{\partial \rho}{\partial x_3} - \frac{\partial p}{\partial x_3} \right) \\ \nu_5 \left(\frac{\partial p}{\partial x_3} + \rho c \frac{\partial u_3}{\partial x_3} \right) \\ \nu_6 \frac{\partial Z}{\partial x_3} \end{pmatrix}. \tag{A.37}$$

Conservation laws in terms of primitive and conservative variables are respectively:

$$\frac{\partial \mathbf{U}}{\partial t} + \mathbf{d} + \mathbf{e} + \mathbf{f} + \mathbf{D} = \mathbf{0}, \tag{A.38}$$

$$\frac{\partial \tilde{\mathbf{U}}}{\partial t} + \mathbf{P} \mathbf{d} + \mathbf{P} \mathbf{e} + \mathbf{P} \mathbf{f} + \frac{\partial \tilde{\mathbf{D}}^i}{\partial x_i} = \mathbf{0}, \tag{A.39}$$

where \mathbf{d} is expressed by Eq. (A.19), \mathbf{e} is expressed by Eq. (A.29) and \mathbf{f} is

$$\mathbf{f} = \mathbf{S}_3 \mathcal{N} = \begin{pmatrix} \frac{1}{c^2} [\mathcal{N}_4 + \frac{1}{2} (\mathcal{N}_5 + \mathcal{N}_1)] \\ \mathcal{N}_2 \\ \mathcal{N}_3 \\ \frac{1}{2\rho c} (\mathcal{N}_5 - \mathcal{N}_1) \\ \frac{1}{2} (\mathcal{N}_5 + \mathcal{N}_1) \\ \mathcal{N}_6 \end{pmatrix}. \tag{A.40}$$

Appendix B. Computing the transverse terms from conservative variables' fluxes

When the solver integrates the Navier–Stokes equations written in conservative form, it may be more convenient to directly relate the transverse terms vector \mathcal{T} to the flux vector $\tilde{\mathbf{F}}^k$. Considering, for instance, a face boundary orthogonal to x_1 , Eq. (13) in vector form reads

$$\frac{\partial \mathbf{U}}{\partial t} + \mathbf{d} - \mathcal{T} = \mathbf{0}, \quad (\text{B.1})$$

where $-\mathcal{T}$ represents the transverse fluxes and pressure gradients along x_2 and x_3 :

$$\mathcal{T} = -\mathbf{F}^t \frac{\partial \mathbf{U}}{\partial x_t} \quad (t = 2, 3). \quad (\text{B.2})$$

By definition, the non-conservative Jacobian matrix \mathbf{F}^k is related to the flux vector $\tilde{\mathbf{F}}^k$ by the following relation:

$$\mathbf{P} \mathbf{F}^k \frac{\partial \mathbf{U}}{\partial x_k} = \frac{\partial \tilde{\mathbf{F}}^k}{\partial x_k}. \quad (\text{B.3})$$

Pre-multiplying the above equation by \mathbf{P}^{-1} , the expression for \mathcal{T} then becomes

$$\mathcal{T} = -\mathbf{P}^{-1} \frac{\partial \tilde{\mathbf{F}}^t}{\partial x_t} \quad (t = 2, 3) \quad (\text{B.4})$$

with components

$$\mathcal{T}_1 = -\frac{\partial F_1^t}{\partial x_t}, \quad (\text{B.5})$$

$$\mathcal{T}_2 = -\frac{1}{\rho} \left(\frac{\partial F_2^t}{\partial x_t} - u_1 \frac{\partial F_1^t}{\partial x_t} \right), \quad (\text{B.6})$$

$$\mathcal{T}_3 = -\frac{1}{\rho} \left(\frac{\partial F_3^t}{\partial x_t} - u_2 \frac{\partial F_1^t}{\partial x_t} \right), \quad (\text{B.7})$$

$$\mathcal{T}_4 = -\frac{1}{\rho} \left(\frac{\partial F_4^t}{\partial x_t} - u_3 \frac{\partial F_1^t}{\partial x_t} \right), \quad (\text{B.8})$$

$$\mathcal{T}_5 = -(\gamma - 1) \left(\frac{\partial F_5^t}{\partial x_t} + \frac{u_k u_k}{2} \frac{\partial F_1^t}{\partial x_t} - u_k \frac{\partial F_{k+1}^t}{\partial x_t} \right), \quad (\text{B.9})$$

$$\mathcal{T}_6 = -\frac{1}{\rho} \left(\frac{\partial F_6^t}{\partial x_t} - Z \frac{\partial F_1^t}{\partial x_t} \right). \quad (\text{B.10})$$

The same relations for an edge boundary can be easily obtained by considering that, in that case, the vector \mathcal{T} represents fluxes and pressure gradients along the edge direction only.

References

- [1] M. Baum, T. Poinsot, D. Thévenin, Accurate boundary conditions for multicomponent reactive flows, *Journal of Computational Physics* 116 (2) (1995) 247–261.
- [2] C. Bogey, C. Bailly, An analysis of the corrections between the turbulent flow and the sound pressure fields of subsonic jets, *Journal of Fluid Mechanics* 583 (2007) 71–97.
- [3] T. Colonius, S. Lele, P. Moin, The free compressible viscous vortex, *Journal of Fluid Mechanics* 230 (1991) 45–73.
- [4] F. Ducros, F. Laporte, T. Soullères, V. Guinot, P. Moinat, B. Caruelle, High-order fluxes for conservative skew-symmetric-like schemes in structured meshes: application to compressible flows, *Journal of Computational Physics* 161 (2000) 114–139.
- [5] C. Hirsch, *Numerical Computation of Internal and External Flows*, vol. 2, John Wiley & Sons Ltd., 1990.
- [6] R. Hixon, S. Shih, R. Mankabadi, Evaluation of boundary conditions for computational aeroacoustics, *AIAA Journal* 33 (11) (1995) 2006–2012.
- [7] G. Jiang, C. Shu, Efficient implementation of weighted ENO schemes, *Journal of Computational Physics* 126 (1996) 202–228.
- [8] M. Klein, A. Sadiki, J. Janicka, A digital filter based generation of inflow data for spatially developing direct numerical or large eddy simulations, *Journal of Computational Physics* 186 (2003) 652–665.

- [9] F. Nicoud, Defining wave amplitude in characteristic boundary conditions, *Journal of Computational Physics* 149 (1999) 418–422.
- [10] F. Nicoud, F. Ducros, Subgrid-scale stress modelling based on the square of the velocity gradient tensor, *Flow, Turbulence and Combustion* 62 (3) (1999) 183–200.
- [11] N. Okong'o, J. Bellan, Consistent boundary conditions for multicomponent real gas mixtures based on characteristic waves, *Journal of Computational Physics* 176 (2) (2002) 330–344.
- [12] T. Poinsot, S. Lele, Boundary conditions for direct simulations of compressible viscous flows, *Journal of Computational Physics* 101 (1992) 104–129.
- [13] W. Polifke, C. Wall, P. Moin, Partially reflecting and non-reflecting boundary conditions for simulation of compressible viscous flow, *Journal of Computational Physics* 213 (1) (2006) 437–449.
- [14] R. Prosser, Improved boundary conditions for the direct numerical simulation of turbulent subsonic flows. I. Inviscid flows, *Journal of Computational Physics* 207 (2005) 736–768.
- [15] D. Rudy, J. Strikwerda, A nonreflecting outflow boundary condition for subsonic Navier–Stokes calculations, *Journal of Computational Physics* 36 (1980) 55–70.
- [16] H. Schlichting, K. Gersten, *Boundary-Layer Theory*, eighth ed., Springer-Verlag, Berlin, Heidelberg, 2000.
- [17] J. Sutherland, C. Kennedy, Improved boundary conditions for viscous, reacting, compressible flows, *Journal of Computational Physics* 191 (2) (2003) 502–524.
- [18] R. Swanson, E. Turkel, On central-difference and upwind schemes, *Journal of Computational Physics* 101 (1992) 292–306.
- [19] C. Tam, Advances in numerical boundary conditions for computational aeroacoustics, *Journal of Computational Acoustics* 6 (4) (1998) 377–402.
- [20] S. Tatsumi, L. Martinelli, A. Jameson, Flux-limited schemes for the compressible Navier–Stokes equations, *AIAA Journal* 33 (2) (1995) 252–261.
- [21] K.W. Thompson, Time dependent boundary conditions for hyperbolic systems, *Journal of Computational Physics* 68 (1987) 1–24.
- [22] K.W. Thompson, Time dependent boundary conditions for hyperbolic systems: II, *Journal of Computational Physics* 89 (1990) 439–461.
- [23] M. Valorani, B. Favini, On the numerical integration of multi-dimensional, initial boundary value problems for the Euler equations in quasi-linear form, *Numerical Methods for Partial Differential Equations* 14 (6) (1998) 781–814.
- [24] C. Yoo, Y. Wang, A. Trouvé, H. Im, Characteristic boundary conditions for direct simulations of turbulent counterflow flames, *Combustion Theory and Modeling* 9 (4) (2005) 617–646.

G. Lodato, P. Domingo and L. Vervisch. A Compressible Wall-Adapting Similarity Mixed Model for Large-Eddy Simulation of the Impinging Round Jet, *Physics of Fluids*, **21(3)**: (2009).

A compressible wall-adapting similarity mixed model for large-eddy simulation of the impinging round jet

Guido Lodato,^{a)} Luc Vervisch,^{b)} and Pascale Domingo^{c)}

INSA-Rouen, UMR-CNRS-6614-CORIA, Campus du Madrillet, Avenue de l'Université, BP 8, 76801 Saint Etienne du Rouvray Cedex, France

(Received 3 July 2008; accepted 12 December 2008; published online 6 March 2009)

Wall-jet interaction is studied with large-eddy simulation (LES) in which a mixed-similarity subgrid scale (SGS) closure is combined with the wall-adapting local eddy-viscosity (WALE) model for the eddy-viscosity term. The macrotemperature and macropressure are introduced to deduce a weakly compressible form of the mixed-similarity model, and the relevant formulation for the energy equation is deduced accordingly. LES prediction capabilities are assessed by comparing flow statistical properties against experiment of an unconfined impinging round jet at Reynolds numbers of 23 000 and 70 000. To quantify the benefit of the proposed WALE-similarity mixed model, the lower Reynolds number simulations are also performed using the standard WALE and Lagrangian dynamic Smagorinsky approaches. The unsteady compressible Navier–Stokes equations are integrated over 2.9 M, 3.5 M, and 5.5 M node Cartesian grids with an explicit fourth-order finite volume solver. Nonreflecting boundary conditions are enforced using a methodology accounting for the three-dimensional character of the turbulent flow at boundaries. A correct wall scaling is achieved from the combination of similarity and WALE approaches; for this wall-jet interaction, the SGS closure terms can be computed in the near-wall region without the necessity of resorting to additional specific treatments. The possible impact of turbulent energy backscatter in such flow configurations is also addressed. It is found that, for the present configuration, the correct reproduction of reverse energy transfer plays a key role in the estimation of near-wall statistics, especially when the viscous sublayer is not properly resolved. © 2009 American Institute of Physics. [DOI: 10.1063/1.3068761]

I. INTRODUCTION

Impinging jets are of great interest in many practical engineering applications where high heat- and mass-transfer performances need to be achieved. This relatively simple configuration can be regarded as characterized by three main regions: (a) free jet flow, (b) stagnation, and (c) wall jet flow. Partly due to this heterogeneity and partly due to some peculiar features, such as the effect of strong curvature over the wall jet turbulence development or the interaction of primary vortices coming from the free jet region and secondary vortices generated close to the wall, the impinging jets are characterized by a series of hard to predict physical phenomena, which are still to be thoroughly understood and described. Thus the intrinsic complexity of this flow configuration^{1–3} makes the impinging round jet a particularly tough test bench for turbulence modeling.

If Reynolds averaged Navier–Stokes computations of impinging jets are well documented (see Hofmann *et al.*⁴ for a review), most of the studies which can be found in literature regarding large-eddy simulation (LES) of impinging round jets are generally focused on wall thermal exchange, without particular attention on subgrid scale (SGS) modeling performances within the most critical near-wall region. A thorough study of wall-round-jet interaction and heat trans-

fer, with particular emphasis on the case of jet's Reynolds number of 20 000 and nozzle to wall distance equal to twice the jet's diameter, was presented by Hällqvist^{5,6} using low-Mach number highly resolved LES on a 6 M cells Cartesian grid without any explicit SGS model. A similar test case, with Reynolds number of 23 000, was analyzed by Hadžiabdić and Hanjalić⁷ using a fully compressible quite well refined LES and the dynamic Smagorinsky model⁸ with clipped model constant, grids ranging from 7.5 M to about 10 M cells and a single quadrant grid with 5 M cells were used, this last representing a total equivalent cell number of about 20 M. In both cases, a precursor simulation of fully developed pipe flow was performed to build the inlet boundary condition. Related flow configurations were also considered with the wall-adapting local eddy-viscosity (WALE) SGS model,⁹ which was used for LES of twin impinging jets in cross flow;¹⁰ while LESs of impinging jets in a confined flow¹¹ have been reported separately.

LES of such wall bounded flows still represents a particularly challenging problem, especially when grid resolution at the wall is kept as low as possible in order to reduce computational cost when the jet-wall interaction is only part of the flow problem to be simulated. When wall boundaries are present, most SGS models, as those based on the eddy-viscosity hypothesis, are generally inadequate in reproducing the correct wall scaling for unresolved quantities. The dynamic approach^{8,12} can be used to recover with success the correct wall scaling, after introducing some spatial or time

^{a)}Electronic mail: guido.lodato@coria.fr.

^{b)}Electronic mail: luc.vervisch@coria.fr.

^{c)}Electronic mail: pascale.domingo@coria.fr.

averaging along fluid particles' path lines.¹³ Nevertheless, the standard eddy-viscosity assumption implies the alignment of the SGS stress tensor with the deformation tensor, which constitutes a quite strong hypothesis and the energy backscatter, which is theoretically permitted using dynamic models, may remain more a mathematical outcome than a fully intended physical model prediction.

Similarity models (see Meneveau and Katz,¹⁴ Sagaut,¹⁵ and references therein for a detailed review) remove the hypothesis of alignment between the SGS stress and the resolved shear stress tensor, thus achieving strong correlation between expected and measured SGS stresses. Moreover, they are able to provide correct wall scaling on each component of the SGS stress tensor¹⁶ and, *a priori*, to predict energy backscatter on a more physical ground. Unfortunately, similarity models are generally not enough dissipative and the addition of an eddy-viscosity term is anyway advisable in practice. The resulting closures are the so-called mixed-similarity models and a number of versions have been proposed which, again, resort to the classical eddy-viscosity hypothesis by Smagorinsky¹⁷ and to dynamic modeling, in order to retain the correct wall scaling that the eddy-viscosity term may have affected.^{18–21}

In this context, the WALE model⁹ is of interest, as it is intrinsically able to retain the correct wall scaling by construction. Along these lines, a compressible version of the similarity mixed model^{20,22} is discussed below, where the eddy-viscosity term is computed by the WALE approximation. The model is tested on turbulent impinging round jets with Reynolds numbers of 23 000 and 70 000; results are compared against the experimental data provided by Cooper *et al.*²³ for both turbulence regimes and by Geers²⁴ and Geers *et al.*²⁵ for the lower Reynolds number. A comparison with the standard WALE model and a compressible extension of the Lagrangian dynamic Smagorinsky model (LDSM) originally developed by Meneveau *et al.*¹³ is also presented for the $Re_D=23\,000$ test case.

Section II reports on the model problem and numerics; the filtered balance equations (continuity, momentum, energy, and scalar) are discussed along with the explicit filtering procedure, then the flow configuration, the numerical formulation, and the grid are discussed. In the subsequent part, the results are analyzed and compared with experimental measurements. In Appendix, the practical use of the explicit filtering is detailed.

II. MODEL PROBLEM AND NUMERICS

A. Filtered balance equations

The flow problem is described by the compressible Navier–Stokes equations set for a Newtonian fluid following the ideal single-component gas law plus one additional transport equation for a passive scalar Z . After introducing the vector of conservative variables $U = [\rho \ \rho u_1 \ \rho u_2 \ \rho u_3 \ \rho e \ \rho Z]^T$ and the flux vector F^k , the problem is formalized as follows:

$$\frac{\partial U}{\partial t} + \frac{\partial F^i}{\partial x_i} = \mathbf{0}, \quad (1)$$

with

$$F^k = \begin{pmatrix} \rho u_k \\ \rho u_1 u_k + \delta_{1k} p - 2\mu A_{1k} \\ \rho u_2 u_k + \delta_{2k} p - 2\mu A_{2k} \\ \rho u_3 u_k + \delta_{3k} p - 2\mu A_{3k} \\ (\rho e + p) u_k - 2\mu u_j A_{kj} - \lambda \frac{\partial T}{\partial x_k} \\ \rho Z u_k - \rho D \frac{\partial Z}{\partial x_k} \end{pmatrix}, \quad (2)$$

$$p = \rho RT, \quad (3)$$

$$\rho e = \frac{1}{2} \rho u_k u_k + \frac{p}{\gamma - 1}, \quad (4)$$

$$A_{ij} = \frac{1}{2} \left(\frac{\partial u_i}{\partial x_j} + \frac{\partial u_j}{\partial x_i} \right) - \frac{1}{3} \delta_{ij} \frac{\partial u_k}{\partial x_k}. \quad (5)$$

In the above equations, ρ is the fluid mass density, p is the thermodynamic pressure, ρe is the total energy density (kinetic+thermal), T is the absolute temperature, $R=R^*/M_w$ is the gas constant computed from the universal gas constant $R^*=8.32$ J/(mol K) and the gas molar weight M_w , and δ_{ij} is the Kronecker's delta; $\gamma=c_p/c_v$ is the ratio between specific heat capacities at constant pressure and constant volume, which, in the present case, can be expressed as

$$c_v = \frac{R}{\gamma - 1}, \quad (6)$$

$$c_p = c_v + R. \quad (7)$$

The dynamic viscosity of the fluid μ is expressed by the Sutherland's law,

$$\mu(T) = \mu_{\text{ref}} \left(\frac{T}{T_{\text{ref}}} \right)^{3/2} \frac{T_{\text{ref}} + S}{T + S}. \quad (8)$$

Finally, the thermal conductivity λ and the diffusion coefficient D are computed using the dynamic viscosity and the Prandtl and Schmidt numbers,

$$\lambda = \frac{\mu c_p}{Pr}, \quad D = \frac{\mu}{\rho Sc}. \quad (9)$$

1. The filtered continuity and momentum equations

In LES, the Navier–Stokes equations are filtered with a low-pass filter, the low frequency components of the flow field, those which represent the large-scale structures of the flow, being directly resolved, and the coupling term arising from the nonlinear convective term being modeled by the SGS model. In the present study, implicit filtering is used, therefore the low-pass filter's cutoff length Δ coincides with the grid spacing. Introducing the filter operator $\bar{\cdot}$ and the

Favre-filter operator *tilde* (namely, $\overline{\rho\tilde{\varphi}} = \overline{\rho\varphi}$ for any quantity φ), the filtered Navier–Stokes equations can be written in the following form:^{26,27}

$$\frac{\partial \overline{\mathbf{U}}}{\partial t} + \frac{\partial \overline{\mathbf{F}}^i}{\partial x_i} = \mathbf{0}, \quad (10)$$

where $\overline{\mathbf{U}} = |\overline{\rho} \ \overline{\rho u_1} \ \overline{\rho u_2} \ \overline{\rho u_3} \ \overline{\rho e} \ \overline{\rho Z}|^T$.

The part of the filtered flux vector relevant to mass and momentum transport equations can be expressed as

$$\overline{\mathbf{F}}_m^k = \begin{pmatrix} \overline{\rho u_k} \\ \overline{\rho u_1 \tilde{u}_k} + \delta_{1k} \overline{p} - \overline{2\mu A_{1k}} - \tau_{1k} \\ \overline{\rho u_2 \tilde{u}_k} + \delta_{2k} \overline{p} - \overline{2\mu A_{2k}} - \tau_{2k} \\ \overline{\rho u_3 \tilde{u}_k} + \delta_{3k} \overline{p} - \overline{2\mu A_{3k}} - \tau_{3k} \end{pmatrix}, \quad (11)$$

where τ_{ij} is the subgrid stress tensor,

$$\tau_{ij} = \overline{\rho \tilde{u}_i \tilde{u}_j} - \overline{\rho u_i u_j}. \quad (12)$$

Introducing the velocity decomposition into resolved and unresolved parts, namely, $u_i = \tilde{u}_i + u'_i$, into Eq. (12), the SGS stress tensor may be written according to the Leonard decomposition as

$$-\tau_{ij} = L_{ij} + C_{ij} + R_{ij}, \quad (13)$$

with

$$L_{ij} = \overline{\rho \tilde{u}_i \tilde{u}_j} - \overline{\rho \tilde{u}_i \tilde{u}_j}, \quad (14)$$

$$C_{ij} = \overline{\rho \tilde{u}_i u'_j} + \overline{\rho u'_i \tilde{u}_j}, \quad (15)$$

$$R_{ij} = \overline{\rho u'_i u'_j}. \quad (16)$$

In the perspective of the scale-similarity hypothesis,^{28,29} generalized to the compressible case,^{22,30} it is postulated that the statistical features of tensors constructed on the SGSs are similar to those of analogous tensors computed on the basis of the smallest resolved scales, which may be estimated as the difference between the filtered field and the twice-filtered field, this difference representing a reasonable estimate of the filtered SGS velocity.²⁸ Hence the cross term and the Reynolds term are approximated as

$$C_{ij} \approx \overline{\rho} [\tilde{u}_i (\tilde{u}_j - \tilde{\tilde{u}}_j) + (\tilde{u}_i - \tilde{\tilde{u}}_i) \tilde{\tilde{u}}_j], \quad (17)$$

$$R_{ij} \approx \overline{\rho} (\tilde{u}_i - \tilde{\tilde{u}}_i) (\tilde{u}_j - \tilde{\tilde{u}}_j), \quad (18)$$

thus leading to the following approximation for the SGS stress tensor:

$$-\tau_{ij} \approx \overline{\rho \tilde{u}_i \tilde{u}_j} - \overline{\rho \tilde{u}_i \tilde{\tilde{u}}_j} + \underbrace{\overline{\rho \tilde{\tilde{u}}_i \tilde{u}_j} - \overline{\rho \tilde{\tilde{u}}_i \tilde{\tilde{u}}_j}}_{C_{ij} + R_{ij}} = \overline{\rho \tilde{u}_i \tilde{u}_j} - \overline{\rho \tilde{\tilde{u}}_i \tilde{\tilde{u}}_j}. \quad (19)$$

If the generalized central moments proposed by Germano³¹ are introduced, the SGS stress tensor is decomposed according to the modified Leonard decomposition as

$$-\tau_{ij} = \mathcal{L}_{ij} + C_{ij} + \mathcal{R}_{ij}, \quad (20)$$

with

$$\mathcal{L}_{ij} = \overline{\rho \tilde{u}_i \tilde{u}_j} - \overline{\rho \tilde{\tilde{u}}_i \tilde{\tilde{u}}_j}, \quad (21)$$

$$C_{ij} = \overline{\rho \tilde{u}_i u'_j} + \overline{\rho u'_i \tilde{u}_j} - \overline{\rho \tilde{\tilde{u}}_i \tilde{\tilde{u}}_j} - \overline{\rho u'_i \tilde{\tilde{u}}_j}, \quad (22)$$

$$\mathcal{R}_{ij} = \overline{\rho u'_i u'_j} - \overline{\rho u'_i u'_j}. \quad (23)$$

Comparing Eq. (19) and the above decomposition, it is clear that the scale-similarity hypothesis is equivalent to neglecting C_{ij} and \mathcal{R}_{ij} . If on one hand, similarity models give very accurate predictions of the structural features of the SGS stresses, on the other hand, they are not generally effective in reproducing the correct average energy transfer, i.e., they are not dissipative enough.¹⁵ A similarity mixed model may be then constructed by adding an eddy-viscosity term to Eq. (19).²⁹ In view of the modified Leonard decomposition, this turns out to be equivalent to assume that $C_{ij} \approx \overline{\rho \tilde{u}_i \tilde{u}_j} - \overline{\rho \tilde{\tilde{u}}_i \tilde{\tilde{u}}_j}$ (Ref. 22) or, as it can be easily verified, that $C_{ij} \approx 0$ and $\overline{\rho u'_i u'_j} \approx 0$. Hence, the SGS stress tensor is modeled as

$$\tau_{ij} \approx -\overline{\rho u'_i u'_j} - \overline{\rho} (\tilde{u}_i \tilde{u}_j - \tilde{\tilde{u}}_i \tilde{\tilde{u}}_j). \quad (24)$$

To obtain the proposed WALE-similarity model, the deviatoric part of the SGS true Reynolds term, namely, the first term in the right-hand side of the above equation, is modeled using the eddy-viscosity WALE model proposed by Nicoud and Ducros⁹ as

$$-\overline{\rho u'_i u'_j} \approx 2\overline{\rho} \nu_t \tilde{A}_{ij}, \quad (25)$$

where \tilde{A}_{ij} is the deviator of the deformation tensor computed on the resolved velocity field using Eq. (5) and

$$\nu_t = C_w^2 \Delta^2 \frac{(\tilde{s}_{ij}^d \tilde{s}_{ij}^d)^{3/2}}{(\tilde{S}_{ij} \tilde{S}_{ij})^{5/2} + (\tilde{s}_{ij}^d \tilde{s}_{ij}^d)^{5/4}}, \quad (26)$$

where Δ is the grid level filter width, which, in the present case, is evaluated as

$$\Delta = f(a_1, a_2) \Delta_{\text{eq}}, \quad (27)$$

where $\Delta_{\text{eq}} = (\Delta_1 \Delta_2 \Delta_3)^{1/3}$ (Ref. 32)— Δ_k being the local grid spacing in the k th direction—and $f(a_1, a_2)$ is the corrective factor for anisotropic grids proposed by Scotti *et al.*,³³ where a_1 and a_2 are the aspect ratios of the two smaller sides of the computational cell to the biggest one.

In Eq. (26), $C_w = 0.5$ is a true model constant, \tilde{S}_{ij} is the strain rate tensor of the resolved field, and \tilde{s}_{ij}^d is the traceless symmetric part of the square of the resolved velocity gradient tensor \tilde{g}_{ij} , namely,

$$\tilde{s}_{ij}^d = \frac{1}{2} (\tilde{g}_{ij}^2 + \tilde{g}_{ji}^2) - \frac{1}{3} \delta_{ij} \tilde{g}_{kk}^2, \quad (28)$$

with $\tilde{g}_{ij}^2 = \tilde{g}_{ik} \tilde{g}_{kj}$. It should be noted that the WALE model has the distinct advantage that it automatically recovers proper scaling in the near-wall region. The following approximation of the SGS stress tensor is then obtained:

$$\tau_{ij} \approx 2\overline{\rho} \nu_t \tilde{A}_{ij} - \frac{1}{3} \delta_{ij} \overline{\rho u'_k u'_k} - \overline{\rho} (\tilde{u}_i \tilde{u}_j - \tilde{\tilde{u}}_i \tilde{\tilde{u}}_j), \quad (29)$$

where only the second term on the right-hand side is not yet closed. Following an analogous approach as in Refs. 26 and

27, we introduce a *macropressure*, which includes the mentioned unclosed term,

$$\bar{\omega} = \bar{p} + \frac{1}{3} \overline{\rho u'_k u'_k}, \quad (30)$$

and neglecting viscous subgrid contributions, namely, $\overline{\mu A_{ij}} - \bar{\mu} \tilde{A}_{ij} \approx 0$, the flux vector Eq. (11) then becomes

$$\bar{F}_m^k = \begin{pmatrix} \bar{\rho} \tilde{u}_k \\ \overline{\rho u_1 \tilde{u}_k} + \delta_{1k} (\bar{\omega} + \frac{1}{3} \mathcal{L}_{jj}) - 2 \bar{\mu} \tilde{A}_{1k} - \tau_{1k}^d \\ \overline{\rho u_2 \tilde{u}_k} + \delta_{2k} (\bar{\omega} + \frac{1}{3} \mathcal{L}_{jj}) - 2 \bar{\mu} \tilde{A}_{2k} - \tau_{2k}^d \\ \overline{\rho u_3 \tilde{u}_k} + \delta_{3k} (\bar{\omega} + \frac{1}{3} \mathcal{L}_{jj}) - 2 \bar{\mu} \tilde{A}_{3k} - \tau_{3k}^d \end{pmatrix}, \quad (31)$$

where $\bar{\mu}$ is computed from the resolved *macrottemperature* [refer to Eqs. (35) and (63) in Sec. II A 2] and τ_{ij}^d is the deviatoric part of the SGS stress tensor, namely,

$$\tau_{ij}^d = 2 \bar{\rho} \nu \tilde{A}_{ij} - \bar{\rho} (\tilde{u}_i \tilde{u}_j - \tilde{u}_i \tilde{u}_j)^d. \quad (32)$$

2. The filtered energy equation

The filtered total energy may be expressed as

$$\begin{aligned} \bar{\rho e} &= \bar{\rho} c_v \bar{T} + \frac{1}{2} \overline{\rho u_k u_k} \\ &= \bar{\rho} c_v \bar{T} + \frac{1}{2} \overline{\rho u_k \tilde{u}_k} + \frac{1}{2} (\overline{\rho u_k u_k} - \overline{\rho u_k \tilde{u}_k}). \end{aligned} \quad (33)$$

It should be noted that, in the above equation, the specific heat capacity c_v has been assumed constant to the filtering operator; this hypothesis, which holds for c_p and R as well, will be implicitly assumed henceforth. Using the modified Leonard decomposition and the scale-similarity hypothesis (see Sec. II A 1), the above equation may be rewritten as

$$\bar{\rho e} \approx \bar{\rho} c_v \bar{T} + \frac{1}{2} \overline{\rho u_k \tilde{u}_k} + \frac{1}{2} \bar{\rho} (\tilde{u}_k \tilde{u}_k - \tilde{u}_k \tilde{u}_k) + \frac{1}{2} \overline{\rho u'_k u'_k}, \quad (34)$$

where, again, the last term on the right-hand side is not closed. It seems natural, therefore, to define a *macrottemperature*,

$$\bar{\vartheta} = \bar{T} + \frac{1}{2 \bar{\rho} c_v} \overline{\rho u'_k u'_k}, \quad (35)$$

which includes the resolved temperature and the spherical part of the SGS true Reynolds term. In this way, the resolved total energy may be computed from resolved quantities,

$$\bar{\rho e} = \bar{\rho} c_v \bar{\vartheta} + \frac{1}{2} \overline{\rho u_k \tilde{u}_k} + \frac{1}{2} \mathcal{L}_{kk}. \quad (36)$$

Taking the filtered ideal gas law, Eq. (3), namely $\bar{p} = \bar{\rho} R \bar{T}$, and substituting the definitions of *macropressure*, Eq. (30), and *macrottemperature*, Eq. (35), the following relation is obtained:

$$\bar{\omega} = \bar{\rho} R \bar{\vartheta} - \frac{3\gamma - 5}{6} \overline{\rho u'_k u'_k}. \quad (37)$$

In particular, under the assumption that the SGS turbulence Mach number,

$$M_{\text{SGS}}^2 = \frac{\overline{\rho u'_k u'_k}}{\gamma \bar{p}}, \quad (38)$$

is sufficiently small, namely,

$$\gamma M_{\text{SGS}}^2 \frac{|3\gamma - 5|}{6} \ll 1, \quad (39)$$

the filtered equation of state results formally identical to its unfiltered counterpart [Eq. (3)], the pressure and temperature being replaced by the *macropressure* and *macrottemperature*, respectively,

$$\bar{\omega} = \bar{\rho} R \bar{\vartheta}. \quad (40)$$

Erlebacher *et al.*²² arrived at a similar conclusion by the assumption that all the spherical part of the Reynolds term could be neglected if

$$\frac{1}{3} \gamma M_{\text{SGS}}^2 \ll 1. \quad (41)$$

On the other hand, the present approach, which only requires *macrottemperature* and *macropressure* to be related via the equation of state, leads to the analogous but less restrictive condition expressed by Eq. (39), which gives a prefactor of about 1/7.5 instead of 1/3 for $\gamma=1.4$, thus extending the range of applicability to higher Mach numbers.

The following relations hold for the resolved total and internal energies:

$$\bar{\rho e} = \frac{\bar{\omega}}{\gamma - 1} + \frac{1}{2} \overline{\rho u_k \tilde{u}_k} + \frac{1}{2} \mathcal{L}_{kk}, \quad (42)$$

$$\bar{e}_I = \frac{\bar{\rho e}}{\bar{\rho}} - \frac{1}{2} \tilde{u}_k \tilde{u}_k - \frac{\mathcal{L}_{kk}}{2 \bar{\rho}}, \quad (43)$$

where $\bar{\rho} \bar{e}_I = \bar{\rho} c_v \bar{\vartheta} = \bar{\omega} / (\gamma - 1)$.

In view of the above development, it seems natural to write the filtered fifth component of the flux vector [Eq. (2)], which is the component relevant to the total energy transport equation, in terms of the resolved quantities just defined,

$$\bar{F}_5^k = (\bar{\rho e} + \bar{\omega}) \tilde{u}_k - \overline{2 \mu u_j A_{kj}} - \lambda \frac{\partial T}{\partial x_k} - q_k, \quad (44)$$

where q_k is the subgrid total energy flux vector, which accounts for heat and kinetic energy subgrid transport and is defined as

$$q_k = (\bar{\rho e} + \bar{\omega}) \tilde{u}_k - \overline{(\rho e + p) u_k}. \quad (45)$$

The above SGS energy flux, as it has been defined, is a combination of the following different terms:

$$\begin{aligned} -q_k &= \overline{\rho e u_k} - \bar{\rho} \tilde{e}_I \tilde{u}_k + \overline{p u_k} - \bar{\omega} \tilde{u}_k \\ &\quad + \frac{1}{2} \overline{\rho u_j u_j u_k} - \frac{1}{2} \overline{\rho \tilde{u}_j \tilde{u}_j \tilde{u}_k} - \frac{1}{2} \mathcal{L}_{jj} \tilde{u}_k. \end{aligned} \quad (46)$$

From Eqs. (3), (6), and (40), the last two terms in the first line of the above equation can be rewritten as

$$\overline{p u_k} - \bar{\omega} \tilde{u}_k = (\gamma - 1) (\overline{\rho e u_k} - \bar{\rho} \tilde{e}_I \tilde{u}_k), \quad (47)$$

and Eq. (46) then becomes

$$-q_k = \gamma (\overline{\rho e u_k} - \bar{\rho} \tilde{e}_I \tilde{u}_k) + \frac{1}{2} \overline{\rho u_j u_j u_k} - \frac{1}{2} \overline{\rho \tilde{u}_j \tilde{u}_j \tilde{u}_k} - \frac{1}{2} \mathcal{L}_{jj} \tilde{u}_k. \quad (48)$$

With regards to the SGS heat flux term, before proceeding with the modified Leonard decomposition, it is worth underlining that, since both the temperature and the macrotemperature are present, i.e.,

$$\overline{\rho e_i u_k} - \overline{\rho \tilde{e}_i \tilde{u}_k} = \overline{\rho c_v} (\widetilde{T u_k} - \widetilde{\vartheta \tilde{u}_k}), \quad (49)$$

the decomposition in terms of resolved and unresolved internal energies is not straightforward. By analogy with the procedure used to obtain the modified Leonard decomposition for the SGS stress tensor, the temperature and the macrotemperature must be decomposed into their resolved and unresolved parts,

$$T = \widetilde{T} + T', \quad \vartheta = \widetilde{\vartheta} + \vartheta'. \quad (50)$$

It should be noted anyway that the fully resolved macrotemperature ϑ is physically meaningless, being the macrotemperature strictly connected with the introduction of SGS terms in the filtered set of equations. Nonetheless, we may observe that, if a resolved macrotemperature ϑ could be defined, this would be the direct numerical simulation (DNS) limit of $\widetilde{\vartheta}$. Observing that, in the DNS limit, the trace of the SGS true Reynolds term vanishes, we conclude that $\vartheta \equiv T$. We may therefore conclude that if the temperature is decomposed as $T = \widetilde{\vartheta} + T'$ (i.e., the unresolved temperature T' is defined as the difference between the temperature T and the macrotemperature $\widetilde{\vartheta}$), then the same decomposition will hold for the fully resolved macrotemperature, namely, $\vartheta = \widetilde{\vartheta} + T'$, and we can write

$$\widetilde{\vartheta} = \widetilde{\widetilde{\vartheta}} + T'. \quad (51)$$

The above decomposition allows the definition of a consistent measure of the unresolved internal energy as $e'_i = c_v T'$, and the SGS heat flux can be then decomposed in the usual way,

$$-q_k^{e_i} = \mathcal{L}_k^{e_i} + C_k^{e_i} + \mathcal{R}_k^{e_i}, \quad (52)$$

with

$$\mathcal{L}_k^{e_i} = \gamma (\overline{\rho \tilde{e}_i \tilde{u}_k} - \overline{\rho \tilde{e}_i' \tilde{u}_k}), \quad (53)$$

$$C_k^{e_i} = \gamma (\overline{\rho \tilde{e}_i' u_k'} + \overline{\rho \tilde{e}_i' \tilde{u}_k} - \overline{\rho \tilde{e}_i' u_k'} - \overline{\rho \tilde{e}_i' \tilde{u}_k}), \quad (54)$$

$$\mathcal{R}_k^{e_i} = \gamma (\overline{\rho e_i' u_k'} - \overline{\rho \tilde{e}_i' u_k'}). \quad (55)$$

By analogy to what has been done with the subgrid stress tensor in Sec. II A 1, we resort to the scale-similarity hypothesis by neglecting $C_k^{e_i}$ and the second term in $\mathcal{R}_k^{e_i}$; we then model the SGS true Reynolds term by the eddy-viscosity assumption, thus obtaining

$$q_k^{e_i} \approx \gamma \frac{\overline{\rho \nu_i}}{\text{Pr}_i} \frac{\partial \tilde{e}_i}{\partial x_k} - \gamma \overline{\rho} (\widetilde{\tilde{e}_i \tilde{u}_k} - \widetilde{\tilde{e}_i' \tilde{u}_k}), \quad (56)$$

where the eddy viscosity ν_i is computed from Eq. (26) and $\text{Pr}_i = 0.5$ (Refs. 22 and 30) is the subgrid Prandtl number.

The remaining terms in Eq. (48) may be rearranged as

$$\begin{aligned} & \frac{1}{2} \overline{\rho} (\widetilde{u_j u_j u_k} - \widetilde{u_j \tilde{u}_j \tilde{u}_k}) - \frac{1}{2} \mathcal{L}_{jj} \tilde{u}_k \\ & = \frac{1}{2} (\overline{\rho u_j u_j} - \overline{\rho \tilde{u}_j \tilde{u}_j} - \mathcal{L}_{jj}) \tilde{u}_k - \overline{\rho} D_k, \end{aligned} \quad (57)$$

where $\overline{\rho} D_k = \frac{1}{2} \overline{\rho u_j u_j} \tilde{u}_k - \frac{1}{2} \overline{\rho \tilde{u}_j \tilde{u}_j} \tilde{u}_k$, evidently, represents the SGS turbulent diffusion of kinetic energy; furthermore, using the usual modified Leonard decomposition and the scale-similarity hypothesis, the term in parentheses in Eq. (57) results equal to $\overline{\rho u_j' u_j'}$, and Eq. (46) is finally rewritten in the following way:

$$q_k = \gamma \frac{\overline{\rho \nu_i}}{\text{Pr}_i} \frac{\partial \tilde{e}_i}{\partial x_k} - \gamma \overline{\rho} (\widetilde{\tilde{e}_i \tilde{u}_k} - \widetilde{\tilde{e}_i' \tilde{u}_k}) + \overline{\rho} D_k - \frac{1}{2} \mathcal{R}_{jj} \tilde{u}_k. \quad (58)$$

The last two terms in the above equation are not closed, and we make the additional hypothesis that they can be neglected under the reasonable assumption that their effect can be considered to be much smaller than that related to the SGS heat flux.³⁴ This hypothesis conforms to that which has been implicitly assumed by Ducros *et al.*²⁶ and Lesieur *et al.*,²⁷ who modeled the SGS transport of total energy using the heat transport contribution only.

Finally, neglecting viscous and diffusive subgrid contributions, namely,

$$\overline{\mu u_j A_{kj}} - \overline{\mu \tilde{u}_j \tilde{A}_{kj}} \approx 0, \quad (59)$$

$$\overline{\lambda \frac{\partial T}{\partial x_k}} - \frac{\overline{\mu c_p}}{\text{Pr}} \frac{\partial \widetilde{\vartheta}}{\partial x_k} \approx 0, \quad (60)$$

the energy flux component, Eq. (44), becomes

$$\overline{F_5^k} = (\overline{\rho e} + \overline{\varpi}) \tilde{u}_k - 2 \overline{\mu \tilde{u}_j \tilde{A}_{kj}} - \frac{\overline{\mu c_p}}{\text{Pr}} \frac{\partial \widetilde{\vartheta}}{\partial x_k} - q_k, \quad (61)$$

with

$$q_k = \gamma \frac{\overline{\rho \nu_i}}{\text{Pr}_i} \frac{\partial \tilde{e}_i}{\partial x_k} - \gamma \overline{\rho} (\widetilde{\tilde{e}_i \tilde{u}_k} - \widetilde{\tilde{e}_i' \tilde{u}_k}), \quad (62)$$

and $\overline{\mu}$ computed from the resolved macrotemperature using Eq. (8),

$$\overline{\mu}(\widetilde{\vartheta}) = \mu_{\text{ref}} \left(\frac{\widetilde{\vartheta}}{T_{\text{ref}}} \right)^{3/2} \frac{T_{\text{ref}} + S}{\widetilde{\vartheta} + S}. \quad (63)$$

3. The filtered scalar equation

The filtered transport equation for the passive scalar Z can be obtained by analogy to what has been done so far for the momentum and energy equations. The main steps are therefore synthetically summarized below.

The filtered scalar flux component is obtained by filtering the sixth component in Eq. (2),

$$\overline{F_6^k} = \overline{\rho Z \tilde{u}_k} - \rho D \frac{\partial Z}{\partial x_k} - q_k^Z, \quad (64)$$

where q_k^Z is the SGS scalar flux vector,

$$q_k^Z = \overline{\rho Z \tilde{u}_k} - \overline{\rho Z u_k}. \quad (65)$$

Introducing the passive scalar decomposition $Z = \tilde{Z} + Z'$, the SGS scalar flux may be decomposed as

$$-q_k^Z = \mathcal{L}_k^Z + \mathcal{C}_k^Z + \mathcal{R}_k^Z, \quad (66)$$

with

$$\mathcal{L}_k^Z = \overline{\rho \tilde{Z} \tilde{u}'_k} - \overline{\rho \tilde{Z}' \tilde{u}'_k}, \quad (67)$$

$$\mathcal{C}_k^Z = \overline{\rho \tilde{Z} u'_k} + \overline{\rho Z' \tilde{u}'_k} - \overline{\rho \tilde{Z} u'_k} - \overline{\rho Z' \tilde{u}'_k}, \quad (68)$$

$$\mathcal{R}_k^Z = \overline{\rho Z' u'_k} - \overline{\rho \tilde{Z}' \tilde{u}'_k}. \quad (69)$$

Under the scale-similarity hypothesis, i.e., neglecting \mathcal{C}_k^Z and the second term in \mathcal{R}_k^Z , and resorting to the eddy-viscosity assumption in order to model the SGS true Reynolds term, the SGS scalar flux then becomes

$$q_k^Z = \frac{\overline{\rho \nu_t} \partial \tilde{Z}}{Sc_t \partial x_k} - \overline{\rho} (\overline{\tilde{Z} \tilde{u}'_k} - \tilde{Z} \tilde{u}'_k), \quad (70)$$

where ν_t is obtained from the WALE model [Eq. (26)] and $Sc_t = 0.5$ is the turbulent Schmidt number. Finally, neglecting molecular subgrid contributions,

$$\overline{\rho D} \frac{\partial \tilde{Z}}{\partial x_k} - \frac{\overline{\mu}}{Sc} \frac{\partial \tilde{Z}}{\partial x_k} \approx 0, \quad (71)$$

the scalar flux component can be computed from resolved quantities and Eq. (70),

$$\overline{F_6^k} = \overline{\rho \tilde{Z} \tilde{u}'_k} - \frac{\overline{\mu}}{Sc} \frac{\partial \tilde{Z}}{\partial x_k} - q_k^Z, \quad (72)$$

with $\overline{\mu}$ computed from Eq. (63).

4. The explicit filtering procedure

As it has been presented in the previous sections, the SGS contributions are modeled by means of an eddy-viscosity term, which is computed from resolved quantities, and the modified Leonard term, which involves explicit filtering of resolved quantities. Within the framework of mixed-similarity modeling,^{28,29} scale invariance is assumed to postulate that the structure of the velocity field at scales below a certain length scale Δ is similar to that at scales above Δ . Consequently, the above closures are, more generally, rewritten as

$$\tau_{ij}^d = 2\overline{\rho} \nu_t \tilde{A}_{ij} - \overline{\rho} (\widehat{\tilde{u}_i \tilde{u}_j} - \hat{\tilde{u}}_i \hat{\tilde{u}}_j)^d, \quad (73)$$

$$q_k = \gamma \frac{\overline{\rho \nu_t} \partial \tilde{e}_l}{Pr_t \partial x_k} - \gamma \overline{\rho} (\widehat{\tilde{e}_l \tilde{u}'_k} - \hat{\tilde{e}}_l \hat{\tilde{u}}_k), \quad (74)$$

$$q_k^Z = \frac{\overline{\rho \nu_t} \partial \tilde{Z}}{Sc_t \partial x_k} - \overline{\rho} (\widehat{\tilde{Z} \tilde{u}'_k} - \hat{\tilde{Z}} \hat{\tilde{u}}_k), \quad (75)$$

the *hat* operator representing filtering at cutoff length $\alpha\Delta$, with $\alpha \geq 1$. Note that the spherical part of the modified Leonard term in Eqs. (31), (42), and (43) is computed accordingly as

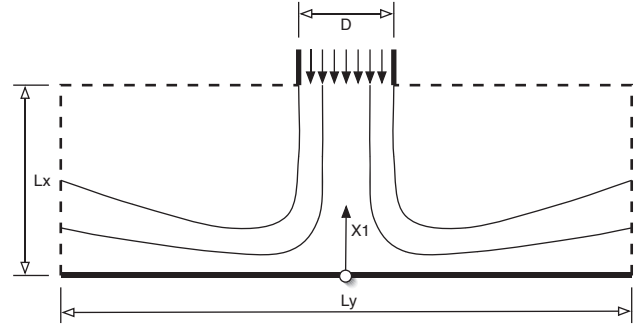


FIG. 1. Schematic of the flow configuration and position of the coordinate system.

$$\mathcal{L}_{kk} = \overline{\rho} (\widehat{\tilde{u}_k \tilde{u}'_k} - \hat{\tilde{u}}_k \hat{\tilde{u}}_k). \quad (76)$$

Different choices of α have been proposed: filtering at the grid level ($\alpha=1$) is a possible solution,^{20–22,28,29} whereas Liu *et al.*¹⁶ and Akhavan *et al.*¹⁸ used $\alpha=2$ and $\alpha=4/3$, respectively.

Akhavan *et al.*,¹⁸ in particular, in their dynamic two-component SGS model, distinguished two contributions: (a) the nonlocal interactions which are responsible for a low-intensity forward energy transfer and (b) the local interactions near the cutoff length scale which are responsible for intense and coherent regions of forward and reverse energy transfer. The former is modeled by the eddy-viscosity assumption, while the latter is represented by an approximation of the modified Leonard term, measuring the interactions between the resolved scales and a narrow band of subgrid wavenumbers. This idea is then applied using pseudospectral methods and results from incompressible LES of turbulent planar jet and turbulent channel flow are validated against DNS data obtaining quite good agreement.

The same assumption generalized to the compressible case is adopted in this study, the details about the implementation of explicit filtering at length $4/3\Delta$ being presented in Appendix. It is worthwhile to stress that the above closures [Eqs. (73)–(75)] have been obtained under the assumption that, as far as the local interactions term in the subgrid contributions are concerned, filtering and Favre-filtering operators behave similarly, as implicitly assumed in Refs. 20 and 22. Moreover, it is assumed that $\hat{\rho} \sim \overline{\rho}$, so that we can write: $\widehat{\rho \phi} \approx \overline{\rho} \hat{\phi}$. These approximations are indeed a necessity dictated by the fact that the fully resolved density is anyway unaccessible and $\hat{\rho}$ cannot be computed rigorously nor can it be any other term of the form $\widehat{\rho \phi}$.

B. Flow configuration

The flow configuration under study consists of an unconfined impinging round jet as schematized in Fig. 1. The jet nozzle to wall distance, namely, L_x , is equal to twice the jet diameter D . Two values of jet Reynolds number have been studied, $Re_D = 23\,000$ and $Re_D = 70\,000$, Re_D being defined with the bulk velocity U_b ,

$$Re_D = \frac{\rho U_b D}{\mu}. \quad (77)$$

TABLE I. Air properties.

	Value	Reference
R	287.7 J/(kg K)	Equation (40)
γ	1.4	Equation (6)
Pr	0.72	Equation (9)
Sc	0.72	Equation (9)
C_w	0.5	Equation (26)
Pr_t	0.50	Equation (62)
Sc_t	0.50	Equation (70)
μ_{ref}	1.827×10^{-5} kg/(m s)	Equation (63)
T_{ref}	291.15 K	Equation (63)
S	120.0 K	Equation (63)

These test cases have been chosen in order to be compared against the experimental database collected by Cooper *et al.*,²³ Geers,²⁴ and Geers *et al.*²⁵ The bottom boundary is an adiabatic no-slip wall, while the lateral and top sides are open boundaries. The jet axis is aligned along x_1 , and the coordinate system origin is located at the impingement wall, hence the impingement wall is contained in the x_2 - x_3 plane of equation $x_1=0$. Hereafter, r will be used to indicate the distance from the jet's axis, namely, $(x_2^2+x_3^2)^{1/2}$.

All the simulations discussed have been performed using the parameters summarized in Table I.

C. Numerical formulation

The simulations have been performed using a parallel solver based on an explicit finite volume scheme written for Cartesian grids. The convective terms are computed resorting to a fourth-order centered skew symmetric-like scheme,³⁵ and the diffusive terms are computed using a fourth-order centered scheme. The scheme is augmented by a blend of second- and fourth-order artificial dissipation terms,^{36–38} these terms are added in order to suppress spurious oscillations and damp high-frequency modes. Time integration is performed using a third-order Runge–Kutta scheme.^{39,40}

The computational grid is stretched toward the wall to ensure accuracy in the wall layer. This stretching is included in the computation of the filter cutoff length Δ , used to obtain the eddy viscosity and also in the determination of the explicit filter operator by means of the corrective function for nonuniform grids³³ [cf. Eq. (27)].

The impacts of in-plane pressure gradient and convection (also called transverse terms' contribution) on the flow at the face boundaries are included in the three-dimensional Navier–Stokes characteristic boundary conditions (3D-NSCBC) approach recently developed by Lodato *et al.*,⁴¹ which is adopted for boundary conditions' treatment. The lateral open boundaries, in particular, are nonreflecting outflows with pressure relaxation coefficient $\sigma=0.28$ and transverse relaxation coefficient $\beta=0.18$ (no target transverse terms have been prescribed), the latter representing a typical value of the Mach number over the outflow boundaries.^{41,42} The incoming wave amplitude variations are prescribed as

$$\mathcal{M}_\psi = \sigma \frac{c(1-M^2)}{L_y} \Delta p + (1-\beta) T_\psi^2 \quad (78)$$

for boundaries orthogonal to x_2 and

$$\mathcal{N}_\chi = \sigma \frac{c(1-M^2)}{L_z} \Delta p + (1-\beta) T_\chi^3 \quad (79)$$

for boundaries orthogonal to x_3 . In the above relations, ψ (resp., χ) is equal to 1 for the outflow located at $x_2=L_y$ (resp., $x_3=L_z$) and 5 for the outflow located at $x_2=0$ (resp., $x_3=0$), $\Delta p = \bar{w} - p_\infty$ ($p_\infty=1$ atm), $c^2 = \gamma R \bar{\theta}$ is the speed of sound and M is the maximum Mach number in the flow. The relevant transverse terms are computed from the following relations:

$$T_\psi^2 = -\tilde{u}_j \frac{\partial \bar{w}}{\partial x_j} - \gamma \bar{w} \frac{\partial \tilde{u}_j}{\partial x_j} - \varsigma(\psi) \bar{\rho} c \tilde{u}_j \frac{\partial \tilde{u}_2}{\partial x_j} \quad (j=1,3), \quad (80)$$

$$T_\chi^3 = -\tilde{u}_j \frac{\partial \bar{w}}{\partial x_j} - \gamma \bar{w} \frac{\partial \tilde{u}_j}{\partial x_j} - \varsigma(\chi) \bar{\rho} c \tilde{u}_j \frac{\partial \tilde{u}_3}{\partial x_j} \quad (j=1,2), \quad (81)$$

with $\varsigma(1)=-1$ and $\varsigma(5)=+1$.

In the inflow section, a nonreflecting inlet is applied with relaxation coefficient $\eta_5=-\eta_2=\eta_3=\eta_4=3.28$, the relevant incoming wave amplitude variations being computed as

$$\mathcal{L}_5 = \eta_5 \frac{\bar{\rho} c^2 (1-M^2)}{L_x} \Delta u_1 + T_5^1 - \bar{\rho} c \frac{dU_1^0}{dt}, \quad (82)$$

$$\mathcal{L}_2 = \eta_2 \frac{\bar{\rho} c R}{L_x} \Delta T + T_2^1, \quad (83)$$

$$\mathcal{L}_3 = \eta_3 \frac{c}{L_x} \Delta u_2 + T_3^1 - \frac{dU_2^0}{dt}, \quad (84)$$

$$\mathcal{L}_4 = \eta_4 \frac{c}{L_x} \Delta u_3 + T_4^1 - \frac{dU_3^0}{dt}, \quad (85)$$

where $\Delta u_k = \tilde{u}_k - U_k$ and $\Delta T = \bar{\theta} - T_0$ ($T_0=300$ K) are the differences between velocity and temperature, and the relevant target values and dU_k^0/dt are the time derivatives of a variable inlet signal to be superimposed to the constant target values.⁴³ The transverse terms are obtained from the following equations:

$$T_5^1 = -\tilde{u}_j \frac{\partial \bar{w}}{\partial x_j} - \gamma \bar{w} \frac{\partial \tilde{u}_j}{\partial x_j} - \bar{\rho} c \tilde{u}_j \frac{\partial \tilde{u}_1}{\partial x_j}, \quad (86)$$

$$T_2^1 = -c^2 \frac{\partial \bar{\rho} \tilde{u}_j}{\partial x_j} + \tilde{u}_j \frac{\partial \bar{w}}{\partial x_j} + \gamma \bar{w} \frac{\partial \tilde{u}_j}{\partial x_j}, \quad (87)$$

$$T_3^1 = -\tilde{u}_j \frac{\partial \tilde{u}_2}{\partial x_j} - \frac{1}{\bar{\rho}} \frac{\partial \bar{w}}{\partial x_2}, \quad (88)$$

$$T_4^1 = -\tilde{u}_j \frac{\partial \tilde{u}_3}{\partial x_j} - \frac{1}{\bar{\rho}} \frac{\partial \bar{w}}{\partial x_3}, \quad (89)$$

with summation over $j=2,3$. For more details about the above relations and 3D-NSCBC implementation on the

edges and the corners of the computational domain, the reader is referred to the original cited paper. The target velocities in the lateral directions were set to zero, while the axial component was prescribed using the power law profile for turbulent pipe flow,

$$\frac{U_1(r)}{U_{cl}} = \left(1 - \frac{2r}{D}\right)^{1/n}, \quad (90)$$

where r represents the distance from the axis and U_{cl} is the centerline velocity. The coefficient n has been tuned, for each simulation (7.23 and 8.3 for Reynolds number 23 000 and 70 000, respectively), in order to attain the same ratio of bulk and centerline inlet velocities as in the experiments,²³

$$\frac{U_b}{U_{cl}} = 0.811 + 0.038[\log(\text{Re}_D) - 4]. \quad (91)$$

To reproduce a turbulent inflow condition, a correlated random noise⁴⁴ is superimposed to the average velocity profile through the terms dU_k^0/dt in Eqs. (82)–(85), with a sampling rate computed from the jet's characteristic time scale. The amplitude of the injected noise varies along the jet diameter from $0.028U_b$ at the axis to a peak value of $0.075U_b$ within the jet's shear layer. These values of amplitude have been determined with *a priori* tests in order to attain correct streamwise fluctuations along the jet axis.

D. Grid spacing

The computational grids and the relevant spacing have been chosen fulfilling three main requirements.

- (1) Maintain the low-pass filter cutoff length within the inertial subrange in order to perform correctly resolved LES.
- (2) Ensure proper resolution of the wall layer while keeping grid stretching to a minimum.
- (3) Retain a reasonable computational cost.

With regards to the first point, the assumption has been made that the inertial subrange includes length scales from approximately $\ell_0/6$ down to length scales of the order of 30η ,⁴⁵ $\ell_0 \sim D/2$ being an estimation of the integral length scale and $\eta \sim \ell_0 \text{Re}^{-3/4}$ being the Kolmogorov length scale, with $\text{Re} = u_0 \ell_0 / \nu$ and $u_0^2 \sim 0.1U_b^2$ (10% turbulence is assumed).

Regarding to the second point, it should be noted that the numerical scheme, which has been used, is designed for uniform grids. This choice, motivated by the necessity of conserving stability properties of the scheme, leads to a variable local discretization error.³⁵ In order to limit accuracy reductions in the refined regions, grid stretching has been done maintaining the maximum stretching ratio below 1.04.

Three different grids were used: (C1) 2.9 M nodes, relatively coarse mesh with dimensions $2D \times 7D \times 7D$, for $\text{Re}_D = 23\,000$; (C2) 5.5 M nodes, more refined grid with dimensions $2D \times 6D \times 6D$, with increased resolution, especially in the near-wall region, for $\text{Re}_D = 23\,000$; (C3) 3.5 M nodes, relatively coarse grid with dimensions $2D \times 5D \times 5D$, for

TABLE II. Computational grid properties.

Re_D	23 000	70 000	
D	2.6 mm	8 mm	
U_b	141 m/s	139.4 m/s	
M	0.41	0.40	
$30\eta/D$	3.2×10^{-2}	1.4×10^{-2}	
$\Delta_{1,\text{min}}/D$	3.5×10^{-3}	9.3×10^{-4}	1.7×10^{-3}
$\Delta_{1,\text{max}}/D$	4.6×10^{-2}	3.5×10^{-2}	4.3×10^{-2}
$\Delta_{2,3}/D$	4.0×10^{-2}	3.1×10^{-2}	2.8×10^{-2}
$\ell_0/6D$	8.3×10^{-2}	8.3×10^{-2}	
Δ_1^+	4.7–6.3	1.2–1.7	5.7–8.4
$\Delta_{r,\phi}^+$	64.2–87.4	49.7–67.7	113.3–165.7
Dimensions	$2D \times (7D)^2$	$2D \times (6D)^2$	$2D \times (5D)^2$
Nodes	90×178^2	146×194^2	110×178^2
CPU time	1360 h	18 650 h	2510 h
Processors	32	512	128

$\text{Re}_D = 70\,000$. The reduction in the computational domain width for test cases C2 and C3 allowed for higher resolution without increasing too much the number of grid points. Reducing the domain size was made possible because of the use of the recently developed 3D-NSCBC boundary conditions,⁴¹ which ensure low numerical perturbations at open boundaries.

With regards to the wall-jet region ($r/D \geq 1.0$), wall-normal grid spacing Δ_1^+ (superscript $+$ indicates wall units, i.e., normalization with respect to the viscous length $\ell_\tau = \nu/u_\tau$, the friction velocity $u_\tau = \tau_w^{1/2}$ being estimated from the experimental average velocity profiles²³) ranges from ~ 4.7 to ~ 6.3 (resp., from ~ 1.2 to ~ 1.7) for the $\text{Re}_D = 23\,000$ test-case C1 (resp., C2) and from ~ 5.7 to ~ 8.4 for the $\text{Re}_D = 70,000$ test case C3, the maximum values being attained near the stagnation region where the average shear stresses are higher.

Due to the use of a Cartesian grid, both radial and azimuthal spacings vary going around the jet's axis, from a minimum of $\Delta_{2,3}$ to a maximum of $\sqrt{2}\Delta_{2,3}$, where $\Delta_{2,3}$ is the grid resolution measured along the coordinate axes x_2 or x_3 (equal spacing was used in both the lateral directions). We will refer, for simplicity, to its average value of $\sim 1.2\Delta_{2,3}$. Radial and azimuthal spacings Δ_r^+ and Δ_ϕ^+ , for the lower Reynolds number case, are in the ranges of 64.2–87.4 for the coarser grid (C1) and 49.7–67.7 for the more resolved grid (C2); for the higher Reynolds number test case (C3), radial and azimuthal spacings are in the range of 113.3–165.7. Again, maximum values are attained close to the stagnation region. A detailed summary of grid dimensions and mesh spacing for the three test cases is reported in Table II.

Grid resolution for test cases C1 and C3 is quite low, compared, for instance, to the recommendations given by Zang,⁴⁶ who suggested that the minimum spacings to capture near-wall dynamics should be $\Delta_{\text{str}}^+ < 80$ and $\Delta_{\text{spn}}^+ < 30$ in the streamwise and spanwise directions, respectively, and a minimum of three points for $\Delta_1^+ < 10$ in the wall-normal

direction. A very strong influence of grid resolution in LES of detached boundary layers was reported by Temmerman *et al.*,⁴⁷ who found high sensitivity of the reattachment position to grid spacing, especially in the streamwise direction, around the mean separation position. They concluded that the use of the no-slip condition at the location where detachment occurs, in conjunction with insufficient grid resolution in the streamwise direction, may lead to substantial errors, even if sufficient wall-normal resolution is used.

Nevertheless, the relevant computational effort when increasing resolution at high Reynolds number may grow significantly (cf. Table II), therefore it is of practical interest to assess the model behavior in cases where a significant percentage of the energy is in the SGSs and when the near-wall resolution is marginal. Moreover, the impinging jet features some peculiarities which make it profoundly different from other wall-bounded flows. As opposed to turbulent boundary layers, where length scales are usually determined by the distance from the wall, the impinging jet, in particular, is characterized by local turbulent length scales in the near-wall region that are strongly affected by the scales of the jet's turbulence. Hence, the criteria on mesh resolution developed for turbulent boundary layers may not be used as a guide line for an impinging jet.

For LES of channel flow at high Reynolds numbers, Piomelli⁴⁸ used grid spacings $\Delta_{\text{str}}^+ = 172$, $\Delta_{\text{spn}}^+ = 26$, $\Delta_1^+ \in [1.25:51]$ for $\text{Re} = 23\,700$ (based on the centerline velocity) and $\Delta_{\text{str}}^+ = 244$, $\Delta_{\text{spn}}^+ = 40$, $\Delta_1^+ \in [1.5:77]$ for $\text{Re} = 47\,100$. Despite the fairly coarse grids used, first- and second-order statistical moments were predicted accurately. The author conjectured that the explanation for that was to be related to the model ability to reproduce backscatter. Purely dissipative models necessitate the energy production events to be resolved by the grid, hence under-resolution of near-wall dynamics may lead to underestimation of the related energy production. On the other hand, models which are able to account for reverse energy transfer, such as the WALE-similarity model (which will be indicated as WSM hereafter) presented in this paper, may effectively give a correction to the average subgrid dissipation, which is reduced due to sufficiently frequent local backscatter. This point will be further discussed in Sec. III D. Moreover, for $\text{Re}_D = 23\,000$, the impact of grid resolution in the wall-boundary layer will be assessed comparing the results from the above mentioned two different computational grids.

III. RESULTS AND DISCUSSION

The WALE-similarity model behavior has been assessed by comparison against the experimental results^{23–25} in terms of resolved average and fluctuating velocities.

Statistical results have been evaluated by time averaging an ensemble of 600 samples of the resolved quantities for total periods of about $17D/U_b$ and $13D/U_b$ for $\text{Re}_D = 23\,000$ (C1) and $\text{Re}_D = 70\,000$, respectively. Due to the reduction in time step of the higher resolved simulation at $\text{Re}_D = 23\,000$ (C2) and the relatively high computational cost, statistical sampling was stopped after $\sim 8D/U_b$; an ensemble of 900 samples was collected. Global statistical convergence

for the three test cases has been checked continuously calculating the L_2 -norm of the change in the statistical quantity $\langle \phi \rangle$ of interest (e.g., the streamwise average velocity, the streamwise fluctuation, and the streamwise/wall-normal correlation) between two successive samplings, indicated with superscripts n and $n-1$,

$$\langle \phi \rangle_{L_2}^{\{n\}} = \sqrt{\sum_{i,j,k} (\langle \phi \rangle_{i,j,k}^{\{n\}} - \langle \phi \rangle_{i,j,k}^{\{n-1\}})^2}, \quad (92)$$

where the summation is extended to the whole computational domain. In the present case, statistical sampling was stopped when the L_2 -norm was below 10^{-1} and 10^{-2} for first- and second-order moments, respectively. Assuming the validity of the Taylor hypothesis, statistical convergence has been further improved by averaging around the jet's axis, for a total statistical ensemble spanning from 50 400 to 637 200, depending on the radial location and the computational grid used. Time/space averaging will be denoted by angled brackets hereafter.

It should be noted that, according to the experimental setup used by Cooper *et al.*, velocity components are measured along the streamwise and wall-normal directions, which are indicated by u_s and u_n , respectively. On the other hand, radial components of velocity are measured by Geers *et al.*: these will be indicated as u_r in the following sections. In order to avoid confusion with SGS quantities, which have been indicated with the prime mark so far, the double prime mark will be used to refer to statistically fluctuating quantities.

A. $\text{Re}_D = 23\,000$ test-case C1 validation

Results for the $\text{Re}_D = 23\,000$ test case (C1), obtained on the coarse grid, are shown in Figs. 2 and 3; error bars relevant to hot-wire anemometry (HWA) measurement uncertainties²³ are displayed for experimental second-order moments. For the same configuration, Figs. 4 and 5 show the comparison against the experimental measurements obtained by Geers²⁴ and Geers *et al.*²⁵ using laser-Doppler anemometry (LDA) and particle image velocimetry (PIV). The WSM is compared to the standard WALE model and the LDSM. Test filtering for the latter model has been performed using the same isotropic filter implementation described in Appendix, but with cutoff length equal to 2Δ .

With regards to the average velocity profiles [Fig. 2(a)], all the three models perform well and no appreciable difference between them is visible. In any case, the correct slope down to the viscous sublayer indicates clearly that correct scaling of SGS stresses is achieved as expected by the three models, and no additional eddy viscosity is produced in regions where this is not expected to be present.

On the other hand, the three models perform quite differently in terms of resolved second-order moments. With regards to the streamwise fluctuations, both the WALE and the LDSM predict fairly well measurements far from the wall but produce a significant overestimation in the near-wall region, especially for $r/D \leq 2.0$, where the flow undergoes strong curvature [Fig. 2(b)]. It seems reasonable to affirm that the dynamic computation of the model constant in the

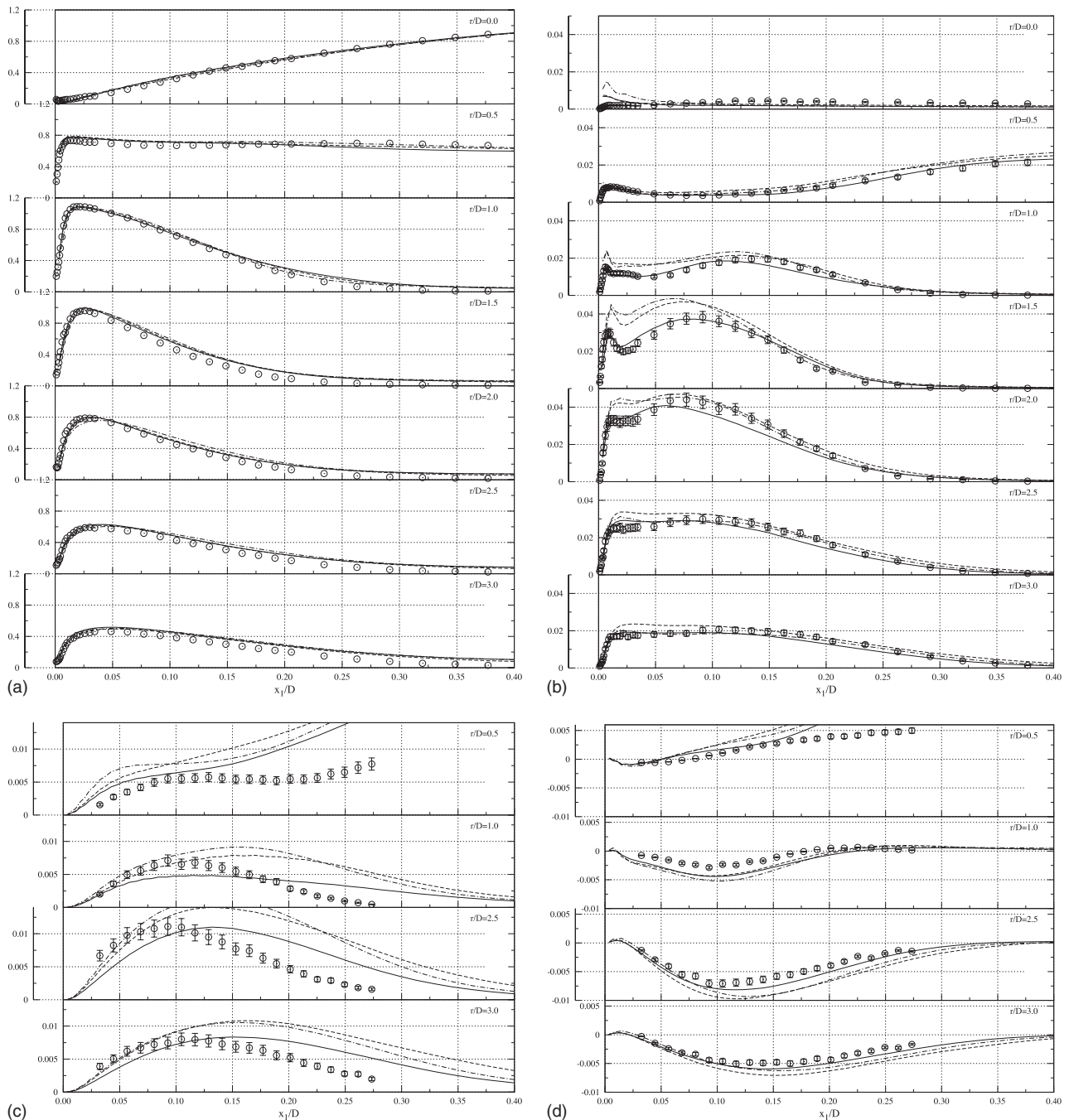


FIG. 2. $Re_D=23\,000$ test case (coarse grid). Streamwise average velocity $\langle u_s \rangle / U_b$ (a); streamwise fluctuating velocity $\langle u_s'' u_s'' \rangle / U_b^2$ (b); wall-normal fluctuating velocity $\langle u_n'' u_n'' \rangle / U_b^2$ (c); and turbulent shear stress $\langle u_s'' u_n'' \rangle / U_b^2$ (d); (—) WSM; (---) WALE; (- - -) LDSM; (O) HWA measures (Ref. 23).

LDSM and the relatively low dissipation of the WALE model allow for a correct representation of subgrid interactions far from the wall. Nonetheless, close to the wall, even the dynamic procedure is not able to adjust properly the subgrid viscosity. These shortcomings are probably due to the fact the both the WALE and the LDSM do not allow energy backscatter, hence resulting, in average, more dissipative than the WSM. The higher subgrid viscosity slows down the process of vortex breakup, thus reducing azimuthal fluctuations and promoting the persistence of toroidal large-scale

structures coming from the jet's shear layer, which eventually result in high levels of resolved radial fluctuations.

The introduction of the modified Leonard term in the WSM has a strong impact on the resolved streamwise velocity fluctuations, these last being slightly underestimated far from the wall in the wall-jet region. It should be noted on this regard that results are expected to improve if the isotropic SGS contribution is included when comparing with measurements, as it will be shown for the $Re_D=70\,000$ test case.

With regards to wall-normal fluctuations, different be-

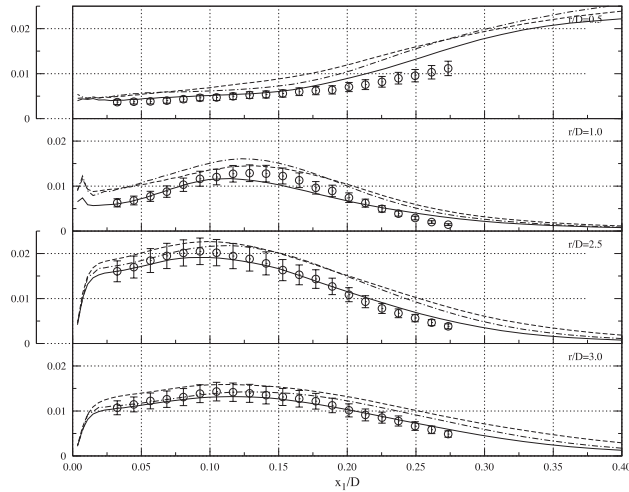


FIG. 3. $Re_D=23\,000$ test case (coarse grid). Turbulent kinetic energy $\frac{1}{2}(\langle u_s''u_s'' \rangle + \langle u_n''u_n'' \rangle)/U_b^2$: (—) WSM; (---) WALE; (-·-) LDSM; (○) HWA measures (Ref. 23).

haviors are observed when comparing with HWA [Fig. 2(c)] and LDA/PIV (Fig. 5) measurements. The WALE and LDSM models predict significant overestimation of vertical fluctuations in the wall-jet region ($r/D \geq 2.5$). This fact, combined with the observed tendency to overestimate streamwise fluctuations in the near-wall region, leads to the prediction of an excess of resolved turbulent kinetic energy over the whole range of interest (Fig. 3). It should be noted that significant backward energy cascade may be generally observed within the buffer layer;^{49–52} purely dissipative models are then expected to give poor results, such as the WALE and the LDSM, as in the original formulation by Meneveau *et al.*,¹³ the dynamically computed model constant is clipped to prevent it from assuming complex values, thus not allowing backscatter. On the other hand, as already mentioned, the WSM intrinsically allows backscatter, and this could be one of the leading mechanism involved in the significant reduction in vertical fluctuations compared to the other two models for $r/D \geq 1.0$ (on this regard more details will be shown with the $Re_D=70\,000$ test case). The mentioned reduction allows significant improvement of the results in terms of turbulent kinetic energy.

If a particularly bad agreement in vertical fluctuations is observed when comparing with HWA measurements, WSM results reproduce fairly well the experimental data extracted from LDA and PIV measurements over the whole range, as it can be seen in Fig. 5(a). Good agreement is also observed on average profiles (Fig. 4) and radial fluctuations [Fig. 5(b)]. The discrepancies observed between the experimental results by Cooper *et al.* and by Geers *et al.* in the measurements of the vertical fluctuations makes it difficult to draw conclusions on this regard.

With regards to the turbulent shear stresses [Fig. 2(d)], results are fairly satisfactory far from the jet's axis, the proposed WSM giving the best agreement.

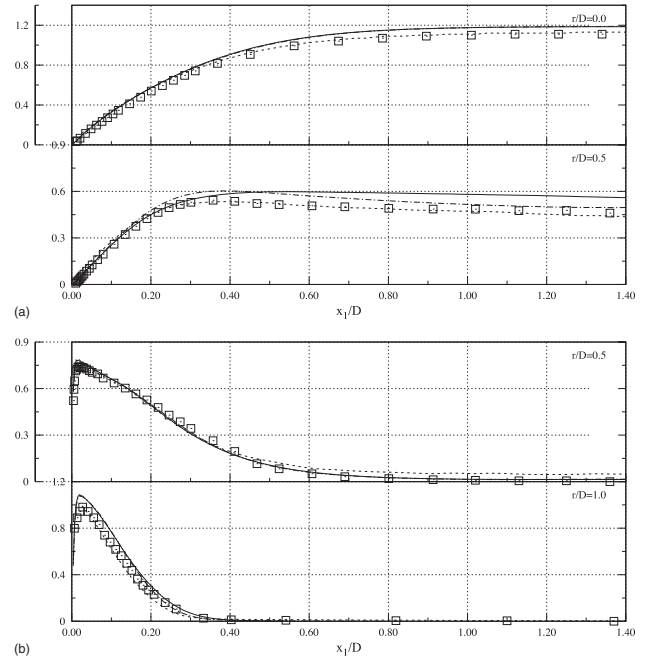


FIG. 4. $Re_D=23\,000$ test case (coarse grid). Average wall-normal velocity $\langle u_n \rangle / U_b$ (a) and average radial velocity $\langle u_r \rangle / U_b$ (b). (—) WSM; (-·-) LDSM; (···) PIV measures (Ref. 25); (□) LDA measures (Ref. 25).

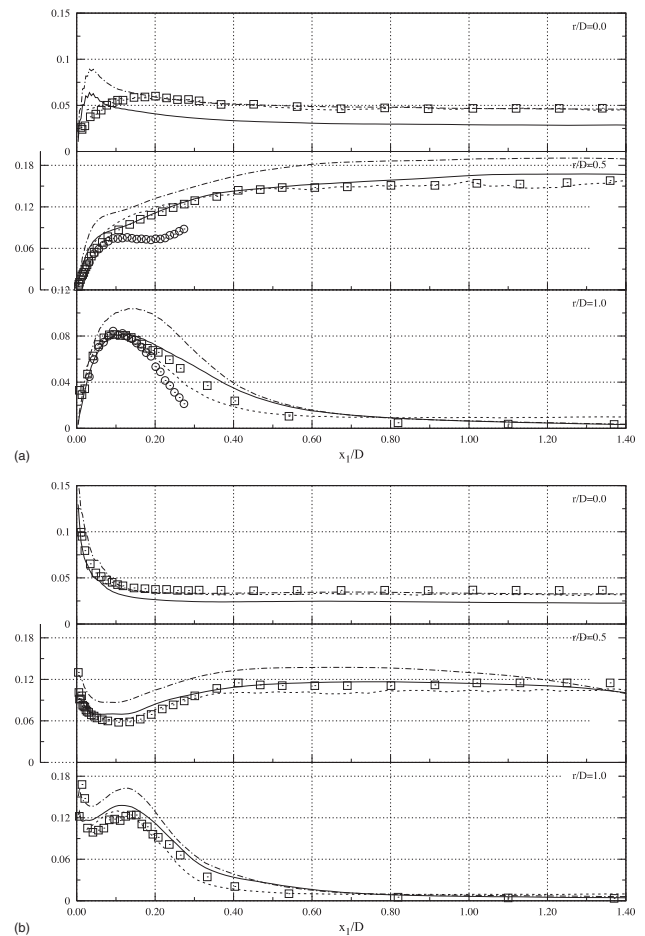


FIG. 5. $Re_D=23\,000$ test case (coarse grid). RMS wall-normal velocity $\sqrt{\langle u_n''u_n'' \rangle} / U_b$ (a) and RMS radial velocity $\sqrt{\langle u_r''u_r'' \rangle} / U_b$ (b). (—) WSM; (-·-) LDSM; (···) PIV measures (Refs. 24 and 25); (□) LDA measures (Refs. 24 and 25); (○) HWA measures (Ref. 23).

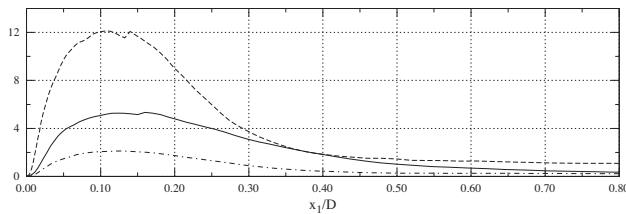


FIG. 6. Average value of ν_{ratio} over horizontal planes: (—) $\text{Re}_D=23\,000$ test case C1 (coarse grid); (---) $\text{Re}_D=23\,000$ test case C2 (refined grid); (-·-) $\text{Re}_D=70\,000$ test case C3.

B. Grid sensitivity assessment

In order to better quantify LES resolution, a normalized SGS energy transfer coefficient is computed as

$$\nu_{\text{ratio}} = \frac{\tau_{ij}^d \tilde{A}_{ij}}{2\bar{\mu} \tilde{A}_{ij} \tilde{A}_{ij}}, \quad (93)$$

which measures the relative intensity between subgrid and viscous energy transfers; note that ν_{ratio} reduces to the ratio ν_t/ν for an eddy-viscosity model and becomes negative in regions characterized by backward SGS energy transfer. The average value of ν_{ratio} has to be positive, anyway, i.e., even if, locally, reverse energy transfer may happen, globally, turbulence is a dissipative phenomenon and the relevant kinetic energy is expected to flow down the energy cascade.

Experience shows that a typical threshold for a well resolved LES is ν_{ratio} , in average, less than about 10. Figure 6 shows the average value of ν_{ratio} produced by the WSM over horizontal planes. With regards to the $\text{Re}_D=23\,000$ test case, the computation performed on the coarse mesh is relatively well resolved, the average ν_{ratio} being always below 6, whereas the computation carried out on the more refined grid has even less energy within the SGSs and $\nu_{\text{ratio}} < 2$ everywhere in the wall-jet region. The higher Reynolds number test case, on the other hand, appears slightly under-resolved, with ν_{ratio} taking values up to ~ 12 . This is consistent with the results which will be presented in Sec. III C, where the resolved turbulent kinetic energy results slightly underpredicted for the $\text{Re}_D=70\,000$ test case.

With regards to the 23 000 Reynolds number jet simulations, the statistical moments computed using the proposed WSM, extracted from the coarse 2.8 M nodes mesh and the refined 5.5 M nodes mesh, are compared in Fig. 7. Results obtained with the WALE and LDSM on the refined grid are also shown. With regards to the new WSM, first order moments match almost perfectly, while some slight difference is visible on second-order moments. The only curve which shows significant improvement is the one related to wall-normal fluctuations at $r/D=1.0$ [cf. Fig. 7(c)]. Clearly the more resolved simulation has less energy in the SGSs, and statistical fluctuations extracted from the resolved flow field give a more accurate representation of the real fluctuations obtained from the experiments.

No significant improvement of the results is observed in the near-wall region where the better resolution of the viscous sublayer in the more refined grid should have implied a more marked improvement.

This result confirms what has been previously said about the positive impact that a model allowing for a correct representation of local interactions near the cutoff length,¹⁸ i.e., the modified Leonard tensor's contribution, connected with local energy backscatter in the simulation, may produce when dealing with not fully resolved wall-bounded flows such as those presented in this paper.

It is worthwhile mentioning that, in order to obtain equivalent results, the more refined computational grid required about 14 times the CPU time required by the coarse grid simulation (cf. Table II), this increase being essentially due to the increased number of grid points and to the reduction in the allowed time step due to the use of explicit time integration and the application of the relevant Courant–Friedrichs–Lewy (CFL) limitation within the viscous sublayer. Moreover, the reduced time step resulted also in a significant reduction in statistical convergence rate and sufficiently converged statistical data required about 56% of the total computational resources.

With regards to the two eddy-viscosity models, i.e., the WALE and the LDSM, results are now slightly improved due to the increased resolution. Yet the streamwise fluctuations are overestimated for $x_1/D \in [0:0.1]$ close to the stagnation region [cf. Fig. 7(b)], giving additional evidence of the inability of purely dissipative models of correctly predicting the average energy transfer in the region where the flow undergoes strong curvature. Similar trends, as in the coarse mesh simulations, are observed on vertical fluctuations [Fig. 7(c)], which are significantly overestimated, and shear stresses [Fig. 7(d)]. The observed inaccuracies in vertical and streamwise fluctuations resulted in the turbulent kinetic energy (not shown) being overpredicted by the WALE and the LDSM at $r/D=1.0$ and $x_1/D \in [0:0.1]$ of about 50%, whereas the WSM results were within experimental measurements' errors. Similar errors were obtained using the dynamic Smagorinsky model (with model constant bound to zero as in the present case) by Hadžiabdić and Hanjalić,⁷ who also observed that, in the early wall-jet region, the turbulent shear stress is not proportional to the mean velocity gradient, thus underlining the weaknesses of the eddy-viscosity hypothesis for this configuration.

In view of these results and the significant extracost that follows from increasing resolution, especially for relatively high Reynolds numbers as in the present study, and considering the small improvements in the results which may be expected (cf. also Sec. III C), the suitability of such a computational effort is questionable. We would rather envisage the possibility of developing improved modeling for the spherical part of the SGS stress tensor in order to better reproduce streamwise and wall-normal fluctuations for slightly under-resolved LES.

C. $\text{Re}_D=70\,000$ test-case C3 validation

The results obtained with the WSM on the $\text{Re}_D=70\,000$ test case are shown in Figs. 8 and 9. Also in this case, error bars are shown to indicate measurement errors on second-order moments. The solid curves refer to statistical quantities extracted directly from the resolved flow field (as

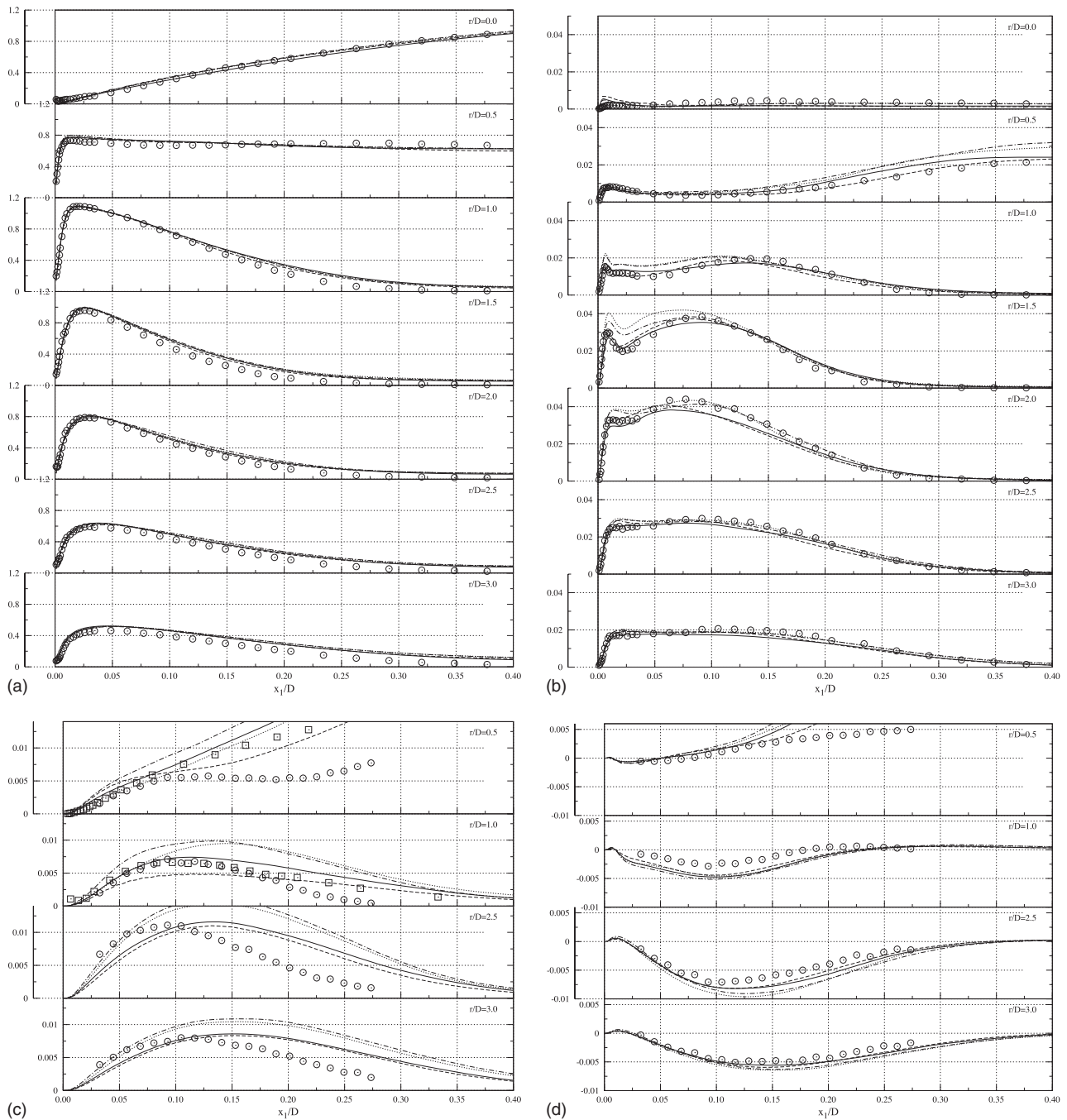


FIG. 7. $Re_D=23\,000$ test case. Streamwise average velocity $\langle u_s \rangle / U_b$ (a); streamwise fluctuating velocity $\langle u_s'' u_s'' \rangle / U_b^2$ (b); wall-normal fluctuating velocity $\langle u_n'' u_n'' \rangle / U_b^2$ (c); and turbulent shear stress $\langle u_s'' u_n'' \rangle / U_b^2$ (d); (—) WSM on highly refined grid (C2); (---) WSM on coarse grid (C1); (···) WALE on highly refined grid (C2); (---) LDSM on highly refined grid (C2); (O) HWA measures (Ref. 23); (□) LDA measures (Refs. 24 and 25).

in the previous test case), while the dashed lines have been obtained including the SGS contribution. If the statistical fluctuation of the resolved velocity is expressed as \bar{u}_i'' and $u_i'^e$ is the exact fluctuation (measured from experiments or obtained from DNS), we may write¹⁵

$$\langle u_i'^e u_j'^e \rangle \approx \langle \bar{u}_i'' \bar{u}_j'' \rangle + \langle \tau_{ij} \rangle, \quad (94)$$

where τ_{ij} is the SGS stress tensor used within the simulation or computed from the resolved field with another SGS model. In the present case, we adopt the former choice and

compute the SGS contribution by time/space averaging the WALE-similarity SGS stress tensor used to perform the simulations,

$$\langle \tau_{ij} \rangle = \langle 2\bar{\rho} \nu_t \tilde{A}_{ij} - \mathcal{L}_{ij} \rangle. \quad (95)$$

Note that \mathcal{L}_{ij} accounts for both the deviatoric and spherical parts. Also note that, in the above formula, the spherical part of the SGS true Reynolds term, i.e., $\rho u_k' u_k'$, which is “absorbed” into the macropressure [see Eq. (30)], is still not included.

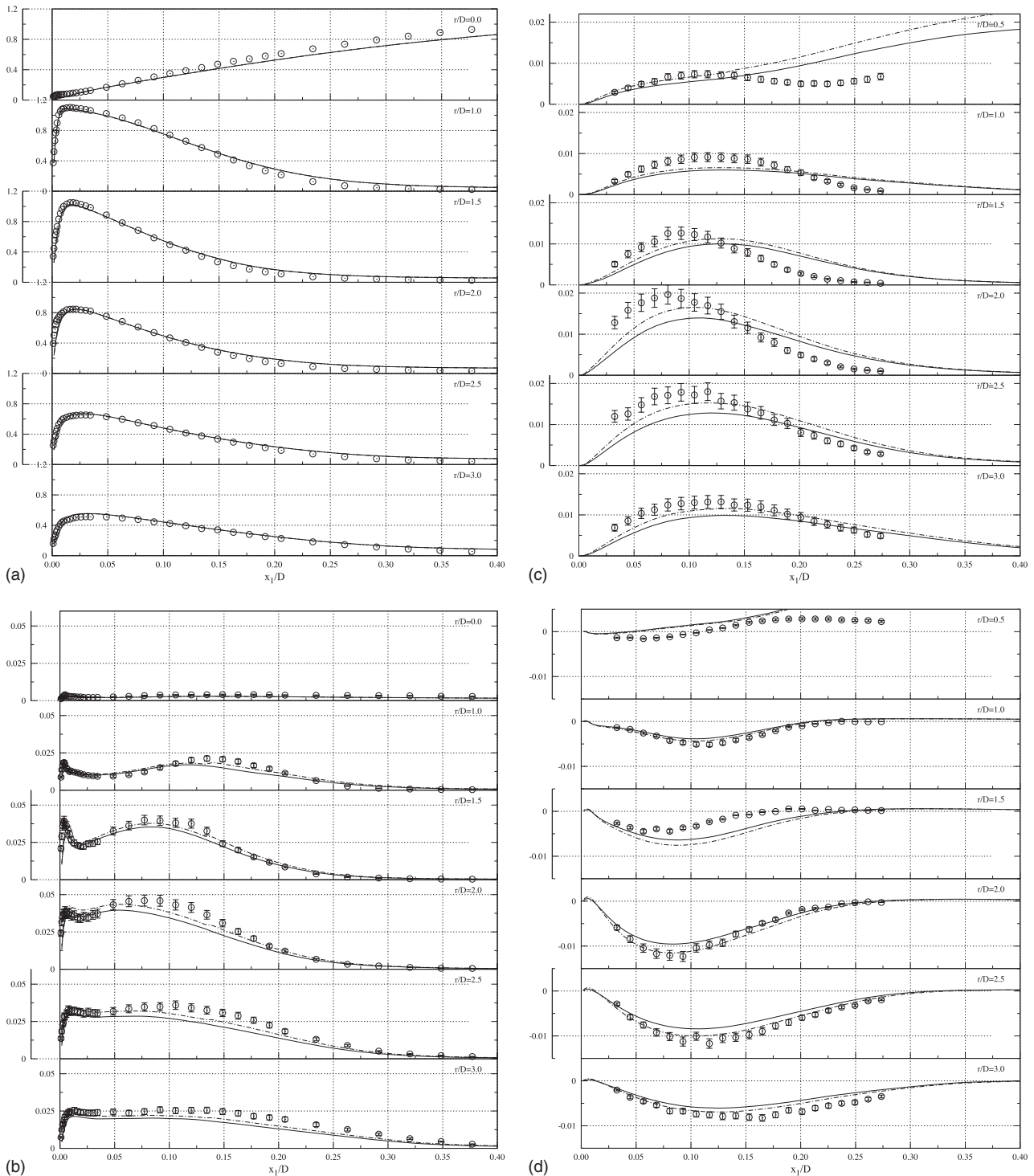


FIG. 8. $Re_D=70\,000$ test case. Streamwise average velocity $\langle u_s \rangle / U_b$ (a); streamwise fluctuating velocity $\langle u''_s u''_s \rangle / U_b^2$ (b); wall-normal fluctuating velocity $\langle u''_n u''_n \rangle / U_b^2$ (c); and turbulent shear stress $\langle u''_s u''_n \rangle / U_b^2$ (d); (—) resolved fluctuations; (---) resolved fluctuations plus SGS contributions; (O) HWA measures (Ref. 23).

For the average velocity profiles [Fig. 8(a)], the matching between experimental data and computed solution is nearly perfect at any location within the computational grid.

As for the $Re_D=23\,000$ test case, the most demanding issue is the computation of the second-order moments. With regards to the streamwise fluctuations [Fig. 8(b)], results show similar trends as in the lower Reynolds number test

case. The model predicts a slight underestimation of fluctuations for $x_1/D \in (0.05:0.2)$. The inclusion of the SGS part produces better agreement but, still, results remain below the measurement errors, especially far from the jet's axis. It should be noted that it is the spherical part of the SGS stress tensor which is playing the key role in this context: it is then reasonable to expect that the inclusion of the modeled trace

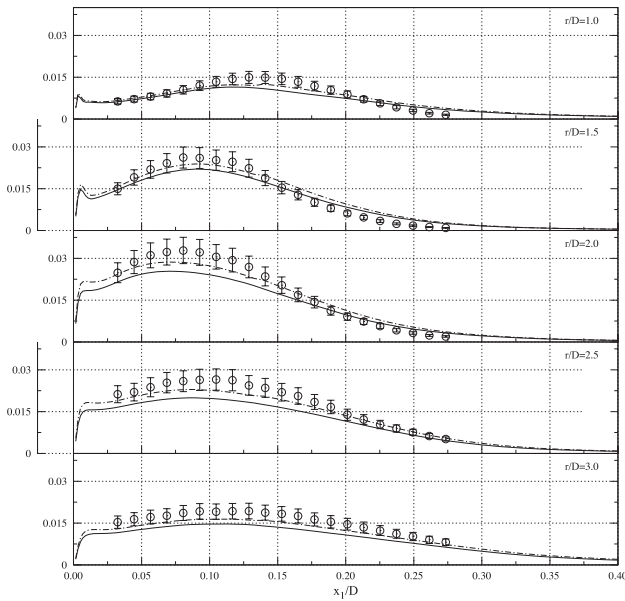


FIG. 9. $Re_D=70\,000$ test case. Turbulent kinetic energy $\frac{1}{2}(\langle u''_x u''_x \rangle + \langle u''_y u''_y \rangle) / U_b^2$: (—) resolved fluctuations; (---) resolved fluctuations plus SGS contributions; (○) HWA measures (Ref. 23).

of the SGS true Reynolds term⁵³ would further improve the results; as it has been pointed out, this is the only missing contribution in the presented results.

Results for wall-normal fluctuations [Fig. 8(c)], again, show the less satisfactory agreement with the experimental results. This is especially true in the impingement region and in the first stages of wall-jet development. Anyway, in sight of the discrepancies observed between HWA and LDA/PIV measurements for the lower Reynolds number test case, it would have been interesting to compare computed vertical fluctuations against alternative measurements; unfortunately, such a database is not available for this Reynolds number. The only reasonable conclusion which may be drawn is that vertical fluctuation profiles show similar trends as those observed at $Re_D=23\,000$.

Turbulent shear stresses [Fig. 8(d)] are well predicted everywhere, except at $r/D=0.5$ and 1.5 . Again, results are globally consistent with those obtained for the $Re_D=23\,000$ test case; the bad agreement on the $r/D=1.5$ profile is quite strange though, considering that the two profiles right ahead and behind it show results in much better agreement with experimentally measured shear stresses. The inclusion of the SGS part, which in this case accounts for all the modified Leonard decomposition's terms, produces a relatively significant improvement in results representing about 10% of the turbulent shear stress (note that error bars in the shear stress plot represent 9% error²³).

The overall behavior of the WSM, as it may be inferred from the computed turbulent kinetic energy in Fig. 9, is quite satisfactory with all the curves falling within the measurement error range. A certain tendency to "align" to the bottom limit of the error range is observed though; this behavior reflects similar tendencies observed in the streamwise and wall-normal directions and is clearly a direct consequence of

the actual distribution of energy between resolved and SGSs for this simulation. Since a significant part of the energy is in the SGSs (cf. Fig. 6), statistically fluctuating quantities extracted from the resolved field cannot match real fluctuations from experiments, unless all the SGS energy is accounted for.

D. Energy backscatter

Even though kinetic energy, in average, is always transferred from the mean motion to the fluctuating one through the well known energy cascade process, the possibility of the existence of isolated events of reverse energy transfer, or backscatter, from the turbulent motion to the mean flow was already envisaged by Monin and Yaglom⁵⁴ and extensively demonstrated using results from DNS, for turbulent boundary layer, in particular, by many authors.^{48–52,55,56} In all these studies, strong anisotropy in *a priori* evaluated subgrid stresses was observed, the main responsible for energy backscatter being identified in the wall SGS shear stress. Therefore, structural SGS models capable of capturing energy backscatter, as it is the case for similarity mixed models, appear to be particularly suited for wall bounded turbulent flows.

In certain regions of the turbulent boundary layer, in fact, typically within the buffer layer,^{49,50,55} the backward energy cascade can become largely dominant over the forward energy cascade. As it has been already observed in Secs. III A and III B, both the standard WALE model and the LDSM show a marked tendency to overestimate velocity fluctuations in the near-wall region, whereas the WSM gives much better results. It is then natural to expect that this behavior may be connected with intrinsic differences between these SGS closures, e.g., the ability of reproducing backscatter, and that computations performed using the WSM should feature some backward energy transfer close to the wall. It is worthwhile mentioning that the similarity closure for the cross and Reynolds terms [cf. Eqs. (17) and (18)] plays a crucial role for backscattering within the buffer layer.⁵⁶ This fact was confirmed by Härtel and Kleiser,⁵⁵ who also emphasized the importance of maintaining the Galilean invariance of the model in order to prevent it from reproducing reverse energy transfer in regions where there should not be any.

Energy backscatter is quantified resorting to the normalized SGS energy transfer coefficient from Eq. (93). For the $Re_D=23\,000$ test case on the coarse grid (C1), in Fig. 10, black regions indicate the occurrence of backscatter over horizontal planes, of dimension $5D \times 5D$, located at different distances from the impingement wall. Approaching the wall, reverse energy transfer regions become more and more numerous, the maximum backscatter activity being observed at a distance $x_1/D \approx 0.015$, and then tend to disappear closer to the viscous sublayer (note that data on the plane at $x_1/D = 0.001$ were extracted from the first computational cell at the wall). Intense backscatter appears for x_1/D in the range of $0.006–0.02$, which corresponds pretty well with the region where the WALE and the LDSM produce excessive streamwise fluctuations [cf. Figs. 2(b) and 7(b)]. The most intense activity is visible in the stagnation region, approximately for

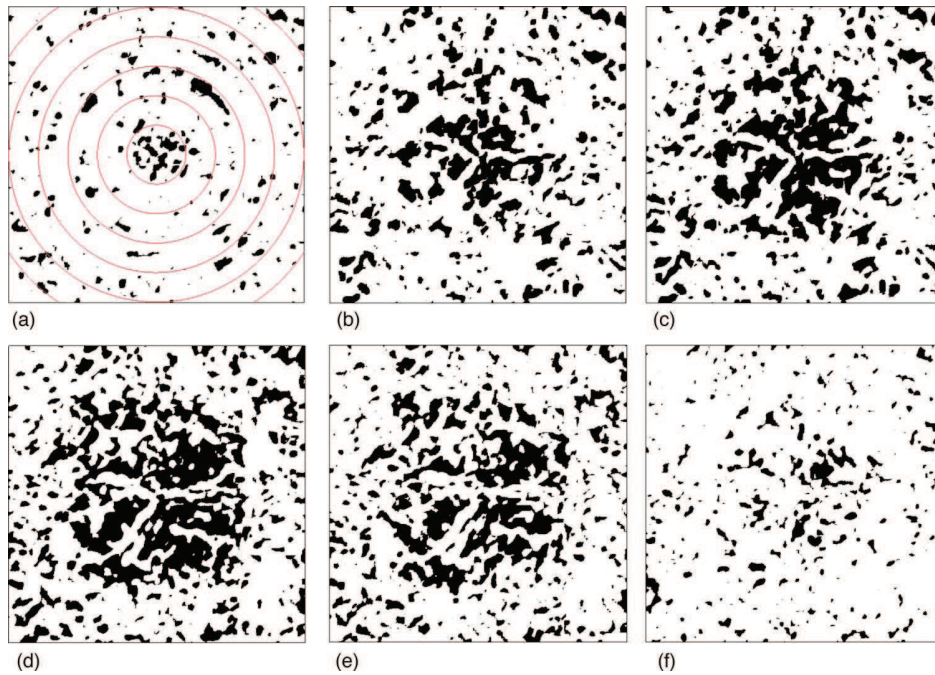


FIG. 10. (Color online) $Re_D=23\,000$ test-case C1 (coarse grid). Localization of regions (colored in black) of negative ν_{ratio} [Eq. (93)] over horizontal planes at different heights: $x_1/D=0.001$ (a), $x_1/D=0.004$ (b), $x_1/D=0.006$ (c), $x_1/D=0.015$ (d), $x_1/D=0.02$ (e), and $x_1/D=0.04$ (f). Circles in (a) indicate radial distances in steps of $0.5D$.

$r < 1.5$, which is also in agreement with the observed behavior of the three models. For the $Re_D=70\,000$ test case (not shown), maximum backscatter activity was registered slightly closer to the wall, at $x_1/D \approx 0.01$, which is consistent with the thinning of the boundary layer at higher Reynolds number.

The same plots for the more resolved grid (C2) are depicted in Fig. 11. The overall behavior is similar to that observed with the less refined mesh. The less frequent events of energy backscatter, registered in the refined grid at x_1/D equal to 0.004 and 0.006, confirm that reverse energy transfer plays a key role in under-resolved turbulent boundary

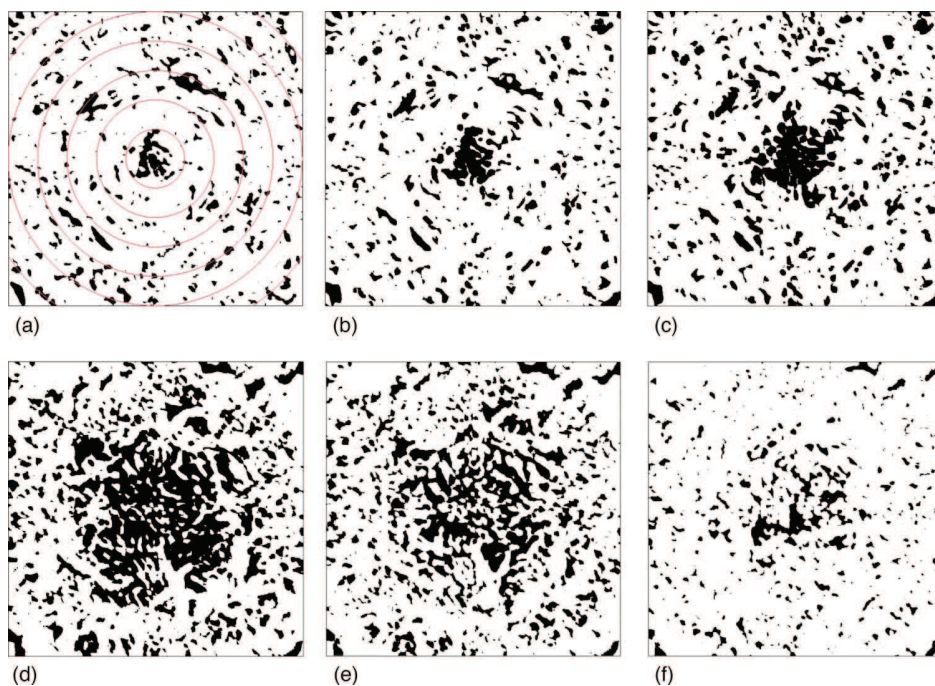
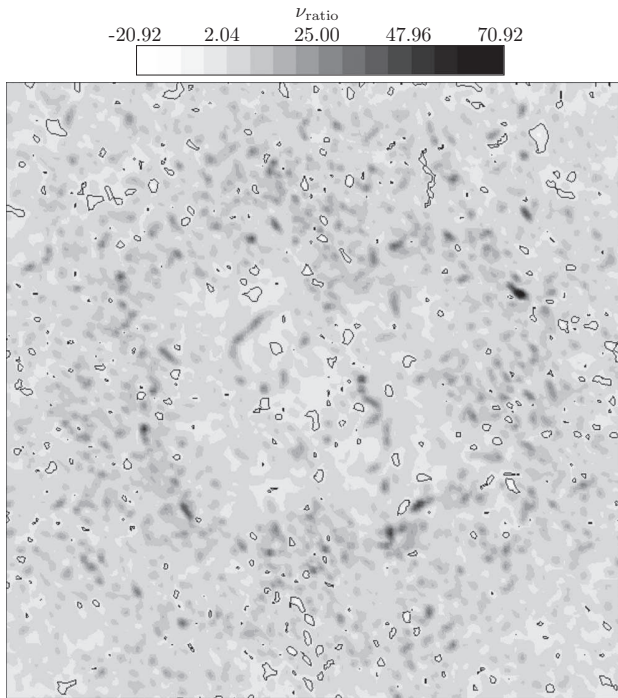
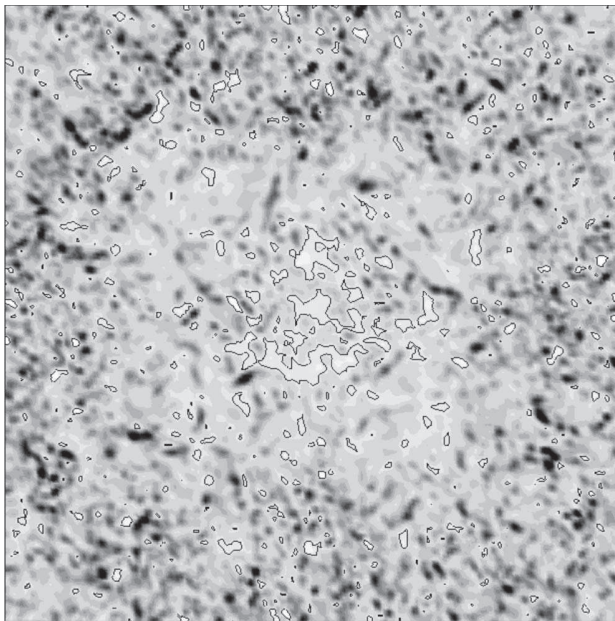


FIG. 11. (Color online) $Re_D=23\,000$ test case C2 (refined grid). Localization of regions (colored in black) of negative ν_{ratio} [Eq. (93)] over horizontal planes at different heights: $x_1/D=0.001$ (a), $x_1/D=0.004$ (b), $x_1/D=0.006$ (c), $x_1/D=0.015$ (d), $x_1/D=0.02$ (e), and $x_1/D=0.04$ (f). Circles in (a) indicate radial distances in steps of $0.5D$.



(a)



(b)

FIG. 12. Maps of normalized SGS energy transfer coefficient ν_{ratio} over a horizontal plane located at $x_1/D=0.1$ for $\text{Re}_D=23\,000$ on coarse grid C1 (a) and for $\text{Re}_D=70\,000$ (b). The black contours indicate regions of energy backscatter.

layers, giving a sort of automatic compensation mechanism that results anyway in the correct amount of average subgrid dissipation being produced.⁴⁸

The visual examination of Figs. 10 and 11 also agrees with the observations of Piomelli *et al.*,⁵¹ who found the fraction of points, in planes parallel to the wall, experiencing backscatter to be between 30% and 50%, when a box filter in physical space was applied to DNS data from channel simu-

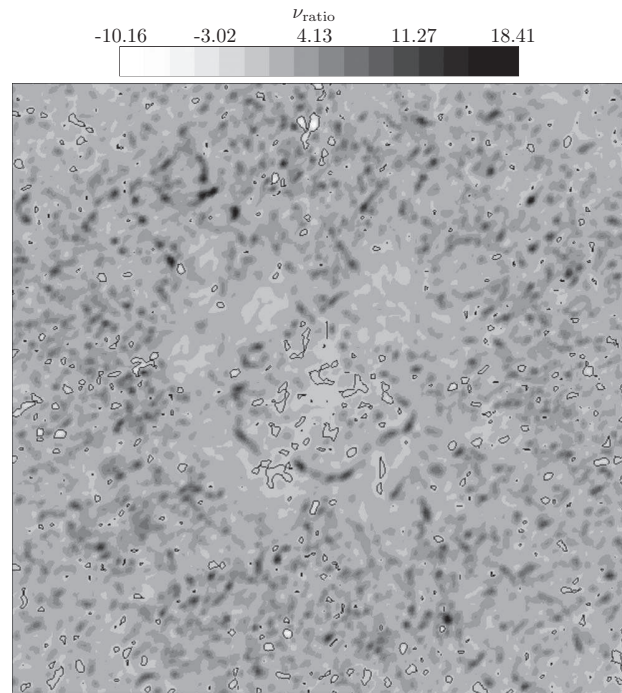


FIG. 13. $\text{Re}_D=23\,000$ test case C2 (refined grid): map of normalized SGS energy transfer coefficient ν_{ratio} over an horizontal plane located at $x_1/D=0.1$. The black contours indicate regions of energy backscatter.

lations at different Reynolds numbers, including transitional turbulence and compressible isotropic decay. No dependence on Mach number was observed, on this regard, in the case of compressible turbulence.

The occurrence of reverse energy transfer is little affected by the Reynolds number,⁴⁹ even though higher Reynolds number flows are typically slightly more susceptible to show backscatter.⁵¹ More frequent occurrence of energy backscatter is expected when the near-wall dynamics of the flow are under-resolved.⁴⁸ This is consistent with the above mentioned dependency on the Reynolds number, as, increasing Re , grid resolution requirements become more stringent.

In Figs. 12 and 13, instantaneous spatial distributions of ν_{ratio} over a horizontal plane located at $x_1/D=0.1$, i.e., the approximate location of maximum turbulent energy production (cf. Figs. 3, 6, and 9), reveal that, when the Reynolds number is increased, subgrid energy transfer becomes much more intermittent, with more frequent occurrence of high peaks of forward energy transfer. Note that, although the two maps in Figs. 12 are represented with the same scale in order to allow direct comparison, the range of values for the lower Reynolds number case was from -12.5 to 96.7 , the maximum being attained in the single black spot which can be observed in the upper right quadrant of Fig. 12(a); that is the only location where values of ν_{ratio} greater than ~ 55 were measured. Also note that, due to the much lower level of SGS energy in the refined $\text{Re}_D=23\,000$ test case C2, the relevant map in Fig. 13 is represented with its own scale. Black contours delimit regions of reverse energy transfer that, of course, at this height has become less frequent.

For the $\text{Re}_D=70\,000$ test case, Fig. 14 shows maps of ν_{ratio} over a radial plane extending from the wall up to

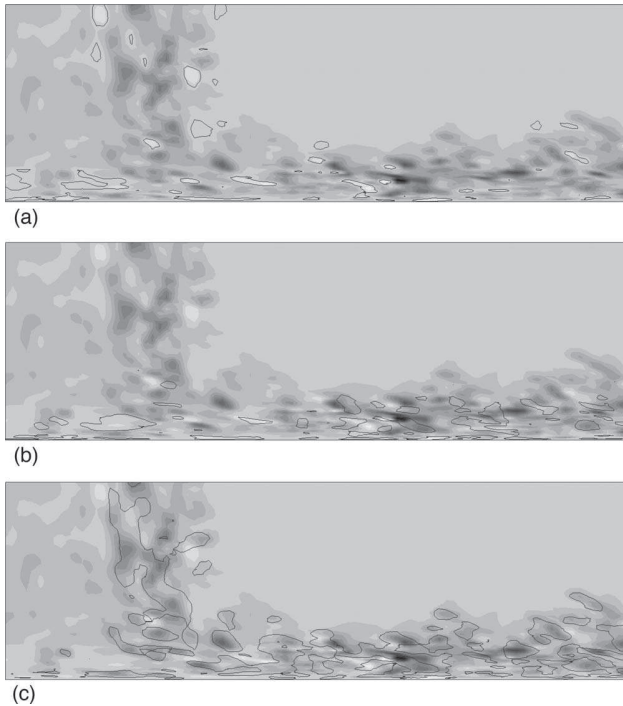


FIG. 14. $Re_D=70\,000$ test case. Maps of normalized SGS energy transfer coefficient ν_{ratio} (same scale as in Fig. 12) over a vertical plane in the range $x_1/D \in [0:0.8]$, $r/D \in [0:2.5]$. The black contours: (a) regions of reverse energy transfer, (b) intense strain, and (c) vorticity.

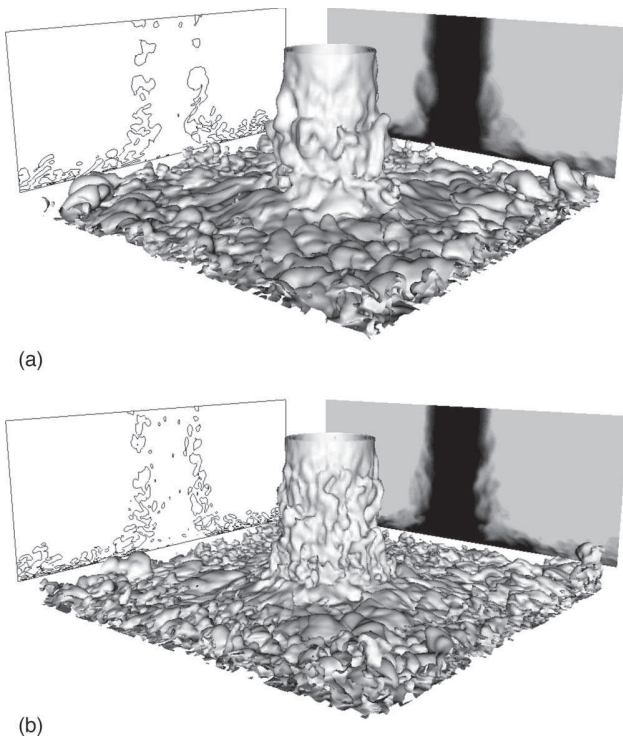


FIG. 15. Tridimensional visualization of the flow at $Re_D=23\,000$ on coarse grid C1 (a) and at $Re_D=70\,000$ (b): isosurfaces of passive scalar Z (center), isocontours of $Q=0.5$ (left), and passive scalar map (right) over axial planes.

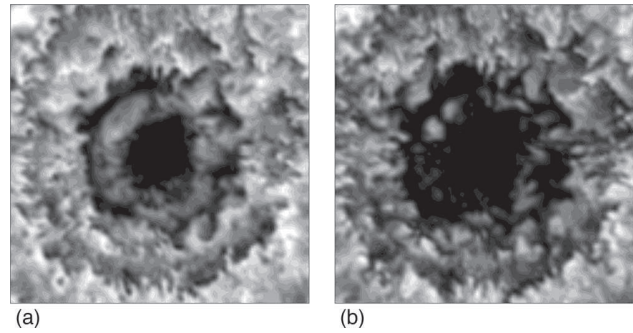


FIG. 16. $Re_D=23\,000$ test case C1: maps of passive scalar Z over a horizontal plane at $x_1/D=0.1$ (a) and $x_1/D=0.05$ (b).

$x_1/D=0.8$; black contours are used to mark regions of negative ν_{ratio} in (a), intense strain in (b), and strong vorticity in (c). The last have been identified by contours at $Q=-10$ and $Q=2$, respectively, Q representing the normalized second invariant of the resolved velocity gradient tensor,

$$Q = -\frac{D^2}{2U_b^2} \frac{\partial \tilde{u}_i}{\partial x_j} \frac{\partial \tilde{u}_j}{\partial x_i}. \quad (96)$$

Consistent with the findings of Piomelli *et al.*,⁵² peaks in forward scatter are well correlated with regions of strong vorticity, for the most coming from the jet's shear layer, and backscatter events generally occur in the middle of intense forward scatter regions. Long and thin pockets of fluid, where backward energy transfer is predominant, originate mostly near the wall and propagate into the boundary layer and downstream in the wall jet. As expected, regions of negative ν_{ratio} are relatively well correlated with regions of negative Q , meaning that the most important events of SGS energy backscatter are observed where the resolved flow field undergoes intense straining due to sweeping motions induced by coherent vortical structures.

E. Flow field and scalar mixing

In this section, we present a brief qualitative comparison of the two test cases C1 and C3, with particular emphasis on the observed differences in turbulence development and scalar mixing. Analogous results from test case C2 (not shown) are consistent with those obtained from test case C1, which is quite expected considering that the WSM gave almost identical statistical features on the two different grids (cf. Sec. III B). A tridimensional representation of the flow field is presented in Fig. 15 for the two test cases. Instantaneous isosurfaces of passive scalar Z are shown, together with its distributions over an axial plane; the development of coherent vortical structures are also represented by means of isocontours of Q . Passive scalar distribution over horizontal planes at $x_1/D=0.1$ and $x_1/D=0.05$ for the two Reynolds numbers is also shown in Figs. 16 and 17, respectively.

As expected, the higher Reynolds number test case presents an earlier development of turbulence within the jet's shear layer, which is characterized by finer structures and increased intermittency, which is particularly evident from the distributions of Z parallel to the impingement wall. Also, increased mixing in the near-wall region is promoted at

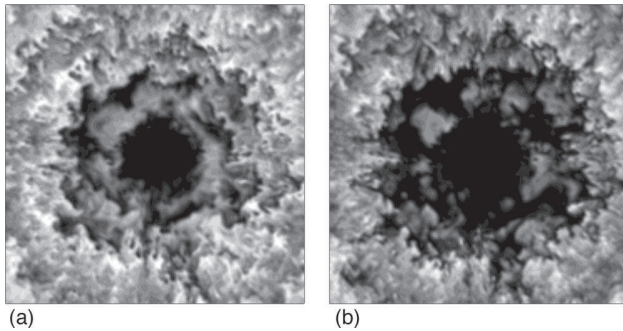


FIG. 17. $Re_D=70\,000$ test case C3: maps of passive scalar Z over a horizontal plane at $x_1/D=0.1$ (a) and $x_1/D=0.05$ (b).

higher Reynolds number, as it may be inferred from the presence of numerous and extended white pockets of fluid with $Z \sim 0$, just around the stagnation region [cf. Fig. 17(b)].

IV. CONCLUSIONS

A WALE-similarity mixed model for LES of compressible turbulent flows was presented and tested on the impinging round jet at two Reynolds numbers: 23 000 (2.8 M and 5.5 M cells) and 70 000 (3.5 M cells), respectively. The use of the WALE eddy-viscosity term together with the modified Leonard tensor allows a good representation of nonlocal interactions as well as local interactions near the cutoff length, these last being responsible for reverse energy transfer, while maintaining proper wall scaling. Furthermore, the unphysical alignment between the SGS stress tensor and the resolved strain tensor—a condition which is intrinsically enforced by any eddy-viscosity model—is automatically removed.

The model was compared to the standard WALE model and the LDSM on the lower Reynolds number test case on two different grids, one relatively coarse and the other with increased resolution. A significant improvement in the results in terms of second-order moments was observed, especially in the near-wall region, where the other two models have a marked tendency to overestimate streamwise turbulent fluctuations. In the outer layer of the wall-jet region, an excessive level of vertical fluctuations was observed with the standard WALE and LDSM models, the proposed mixed model giving better results.

The impact of mesh refinement on the results was also addressed for the $Re_D=23\,000$ test case. An empirical criterion for LES resolution, based on ν_{ratio} —the ratio between subgrid and viscous energy transfer—was assessed. The comparison between resolved fluctuations and exact fluctuations measured from experiments was found to be quite satisfactory for average values of ν_{ratio} lower than about 10. The addition of SGS contributions on resolved fluctuations was deemed to be necessary for less resolved LES, i.e., for average ν_{ratio} greater than 10.

On the higher Reynolds number test case, the new model provided quite satisfactory results on the streamwise fluctuations, the turbulent shear stresses, and the turbulent kinetic energy, the vertical fluctuations representing, again, the most critical issue. On this regard, the unavailability of alternative measurements leaves the question still open for further ex-

amination. The relatively low grid resolution used for such a high Reynolds number made it necessary to account for SGS contributions when comparing with experiments. By accounting for the SGS part, results were generally improved.

Correct representation of energy backscatter was found to play an essential role for the estimation of the average subgrid dissipation, especially when the computational grid does not allow for sufficient resolution in the near-wall region. In that case, backscatter may determine an automatic compensation process for energy production events related to under-resolved near-wall dynamics.

Nonetheless, it is worthwhile stressing that strong backscatter effect using LES may not be always a necessary outcome, as numerical and modeling approximations can easily lead to wrong interpretation of the detail of the physics. Modeled backscatter, in fact, is strictly related with the use of non-Reynolds filtering operators such as the box filter in physical space or the Gaussian filter—the cross term in the usual SGS triple decomposition being the main responsible—and with the location of the cutoff frequency, i.e., the LES resolution. This consideration is consistent with the idea of local interactions near the cutoff length put forward by Akhavan *et al.*,¹⁸ based on *a priori* evaluations on DNS results. Rather, a combination of scale-similarity assumption and WALE model, in order to obtain the proper transient wall-flow behavior in the impinging jet problem, was discussed; indeed, with this modeling formulation and with the modified Leonard term evaluated with a box filter in physical space, backscatter was present due to the anisotropic part of the resolved SGS turbulent transport.

Such a flow configuration, indeed, gave evidence of the weaknesses of functional SGS model based on the Boussinesq approximation and the eddy-viscosity assumption alone, suggesting the use of more performing structural models, as the proposed WSM, in order to correctly capture the complex nature of SGS interactions, in particular, within the strong curvature flow region around the stagnation point.

The proposed model produces a correct representation of the statistical character of the problem under study and demonstrates quite interesting features, especially in consideration of its relatively low computational cost and the complexity of the analyzed flow configuration.

ACKNOWLEDGMENTS

Support was provided by the project NICE (New Integrated Combustion system for Future Passenger Car Engines), Grant No. TIP3-CT-2004-50620 within the Sixth Framework program of the European Union. Computing resources were provided by IDRIS-CNRS (<http://www.idris.fr/>) and CRIHAN (<http://www.crihan.fr/>).

APPENDIX: EXPLICIT FILTER IMPLEMENTATION

The filtering operation at length scale $4/3\Delta$ has been obtained as a generalization of the discrete filter used by Zang *et al.*²¹ With reference to Fig. 18, in the case of uniform grid, the filtered quantity $\hat{\phi}$ is obtained with the trapezoidal rule as

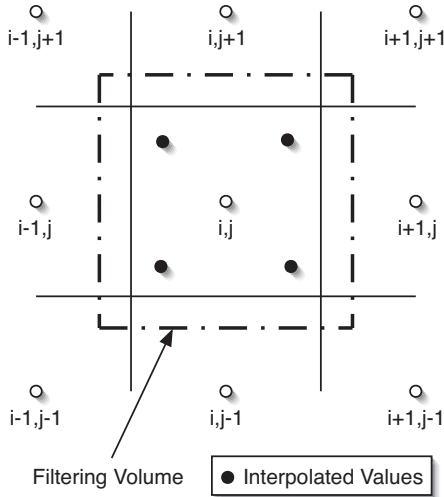


FIG. 18. Explicit filtering volume in two dimensions.

$$\hat{\varphi}_{i,j,k} = \frac{1}{8}(\varphi_{i+1/3,j+1/3,k+1/3} + \varphi_{i-1/3,j+1/3,k+1/3} + \varphi_{i+1/3,j-1/3,k+1/3} + \varphi_{i-1/3,j-1/3,k+1/3} + \varphi_{i+1/3,j+1/3,k-1/3} + \varphi_{i-1/3,j+1/3,k-1/3} + \varphi_{i+1/3,j-1/3,k-1/3} + \varphi_{i-1/3,j-1/3,k-1/3}), \quad (A1)$$

where each of the values in parentheses is obtained by multilinear interpolation of the surrounding nodes. The explicit formulation for interpolated quantities—indicated in Fig. 18 with solid circles—can be expressed as

$$\varphi_{i\pm 1/3,j\pm 1/3,k\pm 1/3} = \frac{1}{27}\varphi_{i\pm 1,j\pm 1,k\pm 1} + \frac{8}{27}\varphi_{i,j,k} + \frac{2}{27}(\varphi_{i\pm 1,j\pm 1,k} + \varphi_{i\pm 1,j,k\pm 1} + \varphi_{i,j\pm 1,k\pm 1}) + \frac{4}{27}(\varphi_{i\pm 1,j,k} + \varphi_{i,j\pm 1,k} + \varphi_{i,j,k\pm 1}), \quad (A2)$$

where the signs in the triplets of indices of the terms on the right-hand side must be chosen in accordance with the signs in the triplet of indices of the relevant interpolated quantity on the left-hand side.

The above formulation may be readily generalized to the case of nonuniform grids. An isotropic filter operator can be built, in this particular case, by computing a different set of the interpolation coefficients for each grid point, thus ensuring the correct filtering cutoff length along the three coordinate directions. The local value of the grid length scale Δ , in particular, may be conveniently computed resorting to the anisotropic grid correction factor proposed by Scotti *et al.*³³ [cf. Eq. (27)]. It is worth stressing that maintaining moderate grid anisotropy¹⁵ and paying particular attention to pencil-like computational cells^{57,58} are anyway advisable. If $\hat{\Delta} = 4/3\Delta$ is the filter cutoff length scale, the nonuniform grid version of Eqs. (A1) and (A2) may be rewritten as

$$\hat{\varphi}_{i,j,k} = \frac{1}{8}[\varphi(x^+, y^+, z^+) + \varphi(x^-, y^+, z^+) + \varphi(x^+, y^-, z^+) + \varphi(x^-, y^-, z^+) + \varphi(x^+, y^+, z^-) + \varphi(x^-, y^+, z^-) + \varphi(x^+, y^-, z^-) + \varphi(x^-, y^-, z^-)], \quad (A3)$$

$$\varphi(x^\pm, y^\pm, z^\pm) = a_0\varphi_{i\pm 1,j\pm 1,k\pm 1} + b_0\varphi_{i,j,k} + c_1\varphi_{i\pm 1,j\pm 1,k} + c_2\varphi_{i\pm 1,j,k\pm 1} + c_3\varphi_{i,j\pm 1,k\pm 1} + d_1\varphi_{i\pm 1,j,k} + d_2\varphi_{i,j\pm 1,k} + d_3\varphi_{i,j,k\pm 1}, \quad (A4)$$

with $x^\pm = x_i \pm \hat{\Delta}/4$, $y^\pm = y_j \pm \hat{\Delta}/4$, and $z^\pm = z_k \pm \hat{\Delta}/4$.

Again, the signs in the triplets of indices on the right-hand side must be chosen according to the location of the interpolated quantity with respect to the filtering location; the same signs shall be used when computing all the following relevant quantities. The multilinear interpolation coefficients in Eq. (A4) are defined by the following relations:

$$a_0 = \xi^\pm \eta^\pm \zeta^\pm, \quad b_0 = [1 - \xi^\pm][1 - \eta^\pm][1 - \zeta^\pm], \\ c_1 = \xi^\pm \eta^\pm [1 - \zeta^\pm], \quad d_1 = \xi^\pm [1 - \eta^\pm][1 - \zeta^\pm], \\ c_2 = \xi^\pm [1 - \eta^\pm] \zeta^\pm, \quad d_2 = [1 - \xi^\pm] \eta^\pm [1 - \zeta^\pm], \\ c_3 = [1 - \xi^\pm] \eta^\pm \zeta^\pm, \quad d_3 = [1 - \xi^\pm][1 - \eta^\pm] \zeta^\pm.$$

ξ^\pm , η^\pm , and ζ^\pm being computed as the ratio between $\hat{\Delta}/4$ and the separation along the three coordinate axes between the filtering location and the neighbor nodes,

$$\xi^\pm = \frac{\hat{\Delta}}{4|x_{i\pm 1} - x_i|}, \\ \eta^\pm = \frac{\hat{\Delta}}{4|y_{j\pm 1} - y_j|}, \\ \zeta^\pm = \frac{\hat{\Delta}}{4|z_{k\pm 1} - z_k|}.$$

As it can be easily verified, Eq. (A1)—or the analogous nonuniform grid version, Eq. (A3)—reduces, globally, to a linear combination of the 27 points involved in the multilinear interpolation procedure,

$$\hat{\varphi}_{i,j,k} = \sum_{\epsilon} \alpha_{i+\epsilon,j+\epsilon,k+\epsilon} \varphi_{i+\epsilon,j+\epsilon,k+\epsilon}, \quad (A5)$$

the factors α being computed from the multilinear interpolation coefficients and the summation being performed over all the possible combinations of indices obtained for $\epsilon = -1, 0, 1$.

The presence of wall boundary conditions poses an additional inevitable issue within the near-wall region, when the filter size becomes greater than the available distance from the wall. In this case, the filtering volume is cut by the wall and a strictly isotropic filter is difficult to be defined. In the present implementation, the scheme is switched to bidimensional filtering over the plane parallel to the solid boundary whenever the filter cutoff length becomes greater than the distance from the wall.

¹E. Baydar and Y. Ozmen, “An experimental investigation on flow structures of confined and unconfined impinging air jets,” *Heat Mass Transfer* **42**, 338 (2006).

²J. W. Hall and D. Ewing, “The development of the large-scale structures in round impinging jets exiting long pipes at two Reynolds numbers,” *Exp. Fluids* **38**, 50 (2005).

- ³J. W. Hall and D. Ewing, "On the dynamics of the large-scale structures in round impinging jets," *J. Fluid Mech.* **555**, 439 (2006).
- ⁴H. M. Hofmann, R. Kaiser, M. Kind, and H. Martin, "Calculations of steady and pulsating impinging jets—an assessment of 13 widely used turbulence models," *Numer. Heat Transfer, Part B* **51**, 565 (2007).
- ⁵T. Hällqvist, "Large eddy simulation of impinging jets with heat transfer," Ph.D. thesis, Royal Institute of Technology, 2006.
- ⁶T. Hällqvist, "Numerical study of impinging jets with heat transfer," Technical Report No. KTH/MEK/TR-03/06-SE, 2003.
- ⁷M. Hadžiabdić and K. Hanjalić, "Vortical structures and heat transfer in a round impinging jet," *J. Fluid Mech.* **596**, 221 (2008).
- ⁸M. Germano, U. Piomelli, P. Moin, and W. Cabot, "A dynamic subgrid-scale eddy viscosity model," *Phys. Fluids A* **3**, 1760 (1991).
- ⁹F. Nicoud and F. Ducros, "Subgrid-scale stress modelling based on the square of the velocity gradient tensor," *Flow, Turbul. Combust.* **62**, 183 (1999).
- ¹⁰Q. Li, G. Page, and J. McGuirk, "Large-eddy simulation of twin impinging jets in cross-flow," *Aeronaut. J.* **111**, 195 (2007).
- ¹¹D. J. Clayton and W. P. Jones, "Large eddy simulation of impinging jets in a confined flow," *Flow, Turbul. Combust.* **77**, 127 (2006).
- ¹²P. Moin, K. Squires, W. Cabot, and S. Lee, "A dynamic subgrid-scale model for compressible turbulence and scalar transport," *Phys. Fluids A* **3**, 2746 (1991).
- ¹³C. Meneveau, T. Lund, and W. Cabot, "A Lagrangian dynamic subgrid-scale model of turbulence," *J. Fluid Mech.* **319**, 353 (1996).
- ¹⁴C. Meneveau and J. Katz, "Scale-invariance and turbulence models for large-eddy simulation," *Annu. Rev. Fluid Mech.* **32**, 1 (2000).
- ¹⁵P. Sagaut, *Large Eddy Simulation for Incompressible Flows: An Introduction*, 2nd ed. (Springer-Verlag, Berlin, 2001).
- ¹⁶S. Liu, C. Meneveau, and J. Katz, "On the properties of similarity subgrid-scale models as deduced from measurements in a turbulent jet," *J. Fluid Mech.* **275**, 83 (1994).
- ¹⁷J. Smagorinsky, "General circulation experiments with the primitive equations," *Mon. Weather Rev.* **91**, 99 (1963).
- ¹⁸R. Akhavan, A. Ansari, S. Kang, and N. Mangiavacchi, "Subgrid-scale interactions in a numerically simulated planar turbulent jet and implications for modeling," *J. Fluid Mech.* **408**, 83 (2000).
- ¹⁹R. Anderson and C. Meneveau, "Effects of the similarity model in finite-difference LES of isotropic turbulence using a Lagrangian dynamic mixed model," *Flow, Turbul. Combust.* **62**, 201 (1999).
- ²⁰M. Salvetti and S. Banerjee, "A priori tests of a new dynamic subgrid-scale model for finite-difference large-eddy simulations," *Phys. Fluids* **7**, 2831 (1995).
- ²¹Y. Zang, R. L. Street, and J. R. Koseff, "A dynamic mixed subgrid-scale model and its application to turbulent recirculating flows," *Phys. Fluids A* **5**, 3186 (1993).
- ²²G. Erlebacher, M. Hussaini, C. Speziale, and T. Zang, "Toward the large-eddy simulation of compressible turbulent flows," *J. Fluid Mech.* **238**, 155 (1992).
- ²³D. Cooper, D. Jackson, B. Launder, and G. Liao, "Impinging jet studies for turbulence model assessment—I. Flow-field experiments," *Int. J. Heat Mass Transfer* **36**, 2675 (1993).
- ²⁴L. Geers, "Multiple impinging jet arrays: an experimental study on flow and heat transfer," Ph.D. thesis, Technische Universiteit Delft, 2004.
- ²⁵L. Geers, M. Tummers, and K. Hanjalić, "Experimental investigation of impinging jet arrays," *Exp. Fluids* **36**, 946 (2004).
- ²⁶F. Ducros, P. Comte, and M. Lesieur, "Large-eddy simulation of a spatially growing boundary layer over an adiabatic flat plate at low Mach number," *Int. J. Heat Mass Transfer* **16**, 341 (1995).
- ²⁷M. Lesieur, O. Métais, and P. Comte, *Large-Eddy Simulations of Turbulence* (Cambridge University Press, Cambridge, 2005).
- ²⁸J. Bardina, J. Ferziger, and W. Reynolds, "Improved subgrid-scale models for large-eddy simulation," *AIAA J.* **1357**, 10 (1980).
- ²⁹J. Bardina, J. Ferziger, and W. Reynolds, "Improved turbulence models based on LES of homogeneous incompressible turbulent flows," Thermosciences Division, Department Mechanical Engineering, Stanford University Report No. TF-19, 1984.
- ³⁰C. Speziale, G. Erlebacher, T. Zang, and M. Hussaini, "The subgrid-scale modeling of compressible turbulence," *Phys. Fluids* **31**, 940 (1988).
- ³¹M. Germano, "A proposal for a redefinition of the turbulent stresses in the filtered Navier–Stokes equations," *Phys. Fluids* **29**, 2323 (1986).
- ³²J. Deardorff, "A numerical study of three-dimensional turbulent channel flow at large Reynolds numbers," *J. Fluid Mech.* **41**, 453 (1970).
- ³³A. Scotti, C. Meneveau, and D. Lilly, "Generalized Smagorinsky model for anisotropic grids," *Phys. Fluids A* **5**, 2306 (1993).
- ³⁴J. DeBonis, "The numerical analysis of a turbulent compressible jet," NASA Report No. TM-2001-210716, 2001.
- ³⁵F. Ducros, F. Laporte, T. Soulères, V. Guinot, P. Moinat, and B. Caruelle, "High-order fluxes for conservative skew-symmetric-like schemes in structured meshes: Application to compressible flows," *J. Comput. Phys.* **161**, 114 (2000).
- ³⁶R. Swanson and E. Turkel, "On central-difference and upwind schemes," *J. Comput. Phys.* **101**, 292 (1992).
- ³⁷R. Swanson, R. Radespiel, and E. Turkel, "On some numerical dissipation schemes," *J. Comput. Phys.* **147**, 518 (1998).
- ³⁸S. Tatsumi, L. Martinelli, and A. Jameson, "Flux-limited schemes for the compressible Navier–Stokes equations," *AIAA J.* **33**, 252 (1995).
- ³⁹S. Gottlieb and C. Shu, "Total variation diminishing Runge–Kutta schemes," *Math. Comput.* **67**, 73 (1998).
- ⁴⁰G. Jiang and C. Shu, "Efficient implementation of weighted ENO schemes," *J. Comput. Phys.* **126**, 202 (1996).
- ⁴¹G. Lodato, P. Domingo, and L. Vervisch, "Three-dimensional boundary conditions for direct and large-eddy simulation of compressible viscous flows," *J. Comput. Phys.* **227**, 5105 (2008).
- ⁴²C. Yoo and H. Im, "Characteristic boundary conditions for simulations of compressible reacting flows with multi-dimensional, viscous and reaction effects," *Combust. Theory Modell.* **11**, 259 (2007).
- ⁴³T. Poinsot and S. Lele, "Boundary conditions for direct simulations of compressible viscous flows," *J. Comput. Phys.* **101**, 104 (1992).
- ⁴⁴M. Klein, A. Sadiki, and J. Janicka, "A digital filter based generation of inflow data for spatially developing direct numerical or large eddy simulations," *J. Comput. Phys.* **186**, 652 (2003).
- ⁴⁵U. Frisch, *Turbulence: The Legacy of A. N. Kolmogorov* (Cambridge University Press, Cambridge, 1995).
- ⁴⁶T. Zang, "Numerical simulation of the dynamics of turbulent boundary layers: Perspectives of a transition simulator," *Philos. Trans. R. Soc. London* **336**, 95 (1991).
- ⁴⁷L. Temmerman, M. Leschziner, C. Mellen, and J. Fröhlich, "Investigation of wall-function approximations and subgrid-scale models in large eddy simulation of separated flow in a channel with streamwise periodic constrictions," *Int. J. Heat Mass Transfer* **24**, 157 (2003).
- ⁴⁸U. Piomelli, "High Reynolds number calculations using the dynamic subgrid-scale stress model," *Phys. Fluids A* **5**, 1484 (1993).
- ⁴⁹C. Härtel and L. Kleiser, "Analysis and modelling of subgrid-scale motions in near-wall turbulence," *J. Fluid Mech.* **356**, 327 (1998).
- ⁵⁰C. Härtel, L. Kleiser, F. Unger, and R. Friedrich, "Subgrid-scale energy transfer in the near-wall region of turbulent flows," *Phys. Fluids* **6**, 3130 (1994).
- ⁵¹U. Piomelli, W. H. Cabot, P. Moin, and S. Lee, "Subgrid-scale backscatter in turbulent and transitional flows," *Phys. Fluids A* **3**, 1766 (1991).
- ⁵²U. Piomelli, Y. Yu, and R. J. Adrian, "Subgrid-scale energy transfer and near-wall turbulence structure," *Phys. Fluids* **8**, 215 (1996).
- ⁵³A. Yoshizawa, "Statistical theory for compressible turbulent shear flows, with the application to subgrid modeling," *Phys. Fluids* **29**, 2152 (1986).
- ⁵⁴A. Monin and A. Yaglom, *Statistical Fluid Mechanics: Mechanics of Turbulence* (Dover, New York, 1971), Vol. I.
- ⁵⁵C. Härtel and L. Kleiser, "Galilean invariance and filtering dependence of near-wall grid-scale/subgrid-scale interactions in large-eddy simulation," *Phys. Fluids* **9**, 473 (1997).
- ⁵⁶K. Horiuti, "The role of the Bardina model in large eddy simulation of turbulent channel flow," *Phys. Fluids A* **1**, 426 (1989).
- ⁵⁷A. Scotti, C. Meneveau, and M. Fatica, "Dynamic smagorinsky model on anisotropic grids," *Proceedings of the Summer Program* (Center for Turbulence Research, Stanford University, Stanford, 1996), pp. 259–276.
- ⁵⁸A. Scotti, C. Meneveau, and M. Fatica, "Dynamic smagorinsky model on anisotropic grids," *Phys. Fluids* **9**, 1856 (1997).

PAPER 3 

G. Lodato, P. Domingo, L. Vervisch and D. Veynante. Scalar variances: LES against measurements and mesh optimization criterion. Scalar gradient: a three-dimensional estimation from planar measurements using DNS. In *Proceedings of the Summer Program* (pp. 387–398), (Center for Turbulence Research, Stanford University, 2008).

Scalar variances: LES against measurements and mesh optimization criterion; scalar gradient: a three-dimensional estimation from planar measurements using DNS

By G. Lodato[†], P. Domingo[†], L. Vervisch[†] AND D. Veynante[‡]

Large-eddy simulation (LES) provides space-filtered quantities to compare with measurements, which may have been obtained using a different filtering operation; hence, numerical and experimental results can be examined side-by-side in a time-averaged statistical sense only. Instantaneous, space-filtered and statistically time-averaged signals feature different characteristic length scales, which can be combined in dimensionless ratios. From a manufactured turbulent flame solution, the critical values of these ratios under which measured and computed variances (resolved plus subgrid scale) can be compared without resorting to additional residual terms are first determined. Then, it is shown that the difference in filter sizes imposes the knowledge of the magnitude of the scalar gradient, to accurately compare LES results against measurements. In premixed turbulent flames, scalar gradients are usually obtained from two-dimensional planar experimental diagnostics, for instance when measuring flame surface density. A transformation to evaluate three-dimensional flame surface density from two-dimensional measurements is discussed and evaluated from direct numerical simulation (DNS) of round and planar premixed jet flames.

1. Introduction

Scalar variances are widely used in large-eddy simulation (LES) of turbulent combustion (Pitsch 2006). These variances appear under different forms, time-averaged, filtered, resolved or at the subgrid scale level. Typically, a scalar signal (*e.g.* species mass fraction, enthalpy, temperature) is denoted $\varphi(\underline{x}, t)$ and $\langle \varphi \rangle(\underline{x})$ is the time average of this signal:

$$\langle \varphi \rangle(\underline{x}) = \lim_{T \rightarrow \infty} \frac{1}{T} \int_0^T \varphi(\underline{x}, t) dt \quad (1.1)$$

and $\overline{\varphi}(\underline{x}, t)$ is the space filtered average:

$$\overline{\varphi}(\underline{x}, t) = \int_{-\infty}^{+\infty} \varphi(\underline{x}', t) \mathcal{G}_\Delta(\underline{x} - \underline{x}') dx' \quad (1.2)$$

where \mathcal{G}_Δ is a space filter of characteristic scale Δ . Mass weighted filtered and time averaged quantities are also defined from these operators as: $\{\varphi\} = \langle \rho \varphi \rangle / \langle \rho \rangle$ and $\tilde{\varphi} =$

[†] LMFN, CORIA - CNRS, Institut National des Sciences Appliquées de Rouen, France

[‡] EM2C - CNRS, Ecole Centrale Paris, France

$\overline{\rho\varphi}/\overline{\rho}$. The three signals $\varphi(\underline{x}, t)$, $\{\varphi\}(\underline{x})$ and $\tilde{\varphi}(\underline{x}, t)$ have three characteristic thicknesses and length scales δ_L , δ_T and δ_Δ , respectively. In LES, $\delta_L < \delta_\Delta \approx \Delta < \delta_T$.

From their definitions, filtering and averaging operators commute; then whatever above length scales $\overline{\langle\varphi\rangle} = \langle\tilde{\varphi}\rangle$. Moreover, for $\Delta \ll \delta_T$ the time averaged signal does not evolve much at the LES scales and $\langle\varphi\rangle$ is left unchanged by the filtering operation: $\overline{\langle\varphi\rangle} \approx \langle\varphi\rangle$. Combining the commutation of operators and the condition $\Delta \ll \delta_T$, the relation $\langle\varphi\rangle \approx \langle\tilde{\varphi}\rangle$ is obtained (Veynante & Knikker 2006). This paper discusses the interplay between these relations and scalar variance measurements, along with implications regarding the estimation of 3-D flame surface density from 2-D measurements.

2. Variance decomposition: Resolved, subgrid scale (SGS) and residual parts

2.1. Definitions

In LES of real combustion systems (Boileau *et al.* 2008), the asymptotic condition $\Delta \ll \delta_T$ is not always verified and non-negligible residual terms r_ρ , $r_{\rho\varphi}$ and $r_{\rho\varphi^2}$ appear which may be defined so that:

$$\langle\rho\rangle = \langle\tilde{\rho}\rangle + r_\rho \quad (2.1)$$

$$\langle\rho\varphi\rangle = \langle\tilde{\rho}\tilde{\varphi}\rangle + r_{\rho\varphi} \quad (2.2)$$

$$\langle\rho\varphi^2\rangle = \langle\tilde{\rho}\tilde{\varphi}^2\rangle + r_{\rho\varphi^2} \quad (2.3)$$

then, φ_v , the time-averaged variance may be written:

$$\varphi_v = \{\varphi^2\} - \{\varphi\}^2 = \frac{\langle\tilde{\rho}\tilde{\varphi}^2\rangle}{\langle\tilde{\rho}\rangle} - \left(\frac{\langle\tilde{\rho}\tilde{\varphi}\rangle}{\langle\tilde{\rho}\rangle}\right)^2 + R_{\rho\varphi^2} - R_{\tilde{\rho}\tilde{\varphi}} \quad (2.4)$$

with

$$R_{\rho\varphi^2} = \frac{\langle\tilde{\rho}\rangle r_{\rho\varphi^2} - \langle\overline{\rho\varphi^2}\rangle r_\rho}{\langle\tilde{\rho}\rangle (\langle\tilde{\rho}\rangle + r_\rho)} ; R_{\tilde{\rho}\tilde{\varphi}} = \frac{\langle\tilde{\rho}\rangle^2 r_{\rho\varphi} (r_{\rho\varphi} + 2\langle\tilde{\rho}\tilde{\varphi}\rangle) - \langle\tilde{\rho}\tilde{\varphi}\rangle^2 r_\rho (r_\rho + 2\langle\tilde{\rho}\rangle)}{\langle\tilde{\rho}\rangle^2 (\langle\tilde{\rho}\rangle^2 + r_\rho^2 + 2\langle\tilde{\rho}\rangle r_\rho)} \quad (2.5)$$

Introducing $\langle\tilde{\rho}\tilde{\varphi}^2\rangle$ into Eq. (2.4) leads to:

$$\varphi_v = \{\varphi^2\} - \{\varphi\}^2 = \underbrace{\frac{\langle\tilde{\rho}\tilde{\varphi}^2\rangle}{\langle\tilde{\rho}\rangle} - \left(\frac{\langle\tilde{\rho}\tilde{\varphi}\rangle}{\langle\tilde{\rho}\rangle}\right)^2}_{T_R: \text{Resolved part}} + \overbrace{\frac{\langle\tilde{\rho}(\tilde{\varphi}^2 - \tilde{\varphi}^2)\rangle}{\langle\tilde{\rho}\rangle}}^{T_{SGS}: \text{SGS part}} + R_v \quad (2.6)$$

This last relation provides the exact decomposition of the total variance φ_v into T_R and T_{SGS} , resolved and SGS parts, with an additional residual term $R_v = R_{\rho\varphi^2} - R_{\tilde{\rho}\tilde{\varphi}}$. T_R is the variance of the filtered field and T_{SGS} the mean of the SGS variance. The constant density case is easily recovered by setting $r_\rho = 0$ and $\rho = cst$ in the above equations.

LES meshes and filters are so that $\Delta = \alpha\delta_L = \beta\delta_T$ with $\alpha > 1$ and $\beta < 1$. The SGS part decreases when $\alpha \rightarrow 1$ and would vanish when $\alpha < 1$, as in DNS. The resolved part is negligible when $\beta \rightarrow 1$, while the contribution of the residual term R_v decreases with β . For a given reactive front, for $\beta > \beta_R$, the residual term R_v cannot be expected to be small compared to other contributions, where β_R is a critical value to be determined. When comparing LES variances obtained from their resolved and SGS parts, the mesh

must therefore verify $\beta = \Delta/\delta_T < \beta_R$, which also implies $\alpha = (\Delta/\delta_L) < \beta_R(\delta_T/\delta_L)$. The value of β_R is now evaluated for a premixed turbulent flame brush in the flamelet regime.

2.2. Manufactured premixed flame solution and LES meshes optimization

Obviously, the analysis of the three terms entering Eq. (2.6) can be performed only in turbulent flame solutions where a sufficiently large number of scales is present. With actual computer capabilities, DNS does not offer the possibility of covering a sufficiently large range of scales to fully investigate these energy-budget questions; a manufactured solution is therefore needed. A synthetic turbulent field is thus manufactured from a large number of laminar flamelets of thickness δ_L , which are randomly distributed to build a mean flame brush. Typically, this solution mimics DNS performed in the flamelet regime; flamelet profiles are transported by turbulence without modification of their internal structure.

The instantaneous progress variable is defined as:

$$c(x, t) = F_L(x - x_L(t)) \tag{2.7}$$

$$x_L(t) = x_o + \xi(t)\kappa(t)\delta_T \tag{2.8}$$

where $F_L(x)$ is the single flamelet distribution obtained from the solution of a methane-air stoichiometric premixed flame computed with detailed GRI chemistry (Smith *et al.* 1999). The progress variable ($c = 0$ in fresh gases and $c = 1$ in fully burnt products) is defined from $Y_c = Y_{CO} + Y_{CO_2}$, normalized by its value in equilibrium products. x_o is the position of the mean flame brush, $x_L(t)$ the position of the flamelet within the turbulent flame brush at time t , $\xi(t)$ is a uniformly distributed random number taking the values ± 1 and $\kappa(t)$ a random Gaussian distribution. The average progress variable profiles of the manufactured solution may be written:

$$\langle c \rangle (x) = \int_{-\infty}^x \overline{P}(x_L^*) dx_L^* \tag{2.9}$$

with $\overline{P}(x_L^*)$ the probability density function (pdf) of the flamelets positions. The manufactured solution is operated over a duration $t = T$, so that $\overline{P}(x_L^*)$ is statistically converged.

The terms of Eq. (2.6) extracted from $c(x, t)$ for various values of α and β are displayed in Fig. 1. As expected, T_R , the resolved part decreases when $\beta = \Delta/\delta_T$ increases, while the SGS contribution, T_{SGS} , becomes greater; the decay of T_R versus β is almost linear. The budget $(T_R + T_{SGS})/c_v$ does not sum to unity, until the always-negative residual part R_v/c_v is added. The sensitivity to $\alpha = \Delta/\delta_L$ is weak for $\beta < 0.2$ and stays moderate for T_{SGS} . For a given β , the resolved part (resp. the SGS part) decreases (resp. increases) when α increases. For a scalar variance budget closed at 1% with the addition of resolved and SGS parts ($R_v/c_v < 0.01$), then β must respect $\beta < \beta_R \approx 0.06$ (Fig. 1), corresponding to $\delta_T/\Delta > 16$.

In LES of a reactive front of characteristic size δ_L , the scalar energy budget can then be completed without resorting to additional residual terms for

$$\alpha_R = \Delta/\delta_L < \beta_R(\delta_T/\delta_L) \tag{2.10}$$

In a typical premixed swirling flow burner (Galpin *et al.* 2008), $\delta_T \approx 0.01$ m and $\delta_L \approx 0.1$ mm, leading to $\alpha_R \approx 6$. This criterion can be used to optimize LES meshes; after a first

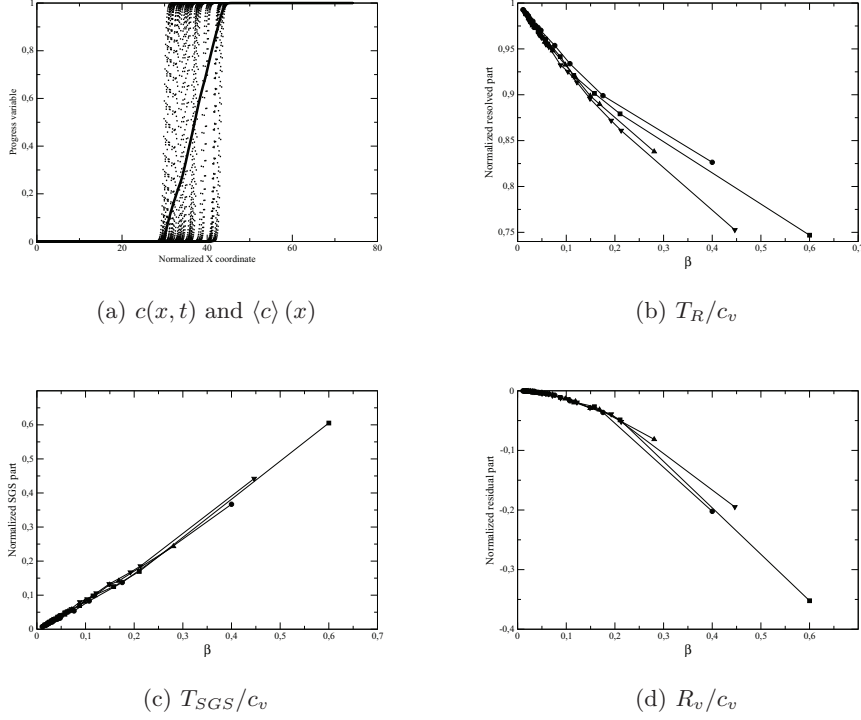


FIGURE 1. (a) - dots: $c(x, t)$ given by Eq. (2.7) for $\delta_T/\delta_L = \alpha/\beta = 12$; line: $\langle c \rangle(x)$. (b) - (c) - (d): Normalized three terms of Eq. (2.6) vs $\beta = \Delta/\delta_T$, normalization is done using c_v . Line with Circle: $\alpha = \Delta/\delta_L = 2$; Square: $\alpha = 3$; Triangle up: $\alpha = 4$; Triangle down: $\alpha = 5$.

simulation performed on a given mesh to estimate δ_T , the grid can be refined at locations where the criterion defined by Eq. (2.10) is not fulfilled.

2.3. Scaling of SGS variance

The SGS variance is usually approximated from mixing modeling closures, mostly derived for non-reactive scalars (Pierce & Moin 2004, Domingo *et al.* 2005), under a production-dissipation hypothesis:

$$T_{SGS} = \frac{\langle \bar{\rho}(\tilde{c}^2 - \tilde{c}^2) \rangle}{\langle \bar{\rho} \rangle} \propto \frac{\langle \bar{\rho}(\Delta|\nabla\tilde{c}|)^2 \rangle}{\langle \bar{\rho} \rangle}. \quad (2.11)$$

Another approach may be followed (Veynante & Knikker 2006) where the flame is supposed as infinitely thin:

$$T_{SGS} \propto \frac{\langle \bar{\rho}\tilde{c}(1-\tilde{c}) \rangle}{\langle \bar{\rho} \rangle} \quad \text{and} \quad \frac{\langle \bar{\rho}|\nabla\tilde{c}| \rangle}{\langle \bar{\rho} \rangle} \propto \frac{\langle \bar{\rho}\tilde{c}(1-\tilde{c}) \rangle}{\Delta \langle \bar{\rho} \rangle} \quad (2.12)$$

leading to:

$$T_{SGS} \propto \frac{\langle \bar{\rho}\Delta|\nabla\tilde{c}| \rangle}{\langle \bar{\rho} \rangle}. \quad (2.13)$$

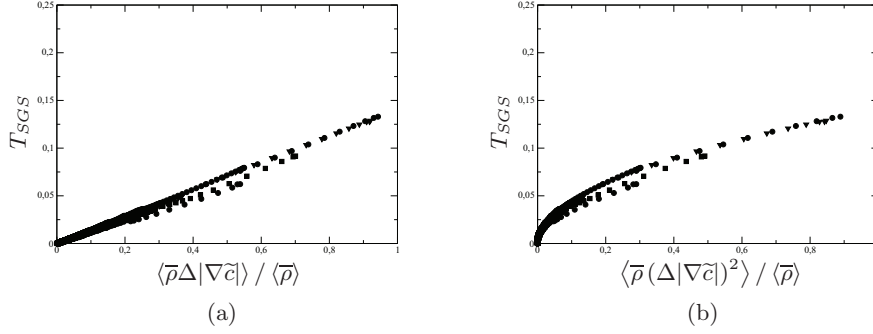


FIGURE 2. T_{SGS} Eq. (2.6) vs (a): $\langle \bar{\rho} \Delta |\nabla \tilde{c}| \rangle / \langle \bar{\rho} \rangle$; (b): $\langle \bar{\rho} (\Delta |\nabla \tilde{c}|)^2 \rangle / \langle \bar{\rho} \rangle$. Circle: $\alpha = \Delta / \delta_L = 2$; Square: $\alpha = 3$, Triangle up: $\alpha = 4$; Triangle down: $\alpha = 5$.

Analyzing local flame front measurements to estimate SGS variances, Veynante & Knikker (2006) found that the best approximation of the SGS variance was obtained with the linear correlation (Eq. (2.13)). Figure 2(a) shows that the manufactured solution reproduces this result, T_{SGS} scales linearly with the filter size and with the gradient of the filtered field, but not with the square of these quantities. For $\beta > \beta_R$, no scaling was found when the residual term R_v is added to the SGS variance.

Scalar measurements, for instance using Raman or PLIF, are obtained from filtering at a level Δ_* , which may differ from the LES filter Δ . The total variance (lhs of Eq. (2.6)) is decomposed for both filters into resolved and SGS parts; using Eq. (2.13), the resolved parts are related according to:

$$\underbrace{\frac{\langle \bar{\rho}_* \tilde{\varphi}_*^2 \rangle}{\langle \bar{\rho}_* \rangle}}_{\text{Measured}} - \left(\frac{\langle \bar{\rho}_* \tilde{\varphi}_* \rangle}{\langle \bar{\rho}_* \rangle} \right)^2 = \underbrace{\frac{\langle \bar{\rho} \tilde{\varphi}^2 \rangle}{\langle \bar{\rho} \rangle}}_{\text{LES}} - \left(\frac{\langle \bar{\rho} \tilde{\varphi} \rangle}{\langle \bar{\rho} \rangle} \right)^2 + C_v \left(1 - \frac{\Delta_*}{\Delta} \frac{\langle \bar{\rho}_* |\nabla \tilde{\varphi}_*| \rangle / \langle \bar{\rho}_* \rangle}{\langle \bar{\rho} |\nabla \tilde{\varphi}| \rangle / \langle \bar{\rho} \rangle} \right) \quad (2.14)$$

where the subscript $*$ indicates measured quantities. This last relation suggests that the knowledge of the gradient is useful when comparing measured and LES variances.

3. Evaluation of 3-D scalar gradients and flame surface density from 2-D measurements

3.1. Background

In premixed turbulent combustion, the gradient of $c(\underline{x}, t)$, the progress variable, is directly related to the flame surface density $\Sigma(c^*; \underline{x}, t) = \left(|\nabla c| |c^* \right) \bar{P}(c^*; \underline{x}, t)$, where $\bar{P}(c^*; \underline{x}, t)$ is the probability density function of c and $\left(|\nabla c| |c^* \right)$ the conditional mean value of the gradient for $c = c^*$, the c -value used to locate the flame surface (Pope 1989; Vervisch *et al.* 1995). Integrating overall surfaces leads to (Veynante & Vervisch 2002):

$$\int_0^1 \Sigma(c^*; \underline{x}, t) dc^* = \int_0^1 \left(|\nabla c| |c^* \right) \bar{P}(c^*; \underline{x}, t) dc^* = |\nabla \bar{c}| = \Xi |\nabla \bar{c}| \quad (3.1)$$

with Ξ the wrinkling factor of the turbulent flame; therefore the knowledge of the flame surface also provides information on gradients, useful in Eq. (2.14).

Flame surface density Σ measures the available flame surface per unit volume and its modeling is one of the key approaches to express reaction rates in RANS or LES (Poinsot & Veynante 2005). The mean (or filtered) reaction rate of a species k is written: $\bar{\omega}_k = \langle \dot{\Omega}_k \rangle_s \Sigma$, where $\langle \dot{\Omega}_k \rangle_s$ is the surface averaged reaction rate of the k -species per unit of flame area, generally estimated from laminar flame studies under flamelet assumptions. The flame surface density may be determined either from algebraic expressions (Bray *et al.* 1989; Boger *et al.* 1998) or by solving a balance equation (Veynante & Vervisch 2002; Hawkes & Cant 2000). Unfortunately, well-resolved instantaneous flame front 3-D visualizations are not yet available and the experimental determination of flame surface densities, either from planar laser tomography (Veynante *et al.* 1996; Lachaux *et al.* 2005) or planar laser-induced fluorescence measurements (Knikker *et al.* 2002), requires the assumption of a 2-D instantaneous flow (*e.g.* the instantaneous flame front is not wrinkled in the direction normal to the measuring plane).

The objective of this section is to investigate, from DNS, the uncertainties linked to this assumption and to explore whether the actual flame surface density Σ may be inferred from 2-D measurements. Note that similar attempts have been conducted to determine scalar dissipation rate distributions from two-dimensional measurements (Dahm & Buch 1989; Hawkes *et al.* 2009). However, the approach proposed here is quite different as we do not attempt to directly estimate the flame surface density distribution.

3.2. DNS of a Bunsen flame

DNS of a turbulent Bunsen flame was performed using the SiTCOM code, a CNRS-CORIA MPI parallelized, fully compressible and explicit Finite Volume flow solver based on cartesian grids. This solver approximates the convective terms resorting to the fourth-order centered skew-symmetric-like scheme (Ducros *et al.*, 2000) and the diffusive terms with a fourth-order centered scheme. Time integration is performed using the third-order Runge-Kutta scheme of Gottlieb & Shu (1998). All the boundary conditions are enforced using the 3D-NSCBC approach (Lodato *et al.*, 2008), which has been modified in order to properly account for the chemical source terms, as discussed below.

Assuming that the equivalence ratio of the mixture is lean (*e.g.* there is an excess of air so that the combustion weakly modifies the oxidizer mass fraction), the progress variable and energy source terms $\dot{\omega}_c$ and $\dot{\omega}_e$ relevant to a single-step chemistry may be written:

$$\dot{\omega}_c = \rho K (1 - c) \exp\left(-\frac{T_{Ac}}{T}\right), \quad \text{and} \quad \dot{\omega}_e = c_p T_0 \left(\frac{\alpha_e}{1 - \alpha_e}\right) \dot{\omega}_c, \quad (3.2)$$

where usual notations are adopted; K is the pre-exponential factor, T_{Ac} the activation temperature and $\alpha_e = (T_b - T_0)/T_b$ the heat release parameter, which may be related to T_{Ac} by the Zeldovitch number $\beta_e = \alpha_e T_{Ac}/T_b$. All the results presented were obtained fixing $\alpha_e = 0.8$ and $\beta_e = 8$.

To better control the behavior of the acoustic-sensitive boundary conditions under the presence of heat release, the chemical source terms are accounted for in the computation of characteristic incoming waves (Yoo & Im, 2007). Source terms, in fact, can be treated in analogy to what is done with transverse terms (in-plane convection and pressure gradient, Lodato *et al.*, 2008). This specific treatment of acoustic boundary conditions allows for the reactive front to cross any boundaries of the computational domain.

Two different flow configurations have been computed: (a) a $Re_D = 2000$ round flame and (b) a $Re_D = 4500$ slot flame (Re_D computed on the bulk velocity U_b). The former

Re_D	D mm	$L_x \times L_y \times L_z$ -	U_b m/s	η μm	h/η min-max	l_t/D -	S_L m/s	u'/S_L -	l_t/δ_l -	Nodes -	Cores (CPUs)
2000	0.5	$4D \times 2D \times 2D$	63.74	2.2	1.2-6.4	0.04	1.7	11.9	2.1	8.5M	2048
4500	1.0	$3D \times 3D \times 1.3D$	71.71	2.4	1.4-10.8	0.025	1.4	16.4	2.2	91M	4096

TABLE 1. Premixed turbulent flame DNS parameters.

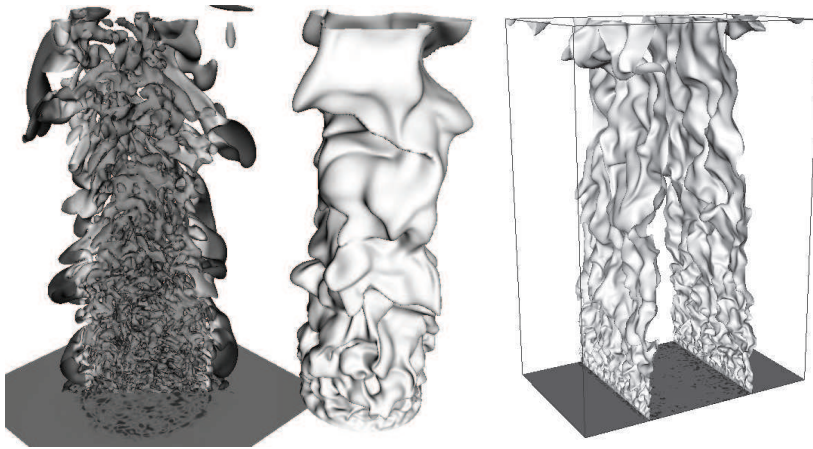


FIGURE 3. Left: $Re_D = 2000$ round jet flame, Q-criterion and flame surface. Right: $Re_D = 4000$ slot burner flame, flame surface.

was computed using subsonic non-reflecting inlet condition and subsonic non-reflecting outflows on all the other five boundaries, the latter had identical boundary types, except in the spanwise direction where periodic conditions were enforced. In both cases, turbulence was promoted by injecting a correlated random noise (Klein *et al.*, 2003) at the inlet, with correlation length l_t and intensity u' .

Grid spacing has been chosen in order to correctly resolve all the relevant scales of turbulence, as well as the flame thickness. With regard to the first point, the Kolmogorov length-scale η has been evaluated from the classical scaling $\eta \sim \ell Re_t^{-3/4}$, $\ell \sim 0.1D$ being an estimation of the integral length-scale, $Re_t \sim u'\ell/\nu$ and $u'^2 \sim 0.1U_b^2$, estimations checked from results. As can be seen in Table 1, grid spacing h is of the order of η in regions where turbulence develops, and the maximum values are attained far from the shear layers, where velocity fluctuations do not exist.

With regard to the flame resolution, 1-D preliminary tests have revealed that a good estimation of the maximum grid spacing h_{\max} can be obtained from the laminar flame speed S_L and the cinematic viscosity ν as $h_{\max} \propto 0.3\nu/S_L$. This criterion, actually, fixes the maximum laminar flame speed that can be resolved on a given computational grid; S_L was set accordingly for both simulations. The main parameters for the two DNS are summarized in Table 1.

3.3. Basic geometrical flame properties

For clarity, the following derivations are conducted for a statistically 2-D turbulent flame in Cartesian coordinates. The proposed relations are easily recast in terms of cylindrical coordinates, considering a statistically axisymmetrical turbulent flame, as observed in the DNS round-jet flame. Let x denote the downstream direction and (x, y) the measuring plane, for which Mie diffusion or laser-induced fluorescence instantaneous flame front visualizations are available. No measurements are conducted along the transverse direction z . In the following, θ is the angle of the projection, in the measuring plane, of the unit vector \mathbf{n} normal to the instantaneous flame front with the transverse direction y , while ϕ measures the angle between \mathbf{n} and the measuring plane (x, y) , as shown in Fig. 4(a). θ is known from measurements and $-\pi \leq \theta \leq +\pi$. For instantaneous flame front parallel to the downstream direction x , $\theta = 0$. The off-measuring plane angle ϕ is unknown and $-\pi/2 \leq \phi \leq +\pi/2$. For instantaneous 2-D flame front, $\phi = 0$.

According to these notations, the unit vector normal to the flame front in the (x, y) -plane and in the 3-D field are respectively:

$$\mathbf{n}_{(x,y)} = (\sin \theta, \cos \theta, 0) \quad \text{and} \quad \mathbf{n} = (\sin \theta \cos \phi, \cos \theta \cos \phi, \sin \phi) \quad (3.3)$$

The density of the isosurface $c = c^*$, Σ , and the corresponding value extracted from 2-D measurements in the (x, y) plane, $\Sigma_{(x,y)}$, are given by Pope (1988):

$$\Sigma = \left(\overline{|\nabla c|} \mid c^* \right) P(c^*) \quad (3.4)$$

$$\Sigma_{(x,y)} = \left(\overline{|\nabla c|_{(x,y)}} \mid c^* \right) P(c^*) . \quad (3.5)$$

the subscript (x, y) denotes 2-D measurements in the (x, y) -plane. Then:

$$\Sigma_{(x,y)} = \left(\overline{\cos \phi} \overline{|\nabla c|} \mid c^* \right) P(c^*) = \langle \cos \phi \rangle_s \Sigma \quad (3.6)$$

Two- and three-dimensional flame surface densities are thus linked through $\langle \cos \phi \rangle_s$, the surface averaged value of $\cos \phi$. For $\phi = 0$, both flame surface densities are equal. Two- and three dimensional mean values of the scalar dissipation rate, proportional to $|\nabla c|^2$ are related through mean values of $\cos^2 \phi$. Dahm & Buch (1989) and Hawkes *et al.* (2009) then propose to estimate the distribution of the scalar dissipation rate from the probability density function of $\cos^2 \phi$; an equivalent approach for flame surface density will be investigated in the future but is not retained here.

Figure 4(b) displays histograms of angles θ and ϕ as extracted from the DNS database. As expected, their mean values are close to zero because of the axi-symmetry of the mean flowfield. They have similar variances, meaning that flame front movements around the y -direction in the plane (x, y) (θ angles) are comparable to off-plane movements (ϕ angles). Also, θ and ϕ are found to be poorly correlated (not shown here) and may be assumed statistically independent.

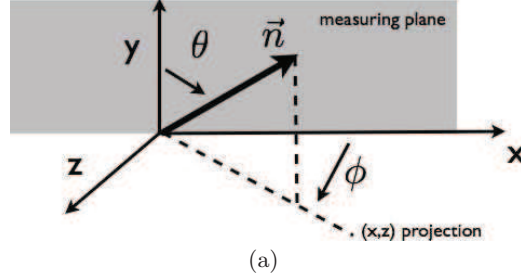
The vector \mathbf{n} normal to the instantaneous flame front is a unit vector:

$$\langle n_x n_x \rangle_s + \langle n_y n_y \rangle_s + \langle n_z n_z \rangle_s = 1 . \quad (3.7)$$

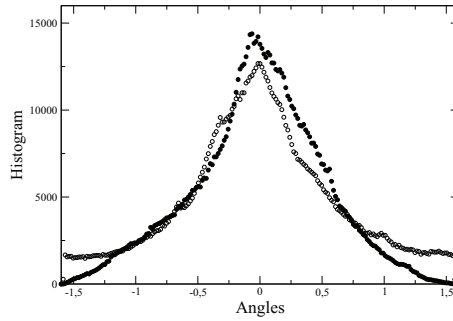
where n_i denotes the component along the i -th direction. Decoupling each component into mean and fluctuation, $n_i = \langle n_i \rangle_s + m_i$, with $\langle m_i \rangle_s = 0$ gives:

$$\langle n_x \rangle_s \langle n_x \rangle_s + \langle m_x m_x \rangle_s + \langle n_y \rangle_s \langle n_y \rangle_s + \langle m_y m_y \rangle_s + \langle n_z \rangle_s \langle n_z \rangle_s + \langle m_z m_z \rangle_s = 1 \quad (3.8)$$

Three additional assumptions are now introduced:



(a)



(b)

FIGURE 4. (a): x is the downstream direction, instantaneous flame front visualizations are performed in the (x, y) plane. θ (respectively ϕ) measures the angle of the projection, in the measuring plane, of the unit vector \mathbf{n} normal to the instantaneous flame front with the y -direction (respectively off the measuring plane). (b): Histograms of angles θ (empty circles) and ϕ (filled circles) from DNS (round-jet flame, points in the flame front $0 < c < 1$, $|\nabla c| > 0$).

(a) In mean, the flow is 2-D (or axi-symmetric), hence $\langle n_z \rangle_s = 0$.

(b) According to Eq. (3.3), $n_x = (\cos \phi)n_{x(x,y)}$ and $n_y = (\cos \phi)n_{y(x,y)}$, where $n_{i(x,y)}$ are the components of $\mathbf{n}_{(x,y)}$, the unit vector normal to the flame front in the (x, y) -plane. When angles θ and ϕ are statistically independent, these relations give $\langle n_i \rangle_s \approx \langle \cos \phi \rangle_s \langle n_{i(x,y)} \rangle_s^{2D}$ and suggest the introduction of $\langle m_i m_i \rangle_s \approx \langle \cos \phi \rangle_s^2 \langle m_{i(x,y)} m_{i(x,y)} \rangle_s^{2D}$, where $i = x, y$ and the suffix $2D$ denotes surface averages in the (x, y) plane.

(c) The fluctuations of the normal vector in the z -direction, $\langle m_z m_z \rangle_s$, remain unknown. Assuming similar statistics for θ and ϕ angles provides an estimation of this quantity from the fluctuations of the normal vector in the plane (x, y) around the y -direction:

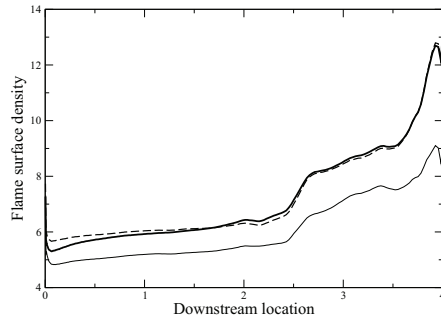
$$\langle m_z m_z \rangle_s \approx \langle m_y m_y \rangle_s \approx \langle \cos \phi \rangle_s^2 \langle m_{y(x,y)} m_{y(x,y)} \rangle_s^{2D} \quad (3.9)$$

Eq. (3.8) then becomes:

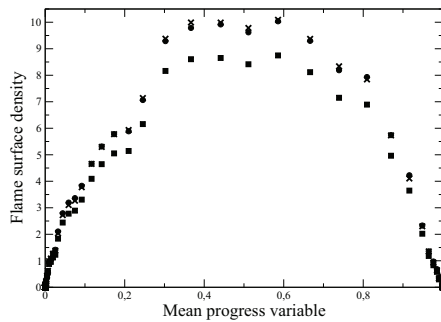
$$\langle \cos \phi \rangle_s^2 \left(1 + \langle m_{y(x,y)} m_{y(x,y)} \rangle_s^{2D} \right) = 1 \quad (3.10)$$

leading to, using Eq. (3.6):

$$\Sigma \approx \left(\sqrt{1 + \langle m_{y(x,y)} m_{y(x,y)} \rangle_s^{2D}} \right) \Sigma_{(x,y)} \quad (3.11)$$



(a)



(b)

FIGURE 5. Flame surface by Eq. (3.12). (a): vs x , normalized bunsen flame downstream location. (b): transverse profile vs mean progress variable. Bold line (a) and Circle (b): DNS 3-D- Σ ; Thin line (a) and Square (b): 2-D measurements ($\Sigma_{(x,y)}$); dashed line (a) and cross (b): 3-D reconstruction from Eq. (3.11).

providing an estimation of the 3-D flame surface density from 2D measurements performed in the (x, y) -plane.

3.4. 3-D estimation against DNS results

Relation (3.11) is now investigated from the DNS data. Flame surface densities are extracted identifying the flame front with the isosurface $c^* = 0.88$, corresponding to the maximum value of the reaction rate. To increase the number of samples, all possible (x, y) -planes are considered, *e.g.* 2-D statistics are extracted from all planes containing the burner centerline (x -axis).

Figure 5(a) displays the evolution of the total flame surface along the burner centerline. This total surface depends on the downstream location and is defined as:

$$\Sigma_{tot}(x) = \int_{-\infty}^{+\infty} \int_{-\infty}^{+\infty} \Sigma \, dy \, dz \quad (3.12)$$

Two-dimensional measurements are found to underestimate the flame surface by about 16% while Eq. (3.11) recovers the true value with an error of about 0.3% on the total flame surface. This finding is confirmed in Fig. 5(b), showing transverse profiles of the flame surface density as a function of the progress variable c . Similar results are found with the slot burner configuration (not shown).

4. Conclusion

A manufactured turbulent premixed flame solution has been introduced to discuss a LES mesh criterion based on characteristic laminar flame and mean flame brush thicknesses. The scaling of scalar variance in terms of scalar gradient was also addressed with this synthetic solution and previous experimental observations recovered. The 3-D estimation of this scalar gradient from 2-D measurements was then addressed using both geometrical derivations and DNS results.

Acknowledgments

The authors have benefited from fruitful discussions with CTR Summer Program participants. Computing resources were provided by IDRIS-CNRS (<http://www.idris.fr/>) and CRIHAN (<http://www.crihan.fr/>).

REFERENCES

- BOGER, M., VEYNANTE, D., BOUGHANEM H. & TROUVÉ A. 1998 Direct numerical simulation analysis of flame surface density concept for large eddy simulation of turbulent premixed combustion. In *Twenty-seventh Symposium (International) on Combustion*, 917–925. Combust. Inst.
- BOILEAU, M., STAFFELBACH, G., CUENOT, B., POINSOT, T. & BÉRAT, C. 2008 LES of an ignition sequence in a gas turbine engine. *Combust. Flame* **154**(1/2): 2-22.
- BRAY, K.N.C., CHAMPION, M. & LIBBY., P. 1989 The interaction between turbulence and chemistry in premixed turbulent flames. In *Turbulent Reacting Flows*, R. Borghi and S. Murphy (Eds.), Vol. 40 of *Lecture Notes in Engineering*, pp. 541 – 563. Springer.
- DAHM, W. & BUCH, K. 1989 Lognormality of the scalar dissipation pdf in turbulent flows. *Phys. Fluids A1* **7**, 1290–1293.
- DOMINGO, P., VERVISCH, L., PAYET, S. & HAUGUEL, R. 2005 DNS of a premixed turbulent V-flame and LES of a ducted-flame using a FSD-PDF subgrid scale closure with FPI tabulated chemistry, *Combust. Flame* **143**(4) 566–586.
- DOMINGO, P., VERVISCH, L. & VEYNANTE, D. 2008 Large-Eddy Simulation of a lifted methane-air jet flame in a vitiated coflow, *Combust. Flame* **153**(3) 415–432.
- DUCROS, F., LAPORTE, F., SOULÈRES, T., GUINOT, V., MOINAT, P. & CARUELLE B. 2000 High-order fluxes for conservative skew-symmetric-like schemes in structured meshes: Application to compressible flows. *J. Comput. Phys.* **161**:114–139.
- GALPIN, J., NAUDIN, A., VERVISCH, L., ANGELBERGER, C., COLIN, O. & DOMINGO, P. 2008 *Combust. Flame* **155**(1):247–266.
- GOTTLIEB, S. & SHU, C. 1998 Total variation diminishing runge-kutta schemes. *Math. Comput.* **67**(221):73–85.

- HAWKES, E. & CANT, S. 2000 A flame surface density approach to large eddy simulation of premixed turbulent combustion. *Proc. Combust. Inst.* **28**:51–58.
- HAWKES, E., SANKARAN, J., CHEN, R., KAISER, S. & FRANCK, J. 2009 Analysis of lower-dimensional approximations to the scalar dissipation rate using direct numerical simulations of plane jet flames. *Proc. Combust. Inst. in press*.
- KLEIN, M., SADIKI, A. & JANICKA, J. 2003 A digital filter based generation of inflow data for spatially developing direct numerical or large eddy simulations. *J. Comput. Phys.* **186**:652–665.
- KNIKKER, R., VEYNANTE, D. & MENEVEAU, C. 2002 A priori testing of a similarity model for large eddy simulations of turbulent premixed combustion. *Proc. Combust. Inst.* **29**:2105–2111.
- LACHAUX, T., HALTER, F., CHAUVEAU, C., GOKALP, I. & SHEPHERD, I. 2005 Flame front analysis of high-pressure turbulent lean premixed methane–air flames. *Proc. Combust. Inst.* **30**:819–826.
- LODATO, G., DOMINGO, P. & VERVISCH, L. 2008 Three-dimensional boundary conditions for direct and large-eddy simulation of compressible viscous flows. *J. Comput. Phys.* **227**(10):5105–5143.
- PIERCE, C. & MOIN, P. 1999 A dynamic model for subgrid-scale variance and dissipation rate. *Phys. Fluids* **10**(12):3041–3044.
- PITSCH, H. 2006 Large-Eddy Simulation of turbulent combustion. *Ann. Rev. Fluid Mech.* **38**:453–482.
- POINSOT, T. & VEYNANTE, D. 2005 *Theoretical and Numerical Combustion* (Second ed.). Edwards Inc., Philadelphia, Penn.
- POPE, S. 1988 The evolution of surfaces in turbulence. *Int. J. Eng. Sci.* **26**(5):445–469.
- SMITH, G. P., GOLDEN, D. M., FRENKLACH, M., MORIARTY, N. W., EITENEER, B., GOLDENBERG, M., BOWMAN, C. T., HANSON, R. K., SONG, S., GARDINER, W., C., LISSANSKI, V., V, QIN, Z. 1999 <http://www.me.berkeley.edu/gri-mech/>.
- TATSUMI, S., MARTINELLI, L. & JAMESON, A. 1995 Flux-limited schemes for the compressible navier-stokes equations. *AIAA Journal* **33**(2):252–261.
- VERVISCH, L., BIDAUX, E., BRAY, K.N.C. & KOLLMANN W. 1995 Surface density function in premixed turbulent combustion modeling, similarities between probability density function and flame surface approaches, *Phys. Fluids* **7**(10):2496–2503.
- VEYNANTE, D. & KNIKKER, R. 2006 Comparison between LES results and experimental data in reacting flows. *J. Turbul.*, 7, DOI: 10.1088/1468-5248/5/1/037.
- VEYNANTE, D., PIANA, J., DUCLOS, J. & MARTEL, C. 1996. Experimental analysis of flame surface density model for premixed turbulent combustion. In *Twenty-sixth Symposium (International) on Combustion*, 413–420. Combust. Inst.
- VEYNANTE, D. & VERVISCH, L. 2002 Turbulent combustion modeling. *Proc. Energy and Comb. Science* **28**(3):193–301.
- YOO, C. & IM., H. 2007 Characteristic boundary conditions for simulations of compressible reacting flows with multi-dimensional, viscous and reaction effects. *Combust. Theor. Model.*, 11(2):259–286.

Appendices

The Lagrangian Averaging Operation

Let $f(\mathbf{x}, t)$ be the value of a generic quantity at position \mathbf{x} and time t , then its weighted average, backward in time, along the fluid particle path-line originating at \mathbf{x} , namely its Lagrangian average, may be obtained as the convolution integral

$$\phi(\mathbf{x}, t) = \int_{-\infty}^t f(\mathbf{z}(t'), t') W(t - t') dt', \quad (\text{A.1})$$

where $W(t)$ is the weighting function and $\mathbf{z}(t')$ defines the Lagrangian trajectory of the fluid particle at some earlier time t' [48],

$$\mathbf{z}(t') = \mathbf{x} - \int_{t'}^t \mathbf{u}(\mathbf{z}(t''), t'') dt''. \quad (\text{A.2})$$

In the case the weighting function is a decaying exponential function with characteristic time \mathbb{T} , Eq. (A.1) becomes:

$$\phi(\mathbf{x}, t) = \int_{-\infty}^t \frac{f(\mathbf{z}(t'), t')}{\mathbb{T}} \exp\left(-\frac{t - t'}{\mathbb{T}}\right) dt'. \quad (\text{A.3})$$

We want to show that, for any sufficiently regular (*i.e.* continuous and differentiable) function $f(\mathbf{x}, t)$, the above Lagrangian average is also solution of the following transport equation:

$$\frac{D\phi}{Dt} = \frac{1}{\mathbb{T}} [f(\mathbf{x}, t) - \phi(\mathbf{x}, t)]. \quad (\text{A.4})$$

In order to evaluate the material derivative $D\phi/Dt$, the fluid particle has to be followed along its path-line and the rate of change of the property ϕ needs to be measured, *i.e.* the following limit is evaluated between two close positions along the pathline:

$$\frac{D\phi}{Dt} = \lim_{dt \rightarrow 0} \frac{\phi(\mathbf{x} + d\mathbf{x}, t + dt) - \phi(\mathbf{x}, t)}{dt}, \quad (\text{A.5})$$

with the infinitesimal displacement $d\mathbf{x}$ lying along the Lagrangian trajectory. From Eq. (A.3) it is easily verified that

$$\phi(\mathbf{x} + d\mathbf{x}, t + dt) = \int_{-\infty}^{t+dt} \frac{f(\mathbf{z}(t'), t')}{\mathbb{T}} \exp\left(-\frac{t + dt - t'}{\mathbb{T}}\right) dt', \quad (\text{A.6})$$

which may be, more conveniently, written as:

$$\begin{aligned} \phi(\mathbf{x} + d\mathbf{x}, t + dt) &= \int_{-\infty}^{t+dt} \frac{f(\mathbf{z}(t'), t')}{\mathbb{T}} \exp\left(-\frac{t - t'}{\mathbb{T}}\right) dt' \\ &\quad + \int_{-\infty}^{t+dt} \frac{f(\mathbf{z}(t'), t')}{\mathbb{T}} \left[\exp\left(-\frac{t + dt - t'}{\mathbb{T}}\right) - \exp\left(-\frac{t - t'}{\mathbb{T}}\right) \right] dt'. \end{aligned} \quad (\text{A.7})$$

From the above relation and Eq. (A.3), the difference $\Delta\phi = \phi(\mathbf{x} + d\mathbf{x}, t + dt) - \phi(\mathbf{x}, t)$ reads:

$$\begin{aligned} \Delta\phi &= \int_{-\infty}^{t+dt} \frac{f(\mathbf{z}(t'), t')}{\mathbb{T}} \left[\exp\left(-\frac{t + dt - t'}{\mathbb{T}}\right) - \exp\left(-\frac{t - t'}{\mathbb{T}}\right) \right] dt' \\ &\quad + \int_t^{t+dt} \frac{f(\mathbf{z}(t'), t')}{\mathbb{T}} \exp\left(-\frac{t - t'}{\mathbb{T}}\right) dt' \end{aligned} \quad (\text{A.8})$$

and, splitting the first integral between $(-\infty : t]$ and $[t : t + dt]$, the ratio $\Delta\phi/dt$ becomes

$$\begin{aligned} \frac{\Delta\phi}{dt} &= \frac{1}{dt} \int_{-\infty}^t \frac{f(\mathbf{z}(t'), t')}{\mathbb{T}} \left[\exp\left(-\frac{t + dt - t'}{\mathbb{T}}\right) - \exp\left(-\frac{t - t'}{\mathbb{T}}\right) \right] dt' \\ &\quad + \frac{1}{dt} \int_t^{t+dt} \frac{f(\mathbf{z}(t'), t')}{\mathbb{T}} \left[\exp\left(-\frac{t + dt - t'}{\mathbb{T}}\right) - \exp\left(-\frac{t - t'}{\mathbb{T}}\right) \right] dt' \\ &\quad + \frac{1}{dt} \int_t^{t+dt} \frac{f(\mathbf{z}(t'), t')}{\mathbb{T}} \exp\left(-\frac{t - t'}{\mathbb{T}}\right) dt'. \end{aligned} \quad (\text{A.9})$$

Assuming that the integrand in the above equation are continuous in $[t : t + dt]$ and differentiable in $(t : t + dt)$, we may invoke the Mean-Value Theorem and say that there exists a $t^* \in (t : t + dt)$ such that

$$\frac{1}{dt} \int_t^{t+dt} g(t') dt' = g(t^*), \quad (\text{A.10})$$

therefore, the second and third integrals become respectively:

$$\frac{f(\mathbf{z}(t_1^*), t_1^*)}{\mathbb{T}} \left[\exp\left(-\frac{t + dt - t_1^*}{\mathbb{T}}\right) - \exp\left(-\frac{t - t_1^*}{\mathbb{T}}\right) \right], \quad (\text{A.11})$$

$$\frac{f(\mathbf{z}(t_2^*), t_2^*)}{\mathbb{T}} \exp\left(-\frac{t - t_2^*}{\mathbb{T}}\right), \quad (\text{A.12})$$

where t_1^* and t_2^* are some suitable instants in $(t : t + dt)$. In the limit for $dt \rightarrow 0$, both t_1^* and t_2^* tend to t and since, by definition, $\mathbf{z}(t') = \mathbf{x}$ for $t' = t$ (cf. Eq. (A.2)), the above quantities assume the following values:

$$\lim_{dt \rightarrow 0} \left\{ \frac{f(\mathbf{z}(t_1^*), t_1^*)}{\mathbb{T}} \left[\exp\left(-\frac{t + dt - t_1^*}{\mathbb{T}}\right) - \exp\left(-\frac{t - t_1^*}{\mathbb{T}}\right) \right] \right\} = 0, \quad (\text{A.13})$$

$$\lim_{dt \rightarrow 0} \left[\frac{f(\mathbf{z}(t_2^*), t_2^*)}{\mathbb{T}} \exp\left(-\frac{t - t_2^*}{\mathbb{T}}\right) \right] = \frac{f(\mathbf{x}, t)}{\mathbb{T}}. \quad (\text{A.14})$$

Taking the limit for $dt \rightarrow 0$ of Eq. (A.9) and using Eq. (A.5), as well as the above two identities, the material derivative of ϕ then becomes:

$$\frac{D\phi}{Dt} = \lim_{dt \rightarrow 0} \frac{1}{dt} \int_{-\infty}^t \frac{f(\mathbf{z}(t'), t')}{\mathbb{T}} \left[\exp\left(-\frac{t+dt-t'}{\mathbb{T}}\right) - \exp\left(-\frac{t-t'}{\mathbb{T}}\right) \right] dt' + \frac{f(\mathbf{x}, t)}{\mathbb{T}}. \quad (\text{A.15})$$

Since, in the above equation, dt is not present in the integral limits anymore, the limit operator can be moved inside the integral sign. Moreover, observing that the term in square brackets represents nothing more than a infinitesimal increment in the exponential function (*i.e.* its time derivative is being taken), the following identity holds true,

$$\lim_{dt \rightarrow 0} \frac{1}{dt} \left[\exp\left(-\frac{t+dt-t'}{\mathbb{T}}\right) - \exp\left(-\frac{t-t'}{\mathbb{T}}\right) \right] = -\frac{1}{\mathbb{T}} \exp\left(-\frac{t-t'}{\mathbb{T}}\right), \quad (\text{A.16})$$

and Eq. (A.15) is rewritten as

$$\frac{D\phi}{Dt} = -\frac{1}{\mathbb{T}} \int_{-\infty}^t \frac{f(\mathbf{z}(t'), t')}{\mathbb{T}} \exp\left(-\frac{t-t'}{\mathbb{T}}\right) dt' + \frac{f(\mathbf{x}, t)}{\mathbb{T}}, \quad (\text{A.17})$$

which, making use of Eq. (A.3), finally proves that the Lagrangian averaging operator $\phi(\mathbf{x}, t)$, of a function $f(\mathbf{x}, t)$, with exponential weighting function may be obtained as solution of Eq. (A.4).

Bibliography

- [1] Akhavan, R., Ansari, A., Kang, S. and Mangiavacchi, N. (2000). Subgrid-scale interactions in a numerically simulated planar turbulent jet and implications for modeling. *Journal of Fluid Mechanics*, **vol. 408**: pp. 83–120.
- [2] Anderson, R. and Meneveau, C. (1999). Effects of the similarity model in finite-difference LES of isotropic turbulence using a lagrangian dynamic mixed model. *Flow, Turbulence and Combustion*, **vol. 62(3)**: pp. 201–225.
- [3] Bardina, J., Ferziger, J. and Reynolds, W. (1980). Improved subgrid-scale models for large-eddy simulation. *AIAA Paper*, **vol. 1980-1357**. Fluid and Plasma Dynamics Conference, 13th, Snowmass, Colo., July 14-16, 1980, 10 p.
- [4] Bardina, J., Ferziger, J. and Reynolds, W. (1984). Improved turbulence models based on LES of homogeneous incompressible turbulent flows. *Report TF-19*, Thermosciences Division, Dept. Mechanical Engineering, Stanford University.
- [5] Baum, M., Poinso, T. and Thévenin, D. (1994). Accurate boundary conditions for multi-component reactive flows. *Journal of Computational Physics*, **vol. 116(2)**: pp. 247–261.
- [6] Bogey, C. and Bailly, C. (2007). An analysis of the corrections between the turbulent flow and the sound pressure fields of subsonic jets. *Journal of Fluid Mechanics*, **vol. 583**: pp. 71–97.
- [7] Colonius, T., Lele, S. and Moin, P. (1991). The free compressible viscous vortex. *Journal of Fluid Mechanics*, **vol. 230**: pp. 45–73.
- [8] Cooper, D., Jackson, D., Launder, B. and Liao, G. (1993). Impinging jet studies for turbulence model assessment—I. flow-field experiments. *International Journal of Heat and Mass Transfer*, **vol. 36(10)**: pp. 2675–2684.
- [9] Davidson, P., *Turbulence: An Introduction for Scientists and Engineers* (Oxford University Press, 2004).
- [10] Deardorff, J. (2006). A numerical study of three-dimensional turbulent channel flow at large Reynolds numbers. *Journal of Fluid Mechanics*, **vol. 41(2)**: pp. 453–480.
- [11] Domingo, P., Vervisch, L. and Bray, K. (2002). Partially premixed flamelets in LES of nonpremixed turbulent combustion. *Combustion Theory and Modelling*, **vol. 6(4)**: pp. 529–551.

- [12] Domingo, P., Vervisch, L., Payet, S. and Hauguel, R. (2005). DNS of a premixed turbulent V flame and LES of a ducted flame using a FSD-PDF subgrid scale closure with FPI-tabulated chemistry. *Combustion and Flame*, **vol. 143(4)**: pp. 566–586.
- [13] Ducros, F., Comte, P. and Lesieur, M. (1995). Large-eddy simulation of a spatially growing boundary layer over an adiabatic flat plate at low Mach number. *International Journal of Heat and Fluid Flow*, **vol. 16(5)**: pp. 341–348.
- [14] Ducros, F., Comte, P. and Lesieur, M. (1996). Large-eddy simulation of transition to turbulence in a boundary layer developing spatially over a flat plate. *Journal of Fluid Mechanics*, **vol. 326**: pp. 1–36.
- [15] Ducros, F., Laporte, F., Soulères, T., Guinot, V., Moinat, P. and Caruelle, B. (2000). High-order fluxes for conservative skew-symmetric-like schemes in structured meshes: Application to compressible flows. *Journal of Computational Physics*, **vol. 161**: pp. 114–139.
- [16] Erlebacher, G., Hussaini, M., Speziale, C. and Zang, T. (1987). Toward the large-eddy simulation of compressible turbulent flows. *ICASE Report 87-20*, Institute for Computer Applications in Science and Engineering, NASA Langley Research Center, Hampton, Virginia 23665. NASA Contractor Report 178273.
- [17] Erlebacher, G., Hussaini, M., Speziale, C. and Zang, T. (1992). Toward the large-eddy simulation of compressible turbulent flows. *Journal of Fluid Mechanics*, **vol. 238**: pp. 155–185.
- [18] Fernandez, G. (2005). Paralelisation du code LES “SiTCom”. *Note Technique NT-11/05*, Modelys – Etudes et Conseil en Mécanique des Fluides.
- [19] Ferziger, J. and Perić, M., *Computational Methods for Fluid Dynamics* (Springer-Verlag Berlin Heidelberg New York, 2002), 3rd edn.
- [20] Frisch, U. (1991). From global scaling, à la kolmogorov, to local multifractal scaling in fully developed turbulence. *Proceedings of the Royal Society of London, series A: Mathematical and Physical Sciences*, **vol. 434(1890)**: pp. 89–99.
- [21] Frisch, U., *Turbulence: The Legacy of A.N. Kolmogorov* (Cambridge University Press, 1995).
- [22] Geers, L. (2004). *Multiple impinging jet arrays: an experimental study on flow and heat transfer*. Ph.D. thesis, Technische Universiteit Delft, Faculty of Applied Sciences. ISBN 90-901-7774-4.
- [23] Geers, L., Tummers, M. and Hanjalić, K. (2004). Experimental investigation of impinging jet arrays. *Experiments in Fluids*, **vol. 36(6)**: pp. 946–958.
- [24] Germano, M. (1986). A proposal for a redefinition of the turbulent stresses in the filtered navier-stokes equations. *Physics of Fluids*, **vol. 29(7)**: pp. 2323–2324.
- [25] Germano, M., Piomelli, U., Moin, P. and Cabot, W. (1991). A dynamic subgrid-scale eddy viscosity model. *Physics of Fluids A: Fluid Dynamics*, **vol. 3(7)**: pp. 1760–1765.

-
- [26] Gottlieb, S. and Shu, C. (1998). Total variation diminishing Runge-Kutta schemes. *Mathematics of Computation*, **vol. 67(221)**: pp. 73–85.
- [27] Härtel, C. and Kleiser, L. (1997). Galilean invariance and filtering dependence of near-wall grid-scale/subgrid-scale interactions in large-eddy simulation. *Physics of Fluids*, **vol. 9(2)**: pp. 473–475.
- [28] Härtel, C. and Kleiser, L. (1998). Analysis and modelling of subgrid-scale motions in near-wall turbulence. *Journal of Fluid Mechanics*, **vol. 356**: pp. 327–352.
- [29] Härtel, C., Kleiser, L., Unger, F. and Friedrich, R. (1994). Subgrid-scale energy transfer in the near-wall region of turbulent flows. *Physics of Fluids*, **vol. 6(9)**: pp. 3130–3143.
- [30] Hirsch, C., *Numerical Computation of Internal and External Flows*, vol. 2 (John Wiley & Sons Ltd., 1990).
- [31] Hixon, R., Shih, S. and Mankabadi, R. (1995). Evaluation of boundary conditions for computational aeroacoustics. *AIAA Journal*, **vol. 33(11)**: pp. 2006–2012.
- [32] Horiuti, K. (1989). The role of the Bardina model in large eddy simulation of turbulent channel flow. *Physics of Fluids A: Fluid Dynamics*, **vol. 1(2)**: pp. 426–428.
- [33] Jameson, A., Schmidt, W. and Turkel, E. (1981). Numerical solution of the euler equations by finite volume methods using runge-kutta time-stepping schemes. *AIAA Paper*, **vol. 1981-1259**. Fluid and Plasma Dynamics Conference, 14th, Palo Alto, CA, June 23–25, 1981.
- [34] Jiang, G. and Shu, C. (1996). Efficient implementation of weighted ENO schemes. *Journal of Computational Physics*, **vol. 126**: pp. 202–228.
- [35] Klein, M., Sadiki, A. and Janicka, J. (2003). A digital filter based generation of inflow data for spatially developing direct numerical or large eddy simulations. *Journal of Computational Physics*, **vol. 186**: pp. 652–665.
- [36] Kolmogorov, A. (1991). Dissipation of energy in the locally isotropic turbulence. *Proceedings of the Royal Society of London, series A: Mathematical and Physical Sciences*, **vol. 434(1890)**: pp. 15–17. English translation of the original paper in *Doklady Akademii Nauk SSSR* (1941), vol. 32(1):19–21.
- [37] Kolmogorov, A. (1991). The local structure of turbulence in incompressible viscous fluid for very large reynolds numbers. *Proceedings of the Royal Society of London, series A: Mathematical and Physical Sciences*, **vol. 434(1890)**: pp. 9–13. English translation of the original paper in *Doklady Akademii Nauk SSSR* (1941), vol. 30(4):299–303.
- [38] Larchevêque, L., Sagaut, P., Mary, I., Labbé, O. and Comte, P. (2003). Large-eddy simulation of a compressible flow past a deep cavity. *Physics of Fluids*, **vol. 15(1)**: pp. 193–210.
- [39] Lenormand, E., Sagaut, P. and Phuoc, L. T. (2000). Large eddy simulation of subsonic and supersonic channel flow at moderate Reynolds number. *International Journal for Numerical Methods in Fluids*, **vol. 32**: pp. 369–406.

- [40] Lesieur, M., Métais, O. and Comte, P., *Large-Eddy Simulations of Turbulence* (Cambridge University Press, 2005).
- [41] Lilly, D. (1992). A proposed modification of the germano subgrid-scale closure method. *Physics of Fluids A: Fluid Dynamics*, **vol. 4(3)**: pp. 633–635.
- [42] Liu, S., Meneveau, C. and Katz, J. (1994). On the properties of similarity subgrid-scale models as deduced from measurements in a turbulent jet. *Journal of Fluid Mechanics*, **vol. 275**: pp. 83–119.
- [43] Lodato, G., Domingo, P. and Vervisch, L. (2008). Three-dimensional boundary conditions for direct and large-eddy simulation of compressible viscous flows. *Journal of Computational Physics*, **vol. 227(10)**: pp. 5105–5143.
- [44] Lodato, G., Domingo, P., Vervisch, L. and Veynante, D., Scalar variances: LES against measurements and mesh optimization criterion. scalar gradient: a three-dimensional estimation from planar measurements using DNS. In *Proceedings of the Summer Program*, (pp. 387–398) (Center for Turbulence Research, Stanford University, 2008).
- [45] Lund, T., On the use of discrete filters for large eddy simulation. In *Annual Research Briefs*, (pp. 83–95) (Center for Turbulence Research, Stanford University, 1997).
- [46] Martín, M. P., Piomelli, U. and Candler, G. V. (2000). Subgrid-Scale Models for Compressible Large-Eddy Simulations. *Theoretical and Computational Fluid Dynamics*, **vol. 13(5)**: pp. 361–376.
- [47] Meneveau, C. and Lund, T. (1997). The dynamic Smagorinsky model and scale-dependent coefficients in the viscous range of turbulence. *Physics of Fluids*, **vol. 9(12)**: pp. 3932–3934.
- [48] Meneveau, C., Lund, T. and Cabot, W. (1996). A lagrangian dynamic subgrid-scale model of turbulence. *Journal of Fluid Mechanics*, **vol. 319**: pp. 353–385.
- [49] Moin, P., Squires, K., Cabot, W. and Lee, S. (1991). A dynamic subgrid-scale model for compressible turbulence and scalar transport. *Physics of Fluids A: Fluid Dynamics*, **vol. 3(11)**: pp. 2746–2757.
- [50] Monin, A. and Yaglom, A., *Statistical Fluid Mechanics: Mechanics of Turbulence*, vol. I (Dover Publications, Inc., 1971).
- [51] Monin, A. and Yaglom, A., *Statistical Fluid Mechanics: Mechanics of Turbulence*, vol. II (Dover Publications, Inc., 1975).
- [52] Nicoud, F. (1999). Defining wave amplitude in characteristic boundary conditions. *Journal of Computational Physics*, **vol. 149**: pp. 418–422.
- [53] Nicoud, F. and Ducros, F. (1999). Subgrid-scale stress modelling based on the square of the velocity gradient tensor. *Flow, Turbulence and Combustion*, **vol. 62(3)**: pp. 183–200.

-
- [54] Okong'o, N. and Bellan, J. (2002). Consistent boundary conditions for multicomponent real gas mixtures based on characteristic waves. *Journal of Computational Physics*, **vol. 176(2)**: pp. 330–344.
- [55] Piomelli, U. (1993). High Reynolds number calculations using the dynamic subgrid-scale stress model. *Physics of Fluids A: Fluid Dynamics*, **vol. 5(6)**: pp. 1484–1490.
- [56] Piomelli, U., Cabot, W. H., Moin, P. and Lee, S. (1991). Subgrid-scale backscatter in turbulent and transitional flows. *Physics of Fluids A: Fluid Dynamics*, **vol. 3(7)**: pp. 1766–1771.
- [57] Piomelli, U., Yu, Y. and Adrian, R. J. (1996). Subgrid-scale energy transfer and near-wall turbulence structure. *Physics of Fluids*, **vol. 8(1)**: pp. 215–224.
- [58] Poinso, T. and Lele, S. (1992). Boundary conditions for direct simulations of compressible viscous flows. *Journal of Computational Physics*, **vol. 101**: pp. 104–129.
- [59] Polifke, W., Wall, C. and Moin, P. (2006). Partially reflecting and non-reflecting boundary conditions for simulation of compressible viscous flow. *Journal of Computational Physics*, **vol. 213(1)**: pp. 437–449.
- [60] Prosser, R. (2005). Improved boundary conditions for the direct numerical simulation of turbulent subsonic flows. I. inviscid flows. *Journal of Computational Physics*, **vol. 207**: pp. 736–768.
- [61] Reynolds, O. (1883). An Experimental Investigation of the Circumstances Which Determine Whether the Motion of Water Shall Be Direct or Sinuous, and of the Law of Resistance in Parallel Channels. *Philosophical Transactions of the Royal Society of London*, **vol. 174**: pp. 935–982.
- [62] Rudy, D. and Strikwerda, J. (1980). A nonreflecting outflow boundary condition for subsonic navier-stokes calculations. *Journal of Computational Physics*, **vol. 36**: pp. 55–70.
- [63] Sagaut, P., *Large Eddy Simulation for Incompressible Flows: An Introduction* (Springer-Verlag Berlin Heidelberg, 2001), 2nd edn.
- [64] Salvetti, M. and Banerjee, S. (1995). *A priori* tests of a new dynamic subgrid-scale model for finite-difference large-eddy simulations. *Physics of Fluids*, **vol. 7(11)**: pp. 2831–2847.
- [65] Samimy, M., Breuer, K., Leal, L. and Steen, P. (Editors), *A Gallery of Fluid Motion*, chap. 8, (p. 82) (Cambridge University Press, 2003).
- [66] Schlichting, H. and Gersten, K., *Boundary-Layer Theory* (Springer-Verlag Berlin Heidelberg, 2000), 8th edn.
- [67] Scotti, A., Meneveau, C. and Fatica, M., Dynamic Smagorinsky model on anisotropic grids. In *Proceedings of the Summer Program*, (pp. 259–276) (Center for Turbulence Research, Stanford University, 1996).

- [68] Scotti, A., Meneveau, C. and Fatica, M. (1997). Dynamic Smagorinsky model on anisotropic grids. *Physics of Fluids*, **vol. 9(6)**: pp. 1856–1858.
- [69] Scotti, A., Meneveau, C. and Lilly, D. (1993). Generalized Smagorinsky model for anisotropic grids. *Physics of Fluids A: Fluid Dynamics*, **vol. 5(9)**: pp. 2306–2308.
- [70] Smagorinsky, J. (1963). General circulation experiments with the primitive equations. *Monthly Weather Review*, **vol. 91(3)**: pp. 99–164.
- [71] Speziale, C. (1985). Galilean invariance of subgrid-scale stress models in the large-eddy simulation of turbulence. *Journal of Fluid Mechanics*, **vol. 156**: pp. 55–62.
- [72] Speziale, C., Erlebacher, G., Zang, T. and Hussaini, M. (1988). The subgrid-scale modeling of compressible turbulence. *Physics of Fluids*, **vol. 31(4)**: pp. 940–942.
- [73] Sutherland, J. and Kennedy, C. (2003). Improved boundary conditions for viscous, reacting, compressible flows. *Journal of Computational Physics*, **vol. 191(2)**: pp. 502–524.
- [74] Swanson, R. and Turkel, E. (1992). On central-difference and upwind schemes. *Journal of Computational Physics*, **vol. 101(2)**: pp. 292–306.
- [75] Tam, C. (1998). Advances in numerical boundary conditions for computational aeroacoustics. *Journal of Computational Acoustics*, **vol. 6(4)**: pp. 377–402.
- [76] Tatsumi, S., Martinelli, L. and Jameson, A. (1995). Flux-limited schemes for the compressible navier-stokes equations. *AIAA Journal*, **vol. 33(2)**: pp. 252–261.
- [77] Temmerman, L., Leschziner, M., Mellen, C. and Fröhlich, J. (2003). Investigation of wall-function approximations and subgrid-scale models in large eddy simulation of separated flow in a channel with streamwise periodic constrictions. *International Journal of Heat and Fluid Flow*, **vol. 24(2)**: pp. 157–180.
- [78] Thompson, K. W. (1987). Time dependent boundary conditions for hyperbolic systems. *Journal of Computational Physics*, **vol. 68**: pp. 1–24.
- [79] Thompson, K. W. (1990). Time dependent boundary conditions for hyperbolic systems, II. *Journal of Computational Physics*, **vol. 89**: pp. 439–461.
- [80] Valorani, M. and Favini, B. (1998). On the numerical integration of multi-dimensional, initial boundary value problems for the euler equations in quasi-linear form. *Numerical Methods for Partial Differential Equations*, **vol. 14(6)**: pp. 781–814.
- [81] Vreman, B. (1995). *Direct and Large-Eddy Simulation of the Compressible Turbulent Mixing Layer*. Ph.D. thesis, Universiteit Twente.
- [82] Vreman, B., Geurts, B. and Kuerten, H. (1995). A priori tests of large eddy simulation of the compressible plane mixing layer. *Journal of Engineering Mathematics*, **vol. 29(4)**: pp. 299–327.
- [83] Wilcox, D., *Turbulence Modeling for CFD* (DCW Industries, Inc., 1993).

-
- [84] Yoo, C. and Im, H. (2007). Characteristic boundary conditions for simulations of compressible reacting flows with multi-dimensional, viscous and reaction effects. *Combustion Theory and Modelling*, **vol. 11(2)**: pp. 259–286.
- [85] Yoo, C., Wang, Y., Trouvé, A. and Im, H. (2005). Characteristic boundary conditions for direct simulations of turbulent counterflow flames. *Combustion Theory and Modelling*, **vol. 9(4)**: pp. 617–646.
- [86] Yoshizawa, A. (1986). Statistical theory for compressible turbulent shear flows, with the application to subgrid modeling. *Physics of Fluids*, **vol. 29**: pp. 2152–2164.
- [87] Zang, T. (1991). Numerical simulation of the dynamics of turbulent boundary layers: Perspectives of a transition simulator. *Philosophical Transactions of the Royal Society: Physical and Engineering Sciences*, **vol. 336(1641)**: pp. 95–102.
- [88] Zang, T., Dahlburg, R. and Dahlburg, J. (1992). Direct and large-eddy simulations of three-dimensional compressible Navier-Stokes turbulence. *Physics of Fluids A: Fluid Dynamics*, **vol. 4(1)**: pp. 127–140.
- [89] Zang, Y., Street, R. L. and Koseff, J. R. (1993). A dynamic mixed subgrid-scale model and its application to turbulent recirculating flows. *Physics of Fluids A: Fluid Dynamics*, **vol. 5(12)**: pp. 3186–3196.

Acknowledgments

When I decided to return to study the fascinating problem of turbulence, I would have never expected that the right set of circumstances would have originated from a country, whose spoken language was not even mentioned in my *curriculum vitae*. And, indeed, it was just by chance that I applied for this PhD position, following this crazy dream of returning to be a student after five years working in industry.

There are events which represent just deviations of the life's trajectory, for better or for worse, and other events which determine veritable and radical changes. When I received the first e-mail from Prof. Luc Vervisch, on September 6th, 2005, I was barely aware that one such fundamental turning points in my life was about to happen.

I wish to express all my gratitude to my Advisors, Prof. Luc Vervisch and Dr. Pascale Domingo, for having trusted my capabilities without any evidence of my skills, aside from what was written in my *curriculum vitae*, thus letting me realize that dream, which, after three years, turned out to represent my greatest professional achievement so far. Without their guess that I would have eventually given some contribution to the scientific community, I would not have had this—maybe any—opportunity to reenter the academic field and to indulge in studying Fluid Dynamics and Turbulence.

Prof. Vervisch and Dr. Domingo, gave me the opportunity but also means and resources that I would have hardly found in my country of origin. I cannot forget my great surprise when, during the first few weeks, I was given the access to the enormous computational resources that I have been using to progress in my studies.

Right from the beginning and during the entire span of these three years of studies, Prof. Vervisch and Dr. Domingo created a fruitful, almost familial, atmosphere of cooperation. They always supported me with enthusiasm and precious advices, especially during the most difficult and frustrating moments of this work, and allowed me to redirect my attention toward unexpected topics somehow, the unpredictable challenges that true research often poses. I regret for not having had time to give a more direct contribution in their specific field of expertise—the turbulent combustion—and I hope that, in some way, they “enjoyed” being involved in some digression.

I also wish to thank the students and the people working in the CORIA laboratory, especially in the Department of *Modélisation de la Combustion Turbulente*. All my encouragements to those who haven't finished their PhD yet and to those who are beginning now: I hope that their experience will be as rich of gratification and satisfaction as mine has been for me.

In particular, I owe special gratitude to Dr. Genesan Subramanian, with whom I shared the office during the first two years, for his precious help during my very first days in Rouen, when I was completely unable to communicate and, nonetheless, I had to arrange my stay “from scratch”. I really enjoyed our exchanges about Indian and Italian cultures.

All my thanks to Dr. Guillaume Ribert for having helped me during the preparation of the assignments relevant to the lectures on Fluid Mechanics I gave at INSA. I remember with pleasure the week-ends spent with him wandering around in California during the last CTR Summer Program and talking about any sort of frivolous issue (at least on my side, of course). Also, I wish to thank Guillaume Godel for having contributed to the correction of the French introductions to the chapters of this thesis (I hope he will eventually find a way to make his complex chemistry live with the 3D-NSCBC procedure) and Mrs. Isabelle Lebon, who made any effort to understand my awful French and helped me to sort out all the administrative issues that came out during these three years. I was lucky to work in this extraordinary group and I regret anyway that, due to my particularly reserved nature, I haven't been able to establish more frequent interactions with my colleagues and to participate more actively in the lab's life.

Of course, without economic support, nothing would have been possible. I want to thank all the partners of the project NICE (New Integrated Combustion system for Future Passenger Car Engines), who, within the 6th Framework program of the European Union (TIP3-CT-2004-50620), provided the funds for my PhD studentship. Computing resources, in particular, were provided by the *Institut du Développement et de Ressources en Informatique Scientifique* (IDRIS-CNRS) and CRIHAN.

Finally, I wish to dedicate the last part of these acknowledgments to my Family for their continuous encouragement and the wholehearted support they have been giving during these three years. In particular, I wish to express all my gratitude to my beloved Wife Monica who followed me here in France, far from her family and far from her friends. I will never forget that summer 2005 when I was struggling to find my way and anything was going wrong. I was about to give up and abandon this PhD idea, when Monica, right at my side as always, told me that, in the end, I had nothing to lose in applying for that position in Rouen. First and foremost, I have been lucky to have somebody trusting and encouraging me during those most difficult moments. And I'm perfectly aware of the great sacrifices she has made during these three years and the enormous difficulties she went through when I was spending our spare time working and yet she was there supporting me and listening to my digressions (or helping me to translate all the french parts of this thesis). I'm perfectly aware that it has not been easy for her to devote so much of her life to my professional achievements.

To Monica I dedicate these last lines as well as each and every single page of this manuscript that represents so much for me.

**Conditions aux Limites Tridimensionnelles pour la Simulation Directe
et aux Grandes Échelles des Écoulements Turbulents.
Modélisation de Sous-Maille pour la Turbulence en Région de Proche Paroi.**

Deux points essentiels ont été abordés dans cette thèse : le traitement des conditions aux limites et la modélisation fine des interactions de sous-maille pour représenter, au mieux, la région de proche paroi.

La formulation caractéristique des conditions aux limites a été analysée et une nouvelle procédure 3D-NSCBC est proposée qui autorise la prise en compte de l'évolution de la vitesse et de la pression dans le plan des frontières, afin d'introduire le caractère tridimensionnel de l'écoulement dans les conditions limites. Les difficultés au niveau des arêtes et des coins du maillage de calcul, liées au couplage des ondes caractéristiques voyageant le long des directions orthogonales et à l'imposition simultanée des différentes conditions aux limites, ont nécessité le développement des nouvelles formulations.

Dans le cadre de la Simulation des Grandes Échelles, pour reproduire correctement la dynamique de la turbulence à la paroi et pour mieux prendre en compte l'anisotropie du tenseur des contraintes de sous-maille, un modèle structural fondé sur l'hypothèse de similarité est développé pour des écoulements modérément compressibles. La reproduction du transfert local inversé d'énergie des petites échelles vers les grandes par le modèle proposé s'est révélée être un ingrédient essentiel contribuant à la représentation correcte du transport énergétique moyen dans la couche limite turbulente.

Des Simulations Numériques Directes de la combustion turbulente sont discutées dans une dernière partie. Une procédure pour prendre en compte les termes sources de la chimie dans les conditions aux limites 3D-NSCBC a été développée, et les résultats obtenus sur une flamme jet prémélangée turbulente de type Bunsen utilisés pour valider un modèle permettant de reconstruire la surface de flamme tridimensionnelle à partir de mesures expérimentales bidimensionnelles.

Mots clés : conditions aux limites caractéristiques non-réfléchissantes ; Simulation aux Grandes Échelles ; modèles de Sous-Maille de similarité-mixte ; comportement asymptotique en région de proche paroi ; transfert inverse d'énergie turbulente ; Simulation Numérique Directe ; combustion turbulente.

**Three-dimensional Boundary Conditions for Direct
and Large-Eddy Simulation of Turbulent Flows.
Sub-Grid Scale Modeling for Near-Wall Region Turbulence.**

Two main topics have been addressed within the present thesis: the treatment of boundary conditions and sub-grid scale interactions' modeling, with particular attention to the near-wall region.

The characteristic formulation of boundary conditions has been analyzed and a novel procedure 3D-NSCBC is proposed, which, accounting for the evolution of velocity and pressure on the boundary planes, allows a better representation of the three-dimensional character of the flow at the boundary. The difficulties on the edges and corners of the computational domain, related to the coupling of characteristic waves traveling along orthogonal directions and to the simultaneous imposition of different boundary conditions, have necessitated new formalisms to be developed.

Within the framework of the Large-Eddy Simulation, in order to give a correct reproduction near-wall turbulence dynamics and in order to better account for the sub-grid scale stress tensor's anisotropy, a structural model based on the similarity hypothesis has been developed for weakly compressible flows. The reproduction of local reversed energy transfer from the small scales to the big ones obtained with the proposed model, has been identified as a key mechanism for the correct representation of the average energy transfer within the turbulent boundary layer.

Direct Numerical Simulations of turbulent combustion are discussed in the last section of this thesis. A procedure to account for chemical source terms in the 3D-NSCBC procedure has been developed, and the results obtained on a premixed turbulent Bunsen flame have been used to validate a model for three-dimensional flame surface reconstruction starting from two-dimensional experimental measurements.

Keywords: non-reflecting characteristic boundary conditions ; Large-Eddy Simulation ; Sub-Grid scale similarity-mixed modelling ; near-wall asymptotic behaviour ; energy backscatter ; Direct Numerical Simulation ; turbulent combustion.